INVESTIGATION OF FRACTURE BEHAVIOUR OF PIPELINES CONTAINING FLAWS SUBJECTED TO PLASTIC STRAINING IN THE PRESENCE OF YIELD DISCONTINUITY

LONGJIE WANG

A thesis submitted for the degree of *Doctor of Philosophy*

Department of Mechanical, Aerospace and Civil Engineering
College of Engineering, Design and Physical Sciences
Brunel University London
Uxbridge, United Kingdom

June 2019

ABSTRACT

An increase in the demand of fossil resources has driven the construction and operation of oil and gas pipelines in remote and harsh environments, such as seismically-active, Arctic and deep-water regions. Pipelines installed and/or operated in these regions are subjected to large plastic straining, which poses a threat to the integrity of pipelines containing crack-like flaws. Pipeline steels often exhibit a yield discontinuity, known as the Lüders plateau, which further complicates analyses and assessments of pipelines containing flaws. This thesis aims to investigate the fracture behaviour of pipelines subjected to plastic straining, and to provide guidance for analysis and assessment of flawed pipes in the presence of yield discontinuity.

This work contained both experiments and numerical analyses, including uniaxial tensile tests with and without notches, and single edged notch tension (SENT) tests, with the utilisation of Digital Image Correlation (DIC) techniques for strain measurement. The fracture behaviour of pipelines containing flaws with Lüders bands were further examined numerically. Finite element analysis (FEA) of pipelines containing circumferential flaws subjected to both uniaxial and biaxial loadings were conducted, respectively. Main contribution to the knowledge includes optimised material models identified by comparing numerical results against the published full-scale test results, and thereafter the influence of various flaw sizes and the pressure-induced stress biaxiality on the development of Lüders bands and the crack driving force of the flawed pipes.

A clear understanding is achieved for the significant effects of the deforming and fracture behaviour of pipelines containing flaws subjected to both uniaxial and biaxial loading conditions, and in turn, of the flaw sizes and stress biaxility on the formation and development of Lüders behaviour. The findings provide enhanced design and operation guidance for pipelines with improved structural integrity.

DECLARATION

I hereby declare no portion of the work referred to in the dissertation has been submitted in support of an application for another degree or qualification of this or any other university or other institute of learning.

Uxbridge, United Kingdom, June 2019

Longjie Wang

If I have seen further,
it is by standing on the shoulders of Giants.

— Isaac Newton, 1675

ACKNOWLEDGMENTS

First and foremost, I would like to express my tremendous gratitude to Dr Bin Wang from Burnel University London and Dr Guiyi Wu from TWI Ltd, who are my academic and industrial supervisors respectively, for their endless support, patience, encouragement and motivation throughout the course of my doctoral study.

My thanks also go to Dr Elvin Eren, Dr Simon Smith and Mr Tyler London from TWI Ltd for their constructive suggestions and useful discussions.

I would like to extend my appreciation to my friends and colleagues at TWI Ltd during PhD study for their support, stimulating and useful discussions, encouragement, and fun time spent together, without whom the doctoral 'journey' would never been as fun and joyful.

Last but not the least, I would like to sincerely thank my parents for their ceaseless love and support throughout my life.

PUBLICATIONS

Wang, L., E. Eren, B. Wang, and G. Wu. 2017. "Consideration of Yield Discontinuity in the Elastic-Plastic Fracture Analysis of Circumferentially Flawed Pipes." In *Proceedings of ASME 2017 Pressure Vessels and Piping Conference*. ASME.

Wang, L., G. Wu, B. Wang, and H. Pisarski. 2019. "Fracture response of X65 pipes containing circumferential flaws in the presence of Lüders plateau." *International Journal of Solids and Structures* 156:29–48.

Wu, G., and L. Wang. 2018. "An Overview of Strain-Based Fracture Assessment of Pipelines." In *Proceedings of ASME 2018 37th International Conference on Ocean, Offshore and Arctic Engineering*. ASME.

Wu, G., L. Wang, T. London, and H. Pisarski. 2019. "Pipe grith welds under plastic straining: full-scale testing and strain-based approaches." In *Proceedings of the Conference on Asset Integrity Management - Pipeline Integrity Management Under Geohazard Conditions*. Houston, TX, USA: ASME.

CONTENTS

List of Figures x

List of Tables xxxi

Nomenclature xxxiii

1 INTRODUCTION 1

1.1 Pipelines subjected to plastic straining 1

1.2 Technological challenges and industry needs 3

1.3 Research objectives and contributions 4

1.4 Thesis structure 4

2 LITERATURE REVIEW 6

2.1 Introduction 6

2.2 Fundamentals of fracture mechanics 6

2.2.1 Crack in elastic solids and the energy release rate 6

2.2.2 Crack-tip stress field and the stress intensity factor 8

2.2.3 Crack-tip opening displacement and J-integral 10

2.2.4 HRR singularity and J-dominance 12

2.2.5 Geometric effect and crack-tip constraint 13

2.2.6 The second crack-tip characterising parameter 15

2.2.7 Engineering Critical Assessment and Failure Assessment Diagram 16

2.3 State of the art on strain-based fracture assessment 19

2.3.1 Overview 19

2.3.2 Modification to existing stress-based method 21

2.3.3 Extension to EPRI scheme for fully-plastic J estimate 24

2.3.4 Budden and Ainsworth 26

2.3.5 Nourpanah approach 28

2.3.6 Jia approach 28

2.3.7 Strain capacity approach 29

2.3.8 SINTEF procedure 32

2.3.9 Comparison of strain-based assessment methods 34

2.3.10 Assessment of pipelines with yield discontinuity 42
2.4 Discontinuous yielding of ferritic steels 43
2.4.1 Yield point phenomenon and strain ageing 43
2.4.2 Numerical modelling of Lüders and Lüders-like phenomenon 46
2.4.3 Influence of yield discontinuity on structural behaviour 47
2.4.4 Cracked component in the presence of yield discontinuity 50
2.5 Summary 52
3 INVESTIGATIONS OF YIELDING BEHAVIOUR OF API X65 PIPELINE STEEL EXHIBITING LÜDERS PLATEAU 53
3.1 Introduction 53
3.2 Experimental procedures 54
3.2.1 Digital image correlation 55
3.2.2 Plain sided specimen 57
3.2.3 Side-notched specimen 58
3.2.4 Results 60
3.3 Computational procedures 70
3.3.1 Constitutive models 70
3.3.2 Finite element models 72
3.3.3 Results 76
3.4 Discussion 84
3.4.1 Mesh sensitivity 84
3.4.2 Effect of rate exponent value 93
3.4.3 Effect of constitutive models 94
3.5 Summary 94
4 SINGLE EDGE NOTCHED TENSION TESTING OF API X65 STEEL EXHIBITING LÜDERS PLATEAU 96
4.1 Introduction 96
4.2 Numerical analysis of crack-tip constraint 97
4.2.1 Stress-strain properties 99
4.2.2 FE models 99
4.2.3 Results and discussion 105
4.2.4 Summary 122

4.3 Single Edge Notched Tension (SENT) testing 123
4.3.1 Testing setup 123
4.3.2 Results 129
4.4 Numerical analysis of SENT testing 135
4.4.1 Material constitutive models 135
4.4.2 Finite element models 140
4.4.3 Results and discussion 140
4.5 Parametric study 150
4.5.1 Finite element models 150
4.5.2 Results and discussion 151
4.6 Summary 164
5 NUMERICAL ANALYSIS OF X65 PIPES CONTAINING FLAWS SUBJECTED TO AXIAL PLASTIC STRAINING WITH LÜDERS PLATEAU 165
5.1 Introduction 165
5.2 FEA of steel pipes containing flaws 166
5.3 Constitutive models 166
5.4 FE model configuration 170
5.4.1 Consideration of ductile tearing 174
5.5 Results 175
5.5.1 Global deformation behaviour 175
5.5.2 Evolution of plasticity 178
5.5.3 Crack driving force 180
5.5.4 Crack tip plastic zone 183
5.5.5 Crack tip stress and strain fields 185
5.6 Discussion 192
5.6.1 Effect of softening modulus on deformation of flawed pipes 192
5.6.2 Application of the UDU material law in fracture analysis of pipes containing crack-like flaws 196
5.7 Summary 196
6 NUMERICAL ANALYSIS OF X65 PIPES CONTAINING FLAWS SUBJECTED TO AXIAL PLASTIC STRAINING AND INTERNAL PRESSURE WITH LÜDERS PLATEAU 198
6.1 Introduction 198

6.2 Parametric FE analysis 198
6.2.1 Summary of FEA cases 198
6.2.2 Results 199
6.3 Discussion 220
6.3.1 Effect of internal pressure on global stress-strain response 220
6.3.2 Effect of internal pressure on crack driving force 225
6.3.3 Effect of flaw sizes on CDF plateau 226
6.4 Summary 236
7 CONCLUSIONS AND RECOMMENDATIONS 237
7.1 Summary 237
7.2 Conclusions 237
7.3 Recommendations for future work 238

Appendix

A TENSILE TEST REPORTS 242
B SENT TEST REPORTS 247
C MISES EQUIVALENT STRAIN MAPS OF SENT SPECIMENS CAPTURED BY DIC 263
D EQUIVALENT PLASTIC STRAIN MAPS OF SENT SPECIMENS CALCULATED FROM FEA 266

BIBLIOGRAPHY 271

LIST OF FIGURES

Figure 1.1 Strain-based scenarios of pipelines undergoing considerable plastic straining: (a) Offshore pipeline installation via reeling (from Kyriakides and Corona (2007b)), (b) Iceberg gouging in Arctic regions (from Barrette (2011)), (c) lateral buckling (snaking) of subsea pipelines lying on the seabed (taken from Pangeranlaut (2016)), and (d) thaw settlement in permafrost terrains (adapted from National Energy Board (2016)) 2

Figure 1.2 Strain demand of pipelines during installation and operation 2

Figure 2.1 Schematic of an elliptical hole in an infinite plate subjected to applied tensile stress 7

Figure 2.2 Schematic of stress components at an arbitrary location in a coordinate system originating from the crack tip 9

Figure 2.3 Schematic of cracked body under various loading mode 10

Figure 2.4 Illustration of an arbitrary contour around the crack tip for calculation of the path-independent line integral 11

Figure 2.5 Effect of plasticity on the crack-tip stress field: (a) SSY conditions, (b) elastic-plastic conditions, and (c) LSY conditions 14

Figure 2.6 Schematic of a typical failure assessment diagram spanning the range of fully brittle to fully plastic behaviour 17

Figure 2.7 A schematic of strain-based FAD where the FAC is defined by function $f^*(D_r)$ 27

Figure 2.8 CTOD versus strain relationship showing predominant linearity strains ranging from 0.2% to 1.6% (adapted from Østby (2005)) 32

Figure 2.9 Experimental setup of the full-scale pipe tests carried out by TWI (adapted from (Pisarski et al. 2014)) 37
Figure 2.10 Comparison of crack driving force predicted with strain-based assessment methods (Category 1) against TWI pipe test for nominal flaw size 6 × 50 mm 38
Figure 2.11 Comparison of crack driving force predicted with strain-based assessment methods (Category 2) against TWI pipe test for nominal flaw size 6 × 50 mm 38
Figure 2.12 Comparison of crack driving force predicted with strain-based assessment methods (Category 3) against TWI pipe test for nominal flaw size 6 × 50 mm 39
Figure 2.13 Comparison of crack driving force predicted with strain-based assessment methods (Category 4) against TWI pipe test for nominal flaw size 6 × 50 mm 39
Figure 2.14 Comparison of crack driving force predicted with strain-based assessment methods (Category 1) against TWI pipe test for nominal flaw size 5 × 100 mm 40
Figure 2.15 Comparison of crack driving force predicted with strain-based assessment methods (Category 2) against TWI pipe test for nominal flaw size 5 × 100 mm 40
Figure 2.16 Comparison of crack driving force predicted with strain-based assessment methods (Category 3) against TWI pipe test for nominal flaw size 5 × 100 mm 41
Figure 2.17 Comparison of crack driving force predicted with strain-based assessment methods (Category 4) against TWI pipe test for nominal flaw size 5 × 100 mm 41
Figure 2.18 Example of a FAD with a Lüders plateau (in accordance with Option 1 FAD of BS 7910) 43
Figure 2.19 Stress-strain response of an X60 steel exhibiting yield point elongation(adapted from Kyriakides and Corona (2007a)) 44
Figure 2.20 Evolution of Lüders band on a uniaxial tensile strip of X70 steel (from Kyriakides and Miller (2000)) 45

Figure 2.21 Development of yield point phenomenon during strain ageing of mild steels (adapted from Wilson et al. (1959), cited in O. Hall (1970)) 48
Figure 2.22 Simple phenomenological material law for numerical simulation of Lüders band (adapted from Kyriakides and Miller (2000) 48
Figure 2.23 Moment-curvature behaviour and the bent configurations of tube loaded in bending (adapted from Hallai and Kyriakides (2011a)) 49
Figure 2.24 Lüders band patterns on the tube/pipe under bending: (a) band patterns on compressed side of the tube observed in experiment (adapted from Hallai and Kyriakides (2011a)); numerical simulation of Lüders band on pipe (b) under pure bending (adapted from Hallai and Kyriakides (2011b)) and (c) during reeling (adapted from Liu et al. (2015)) 50
Figure 2.25 Effect of Lüders behaviour on the equivalent plastic strain development in the near-tip region of: (a) 3D FE model of double-edged cracked plate (adapted from Beardsmore et al. (2013)); (b) 2D FE model of CT specimens in plane stress and plane strain, respectively (adapted from Belotteau et al. (2009)); (c) 3D FE model of CT specimens (adapted from Wenman and Chard-Tuckey (2010)) 51
Figure 3.1 Experimental setup of the tensile testing at TWI 55
Figure 3.2 Speckle patterns applied to the surface of the tensile specimen (M01-02) 56
Figure 3.3 Schematic of the plain tensile specimen M01-01 instrumented with strain gauges 57
Figure 3.4 Schematic of the plain tensile specimen M01-02 instrumented with strain gauges and a extensometer 58
Figure 3.5 Schematic of the notched tensile specimen M01-03 instrumented with strain gauges 59
Figure 3.6 Schematic of the notched tensile specimen M01-04 instrumented with strain gauges and an extensometer 60

Figure 3.7 Measured engineering stress-strain curve of M01-01 61
Figure 3.8 Longitudinal strain ϵ_{yy} maps of plain tensile specimen M01-01 at various stages of loading 61
Figure 3.9 Local strain and overall strain measurements of M01-01 63
Figure 3.10 Comparison between the engineering stress-strain curves measured for M01-1 and M01-02 63
Figure 3.11 Local strain and overall strain measurements of M01-02 64
Figure 3.12 Longitudinal strain ε_{yy} map of M01-02 65
Figure 3.13 Comparison of strain measurements by DIC and strain gauges in M01-02 66
Figure 3.14 Load-extension response of M01-03: (a) global measured load-extension curve (b) close-up of the load-extension curve in the range of extension from 0.5 mm to 1.5 mm 67
Figure 3.15 Longitudinal strain ε_{yy} maps of notched tensile specimen M01-03 at various stages of loading of Figure 3.14 68
Figure 3.16 Comparison between load-extension responses of M01-03 and M01-04 (notched tensile tests) 69
Figure 3.17 Close-up of the load-extension (P-ΔL) curve of M01-04 in the range of extension from 0.5 to 1.5mm 70
Figure 3.18 Longitudinal strain ε_{yy} maps of notched tensile specimen M01-04 at various stages of loading 71
Figure 3.19 Stress-strain curves used in FE simulation of M01-02 73
Figure 3.20 Definitions of gauge length in FE model of the plain-sided specimen 73
Figure 3.21 Mesh configuration and the applied boundary conditions of FE model of the plain-sided specimen 74
Figure 3.22 Mesh configuration and the applied boundary conditions of FE model of the side-notched specimen 75
Figure 3.23 Global stress-strain responses of the FE models using different material models in comparison with that measured from the test 77

Figure 3.24 Longitudinal strain ε^{p}_{eq} maps in FE simulation of X65 plain-sided tensile specimen with various material models at 0.37% strain 78
Figure 3.25 Longitudinal strain ε^{p}_{eq} maps in FE simulation of X65 plain-sided tensile specimen with various material models at 1.5% strain 78
Figure 3.26 Longitudinal strain ε^{p}_{eq} maps in FE simulation of X65 plain-sided tensile specimen with various material models at 2.4% strain 79
Figure 3.27 Longitudinal strain ε^{p}_{eq} maps in FE simulation of X65 plain-sided tensile specimen with various material models at 2.9% strain 79
Figure 3.28 Equivalent plastic strain ε^{p}_{eq} map in FE simulation of X65 plain-sided tensile specimen with various material models at 0.37% strain 80
Figure 3.29 Equivalent plastic strain ε^{p}_{eq} map in FE simulation of X65 plain-sided tensile specimen with various material models at 1.5% strain 80
Figure 3.30 Equivalent plastic strain ε^{p}_{eq} map in FE simulation of X65 plain-sided tensile specimen with various material models at 2.4% strain 81
Figure 3.31 Equivalent plastic strain ε^{p}_{eq} map in FE simulation of X65 plain-sided tensile specimen with various material models at 2.9% strain 81
Figure 3.32 Global stress-strain responses of the FE models of side-notched specimen using different material models in comparison with that measured from the test 82
Figure 3.33 Longitudinal strain ε_{yy} map of FE models of notched tensile specimen with various material models at 0.27% strain 84
Figure 3.34 Longitudinal strain ε_{yy} map of FE models of notched tensile specimen with various material models at 0.66% strain 85

Figure 3.35 Longitudinal strain ε_{yy} map of FE models of notched tensile specimen with various material models at 1.21% strain 85
Figure 3.36 Longitudinal strain ε_{yy} map of FE models of notched tensile specimen with various material models at 3.32% strain 86
Figure 3.37 Equivalent plastic strain ε^{p}_{eq} map of FE models of notched tensile specimen with various material models at 0.27% strain 86
Figure 3.38 Equivalent plastic strain ε^{p}_{eq} map of FE models of notched tensile specimen with various material models at 0.66% strain 87
Figure 3.39 Equivalent plastic strain ε^{p}_{eq} map of FE models of notched tensile specimen with various material models at 1.21% strain 87
Figure 3.40 Equivalent plastic strain ε^{p}_{eq} map of FE models of notched tensile specimen with various material models at 3.32% strain 88
Figure 3.41 FE model of the plain-sided specimen with various mesh densities 89
Figure 3.42 Influence of the size of elements on the calculated global stress-strain response for M01-02 89
Figure 3.43 Influence of the size of elements on the calculated ε^{p}_{eq} contours of M01-02 90
Figure 3.44 Influence of the size of elements on the calculated ε^{p}_{eq} profiles along the centreline of M01-02 90
Figure 3.45 Influence of the size of elements on the calculated ε^{p}_{eq} propagating front of the Lüders band in M01-02 91
Figure 3.46 FE model of the side-notched specimen with various mesh densities 91
Figure 3.47 Load-elongation response of the side-notched specimen FE model calculated using various mesh densities 92
Figure 3.48 Influence of the number of elements on the calculated ε^{p}_{eq} contours in the side-notched tensile specimen 92

Figure 3.49 Influence of the rate exponent value on the calculated global stress-strain curve of M01-02 93
Figure 3.50 Extracted stress-strain response of a carbon steel strip exhibiting Lüders plateau (from (Hallai and Kyriakides 2013)) 94
Figure 4.1 Illustration of in-plane and out-of-plane directions for a through-thickness crack in a three-dimensional body 98
Figure 4.2 Stress-strain curve used in FE analysis of the fracture toughness specimens: (a) the engineering and true stress-strain form, (b) the true stress-strain curve with the post-necking response based on a power law extrapolation 100
Figure 4.3 (a) Mesh configuration of the SENT specimen models and (b) applied boundary conditions for the SENT specimen models 101
Figure 4.4 (a) Mesh configuration of the SENB specimen models and (b) applied boundary conditions for the SENB specimen models 102
Figure 4.5 Mesh configuration of FE pipe model and the applied boundary conditions 103
Figure 4.6 (a) Mesh configuration of the MBL model with the applied bounday conditions and (b) close-up of the crack tip with initial notch radius 104
Figure 4.7 In-plane crack-tip constraint parameter in terms of Q versus normalised J calculated from FE analysis of SENT B×B 105
Figure 4.8 In-plane crack-tip constraint parameter in terms of Q versus normalised J calculated from FE analysis of SENT 2B×B 106
Figure 4.9 In-plane crack-tip constraint parameter in terms of Q versus normalised J calculated from FE analysis of SENB B×B 106

Figure 4.10 In-plane crack-tip constraint parameter in terms of Q versus normalised J calculated from FE analysis of circumferentially cracked pipes 107

Figure 4.11 In-plane crack-tip constraint parameter in terms of Q versus normalised J calculated from FE analysis of circumferentially cracked pipe with crack depth of $a/t = 0.1$ for various internal pressure levels 108

Figure 4.12 In-plane crack-tip constraint parameter in terms of Q versus normalised J calculated from FE analysis of circumferentially cracked pipe with crack depth of $a/t = 0.2$ for various internal pressure levels 108

Figure 4.13 In-plane crack-tip constraint parameter in terms of Q versus normalised J calculated from FE analysis of circumferentially cracked pipe with crack depth of $a/t = 0.3$ for various internal pressure levels 109

Figure 4.14 In-plane crack-tip constraint parameter in terms of Q versus normalised J calculated from FE analysis of circumferentially cracked pipe with crack depth of $a/t = 0.4$ for various internal pressure levels 109

Figure 4.15 In-plane crack-tip constraint parameter in terms of Q versus normalised J calculated from FE analysis of circumferentially cracked pipe with crack depth of $a/t = 0.5$ for various internal pressure levels 110

Figure 4.16 Comparison of Q for SENB, SENT and cracked pipes at various crack-tip loadings: (a) $J/(\sigma_y b) = 0.02$, (b) $J/(\sigma_y b) = 0.03$, (c) $J/(\sigma_y b) = 0.05$ and (d) $J/(\sigma_y b) = 0.07$ 111

Figure 4.17 Crack-tip stress triaxiality parameter h versus normalised J calculated from FE analysis of SENT B×B 112

Figure 4.18 Crack-tip stress triaxiality parameter h versus normalised J calculated from FE analysis of SENT 2B×B 112

Figure 4.19 Crack-tip stress triaxiality parameter h versus normalised J calculated from FE analysis of SENB B×B 113

Figure 4.20 Crack-tip stress triaxiality parameter h versus normalised J calculated from FE analysis of circumferentially cracked pipes 113
Figure 4.21 Crack-tip stress triaxiality parameter h versus normalised J calculated from FE analysis of circumferentially cracked pipes with crack depth of $a/t = 0.1$ for various internal pressure levels 114
Figure 4.22 Crack-tip stress triaxiality parameter h versus normalised J calculated from FE analysis of circumferentially cracked pipes with crack depth of $a/t = 0.2$ for various internal pressure levels 114
Figure 4.23 Crack-tip stress triaxiality parameter h versus normalised J calculated from FE analysis of circumferentially cracked pipes with crack depth of $a/t = 0.3$ for various internal pressure levels 115
Figure 4.24 Crack-tip stress triaxiality parameter h versus normalised J calculated from FE analysis of circumferentially cracked pipes with crack depth of $a/t = 0.4$ for various internal pressure levels 115
Figure 4.25 Crack-tip stress triaxiality parameter h versus normalised J calculated from FE analysis of circumferentially cracked pipes with crack depth of $a/t = 0.5$ for various internal pressure levels 116
Figure 4.26 Comparison of stress triaxiality parameter h for SENB, SENT and cracked pipes 117
Figure 4.27 Out-of-plane crack-tip constraint parameter in terms of T_z versus normalised J calculated from FE analysis of SENT B×B 118
Figure 4.28 Out-of-plane crack-tip constraint parameter in terms of T_z versus normalised J calculated from FE analysis of SENT 2B×B 118
Figure 4.29 Out-of-plane crack-tip constraint parameter in terms of T_z versus normalised J calculated from FE analysis of circumferentially cracked pipes 119

Figure 4.30 Out-of-plane crack-tip constraint parameter in terms of T_z versus normalised J calculated from FE analysis of circumferentially cracked pipes with crack depth of $a/t = 0.1$ for various internal pressure levels 119

Figure 4.31 Out-of-plane crack-tip constraint parameter in terms of T_z versus normalised J calculated from FE analysis of circumferentially cracked pipes with crack depth of $a/t = 0.2$ for various internal pressure levels 120

Figure 4.32 Out-of-plane crack-tip constraint parameter in terms of T_z versus normalised J calculated from FE analysis of circumferentially cracked pipes with crack depth of $a/t = 0.3$ for various internal pressure levels 120

Figure 4.33 Out-of-plane crack-tip constraint parameter in terms of T_z versus normalised J calculated from FE analysis of circumferentially cracked pipes with crack depth of $a/t = 0.4$ for various internal pressure levels 121

Figure 4.34 Out-of-plane crack-tip constraint parameter in terms of T_z versus normalised J calculated from FE analysis of circumferentially cracked pipes with crack depth of $a/t = 0.5$ for various internal pressure levels 121

Figure 4.35 Comparison of out-of-plane constraint parameter T_z for SENB, SENT and cracked pipes at various crack-tip loadings: (a) $J/(\sigma_y b) = 0.02$, (b) $J/(\sigma_y b) = 0.03$, (c) $J/(\sigma_y b) = 0.05$ and (d) $J/(\sigma_y b) = 0.07$ 122

Figure 4.36 Pipe section from which the SENT specimens were extracted (a) pipe section (b) cutting plan for manufacturing SENT specimens 124

Figure 4.37 SENT specimens to be tested using multiple specimen method 125

Figure 4.38 SENT specimen configuration 126

Figure 4.39 Speckle pattern applied to the surface of SENT specimens for DIC measurement 127

Figure 4.40 SENT specimen loaded using servo hydraulic testing machine 129

Figure 4.41 Force-CMOD responses of SENT specimens with nominal initial crack depth of $a/W = 0.35$ 130
Figure 4.42 CTOD J-curves of SENT specimens with nominal crack depth of $a/W = 0.35$ 131
Figure 4.43 CTOD R-curves of SENT specimens with nominal crack depth of $a/W = 0.35$ 131
Figure 4.44 Longitudinal strain ε_{yy} maps of SENT test (Set-1) M01-02 captured by DIC 132
Figure 4.45 Gauge length for global strain extraction from SENT test Set-1 specimens 133
Figure 4.46 CMOD versus global strain (65 mm GL) of SENT test Set-2 134
Figure 4.47 Force-CMOD responses of SENT specimens with nominal initial crack depth of $a/W = 0.15$ 134
Figure 4.48 Longitudinal strain ε_{yy} maps of SENT test Set-2 (M01-08) captured by DIC 136
Figure 4.49 Longitudinal strain ε_{yy} maps of SENT test Set-2 (M01-09) captured by DIC 137
Figure 4.50 CMOD versus global strain (80 mm GL) of SENT test Set-2 138
Figure 4.51 Measured stress-strain curves of the uniaxial round-bar tensile specimens 138
Figure 4.52 Stress-strain curves adopted in FE analyses of SENT specimens 139
Figure 4.53 Mesh configuration and boundary conditions of FE model of SENT test (Set-1) 141
Figure 4.54 Mesh configuration and boundary conditions of FE model of SENT test (Set-2) with additional mesh refinement 141
Figure 4.55 Comparison between the Load-CMOD responses calculated from FEA and those from the SENT tests 142
Figure 4.56 Comparison between the longitudinal strain map calculated from FEA and that from the SENT test at CMOD = 0.05 143

Figure 4.57 Comparison between the longitudinal strain map calculated from FEA and that from the SENT test at CMOD = 0.11 mm 143
Figure 4.58 Comparison between the longitudinal strain map calculated from FEA and that from the SENT test at CMOD = 0.21 mm 144
Figure 4.59 Comparison between the longitudinal strain map calculated from FEA and that from the SENT test at CMOD = 0.29 mm 144
Figure 4.60 Comparison between the longitudinal strain map calculated from FEA and that from the SENT test at CMOD = 0.41 mm 144
Figure 4.61 Comparison between the longitudinal strain map calculated from FEA and that from the SENT test at CMOD = 0.61 mm 144
Figure 4.62 Comparison between the load-CMOD responses calculated from FEA and those from the SENT tests Set-2 146
Figure 4.63 Comparison between the equivalent plastic strain map calculated from FEA and that from the SENT test (equivalent von Mises strain) at CMOD = 0.031 mm 147
Figure 4.64 Comparison between the equivalent plastic strain map calculated from FEA and that from the SENT test (equivalent von Mises strain) at CMOD = 0.166 mm 147
Figure 4.65 Comparison between the equivalent plastic strain map calculated from FEA and that from the SENT test (equivalent von Mises strain) at CMOD = 0.449 mm 148
Figure 4.66 Comparison between the equivalent plastic strain map calculated from FEA and that from the SENT test (equivalent von Mises strain) at CMOD = 0.782 mm 148
Figure 4.67 Comparison between the equivalent plastic strain map calculated from FEA and that from the SENT test (equivalent von Mises strain) at CMOD = 0.923 mm 149

Figure 4.68 Comparison between the equivalent plastic strain map calculated from FEA and that from the SENT test (equivalent von Mises strain) at CMOD = 0.950 mm 149
Figure 4.69 Comparison between the CMOD versus global strain (80 mm GL) responses calculated from FEA and those from the SENT tests Set-2 150
Figure 4.70 Load-CMOD responses of the SENT FEA models with various notch depths (a/W) 152
Figure 4.71 CMOD versus global strain responses of the SENT FEA models with various notch depths (a/W) 153
Figure 4.72 Equivalent plastic strain (ε^p_{eq}) distributions in the symmetric plane (plain strain) of SENT FE model with $a/W = 0.1$ 154
Figure 4.73 Equivalent plastic strain (ε^p_{eq}) distributions in the surface (plain stress) of SENT FE model with $a/W = 0.1$ 155
Figure 4.74 Equivalent plastic strain (ε^p_{eq}) distributions in the symmetric plane (plain strain) of SENT FE model with $a/W = 0.2$ 156
Figure 4.75 Equivalent plastic strain (ε^p_{eq}) distributions in the surface (plain stress) of SENT FE model with $a/W = 0.2$ 157
Figure 4.76 Equivalent plastic strain (ε^p_{eq}) distributions in the symmetric plane (plain strain) of SENT FE model with $a/W = 0.3$ 158
Figure 4.77 Equivalent plastic strain (ε^p_{eq}) distributions in the surface (plain stress) of SENT FE model with $a/W = 0.3$ 159
Figure 4.78 Equivalent plastic strain (ε^p_{eq}) distributions in the symmetric plane (plain strain) of SENT FE model with $a/W = 0.4$ 160
Figure 4.79 Equivalent plastic strain (ε^p_{eq}) distributions in the surface (plain stress) of SENT FE model with $a/W = 0.4$ 161
Figure 4.80 Equivalent plastic strain (ε^p_{eq}) distributions in the symmetric plane (plain strain) of SENT FE model with $a/W = 0.5$ 162

Figure 4.81 Equivalent plastic strain (ε^{p}_{eq}) distributions in the surface (plain stress) of SENT FE model with $a/W = 0.5$ 163
Figure 5.1 Schematic of the pipe containing a surface-breaking flaw: (a) geometric features of the pipe in the longitudinal view; (b)geometric features of the pipe cross-section containing an external surface-breaking flaw 167
Figure 5.2 Illustrative schematic of the UDU stress-strain model 168
Figure 5.3 Constitutive models used in FE analyses 169
Figure 5.4 Mesh configuration of the circumferentially-flawed pipe FE model 171
Figure 5.5 Paths AB and A'B' selected to extract the equivalent plastic strain distribution 173
Figure 5.6 Illustration of the J contours at the crack tip and near-tip regions 173
Figure 5.7 Calculated J-integral of cracked pipes for UDU model with $\overline{E}_L = 0.005$ 174
Figure 5.8 Incorporation of ductile tearing by driving force mapping and tangency approach 176
Figure 5.9 Comparison between global deformation behaviour (s-$e_{o,avg}$) calculated from FEA and that measured from full-scale test 177
Figure 5.10 Equivalent plastic strain (ε^{p}_{eq}) contours of the simulated cracked pipe with different material models at various average overall strain ($e_{o,avg}$) levels 178
Figure 5.11 Equivalent plastic strain distribution along path AB in the pipes 181
Figure 5.12 Equivalent plastic strain distribution along path A'B' in the pipes 182
Figure 5.13 Comparison of CTOD for average flaw size 5.68×50 mm from full-scale test and FE analyses without consideration of ductile tearing 183
Figure 5.14 Comparison of CTOD for average flaw size 4.6×100 mm from full-scale test and FE analyses without consideration of ductile tearing 184

Figure 5.15 Comparison of CTOD for average flaw size 5.68×50 mm from full-scale test and FE analyses with consideration of ductile tearing 184

Figure 5.16 Equivalent plastic strain contours in the near-tip region at $e_{o,avg} = 0.002$ from FE analyses using different material models 186

Figure 5.17 Equivalent plastic strain contours in the near-tip region at $e_{o,avg} = 0.003$ from FE analyses using different material models 187

Figure 5.18 Equivalent plastic strain contours in the near-tip region at $e_{o,avg} = 0.01$ from FE analyses using different material models 188

Figure 5.19 Equivalent plastic strain contours in the near-tip region at $e_{o,avg} = 0.02$ from FE analyses using different material models 188

Figure 5.20 Local polar coordinate system defined originating at the crack tip 189

Figure 5.21 Crack-tip fields at $e_{o,avg} = 0.002$: (a) radial distribution of tangential stress component $\sigma_{\theta\theta}$, (c) radial stress component σ_{rr}, (e) von Mises effective stress σ_e and (g) equivalent plastic strain ε^p_{eq} at angle $\theta = 0$; angular distribution of (b) tangential stress component $\sigma_{\theta\theta}$, (d) radial stress component σ_{rr}, (f) von Mises effective stress σ_e and (h) equivalent plastic strain ε^p_{eq} at normalised radial distance $r/\delta = 2$ 190

Figure 5.22 Crack-tip fields at $e_{o,avg} = 0.01$: (a) radial distribution of tangential stress component $\sigma_{\theta\theta}$, (c) radial stress component σ_{rr}, (e) von Mises effective stress σ_e and (g) equivalent plastic strain ε^p_{eq} at angle $\theta = 0$; angular distribution of (b) tangential stress component $\sigma_{\theta\theta}$, (d)radial stress component σ_{rr}, (f) von Mises effective stress σ_e and (h) equivalent plastic strain ε^p_{eq} at normalised radial distance $r/\delta = 2$ 191

Figure 5.23 Crack-tip fields at $e_{o,avg} = 0.002$: Radial distribution of (a) hydrostatic stress, (b) triaxiality parameter; Angular distribution of (c) hydrostatic stress, (d) triaxiality parameter; at normalised radial distance $r/\delta = 2$ 193
Figure 5.24 Crack-tip fields at $e_{o,avg} = 0.01$: Radial distribution of (a) hydrostatic stress, (b) triaxiality parameter; Angular distribution of (c) hydrostatic stress, (d) triaxiality parameter; at normalised radial distance $r/\delta = 2$ 194
Figure 5.25 Illustration of Lüders band pattern simulated using different material laws 195
Figure 6.1 Schematic illustrating the loading steps in the FEA of cracked pipes subjected to axial straining and internal pressure 200
Figure 6.2 Global stress-strain response of FE pipe models with 3×10 mm circumferential flaw with various levels of internal pressure 201
Figure 6.3 Global stress-strain response of FE pipe models with 3×25 mm circumferential flaw with various levels of internal pressure 201
Figure 6.4 Global stress-strain response of FE pipe models with 3×50 mm circumferential flaw with various levels of internal pressure 202
Figure 6.5 Global stress-strain response of FE pipe models with 3×75 mm circumferential flaw with various levels of internal pressure 202
Figure 6.6 Global stress-strain response of FE pipe models with 3×100 mm circumferential flaw with various levels of internal pressure 203
Figure 6.7 Global stress-strain response of FE pipe models with 5×25 mm circumferential flaw with various levels of internal pressure 203
Figure 6.8 Global stress-strain response of FE pipe models with 5×50 mm circumferential flaw with various levels of internal pressure 204

Figure 6.9 Global stress-strain response of FE pipe models with 5×75 mm circumferential flaw with various levels of internal pressure 204
Figure 6.10 Global stress-strain response of FE pipe models with 5×100 mm circumferential flaw with various levels of internal pressure 205
Figure 6.11 Global stress-strain response of FE pipe models with 7×25 mm circumferential flaw with various levels of internal pressure 205
Figure 6.12 Global stress-strain response of FE pipe models with 7×50 mm circumferential flaw with various levels of internal pressure 206
Figure 6.13 Global stress-strain response of FE pipe models with 7×75 mm circumferential flaw with various levels of internal pressure 206
Figure 6.14 Global stress-strain response of FE pipe models with 7×100 mm circumferential flaw with various levels of internal pressure 207
Figure 6.15 CTOD versus average overall strain of FE pipe models with 3×10 mm circumferential flaw with various levels of internal pressure 208
Figure 6.16 CTOD versus average overall strain of FE pipe models with 3×25 mm circumferential flaw with various levels of internal pressure 208
Figure 6.17 CTOD versus average overall strain of FE pipe models with 3×50 mm circumferential flaw with various levels of internal pressure 209
Figure 6.18 CTOD versus average overall strain of FE pipe models with 3×75 mm circumferential flaw with various levels of internal pressure 209
Figure 6.19 CTOD versus average overall strain of FE pipe models with 3×100 mm circumferential flaw with various levels of internal pressure 210

Figure 6.20 CTOD versus average overall strain of FE pipe models with 5 × 25 mm circumferential flaw with various levels of internal pressure 210
Figure 6.21 CTOD versus average overall strain of FE pipe models with 5 × 50 mm circumferential flaw with various levels of internal pressure 211
Figure 6.22 CTOD versus average overall strain of FE pipe models with 5 × 75 mm circumferential flaw with various levels of internal pressure 211
Figure 6.23 CTOD versus average overall strain of FE pipe models with 5 × 100 mm circumferential flaw with various levels of internal pressure 212
Figure 6.24 CTOD versus average overall strain of FE pipe models with 7 × 25 mm circumferential flaw with various levels of internal pressure 212
Figure 6.25 CTOD versus average overall strain of FE pipe models with 7 × 50 mm circumferential flaw with various levels of internal pressure 213
Figure 6.26 CTOD versus average overall strain of FE pipe models with 7 × 75 mm circumferential flaw with various levels of internal pressure 213
Figure 6.27 CTOD versus average overall strain of FE pipe models with 7 × 100 mm circumferential flaw with various levels of internal pressure 214
Figure 6.28 Equivalent plastic strain ε^{p}_{eq} (PEEQ) distribution of FE pipe model with flaw size 3 × 10 mm under various internal pressure levels at 0.39% global strain ($e_{o,avg}$ = 0.39%) 215
Figure 6.29 Equivalent plastic strain ε^{p}_{eq} (PEEQ) distribution of FE pipe model with flaw size 3 × 10 mm under various internal pressure levels at 0.98% global strain ($e_{o,avg}$ = 0.98%) 216

Figure 6.30 Equivalent plastic strain ε_{eq}^{p} (PEEQ) distribution of FE pipe model with flaw size 3×10 mm under various internal pressure levels at 1.31% global strain ($e_{o,avg}$ = 1.31%) 216

Figure 6.31 Equivalent plastic strain ε_{eq}^{p} (PEEQ) distribution of FE pipe model with flaw size 3×10 mm under various internal pressure levels at 1.44% global strain ($e_{o,avg}$ = 1.44%) 217

Figure 6.32 Equivalent plastic strain ε_{eq}^{p} (PEEQ) distribution of FE pipe model with flaw size 3×10 mm under various internal pressure levels at 2.04% global strain ($e_{o,avg}$ = 2.04%) 218

Figure 6.33 Equivalent plastic strain ε_{eq}^{p} (PEEQ) distribution of FE pipe model with flaw size 3×10 mm under various internal pressure levels at 2.86% global strain ($e_{o,avg}$ = 2.86%) 218

Figure 6.34 Equivalent plastic strain ε_{eq}^{p} (PEEQ) distribution of FE pipe model with flaw size 7×100 mm under various internal pressure levels at 0.4% global strain ($e_{o,avg}$ = 0.4%) 219

Figure 6.35 Equivalent plastic strain ε_{eq}^{p} (PEEQ) distribution of FE pipe model with flaw size 7×100 mm under various internal pressure levels at 0.8% global strain ($e_{o,avg}$ = 0.8%) 219

Figure 6.36 Equivalent plastic strain ε_{eq}^{p} (PEEQ) distribution of FE pipe model with flaw size 7×100 mm under various internal pressure levels at 1.1% global strain ($e_{o,avg}$ = 1.1%) 220

Figure 6.37 Effect of flaw sizes on the normalised gross stress ($s_{Plateau}/R_{eL}$) level during Lüders plateau phase of the cracked pipe with flaw height of (a) $a = 3$ mm, (b)$a = 5$ mm, and (c)$a = 7$ mm subjected to various levels of internal pressure 222

Figure 6.38 Effect of flaw sizes on extent of Lüders plateau (Δe_L) during Lüders plateau phase of the cracked pipe with flaw height of (a) $a = 3$ mm, (b)$a = 5$ mm, and (c)$a = 7$ mm subjected to various levels of internal pressure 223

Figure 6.39 Schematic of the global stress-strain response calculated from the FEA with associated parameters 224

Figure 6.40 Stress state of a pipe subjected to combined axial straining and internal pressure 224

Figure 6.41 Schematic of the von Mises yield criterion illustrating the effect of hoop stress induced by internal pressure 225

Figure 6.42 Schematic illustrating the effect of internal pressure on the strain energy of the cracked pipe 226

Figure 6.43 Effect of flaw depth on the CDF calculated from FEA for (a) $2c = 25$ mm (b) $2c = 50$ mm subjected to combine axial straining and internal pressure ($\sigma_{hoop}/\sigma_y = 0.2$) 228

Figure 6.44 Effect of flaw length on the CDF calculated from FEA for (a) $a = 3$ mm (b) $a = 5$ mm subjected to combined axial straining and internal pressure ($\sigma_{hoop}/\sigma_y = 0.2$) 229

Figure 6.45 Effect of flaw sizes on the CTOD during plateau phase of the cracked pipe with flaw height of (a) $a = 3$ mm, (b) $a = 5$ mm, and (c) $a = 7$ mm subjected to various levels of internal pressure 230

Figure 6.46 Effect of flaw sizes on the extent of CTOD plateau of the cracked pipe with flaw height of (a) $a = 3$ mm, (b) $a = 5$ mm, and (c) $a = 7$ mm subjected to various levels of internal pressure 231

Figure 6.47 Schematic of the CTOD versus global strain response calculated from the FEA with associated parameters 232

Figure 6.48 Illustration showing the necking in the uncracked ligament due to significant straining in the crack region (flaw 7×75 mm with $\sigma_{hoop}/\sigma_y = 0.5$ as an example) 235

Figure C.1 Equivalent von Mises strain ε_{eq} maps of SENT test (Set-2) M01-02 captured by DIC 263

Figure C.2 Von Mises equivalent strain ε_{yy} maps of SENT test Set-2 (M01-08) captured by DIC 264
Figure C.3 Von Mises equivalent strain ε_{yy} maps of SENT test Set-2 (M01-09) captured by DIC 265
Figure D.1 Comparison between the equivalent plastic strain map calculated from FEA and that from the SENT test (equivalent von Mises strain) at CMOD = 0.05 mm 266
Figure D.2 Comparison between the equivalent plastic strain map calculated from FEA and that from the SENT test (equivalent von Mises strain) at CMOD = 0.11 mm 266
Figure D.3 Comparison between the equivalent plastic strain map calculated from FEA and that from the SENT test (equivalent von Mises strain) at CMOD = 0.21 mm 267
Figure D.4 Comparison between the equivalent plastic strain map calculated from FEA and that from the SENT test (equivalent von Mises strain) at CMOD = 0.29 mm 267
Figure D.5 Comparison between the equivalent plastic strain map calculated from FEA and that from the SENT test (equivalent von Mises strain) at CMOD = 0.41 mm 267
Figure D.6 Comparison between the equivalent plastic strain map calculated from FEA and that from the SENT test (equivalent von Mises strain) at CMOD = 0.61 mm 267
Figure D.7 Comparison between the equivalent plastic strain map calculated from FEA and that from the SENT test (equivalent von Mises strain) at CMOD = 0.031 mm 268
Figure D.8 Comparison between the equivalent plastic strain map calculated from FEA and that from the SENT test (equivalent von Mises strain) at CMOD = 0.166 mm 268
Figure D.9 Comparison between the equivalent plastic strain map calculated from FEA and that from the SENT test (equivalent von Mises strain) at CMOD = 0.449 mm 269
Figure D.10 Comparison between the equivalent plastic strain map calculated from FEA and that from the SENT test (equivalent von Mises strain) at CMOD = 0.782 mm 269

Figure D.11 Comparison between the equivalent plastic strain map calculated from FEA and that from the SENT test (equivalent von Mises strain) at CMOD = 0.923 mm 270
Figure D.12 Comparison between the equivalent plastic strain map calculated from FEA and that from the SENT test (equivalent von Mises strain) at CMOD = 0.950 mm 270

LIST OF TABLES

Table 2.1 A summary of the range of validity of the strain-based fracture assessment methods 35
Table 2.2 Actual notch sizes in TWI full-scale pipe tests 36
Table 2.3 Categorisation of strain-based CDF estimation approaches 37
Table 3.1 Chemical composition of the tested steel (wt%) 54
Table 3.2 Parameters of material models used in FE simulation of M01-02 72
Table 4.1 Summary of FEA cases for analysis of crack-tip constraint of fracture mechanics test specimens 98
Table 4.2 Summary of FEA cases for analysis of crack-tip constraint of fracture mechanics test specimens 98
Table 4.3 Actual dimensions of Set-1 SENT specimens with a nominal crack depth of $a_0/W = 0.35$ 125
Table 4.4 Actual dimensions of Set-2 SENT specimens with a nominal crack depth of $a_0/W = 0.15$ 125
Table 4.5 Results of SENT fracture test Set-1 using multiple specimen method 129
Table 4.6 Summary of average tensile properties measured by the round-bar tensile testing 139
Table 4.7 Dimensions of the FE models in the parametric study of SENT specimens 151

Table 5.1 Parameters of material laws used in FEA of cracked pipes 169

Table 6.1 FEA cases covering various flaw sizes and internal pressure levels 199

Table 6.2 Summary of CTOD and stress plateau calculated from FEA 232

NOMENCLATURE

Abbreviations

BS British Standard

CDF Crack Driving Force

CMOD Crack Mouth Opening Displacement

CRES Centre for Reliable Energy Systems

CT Compact Tension

CTOD Crack Tip Opening Displacement

DIC Digital Image Correlation

DNV Det Norske Veritas

ECA Engineering Critical Assessment

EDM Electric Discharge Machining

EPFM Elastic-Plastic Fracture Mechanics

EPRI Electric Power Research Institute

FAC Failure Assessment Curve

FAD Failure Assessment Diagram

FCAW Flux-Cored Arc Welding

FE Finite Element

FEA Finite Element Analysis

FFS Fitness-For-Service

GL Gauge Length

GL Germanischer Lloyd

GMAW Gas Metal Arc Welding

GTN Gurson-Tvergaard-Needleman

HAZ Heat Affected Zone

HRR Hutchinson-Rice-Rosengren

ID Inside Diameter

JIP Joint Industry Project

LEFM Linear Elastic Fracture Mechanics

LGC Large Geometry Change

LSY Large-Scale Yielding

LVDT Linear Variable Differential Transformer

MBL Modified Boundary Layer

NLG Nonlinear Geometry

OD Outside Diameter

PDE Partial Differential Equation

PF Pressure Factor

PHMSA Pipeline and Hazardous Materials Safety Administration

PLC Portevin-Le Chatelier

PRCI Pipeline Research Council International

SBD Strain-Based Design

SEM Scanning Electron Microscope

SENB Single Edge Notch Bend

SENT Single Edge Notch Tension

SG Strain Gauge

SGC Small Geometry Change

SIF Stress Intensity Factor

SINTEF Stiftelsen for Industriell og Teknisk Forskning (The Foundation for Scientific and Industrial Research)

SMAW Shielded Metal Arc Welding

SSY Small-Scale Yielding

TSC Tensile Strain Capacity

TWI The Welding Institute

UDU Up-down-up

UEL Uniform Elongation

Greek Symbols

α Ramberg-Osgood fitting parameter

δ_{ij} Kronecker delta

ν Poisson's ratio

σ True stress

$\sigma_{0.2}$ 0.2% proof stress on the true stress-strain curve

σ_0 Normalising stress

$\sigma_{\theta\theta}$ Tangential component of crack-tip stress in the polar coordinate system

σ_{hoop} Hoop stress induced by the internal pressure in the pipelines

σ_h Hydrostatic stress

σ_{ij} The Cauchy (true) stress tensor

σ_m Mean stress

σ_{rr} Radial component of crack-tip stress in the polar coordinate system

σ_{ref} Reference stress

σ_u Tensile strength

σ_y Yield stress

θ Angular position ahead of the crack tip in the polar coordinate system

ε true strain

ε_{eq}^{p} Equivalent plastic strain

ε_c Critical strain or tensile strain capacity

ε_{ij} Strain tensor

ε_{ref} Reference strain

ε_{unc} Uncracked strain

ε_{UTS} Uniform elongation strain at UTS

ε_{YS} Yield strain

Roman Symbols

$2c$ Flaw length

$\bar{E}_L$ Normalised softening modulus

Δa Flaw extension

Γ Arbitrary contour around the crack

Π Potential energy

ρ_t Radius of the notch in the side-notched tensile specimen

$\tilde{\sigma}_{ij}$, $\tilde{\varepsilon}_{ij}$ Dimensionless functions in the formulation of HRR field

A Cross-section area of the uncracked end of the pipe

a Flaw depth

a Length of the notch in the side-notched tensile specimen

a_0 Initial flaw depth

a_{eff} Effective flaw depth

b	Remaining ligament
c_1, c_2	Coefficients used in strain-based FAD proposed by Smith
d_n	Dimensionless constant of J-CTOD correlation mainly depending on strain hardening
D_r	Strain ratio of reference strain to yield strain
E	Softening modulus of the softening segment in the UDU stress-strain model
E	Total energy
E	Young's modulus
e	Engineering strain
$e_{o,avg}$	Average overall strain
F	Applied force at the uncracked end of the pipe
f	Function of stress-based failure assessment curve
f^*	Function of strain-based failure assessment curve
f_1, f_2	Dimensionless functions of the reference strain method proposed by Nourpanah
f_{ij}	Dimensionless function in the formulation of crack-tip stress field
G	Energy release rate
g_1	dimensionless proportionality parameter between J_{pl} and applied strain
h	Stress triaxiality parameter
h	Weld 'hi-lo' misalignment
h_1	dimensionless proportionality parameter between J_{pl} and applied loading
h_2	dimensionless proportionality parameter between δ_{pl} and applied loading

J J-integral

J_{el} Elastic component of J

J_{pl} Plastic component of J

J_{tot} Total or elastic-plastic J

K Strength coefficient in ExxonMobil TSC predictive equation

K Stress intensity factor

K_I Mode I stress intensity factor

K_r Fracture ratio of applied elastic K to K_{mat}

K_{III} Mode III stress intensity factor

K_{II} Mode II stress intensity factor

K_{mat} Material fracture toughness measured by stress intensity factor

L Half-length of the pipe,also the length of quarter FE pipe model

L_e Gauge length of the extensometer

L_o Gauge length of the uniaxial tensile specimen

L_t Parallel length of the uniaxial tensile specimen

$L_{GL1,0}$, ΔL_{GL1} Original length and elongation over the 25 mm gauge length of the side-notched tensile specimen, respectively

$L_{r,max}$ Cut-off limit of L_r

L_r Load ratio of applied load to yield load

M Applied bending moment

m J-CTOD conversion constant

M_0 Limit bending moment

N Coefficient of the power-law strain rate-dependence law

N	Number of elements n the radial direction of the notch in the FE model of side-notched specimen
n	Components of the unit vector n normal to Γ
n	Strain hardening exponent in Ramberg-Osgood material model
n_j	Components of n
N_t	Number of elements through thickness in FEA
OD	Outside diameter
P	Applied load
P	Internal pressure
P_0	Reference load, often defined as P_L
P_L	Limit load
Q	Elastic-plastic crack-tip constraint parameter
r	Radial distance from the crack tip
R_0	Intrinsic yield stress of material prior to strain ageing
R_a	Increase in stress due to strain ageing
R_{eH}	Upper yield strength of material
R_{eL}	Lower Yield strength of discontinuously yielding material
R_h	Increase in stress due to strain hardening
s	Engineering stress, or gross stress of the flawed structure
s_{ly}	Lower yield stress of the UDU stress-strain model in the form of engineering stress-strain curve
$s_{Plateau}$	Gross stress level of the Lüders plateau phase
s_{uy}	Upper yield stress of the UDU stress-strain model in the form of engineering stress-strain curve
T	Elastic crack-tip constraint parameter

T	Traction vector
t	Pipe wall thickness
T_i	Components of T
U	Strain energy
u	Components of the displacement vector T
u_i	Components of T
u_x, u_y, u_z	Displacement in x, y and z directions, respectively
W_s	Energy required for the formation of new crack surfaces
X	Correction factor used in strain-based FAD proposed by Smith
Y	Dimensionless constant in the formulation of stress intensity factor
GL-1, GL-2	25 mm and 80 mm gauge length in the FEA of plain tensile specimen
UTS	Ultimate tensile strength
YS	Yield strength

1

INTRODUCTION

1.1 PIPELINES SUBJECTED TO PLASTIC STRAINING

Fossil resources are crucial for engineering production and daily life of human beings. They are usually located underground in remote areas. The resources need to be extracted from the earth and then transported to the sites where the hydrocarbon is treated before distributed to customers. The hydrocarbon is usually transmitted via pipelines, which are effective means for transporting crude oil and natural gas.

Pipelines are subjected to plastic straining during installations, such as S-lay, J-lay and reeling for offshore applications, and in service where the geophysical events such as ice gouging, thaw settlement and landslide may exert forces on the buried pipelines. Figure 1.1 shows some of the aforementioned scenarios of pipelines undergoing plastic deformation. In reeling installation of offshore pipelines (as depicted in Figure 1.1(a)), the pipes are spooled to a large reel at onshore facilities before being conveyed to the construction location at sea via a large barge. During the pipe laying, the pipes spooled on the reel are un-reeled and straightened before laying off to the seabed. During the reeling and un-reeling processes, the pipes are plastically strained up to 3% strain under low-cycle fatigue. In-service pipelines at the seabed may also undergo plastic straining, exerted by lateral buckling or 'snaking' that is a result of the combination of thermal stresses and pipe-soil interactions. Other geophysical events such as ice gouging, frost heave and thaw settlement, usually found in Arctic or permafrost regions, can impose large deformations to the operating pipelines, resulting in a longitudinal strain up to 4%. The magnitude of the

longitudinal strains pipelines may undergo (known as the strain demand) during installation or service are summarised in Figure 1.2.

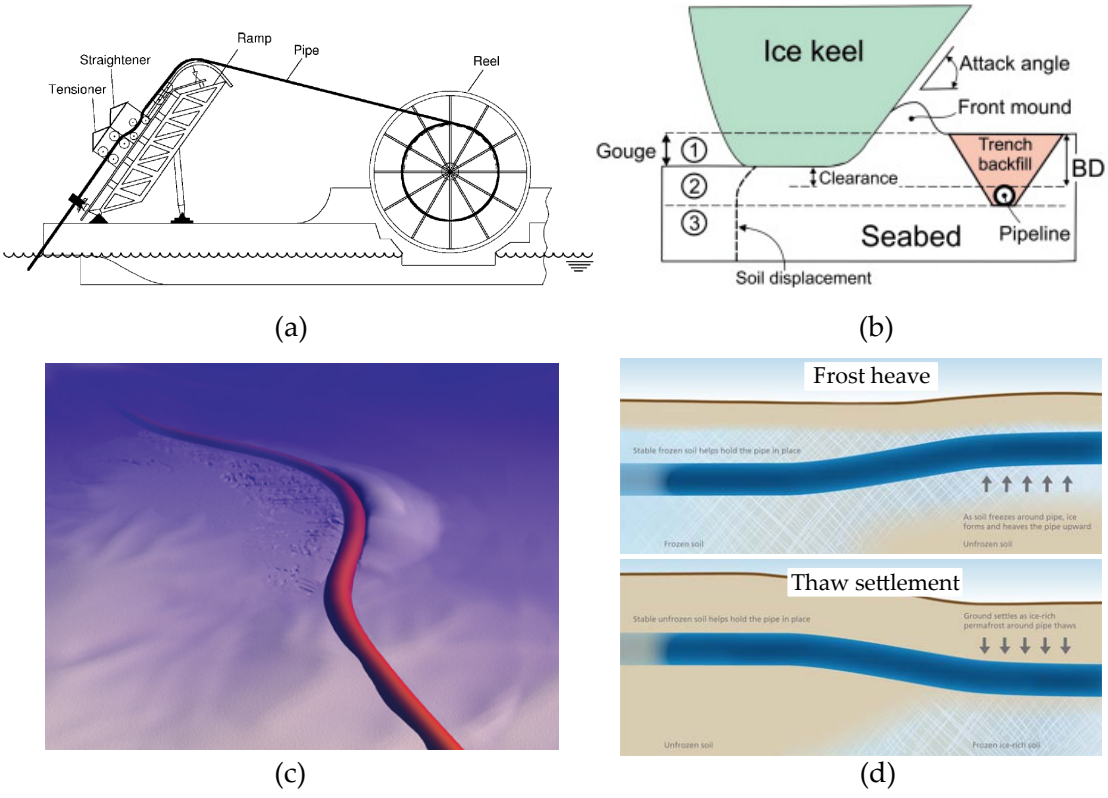

Figure 1.1: Strain-based scenarios of pipelines undergoing considerable plastic straining: (a) Offshore pipeline installation via reeling (from Kyriakides and Corona (2007b)), (b) Iceberg gouging in Arctic regions (from Barrette (2011)), (c) lateral buckling (snaking) of subsea pipelines lying on the seabed (taken from Pangeranlaut (2016)), and (d) thaw settlement in permafrost terrains (adapted from National Energy Board (2016))

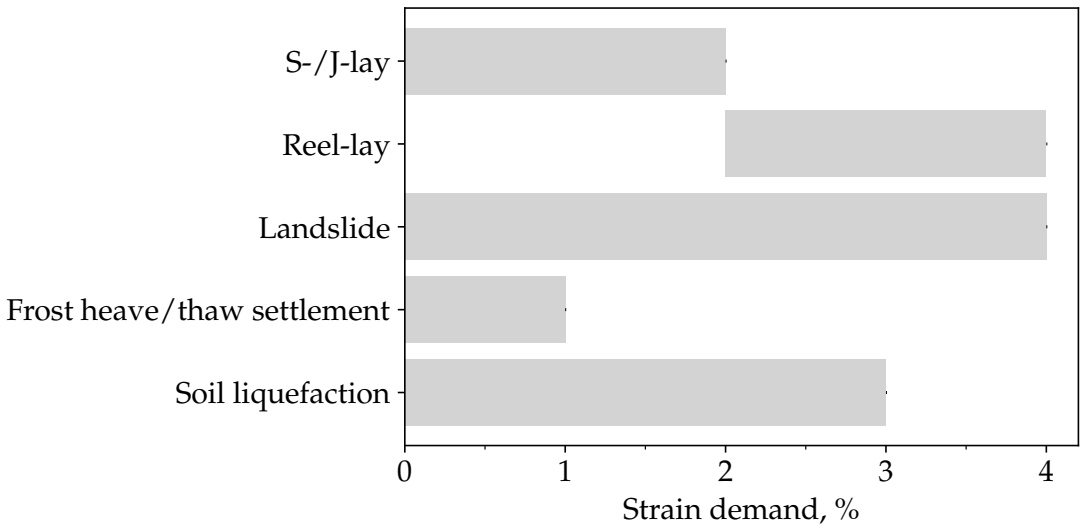

Figure 1.2: Strain demand of pipelines during installation and operation

Girth welds, via which pipelines are jointed and constructed, may have crack-like flaws that pose risks to the integrity and serviceability of the pipelines. Therefore, the criticality of the weld flaws needs to be assessed, usually via fracture mechanics-based techniques, to determine whether the equipment is fit for service or repairs are required.

1.2 TECHNOLOGICAL CHALLENGES AND INDUSTRY NEEDS

Conventional assessment methods codified in commonly-used codes and standards such as BS 7910:2013+A1:2015 (Incorporating Corrigenda Nos. 1 and 2) (BSI 2013a), R6 (EDF Energy 2015) and API 579/ASME FFS-1 (API/ASME 2016) are preferably applicable to equipments that are elastically loaded and have been found not suited to scenarios where pipelines are subjected to plastic straining.

During the plastic straining phase, the deformation behaviour of pipelines are further complicated by a yielding behaviour of the materials, known as yield discontinuity, which is usually manifested by a yield plateau or Lüders plateau.

Simplified guidelines are provided in the aforementioned codes and standards on the incorporation of the effect of yield discontinuity on fracture analysis of pipelines, but a detailed approach involving sophisticated analysis of discontinuous yielding behaviour is lacking.

The following technological gaps and challenges, which impede accurate and reliable assessment of flawed pipelines in the presence of yield discontinuity, are yet to be addressed:

- No clear guidance is given in current codes and standards for detailed analysis and assessment of pipelines containing flaws with Lüders bands.
- Very limited studies and researches have been carried out to investigate thoroughly the crack-tip behaviour of pipelines made of steels exhibiting yield discontinuity.
- Current methods adopted in industry may lead to non-conservatism in assessment of pipelines subjected to plastic straining with Lüders bands.

1.3 RESEARCH OBJECTIVES AND CONTRIBUTIONS

To address the technological gaps and challenges, the research reported in this thesis aims to achieve the following objectives and original contributions to knowledge:

- Identify effective material models for numerical analysis of Lüders bands in tensile specimens and fracture mechanics test specimens.
- Investigate the effect of flaws on the development of Lüders banding in steels.
- Understand the structural behaviour and crack-tip conditions of pipelines subjected to axial straining with and without internal pressure, in the presence of yield discontinuity.
- Provide guidance on fracture analysis of pipelines in the presence of yield discontinuity.

1.4 THESIS STRUCTURE

The thesis consists of seven chapters, including both experimental and numerical work. The thesis structure is described as follows:

- Chapter 1 introduces the background, significance, research gap and original contributions of the thesis.
- Chapter 2 reports an insightful and critical review of the current status of the research, including fundamental concepts of fracture mechanics that were utilised in the study, progresses in strain-based pipeline assessment and the significance of Lüders banding phenomenon.
- Chapter 3 reports both the experimental and numerical analysis of uniaxial tensile specimens with and without notches. DIC technique was employed in the tests to quantify the deformation. Various material models were examined for numerical analysis of Lüders banding in both plain and notched tensile specimens.

- Chapter 4 reports both the experimental and numerical analysis of the single edged notch tension (SENT) specimens. A systematic numerical analysis of crack-tip constraint was performed to establish the optimal specimen configuration in the light of the transferability in constraint level to the pressurised pipes containing flaws. Testing of the SENT specimens with the established notch size and additional specimens with a shallow notch was carried out with the employment of DIC. The appropriate material model was identified by validation of the FEA against the DIC. Parametric FEA study using the identified material model was performed to investigate the effect of notch size on the development of plasticity associated with Lüders bands.

- Chapter 5 investigates the fracture behaviour of pipelines containing circumferential flaws subjected to axial straining only. Numerical analysis was performed and then validated against the published full-scale test data. Effect of different material models on the calculated crack driving force, development of plasticity associated with Lüders bands and the crack-tip field were examined. Appropriate material model was identified in order to obtain a suitable level of conservatism in the fracture assessment of pipelines in the presence of yield discontinuity.

- Chapter 6 reports a parametric FEA study of pipelines containing circumferential flaws subjected to combined axial straining and internal pressure. The effect of internal pressure on the global structural response, development of plasticity associated with Lüders bands and the crack driving force were investigated.

- Chapter 7 draws the conclusions based on the work reported and provide recommendations on the future work which extends and deepens the current research scope of the thesis.

2

LITERATURE REVIEW

2.1 INTRODUCTION

This chapter presents a comprehensive literature review on the relevant concepts and previous studies. The fundamental concepts of fracture mechanics that are essential to the work carried out are introduced, focusing on the stress field of a cracked body, crack driving force and crack-tip constraint. The previous studies on fracture assessment of pipelines strained plastically are critically reviewed, which identifies current status and the research gaps. The importance of the yield discontinuity on fracture behaviour of pipelines is highlighted.

2.2 FUNDAMENTALS OF FRACTURE MECHANICS

2.2.1 *Crack in elastic solids and the energy release rate*

Early studies of fracture mechanics focused on linear-elastic brittle solids containing flaws. By analysing elliptical holes in elastic flat plates (shown in Figure 2.1), Inglis (1913) investigated the stress concentration effect due to flaws, and established its correlation with the hole dimensions. The correlation reads as the following:

$$\sigma_A = \sigma\left(1 + 2\sqrt{\frac{a}{\rho}}\right) \tag{2.1}$$

where σ_A is the local stress at the tip of the hole (Point A), σ is the applied stress, and ρ is the radius of the curvature at the hole tip. The radius ρ is related to the hole dimensions by $\rho = b^2/a$. Based on Equation 2.1, it can be

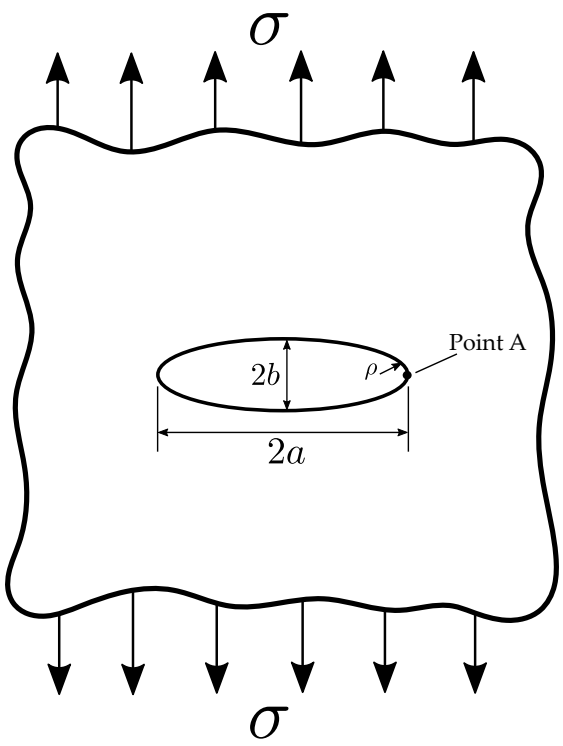

Figure 2.1: Schematic of an elliptical hole in an infinite plate subjected to applied tensile stress

envisaged that when ρ becomes infinitely small, or in others words the hole becomes a sharp crack, the local stress at the tip would be infinite. However, with an infinite local stress at the tip of a sharp crack, the material could fail at an infinitesimal stress. To establish a more robust fracture criterion, Griffith (1920) used an energy approach assuming that a crack can form (or an existing crack can grow) only if the external work causes the total energy to decrease or remain constant. In other words, the potential energy must suffice to overcome the surface energy of the material for new crack faces to form. For an infinite plate subjected to a nominal stress σ containing a through-thickness crack 2a long, based on the Griffith energy balance approach, the following conditions must be met for the new crack faces to form:

$$\frac{dE}{dA} = \frac{d\Pi}{dA} + \frac{dW_s}{dA} = 0 \tag{2.2}$$

or rearranged as:

$$-\frac{d\Pi}{dA} = \frac{dW_s}{dA} \tag{2.3}$$

where E is the total energy, Π is the potential energy consisting of the internal strain energy and external work, and W_s is the energy required for the formation of new crack surfaces. Based on the energy balance, Griffith derived the fracture stress of the cracked plate shown in Figure 2.1, which was then modified by Irwin (1948) and Orowan (1949) to accommodate elastic-plastic materials.

Later Orowan (1956) proposed an energy approach featuring the use of energy release rate G, which quantifies the energy required for crack extension:

$$G = -\frac{d\Pi}{dA} \tag{2.4}$$

The energy release rate G is the rate of change in potential energy with the crack area. G is also known as the crack driving force and is quantitatively related to the crack stress field, which will be elaborated in the following subsections.

2.2.2 *Crack-tip stress field and the stress intensity factor*

Stress field of elastic cracked solids was studied by a number of researchers, such as Westergaard (1939), Irwin (1939), and Williams (1957). The derived closed-form solution of the stresses ahead of a crack tip takes the following form:

$$\sigma_{ij} = \frac{K}{\sqrt{2\pi r}} f_{ij}(\theta) + \sum_{m=0}^{\infty} A_m r^{\frac{m}{2}} g_{ij}^{(m)}(\theta) \tag{2.5}$$

where σ_{ij} is the stress tensor; r and θ are defined in the polar coordinate system shown in Figure 2.2; K is the stress intensity factor, and f_{ij} is a dimensionless function depending on θ. In Equation 2.5, the higher-order terms (second term) vanish as the distance to crack tip (r) approaches to zero, which describes a $1/\sqrt{r}$ singularity in the vicinity of the crack tip. In the regions far from the crack tip, the stresses are governed by the remote boundary conditions, whereas in the singularity-dominated zone, the stresses are uniquely described by the parameter K. This important concept lays the ground for the single-parameter fracture mechanics.

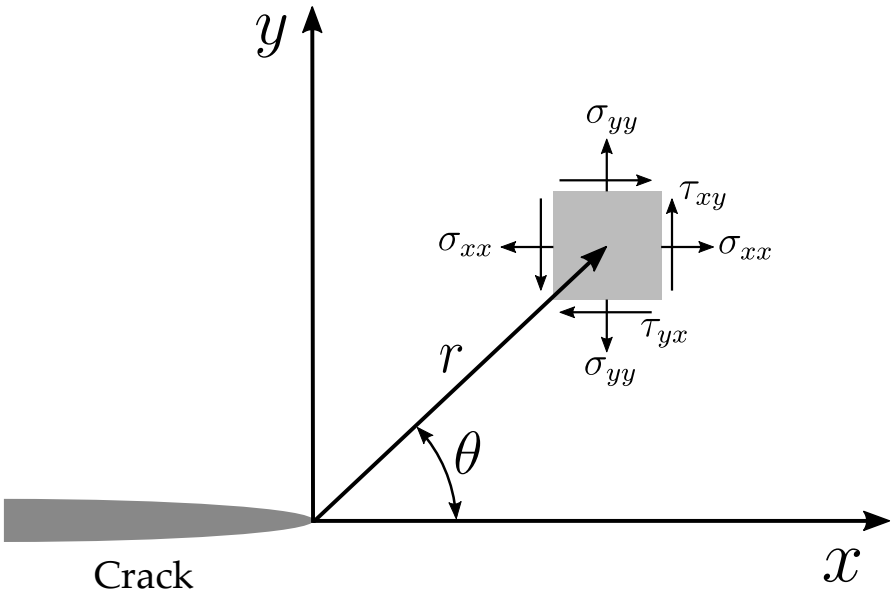

Figure 2.2: Schematic of stress components at an arbitrary location in a coordinate system originating from the crack tip

While most closed-form K solutions were derived for a crack with a simple shape in an infinite plate, K is additionally dependent on the specific geometry of the structure provided the dimensions of the crack is not small enough in comparison with the structure to be free from the influence by external boundaries. Thus, a general form of K for a cracked body is given by:

$$K_{I,II,III} = Y\sigma\sqrt{\pi a} \tag{2.6}$$

where I, II, III represent the three modes of loading applied to the cracked body, as illustrated in Figure 2.3; a is the characteristic crack dimension; Y is a dimensionless constant depending on the geometry and the mode of loading. The K is uniquely related to the energy release rate G via:

$$G = \frac{K^2}{E'} \tag{2.7}$$

where $E' = E$ for plane stress and $E' = E/(1-\nu^2)$ for plane strain. Since the K is originally defined for linear-elastic body, modifications were proposed to accommodate the plasticity for elastic-plastic materials (Irwin 1961; Dugdale 1960; Burdekin and Stone 1966).

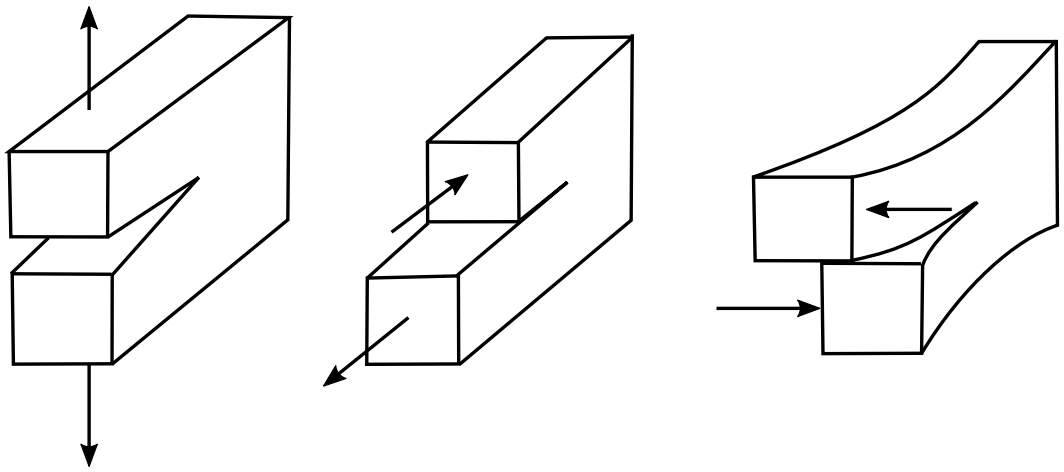

Mode I (Opening) Mode II (In-plane shear) Mode III (Out-of-plane shear)

Figure 2.3: Schematic of cracked body under various loading mode

2.2.3 *Crack-tip opening displacement and J-integral*

For inelastic materials in which the spread of plasticity is beyond K-dominated regime, the elastic-plastic fracture mechanics are applicable. The Crack Tip Opening Displacement (CTOD) and the J-integral are important parameters that describe the crack-tip conditions in the elastic-plastic materials.

The concept of CTOD was originally envisaged by Wells (1961) in an attempt to measure the fracture toughness of structural steels. He was motivated by the observation that the plastic deformation resulted in crack blunting, of which the degree increased in proportion to the toughness of the material. The CTOD was demonstrated to be related to K and G in the limit of Small Scale Yielding (SSY) (Wells 1961; Burdekin and Stone 1966) which implies that CTOD could be a characterising parameter of crack-tip conditions. The CTOD is usually defined as the displacement at the original crack tip before blunting or the 90° intercepts. The latter is a common approach to compute the CTOD in FEA.

Another crack-tip parameter, the J-integral, was proposed by Rice (1964) based on non-linear elastic material behaviour (i.e. deformation theory of plasticity) and small strain assumption. The J takes the following form:

$$J = \int_{\Gamma} \left(w dy - T_i \frac{\partial u_i}{\partial u_x} ds \right) \tag{2.8}$$

where w is the strain energy density; ds is the length increment along the contour Γ around the crack (see Figure 2.4); u_i are the components of

displacement vector; T_i are the components of the traction vector, which are given by:

$$T_i = \sigma_{ij} n_j \tag{2.9}$$

where n_j are the components of the unit vector n normal to Γ. The J-integral was demonstrated to not be affected by the path of integration around the crack (known as path-independence), and able to quantify the crack-tip conditions (Hutchinson 1968; Rice and Rosengren 1968).

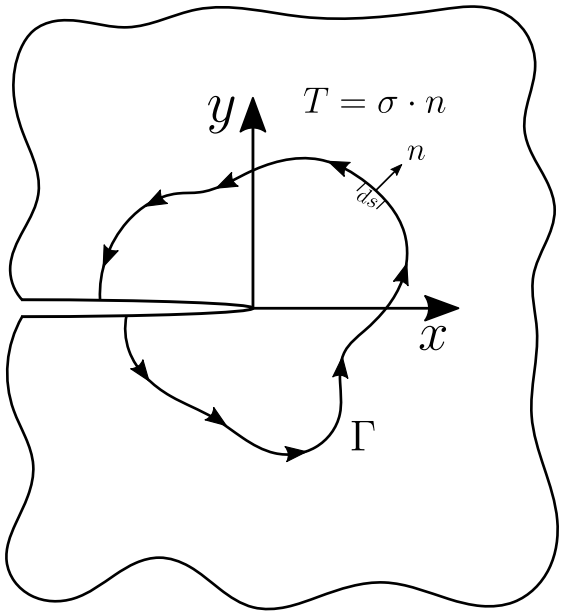

Figure 2.4: Illustration of an arbitrary contour around the crack tip for calculation of the path-independent line integral

J was shown to be equal to the energy release rate in non-linear elastic materials, which is defined by the following:

$$J = -\frac{d\Pi}{dA} \tag{2.10}$$

For linear elastic materials, J is related to K for Mode I loading via:

$$J = \frac{K_I^2}{E'} \tag{2.11}$$

It should be noted that the energy release rate is typically defined as the potential energy that is released from a structure when the crack grows in an elastic material. However, for inelastic materials containing a growing crack

or being unloaded, the strain energy absorbed is not recovered, rendering a plastic wake.

2.2.4 *HRR singularity and J-dominance*

Assuming a power law material behaviour, Hutchinson (1968), Rice and Rosengren (1968) obtained the solutions of crack-tip stress and strain fields in elastic-plastic materials. The solutions are given as:

$$\sigma_{ij} = \sigma_0 \left(\frac{EJ}{\alpha \sigma_0^2 I_n r} \right)^{\frac{1}{n+1}} \tilde{\sigma}_{ij}(n, \theta) \tag{2.12}$$

$$\varepsilon_{ij} = \frac{\alpha \sigma_0}{E} \left(\frac{EJ}{\alpha \sigma_0^2 I_n r} \right)^{\frac{n}{n+1}} \tilde{\varepsilon}_{ij}(n, \theta) \tag{2.13}$$

where $\tilde{\sigma}_{ij}$ and $\tilde{\varepsilon}_{ij}$ are the dimensionless functions of n and θ, and I_n is a constant depending on n. Equations 2.12 and 2.13 describe a type of singularity, as known as the HRR singularity where the stress and strain vary as $r^{-1/(n+1)}$ and $r^{-n/(n+1)}$, respectively. It can be noted that the J integral, as in Equations 2.12 and 2.13, uniquely determines the magnitude of the stress and strain fields of the HRR singularity. These formulations bound both the elastic and plastic region in the SSY condition.

In the close proximity to the crack tip (as r approaches zero), the crack tip is blunted by large strains, diminishing the singularity of the HRR field. This effect of crack tip blunting and large strains was not accounted for in the establishment of HRR field which considered small strain theory. By finite strain analysis of cracked geometries, McMeeking and Parks (1979) showed that the crack-tip blunting caused by large strain invalidate the HRR solution within a distance about 2δ or $x\sigma_0/J$.

By invoking the HRR solutions and 90° intercept definition of CTOD, Shih investigated the displacements at the crack tip and established a unique rela-

tionship between J and CTOD for a given material, which takes the following form:

$$\delta = \frac{d_n}{\sigma_0} \tag{2.14}$$

where d_n is a dimensionless constant mainly depending on strain hardening. The unique relationship between J and CTOD indicates that both parameters are equivalent in characterizing the crack-tip field of elastic-plastic materials.

J-dominance refers to situations where J completely characterizes crack-tip conditions. However, as the spread of plasticity progresses, the J-dominance may no longer remains valid. Figure 2.5 illustrates the influence of plasticity on the crack-tip stress field. It can be seen that in SSY conditions where plasticity is limited, both K- and J-dominated regions exist. Well within the plastic zone, the $1/\sqrt{r}$ singularity vanishes while the HRR singularity still hold valid. Despite the invalidity of $1/\sqrt{r}$ singularity at very short distance from the crack tip, the K still uniquely describes the crack-tip conditions in SSY. Likewise, J still uniquely characterises the crack-tip conditions even though the HRR field is invalid due to large strains within approximately 2δ from the crack tip. It is noteworthy that the HRR singularity is not a necessity for J-dominance as HRR singularity is only one possible solution to the J-dominated region.

In Large Scale Yielding (LSY) conditions where plastic deformation is widespread, J-dominance no longer exists due to significant size of finite strain region. In this situation, single-parameter fracture mechanics is invalid and additional parameters were established to describe the crack tip conditions. This will be elaborated in Section 2.2.5.

2.2.5 *Geometric effect and crack-tip constraint*

By examining stresses in various specimens under plain strain and fully plastic conditions, McClintock (1971) found that the near-tip stresses were dependent on the geometry. Anderson (1988) observed dependence of fracture toughness on crack depth and specimen size for brittle materials. The size dependence was also evidenced for R-curve of ductile materials (Towers and Garwood 1986). According to Towers and Garwood (1986), the specimens with a high level of crack-tip constraint has a lower tearing modulus, and vice versa. Therefore,

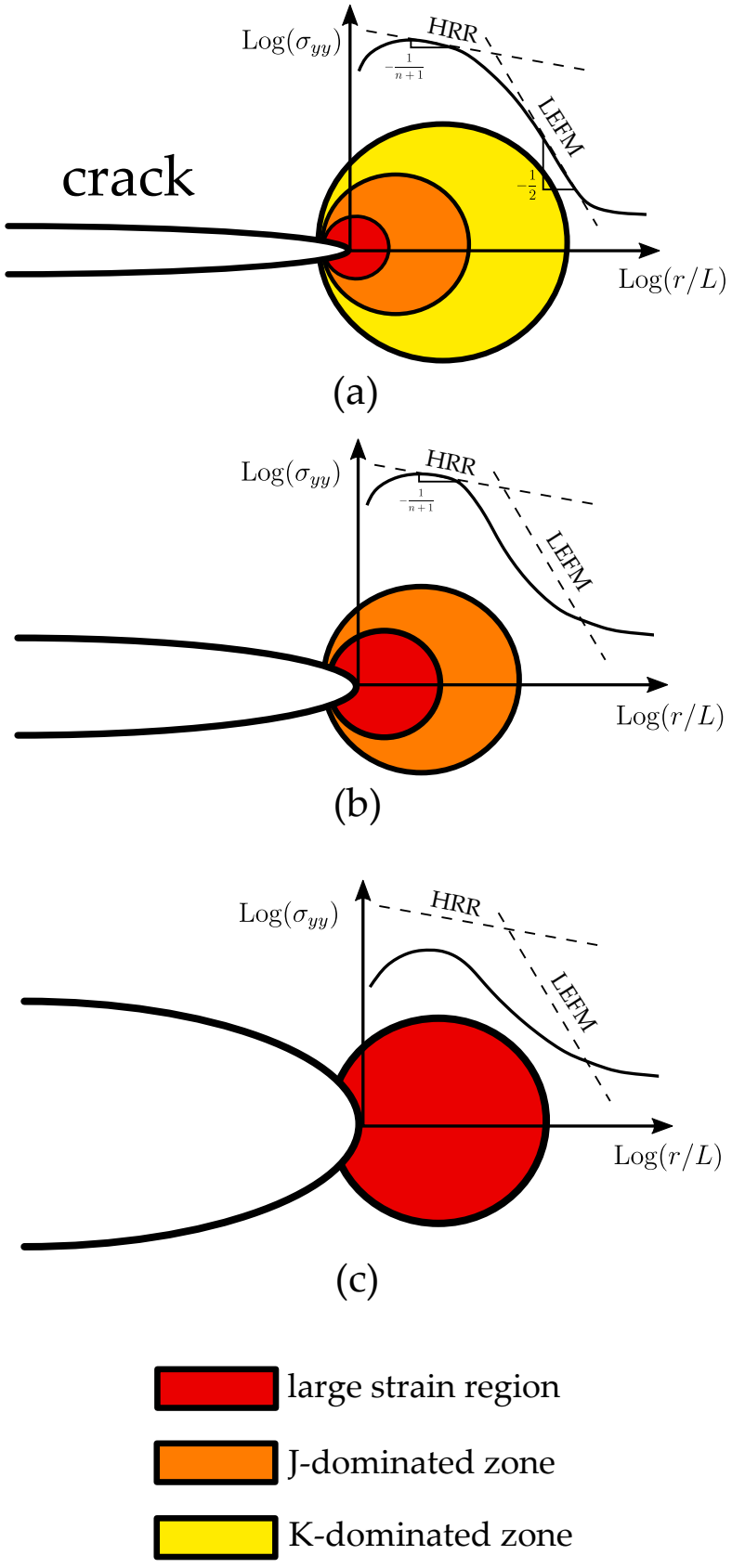

Figure 2.5: Effect of plasticity on the crack-tip stress field: (a) SSY conditions, (b) elastic-plastic conditions, and (c) LSY conditions

herein a single-parameter fracture mechanics may not suffice to uniquely characterises the crack-tip conditions. This has motivated a number of studies that led to the development of a second crack-tip characterising parameter, which will be discussed in the following section.

2.2.6 *The second crack-tip characterising parameter*

2.2.6.1 *The elastic* T *stress*

According to Williams (1957), the stresses ahead of the crack tip can be expressed in an infinite power series. When approaching to the crack tip ($r \to 0$), the third term vanishes, leaving the first and second term in the solution. For an isotropic elastic solid subjected to Mode I loading under plane strain condition, the first two terms of the aforementioned crack-tip stress solution are expressed as:

$$\sigma_{ij} = \frac{K}{\sqrt{2\pi r}} f_{ij}(\theta) + T\delta_{1i}\delta_{1j} \tag{2.15}$$

where T is a uniform stress in the transverse direction perpendicular to the crack opening, and δ_{ij} is the the Kronecker's delta, which is defined as follows:

$$\delta_{ij} = \begin{cases} 0, & \text{for } i \neq j \\ 1, & \text{for } i = j \end{cases} \tag{2.16}$$

FE analysis of the Modified Boundary Layer (MBL) model performed by Kirk et al. (1994) showed that T stress affects the crack opening stress profile, especially when T is negative. When $T = 0$, the stress field corresponds to the limit of SSY where K uniquely characterises the crack-tip field. It should be cautioned that T is an elastic parameter, and will lose its validity and physical meaning when the size of plastic zone is significant relative to the size of the cracked body, as in LSY conditions. Thus, the Q parameter was proposed therein to accommodate the widespread plasticity.

2.2.6.2 *The Q parameter*

O'Dowd and Shih (1991, 1992) showed that crack-tip stresses in the forward sector of the crack-tip region ($|\theta| \leqslant \pi/2$) can be approximately expressed in terms of a sum of a reference field and a difference field as follows:

$$\sigma_{ij} \approx \sigma_{ij(ref)} + Q\sigma_0\delta_{ij} \quad \text{for} \quad |\theta| \leqslant \frac{\pi}{2} \tag{2.17}$$

where $\sigma_{ij(ref)}$ is the reference stress field and is defined as the HRR field, or alternatively, as that for $T = 0$; Q is dimensionless constant that scales with the difference field (or deviation) from the former; σ_0 is the yield stress. It was recommended that the Q parameter be calculated at $r = 2J/\sigma_0$, where the finite strain effects vanish (McMeeking and Parks 1979; Rice et al. 1979; Dodds et al. 1993b). It should be noted that Q is applicable to stationary crack only, as the stress and strain fields ahead of a growing crack render it invalid (Dodds et al. 1993b, 1993a).

2.2.7 *Engineering Critical Assessment and Failure Assessment Diagram*

Engineering Critical Assessment (ECA) or Fitness-For-Service (FFS) is a procedure based on fracture mechanics principles for determining the flaw tolerance of engineering structural components. The key ingredients include applied stresses, structure geometry and material properties. To the best knowledge of the authors, the Failure Assessment Diagram (FAD) is probably the most widely used approach for performing an ECA. This approach has been included in industry ECA/FFS standards and recommended procedures, such as R6, BS 7910, API 579 and DNVGL-RP-F108. The FAD is originally derived from the strip-yield model with modifications (Dowling and Townley 1975; Harrison et al. 1976) and was later developed into a more robust version based on elastic-plastic J solution (Bloom 1980; Shih et al. 1981). As shown in Figure 2.6, the FAD consists of a Failure Assessment Line (FAL) and a cut-off line representing the limit of plastic collapse. The FAL represents the locus of predicted failure points

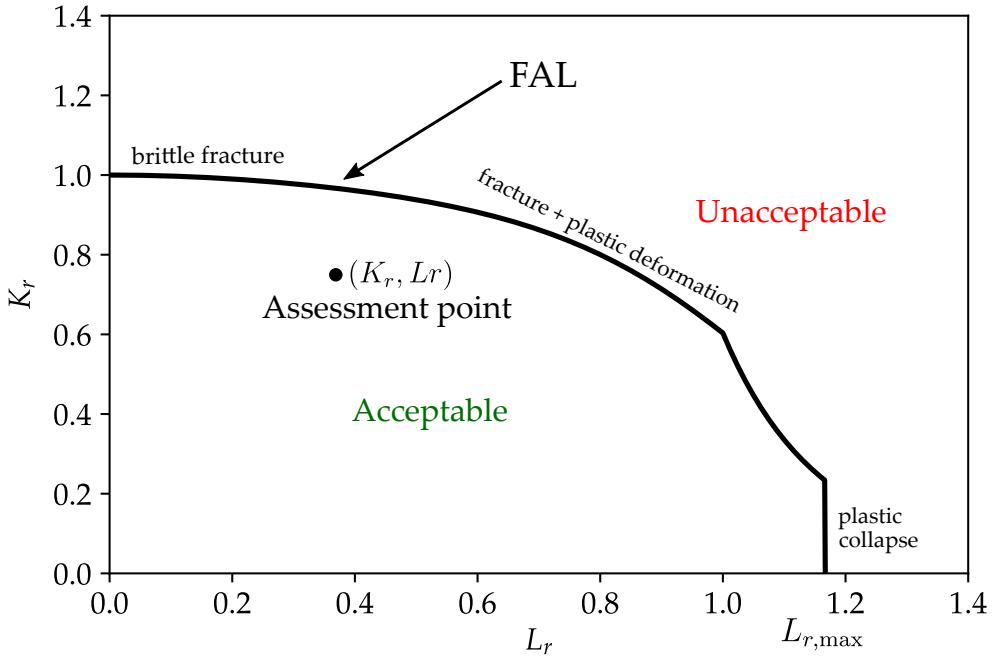

Figure 2.6: Schematic of a typical failure assessment diagram spanning the range of fully brittle to fully plastic behaviour

defined by coordinates (L_r, K_r). The ordinate K_r is a measure of the proximity to brittle fracture, and is defined as:

$$K_r = \frac{K_I}{K_{mat}} \tag{2.18}$$

where K_I is the applied stress intensity factor of cracked component subjected to Mode I loading, and K_{mat} is the fracture toughness. The abscissa L_r is a measure of the proximity to plastic collapse, and is defined as:

$$L_r = \frac{\sigma_{ref}}{\sigma_y} \tag{2.19}$$

The FAD covers failure modes ranging from full brittle fracture where $K_r = 1$ to fully ductile behaviour where $L_r = 1$ and the structure fails by plastic collapse, and the interaction of both mechanisms ($K_r < 1$ and $L_r < 1$). The structure is considered acceptable (safe) if the assessment point is situated within the FAC, and unacceptable (potentially unsafe) otherwise. Elastic-plastic J analysis is required to establish a rigorous FAD due to its J-based nature. This approach, however, is computationally-expensive and time-consuming. Therefore, simplified approaches were envisaged, one of which is the well-known reference

stress method proposed by Ainsworth (1984). The reference stress method was originally a modification based on the Electric Power Research Institute (EPRI) J estimation scheme. The EPRI scheme postulates that the total J is calculated separately as the sum of elastic and plastic components as follows:

$$J_{tot} = J_{el} + J_{pl} \tag{2.20}$$

where J_{el} is the elastic component of J and can be obtained from K_I; J_{pl} is the plastic component of J, which is expressed as:

$$J_{pl} = \alpha \varepsilon_0 \sigma_0 b h_1 \left(a/W, n\right) \left(\frac{P}{P_0}\right)^{n+1} \tag{2.21}$$

where b is the length of uncracked ligament; a is the crack length; h is the function of geometry and hardening exponent, and has been tabulated for various geometries in literature (Kumar et al. 1981, 1984; Kumar and German 1988; Zahoor 1989); P is the applied load and P_0 is the limit load. Since Equation 2.21 assumes a power law material behaviour, therefore it is not readily suitable for materials with a non-power law behaviour, such as those with a yield plateau. Ainsworth (1984) generalised the EPRI approach to accommodate the flow behaviour of real materials by invoking the concept of reference stress σ_{ref} defined by:

$$\sigma_{ref} = \frac{P}{P_0}\sigma_0 \tag{2.22}$$

By making appropriate assumptions, Ainsworth (1984) arrived at a J solution which was later developed into the current form as follows, by further modifications and incorporation of the SSY correction:

$$J = \frac{K_I^2}{E'}\left[\frac{E\varepsilon_{ref}}{\sigma_{ref}} + \frac{\sigma_{ref}^3}{2\sigma_0^2 E\varepsilon_{ref}}\right] \tag{2.23}$$

where ε_{ref} is the reference strain defined as the strain corresponding to the reference stress σ_{ref} on the uniaxial true stress-true strain curve; σ_0 is usually

defined as the yield stress σ_y. By recasting Equation 2.23 into the form of a FAL, the following formulation is obtained:

$$K_r = \left[\frac{E\varepsilon_{ref}}{L_r\sigma_y} + \frac{L_r^3\sigma_y}{2E\varepsilon_{ref}}\right]^{-0.5} \tag{2.24}$$

The above equation is the formulation of the Option 2 FAD provided in BS 7910:2013 (or Level 2B/3B as in its predecessor BS 7910:2005) and R6, in which compendium of stress intensity factor solutions and reference stress (or limit load) solutions for various geometries and configurations are given.

The FAD approach as in BS 7910, R6 and API 579 have been widely-used for ECA of engineering components across various sectors with evidenced conservatism and versatility. In accessing the flaw tolerance of pipelines subjected to plastic straining, however, uncertainties and deficiencies of the conventional FAD approach have been reported. This has led to the research and development of methodologies for assessing pipelines under large strains. Section 2.3 will elaborate on the current status, technological gaps and outlook of pipeline strain-based assessment.

2.3 STATE OF THE ART ON STRAIN-BASED FRACTURE ASSESSMENT

2.3.1 *Overview*

Over the past few decades, extensive research has been carried out to develop strain-based fracture assessment methods. To the best of author's knowledge, Bratfos (2002) is among the first to propose a strain-based ECA approach which is applicable to scenarios where the applied stress is well in excess of yield strength. This procedure is based on the BS 7910:2005[1] Level 2 (equivalent to Option 2 of BS 7910:2013) FAD with adjustment to the cut-off limit, $L_{r,max}$. Later in 2006, DNV published a recommended practice DNV-RP-F108[2] as an outcome of the collaborative research with other two research institutes, TWI and SINTEF. The recommended practice given in DNVGL-RP-F108 follows BS 7910:2013 Option 2 FAD with adjustments and modifications.

1 now superseded by BS 7910:2013 (refereed to as BS 7910 hereafter)
2 now superseded by DNVGL-RP-F108

Upon the completion of a Joint Industry Projecct (JIP) - 'Fracture Control-Offshore Pipelines' which includes a series of studies on fracture behaviour of offshore pipelines, SINTEF has published a procedure dedicated for the strain-based fracture assessment. The procedure featuring parametric equations used to estimate crack driving force was proposed for offshore pipelines containing circumferential surface-breaking flaws (Østby 2005; Østby 2007). The equations were fine-tuned to the parametric FEA using LINKpipe software, and the CDF in terms of CTOD was formulated as a function of the applied strain, pipe geometry, flaw sizes, weld misalignment, material properties, weld strength mismatch and internal pressure. The effect of misalignment, weld strength mismatch and internal pressure were accounted for by using the concepts of effective wall thickness and ligament (Østby 2005).

Modifications to the existing stress-based methods, such as BS 7910:2013 Option 2 FAD, have been also proposed by other researchers. For example, Tkaczyk et al. (2009a) applied a correction factor to Kastner limit load solution (Kastner et al. 1981); Smith (2012) proposed a correction factor to the fully-plastic term of the BS 7910:2013 Option 2 FAD equation.

In North America, the construction and operation of strain-based pipelines has driven the development of Strain-Based Design (SBD) methods which enable the Tensile Strain Capacity (TSC) to be evaluated (Wang et al. 2006, 2008; Wang et al. 2011b; Kibey et al. 2010; Tang et al. 2010; Tang et al. 2014; CSA 2007; Wang et al. 2004; Wang et al. 2011a; Fairchild et al. 2011b, 2014). These models formulated the maximum tensile strain that can be safely sustained by pipeline girth welds as a function of influencing parameters, including pipe geometry, flaw sizes, material properties and internal pressure.

Center for Reliable Energy Systems (CRES) has developed a four-tier procedure for predicting tensile strain capacity (Wang et al. 2011c). The CRES procedure is applicable when pipes are subjected to biaxial loading. The tensile strain capacity was expressed as a function of a number of parameters, including pipe diameter, wall thickness, flaw sizes, the apparent toughness of the weld/heat affected zone (HAZ) and the parent material yield to tensile ratio (Y/T). However, the aforementioned equations do not account for weld mismatch, hi-lo misalignment and the biaxial loading effect induced by internal pressure.

ExxonMobil has undertaken a considerable amount of work to establish methods for TSC prediction. A three-tier procedure has been reported (Fairchild et al. 2011b). The procedure consists of three tiers of assessment with increasing complexity and accuracy, comprising simplified closed-form equations and a detailed numerical modelling scheme. More recently, ExxonMobil proposed a new TSC prediction procedure featuring the utilisation of the Gurson-Tvergaard-Needleman (GTN) model in lieu of conventional fracture mechanics model which simulates a known static crack (Fairchild et al. 2014). Numerous full-scale pipe tests were performed to validate the FE models and the proposed closed-form solutions.

2.3.2 *Modification to existing stress-based method*

Research work was also carried out to modify current stress-based procedures such as those codified in BS 7910 and R6 to extend their applicability to strain-based assessment. The greatest merit is that these approaches maximally utilise the existing analytical solutions, including elastic stress intensity factor and reference stress/limit load solutions.

2.3.2.1 *DNVGL-RP-F108*

DNVGL-RP-F108 provides recommendations on the assessment of pipeline girth welds subjected to large straining. For strains beyond 0.4%, an ECA "static, full" assessment is advised, based on a BS 7910 Option 2 FAD and taking into account the effect of ductile tearing. For strains below 0.4%, an assessment based on BS 7910 Option 2 FAD without consideration of tearing is suggested. Weld mismatch is not explicitly incorporated, but weld strength overmatching is required. If the effect of hoop stress generated by internal pressure is not included in the applied stress, DNVGL-RP-F108 recommends compensating for the non-conservatism by using high constraint Single Edge Notched Bend (SENB) specimens. This has been nevertheless criticised for being arbitrary, as no quantitative estimation was given in order to compensate the effect of internal pressure by using a high constraint fracture toughness specimen in an ECA (Cosham and Macdonald 2015). It is therefore recommended that for assessment of situations with longitudinal strain above 0.4% under internal

pressure solid 3D FEA shall be performed. The treatment of residual stresses in the assessment follows the guidance given in BS 7910, allowing for relaxations at higher loadings.

The parent pipe stress-strain curve is used to obtain an equivalent stress that corresponds to the maximum strain that the pipe will undergo during reeling and un-reeling. For the first strain cycle, the “as-received" stress strain curve is adopted. For the second and subsequent strain cycles, the stress-strain curve of the parent pipe in the pre-strained condition is used. This aims to account for the Bauschinger effect. To assess the stable crack extension during the whole reeling process, analyses should be conducted for each tensile strain increment during reeling. The allowable crack extension is restricted to 1 mm. The weld ‘hi-lo’ misalignment is considered using the Neuber method for applied strains above 0.4%, but the weld toe effect is neglected.

As mentioned above, DNVGL-RP-F108 uses the same FAD as BS 7910 Option 2, but with an extension for displacement controlled loading in which pipe is plastically strained globally. The cut-off limit, $L_{r,max}$, can be adjusted based on experimental tests, or via the following equation in which the flow stress (which, in the case of BS 7910 analyses, appears in the numerator of Equation 2.25) is replaced by ultimate tensile strength (UTS) if the reference stress for cylinder (Kastner limit load (Kastner et al. 1981)) is used:

$$L_{r,max} = \frac{UTS}{YS} \tag{2.25}$$

Alternatively, if the reference stress for a plate containing surface flaw is used, the true values of the yield strength (YS) and ultimate tensile strength (UTS) are used instead:

$$L_{r,max} = \frac{(1 + \varepsilon_{UTS}) \cdot UTS}{(1 + \varepsilon_{YS}) \cdot YS} \tag{2.26}$$

Tkaczyk et al. (2009a) demonstrated Kastner limit load solution (Kastner et al. 1981), used by DNVGL-RP-F108, to be inappropriate for pipelines subjected to plastic straining. Instead, they modified it by applying a correction factor.

The correction factor was fine-tuned with extensive FEA of pipes containing an external surface-breaking crack subjected to tensile load.

2.3.2.2 *Smith*

Smith (2012) applied a correction factor to the BS 7910 Option 2 FAD to extend its use for the large-scale yielding condition. In contrast to Tkaczyk et al. (2009a), the correction was applied to the first term of the FAD equation rather than to the reference stress solution. Based on a theoretical analysis of the J-integral for a cracked geometry, Smith (2018) arrived at the following relationship:

$$\frac{J_p}{J_e} = \frac{2n}{n+1}\frac{E\epsilon_{ref}}{\sigma_{ref}} \tag{2.27}$$

where J_p and J_e are the plastic and elastic J-integrals respectively, ϵ_{ref} is the reference strain, σ_{ref} is the reference stress, and n is the hardening exponent. For low strain hardening materials (high strain hardening exponent, n), Equation 2.27 becomes:

$$\frac{J_p}{J_e} \approx \frac{2E\varepsilon_{ref}}{\sigma_{ref}} \tag{2.28}$$

Equation 2.28 implies that the current BS 7910:2013 Option 2 FAD method, in which $J_p/J_e = E\varepsilon_{ref}/\sigma_{ref}$, may significantly under-estimate the CDF for a cracked body that undergoes large-scale yielding. Smith (2012) demonstrated that the potential non-conservatism could be removed by using a correction factor, denoted as X, to the first term in the equation of the BS 7910 Option 2 FAD:

$$K_r = \left(\frac{X \cdot E\epsilon_{ref}}{L_r\sigma_y} + \frac{{L_r}^3\sigma_y}{2E\varepsilon_{ref}}\right)^{-0.5} \tag{2.29}$$

where X ranges from unity to two as the applied loading increases, and is expressed as follows:

$$X = \frac{3 + \tanh(c_1(L_r - c_2))}{2} \tag{2.30}$$

Smith (2012) preliminarily compared the modified FAD using the upper bound value of X (equal to 2) with the EPRI-type equation of Chiodo and Ruggieri (2010) and the BS 7910 Option 2 FAD. It was demonstrated that BS 7910 Option 2 FAD was non-conservative for low-hardening material and small cracks, whereas the modified FAD was unduly conservative. Further development may be required to fine-tune the value of c_1 and c_2 for a wide range of geometries and flaw sizes.

This approach may be very sensitive to stress-strain response for materials with low strain hardening and those with yield discontinuity (i.e. Lüders plateau). For a slight increase in the applied strain, a dramatic increase in the CDF is found. This may result in considerable error in CDF estimation when a minor error is made in evaluating the loads. The comparison made between the modified FAD and the method of Chiodo and Ruggieri (2010) as well as the full-scale test imply that in order to make the modified FAD suitably conservative the correction factor may be expressed as a function including parameters of the crack configurations and material properties. However, this wipes out the geometry-independent nature of the original BS 7910 Option 2 FAD, rendering the assessment less convenient. In addition, as BS 7910 Option 2 FAD combined with Kastner limit load solution was found to under-estimate J for some cases and over-estimate J for other cases (Tkaczyk et al. 2009a), the correction factor X will accordingly be above and below unity, respectively. This is contradictory to the range of value mentioned in the work of Smith (2012). Therefore, further study and justification may be required for robust use of this approach.

2.3.3 *Extension to EPRI scheme for fully-plastic J estimate*

2.3.3.1 *Chiodo and Ruggieri*

Chiodo and Ruggieri (2010) put their efforts into extending the use of the EPRI framework to pipes containing a circumferential flaw subjected to plastic

bending. Both fully plastic J and CTOD estimations were formulated. The equations for J and CTOD are:

$$J_p = \alpha\varepsilon_y\sigma_y b h_1\left(\frac{a}{t}, \frac{D}{t}, \frac{2c}{\pi D}, n\right)\left(\frac{M}{M_0}\right)^{n+1} \tag{2.31}$$

$$\delta_p = \alpha\varepsilon_y\sigma_y b h_2\left(\frac{a}{t}, \frac{D}{t}, \frac{2c}{\pi D}, n\right)\left(\frac{M}{M_0}\right)^{n+1} \tag{2.32}$$

where b is the uncracked ligament ($b = t - a$). A total of 405 3D FE analyses were performed to calibrate the above equations. The values of non-dimensional functions, h_1 and h_2, are determined by applying least squares fit to the linear progression of the normalised fully plastic J ($J_p/\alpha\varepsilon_y\sigma_y b$) and normalised CTOD ($\delta_p/\alpha\varepsilon_y b$) with $M/M^{(n+1)}$ data. Values of h_1 and h_2 are tabulated in the work of Chiodo and Ruggieri (2010).

Validations of Equations 2.31 and 2.32 against FEA of realistic pipeline reeling scenarios were also conducted by Chiodo and Ruggieri (2010). Good agreement was observed between the estimated crack driving force and the numerical results. Nevertheless, there are some shortcomings for this approach:

- For low hardening material (e.g. n=20) and longer crack length ($0.12 \leqslant 2c/\pi D \leqslant 0.20$), the linear relation is guaranteed for crack sizes in the range of $a/t \leqslant 0.25$, hence the validity of this approach is limited to this range of crack sizes.

- This approach does not consider the effect of Lüders plateau. Instead, a continuous yielding fit with a Ramberg-Osgood model was adopted for the establishment of the fully plastic crack driving force equation. However, a minor difference in J-integral was demonstrated between discontinuous yielding material and Ramberg-Osgood power-law material when the applied load (M/M_0) was sufficiently high to cause large plastic deformation.

- Due to the stress-based nature of Equations 2.31 and 2.32, they are very sensitive to the applied loads. Therefore, a minor error made in the

evaluation of the applied bending moment may lead to inaccuracy in the crack driving force estimation.

2.3.3.2 *Parise approach*

The stress-based nature of the approach proposed by Chiodo and Ruggieri (2010) was demonstrated to be a disadvantage due to its sensitivity to high applied load (Parise et al. 2015). It was advocated by Parise et al. (2015) that a strain-based approach may be more suitable for high strain and displacement-controlled scenarios, such as reeling installation. Parise et al. (2015) recast the EPRI framework in a strain-based form as:

$$J_p = \alpha \varepsilon_0 b g_1 \left(\frac{a}{t}, \frac{2c}{\pi D}, \frac{D}{t}, n\right) \left(\frac{\varepsilon_p}{\varepsilon_0}\right)^{\frac{n+1}{n}} \tag{2.33}$$

where b is the uncracked ligament and g_1 is the dimensionless scaling factor that depends on the crack sizes and strain hardening exponent, n.

Extensive parametric FE analyses were performed to calibrate the proposed strain-based framework. A library of dimensionless factor, g_1 , is provided in Parise et al. (2015). Good agreement was achieved between the proposed method and the numerical results. Note that this approach has not been fully validated by experiments. The range of application is based on the FE analyses performed.

2.3.4 *Budden and Ainsworth*

Budden (2006) established a strain-based FAD framework which is similar to the stress-based Option 2 FAD in BS 7910 or R6. The strain-based assessment procedure was later refined by Budden and Ainsworth (2012). In the strain-based FAD, the strain ratio, D_r, is used in lieu of the load ratio, L_r, and is expressed by:

$$D_r = \frac{\varepsilon_{ref}}{\varepsilon_y} \tag{2.34}$$

Substituting Equation 2.34 in the stress-based Option 2 FAD in R6 leads to the expression of the strain-based FAD equation:

For $D_r \leqslant 1$

$$K_r = f^*(D_r) = \left[\frac{D_r}{\sigma_{ref}/\sigma_y} + \frac{\sigma_{ref}/\sigma_y}{2D_r}\right]^{-0.5} \tag{2.35}$$

And for $D_r > 1$

$$K_r = f^*(D_r) = \left[\frac{2E\varepsilon_{ref}}{\sigma_{ref}}\right]^{-0.5} \tag{2.36}$$

Figure 2.7 shows an example of a typical strain-based FAD. The research work carried out by Cheaitani (2016) demonstrated that the strain-based FAD approach is likely to provide increasingly more conservative assessments for small flaws, and less conservative (potentially non-conservative) assessments for larger flaws and/or materials with no or low work hardening. Both of these limitations are highly relevant to assessment of pipelines.

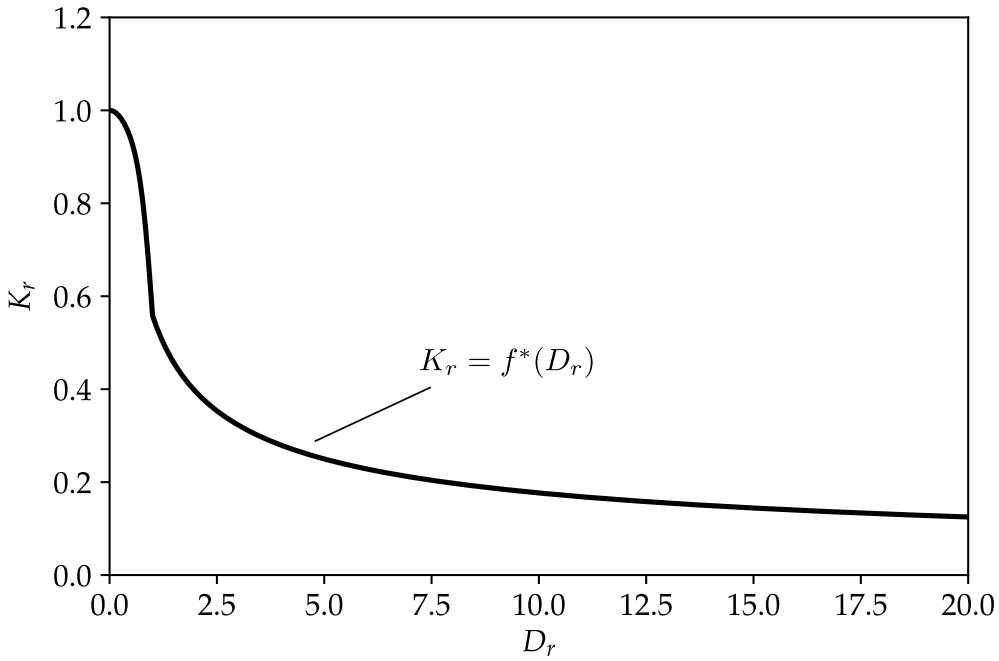

Figure 2.7: A schematic of strain-based FAD where the FAC is defined by function $f^*(D_r)$

2.3.5 *Nourpanah approach*

Nourpanah and Taheri (2010) developed a reference strain J estimation equation primarily for offshore pipelines. The reference strain was determined as the equivalent strain in the uncracked body, ε_{unc}. The J estimation is expressed as:

$$\frac{J}{\sigma_y t} = f_1 \varepsilon_{unc} + f_2 \tag{2.37}$$

where f_1 and f_2 are functions of pipe and crack geometries and material properties. A total of 300 FE analyses of pipes containing externally circumferential surface cracks were performed to evaluate f_1 and f_2, which are tabulated in (Nourpanah and Taheri 2010).

The parametric FE analyses suggested that the normalised crack driving force $J/\sigma_y t$, was independent of the yield strength. Therefore, the fact that the proposed equation is applicable to a range of pipeline materials, despite the fact that that only one yield strength value was adopted for the parametric FE analyses. The solution was recommended to be used for strains ranging from 1.5% to 4%.

2.3.6 *Jia approach*

To make the strain-based FAD framework proposed by Budden (2006) more robust, Jia et al. (2016) established a new reference strain solution for offshore pipelines installed by reeling. The reference strain was evaluated using the J solutions derived by Nourpanah and Taheri (2010). Equation 2.37 was rearranged by Jia et al. (2016) as:

$$J = J_e \frac{2E\varepsilon_{ref}}{\sigma_{ref}} \tag{2.38}$$

By substituting Equation 2.38 into Equation 2.38, Jia et al. (2016) obtained:

$$\begin{aligned} f_1\varepsilon_{unc} + f_2 &= \frac{J}{\sigma_y t} \\ &= 2E\varepsilon_{ref}\frac{J_e}{\sigma_y \sigma_{ref} t} \end{aligned} \tag{2.39}$$

Jia et al. (2016) examined the effects of geometry and material properties on the reference strain using Equation 2.39. It was shown that the uncracked strain had only a marginal effect on the $\varepsilon_{ref}/\varepsilon_{unc}$ ratio when applied strains greater than 2% determined from the uncracked pipe were applied to the cracked pipe. In addition, the effect of the outer diameter of a pipe on the $\varepsilon_{ref}/\varepsilon_{unc}$ ratio was demonstrated to be negligible. Hence, the $\varepsilon_{ref}/\varepsilon_{unc}$ ratio can be expressed by:

$$\frac{\varepsilon_{ref}}{\varepsilon_{unc}} = f\left(\frac{a}{t}, \frac{a}{c}, \frac{\sigma_y}{\sigma_u}\right) \tag{2.40}$$

A polynomial equation was fitted to 300 sets of ref $\varepsilon_{ref}/\varepsilon_{unc}$ ratios calculated using Equation 2.40. The detailed form of the equation and values of coefficients were given in Jia et al. (2016). Comparisons of J versus strain for some specific cases using the methods of Jia et al. (2016) , Tkaczyk et al. (2009a), Parise et al. (2015) and SINTEF (Østby 2005) suggested that the method of Jia et al. (2016) was in better agreement with that of Tkaczyk et al. (2009a), the methods from Jia et al. (2016) and Tkaczyk et al. (2009a) predicted higher crack driving force than that predicted using other methods (Budden and Ainsworth 2012).

2.3.7 *Strain capacity approach*

2.3.7.1 *PRCI/CRES approach*

CRES, C-FER Technologies (C-FER) and Microalloying International for Pipeline cooperatively performed a project to develop a TSC prediction procedure. The project was funded by the Pipline Research Council International (PRCI) and the Pipeline and Hazardous Materials Safety Administration (PHMSA) of the US Department of Transportation. Liu et al. (2012) presented a TSC procedure that comprises four tiers of assessments with increasing complexity and accuracy.

The Level 1 model aims at a quick estimation of the TSC. The values of TSC for selected cases were tabulated in the work of Wang et al. (2011b). Level 2 provides parametric equations for TSC estimation that were developed for fixed wall thickness (15.9 mm) and internal pressure (corresponding to σ_{hoop}/σ_y where σ_{hoop} is hoop stress arising from internal pressure). Two sets of equations were formulated for girth welds fabricated using Gas Metal Arc Welding (GMAW) and Flux Cored Arc Welding (FCAW) / Shielded Metal Arc Welding (SMAW) techniques, respectively. The TSC is expressed as a function of a number of influencing parameters, as shown below:

$$\varepsilon_c = f\left(\frac{a}{t}, \frac{2c}{t}, \frac{h}{t}, \frac{\sigma_y}{\sigma_u}, \frac{\sigma_{hoop}}{\sigma_y}\right) \tag{2.41}$$

where σ_{uw} is the ultimate tensile strength of weld metal, and h is the weld misalignment.

Level 3 includes two options, Level 3a and 3b. Level 3a adopts the single value of the fracture toughness obtained at the tearing initiation point. Level 3b uses the fracture resistance curve (CTOD-R) curve in the assessment. The failure or tearing instability is determined using the tangency approach. In Level 4, detailed 3D FEA is recommended.

Note that the above procedure is established based on numerical and experimental analyses of internal surface flaws. The equations used in Levels 2 and 3 are valid for internal pressure producing hoop stress in the range of 60% to 80% of the base metal yield strength.

2.3.7.2 *ExxonMobil approach*

Recently, ExxonMobil published its newly developed procedure for TSC prediction (Tang et al. 2014; Fairchild et al. 2014), which explicitly simulates ductile tearing with the utilisation of damage mechanics (GTN model). To facilitate the use of the GTN model, a calibration needs to be performed to determine the GTN damage parameters. A series of small-scale tests including notched round bar tensile tests, small-punch tests and SENT tests were performed. Initially, basic sets of parameters were determined based on the notched round bar tensile tests and small punch tests. Then, the remaining parameters were

calibrated by matching the CTOD-R curve evaluated from FEA of the SENT specimens to that determined from the SENT tests.

Full-scale pipe tests were performed to validate the GTN-based FE model and fairly good agreement was reached. Note that the TSC obtained from experiments and FEA were determined as the strain at the maximum load by tracing the load-strain response. The difference between TSC determined at tearing initiation and at maximum load was also investigated. It was shown that TSC determined at tearing initiation was over-conservative compared with that determined at the maximum load (Tang et al. 2014; Fairchild et al. 2014). Hence, the maximum load criterion is deemed suitable and is used throughout the FE analyses.

Closed-form equations have been developed based on the FE results using the GTN model. A single set of equations is expressed Tang et al. (2014):

$$\varepsilon_{c,0.8} = f\left(\frac{D}{t}, \frac{a}{t}, \frac{2c}{t}, \frac{h}{t}, \frac{\delta_1}{t}, \frac{K}{\sigma_y}, n, \frac{\sigma_{uw}}{\sigma_u}\right) \tag{2.42}$$

where δ_1 is the crack opening displacement at 1 mm crack growth, K is the strength coefficient, n is the hardening exponent, σ_{uw} is the ultimate strength of the weld metal and σ_u is the ultimate strength of the parent material.

A pressure factor was developed to correlate the TSC at the internal pressure (generating a hoop stress of 80% of the yield strength of the parent material) with that at an arbitrary internal pressure level. The Pressure Factor (PF) is expressed as a function of the normalised hoop stress (percentage of σ_{hoop}/σ_y) created by the pressure of interest. Then, the TSC at a pressure of interest can be calculated using:

$$\varepsilon_c = \begin{cases} PF \cdot \varepsilon_{c\text{-}0.8}, & \text{if } \varepsilon_c < \frac{2}{3}UEL. \\ \frac{2}{3}UEL, & \text{if } \varepsilon_c \geqslant \frac{2}{3}UEL. \end{cases} \tag{2.43}$$

where ε_{crit} is the critical strain or tensile strain capacity at a pressure of interest and $\varepsilon_{crit,0.8}$ is the tensile strain capacity at an internal pressure inducing a hoop stress with a magnitude of 80% of yield strength.

A total of 93 full-scale pipe tests were carried out to validate the FEA that used the GTN model and also the proposed TSC equation. An extensive range of variables was covered in the tests. Tang et al. (2014) showed that good agreement was obtained between the proposed TSC equation and full-scale tests.

2.3.8 *SINTEF procedure*

Stiftelsen for Industriell og Teknisk Forskning (SINTEF) procedure was developed during the Joint Industry Project 'Fracture Control – Offshore Pipelines' (Østby 2007). A simplified strain-based assessment procedure featuring the approximation of a linear relationship between the increment in the CTOD and the applied strain has been developed by SINTEF. This linear relationship was utilised in other studies to develop strain-based assessment methods (Nourpanah and Taheri 2010).

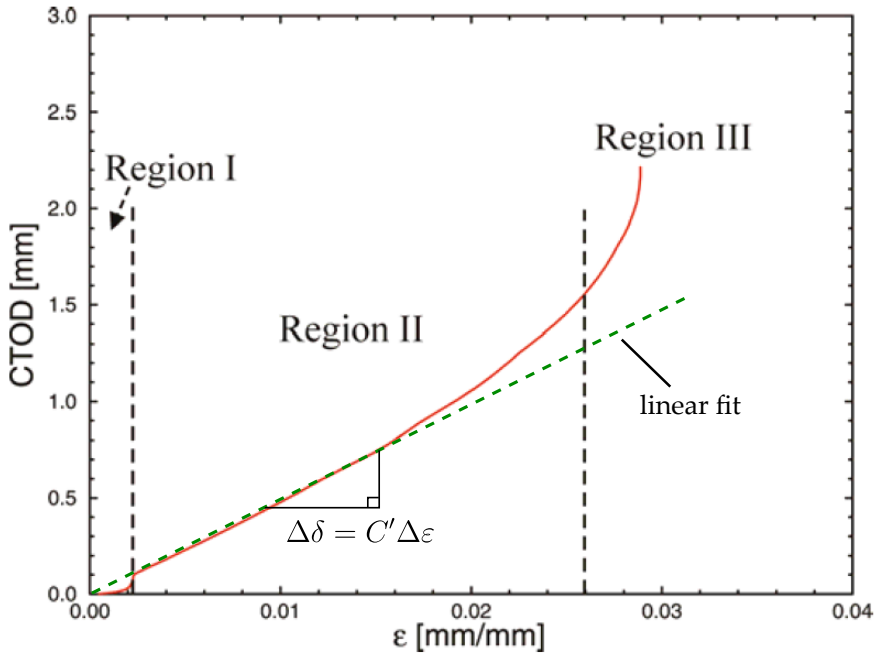

Figure 2.8: CTOD versus strain relationship showing predominant linearity strains ranging from 0.2% to 1.6% (adapted from Østby (2005))

The evolution of the CTOD versus the applied strain is split into three regions, as shown in Figure 2.8. In Region I, the global behaviour of pipe is elastic and CTOD increases quadratically with the applied strain. As the plasticity spreads through the uncracked ligament, CTOD increases rapidly. At the end of Region

I, net section yielding occurs. CTOD begins to increase linearly with the applied strain throughout Region II, and the increase of CTOD can be expressed as:

$$\Delta\delta = C\prime\Delta\varepsilon \tag{2.44}$$

where $\Delta\delta$ is the increment of CTOD, $\Delta\varepsilon$ is the increment of applied strain and C' is a function depending on crack geometry, material properties, weld mismatch, weld misalignment and internal pressure. Replacing $C\prime$ with a normalised $C = C'/t$ leads to:

$$\Delta\delta = tC\Delta\varepsilon \tag{2.45}$$

The 'total' CTOD can thus be obtained via integration over the whole applied strain range:

$$\begin{aligned}\delta &= t\int_0^{\varepsilon} C\,(a_{eff}/t)\,d\varepsilon \\ &= t\int_0^{\varepsilon} f\left(\frac{a}{t}, \frac{2c}{\pi D}\right)\cdot g\left(\frac{a}{t}, \frac{2c}{\pi D}, \frac{\sigma_y}{\sigma_u}\right) d\varepsilon\end{aligned} \tag{2.46}$$

where f is a dimensionless function depending on a/t and $2c/\pi D$, and g is a dimensionless function depending on a/t, $2c/\pi D$ and σ_y/σ_u. It is known that the yielding behaviour of the cracked pipe is affected by the biaxial loading, weld mismatch and weld misalignment. Biaxial loading increases the axial load at yield for a pipe with and without a crack, while weld mismatch and misalignment modify the axial load at yield for a pipe with a crack. To incorporate these effects in the crack driving force estimation, Østby (2005) proposed the concept of effective wall thickness and ligament height. The effects of biaxial loading, weld strength mismatch and misalignment on the crack driving force are quantified by the changes in the effective wall thickness and ligament height. This concept may be promising as the structure of the crack driving force equation remains unchanged.

Validations against full-scale pressurised pipe tests were performed to provide confidence in the SINTEF approach (Østby 2007). Nevertheless, based on the assumptions and the cases studied in the numerical modelling, the following limitations can be identified:

- The crack driving force equation does not account for the effect of D/t ratio.
- Only Power-law hardening materials are considered in the numerical modelling to establish the SINTEF procedure, thus restricting its use for other shapes of stress-strain behaviour, particularly, for material exhibiting Lüders plateau.

2.3.9 *Comparison of strain-based assessment methods*

Each method aforementioned has its range of validity and applicability depending on its formulation, associated numerical simulation and possible experimental validation programme. Table 2.1 compares the range of validity and capability of different strain-based assessment methods covered in the literature review.

While each method has its own validity and capability range of flaw sizes and pipe geometry, the DNV and BS 7910 Smith approach (based on BS 7910 stress intensity factor (SIF) and reference stress solutions) seem more flexible and robust in terms of geometry limitations.

While the FAD-based approaches provide generic solutions, more comprehensive and pipeline-specific procedures are given by CRES, ExxonMobil and SINTEF methods, with accommodation of weld mismatch, 'hi-lo' misalignment and internal pressure.

Table 2.1: A summary of the range of validity of the strain-based fracture assessment methods

Approach	Pipe geometry		Flaw sizes		Pipe material				Weld property		Loading	
	t	D	a	2c	Steel grade	Y/T	hardening exponent	UEL	Overmatch	Misalignment	Applied strain	Internal pressure
DNV	N/A	N/A	N/A	$0a/2c \leqslant 1.0$	N/A	N/A	N/A	N/A	Required	Neuber's rule	N/A	conservative approach
BS 7910 Smith	N/A	N/A	N/A	$0a/2c \leqslant 1.0$	N/A	N/A	N/A	N/A	N/A	Annex D	N/A	N/A
Chiodo	N/A	N/A	$0.1 < a/t < 0.5$	$0.04 < 2c/\pi D < 0.2$	N/A	N/A	N/A	N/A	N/A	N/A	N/A	N/A
Parise	N/A	$10 < D/t < 20$	$0.1 < a/t < 0.5$	$0.04 < 2c/\pi D < 0.2$	N/A	N/A	5 - 20	N/A	N/A	N/A	N/A	N/A
Nourpanah	N/A	$10 < D/t < 30$	$0.1 < a/t < 0.5$	$0.05 < 2c/\pi D < 0.2$	X60 - X80	0.659 - 0.846	10 - 25	N/A	N/A	N/A	1.5 % - 4%	N/A
Jia	N/A	$10 < D/t < 30$	$0.1 < a/t < 0.5$	$0.05 < 2c\pi D < 0.2$	X60 - X80	0.659 - 0.846	10 - 25	N/A	N/A	N/A	2 % - 4 %	N/A
CRES	12.7 - 25.4mm	304 - 1219mm	$0.05 < t/D < 0.5$	$1 < 2c/t < 20$	X56 - X100	0.75 - 0.94	N/A	$5.9\% - 13\%$	0 - 30%	$0 < h/t < 0.2$	N/A	0 - 80%
ExxonMobil	13 - 36mm	8.625 - 48 inch	1.35-6.7mm	15 - 200mm	<X80	0.71 - 0.93	N/A	5.9%-13%	0 - 40%	0 - 4.3mm	N/A	0 - 80%
SINTEF	15 - 35mm	$20 < D/t < 40$	$a/t < 0.35$	<300mm	N/A	0.82 - 0.93	N/A	N/A		$h/t < 0.15$ (when $a/t < 0.3$)	N/A	<80%

Validation of the strain-based approaches was conducted against the full-scale pipe tests described in (Pisarski et al. 2014). The reported pipe tests included two seamless pipes with an average outside diameter (OD) of 273.3 mm and a wall thickness of 18.4 mm. The pipes were loaded with a machine consisting of a pair of pistons that reacted against the face plates to which the test pipes were bolted via the flange arrangement, as shown in Figure 2.9. The pipes were 2000 mm long and had four notches machined at the mid-length in the circumferential direction at each of the cardinal points. The flaws have a nominal size of 5×100 mm, 6×50 mm, 3×100 mm and 4×50 mm, respectively. Table 2.2 gives the details of the actual notch sizes measured after the completion of the tests. In the comparison study presented in this Chapter, the pipe subjected to axial loading only with the nominal flaw sizes was used for validation.

Table 2.2: Actual notch sizes in TWI full-scale pipe tests

Pipe test	Clock position	Nominal size $a \times 2c$, mm	Actual size $a \times 2c$, mm
TWI 2-1 (Axial loading)	12	5×100	4.6×92.3
	6		4.6×92.4
	9	6×50	5.8×46.5
	3		5.7×45.8
TWI 2-2a (Internal pressure and axial loading)	12	3×100	2.5×98.7
	6		2.9×98.7
	9	4×50	3.7×50.0
	3		3.9×50.0

For readability and clarity, the CDF curves predicted using analytical strain-based assessment approaches are four categories based on its nature and characteristics, as shown in Table 2.3. Both the predicted CDF for initial flaw sizes and those considering ductile tearing were plotted and shown in Figure 2.10 to 2.17. The ductile tearing was accounted for using the tangency approach, which will be elaborated in Chapter 5.

The DNV, Smith and Budden & Ainsworth methods, which are based on FAD approach (stress-based and strain-based), are shown to capture the CTOD plateau phase due to Lüders behaviour. Other methods, which were developed

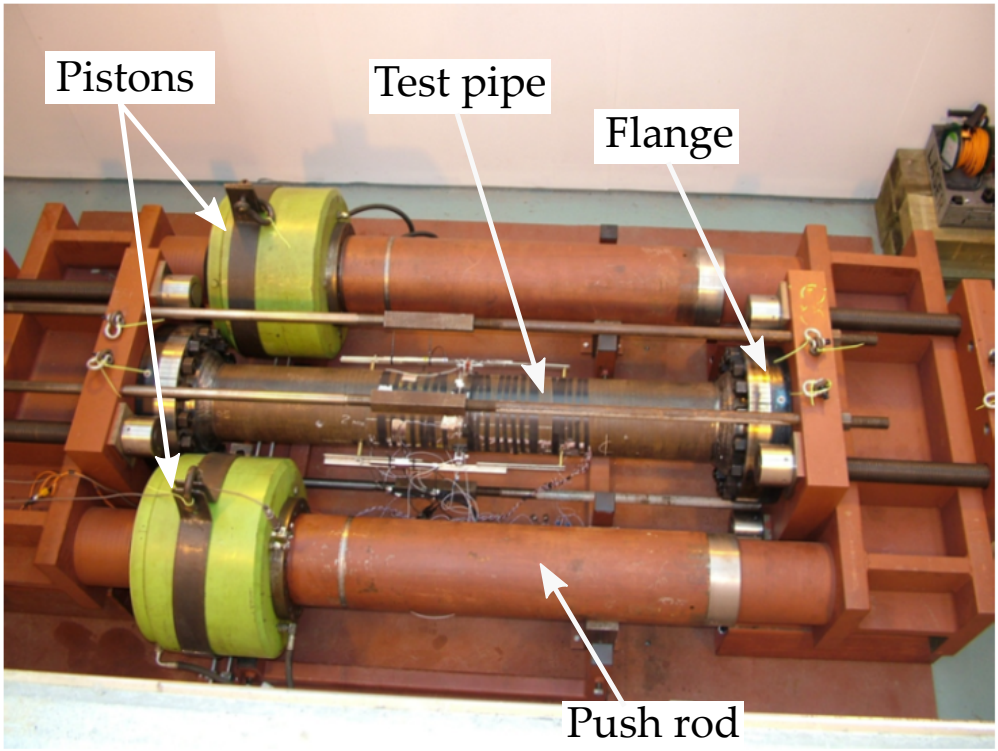

Figure 2.9: Experimental setup of the full-scale pipe tests carried out by TWI (adapted from (Pisarski et al. 2014))

Table 2.3: Categorisation of strain-based CDF estimation approaches

Category	Methods	Description
1	DNV BS 7910 Smith	modified from Option 2 FAD of BS 7910
2	Budden and Ainsworth Nourpanah and Taheri Jia et al.	reference strain method and its modification
3	Chiodo and Ruggieri Parise et al.	EPRI-type CDF estimation scheme
4	SINTEF CRES	CDF relations established from FEA

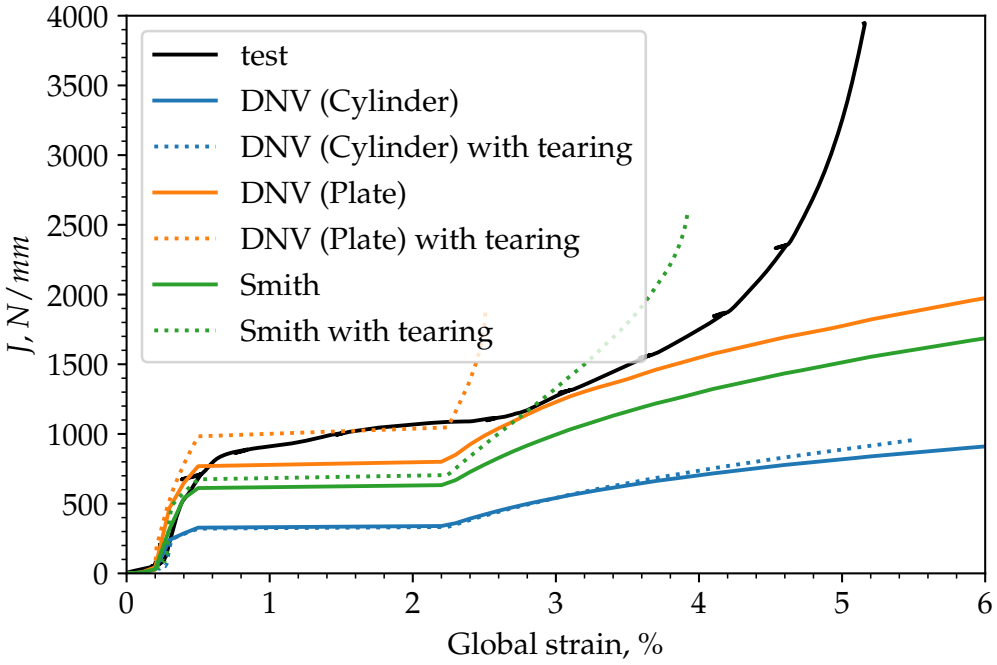

Figure 2.10: Comparison of crack driving force predicted with strain-based assessment methods (Category 1) against TWI pipe test for nominal flaw size 6×50 mm

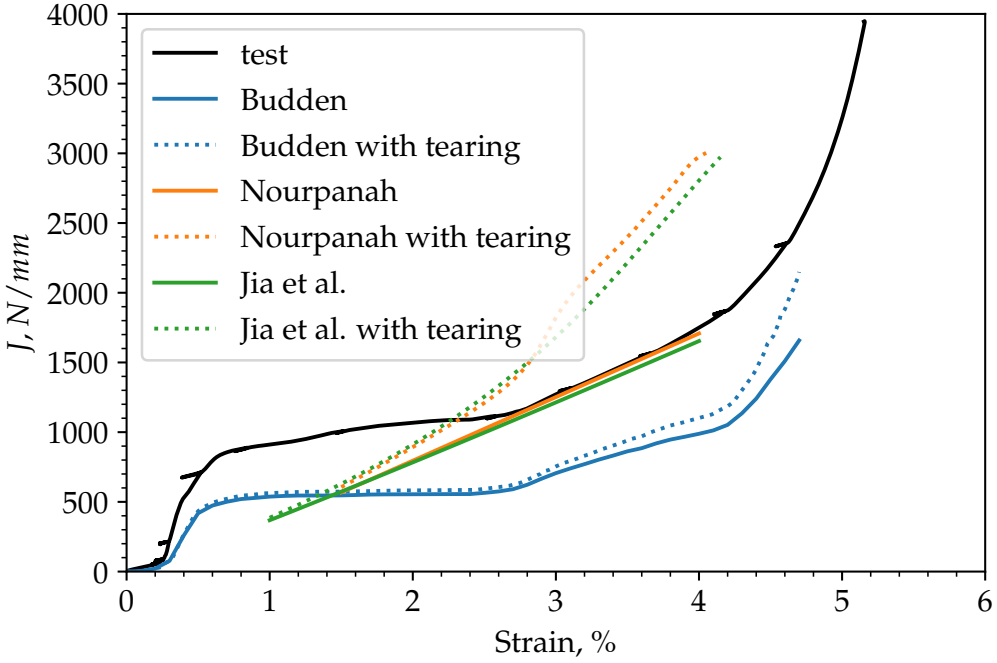

Figure 2.11: Comparison of crack driving force predicted with strain-based assessment methods (Category 2) against TWI pipe test for nominal flaw size 6×50 mm

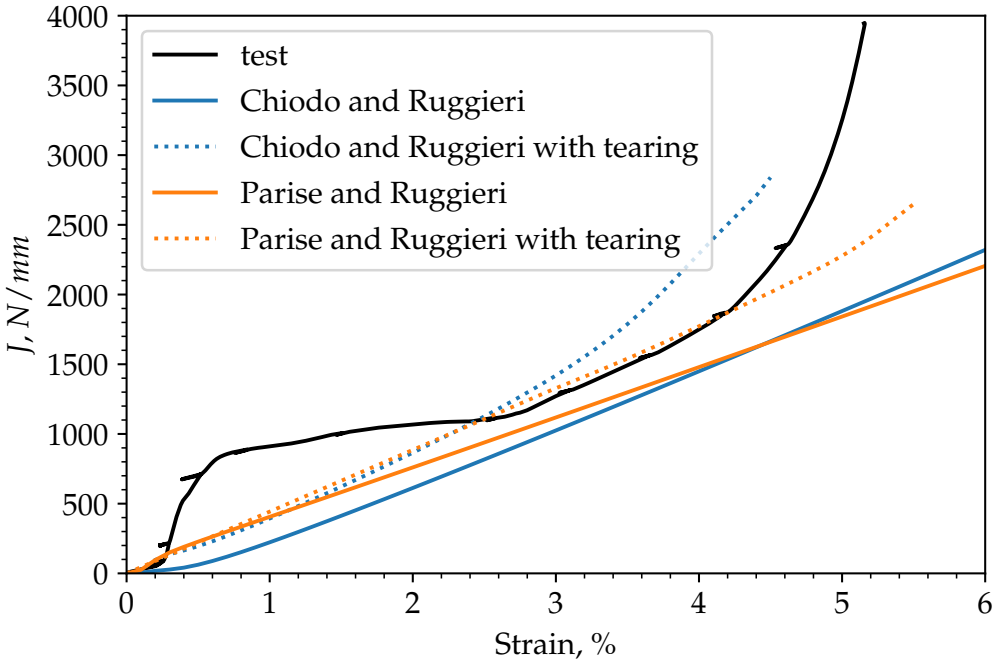

Figure 2.12: Comparison of crack driving force predicted with strain-based assessment methods (Category 3) against TWI pipe test for nominal flaw size 6×50 mm

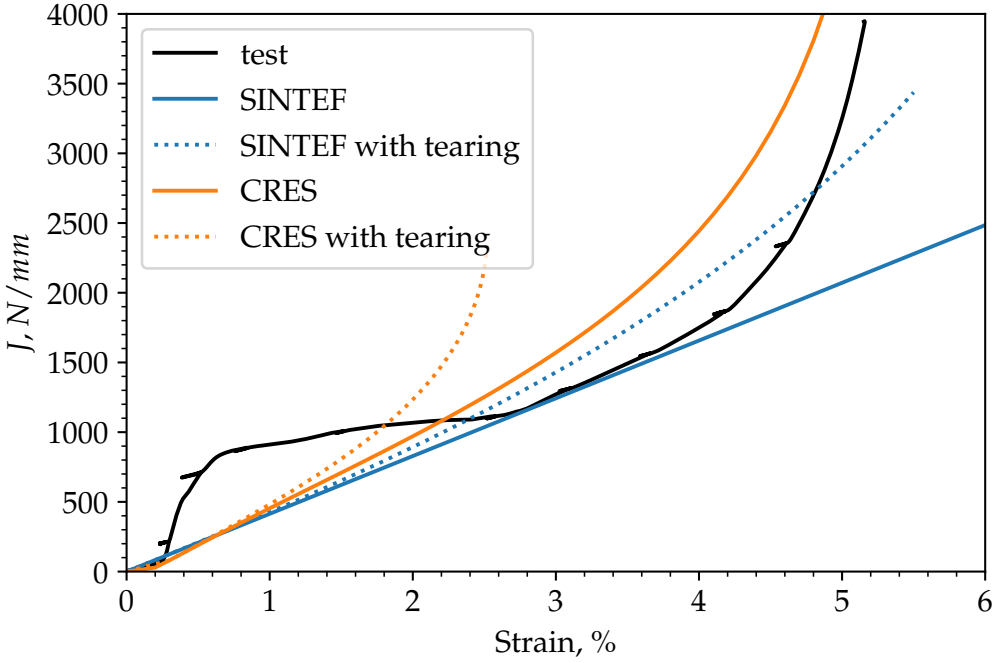

Figure 2.13: Comparison of crack driving force predicted with strain-based assessment methods (Category 4) against TWI pipe test for nominal flaw size 6×50 mm

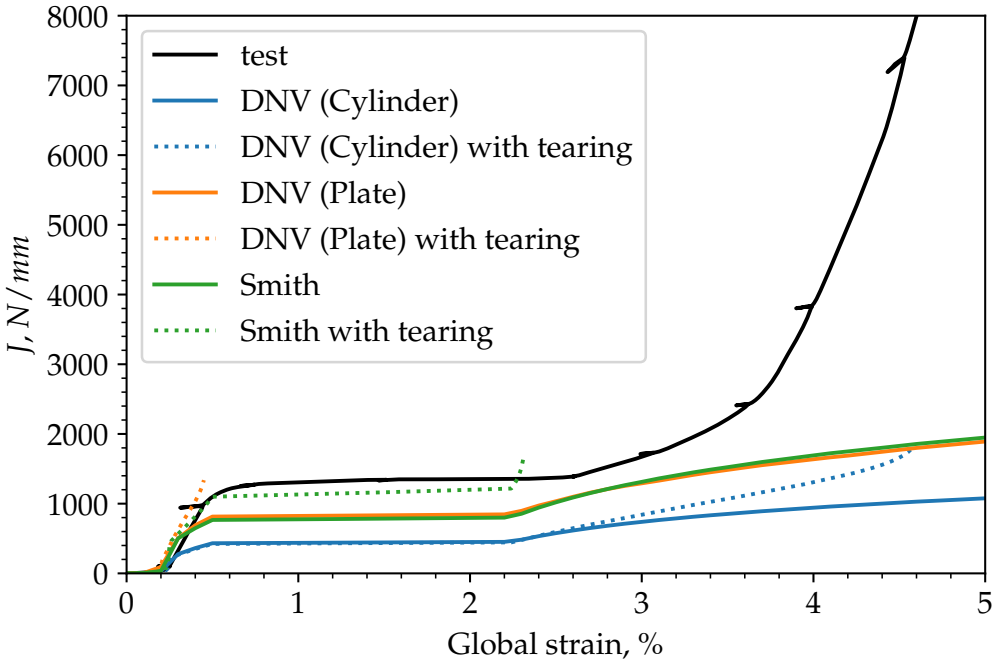

Figure 2.14: Comparison of crack driving force predicted with strain-based assessment methods (Category 1) against TWI pipe test for nominal flaw size 5 × 100 mm

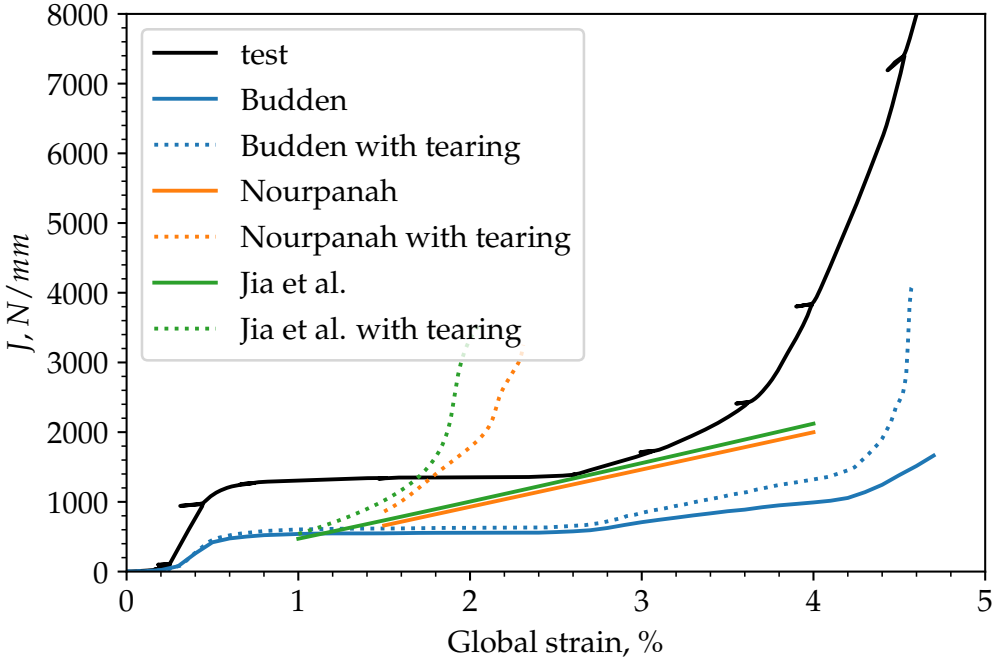

Figure 2.15: Comparison of crack driving force predicted with strain-based assessment methods (Category 2) against TWI pipe test for nominal flaw size 5 × 100 mm

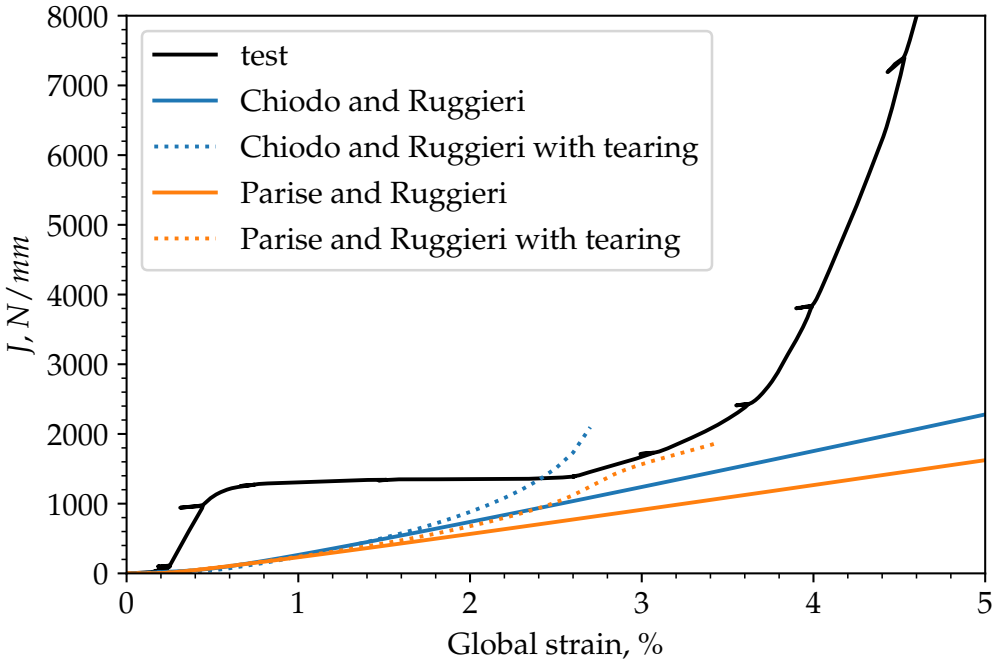

Figure 2.16: Comparison of crack driving force predicted with strain-based assessment methods (Category 3) against TWI pipe test for nominal flaw size 5 × 100 mm

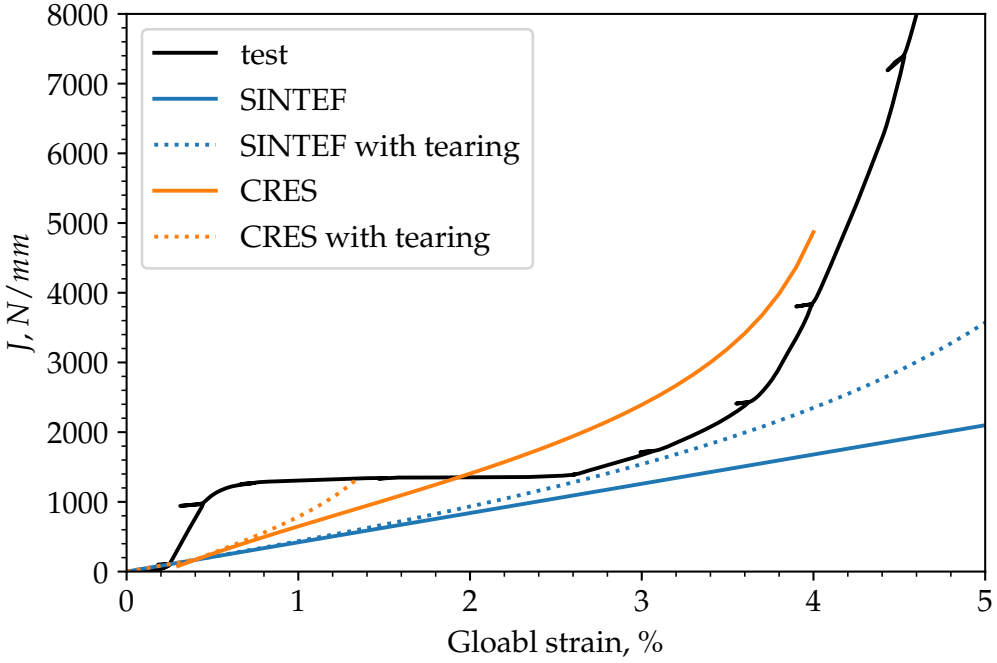

Figure 2.17: Comparison of crack driving force predicted with strain-based assessment methods (Category 4) against TWI pipe test for nominal flaw size 5 × 100 mm

assuming a Power-law material behaviour, failed to reproduce the CTOD plateau.

Most of the methods examined are shown to under-predict the J in comparison with that from the test, in particular in the Lüders plateau phase (about strain 0.5% to 2.7 %). With the incorporation of ductile tearing, the non-conservatisms were greatly reduced, and excessively over-prediction of CDF can be noticed at higher strains for some methods.

2.3.10 *Assessment of pipelines with yield discontinuity*

As can be seen from the analysis of the contemporary strain-based methods presented in Section 2.3.9, most of the current methods do not have the capability of capturing the yield discontinuity in the estimation of CDF. Among all methods examined, only those that originally derived from the FAD approach were found effective in reproducing the CDF with the effect of yield discontinuity. The stress-strain curves, however, are normally simplified as a flat stress plateau following the yield point, without thoroughly investigating the effect of yield discontinuity on the pipelines.

A few studies have been reported regarding the effect of flaws with yield discontinuity, for example, on the crack-tip fields of pipelines loaded in bending (Nourpanah and Taheri 2011), crack driving force and ductile crack growth of SENT specimens (Dahl et al. 2018; Tu et al. 2018). In these studies, a simplified stress-strain curve as aforementioned was used to represent the material property exhibiting Lüders behaviour. This type of representation is commonly used in industry (e.g. Tkaczyk et al. 2009b; Tang et al. 2014), and codes and standards such as BS 7910 and R6. An example of FAD in accordance with BS 7910 for materials exhibiting a Lüders plateau is shown in Figure 2.18. Notwithstanding that the actual stress-strain curves are used for Option 2 FAD, the stress-strain curves for Lüders materials are often simplified without considering the yield drop response (e.g. Pisarski et al. 2014; Tkaczyk et al. 2009c; Pisarski 2011).

Nevertheless, a number of studies are available in the literature, closely examining the effect of yield discontinuity with more sophisticated approaches. Therefore, the following section (Section 2.4) the review of those studies as

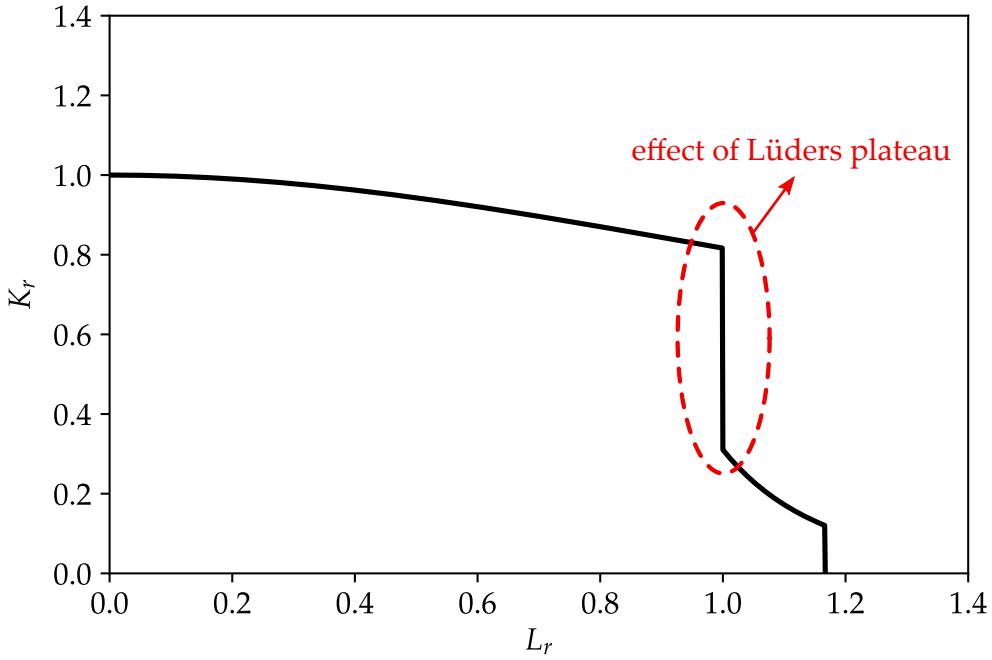

Figure 2.18: Example of a FAD with a Lüders plateau (in accordance with Option 1 FAD of BS 7910)

well as the significance of the yield discontinuity in the structural behaviour of engineering equipment, in particular, containing flaws.

2.4 DISCONTINUOUS YIELDING OF FERRITIC STEELS

2.4.1 *Yield point phenomenon and strain ageing*

Many materials such as structural steels, titanium and tungsten alloys frequently exhibit a yield point phenomenon during a uniaxial tensile test. On a typical stress-strain curve showing yield point phenomenon shown in Figure 2.19, the stress drops suddenly from the upper yield point to the lower one, followed by a fluctuating but overall constant stress plateau.

Lüders bands, also known as “slip bands" or “stretcher-strain marks," are bands of localized plastic deformation in metals under tension, commonly observed on mild steels and certain Al-Mg alloys. It is a dislocation-driven phenomenon that macroscopically manifests as localized deformation. In the simplest setup involving a uniaxial tension test on a low carbon steel strip, immediately after first yielding, included bands of plastic deformation develop

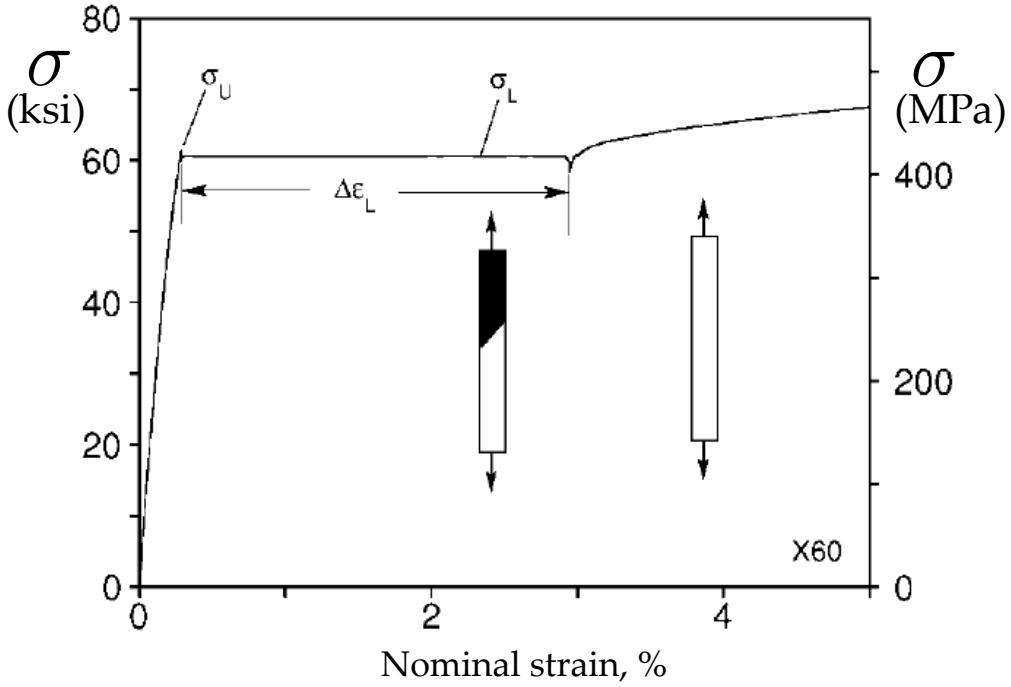

Figure 2.19: Stress-strain response of an X60 steel exhibiting yield point elongation(adapted from Kyriakides and Corona (2007a))

locally. Under displacement controlled stretching, the bands propagate gradually consuming the test section, as depicted in Figure 2.20. During this process, the stress remains essentially unchanged tracing a plateau.

The above phenomenon was first observed by Lüders (1860) and Piobert et al. (1842) about 150 years ago, and are thus known as the Lüders or Lüders-Piobert band. Extensive studies have been carried out with regard to the characterization of Lüders-type deformation, such as the general nature of Lüders banding behaviour (Ananthan and Hall 1991; O. Hall 1970), the velocity of the Lüders front (Sylwestrowicz and Hall 1951), the orientation of the band front (Delwiche and Moon 1971), and the kinetics of the Lüders front propagation (Fortes 1984).

Two main theories have been established to account for the mechanisms of Lüders phenomenon, which are known as the dislocation pinning and unpinning and dislocation multiplication. The dislocation pinning theory was attributed to Cottrell and B.A.Bilby (1949), who postulated that the upper yield point in low-carbon steel was due to the pining of dislocations by interstitial atoms such as carbon and nitrogen. They found that those atoms can naturally form solute atmospheres, known as the Cottrell atmosphere, which precluded the dislocations from moving. Thus, to move the dislocations preceding the plastic deformation, a higher stress is required, which is referred to as the initial

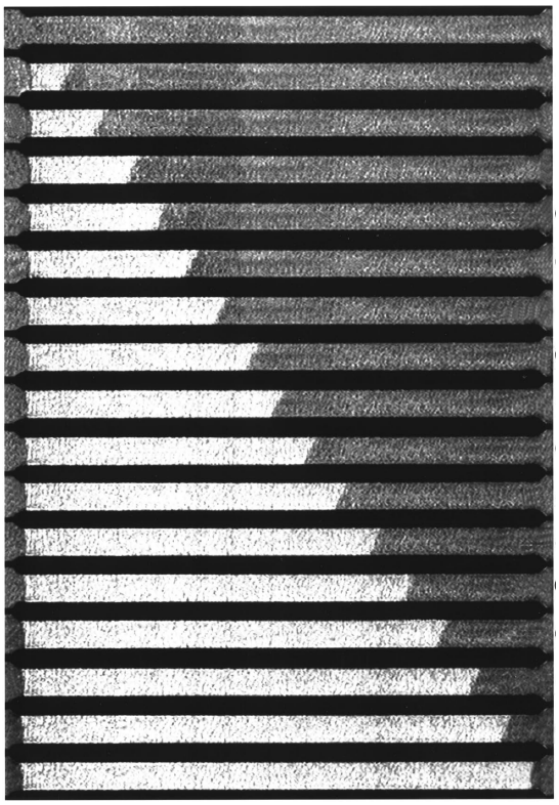

Figure 2.20: Evolution of Lüders band on a uniaxial tensile strip of X70 steel (from Kyriakides and Miller (2000))

yielding or upper yield point. Thereafter the dislocations can be moved by a lower stress, causing a drop in the flow stress. The other theory, dislocation multiplication proposed by Johnston and Gilman (1959), postulated that the yield drop was caused by the multiplication of dislocations. They observed that the stress required to move the dislocations decreased when the number of dislocations increased.

For a certain range of strain rates and temperatures, particularly in Al-Mg alloys, the increasing mobility of solutes leads to repetitive pinning and unpinning of dislocations, associated with stress drops and rises in the flow curve. This phenomenon is known as the Portevin–Le Chatelier (PLC) effect, initially discovered by Le Chatelier (1909) and Portevin and Le Chatelier (1923), and is associated with negative strain rate sensitivity (Penning 1972).

The yield point is found to often appear after the material has been pre-strained and undergone heat treatment with low-temperature, as known as the strain ageing. In this process, the aforementioned solute atoms diffuse to the dislocations, and act as obstacles to the dislocations as described earlier,

resulting in the upper yield point followed by a Lüders plateau. Figure 2.21 illustrates the impact of strain ageing on the shape of the stress-strain curve.

2.4.2 *Numerical modelling of Lüders and Lüders-like phenomenon*

Simulation of Lüders phenomenon requires the use of appropriate material laws in FEA. Two types of constitutive models have been shown capable of capturing the Lüders banding events. The first and simplest material law is a stress-strain response with strain softening in the flow curve prior to the strain hardening. It is usually used by being supplied to FE code in a form of tabulated stress-plastic strain data. Shaw and Kyriakides (1997) and Kyriakides and Miller (2000) are believed to be among the first to utilise this type of material law in numerical modelling of Lüders phenomenon. Other researchers have shown its efficacy in various studies, such as numerical simulation of Lüders-like behaviours on bent pipes/tubes (Hallai and Kyriakides 2011b; Kyriakides et al. 2008; Aguirre et al. 2004), reeled pipes (Liu et al. 2015), NiTi strips and tubes (Jiang et al. 2017b, 2017a), tensile strips (Belotteau et al. 2006) and fracture specimens (Wenman and Plant 2006). However, as suggested by a number of researchers, this type of material model is phenomenological and does not take account of the strain rate effect, testing temperature and the mechanisms of strain ageing. Therefore, this phenomenological law may not be suitable for complex loading process with strain rate and temperature changes, and the more complex strain ageing process such as the dynamic strain ageing and the associated PLC bands.

The second and more sophisticated material law is the strain ageing model which accounts for the intrinsic mechanism of interactions between dislocations and solute atoms. This type of material model was specifically proposed to simulate the PLC effect (McCormick 1988; Zhang et al. 2001), but also has been modified to accommodate Lüders phenomenon (Graff et al. 2004). A number of studies have reported the effect of static/dynamic strain ageing on the behaviour of steel strips and fracture specimens using this type of constitutive laws (Beardsmore et al. 2013; Wenman and Chard-Tuckey 2010; Graff et al. 2004;

Belotteau et al. 2009; Marais et al. 2015). The constitutive model generally takes the following form:

$$\sigma_{eq} = R_0 + R_h(p, \dot{p}) + R_a(p, t_a) \tag{2.47}$$

where R_0 is the intrinsic yield stress before the strain ageing, in other words, without the discontinuous yielding mechanism; R_h is the conventional strain hardening considering the strain rate effect; R_a is the stress contribution due to strain ageing. The term R_a is a function of plastic strain p, ageing time, waiting time and several other variables accounting for the interactions between the dislocations and obstacles (interstitial atoms). This type of material model seems robust in handling complex discontinuous yielding phenomena such as dynamic strain ageing. However, many tests are required to calibrate the variables relevant to strain ageing and strain rate sensitivity. This may render this type of model undesirable for engineering applications which require efficiency and convenience due to a tight time scale.

2.4.3 *Influence of yield discontinuity on structural behaviour*

Many studies have been conducted to investigate the effect of Lüders band on the structural behaviour of steel pipes/tubes subjected to bending, such as the interaction between Lüders instability and wrinkling (Aguirre et al. 2004), effect of Lüders strain on the bending capacity of pipes (Kyriakides et al. 2008; Hallai and Kyriakides 2011a, 2011b), the evolution of Lüders band in the pipe during reeling (Liu et al. 2015). It was found that when the pipe was bent well into the plastic regime, Lüders banding could precipitate structural instabilities and plastic collapse. Pockets of inclined localisation bands were observed to emanate from peaks of wrinkles during the moment plateau in the numerical analysis of bent pipes (Aguirre et al. 2004). In the moment plateau phase, two curvature regimes were found to co-exist, one approximately corresponding to the strain at the end of the Lüders plateau (known as Lüders strain ε_L) and the second to that at the beginning of the plateau. Local inclined deformation bands were shown to develop on the top and bottom surfaces of the tube, which in turn led to a structural localization where the Lüders affected parts of the tube

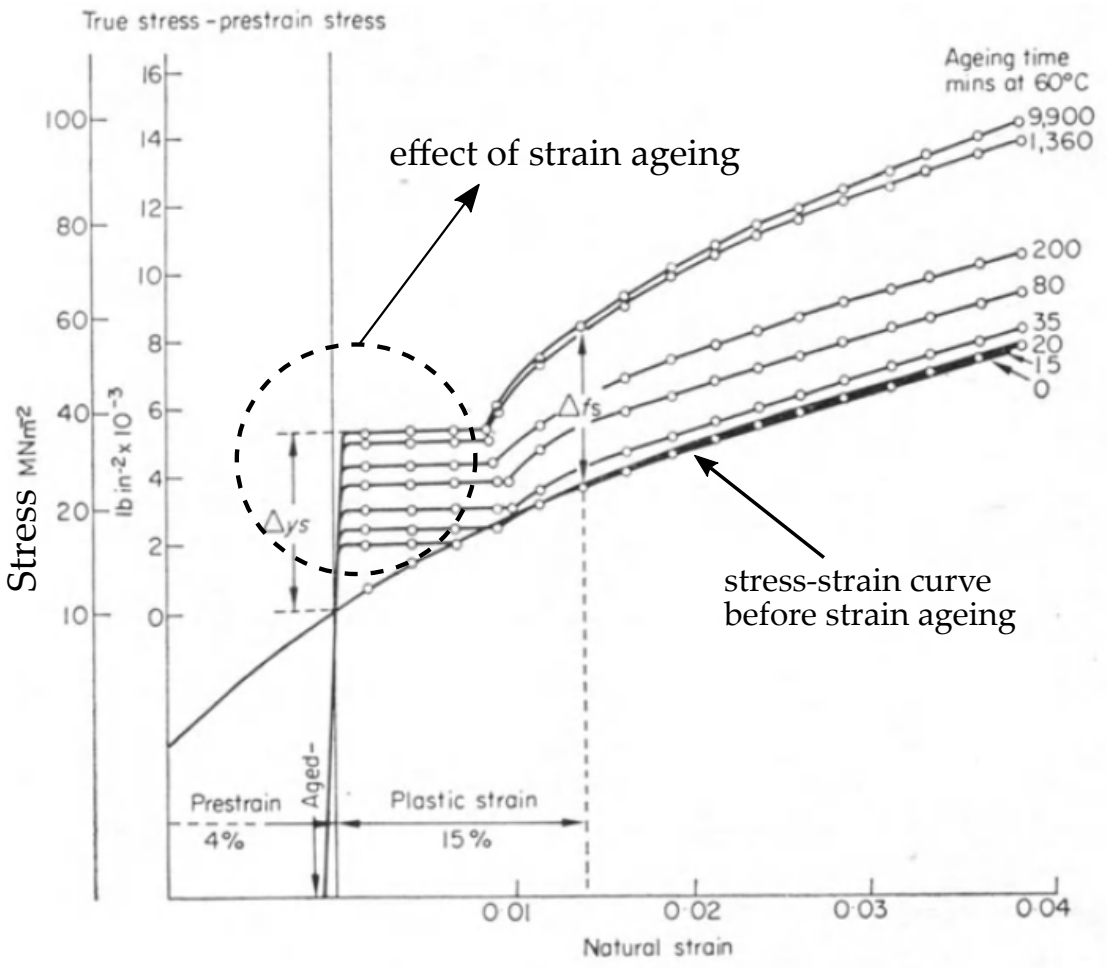

Figure 2.21: Development of yield point phenomenon during strain ageing of mild steels (adapted from Wilson et al. (1959), cited in O. Hall (1970))

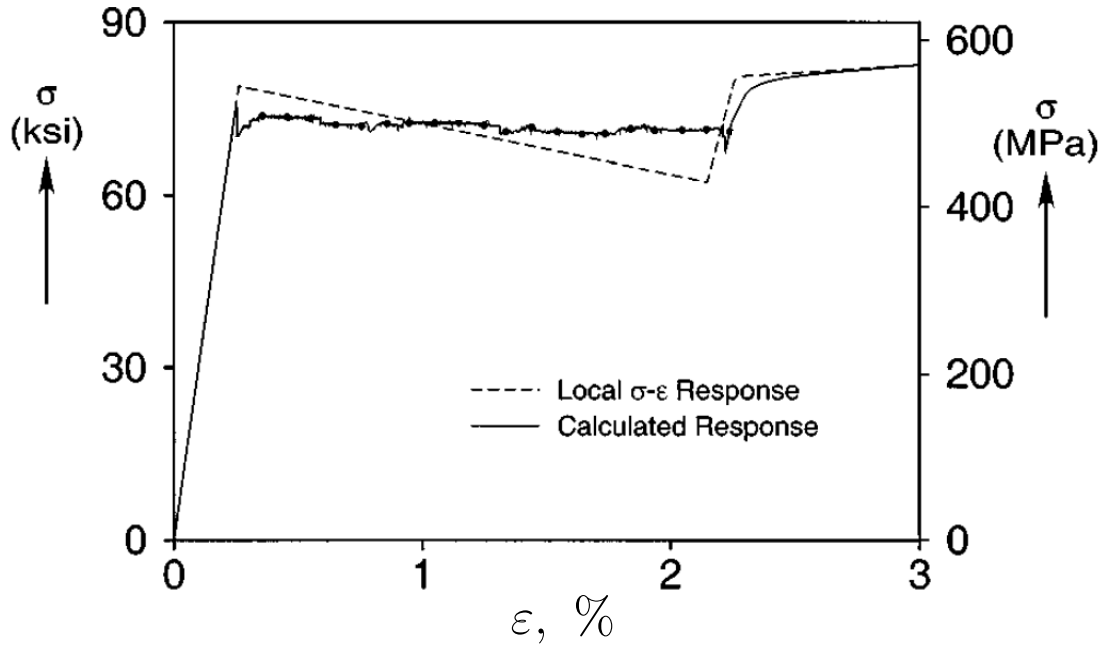

Figure 2.22: Simple phenomenological material law for numerical simulation of Lüders band (adapted from Kyriakides and Miller (2000)

deformed to a relatively high curvature while the rest remains at the curvature corresponding to the beginning of the moment plateau. The length of Lüders plateau together with the D/t ratio were shown to affect the bending behaviour and collapse significantly (Hallai and Kyriakides 2011a, 2011b).

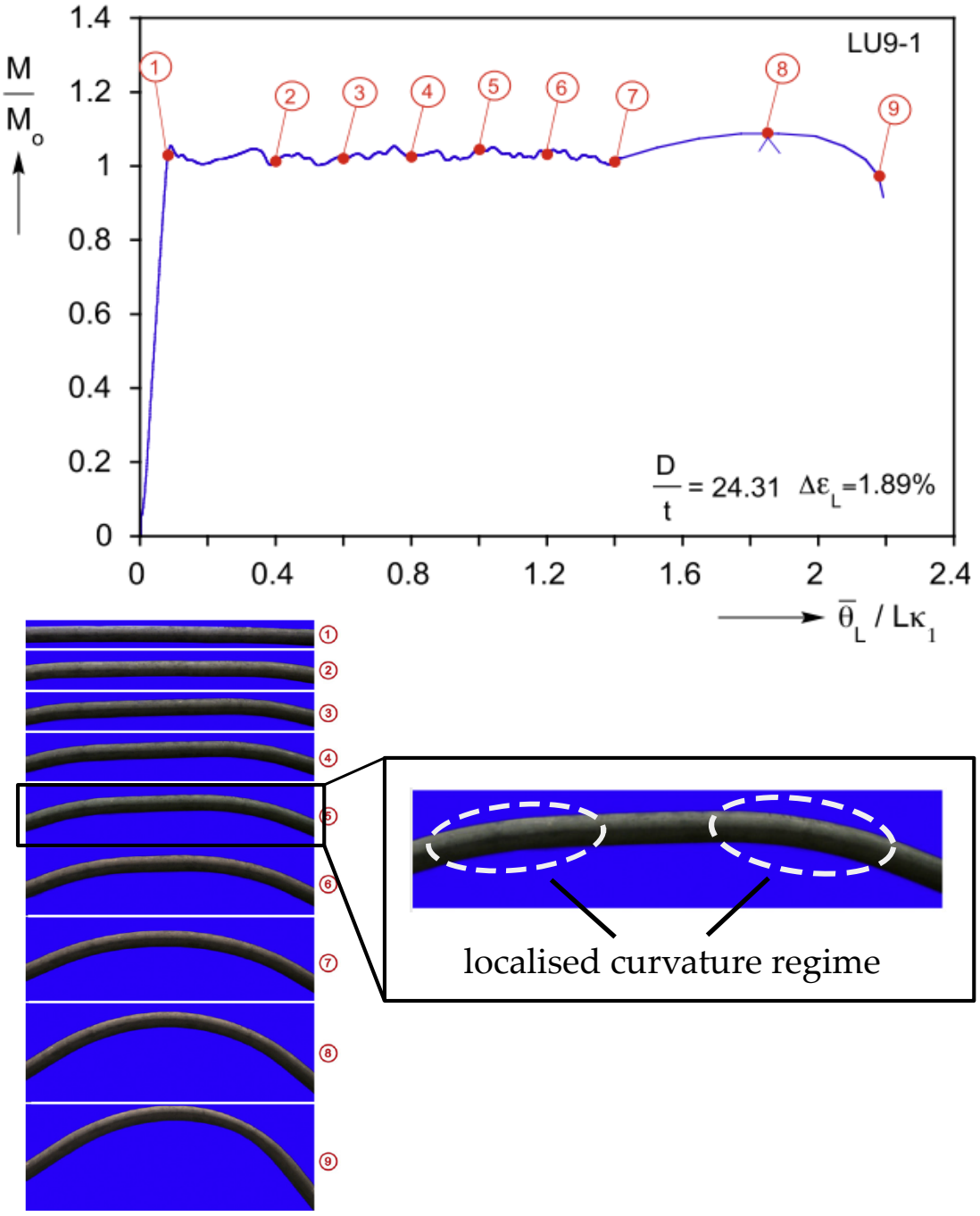

Figure 2.23: Moment-curvature behaviour and the bent configurations of tube loaded in bending (adapted from Hallai and Kyriakides (2011a))

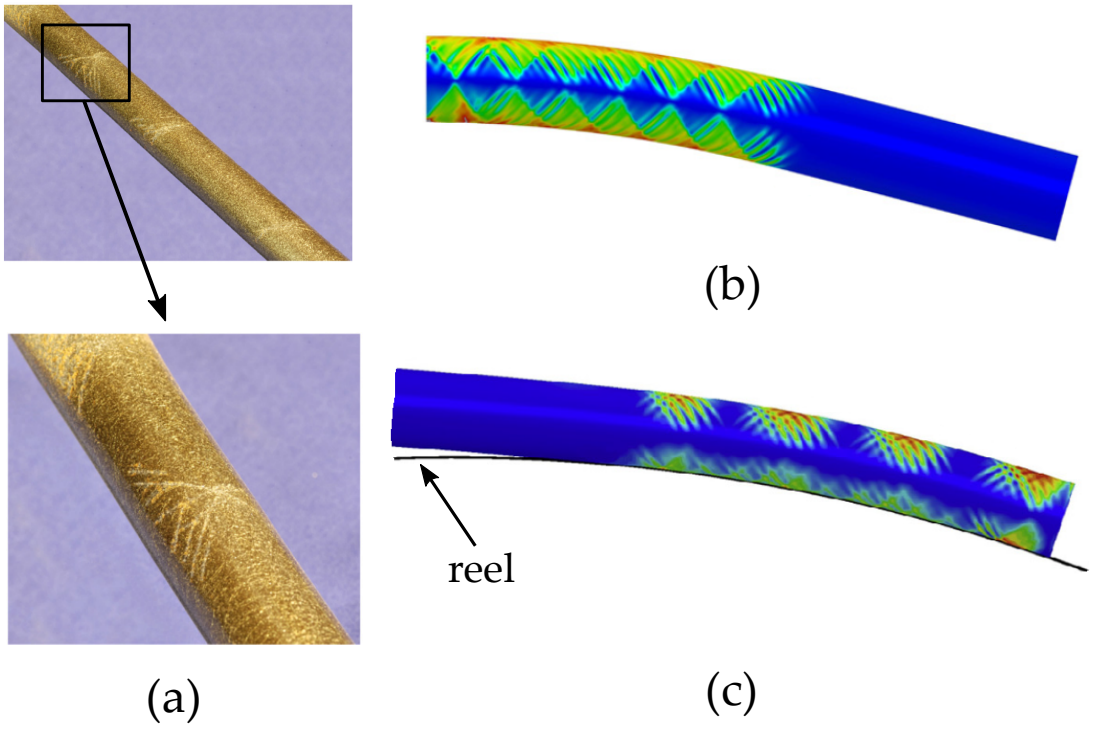

Figure 2.24: Lüders band patterns on the tube/pipe under bending: (a) band patterns on compressed side of the tube observed in experiment (adapted from Hallai and Kyriakides (2011a)); numerical simulation of Lüders band on pipe (b) under pure bending (adapted from Hallai and Kyriakides (2011b)) and (c) during reeling (adapted from Liu et al. (2015))

2.4.4 *Cracked component in the presence of yield discontinuity*

A number of researchers have examined the effects of the Lüders or Lüders-like behaviour on the formation of crack-tip plasticity. These studies mostly examined the deformation behaviour of small-scale test samples, such as Compact Tension (CT) specimens (Wenman and Plant 2006; Wenman and Chard-Tuckey 2010; Belotteau et al. 2009; Wang et al. 2012; Belotteau 2009), tensile strips with cracks (Beardsmore et al. 2013), and Charpy V-notched specimens (Marais et al. 2015). As shown in Figure 2.25, the CT specimens with Lüders behaviour exhibits distinctly different strain distribution from the one with continuous yielding behaviour. In the near-tip region, highly localised strain region can be observed, which shows a cluster of complex plasticity bands of a multi-pronged pattern.

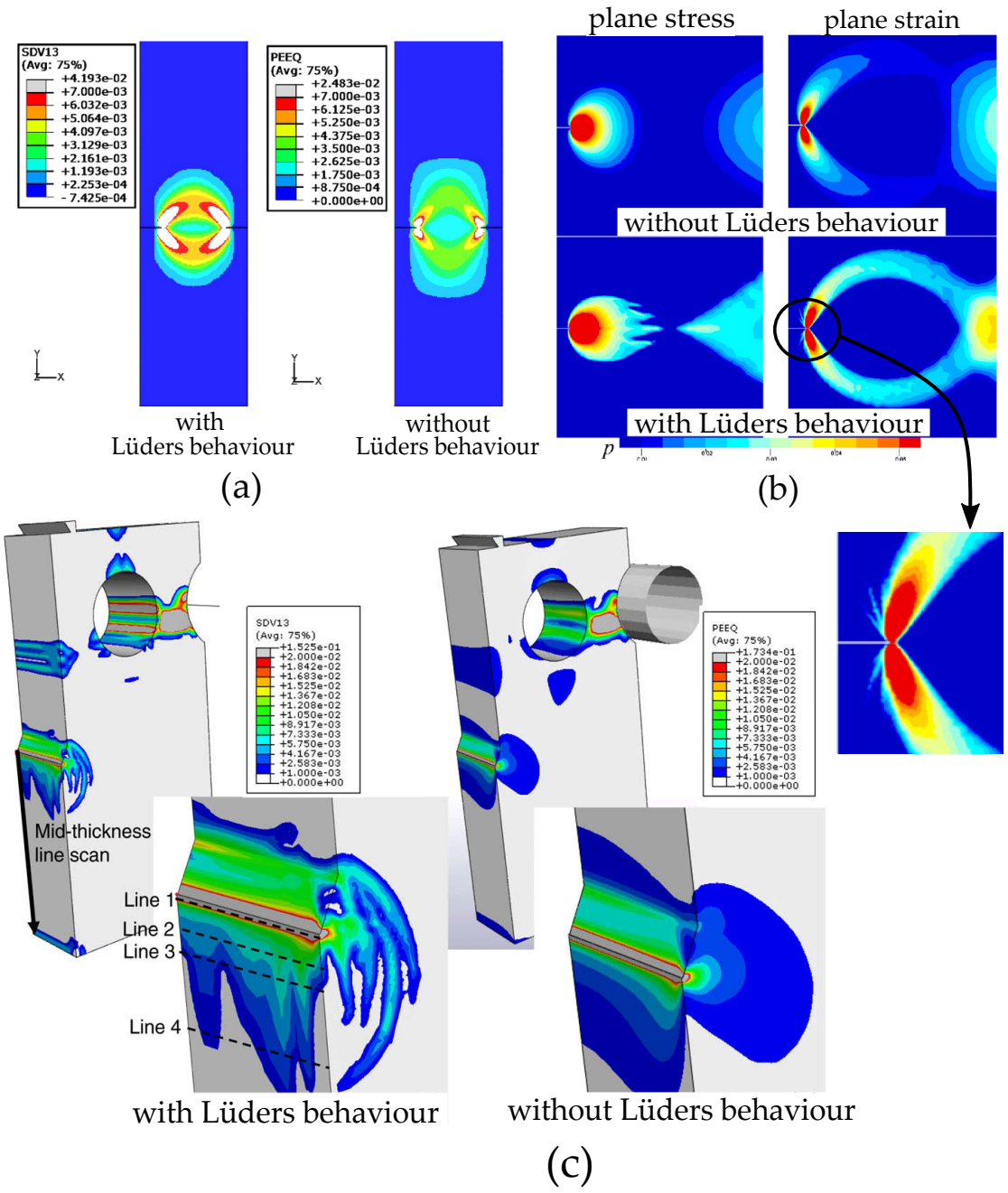

Figure 2.25: Effect of Lüders behaviour on the equivalent plastic strain development in the near-tip region of: (a) 3D FE model of double-edged cracked plate (adapted from Beardsmore et al. (2013)); (b) 2D FE model of CT specimens in plane stress and plane strain, respectively (adapted from Belotteau et al. (2009)); (c) 3D FE model of CT specimens (adapted from Wenman and Chard-Tuckey (2010))

2.5 SUMMARY

Chapter 2 conducted a thorough review of the assessment of pipelines under inelastic deformation and the significance of Lüders plateau. Comparisons of the current assessment methods against the test data in the public domain were made to further highlight the need to investigate the fracture response with the effect of Lüers phenomenon. Based on the literature review presented, the following conclusions are drawn:

- Most methods available for strain-based fracture assessment are not capable of capturing the effect of Lüders plateau on the crack driving force as measured in full-scale tests.
- Further studies on crack-tip behaviour of pipelines with Lüders bands may be required.
- More investigations are desired to understand whether a more realistic modelling of Lüders behaviour would offer benefits to the assessment of cracked pipes.

3

INVESTIGATIONS OF YIELDING BEHAVIOUR OF API X65 PIPELINE STEEL EXHIBITING LÜDERS PLATEAU

3.1 INTRODUCTION

Experimental observation of Lüders band has been extensively reported in the literature (e.g. Kyriakides and Miller 2000; Beardsmore et al. 2013; Butler 1962; Wenman and Chard-Tuckey 2010). However, limited studies were reported on the experimental observation of Lüders banding behaviour in the materials employed in the pipeline industry, such as API 5L Grade steel X65 - X100 (Kyriakides and Miller 2000; Liu et al. 2015; Zhao et al. 2012; Han et al. 2017). It is acknowledged that yield discontinuity (appeared as yield plateau) may occur during the fabrication of seamless pipes that are later used for offshore pipeline installation via reeling procedure. Many studies have reported the occurrence of the yield plateau in the pipeline materials for offshore applications (e.g. Pisarski et al. 1994; Tkaczyk et al. 2011; Tkaczyk et al. 2009b, 2009c). Nonetheless, little work has reported the optical observation of Lüders banding phenomenon of pipeline steels during a typical tensile test. In order to gain further insights into the Lüders behaviour exhibited in the pipeline steel, uni-axial tensile tests of API 5L Grade X65 steel strips were conducted. Both plain strips and notched strips were tested. Digital image correlation (DIC) technique was used to record the full-field deformations of the test samples for clear and accurate observation of Lüders banding and associated strain localisations.

As elaborated in Chapter 2, there are a number of approaches available to simulate the initiation and propagation of Lüders bands. Among those approaches, the 'up-down-up'(UDU) method is deemed the simplest to satisfactorily capture the main macroscopic event of Lüders banding observed in an

experiment. Nevertheless, few studies have addressed the effect of the shape of UDU stress-strain models on the simulated structural behaviour and the practicality of the UDU method. Therefore, in this chapter, the UDU stress-strain model with various softening modulus was investigated with regard to the simulated Lüders banding behaviour and the global structural response.

3.2 EXPERIMENTAL PROCEDURES

Four tests with two plain tensile specimens and two notched tensile specimens were conducted, respectively. All of the tests were compared with the use of DIC to capture the deformation characteristics. The test samples were extracted by electro-discharge machining (EDM) from various circumferential locations in a parent seamless pipe. The axis of the samples was in parallel with the pipe axis. The pipe is made of API 5L X65 steel with the chemical compositions presented in Table 3.1.

Table 3.1: Chemical composition of the tested steel (wt%)

Material	C	Mn	Si	Ni	Cr	Mo	V	Cu	P	S
X65	0.11	1.12	0.24	0.10	0.12	0.10	0.05	0.15	0.011	0.004

During the testing, the specimens were loaded quasi-statically under displacement-control using a servo-hydraulic testing machine (INSTRON 8500 B530). The testing machine has a loading capacity of 100kN, which is sufficient to load the specimens to failure. DIC was used throughout the testing to monitor the full-field deformations of the test samples. The DIC system comprises a high-resolution camera with a Titanar A 75mm lens (ARAMIS 5M with a resolution of 2448 $\times$ 2050 Pixels). The illumination was supplied by a halogen light fitted on the tripod. Figure 3.1 shows the experimental set-up of the tensile testing machine and DIC system. All tests proceeded until fracture occurred. The details of the geometry of the test samples, loading parameters and DIC configurations were elaborated in the subsections that follow.

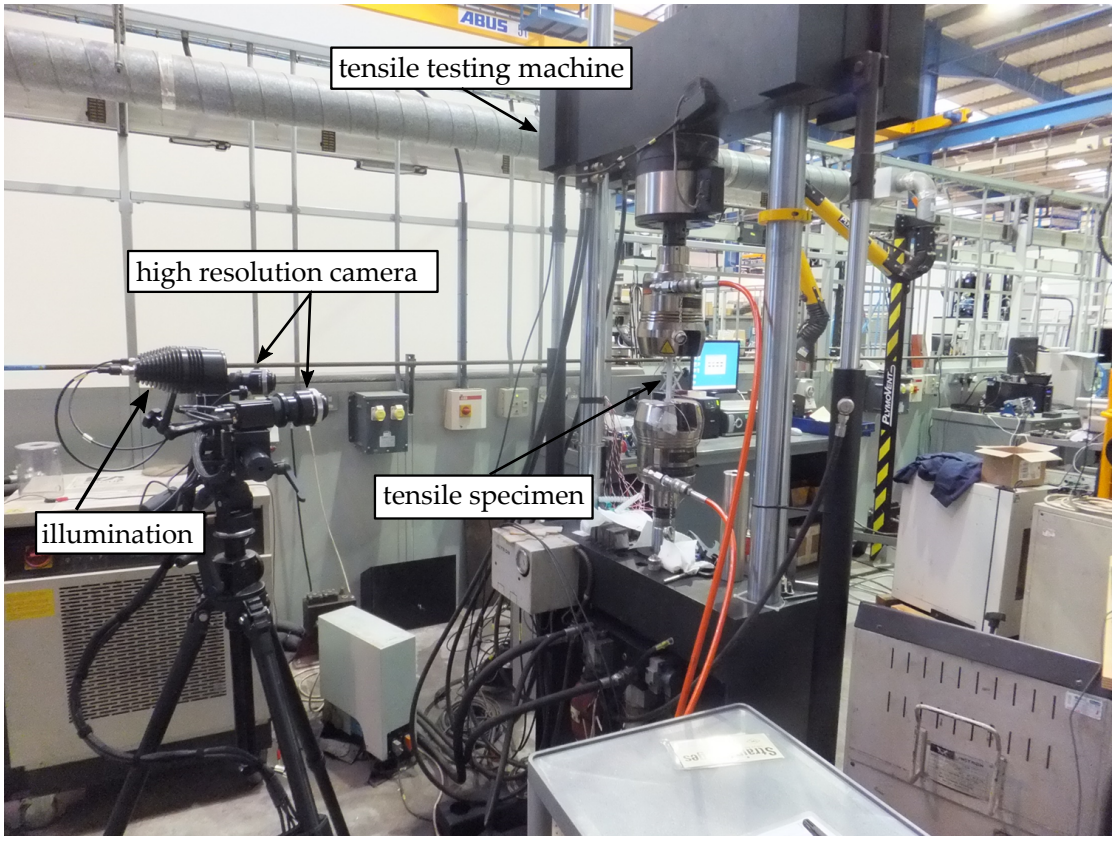

Figure 3.1: Experimental setup of the tensile testing at TWI

3.2.1 *Digital image correlation*

3.2.1.1 *Principles*

Digital image correlation (DIC) is an effective non-contact optical technique to measure the deformation of an object. DIC calculates the strains by analysing the images of the specimens captured during testing. Prior to testing, a random speckle pattern is applied to the specimen surface to be monitored (Sutton et al. 2010). The pattern can be generated by either using a spray or marker. During testing, the specimen pattern changes as the specimen deforms. The deformation is quantified by analysing the displacements and rotations the pattern. The captured images of the deformed object are divided into a two-dimensional matrix of nodes or facets. At each node, the grey-scale intensity is evaluated as a weighted average of a square box surrounding the node. The size of this box is determined by a parameter named subset size, again expressed in pixels. Two subsequently taken images can thus be compared to each other

based on their resulting grey-scale intensity matrix. By matching the grey-scale distribution between these two images, the deformation can be quantified.

3.2.1.2 *Procedure*

A larger subset size will result in a more accurate correlation, while the spatial resolution will improve for a smaller subset. Since the preferred speckle size equals 3×3 pixels and a subset preferably contains three speckles (Sutton et al. 2010). In the tensile testing, the speckle patterns were applied to the specimen surface either by using a black spray or marker with a white painted background. Below is a typical photo of the speckle pattern applied to the specimen surface to be monitored:

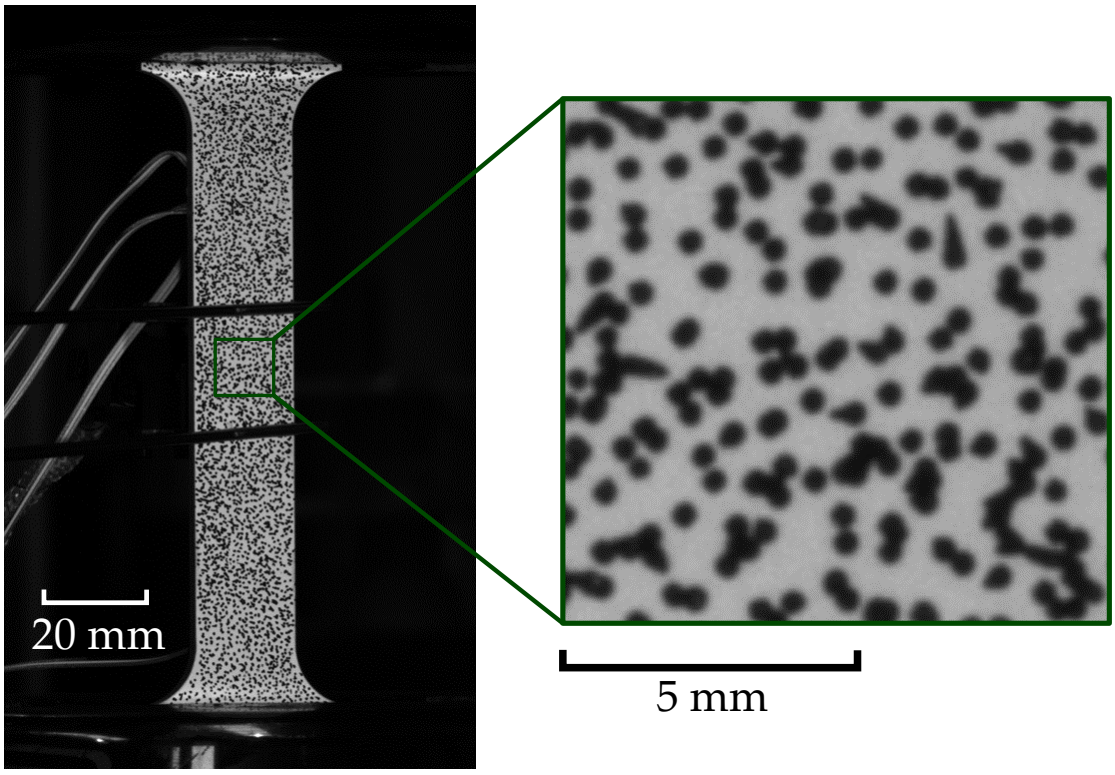

Figure 3.2: Speckle patterns applied to the surface of the tensile specimen (M01-02)

The speckle pattern shown in Figure 3.2 comprises the stochastic black dots drawn by a black marker and a white paint underneath. For other specimens, such as M01-01 and M01-03, the speckles were created using a black spray, which was as effective as that using a marker.

3.2.2 *Plain sided specimen*

The two plain tensile specimens (denoted by M01-01, M01-02) are identical and have a rectangular cross-section of 20×5 mm and a gauge length of 80 mm. Both specimens were installed with strain gauges. M01-01 contained strain gauges at both sides so that only the area between the strain gauges was observed by DIC. M01-02 contained strain gauges at only one side for a larger area of measurement. Figures 3.3 and 3.4 illustrate the geometry and applied instrumentation of the test samples M01-01 and M01-02, respectively.

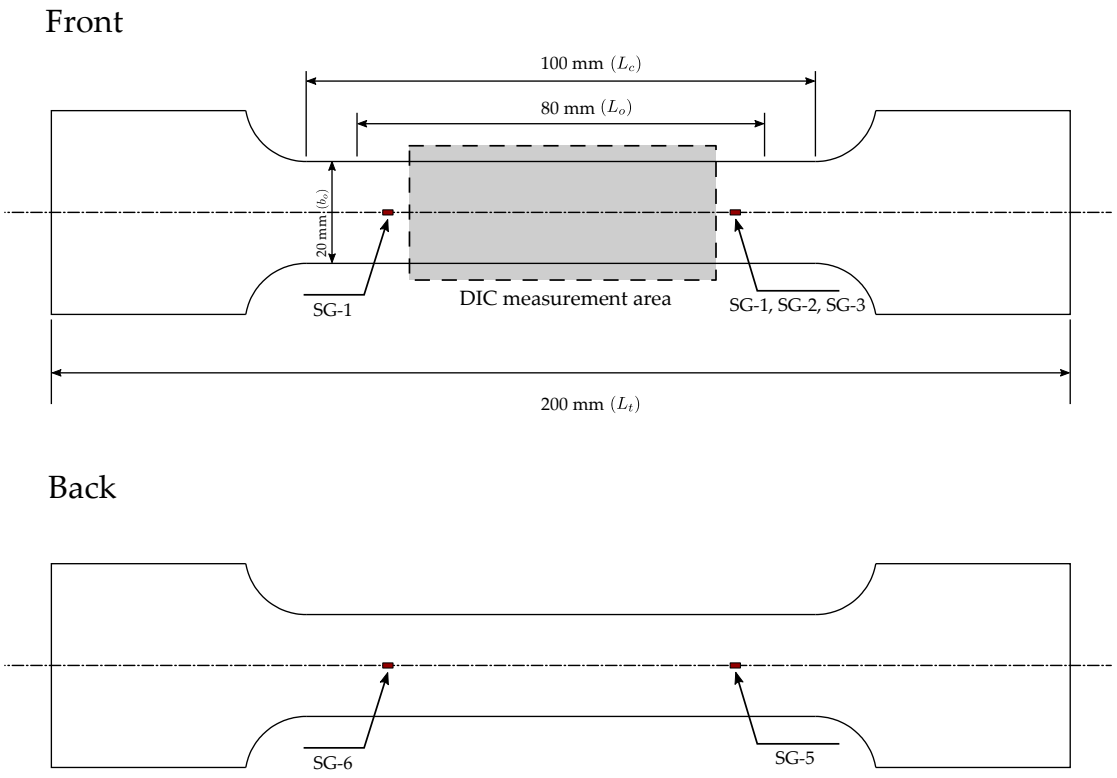

Figure 3.3: Schematic of the plain tensile specimen M01-01 instrumented with strain gauges

As shown in the instrumentation in Figure 3.3, the elongation of specimen M01-01 was directly measured by DIC. By contrast, in the testing of M01-02 (shown in Figure 3.4) an extensometer of a 25 mm gauge length (L_e) was used for supposedly more accurate measurement of the elongation and the verification of the accuracy of DIC. A cross-head velocity of 0.6 mm/min was applied for both samples such that a nominal strain rate of approximately $10^{-4}s^{-1}$ was obtained. The frame size for DIC measurement was set as 125×100 mm, and the images of the sample were taken at a frequency of 1Hz.

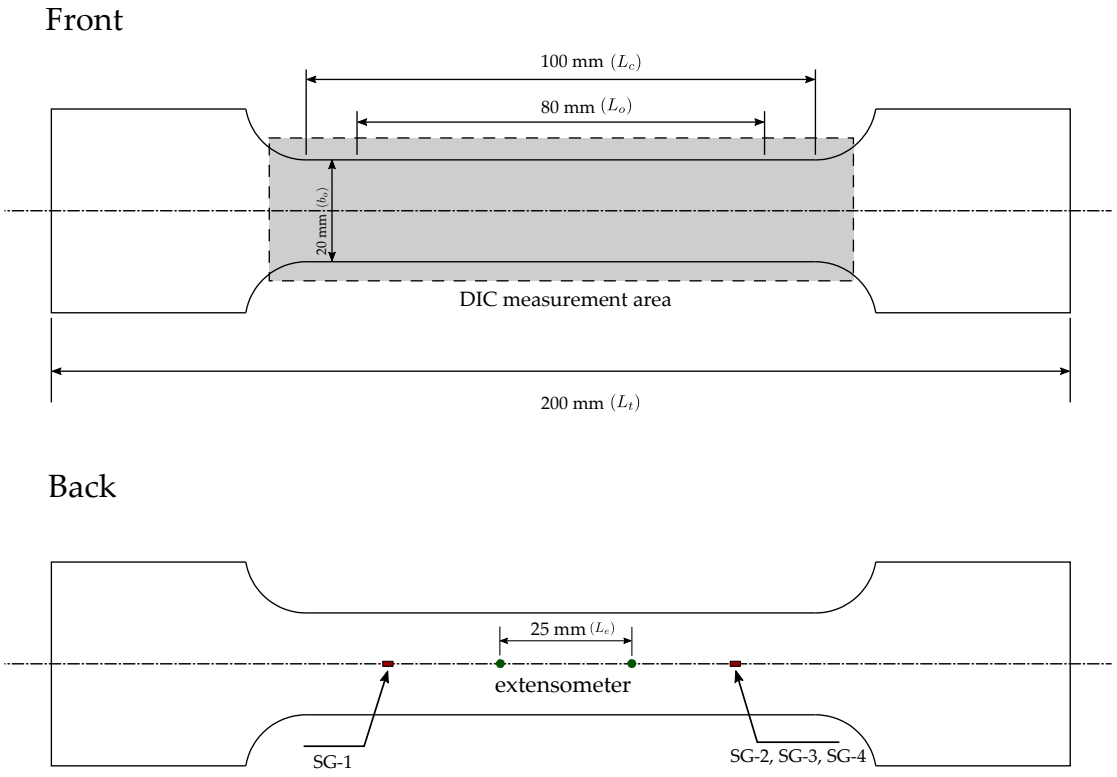

Figure 3.4: Schematic of the plain tensile specimen M01-02 instrumented with strain gauges and a extensometer

3.2.3 *Side-notched specimen*

The notched specimens had the same dimensions as that of the plain specimens with the exception of the notches machined on the sides. The notches were semi-circular and had radii of 3 mm, as shown in the schematic in Figures 3.5 and 3.6. Like the plain tensile tests, one of the notched tensile specimen (M01-03) was instrumented with strain gauges on both sides and the other one (M01-04) on only one side. As for M01-04, an extensometer of 25 mm gauge length was used to measure the extension over a span of 25 mm cross the notched locations. A cross-head velocity of 0.6 mm/min (same as for plain tensile specimens) was applied to M01-03. Since the notched locations had a reduced specimen width and the notches acted as stress concentrators, the resulting strain rate in the ligament was certainly above the nominal strain rate of $10^{-4}s^{-1}$. Thus, we applied a more reasonable cross-head velocity that results in an equivalent strain rate of $10^{-4}s^{-1}$ in the ligament. The cross-head velocity for M01-04 was determined with the consideration of the stress concentrations.

The magnified stress at the notch tip can be calculated by the following equation (William D. Callister 2007):

$$\sigma_m = \sigma_0 \left[\left(1 + 2\frac{a}{\rho_t} \right)^{0.5} \right] \tag{3.1}$$

where σ_0 is the magnitude of the nominal applied tensile stress, ρ_t and a are the radii of the curvature and the length of the notch, respectively. The stress concentration factor, σ_m/σ_0, for the notched tensile specimen was calculated as 2.4. Then the cross-head velocity was determined in proportion to the stress concentration factor as 0.25 mm/min. In the work of Beardsmore et al. (2013), Equation 3.1 was also used to define the loading rate of tensile testing.

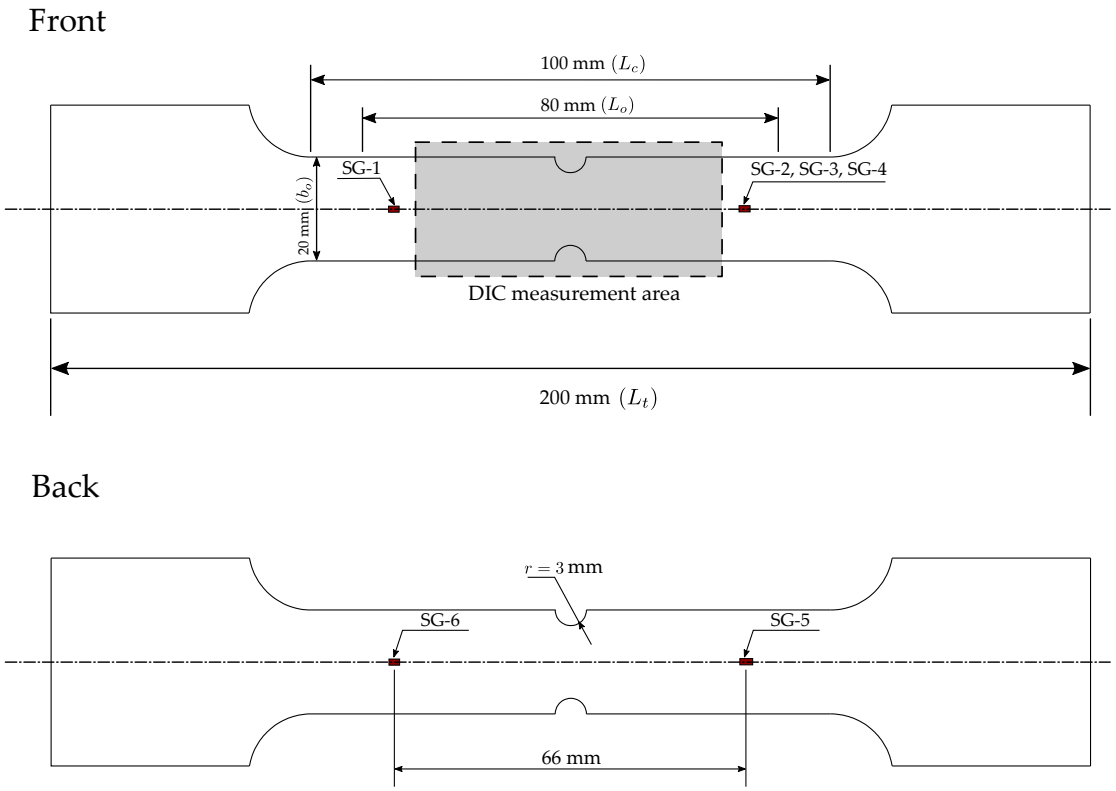

Figure 3.5: Schematic of the notched tensile specimen M01-03 instrumented with strain gauges

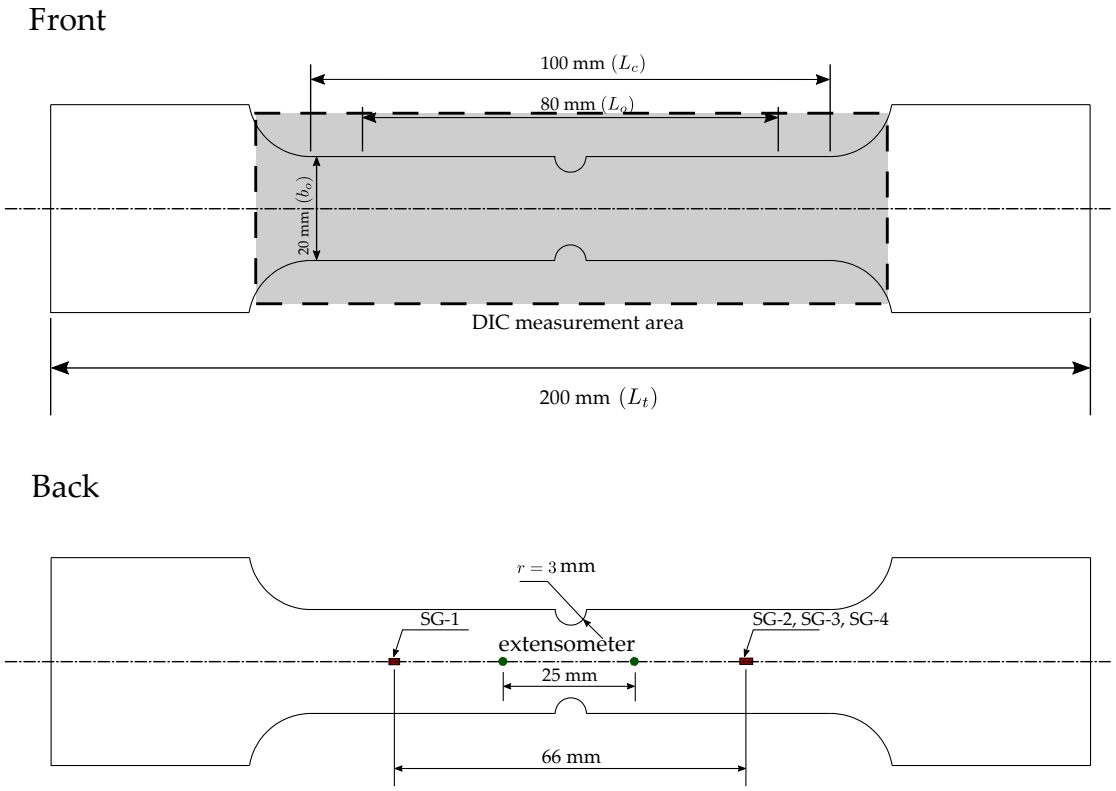

Figure 3.6: Schematic of the notched tensile specimen M01-04 instrumented with strain gauges and an extensometer

3.2.4 *Results*

3.2.4.1 *M01-01*

Figure 3.7 shows the measured engineering stress-strain curve of M01-01. The extension was computed in ARAMIS software over the span between the two strain gauges on the side that was monitored by DIC. It can be seen a pronounced yield point of 477 MPa, followed by a nearly constant stress plateau with the average magnitude of 460 MPa. The stress plateau extends from strain 0.25% to 2.32%, which is followed by a conventional strain hardening curve.

On the engineering stress-strain (s-e) curve, we selected a sequence of points that correspond to the longitudinal strain (ε_{yy}) maps presented in Figure 3.8. These strain maps depict the Lüders band evolutions at various stages of the testing. From configuration ② to ⑤, a localised deformation band propagates at nearly constant speed and gradually spreads through the whole gauge length monitored. The band front is relatively narrow and separates the specimen into plastically-deformed and plastically-undeformed regimes. The band is expected to initiate at the lower-left grip fillet because of the stress concentration.

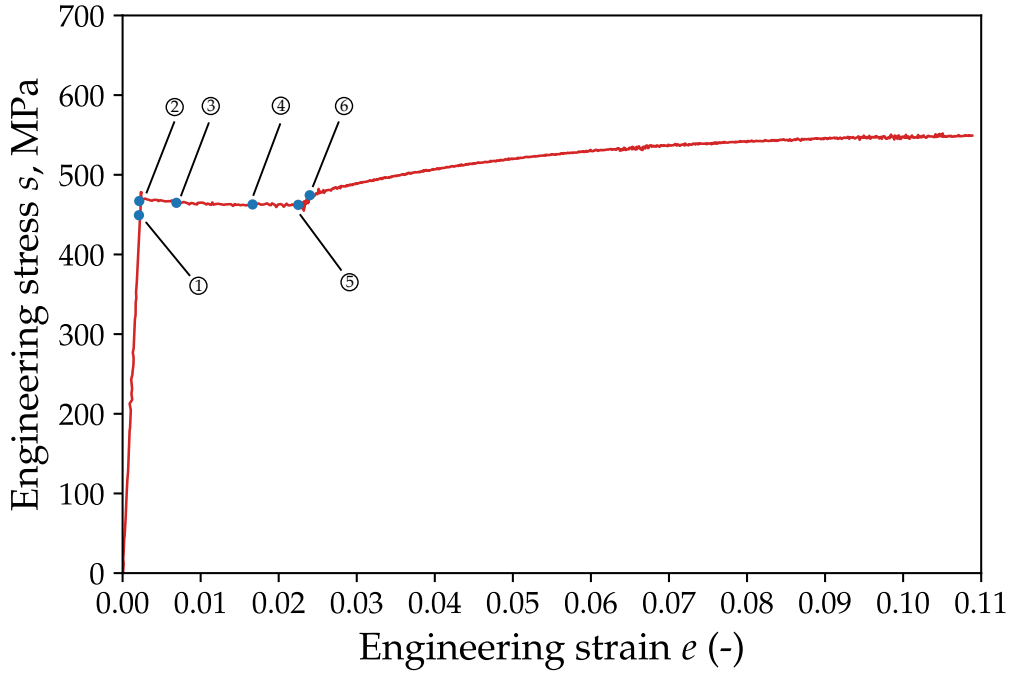

Figure 3.7: Measured engineering stress-strain curve of M01-01

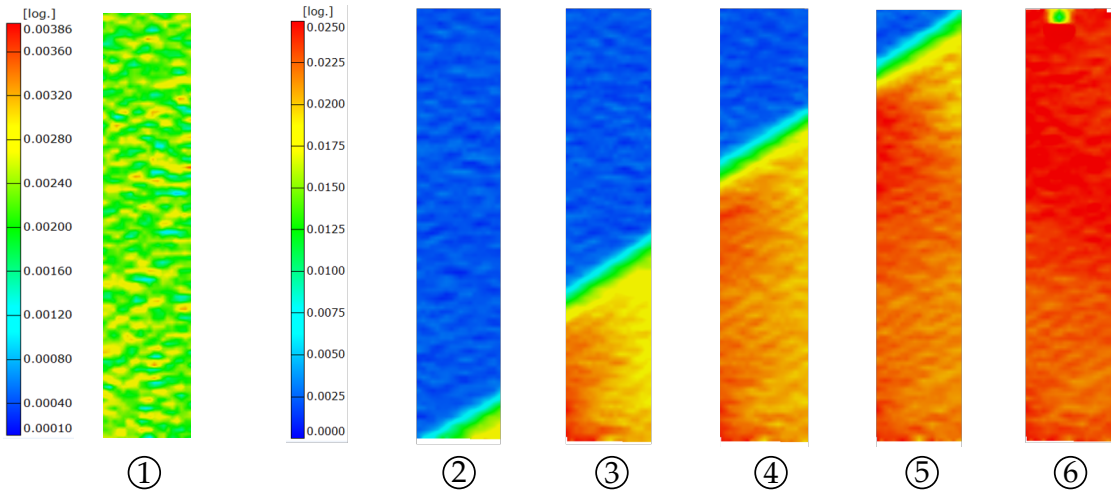

Figure 3.8: Longitudinal strain ϵ_{yy} maps of plain tensile specimen M01-01 at various stages of loading

However, this was not observed in the testing of M01-01 as only the region between strain gauges was observed. In the testing of M01-02, a full view of the specimen was captured and is presented in the subsection that follows.

The band inclines at a certain angle, from approximately 55° when the band initially starts at the lower-left end to around 70° at a later stage (configuration ⑤). In configuration ①, a homogeneous strain distribution is observed, indicating the plate deforms uniformly. It is shown in Figure 3.7 to be located in the elastic regime, in which no plasticity occurs throughout the plate. At the onset of yielding, a stress peak is noticed, followed by a sharp stress drop. Subsequent to the stress drop is the configuration ② in which we can see a distinguishable deformation band. The propagation of Lüders band is well described in the configurations ② to ⑤. In the strain hardening phase, the deformation of the plate is generally uniform, as shown in ⑥.

The general trend of strain evolution presented in Figures3.8 is also reflected by the local strain measurements of the strain gauges shown in Figure 3.9. Initially, when the plate is in linear-elastic regime, the local strains e_{loc} at all strain gauges increase with the overall strain e_o, indicating homogeneous deformation. Upon the termination of the elastic regime, it can be seen a significant boost in strain at SG-1 and SG-6, where the band reaches these two locations. Similar increases in strain occurs at the SG-4 and SG-5 are noticed at later stage of loading. Plummet in strains of SG-1, SG-4 and SG-5 are noticed at overall strain of about 0.029 , 0.036 and 0.023, respectively, which is due to the detachment of the strain gauges caused by excessive plastic deformations . Meanwhile, the strains at SG-4 and SG-5 are constant, which indicates the inhomogeneous deforming nature of the tested material.

3.2.4.2 *M01-02*

Figure 3.10 presents the measured stress-strain curve of M01-02 alongside that of M01-01. The measured stress-strain curve of M01-02 is in good agreement with that of M01-01. Like M01-01, local strains at the strain gauges were plotted and the overall strain measured by the extensometer, as shown in Figure 3.11. Sharp increase in strain at SG-4 is noticed at the onset of yielding while the strain at SG-4 remains constant. Both strain gauges became detached from the test sample when the deformation was excessive.

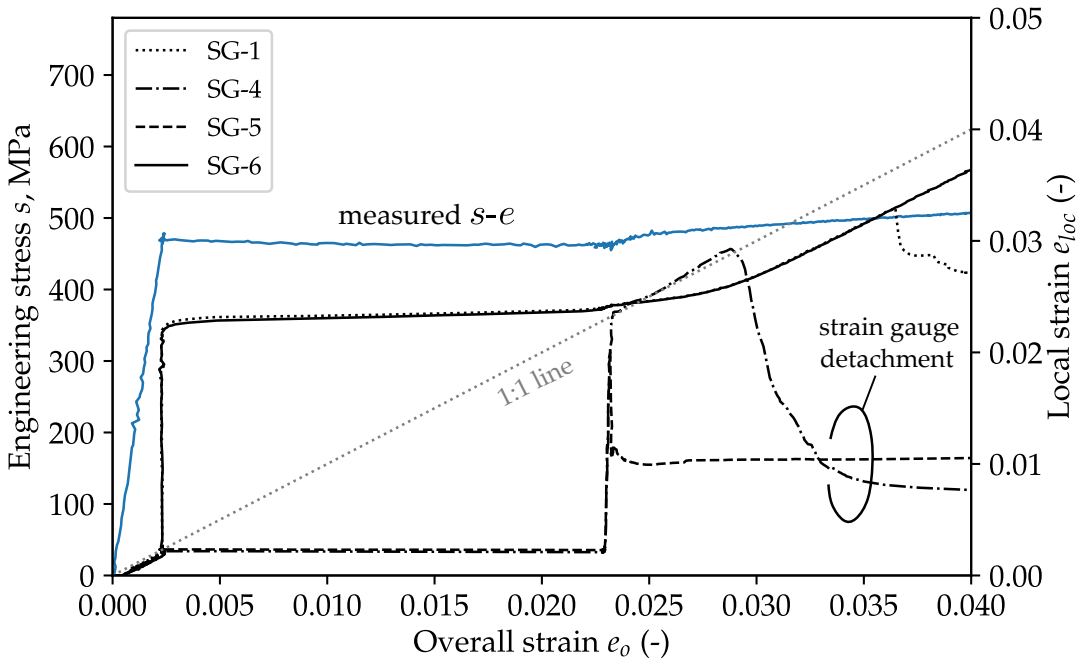

Figure 3.9: Local strain and overall strain measurements of M01-01

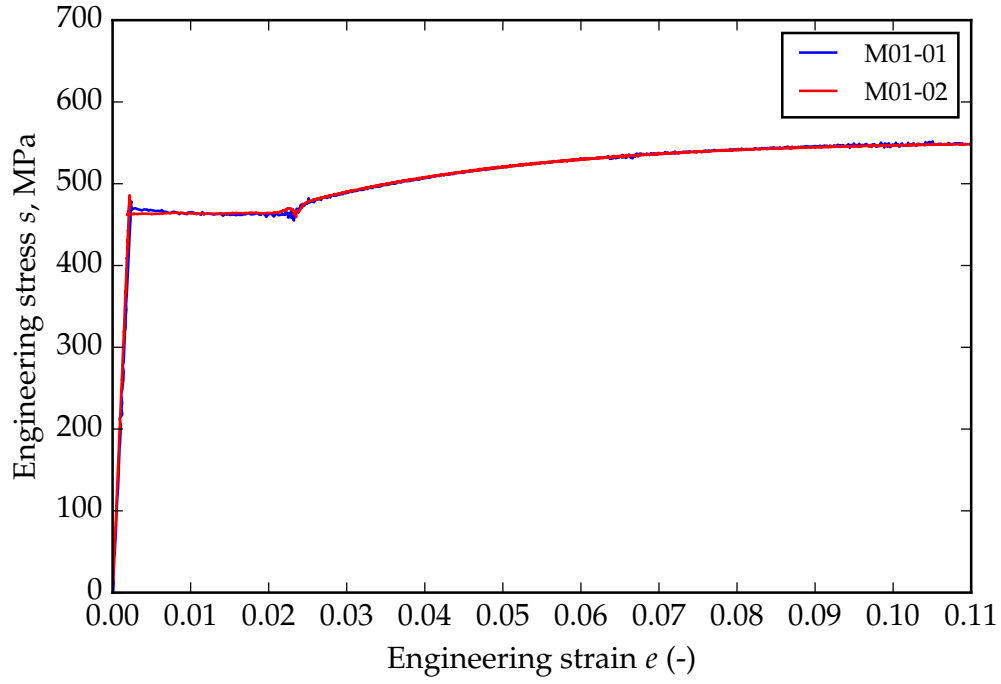

Figure 3.10: Comparison between the engineering stress-strain curves measured for M01-1 and M01-02

Figure 3.12 shows the longitudinal strain ε_{yy} maps of M01-02 during testing, which enables wider view than the strain maps of M01-01 shown earlier in Figure 3.8. In configuration ①, we can clearly see that the Lüders band initiates at the lower-left fillet that acts as a stress concentrator. Similar pattern of the propagating band is seen in configurations in ② to ⑤ as can be seen in Figure (strain maps of M01-01). No strain maps can be seen in a small amount of area as it was clamped by the extensometer.

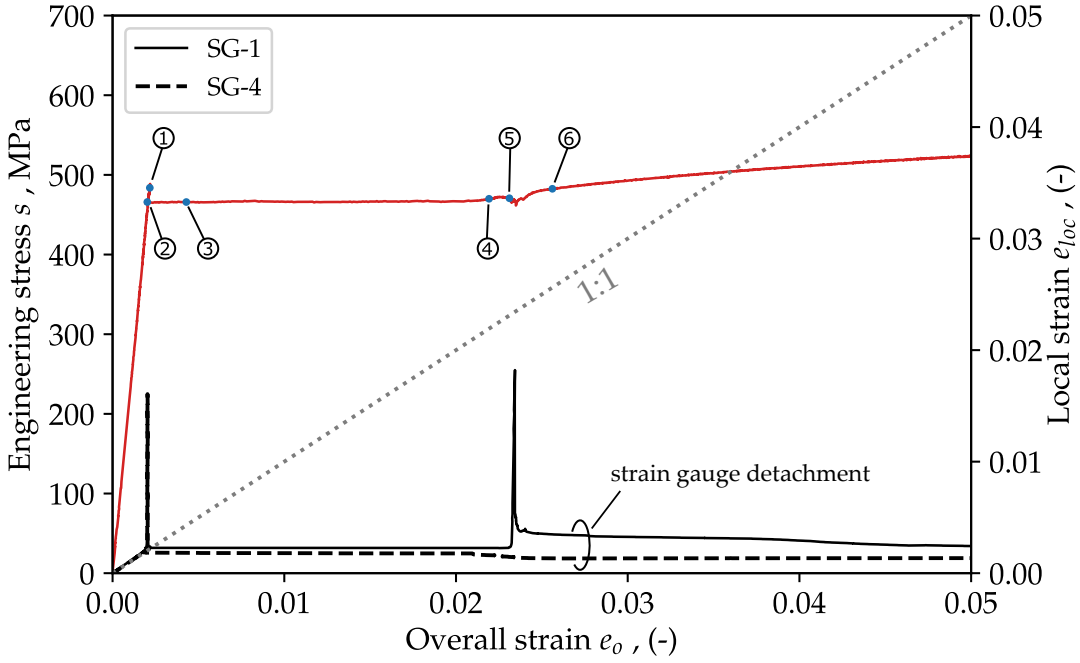

Figure 3.11: Local strain and overall strain measurements of M01-02

To verify the accuracy of strain measurements by DIC, the strain values measured by DIC were compared with the strain gauges at exactly the same location. The comparison of strains as a function of time is shown in Figure 3.13. Clearly, the local strain e_{loc} measurements by DIC are generally in good agreement with that by strain gauges except that some undulations can be seen for the DIC measurements.

3.2.4.3 *M01-03*

Figure 3.14 presents the load-extension (P-ΔL) response of M01-03. The P-ΔL response was chosen because the sample has a reduced section and thus the gross stress (P/A_0) is meaningless as a parameter describing material property.

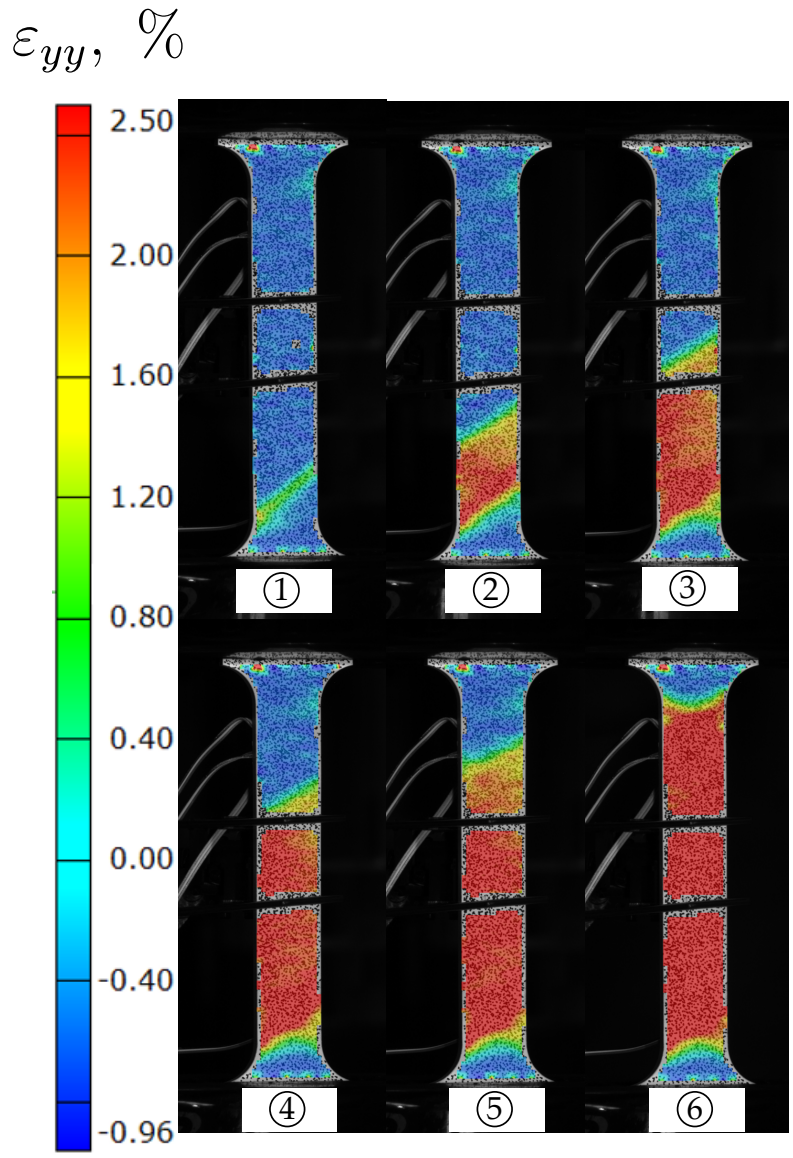

Figure 3.12: Longitudinal strain ε_{yy} map of M01-02

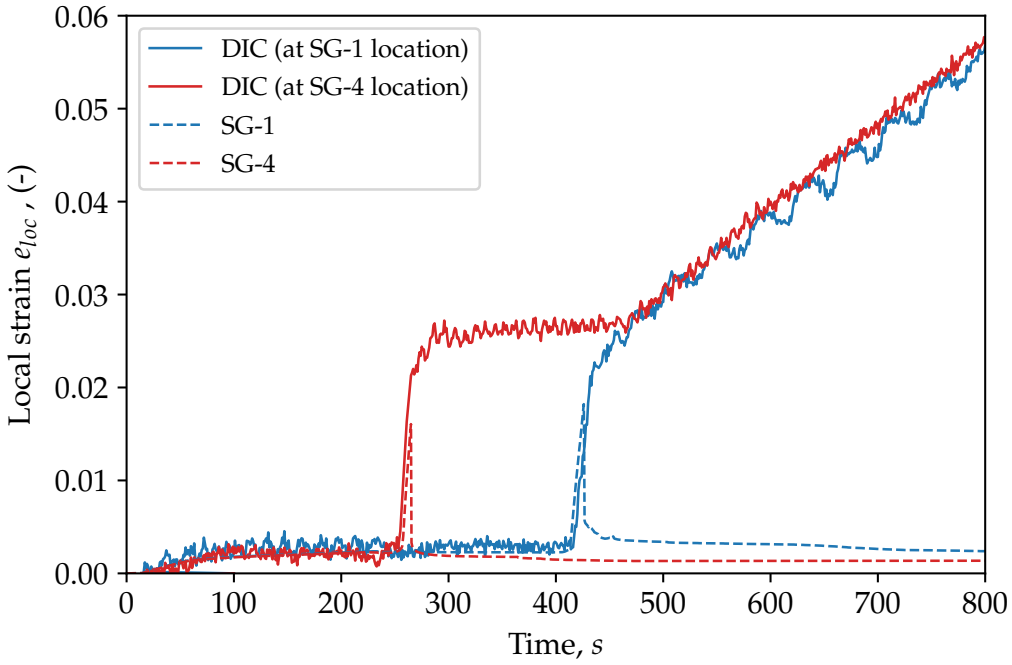

Figure 3.13: Comparison of strain measurements by DIC and strain gauges in M01-02

The P-ΔL curve exhibits roughly a roundhouse shape and neither a pronounced load peak nor load plateau is observed. A slight bump in load can be observed, which is followed by a very short ascending plateau. This may suggest that the Lüders strain localisation does not occur or propagate. In the study of Lüders band in RPV steels, Beardsmore et al. (2013) suggested that the mechanism of Lüders effect was still active despite that no band propagation was observed in cracked plates.

To find out the cause, we captured a series of deformation configurations that correspond to the points situated on the P-ΔL curve shown in Figure 3.14. In configuration ① which is close to the yield point, two localised plastic bands initiate at the tip of the left notch. The bands emanate and spread to the notch on the right. From ② to ③, the strain localisation passes across the net section of the reduced region to reach the tip of the notch on the right. Configurations ④ and ⑤ present the propagation of the strain localisation at the ligament of the notches. The the strain localisation intensifies in the notched area, and new localised plastic bands are formed at approximately 55° with respect to the loading axis. In configuration ⑨, another pair of bands are generated forming a symmetric strain localisation region that assembles a bowel. The strains in

the plastic localisation region continues to build up until the necking and the subsequent fracture occurs.

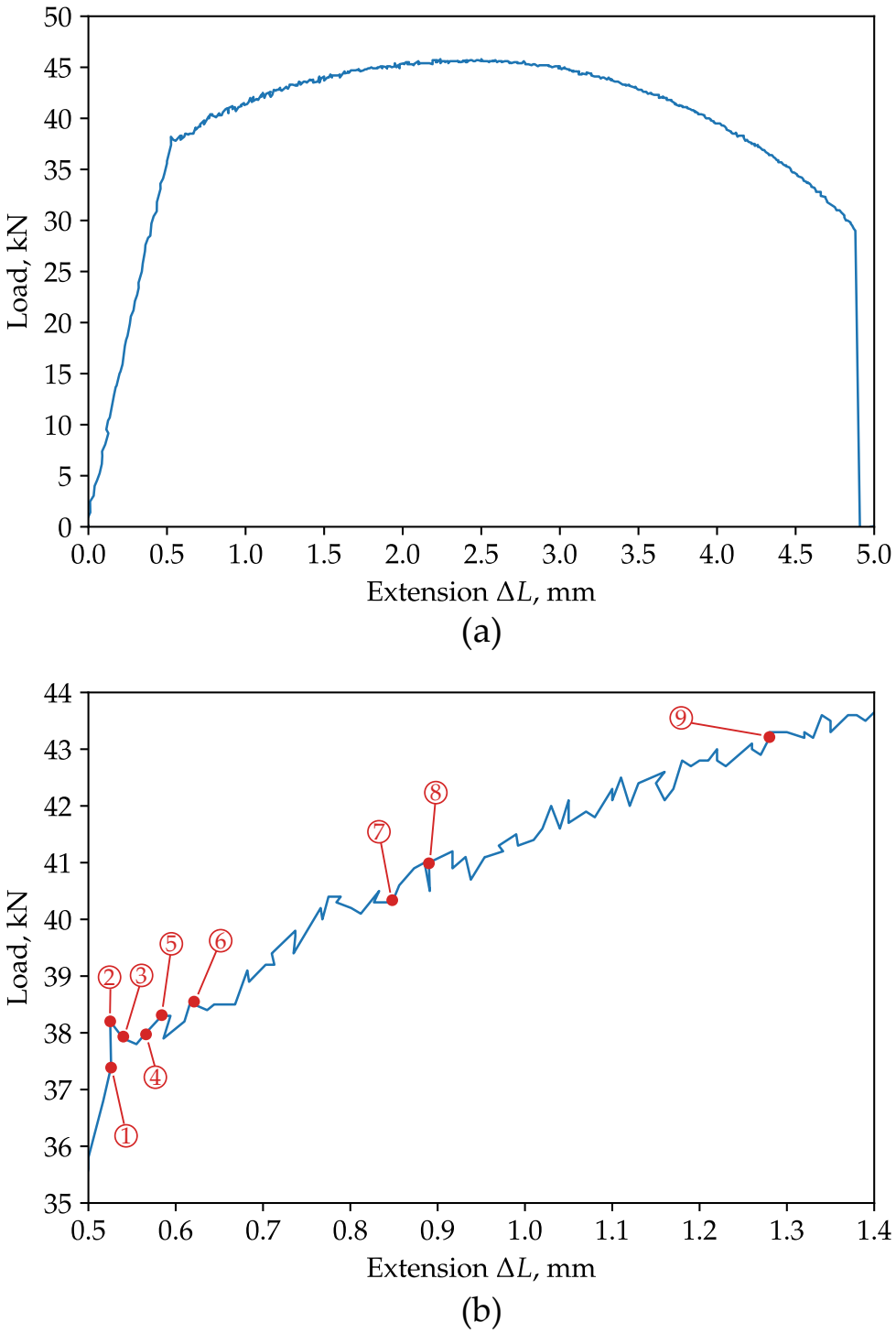

Figure 3.14: Load-extension response of M01-03: (a) global measured load-extension curve (b) close-up of the load-extension curve in the range of extension from 0.5 mm to 1.5 mm

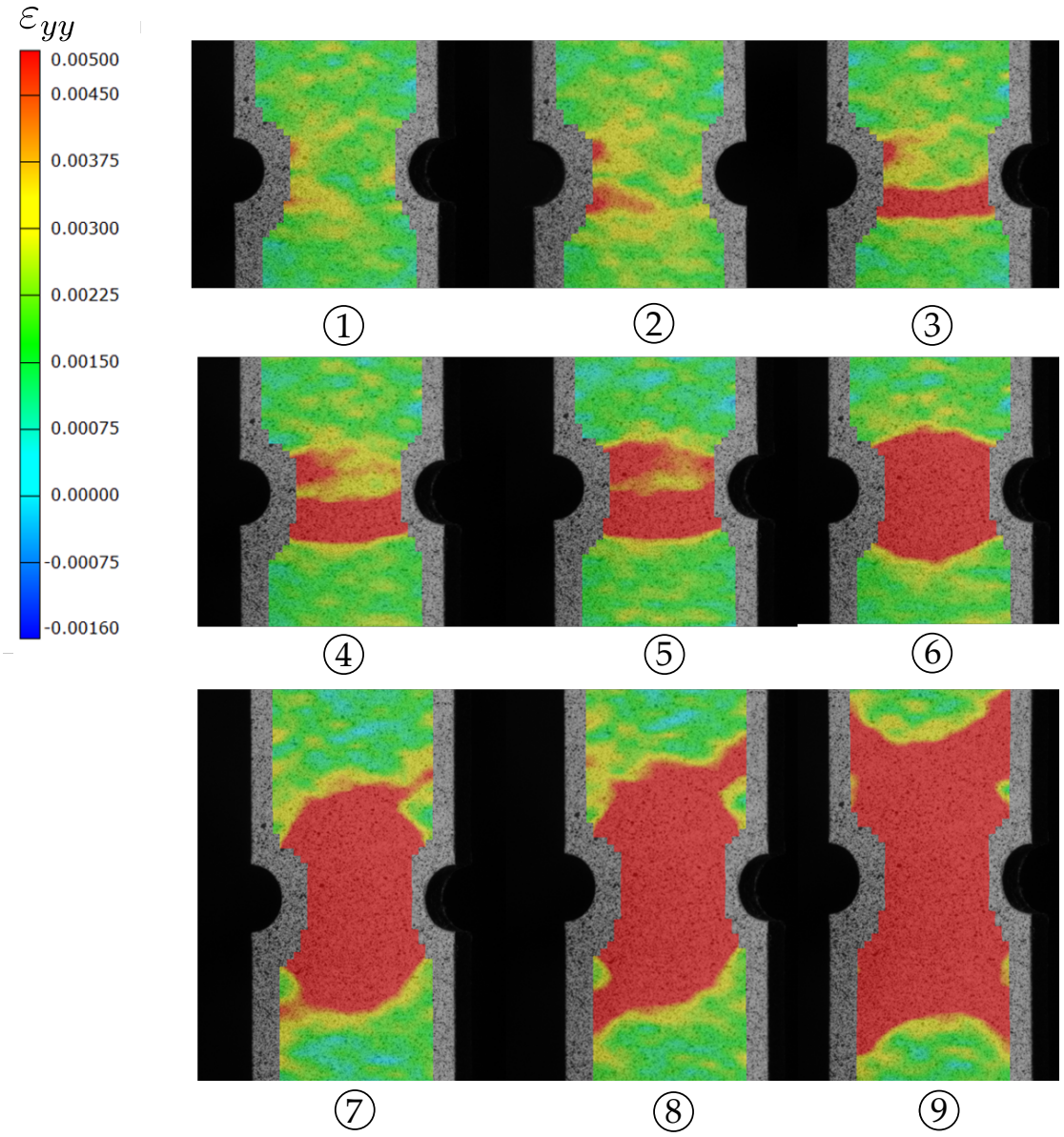

Figure 3.15: Longitudinal strain ε_{yy} maps of notched tensile specimen M01-03 at various stages of loading of Figure 3.14

3.2.4.4 *M01-04*

In the testing of M01-04, as we used a lower loading rate that accommodates the stress concentration effect due to the notches, we obtained a P-ΔL curve that is lower than that of M01-03. Figure 3.16 shows the comparison between the P-ΔL responses of M01-03 and M01-04. Both curves are in good agreement in elastic regime but start to diverge at the onset of yielding. The elastic limit of M01-04 appears higher than that of M01-03 as higher loading rate was applied to M01-03.

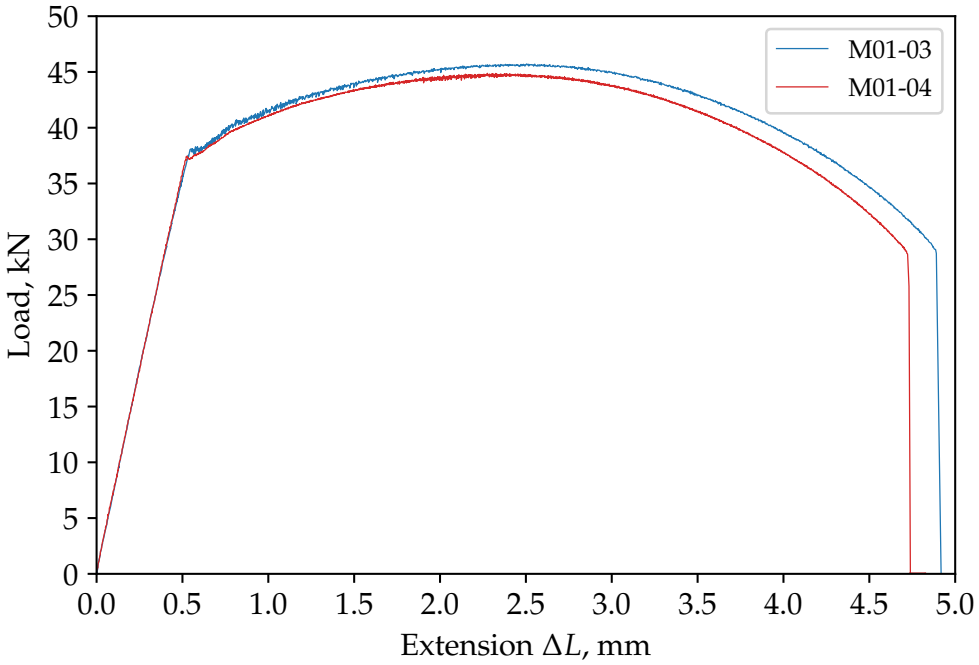

Figure 3.16: Comparison between load-extension responses of M01-03 and M01-04 (notched tensile tests)

Like M01-03, we selected a series of deformation configurations that correspond to the numbered points in the close-up P-ΔL curve of M01-04 in Figure 3.17. Figure 3.18 shows the longitudinal strain (ε_{yy}) maps in the notched regions of M01-04 during testing. From the ε_{yy} maps, we can see that the deformation in the notched region of M01-04 is very similar to that in M01-03. The only exception is that the upper band of strain localisation propagates across the ligament first. Therefore, in favour of brevity, we will not elaborate the plasticity evolutions in M01-04 further.

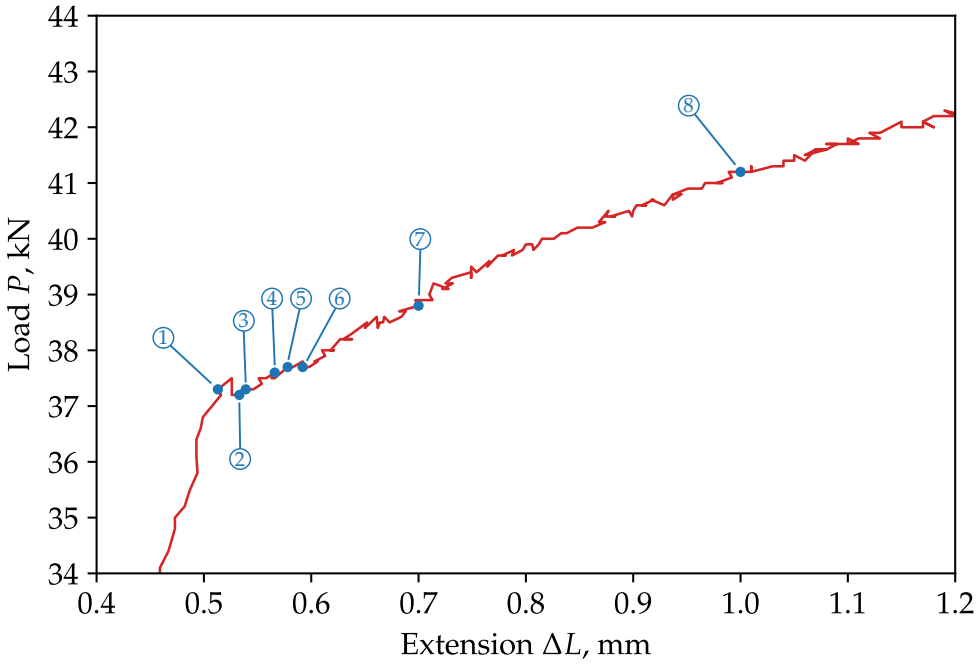

Figure 3.17: Close-up of the load-extension (P-ΔL) curve of M01-04 in the range of extension from 0.5 to 1.5mm

3.3 COMPUTATIONAL PROCEDURES

3.3.1 *Constitutive models*

The UDU stress-strain model was used to simulate the Lüders propagation in commercial FE software Abaqus 6.14. The measured stress-strain curve of M01-02 is taken as the base stress-strain curve and is fitted to the UDU framework. The reason for doing so is that the DIC measurement of M01-02 will be used to validate the FE analysis, therefore we selected the measured stress-strain curve of M01-02 instead of the average of the two tests. Figure 3.19 presents the stress-strain curves to be used in FE simulations, which are based on the measured stress-strain curve of M01-02. The Flat stress-strain model is the simplest model that is based on the measured stress-strain curve of M01-02 and neglects the upper yield point and the subsequent stress drop. The Flat model has a flat stress plateau with a plateau stress level of the average of the measured stress plateau. Following Shaw and Kyriakides (1997), Kyriakides and Miller (2000), Kyriakides et al. (2008), Aguirre et al. (2004), and Hallai and Kyriakides (2011b), we constructed the UDU models on the basis of the Flat

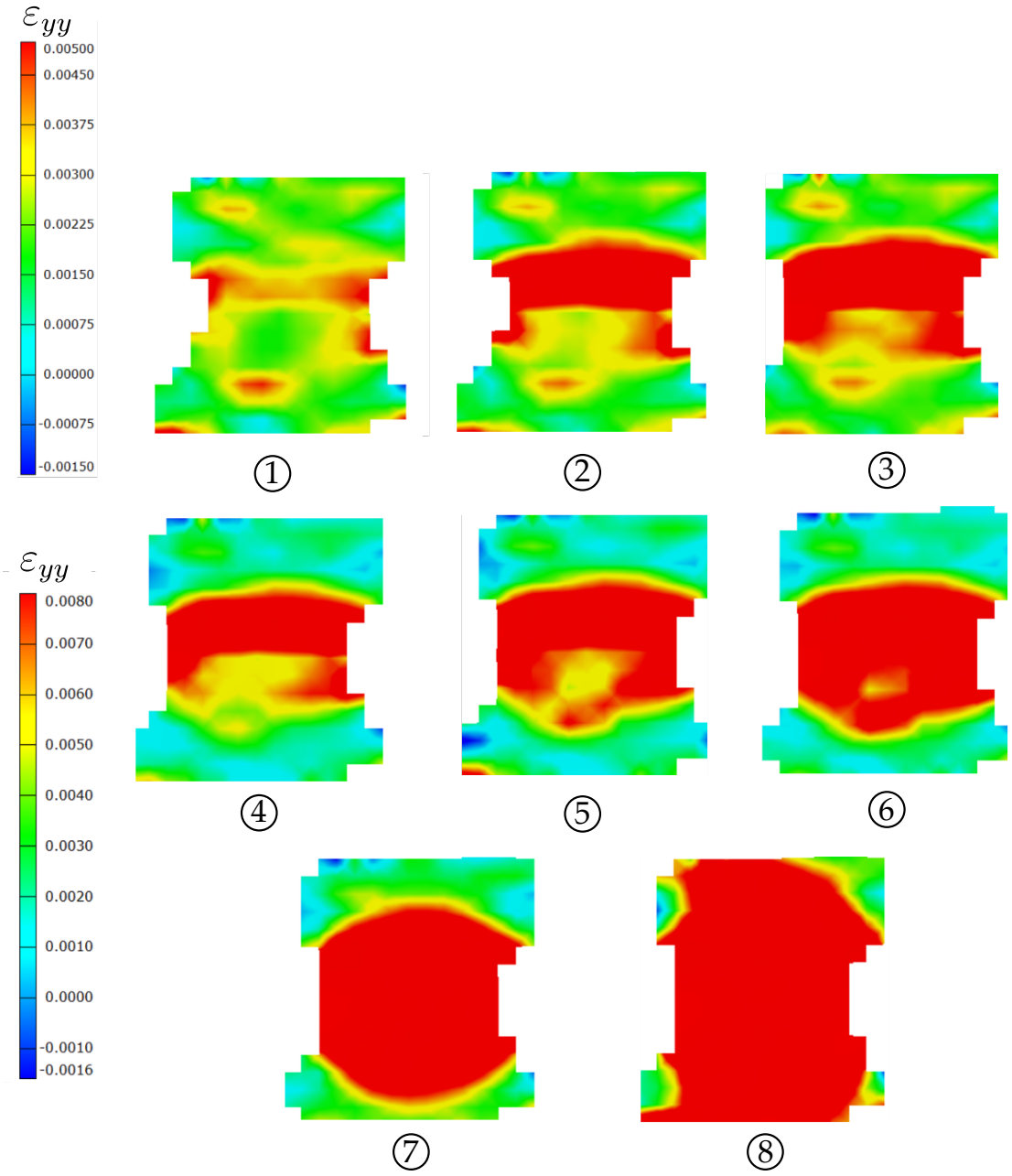

Figure 3.18: Longitudinal strain ε_{yy} maps of notched tensile specimen M01-04 at various stages of loading

stress-strain curve. Various softening modulus E_L($\partial s/\partial e$, the slope of the linear softening branch) were used to investigate effect of the strain softening on the simulated structural behaviour. The resulting normalised softening modulus ($\bar{E}_L \equiv |E_L/E|$) are 0.005, 0.015 and 0.025. The parameters of the UDU models are listed in Table 3.2.

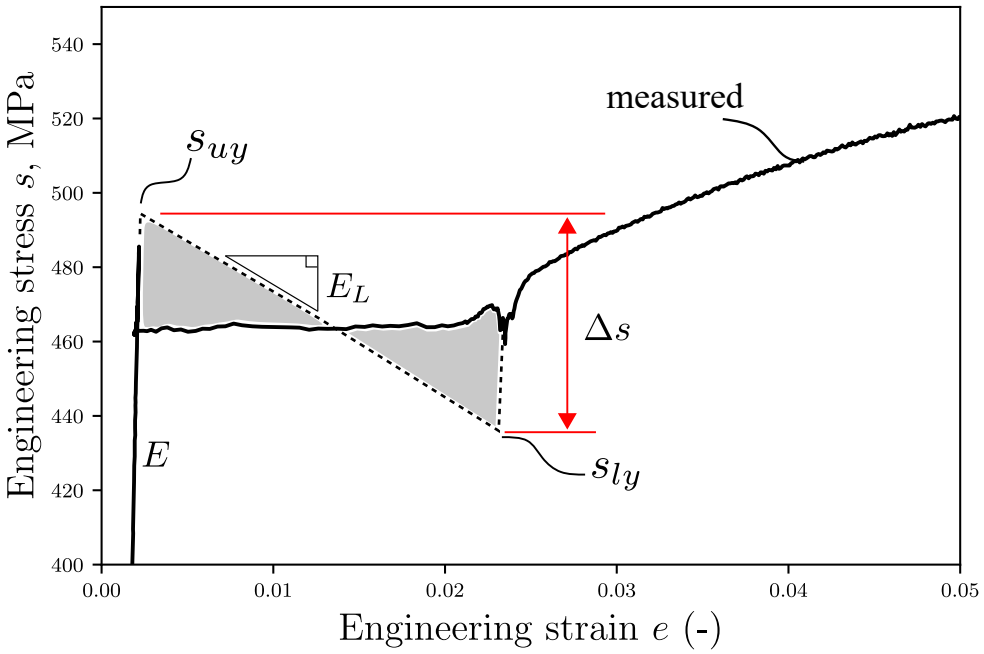

Table 3.2: Parameters of material models used in FE simulation of M01-02

Material model	E(MPa)	R_{eL}(MPa)	Δe_L%	$\bar{E}_L$	$\Delta s/R_{eL}$
Flat	222409	463	2.1	0	0
UDU-1				0.005	0.0504
UDU-2				0.015	0.151
UDU-3				0.025	0.252

3.3.2 *Finite element models*

3D FE model of the specimen was generated in Abaqus 6.14. The model was meshed with 20-node, reduced integration hexahedral elements (type C3D20R). Figure 3.21 shows the mesh configuration of the model and the applied boundary conditions. The mesh has two elements through the thickness with the dimensions in all directions (x, y and z) being equal. A prescribed

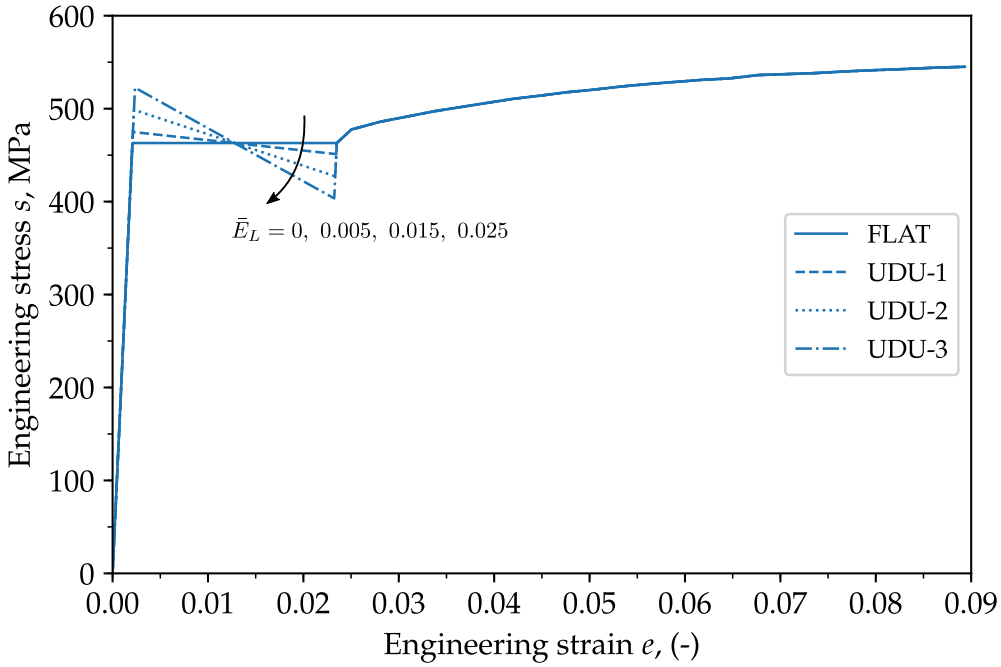

Figure 3.19: Stress-strain curves used in FE simulation of M01-02

displacement was applied to the nodes at the upper end while the lower end was fixed.

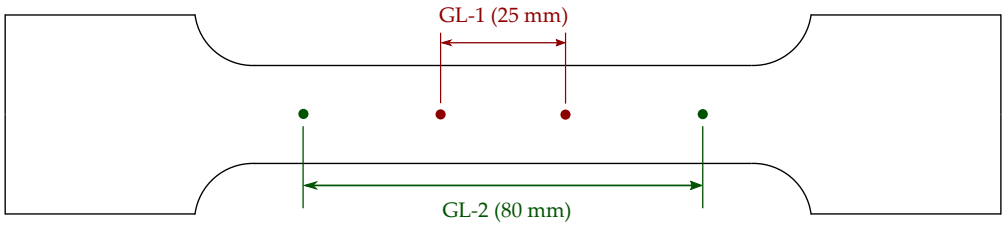

Figure 3.20: Definitions of gauge length in FE model of the plain-sided specimen

In the test, Lüders band initiated near the lower-left grip shoulder and propagated towards the upper end. The initiation of single Lüders localisation regime may be due to the inherent imperfections such as flaws or material inclusions. As the FE model is 'perfect' and symmetric, two identical bands are expected to initiate at both grip fillets and propagate towards each other. Therefore, to generate Lüders localisation similar to experiment, a certain extent of asymmetry must be introduced. The asymmetry could be in the form of asymmetry loading, material imperfection (an element with a lower yield stress) or geometric imperfection.

In this work, we introduced a geometric imperfection by misplacing the nodes on the side by 0.1 mm. The imperfection is sufficient to initiate Lüders localisation at the wanted location while is small such that the global structural behaviour is not affected.

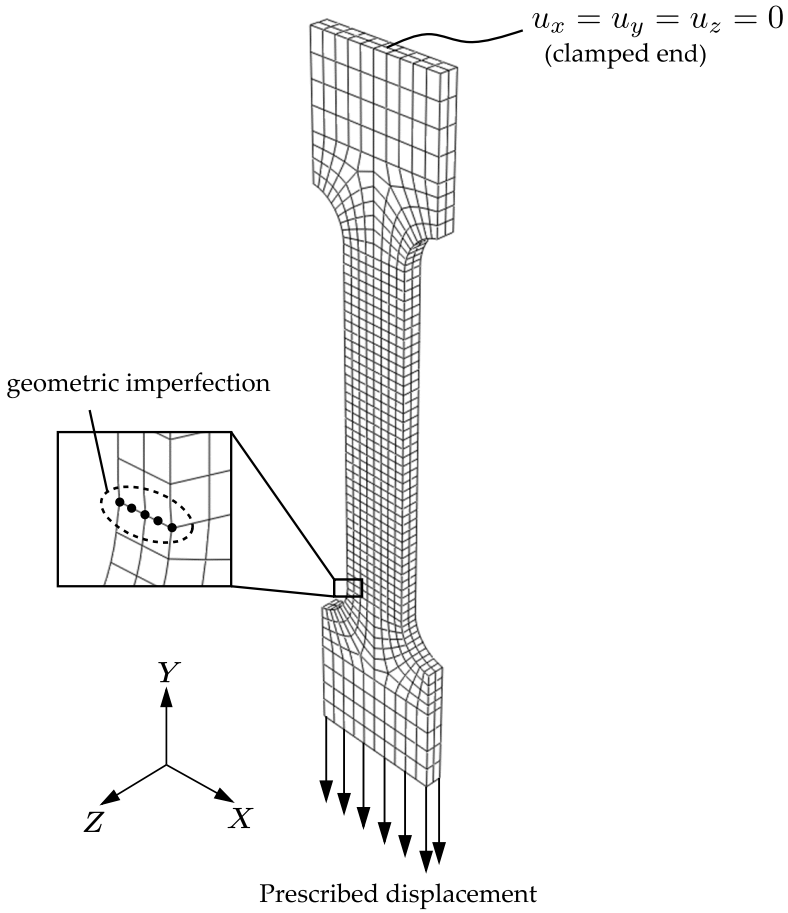

Figure 3.21: Mesh configuration and the applied boundary conditions of FE model of the plain-sided specimen

Figure 3.22 shows the mesh configuration of the side-notched specimen. The model has a focused and refined mesh pattern at the notched region and relatively coarser mesh in the regions far away from the notches. In the notched region, the mesh consists of 32 elements in the half annulus (eight elements in the $\pi/4$ region). The radial dimensions of the element in the notch tip region are in the order of 0.03.

The rate-dependent solution of FE simulations containing strain softening can be regularised by introducing rate-dependence or higher order gradients in the formulation with an intrinsic length scale. In the present work, we used a simple power-law rate-dependence which has been demonstrated to effectively reduce the mesh sensitivity due to strain softening (Needleman 1988; Nacar

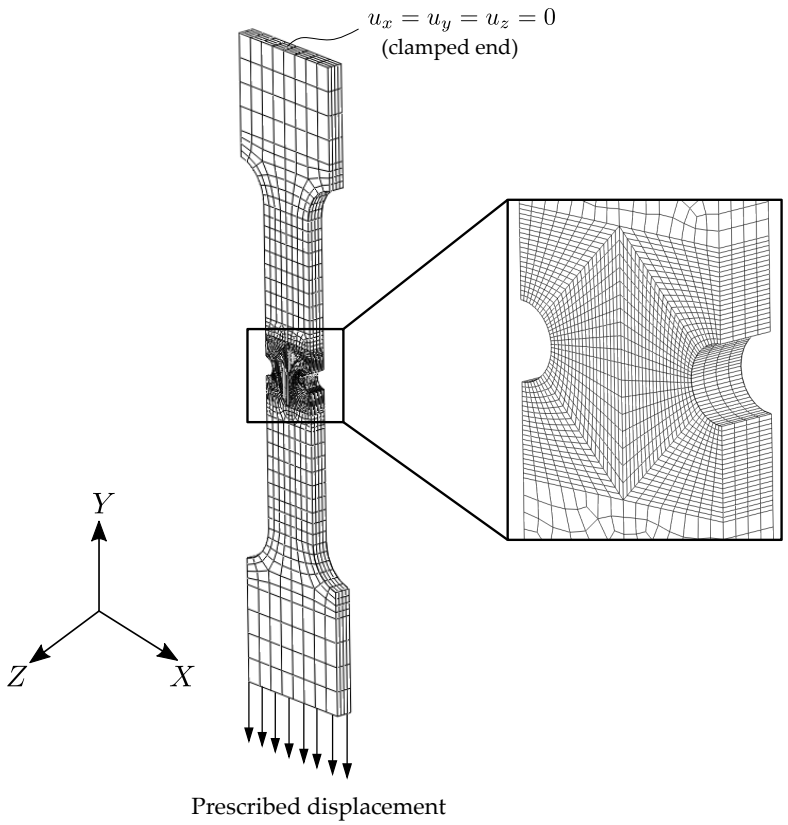

Figure 3.22: Mesh configuration and the applied boundary conditions of FE model of the side-notched specimen

et al. 1989). Other researchers (Hallai and Kyriakides 2011b, 2013; Liu et al. 2015) have employed this regularisation approach to achieve better convergence and remove mesh sensitivity. The rate-dependence takes the following form:

$$\frac{\dot{\varepsilon}^{p}_{eq}}{\dot{\varepsilon}_0} = \frac{\sigma}{\Sigma\left(\varepsilon^{p}_{eq}\right)} \tag{3.2}$$

where ε_0 is a reference rate, $\Sigma\left(\varepsilon^{p}_{eq}\right)$ is the measured stress-plastic strain response (in terms of true stress-strain curve) at this strain rate and m is the rate exponent. Rate exponent $m = 0.001$ is found to be most suitable in that it removed mesh sensitivity while having marginal effects on the global stress-strain (load-elongation) behaviour.

3.3.3 *Results*

3.3.3.1 *Plain sided specimen*

Figure 3.23 compares the engineering stress-strain curve measured from the test and that calculated from FE simulations using various material models. It can be seen that the curves produced using all material models were able to predict the general trend of that measured. However, the Flat model did not reproduce the upper yield stress, but instead a perfectly flat stress plateau. The UDU models, on the other hand, predicted a sharp stress peak preceding a plunge, subsequently followed by a stress plateau. As can be observed in the zoomed-in image of the stress plateau segment, the value of the upper yield stress predicted depends on the material model used. Precisely, the UDU model with a higher $\bar{E}_L$ ratio produces a higher value of the upper yield stress. The UDU model with a $\bar{E}_L = 0.005$ did not seem exhibit the upper yield point, as this $\bar{E}_L$ ratio may be insufficiently large to reproduce the experimental events. Interestingly, the $\bar{E}_L$ ratio is found to also influence the predicted stress plateau, in terms of its height and length. A higher $\bar{E}_L$ tends to produce a higher and longer stress plateau. After the Lüders plateau terminates of each stress-strain curve predicted, all these curves start to converge and agree well with experimentally-measured one.

To compare the macroscopic events of Lüders banding predicted from FEA against those captured from DIC, the longitudinal strain (ε_{yy}) and equivalent plastic strain (ε^p_{eq}) maps are presented in Figures 3.24 to 3.27 and Figures 3.28 to 3.40, respectively, for various nominal strain levels. Apparently, no localised deformation was observed in the model using Flat stress-strain curve. Rather, the deformation predicted was fairly uniform over the parallel length of the modelled specimen throughout the tensile loading, in terms of both ε_{yy} and ε^p_{eq}. The models using the UDU material laws all show the propagating band of localised deformation that initiated at the fillet near the grip region, as shown in Figures 3.24 and 3.28. Figures 3.25 to 3.31 present the propagation of the simulated Lüders band from the lower fillet region of the modelled specimen to the other. Notwithstanding that the UDU with $\bar{E}_L = 0.005$ (referred to as UDU-1) produces the propagating strain localisation, the front of the simulated Lüders band appear very diffused and blunted, which is largely

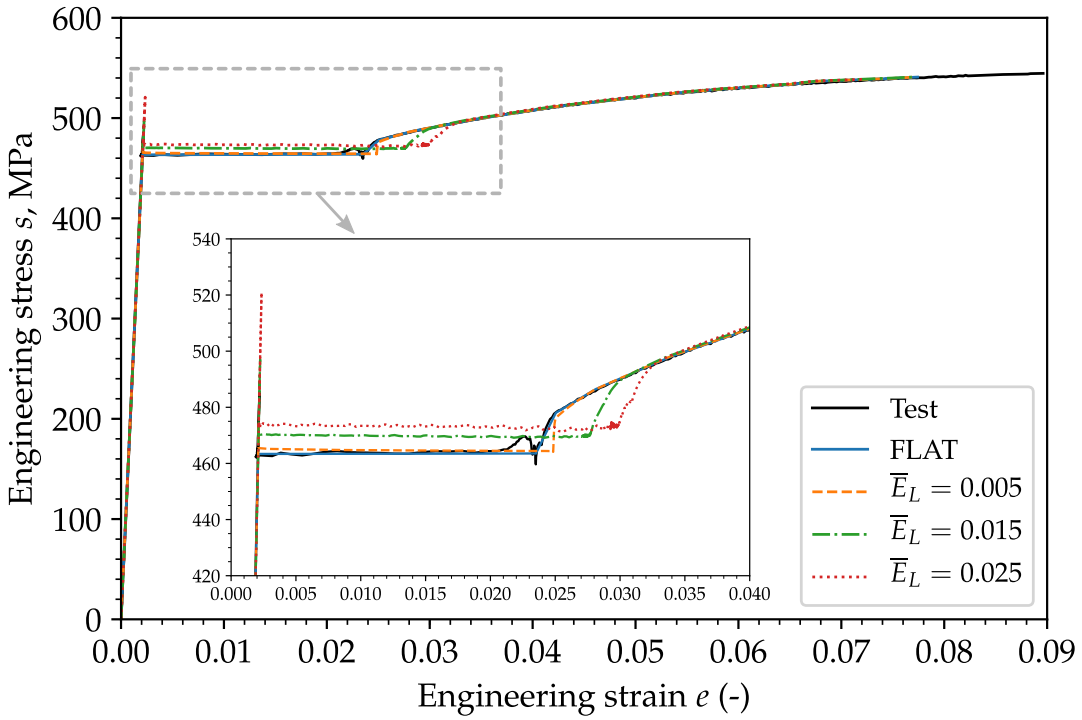

Figure 3.23: Global stress-strain responses of the FE models using different material models in comparison with that measured from the test

different from that observed in the test. The models using the UDU-2 and UDU-3, in comparison, reproduced a sharp, straight and inclined band front in line with the one observed from DIC (see Figure 3.8). From Figures 3.35 to 3.30, it is observed that among the models using the UDU material laws, the band in the UDU-1 model reached the upper end first, followed by UDU-2 and then UDU-3. This agrees with the effect of the E_L ratio adopted for the UDU material law on the predicted length of Lüders plateau shown in Figure 3.23. On the grounds of the nominal stress-strain response and strain distribution, the UDU-2 ($\bar{E}_L = 0.015$) is considered optimal in reproducing the macroscopic events associated with Lüders banding observed in the test.

3.3.3.2 *Side-notched specimen*

The global response and strain distributions are presented herein to compare the FE results of the side-notched specimen against those observed in the test. Similar to the results presented for FEA of plain-sided specimen (see Figure 3.23), the gross stress versus elongation response is shown in Figure 3.32. It should be noted, however, the gross stress P/A represents the stress in the region of parallel length, which is away from the notches where the stress are

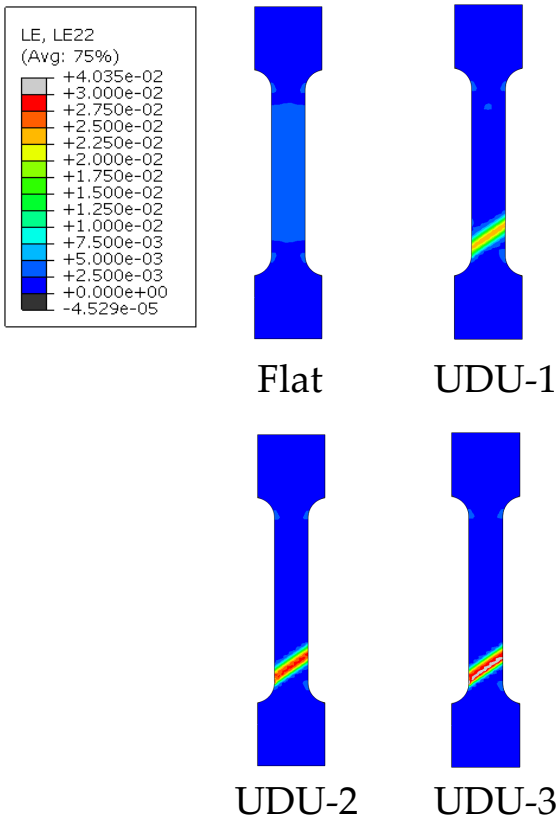

Figure 3.24: Longitudinal strain ε^{p}_{eq} maps in FE simulation of X65 plain-sided tensile specimen with various material models at 0.37% strain

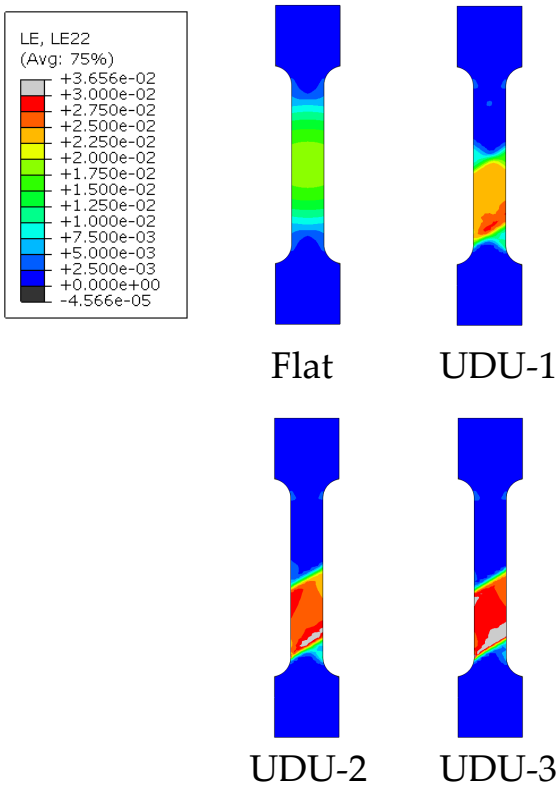

Figure 3.25: Longitudinal strain ε^{p}_{eq} maps in FE simulation of X65 plain-sided tensile specimen with various material models at 1.5% strain

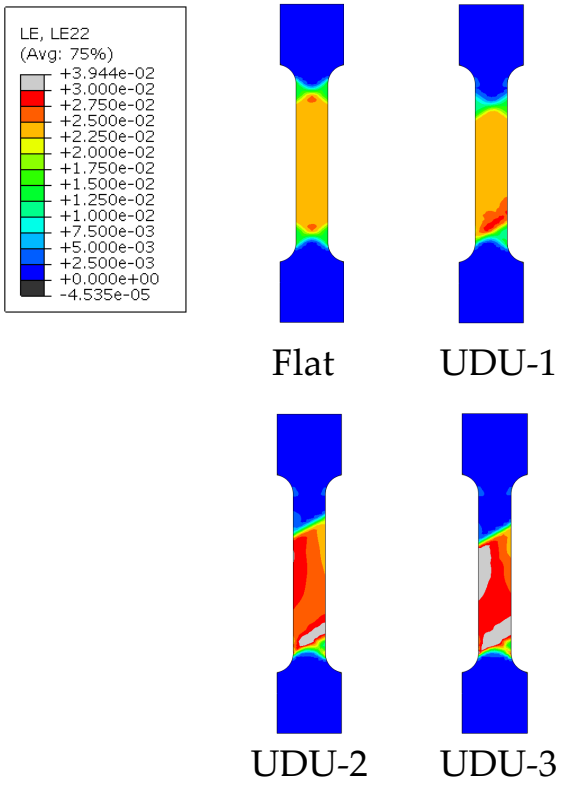

Figure 3.26: Longitudinal strain ε^p_{eq} maps in FE simulation of X65 plain-sided tensile specimen with various material models at 2.4% strain

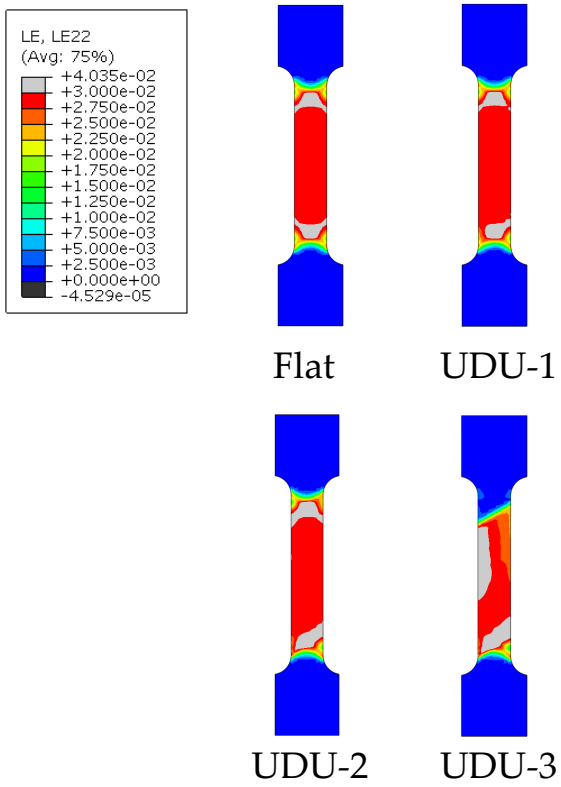

Figure 3.27: Longitudinal strain ε^p_{eq} maps in FE simulation of X65 plain-sided tensile specimen with various material models at 2.9% strain

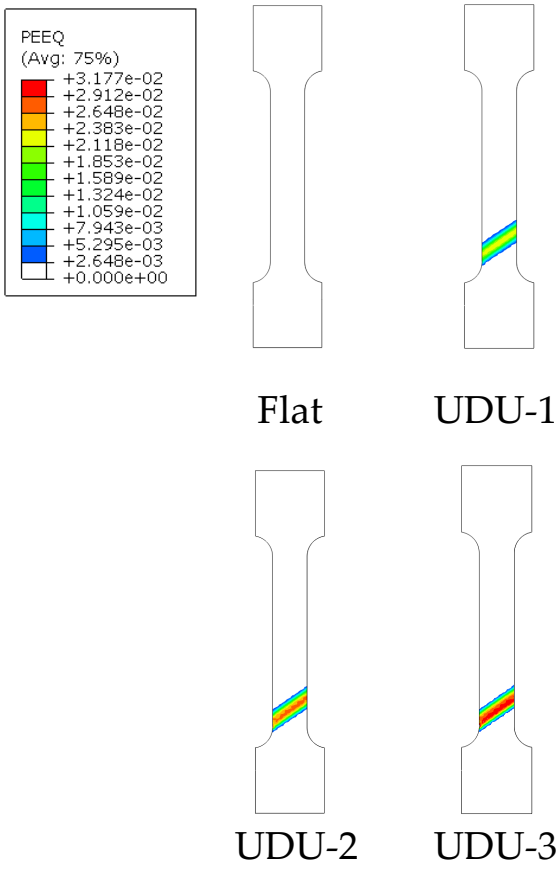

Figure 3.28: Equivalent plastic strain ε^{p}_{eq} map in FE simulation of X65 plain-sided tensile specimen with various material models at 0.37% strain

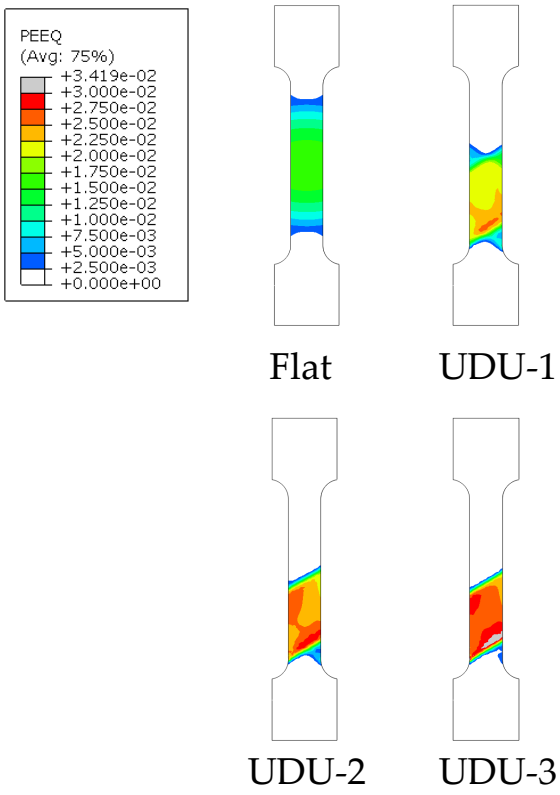

Figure 3.29: Equivalent plastic strain ε^{p}_{eq} map in FE simulation of X65 plain-sided tensile specimen with various material models at 1.5% strain

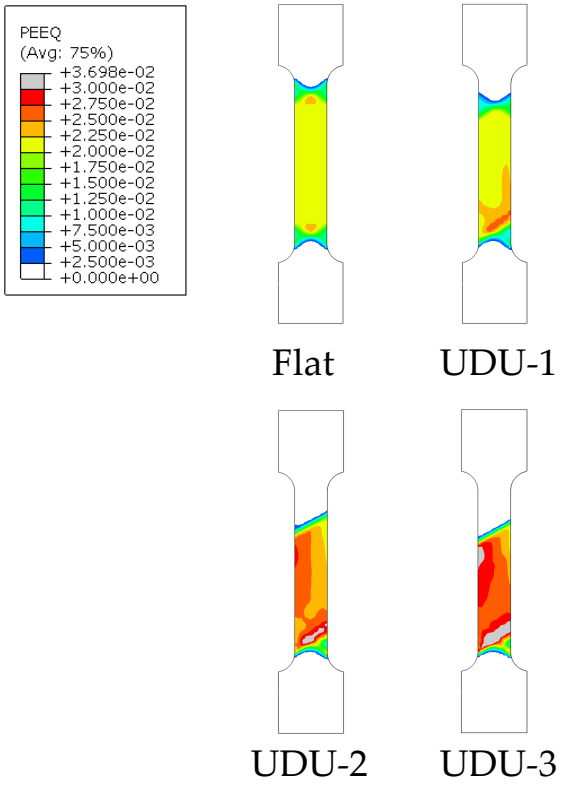

Figure 3.30: Equivalent plastic strain ε^p_{eq} map in FE simulation of X65 plain-sided tensile specimen with various material models at 2.4% strain

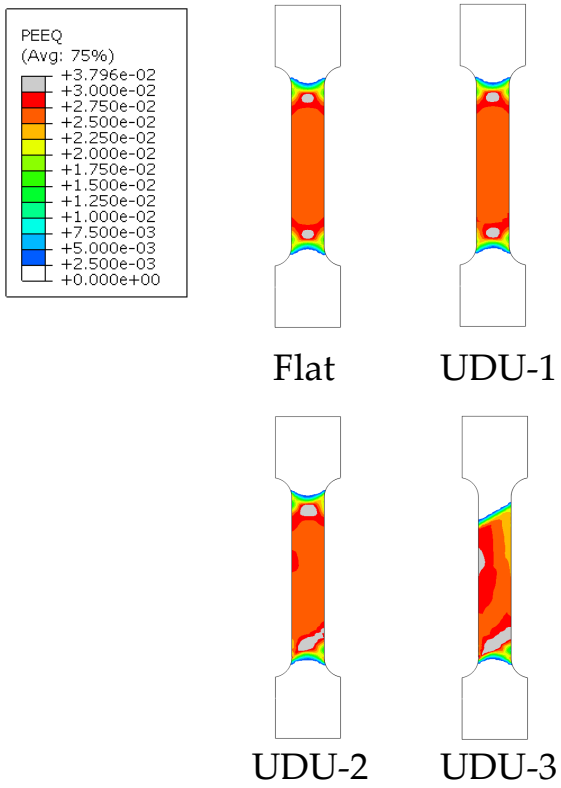

Figure 3.31: Equivalent plastic strain ε^p_{eq} map in FE simulation of X65 plain-sided tensile specimen with various material models at 2.9% strain

significantly higher due to stress concentrations, and the elongation is extracted over the extensometer length (25 mm). Hence the plotted gross stress versus elongation response does not quantify the stress-strain behaviour of the notch specimen as the deformation is rather inhomogeneous. Instead, the behaviour is a qualitative measure of the overall deformation in the notched region, and also a way that enables the comparison against the test to be made.

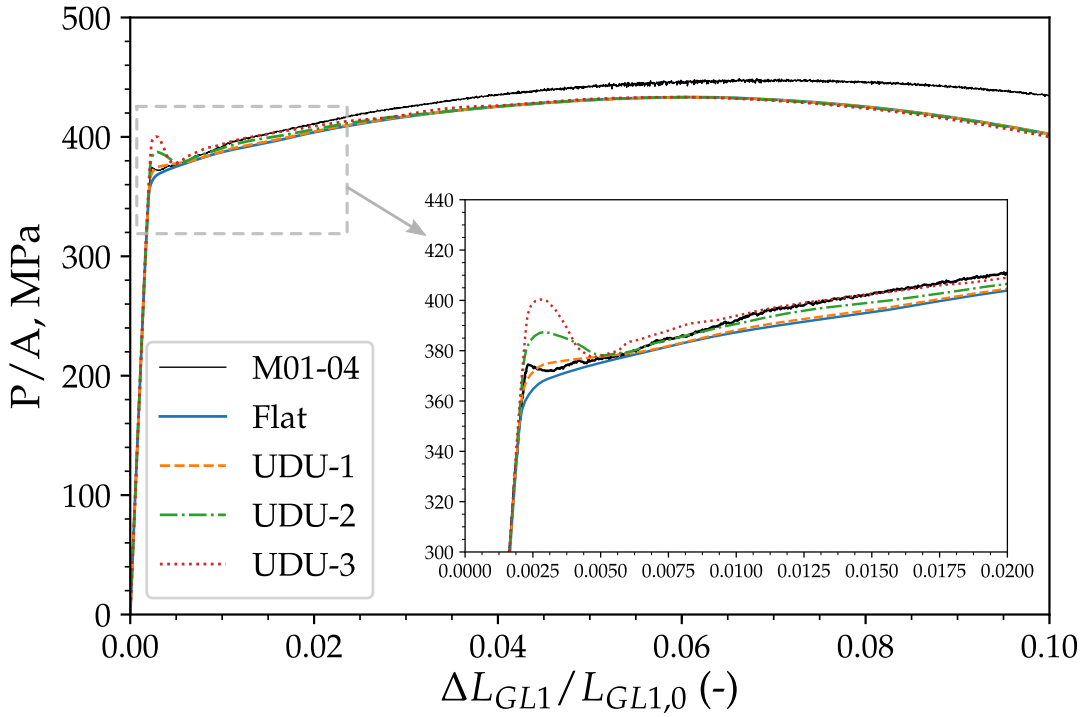

Figure 3.32: Global stress-strain responses of the FE models of side-notched specimen using different material models in comparison with that measured from the test

From Figure 3.32, it is shown that the general behaviour of the load-displacement (or stress-elongation) response was captured by the FEA, exhibiting an initially upward and subsequently downward trajectory. Deviations between the FEA and test is noticed in terms of the global behaviour and is shown to enlarge as the elongation increases. This may be due to the nature of the analysis undertaken, which is essentially rate-independent, and the material properties adopted were measured from quasi-static tensile tests loaded in a single loading rate. When the material properties were used in a rate-independent analysis, the strain rate effect may not be captured in the notched region where the local strain rate was expected to be higher than that in the parallel-length region. Since the material properties were measured from a fixed loading rate and

thus treated as rate-independent, it is unclear to what extent the strain rate effect has come to play and what exactly the strain rate sensitivity should be. Like the observation shown in Figure 3.23 for the FEA of the plain tensile specimen, the value of $\bar{E}_L$ is found to have an impact on the global response of the side-notched specimen, in particular, in the elongation 0.25% to 0.5% where the plasticity started to propagate from one notch to another. The UDU models are observed to produce a bump on the global response curve when the elastic loading phase is terminated. This is in line with the global response of the test which contains a slight bump between the globally elastic and plastic segments. The bump resembles the yield point phenomenon observed in a uniaxial tensile test and is considered to be the process where the Lüders instability came into effect. Note the simulated bumps or peak stresses, similar to those for uniaxial tensile test (see Figure 3.23), are affected by the value of $\bar{E}_L$ used. Clearly, a higher value of $\bar{E}_L$ ratio leads to a higher and sharper bump or peak stress, whereas the Flat material law ($\bar{E}_L = 0$) produces no bump altogether but a smooth elastic-plastic transition instead. Following the bumps, all simulated curves started to gradually converge.

Figures 3.33 to 3.36 and Figures 3.37 to 3.40 show the longitudinal strain and equivalent plastic strain maps of the notched specimen model for various elongation or global strain. Only the strains near the notched region are shown as the deformation is fairly localised due to stress concentration of the notches, and thus the regions distant from the notches remained essentially elastic. Note that the colour scale of the longitudinal strain maps shown in Figures 3.33 to 3.36 was set similar to that captured by DIC (shown in Figure 3.18). This facilitates the comparison of the deformation between the test and FEA, but may not show minor details at higher loadings where the plasticity has engulfed the whole notched region, as shown in Figures 3.35 and 3.36. It can be seen that the development of longitudinal strains predicted in FEA using both Flat and UDU material laws exhbits a similar trend as that captured with DIC (shown in Figure 3.15). The UDU models seem to predict a more localised deformation regime than the Flat model. It can be noted that the extent of strain localisation depends on the value of $\bar{E}_L$ employed.

As presented in Figures 3.35 and 3.36, the models using UDU-2 and UDU-3 exhibit fairly localised strain region which tends to branch off and emanate.

This is more pronounced in terms of the equivalent plastic strain distributions at higher loadings shown in Figures 3.39 and 3.40. Note that no additional stress concentrations or perturbations were applied to the FE models, the FE models therefore produce a nearly symmetric strain distributions, rather than the ones observed in the test where the strain localisation spreads from one notch to another. The model using UDU-3, however, exhibits an asymmetric behaviour at a higher loading (3.32%), which can be seen from Figure 3.40. This may due to the significant strain localisation induced by the UDU-3 model ($\bar{E}_L = 0.025$), which led to the deviation of the tensile deformation from the loading axis and the associated bending moment.

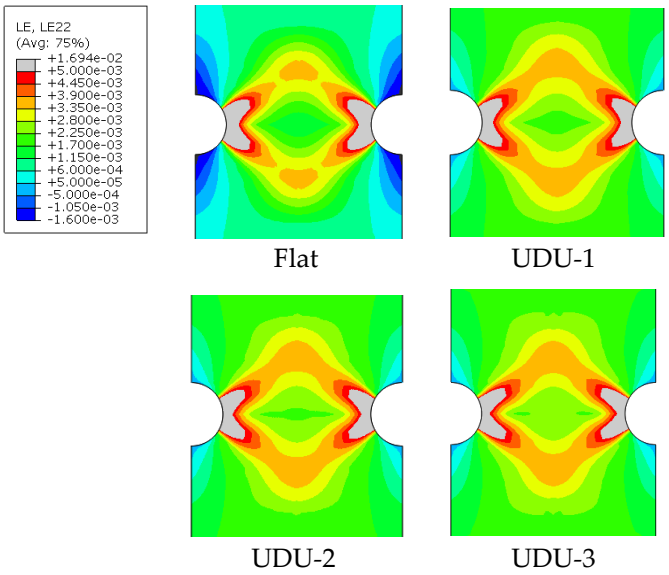

Figure 3.33: Longitudinal strain ε_{yy} map of FE models of notched tensile specimen with various material models at 0.27% strain

3.4 DISCUSSION

3.4.1 *Mesh sensitivity*

Strain softening is well-known to be problematic in FE analysis, leading to difficulties in convergence and mesh sensitivity. Non-convergence may be present if the tangent stiffness of the material law changes dramatically or become negative (as in strain softening), which makes it harder for conventional numerical methods to find a solution, such as the Newton-Raphson method.

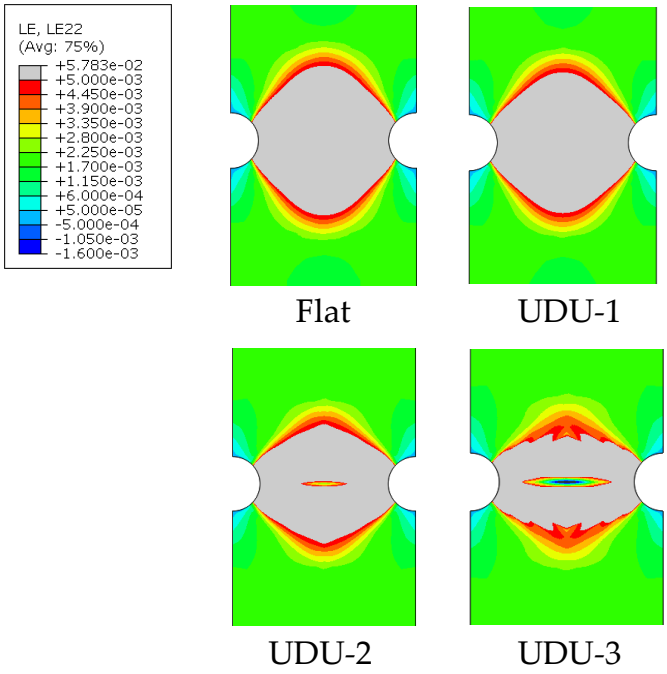

Figure 3.34: Longitudinal strain ε_{yy} map of FE models of notched tensile specimen with various material models at 0.66% strain

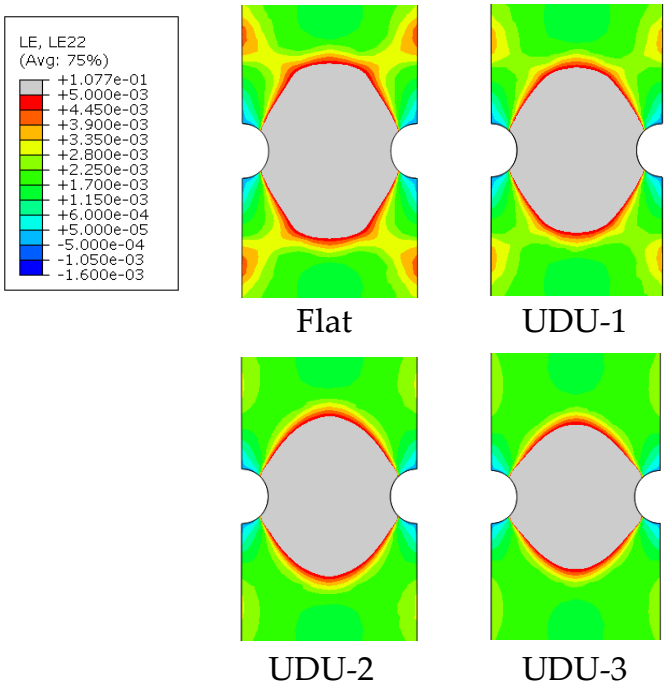

Figure 3.35: Longitudinal strain ε_{yy} map of FE models of notched tensile specimen with various material models at 1.21% strain

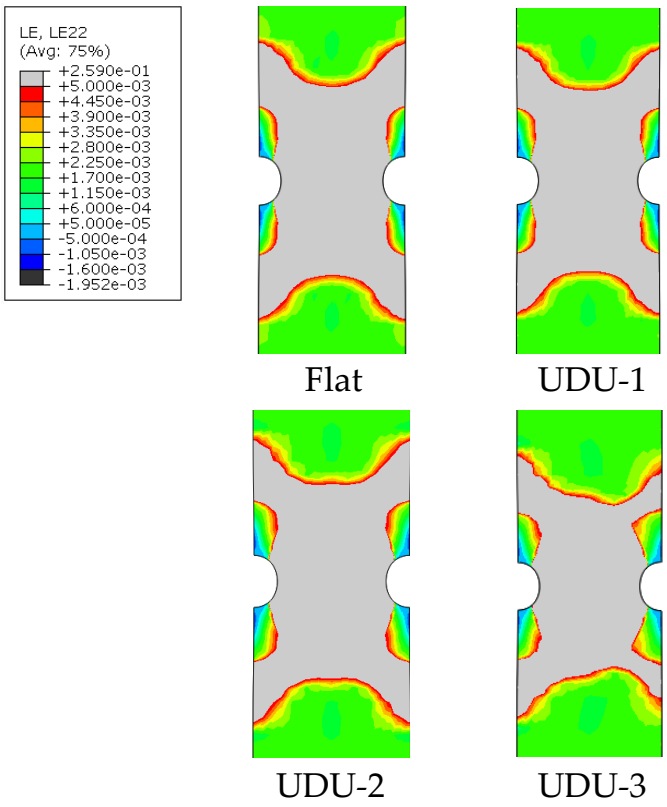

Figure 3.36: Longitudinal strain ε_{yy} map of FE models of notched tensile specimen with various material models at 3.32% strain

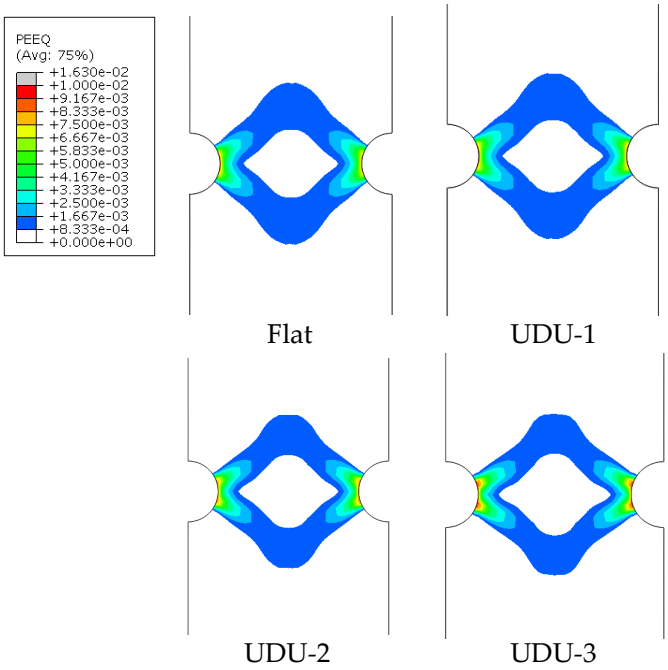

Figure 3.37: Equivalent plastic strain ε^{p}_{eq} map of FE models of notched tensile specimen with various material models at 0.27% strain

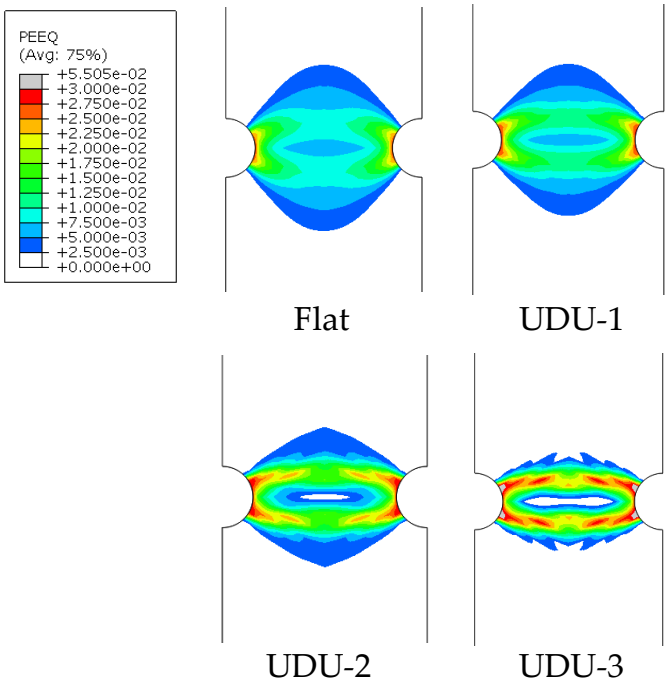

Figure 3.38: Equivalent plastic strain ε^{p}_{eq} map of FE models of notched tensile specimen with various material models at 0.66% strain

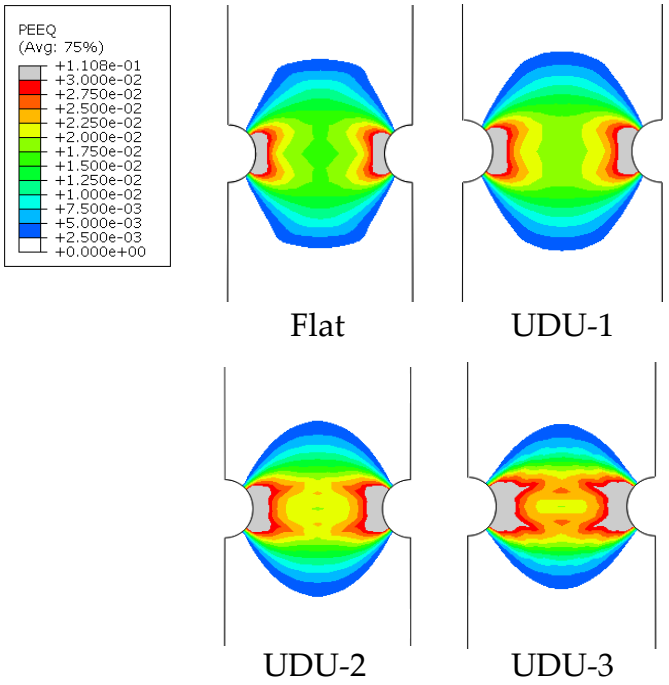

Figure 3.39: Equivalent plastic strain ε^{p}_{eq} map of FE models of notched tensile specimen with various material models at 1.21% strain

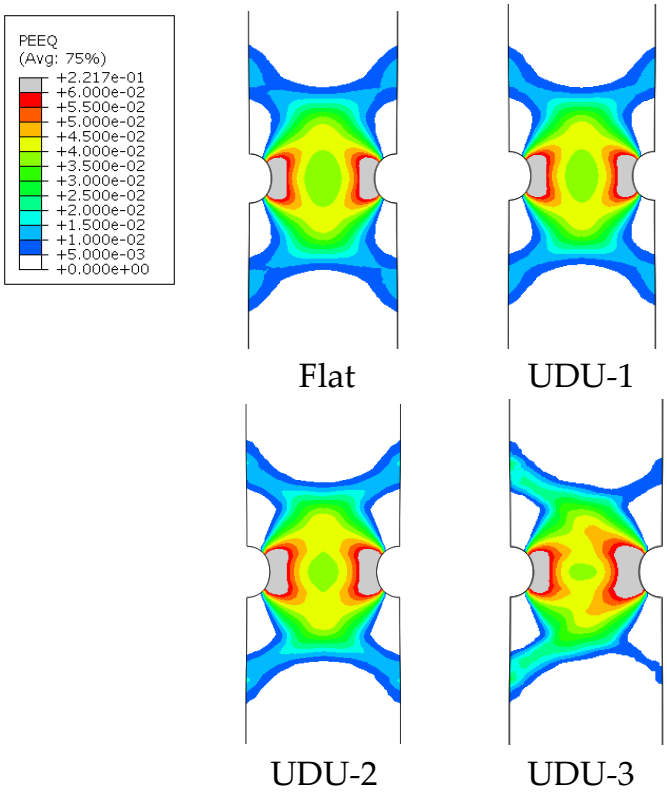

Figure 3.40: Equivalent plastic strain ε^{p}_{eq} map of FE models of notched tensile specimen with various material models at 3.32% strain

This can be overcome by adopting a displacement-control loading mode or using viscous damping to achieve convergence in the presence of instability.

Strain softening introduced in a constitutive model can lead to pathological problem that manifests as mesh sensitivity in the FE simulation. In the presence of strain softening, the partial differential equation of physical field is ill-posed, leading to non-uniqueness of the solutions. The solution becomes uncertain and highly dependent on the mesh sizes, and is thus meaningless. However, in the current problems where the UDU stress-strain curve is used, the strain localisation is eventually arrested when the material tangent stiffness recovers (at the onset of the strain hardening branch). The subsequent strain hardening acts as stabilising effect on the solution. Other researchers (Shaw and Kyriakides 1997; Kyriakides et al. 2008; Hallai and Kyriakides 2011b; Jiang et al. 2017b, 2017a) noticed the mesh sensitivity associated with the simulation of Lüders-like behaviour, and suggested that the mesh size only affects the minor details of the band front but marginally influence the global structural behaviour. In the current work, the mesh sensitivity of the FE model was examined. As for FE models of the plain-sided specimens, different mesh densities were used

by specifying a various number of elements (N_t) through the thickness. Four N_t values were adopted, namely $N_t = 1$, 2, 3 and 4, which results in total number of elements 220, 1,128, 4,176 and 6,800, respectively. Figure 3.41 shows the FE model of the plain-sided specimen discretized with meshes of different densities.

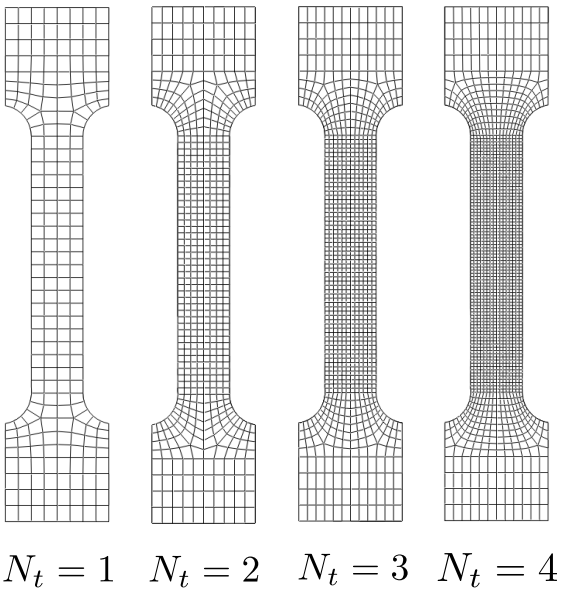

Figure 3.41: FE model of the plain-sided specimen with various mesh densities

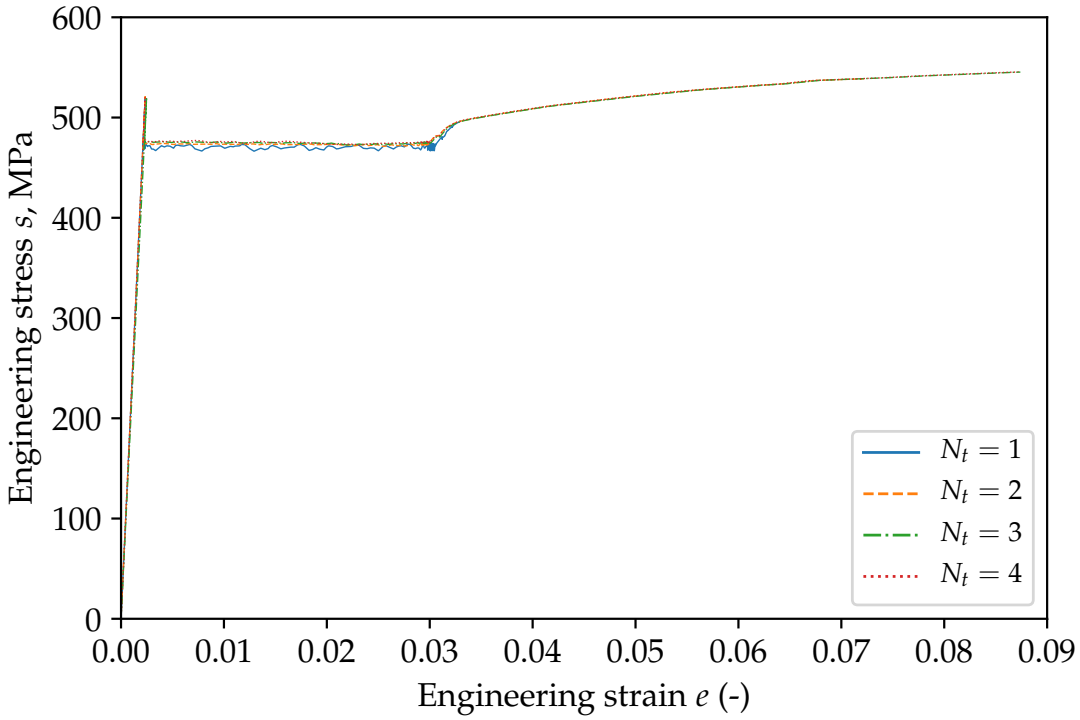

Figure 3.42: Influence of the size of elements on the calculated global stress-strain response for M01-02

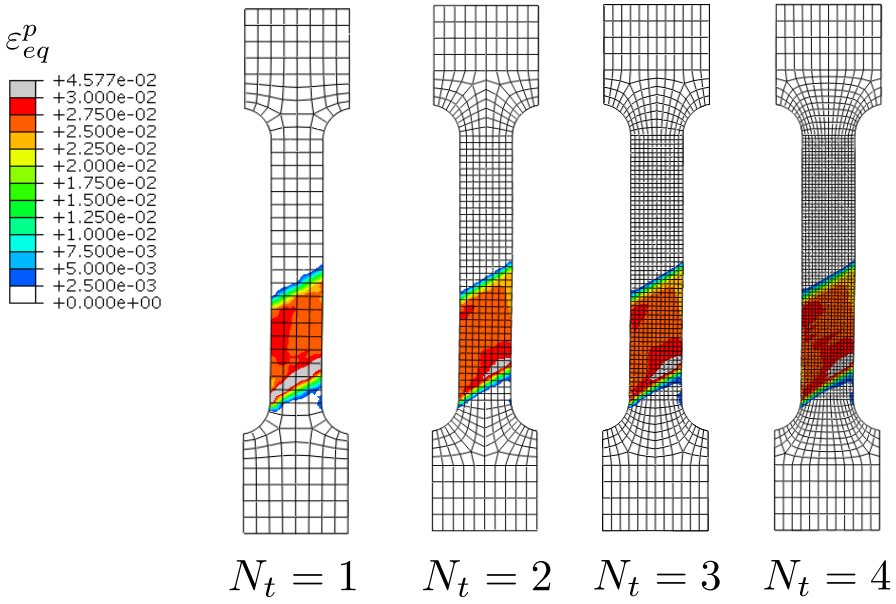

Figure 3.43: Influence of the size of elements on the calculated ε^{p}_{eq} contours of M01-02

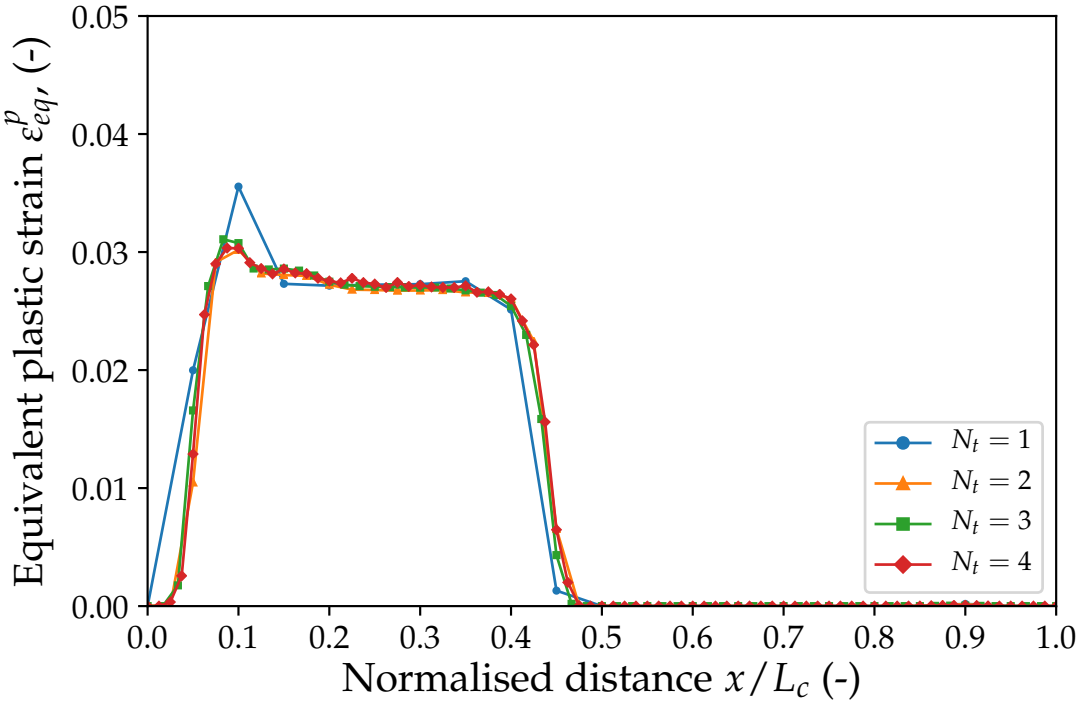

Figure 3.44: Influence of the size of elements on the calculated ε^{p}_{eq} profiles along the centreline of M01-02

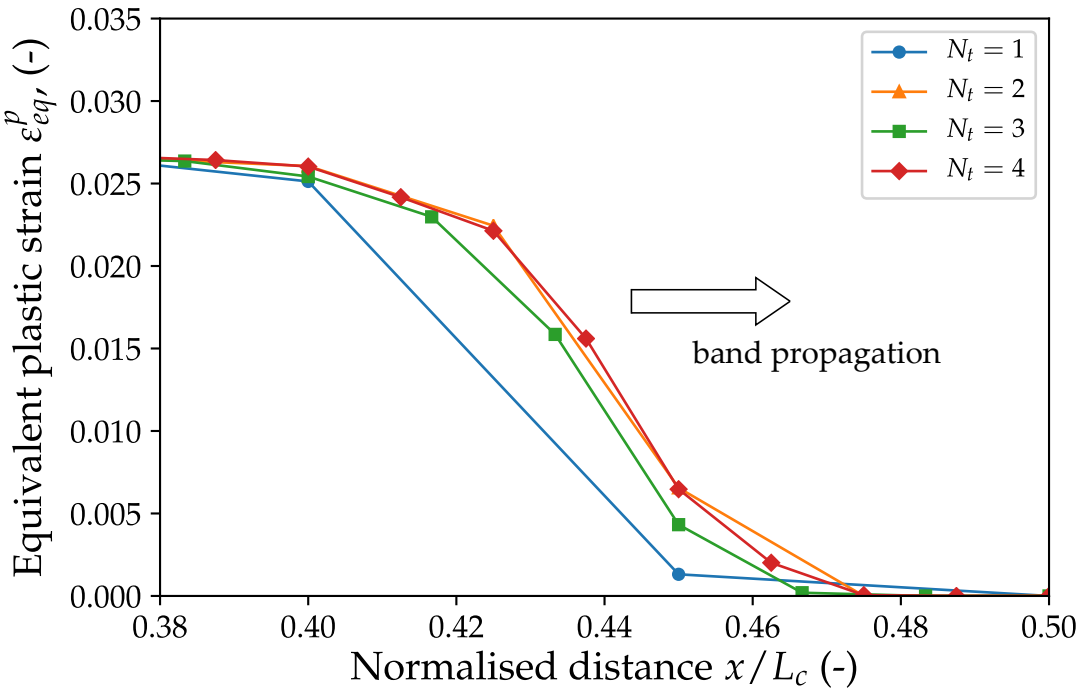

Figure 3.45: Influence of the size of elements on the calculated ε^{p}_{eq} propagating front of the Lüders band in M01-02

As for the FE models of the side-notched specimens, different mesh densities were applied by specifying different number of elements (N = 16, 24, 32, 40) along the notch annulus. The corresponding numbers of the elements in the radial direction were 12, 16, 20 and 24, respectively. This meshing strategy resulted in a total of 6,144, 9,336, 13,576 and 18,936, respectively.

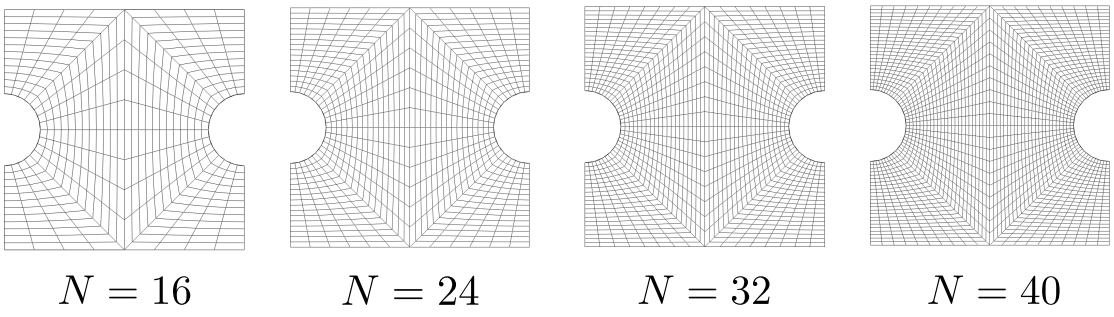

Figure 3.46: FE model of the side-notched specimen with various mesh densities

From the FE results, it was observed that the simulated macroscopic features of Lüders band and global stress-strain response exhibit limited mesh sensitivity. Noticeable mesh dependency is found in the band front, influencing the width of the propagating localisation. Others (Kyriakides et al. 2008; Hallai and Kyriakides 2011b; Liu et al. 2015; Hallai and Kyriakides 2013) reported marginal

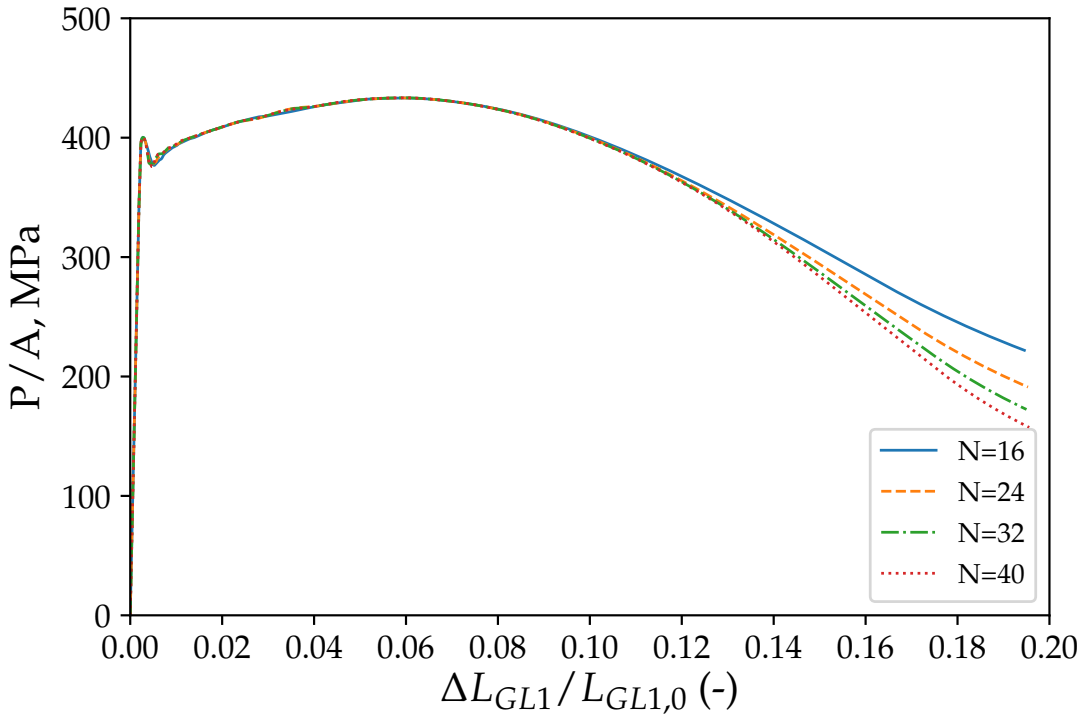

Figure 3.47: Load-elongation response of the side-notched specimen FE model calculated using various mesh densities

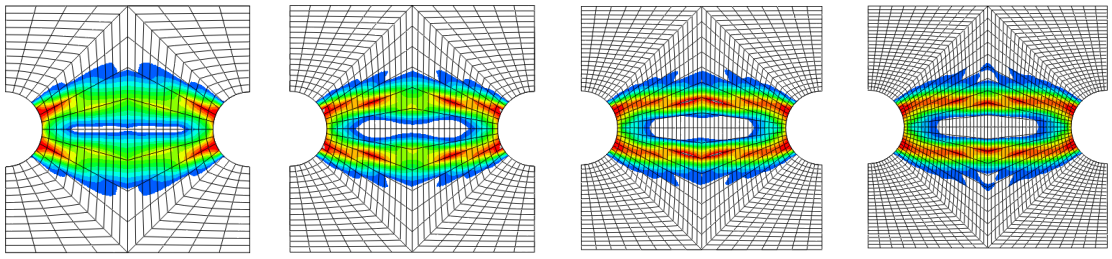

Figure 3.48: Influence of the number of elements on the calculated ε_{eq}^{p} contours in the side-notched tensile specimen

influence of the mesh density on the simulated global structural behaviour in the numerical analysis of steel strips and tubes/pipes. Furthermore, Jiang et al. (2017a, 2017b) noted that the mesh sensitivity due to strain softening was only noticeable in the band front region in the simulated NiTi tubes and strips. The width of the localisation front was shown some degree of mesh dependency in that the localisation tends to form along the element boundary with band front crossing over about 2 to 3 element widths. The overall behaviour and the macroscopic events, however, are marginally affected by the mesh density.

3.4.2 *Effect of rate exponent value*

Various rate exponent $m = 0.001$, 0.01 and 0.1 were used to investigate the effect of rate dependence on the simulated structural behaviour and identify a most suitable rate exponent value for the rest of the FE analyses. Figure 3.49 shows the comparison of the calculated stress-strain responses using various values of m. It can be implied from the figure below that $m = 0.001$ is found to have negligible effect on the calculated stress-strain behaviour.

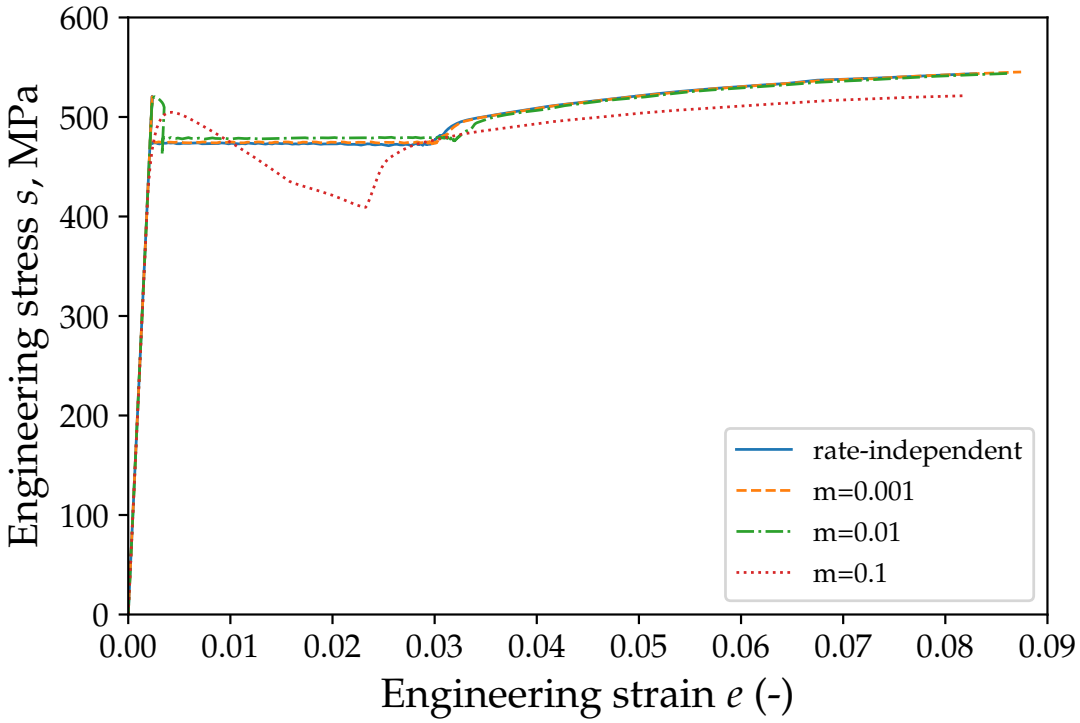

Figure 3.49: Influence of the rate exponent value on the calculated global stress-strain curve of M01-02

3.4.3 *Effect of constitutive models*

It is evident the softening modulus of the UDU model affects the calculated structural response of the FE model. As for the magnitude of the stress plateau and its length, it is observed that the FE simulation using UDU material models tends to predict a stress plateau that is above the measured one and has a longer extent. This type of deviation from the test can be observed in Kyriakides and Miller (2000) and Hallai and Kyriakides (2011b). However, since the studies by Kyriakides and Miller (2000), Hallai and Kyriakides (2011b), and Aguirre et al. (2004) mainly concerned the macroscopic behaviour of the Lüders banding phenomenon, little attention was paid to the quantitative aspects of the simulated stress plateau, such as its stress level and length. Also, in the study of bent pipes with Lüders bands, the softening modulus seemed to have a marginal effect on the magnitude of the bending moment.

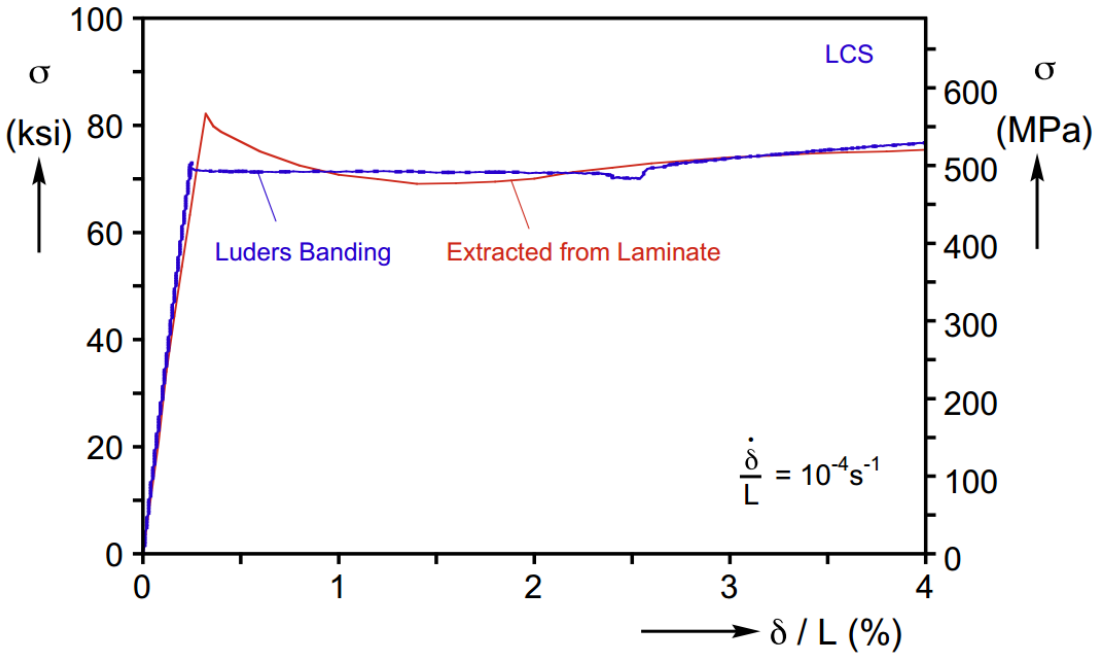

Figure 3.50: Extracted stress-strain response of a carbon steel strip exhibiting Lüders plateau (from (Hallai and Kyriakides 2013))

3.5 SUMMARY

Uniaxial tensile tests of API 5L X65 plate with and without notches were carried out. DIC technique was used to quantitatively capture the inhomogeneous

deformation of Lüders banding phenomenon. FE modelling was performed to simulate the tensile tests following a simple and phenomenological constitutive model of an 'up-down-up' trajectory. The effect of various shapes of the UDU stress-strain response on the simulated Lüders band and global stress-strain response were explored. Based on the results presented in this work, the key findings are:

- The typical idealisation for materials exhibiting Lüders plateau as a flat stress-strain response in engineering stress-strain curve is a gross simplification. This type of Lüders representation does not produce strain localisation (and Lüders banding) in FE modelling, even though the simulated nominal stress-strain curve matches the experiment best. In FE simulation of cracked pipes (in Chapter 4), this type of idealisation generally produces uniform deformation and no abrupt increase in crack driving force (characteristic of Lüders-deforming material) is simulated.

- The UDU stress-strain approach is useful in simulating the Lüders band initiation and propagation in a uniaxial tensile specimen. However, the simulated nominal stress-strain curve is not completely in agreement with that measured in the experiment. This seems admissible as the simulated Lüders band formation is of more interest, but it may cause over-prediction of the crack driving force in cracked component as it produces a higher nominal stress-strain response.

- Lüders plateau elevates the strain localisation near existing strain concentrators (or defects), and the strain localisation is more constrained in comparison to continuous yielding material. This indicates that for assessing defective component with discontinuous yielding, the effect of Lüders plateau must be incorporated. This also indirectly explains the considerably higher crack driving force in a cracked component when the global strain reaches yield strain.

- The shape of UDU stress-strain curve has a significant impact on the simulated Lüders band and nominal stress-strain response. The stronger the softening and higher peak stress, the more pronounced Lüders band and higher plateau stress level.

4

SINGLE EDGE NOTCHED TENSION TESTING OF API X65 STEEL EXHIBITING LÜDERS PLATEAU

4.1 INTRODUCTION

In Chapter 3, the author investigated the deformation of API X65 steel exhibiting Lüders plateau and the effect of various material models on the FE simulation of Lüders banding. To further understand the behaviour of the cracked component in the presence of Lüders plateau, fracture toughness tests were conducted with the use of DIC technique.

It is generally acknowledged that the commonly-used SENB specimens produce over-conservative toughness results for assessing the flaw tolerance of cracked pipes. The reason is that the crack-tip constraint of the SENB is considerably higher than that of the surface-cracked pipes. Therefore, in recent years the use of SENT specimens as an alternative has gained significant popularity in the oil and gas industry. However, the specific dimensions of the SENT specimens, including the a_0/W ratio, specimen breadth (whether B×B or 2B×B), the side groove depths and the daylight length are yet to be investigated. In this study, a thorough analysis of the crack-tip constraint conditions was performed in light of defining the optimum dimensions of the fracture toughness specimens used in SBD and SB-ECA of oil and gas pipelines.

Experimental study of the SENT specimens made from the API 5L Grade X65 steel was then carried out. The geometry of the SENT specimens was based on the results of the crack-tip constraint analyses. The DIC was employed to monitor the deformation of the surface of the specimen to study how the Lüders strain influences the crack tip conditions. Additional tests of SENT with

a shallow notch was also carried out to examine the effect of notch size on the development of Lüders-related strain localisation.

Subsequently, a parametric study of the effect of a_0/W on the formation and propagation of Lüders localisations was conducted.

4.2 NUMERICAL ANALYSIS OF CRACK-TIP CONSTRAINT

Numerous studies have looked into the constraint conditions of the cracked pipes subjected to axial straining with and without internal pressure. The effect of internal pressure has been found to be marginal on the crack-tip constraint and crack growth resistance curves of pressurised pipes containing circumferential flaws (Cravero et al. 2008; Xu et al. 2010; Tyson et al. 2007; Verstraete et al. 2014). However, Verstraete et al. (2014) additionally found that internal pressure slightly increases the out-of-plane constraint. In this work, we have conducted a systematic analysis of the crack-tip constraint of SENT, SENB and circumferentially flawed pipes subjected to uni-axial and bi-axial loadings. Both in-plane and out-of-plane constraints were investigated. Figure 4.1 illustartes the in-plane and out-of-plane directions for a through-thickness crack. Tables 4.2 and 4.2 summarise the FEA performed for the constraint analysis of fracture mechanics test specimens and cracked pipes, respectively. The FEA of SENB (B $\times$ B) and SENT (B $\times$ B and 2B $\times$ B) were performed with a variety of crack depth (a_0/W ranging from 0.1 to 0.5), resulting in a total of 15 FE cases. The FEA of cracked pipes had a crack depth (a_0/t) ranging from 0.1 to 0.5, which were loaded in tension with and without internal pressure. The internal pressure level in terms of the hoop stress to yield stress ratio (σ_{hoop}/σ_y ranges from 0 (tension only) to 0.8, leading to a sum of 20 FEA cases.

Apart from the in-plane constraint parameter Q, the out-of-plane parameter T_z proposed by a number of researchers (Guo 1993; Zhao et al. 2007; Zhang and Guo 2007) was also investigated for each FEA case. The T_z parameter is defined as:

$$T_z = \frac{\sigma_{zz}}{\sigma_{xx} + \sigma_{yy}} \tag{4.1}$$

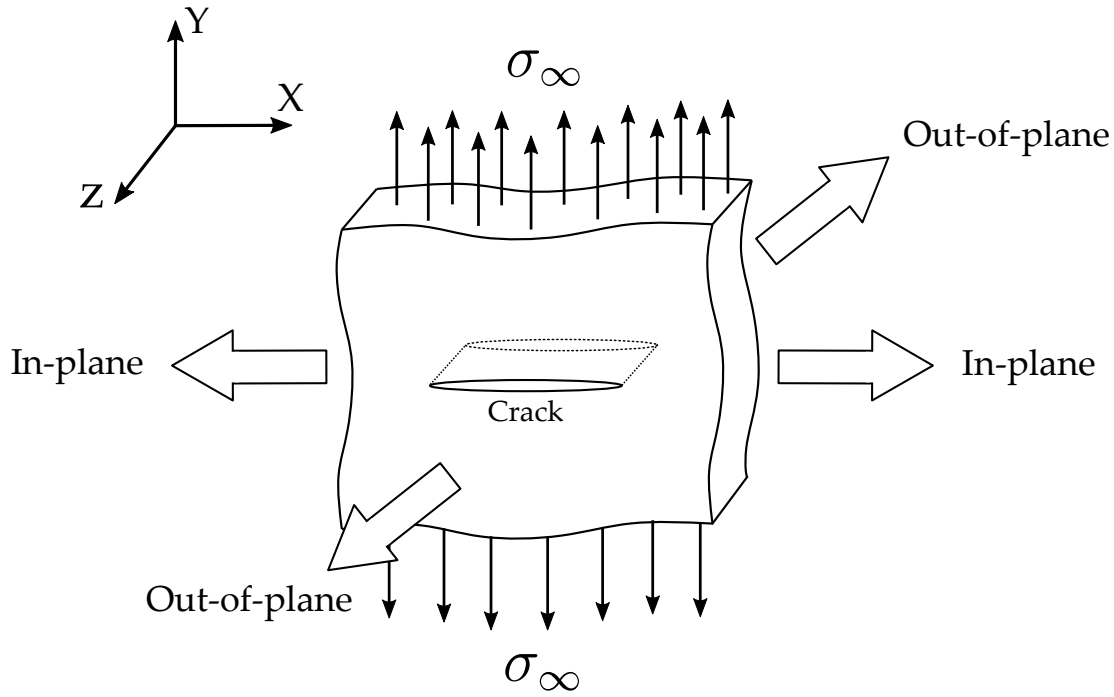

Figure 4.1: Illustration of in-plane and out-of-plane directions for a through-thickness crack in a three-dimensional body

Table 4.1: Summary of FEA cases for analysis of crack-tip constraint of fracture mechanics test specimens

FE model	B, mm	W, mm	a_0/W
SENB (B × B)	17	17	0.1, 0.2, 0.3, 0.4, 0.5
SENT (B × B)	17	17	0.1, 0.2, 0.3, 0.4, 0.5
SENT (2B × B)	34	17	0.1, 0.2, 0.3, 0.4, 0.5

Table 4.2: Summary of FEA cases for analysis of crack-tip constraint of fracture mechanics test specimens

FE model	OD, mm	t, mm	a_0/t	Internal Pressure
Cracked pipe	355.6	19	0.1	σ_{hoop}/σ_y = 0, 0.2, 0.6, 0.8
			0.2	σ_{hoop}/σ_y = 0, 0.2, 0.6, 0.8
			0.3	σ_{hoop}/σ_y = 0, 0.2, 0.6, 0.8
			0.4	σ_{hoop}/σ_y = 0, 0.2, 0.6, 0.8
			0.5	σ_{hoop}/σ_y = 0, 0.2, 0.6, 0.8

4.2.1 *Stress-strain properties*

The UDU model described in Chapter 3 has a strain softening segment in the stress-strain curve, which invalidates the validity requirement of J-integral. Therefore, the stress-strain curve containing a flat stress plateau was used to represent the Lüders deforming material in the numerical analysis of crack-tip constraint, as shown in Figure 4.2. The upper yield point was neglected. As illustrated in Figure 4.2(b), the stress-strain curve was extended upon the true UTS (σ_U), following the power-law extrapolation described in Ling (1996) and Hertelé (2012).

4.2.2 *FE models*

Figure 4.27 to 4.5 show the mesh configuration of the FE models of SENT, SENB and cracked pipe, respectively, alongside the applied boundary conditions. Three-dimensional solid quadratic brick elements with reduced integration (element type C3D20R) were used to construct all the FE models.

As illustrated in Figure 4.3, SENT B×B and 2B×B have similar mesh arrangements, and are subjected to identical loadings and boundary conditions. Only the length between grips (the so-called 'daylight') was modelled and the clamped regions were neglected. Prescribed displacement was applied to the nodes at the uncracked end such that a global strain up to 5% was obtained. The top and bottom nodes at the uncracked end were not permitted to move vertically to simulate the boundary conditions due to clamping. Symmetry boundary conditions were applied to the uncracked ligament such that the nodes were not permitted to move in the loading direction. Similar mesh arrangements were applied to the SENB models (see Figure 4.4). The rollers were modelled as rigid half-circular surfaces. Mesh refinement was applied to the contact surfaces between the rollers and the SENB model.

The FE model of cracked pipe, as shown in Figure 4.5, has a similar mesh arrangement in the near-tip region and the mesh transits smoothly from small element in the near-tip region to larger element near the uncracked end. Like SENT model, prescribed displacement was applied to the nodes at the uncracked end. The bottom node was restrained in the vertical direction in order

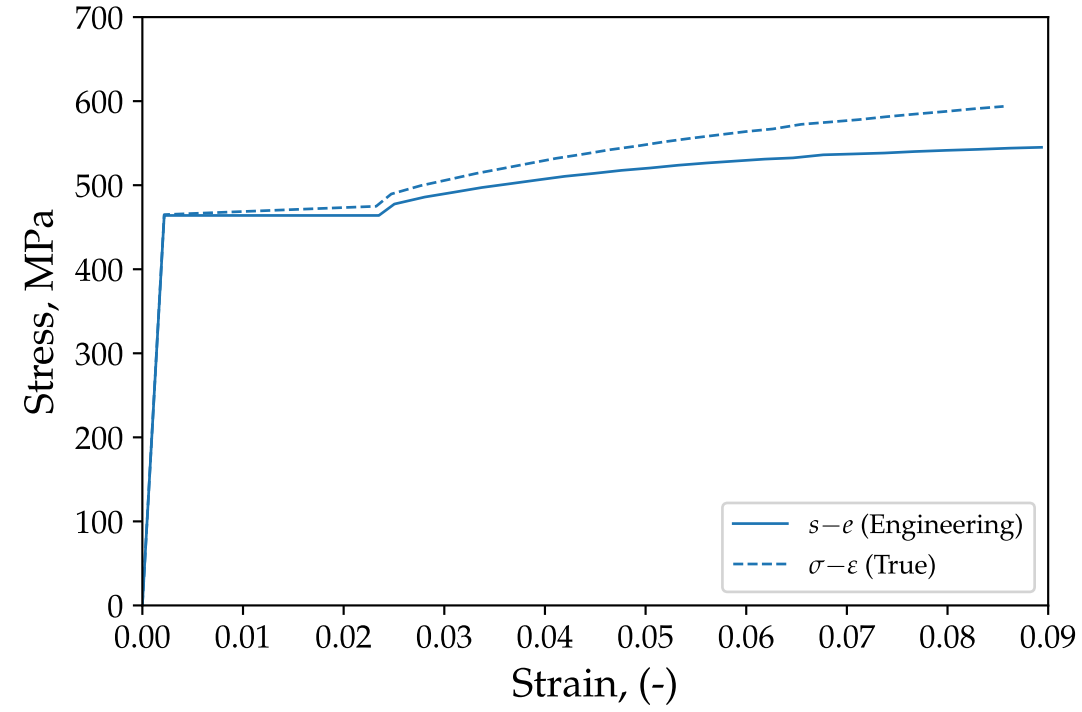

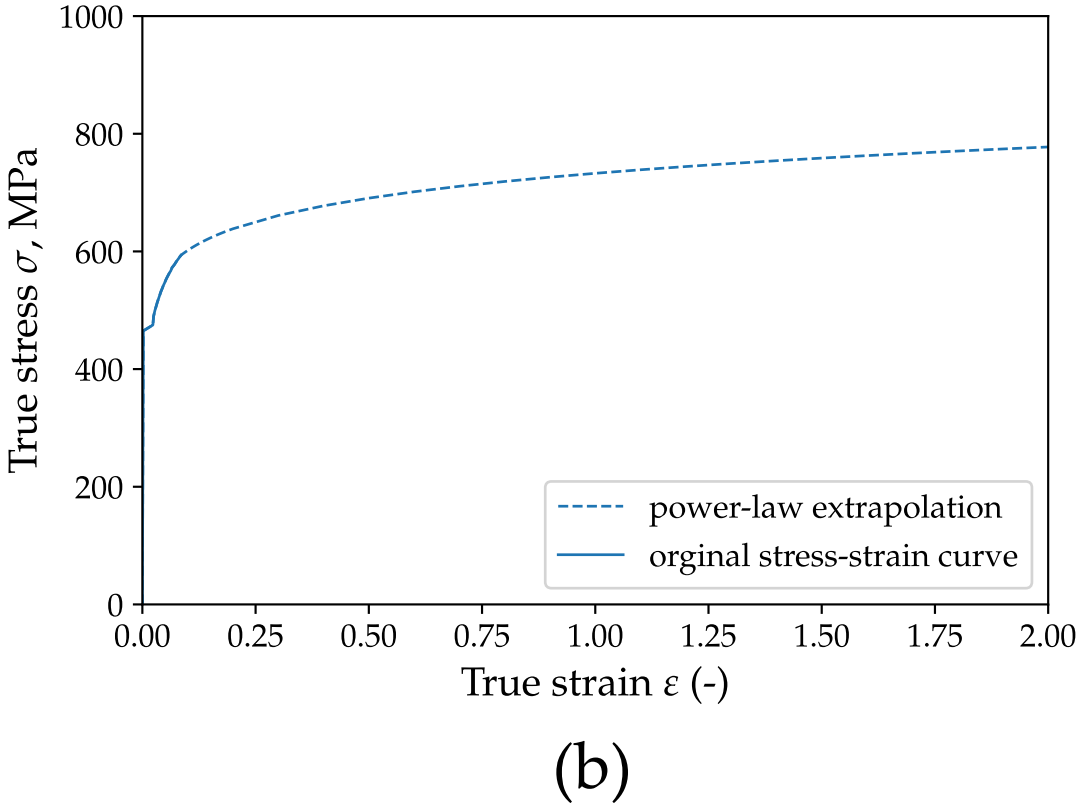

Figure 4.2: Stress-strain curve used in FE analysis of the fracture toughness specimens: (a) the engineering and true stress-strain form, (b) the true stress-strain curve with the post-necking response based on a power law extrapolation

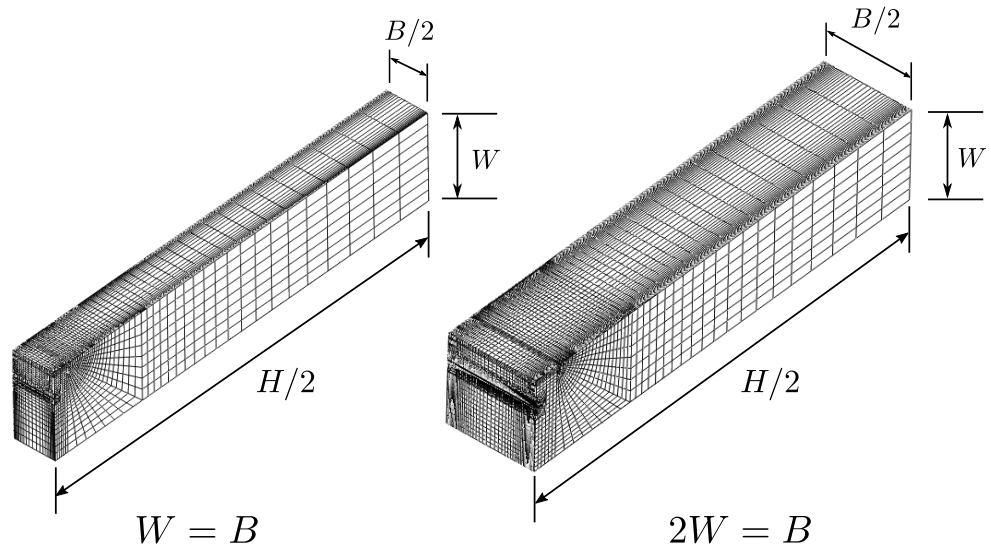

(a)

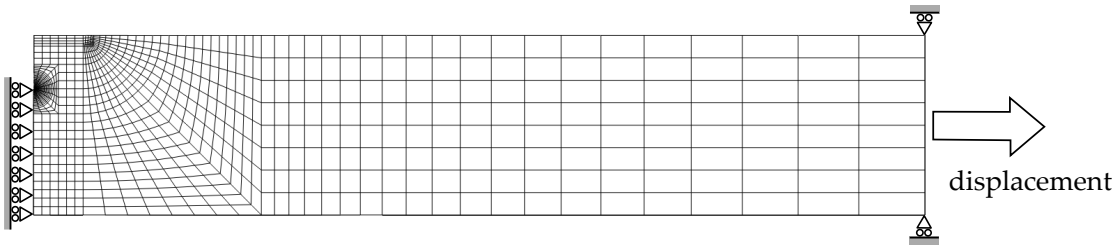

(b)

Figure 4.3: (a) Mesh configuration of the SENT specimen models and (b) applied boundary conditions for the SENT specimen models

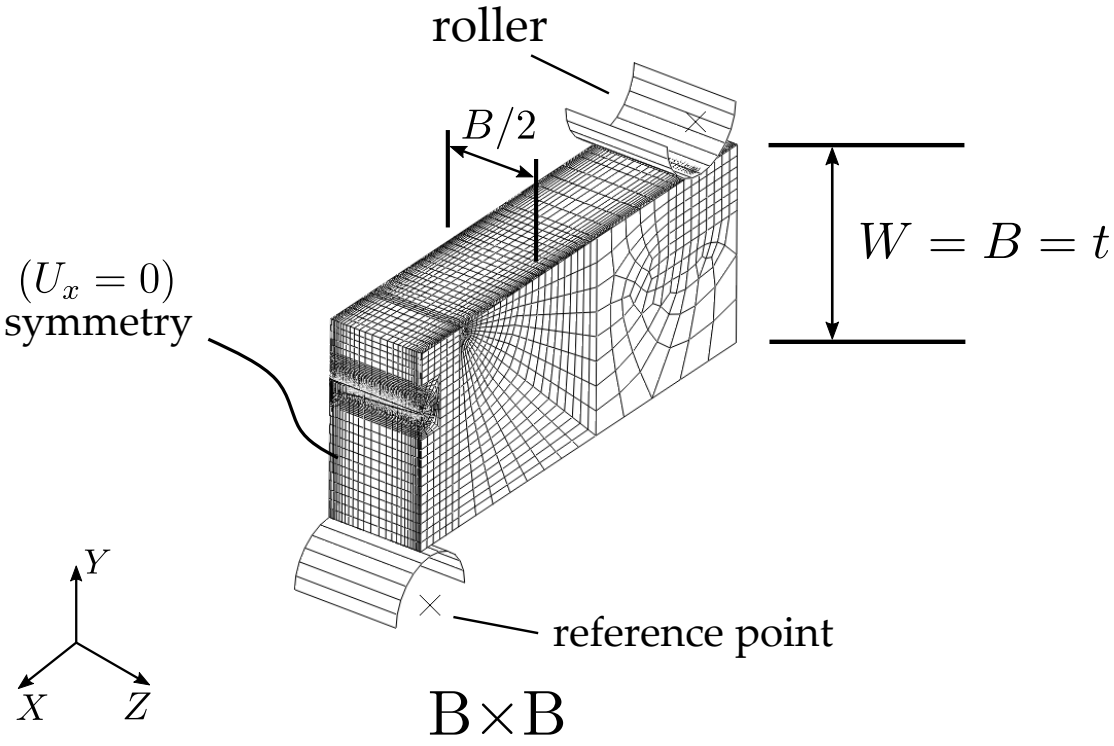

(a)

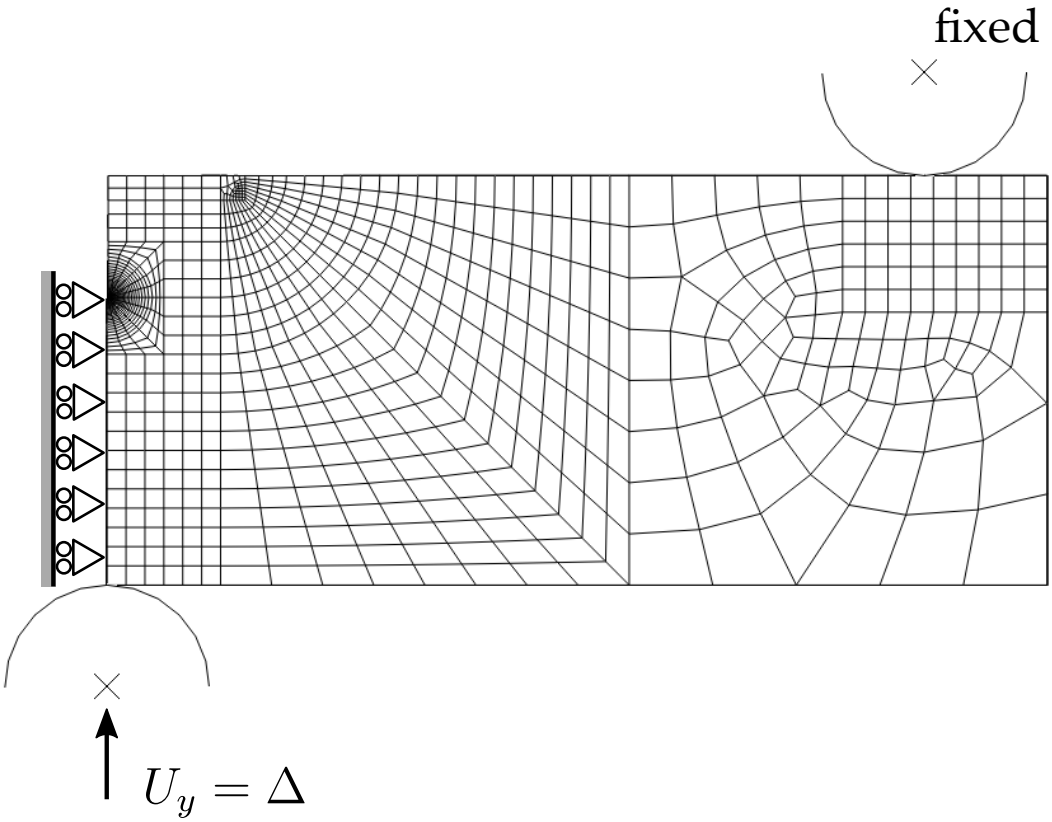

(b)

Figure 4.4: (a) Mesh configuration of the SENB specimen models and (b) applied boundary conditions for the SENB specimen models

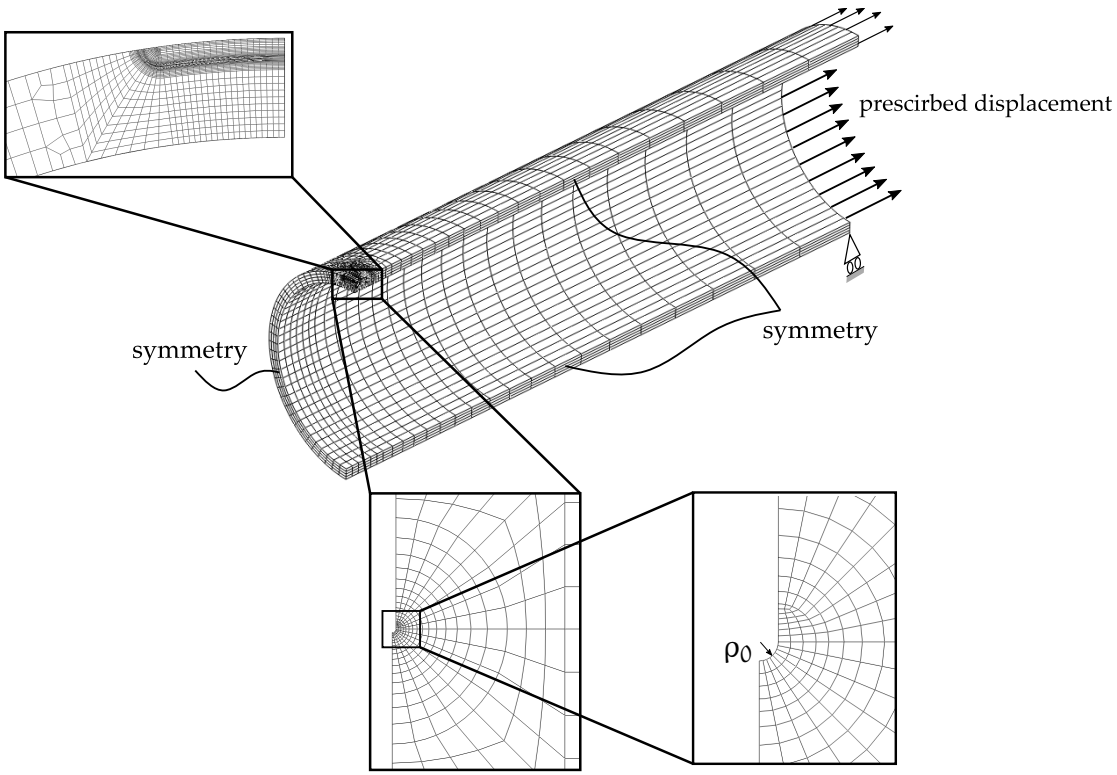

Figure 4.5: Mesh configuration of FE pipe model and the applied boundary conditions

to prevent rigid body motion. Symmetry conditions were applied to the cracked end and the edge surfaces.

MBL model was constructed to generate the reference crack-tip stress field used in the calculation of Q parameter. The mesh configuration and boundary conditions were shown in Figure 4.6. It is noted that due to symmetry only a half MBL model was constructed. Prescribed displacements were applied to the nodes at the outer circumference of the MBL model. The displacements were based on the first two terms of the Williams linear elastic singularity solution, which takes the following form:

$$u_x = \frac{K_I}{E}(1+\upsilon)\sqrt{\frac{r}{2\pi}}\cos(\theta/2)\left[\kappa - \cos\theta\right] + \left(1-\upsilon^2\right)\frac{T}{E}x \tag{4.2}$$

$$u_y = \frac{K_I}{E}(1+\upsilon)\sqrt{\frac{r}{2\pi}}\sin(\theta/2)\left[\kappa - \cos\theta\right] - \upsilon(1+\upsilon)\frac{T}{E}y \tag{4.3}$$

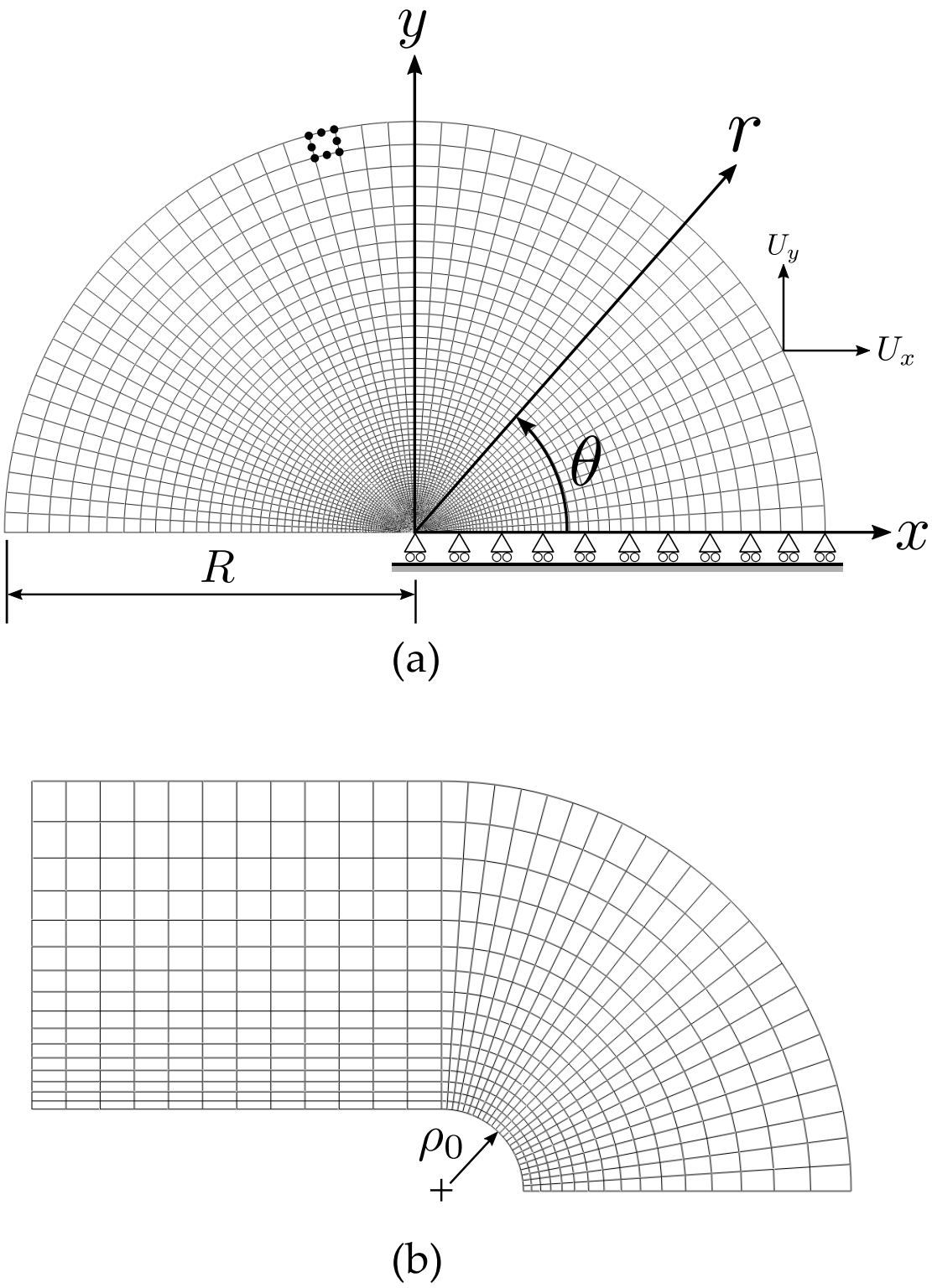

Figure 4.6: (a) Mesh configuration of the MBL model with the applied bounday conditions and (b) close-up of the crack tip with initial notch radius

4.2.3 *Results and discussion*

4.2.3.1 J-Q *analysis*

Figures 4.9 to 4.10 present the Q parameter versus normalised J of SENT B×B, SENT 2B×B, SENB B×B and cracked pipes (subjected to tensile loading only), respectively. It is clear that, for all types of components analysed, Q is found to decline with increasing notch depth, i.e. a_0/W for SENT and SENB, and a/t for cracked pipes.

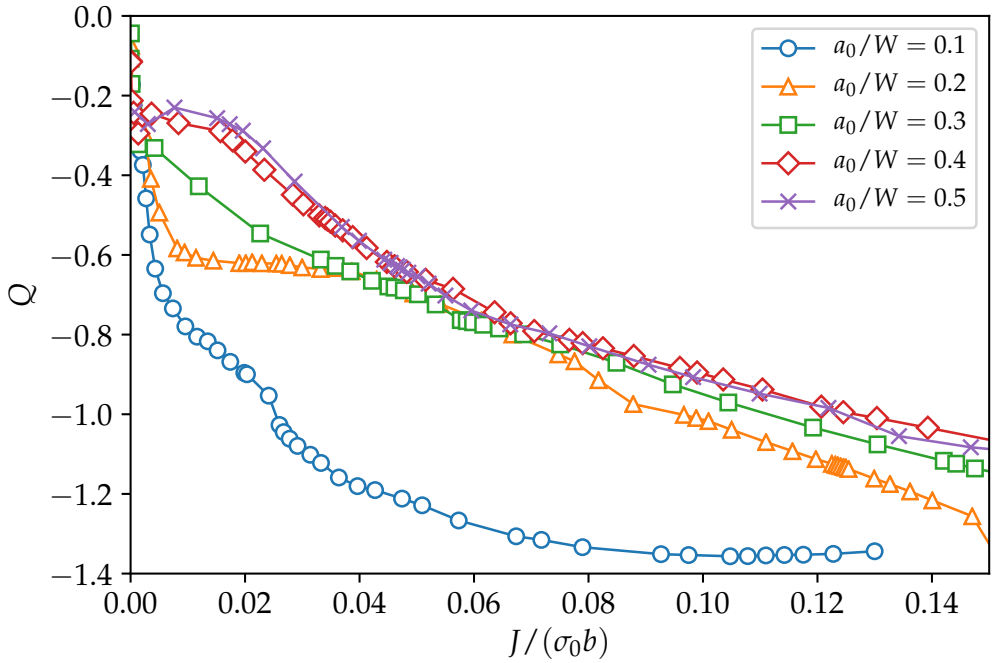

Figure 4.7: In-plane crack-tip constraint parameter in terms of Q versus normalised J calculated from FE analysis of SENT B×B

From Figures 4.7 and 4.8, a significant increase of Q with increasing a_0/W can be noticed, particularly between $a_0/W = 0.1$ and $a_0/W = 0.2$. The increase of Q becomes less significant with a_0/W when $a_0/W = 0.2$ - 0.4 and marginal when $a_0/W = 0.4$ - 0.5. For shallow notch ($a/W = 0.1$), the stress state is essentially tensile (membrane). When the notch depth increases, a bending moment may be induced due to the reduced thickness of ligament. The induced compressive bending stresses contribute to the crack-tip constraint, resulting in an increase in Q parameter. A similar trend of the increase in Q with notch depths to SENT

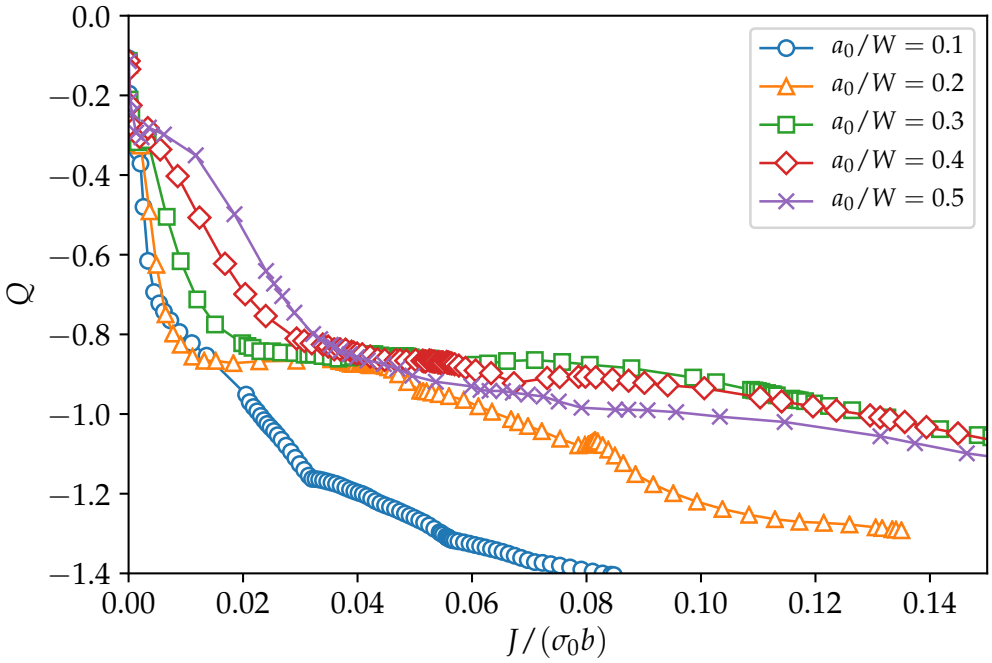

Figure 4.8: In-plane crack-tip constraint parameter in terms of Q versus normalised J calculated from FE analysis of SENT 2B×B

models were found in SENB and cracked pipe models, as depicted in Figures 4.9 and 4.10, respectively.

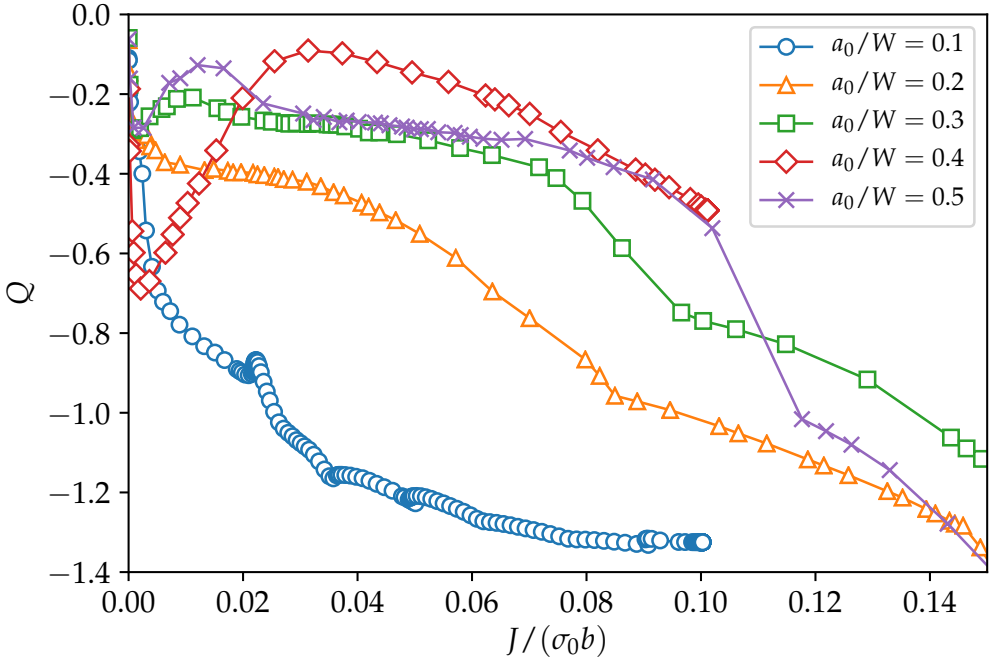

Figure 4.9: In-plane crack-tip constraint parameter in terms of Q versus normalised J calculated from FE analysis of SENB B×B

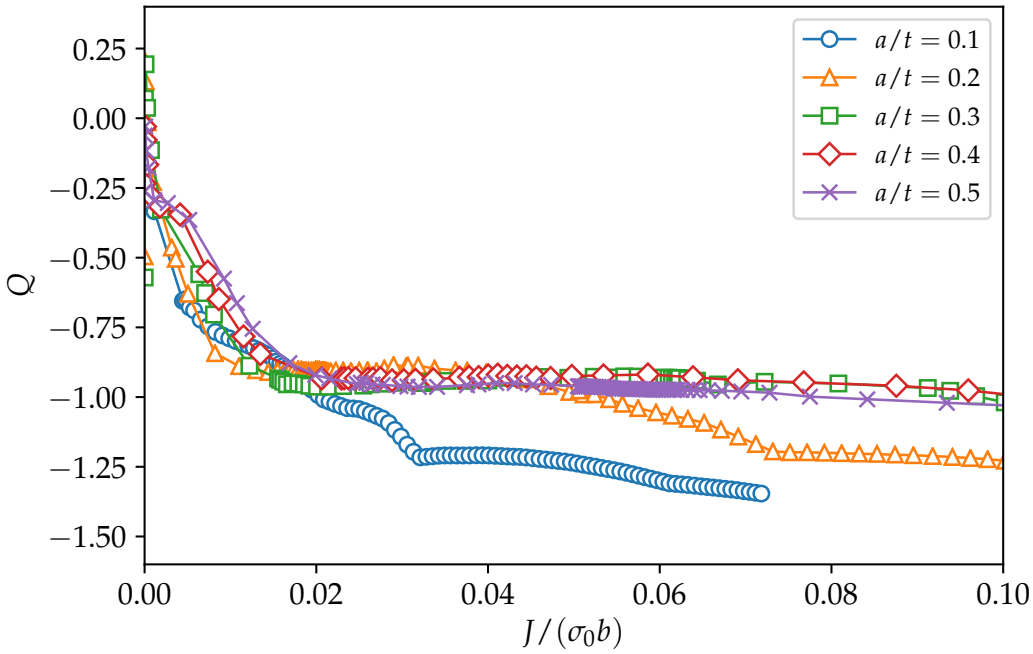

Figure 4.10: In-plane crack-tip constraint parameter in terms of Q versus normalised J calculated from FE analysis of circumferentially cracked pipes

Figures 4.11 to 4.15 present the effect of internal pressure (in terms of the ratio of the pressure induced hoop stress to the yield stress, $\sigma_{hoop}/\sigma_{ys}$). From Figure 4.11 we can see that increase in internal pressure ($\sigma_{hoop}/\sigma_0 = 0.2$ - 0.6 slightly increases the Q values. For $\sigma_y/\sigma_0 = 0.6$ - 0.8, the effect of internal pressure on the Q values is found insignificant. For cracked pipe with $a/t = 0.2$ (see Figure 4.12), a similar trend to Figure 4.11 can be seen. For cracked pipe with $a/t = 0.3$ - 0.5, as shown in Figures 4.13 to 4.15, respectively, it is shown that the increase in σ_{hoop}/σ_0 leads to a slight decline of the Q values, particularly between non-pressursied and pressurised pipes. For pressure level $\sigma_{hoop}/\sigma_0 = 0.2$ - 0.8, the effect of pressure on Q is found insignificant.

Figure 4.16 compares the Q parameter versus the normalised crack depth (a_0/W or a_0/t) for SENB, SENT and cracked pipes at various normalised J levels ($J/\sigma_y b = 0.02, 0.03, 0.05$ and 0.07). It is apparent that the Q values of SENB specimens are significantly higher than those of other geometries, particularly for deeper cracks ($a_0/W \geqslant 0.2$) and higher crack loadings in terms of J. The SENT specimens are shown to have a higher Q than the cracked pipes for all crack depths. It is worth noting that the SENT with B × B has higher Q than that with 2B × B, which indicates that greater thickness results in a lower in-plane

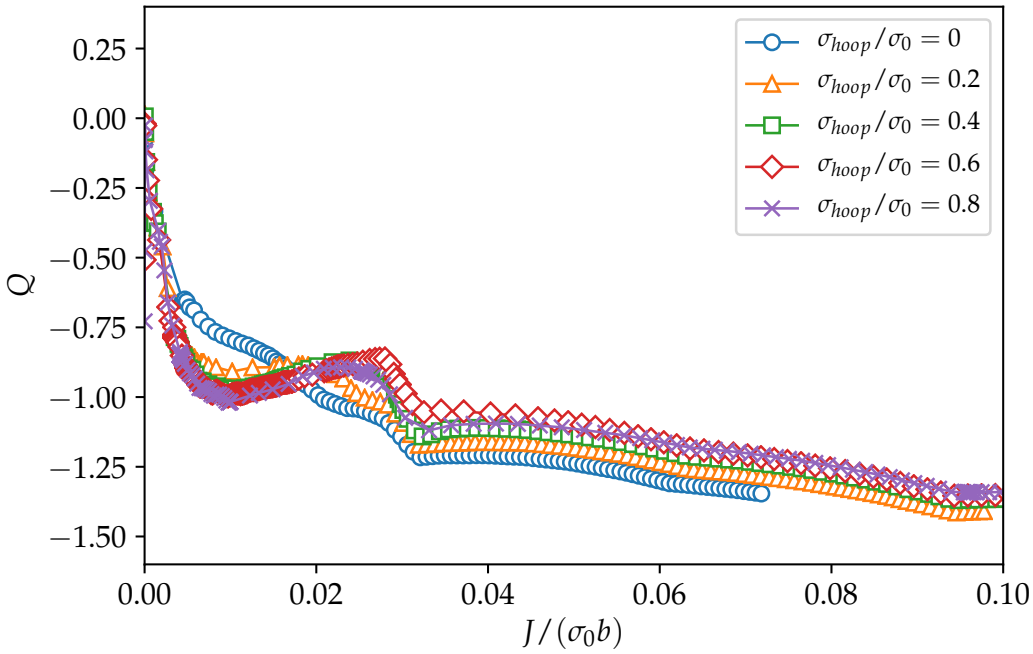

Figure 4.11: In-plane crack-tip constraint parameter in terms of Q versus normalised J calculated from FE analysis of circumferentially cracked pipe with crack depth of $a/t = 0.1$ for various internal pressure levels

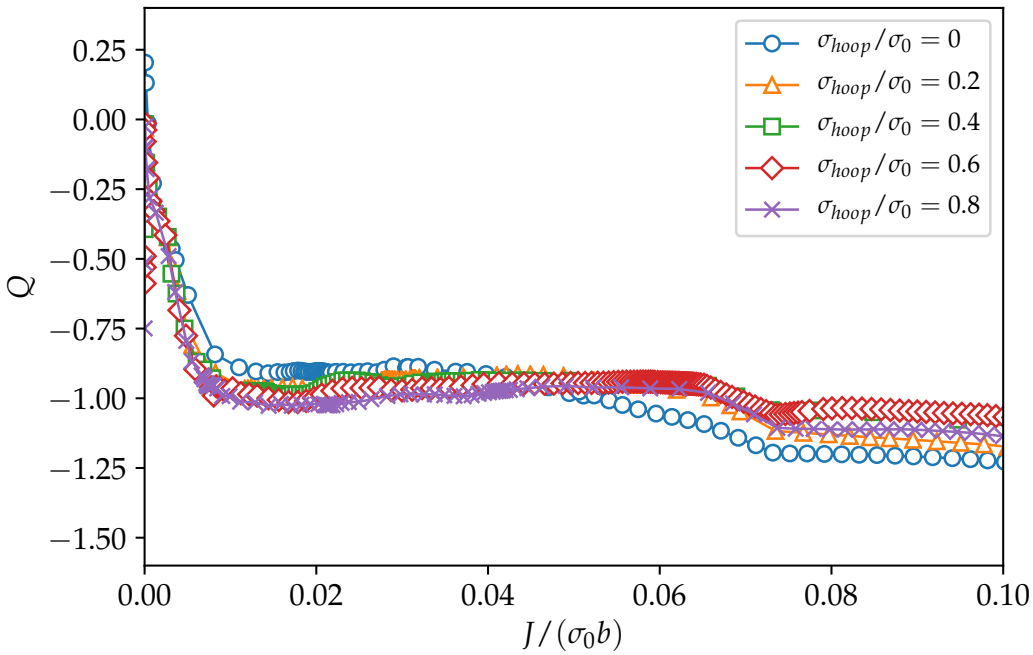

Figure 4.12: In-plane crack-tip constraint parameter in terms of Q versus normalised J calculated from FE analysis of circumferentially cracked pipe with crack depth of $a/t = 0.2$ for various internal pressure levels

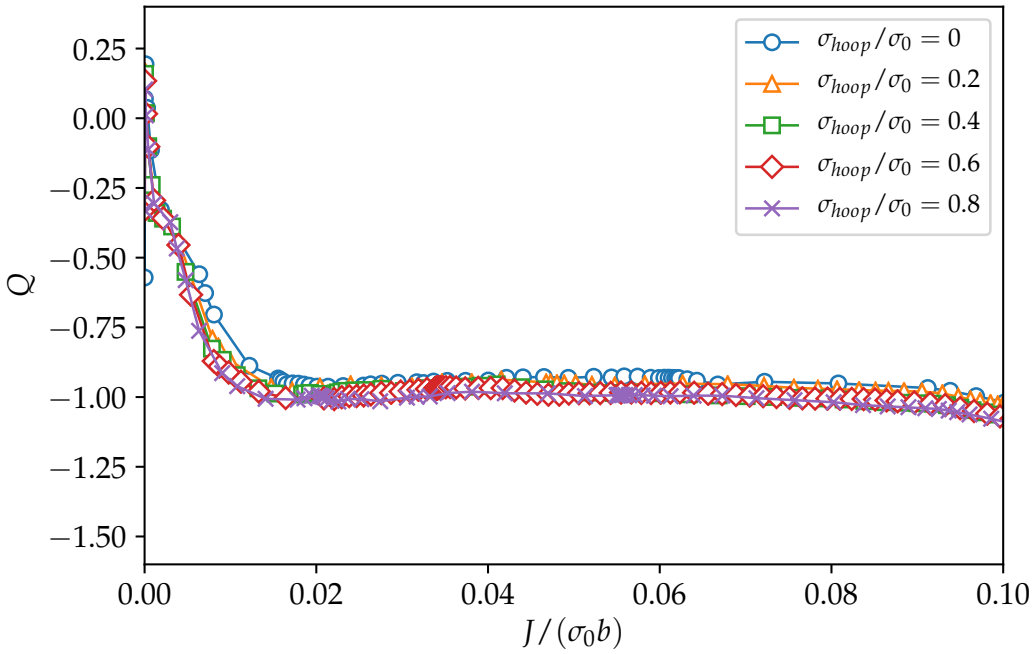

Figure 4.13: In-plane crack-tip constraint parameter in terms of Q versus normalised J calculated from FE analysis of circumferentially cracked pipe with crack depth of $a/t = 0.3$ for various internal pressure levels

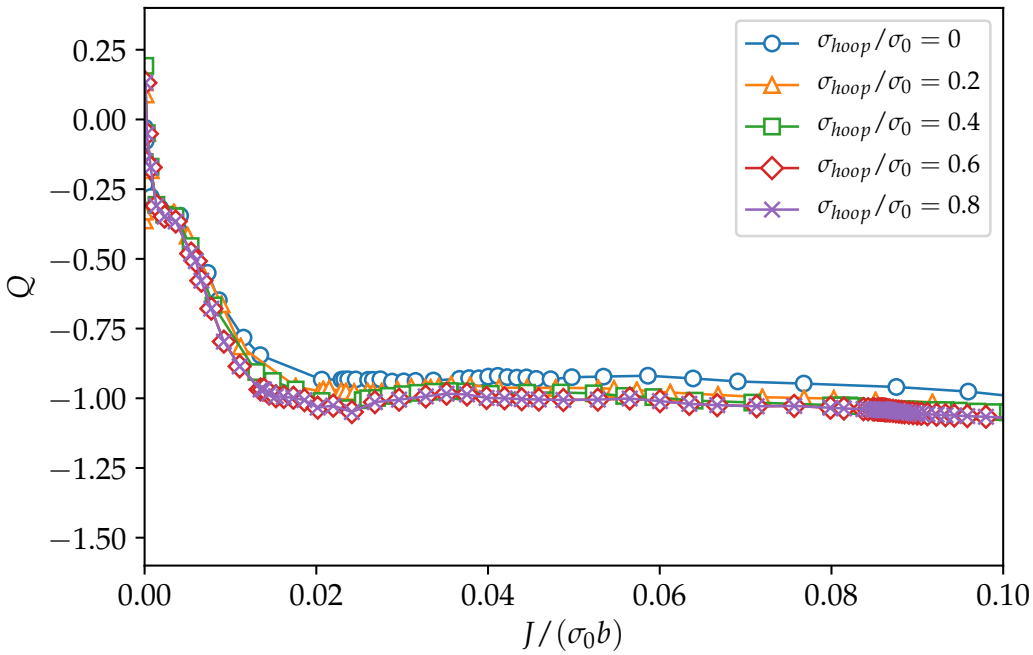

Figure 4.14: In-plane crack-tip constraint parameter in terms of Q versus normalised J calculated from FE analysis of circumferentially cracked pipe with crack depth of $a/t = 0.4$ for various internal pressure levels

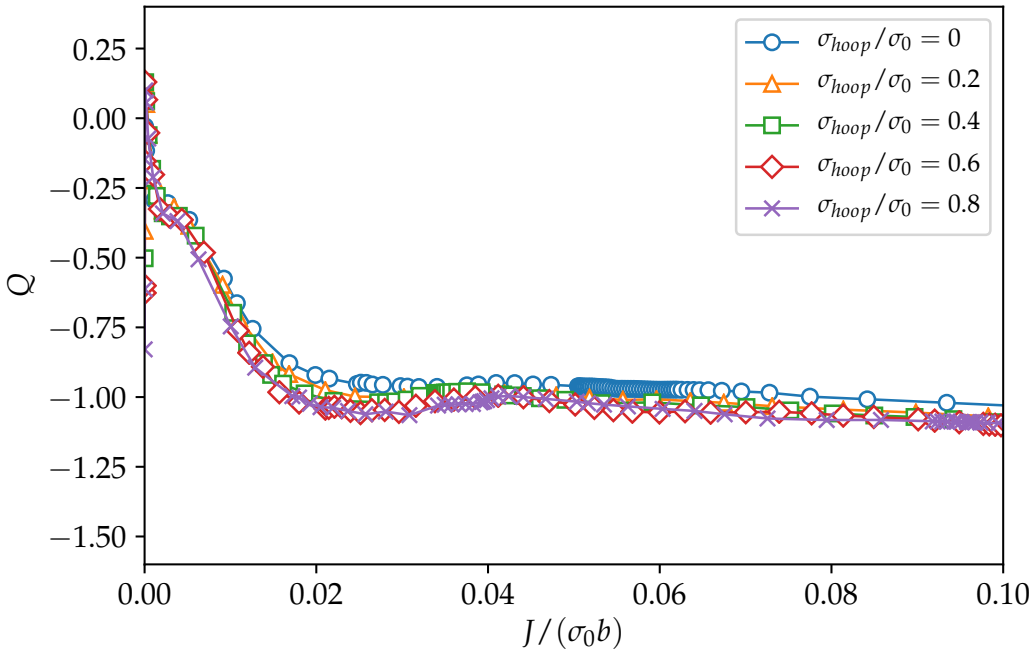

Figure 4.15: In-plane crack-tip constraint parameter in terms of Q versus normalised J calculated from FE analysis of circumferentially cracked pipe with crack depth of $a/t = 0.5$ for various internal pressure levels

constraint. As for cracked pipes, generally low values of Q are observed for all crack depths examined. The Q seems to be slightly reduced by increasing internal pressure at lower $J/\sigma_y b$, which diminishes at higher $J/\sigma_y b$.

4.2.3.2 J-h *analysis*

Figures 4.17 to 4.20 show the triaxiality parameter h versus normalised J for SENT B×B, SENT 2B×B, SENB B×B and cracked pipes (subjected to tensile loading only), respectively. Figures 4.21 to 4.25 show the effect of internal pressure (in terms of the ratio of the pressure induced hoop stress to the yield stress, $\sigma_{hoop}/\sigma_{ys}$). The comparison of the Q parameter versus the normalised crack depth (a_0/W or a_0/t) for SENB, SENT and cracked pipes at various normalised J levels ($J/\sigma_y b = 0.02, 0.03, 0.05$ and 0.07) is shown in Figure 4.16.

As can be seen from Figures 4.17 to 4.26, the J-h behaviour is observed to resemble that of J-Q, which indicates the validity of both parameters in quantifying the stress triaxiality of the crack tip. The triaxiality parameter h is also different from the Q in that the h parameter measures both in-plane and out-of-plane constraint.

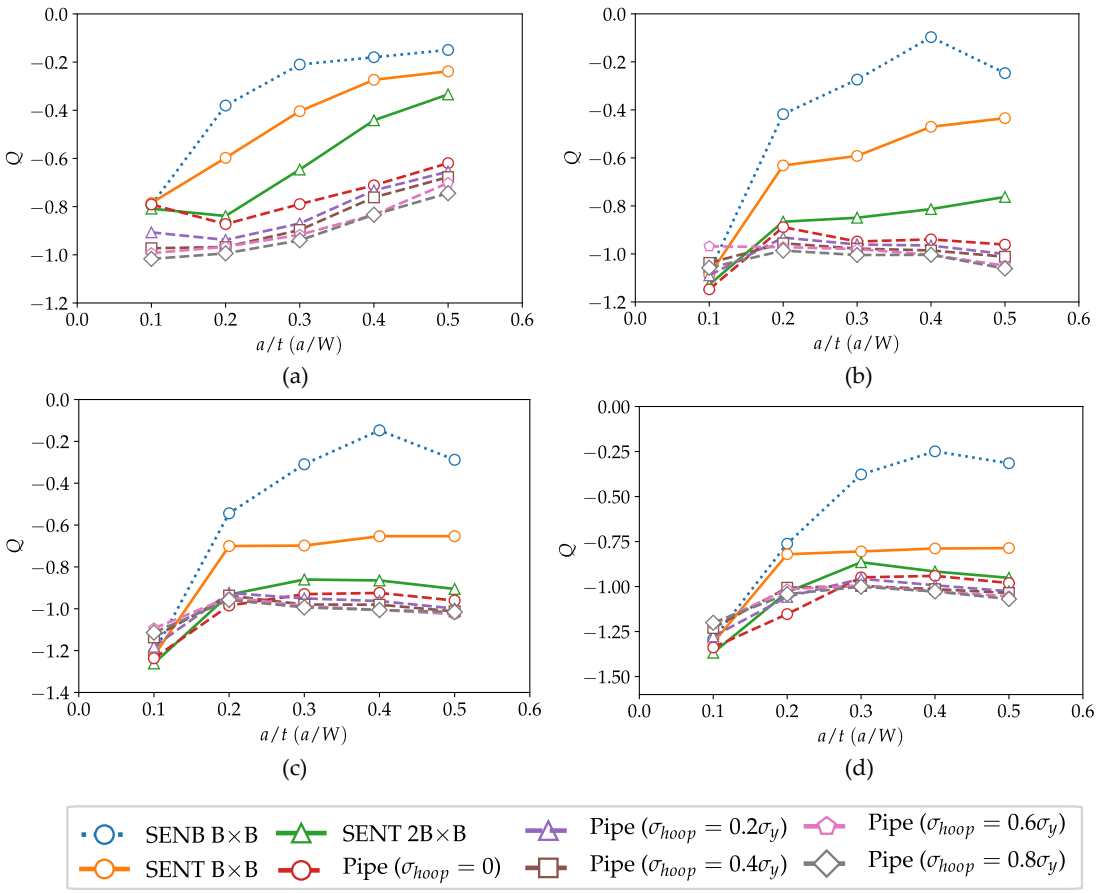

Figure 4.16: Comparison of Q for SENB, SENT and cracked pipes at various crack-tip loadings: (a) $J/(\sigma_y b) = 0.02$, (b) $J/(\sigma_y b) = 0.03$, (c) $J/(\sigma_y b) = 0.05$ and (d) $J/(\sigma_y b) = 0.07$

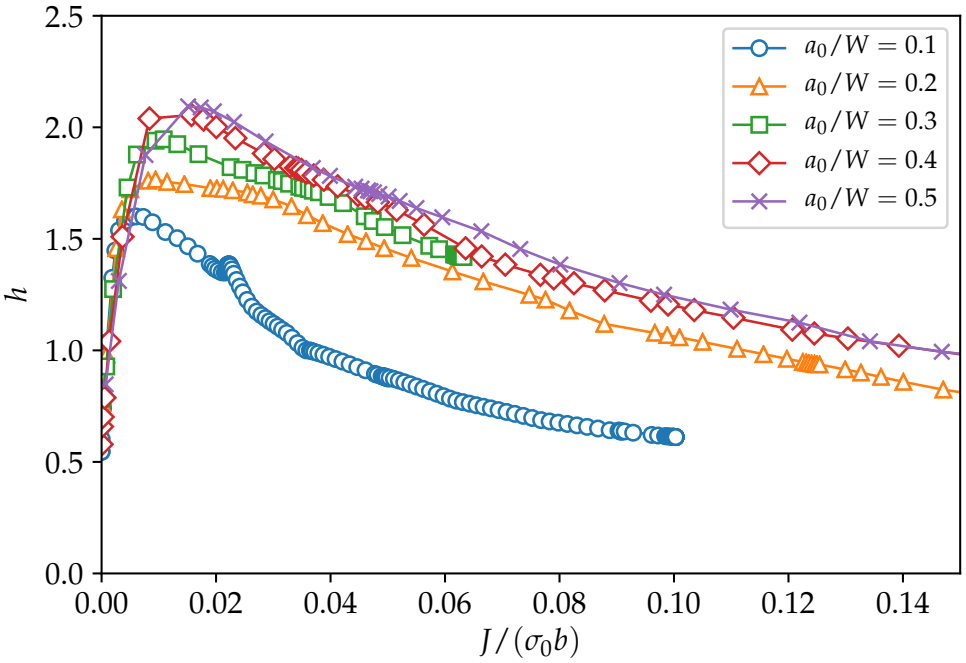

Figure 4.17: Crack-tip stress triaxiality parameter h versus normalised J calculated from FE analysis of SENT B×B

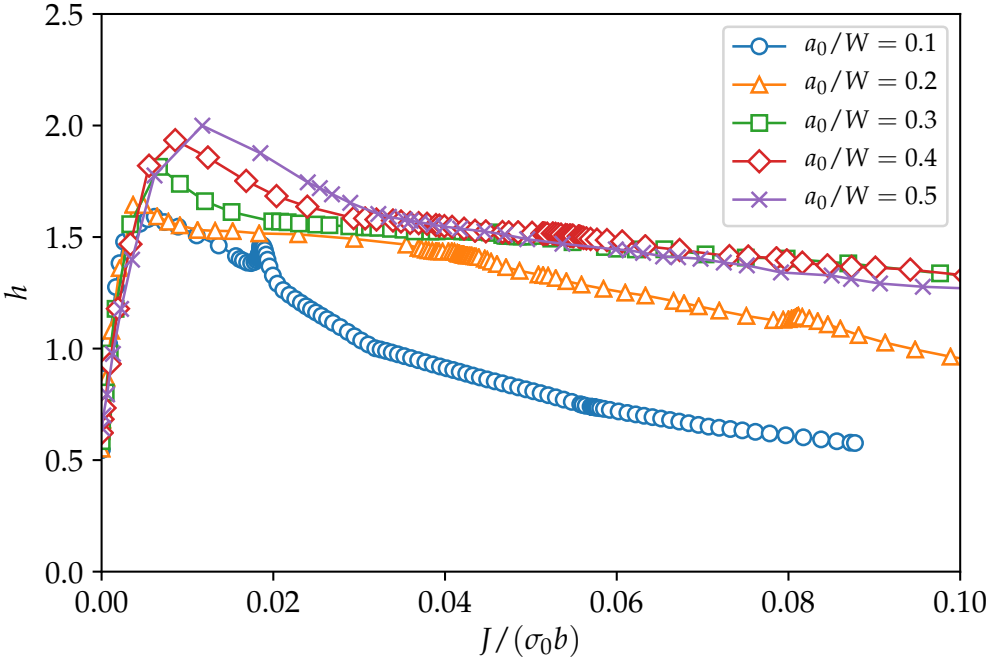

Figure 4.18: Crack-tip stress triaxiality parameter h versus normalised J calculated from FE analysis of SENT 2B×B

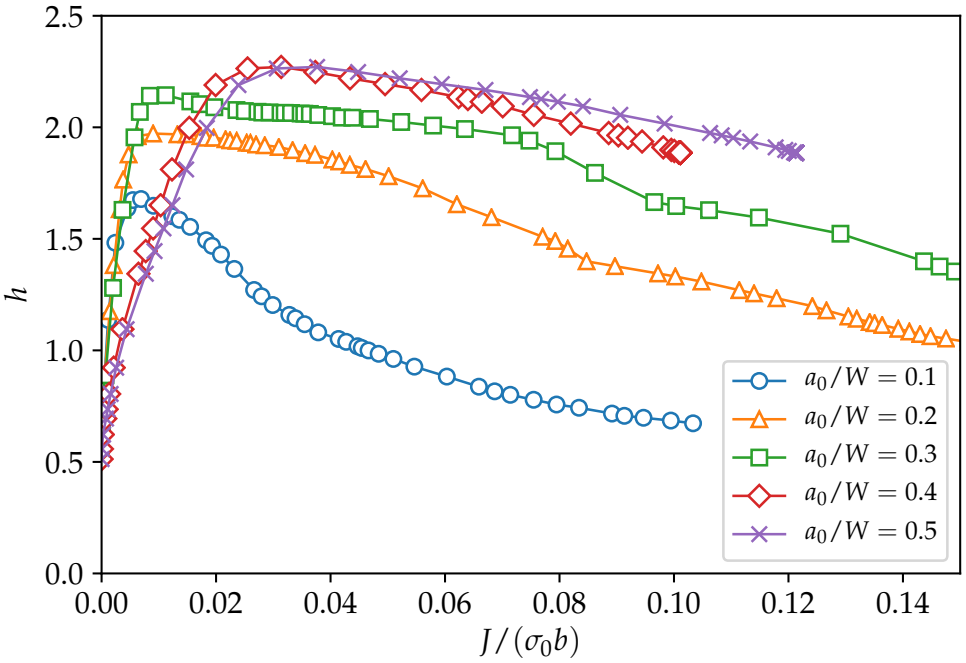

Figure 4.19: Crack-tip stress triaxiality parameter h versus normalised J calculated from FE analysis of SENB B×B

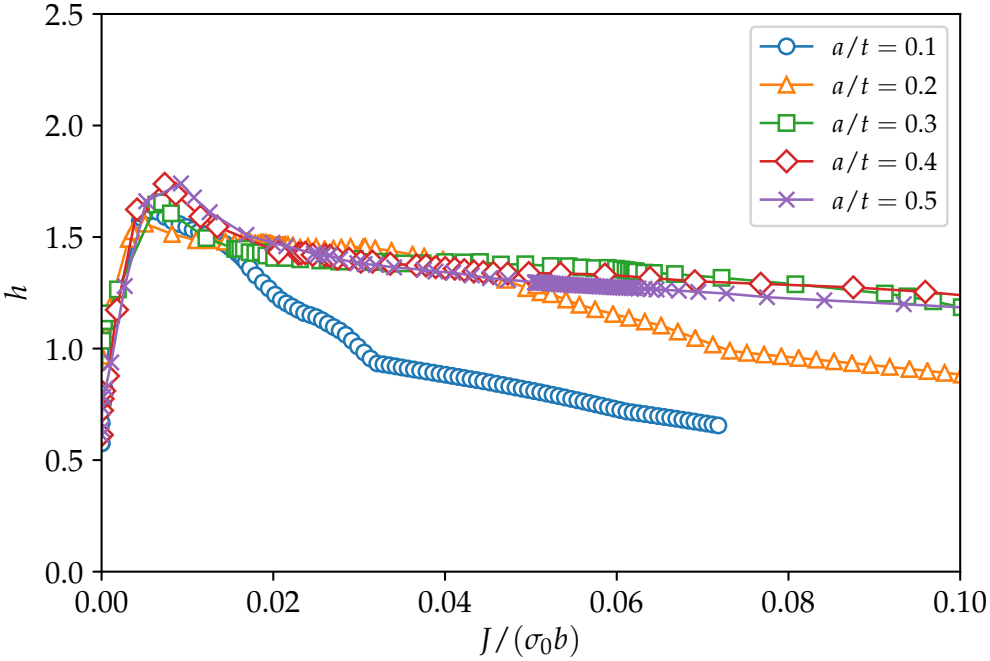

Figure 4.20: Crack-tip stress triaxiality parameter h versus normalised J calculated from FE analysis of circumferentially cracked pipes

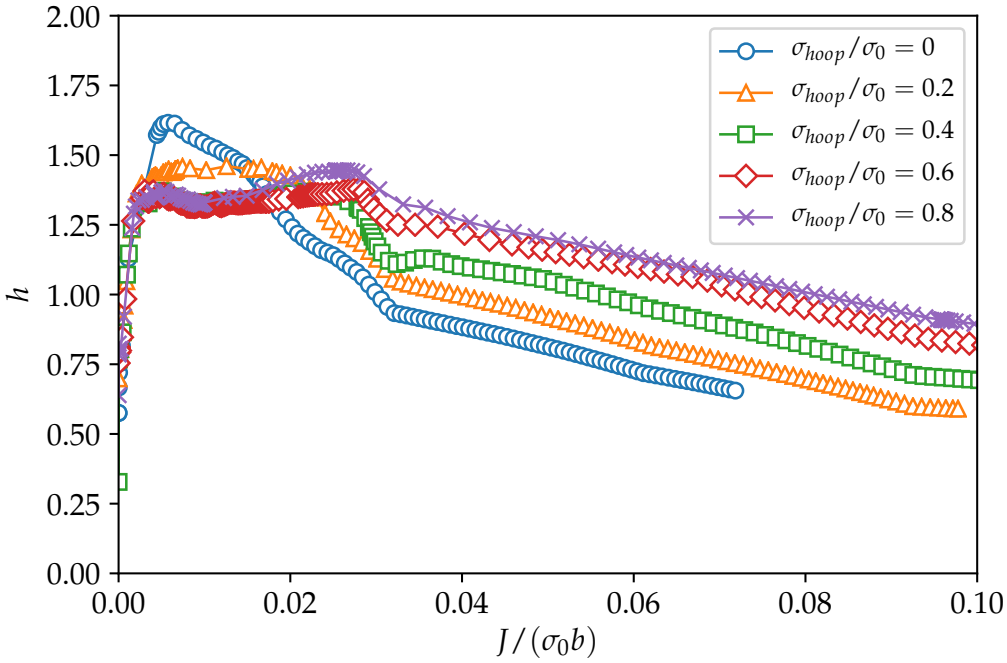

Figure 4.21: Crack-tip stress triaxiality parameter h versus normalised J calculated from FE analysis of circumferentially cracked pipes with crack depth of $a/t = 0.1$ for various internal pressure levels

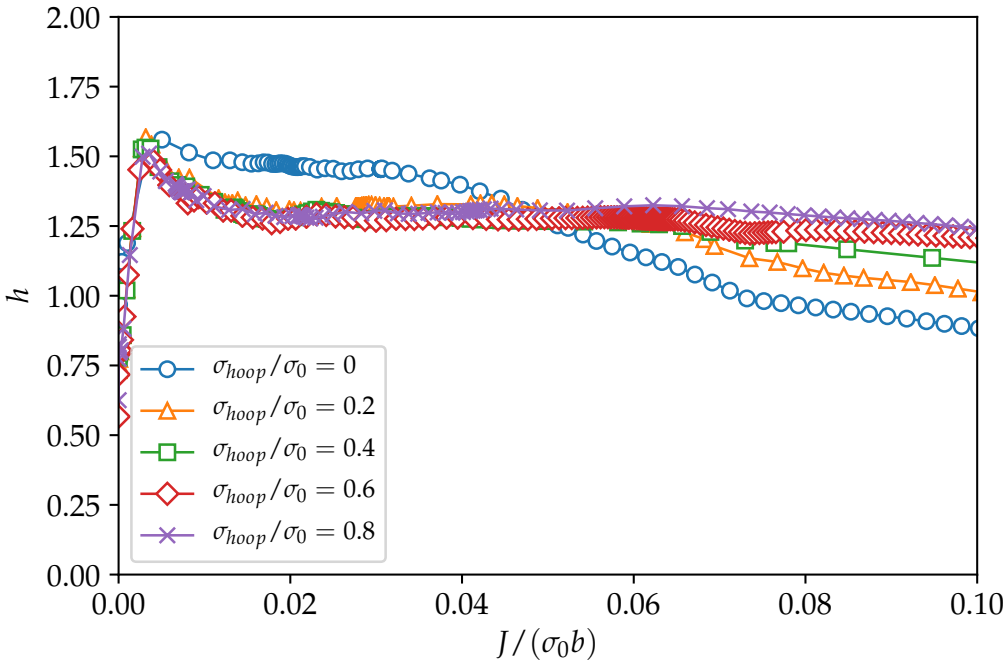

Figure 4.22: Crack-tip stress triaxiality parameter h versus normalised J calculated from FE analysis of circumferentially cracked pipes with crack depth of $a/t = 0.2$ for various internal pressure levels

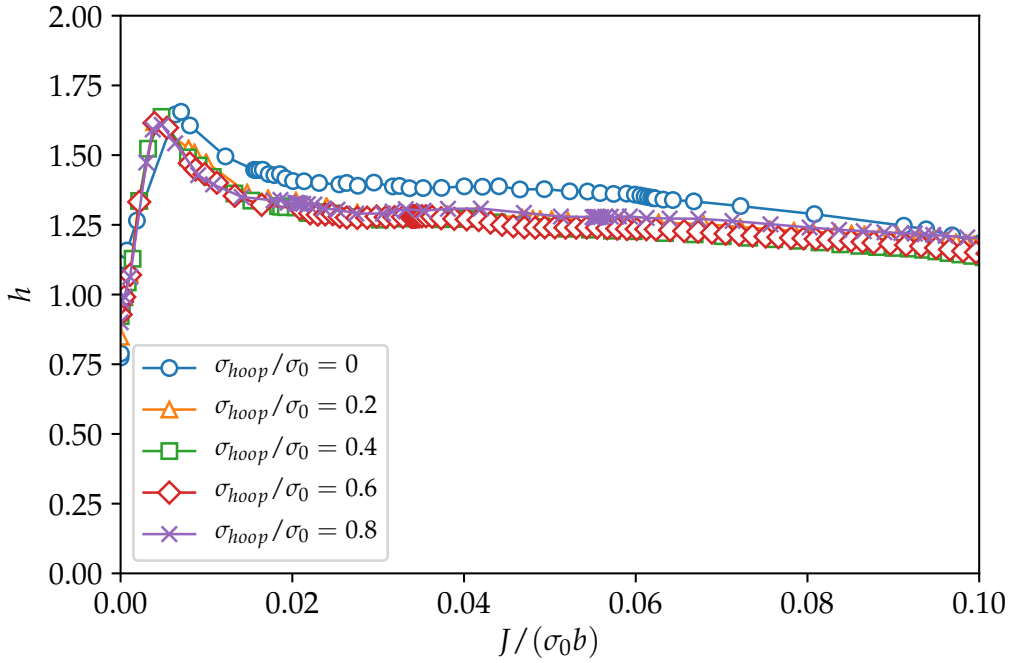

Figure 4.23: Crack-tip stress triaxiality parameter h versus normalised J calculated from FE analysis of circumferentially cracked pipes with crack depth of $a/t = 0.3$ for various internal pressure levels

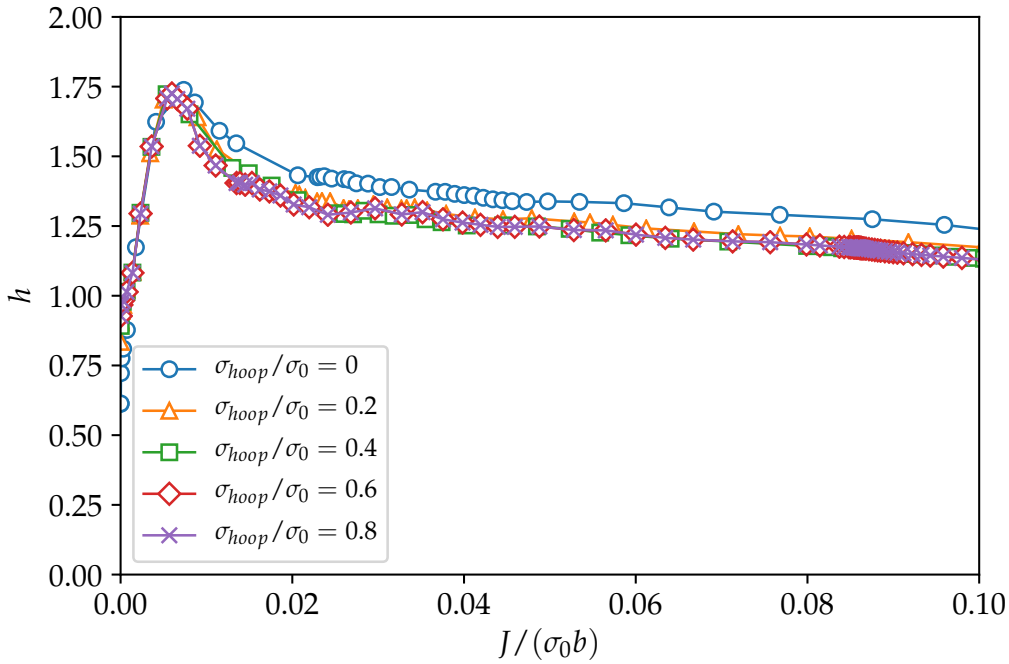

Figure 4.24: Crack-tip stress triaxiality parameter h versus normalised J calculated from FE analysis of circumferentially cracked pipes with crack depth of $a/t = 0.4$ for various internal pressure levels

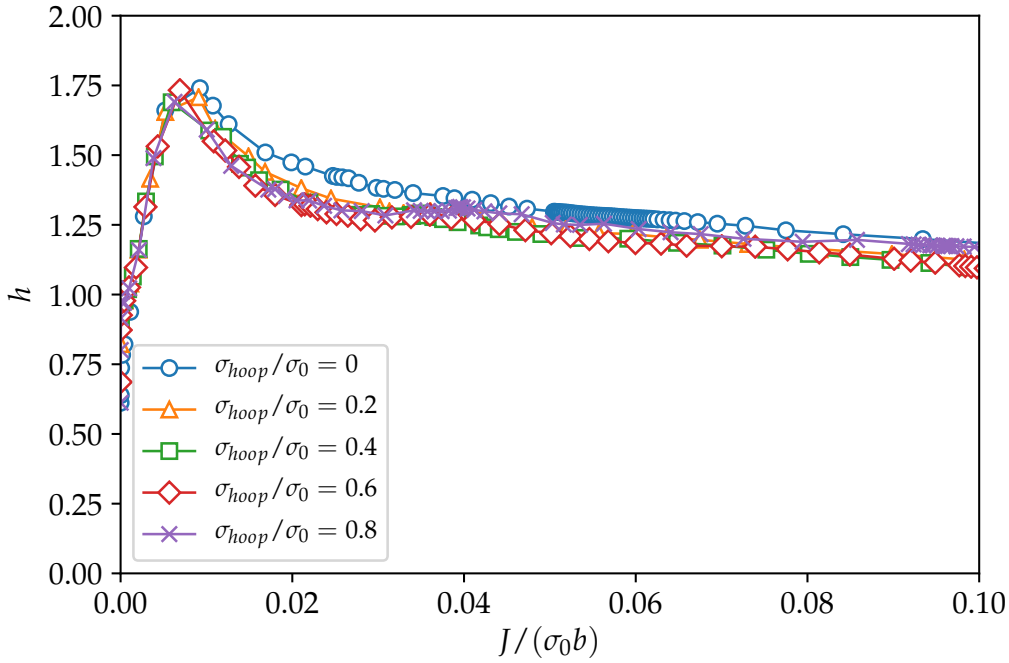

Figure 4.25: Crack-tip stress triaxiality parameter h versus normalised J calculated from FE analysis of circumferentially cracked pipes with crack depth of $a/t = 0.5$ for various internal pressure levels

4.2.3.3 J-T_z *analysis*

Unlike the constraint parameters Q and h, T_z explicitly measures the out-of-plane constraint at the crack-tip. Figures 4.27 to 4.29 show T_z versus the normalised J for SENT specimens and the cracked pipes subjected to tension only. Similar to Q and h, geometries (SENT and cracked pipes) with deeper notches show a higher T_z, indicating higher out-of-plane crack-tip constraint. When the notch depth ratio (a/t or a/W) is greater than 0.3, the effect of notch depth on T_z is found to be diminished.

Figures 4.30 to 4.34 show the effect of internal pressure (measured in terms of the ratio of the hoop stress to the yield strength, σ_{hoop}/σ_0) on T_z for cracked pipes with various flaw depth, respectively. It can be seen that for shallow cracks, as shown in Figure 4.30, the internal pressure is found to increase T_z, especially at higher J levels. This increase is found to be less considerable for a crack depth of $a/t = 0.2$. For deeper crack depths ($a/t = 0.3$ - 0.5), the effect of internal pressure on T_z is shown negligible.

A comprehensive comparison of T_z for all types of geometries are shown in Figure 4.35. SENT (B $\times$ B) is found to have the lowest out-of-plane constraint

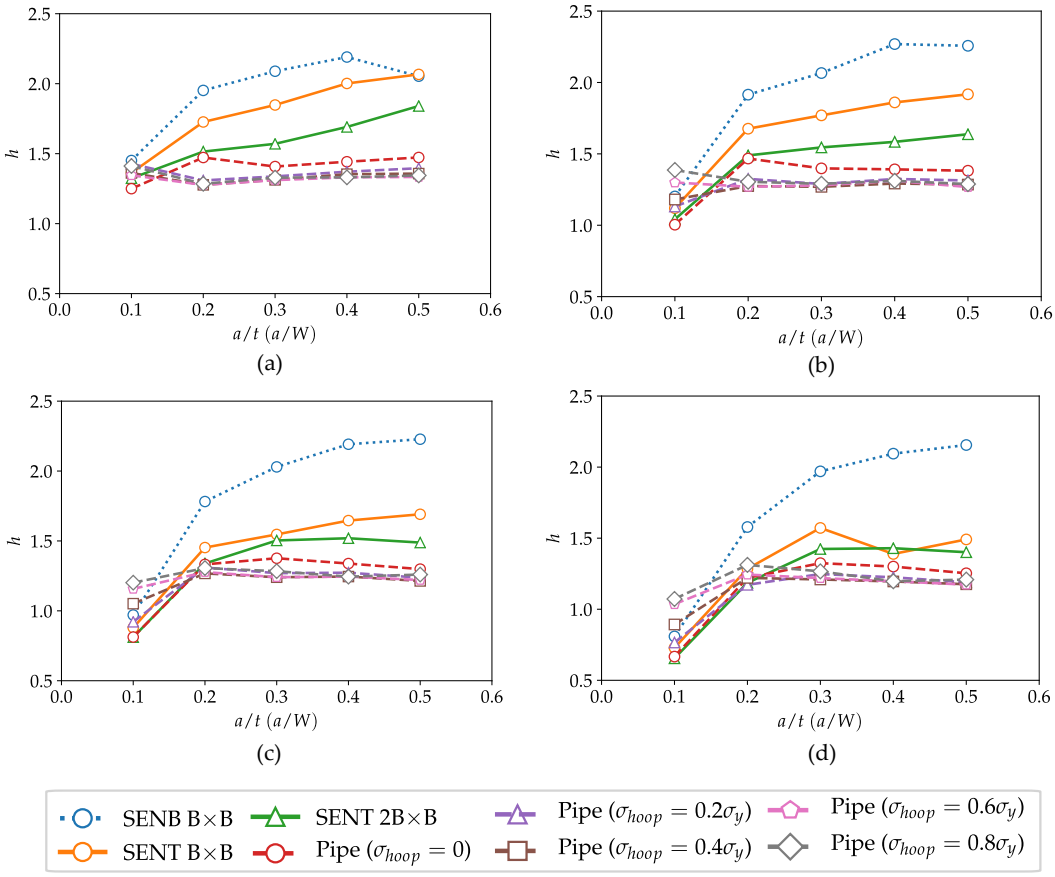

Figure 4.26: Comparison of stress triaxiality parameter h for SENB, SENT and cracked pipes

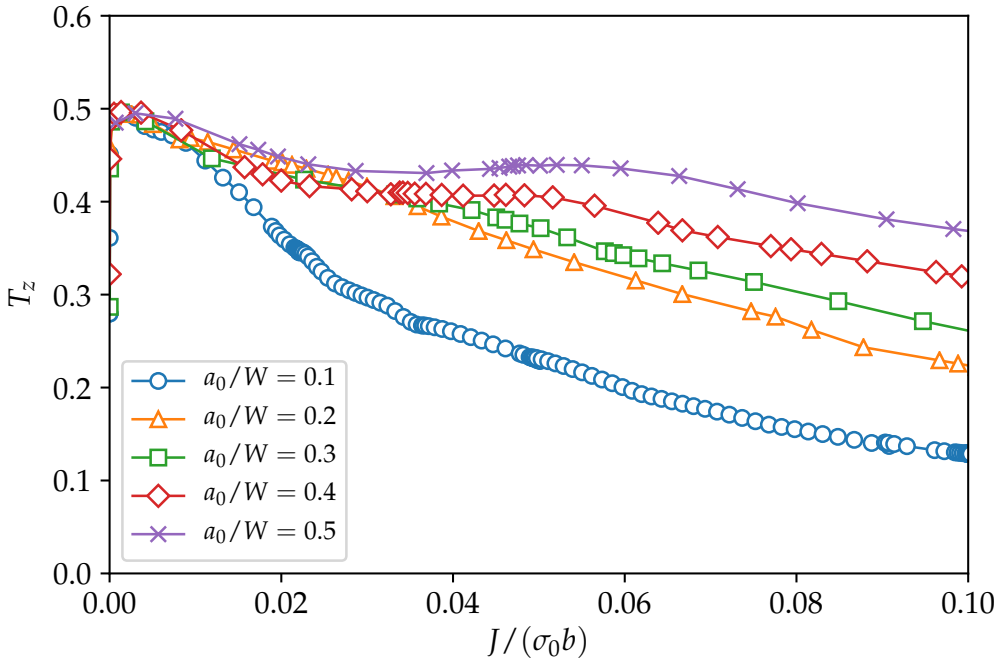

Figure 4.27: Out-of-plane crack-tip constraint parameter in terms of T_z versus normalised J calculated from FE analysis of SENT B×B

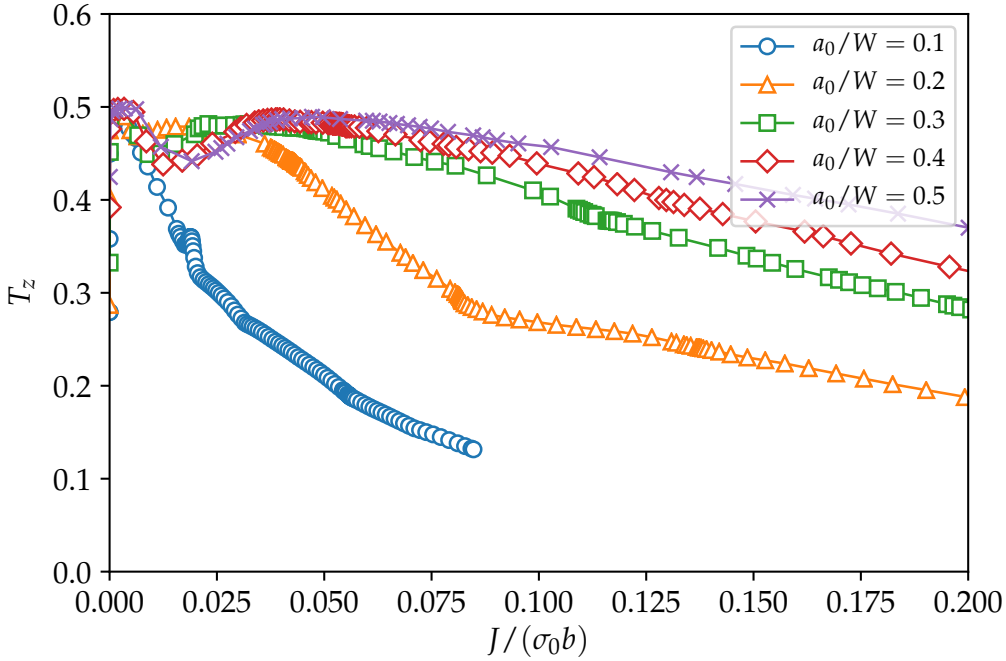

Figure 4.28: Out-of-plane crack-tip constraint parameter in terms of T_z versus normalised J calculated from FE analysis of SENT 2B×B

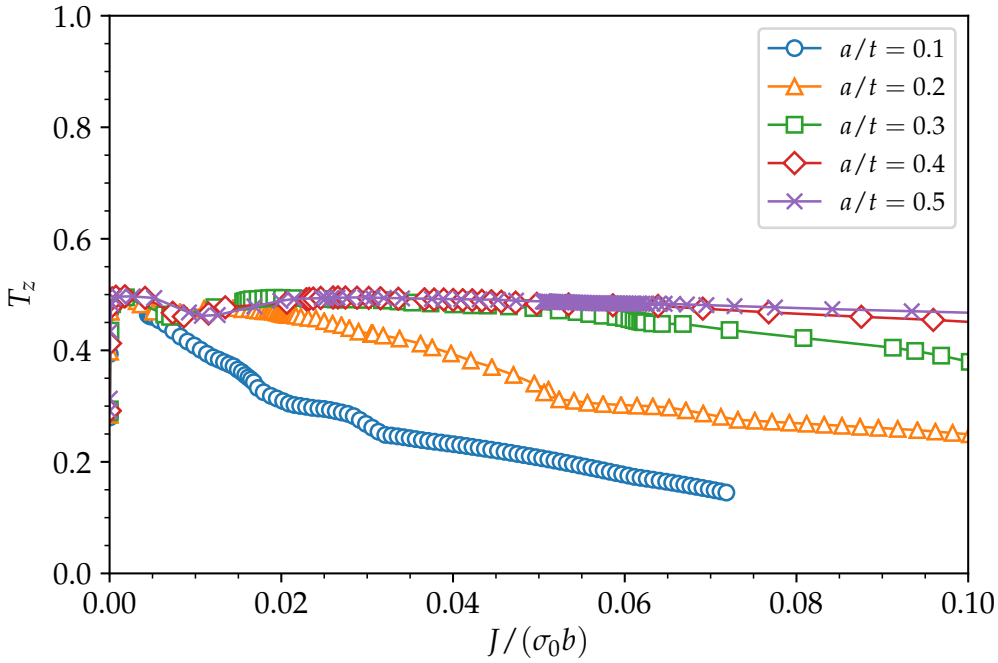

Figure 4.29: Out-of-plane crack-tip constraint parameter in terms of T_z versus normalised J calculated from FE analysis of circumferentially cracked pipes

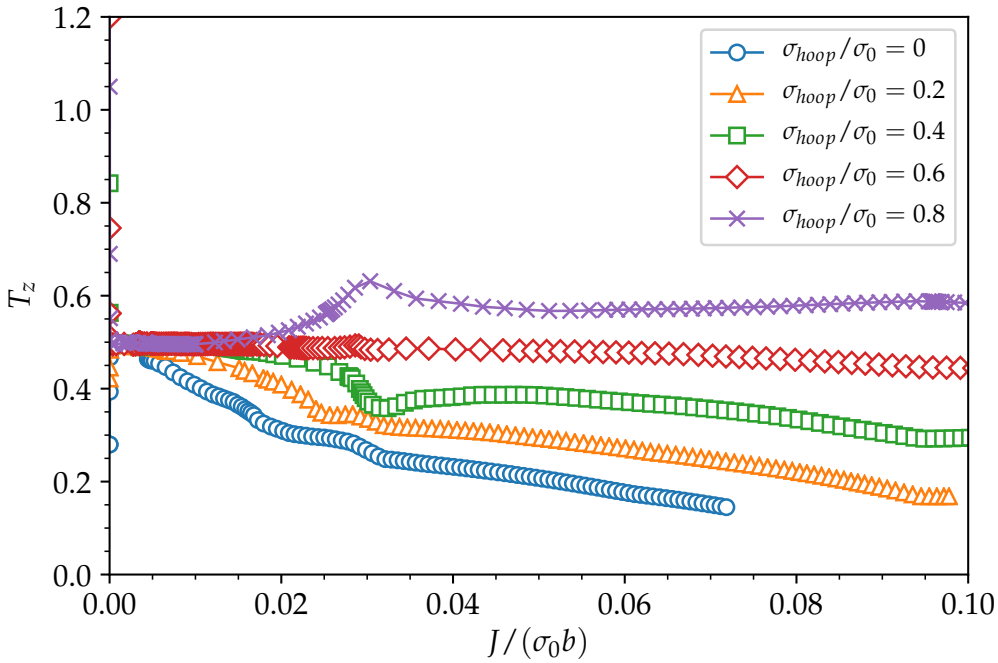

Figure 4.30: Out-of-plane crack-tip constraint parameter in terms of T_z versus normalised J calculated from FE analysis of circumferentially cracked pipes with crack depth of $a/t = 0.1$ for various internal pressure levels

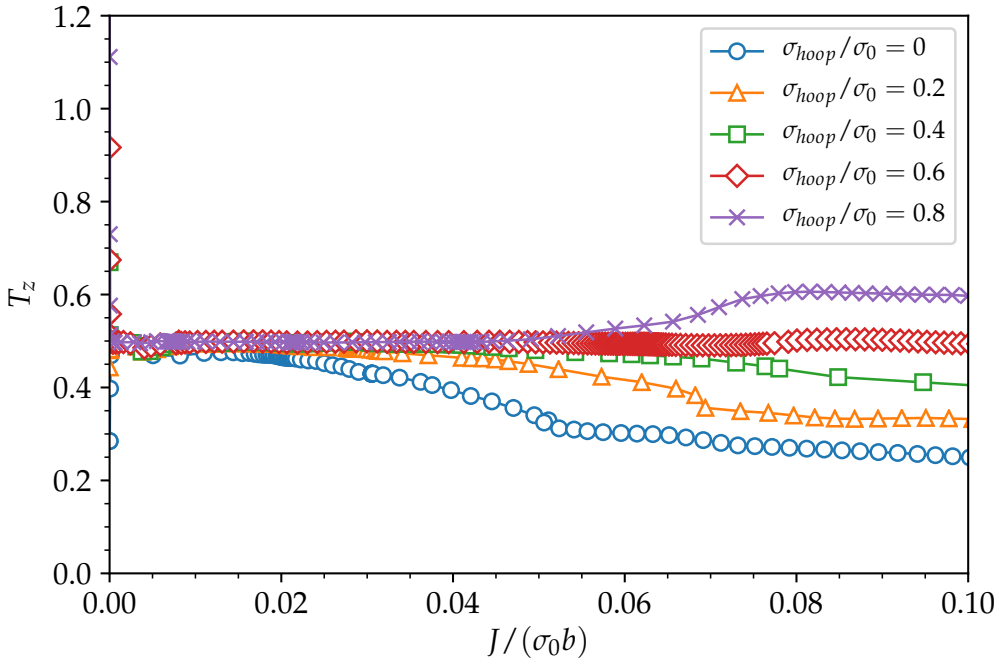

Figure 4.31: Out-of-plane crack-tip constraint parameter in terms of T_z versus normalised J calculated from FE analysis of circumferentially cracked pipes with crack depth of $a/t = 0.2$ for various internal pressure levels

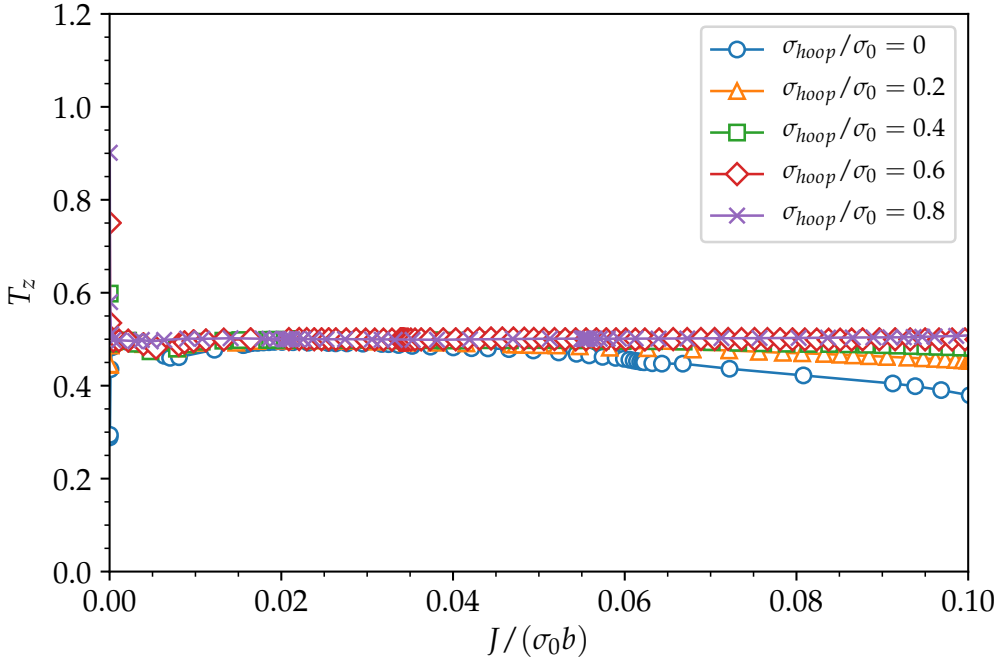

Figure 4.32: Out-of-plane crack-tip constraint parameter in terms of T_z versus normalised J calculated from FE analysis of circumferentially cracked pipes with crack depth of $a/t = 0.3$ for various internal pressure levels

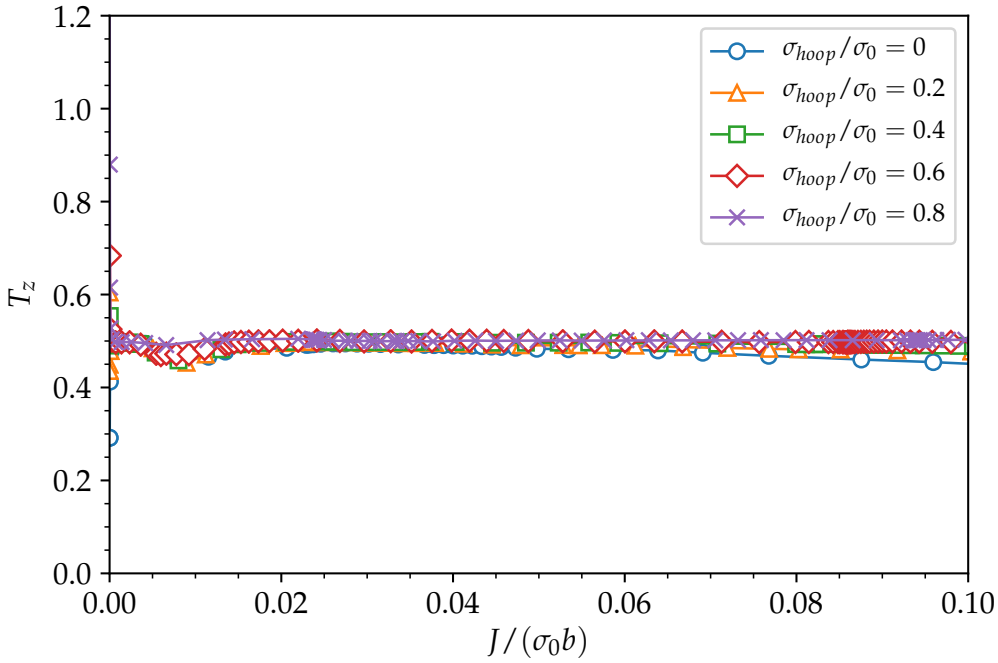

Figure 4.33: Out-of-plane crack-tip constraint parameter in terms of T_z versus normalised J calculated from FE analysis of circumferentially cracked pipes with crack depth of $a/t = 0.4$ for various internal pressure levels

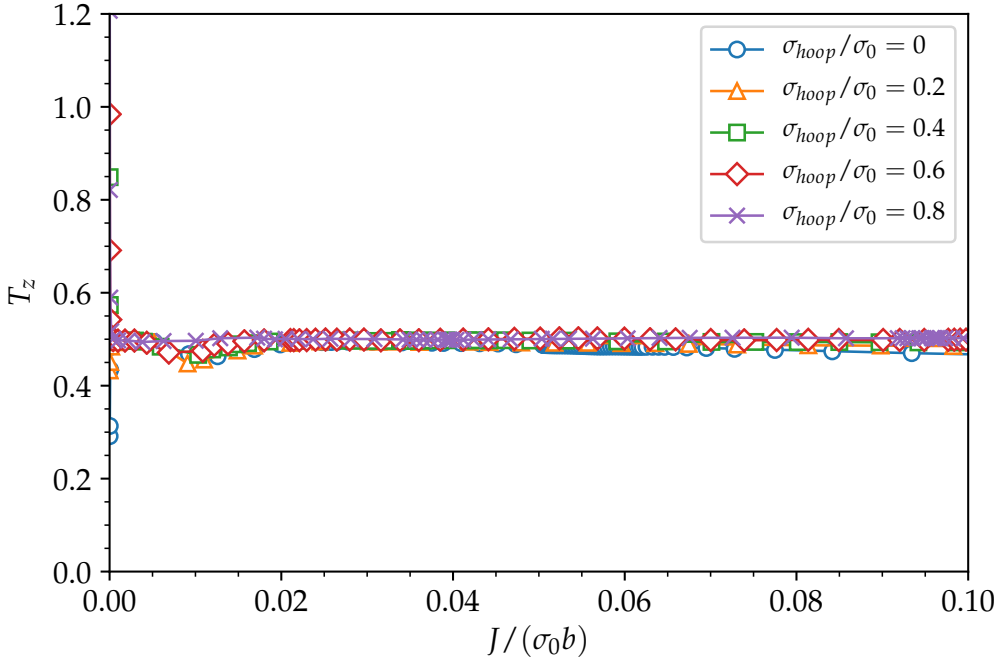

Figure 4.34: Out-of-plane crack-tip constraint parameter in terms of T_z versus normalised J calculated from FE analysis of circumferentially cracked pipes with crack depth of $a/t = 0.5$ for various internal pressure levels

among all geometries and loadings investigated. SENT (2B × B) is found to have a similar out-of-plane constraint to that of cracked pipes subjected to various internal pressure levels for deeper notch depths ($a_0/t = 0.3$ - 0.5). The notch depth (a_0/t or a_0/W) is shown to have less effect on T_z for deeper notches (a_0/t or a_0/W greater than 0.3).

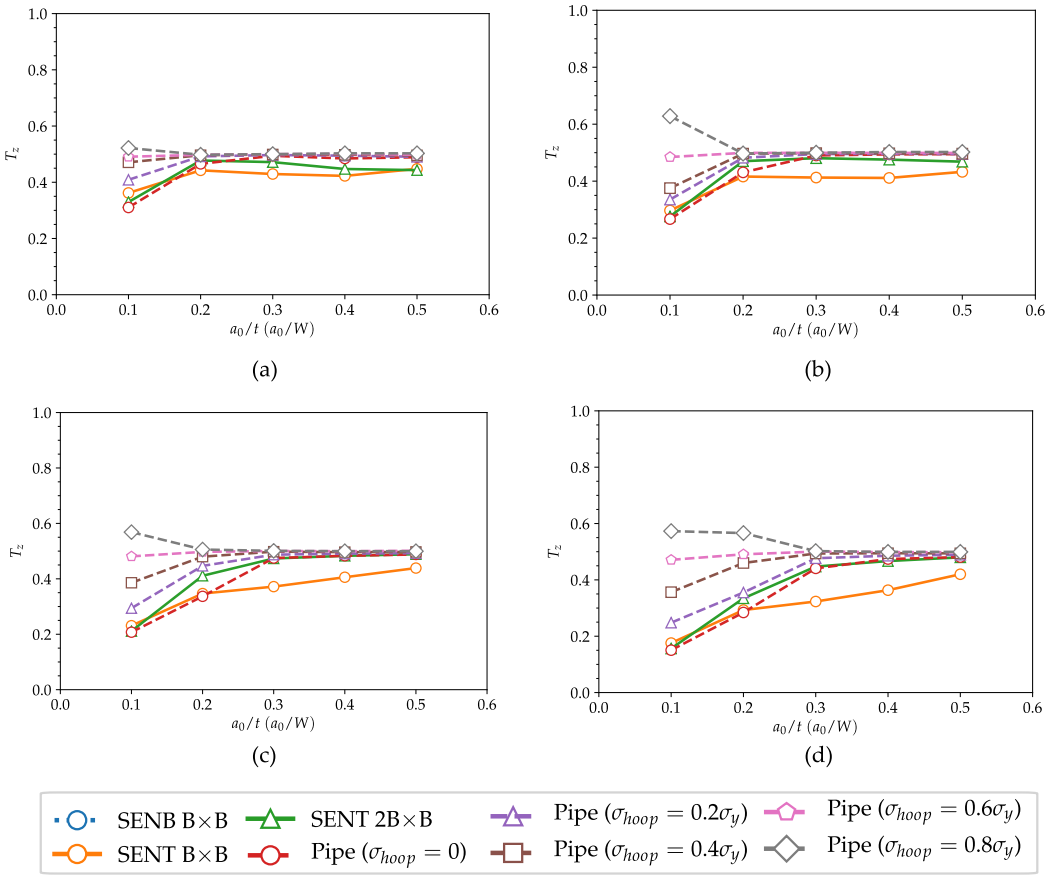

Figure 4.35: Comparison of out-of-plane constraint parameter T_z for SENB, SENT and cracked pipes at various crack-tip loadings: (a) $J/(\sigma_y b) = 0.02$, (b) $J/(\sigma_y b) = 0.03$, (c) $J/(\sigma_y b) = 0.05$ and (d) $J/(\sigma_y b) = 0.07$

4.2.4 *Summary*

Numerical analyses of the crack-tip constraint of fracture mechanics test specimens (SENB and SENT) and cracked pipes were performed. The in-plane constraint Q, triaxiality parameter h and the out-of-plane constraint T_z for aforementioned geometries were investigated. Based on the results presented, it is found that:

- For small a_0/W, the crack-tip constraint of SENB is similar to that of SENT, while for larger a_0/W, the crack tip constraint of SENB is much higher than that of SENT.
- Biaxial loading induced by internal pressure decreases the crack tip constraint at lower crack-tip loadings but has marginal effect at higher crack-tip loadings.
- SENT (2B $\times$ B) has lower in-plane constraint than SENT (B $\times$ B), but higher out-of-plane constraint.
- The SENT (2B $\times$ B) with $a/W \leqslant 0.3$ seems optimal in terms of the transferability in crack-tip constraint to the cracked pipes subjected to axial straining with and without internal pressure.

4.3 SINGLE EDGE NOTCHED TENSION (SENT) TESTING

4.3.1 *Testing setup*

SENT specimens were extracted from a seamless pipe segment at different locations around the circumference. A total of six specimens were taken from the pipe section, as shown in Figure 4.36 and 4.37. The specimens were machined to standard BS 8571:2014 [1] (BSI 2013b), having a rectangular cross-section (2B $\times$ B).

Figure 4.37 shows the configuration of the SENT specimens. The length between the grips is $10W$. Knife edges were attached on each side of the machined notch, at two different heights (z_1 and z_2, respectively). A fatigue pre-crack was produced by applying a controlled alternating force using three-point bending such that the total crack depth reaches the intended value. A close-up view of the machined notch and the fatigue pre-crack is shown in Figure 4.38 (b). Tables 4.3 and 4.4 show the actual dimensions of the manufactured specimens and the machined total crack depths for nominal deeper and shallow crack depth, respectively.

The Set-1 SENT specimens were tested to BS 8571 using multiple specimen method to generate an R-curve, while in Set-2 only single point tests were

1 now superseded by BS 8571:2018

(a)

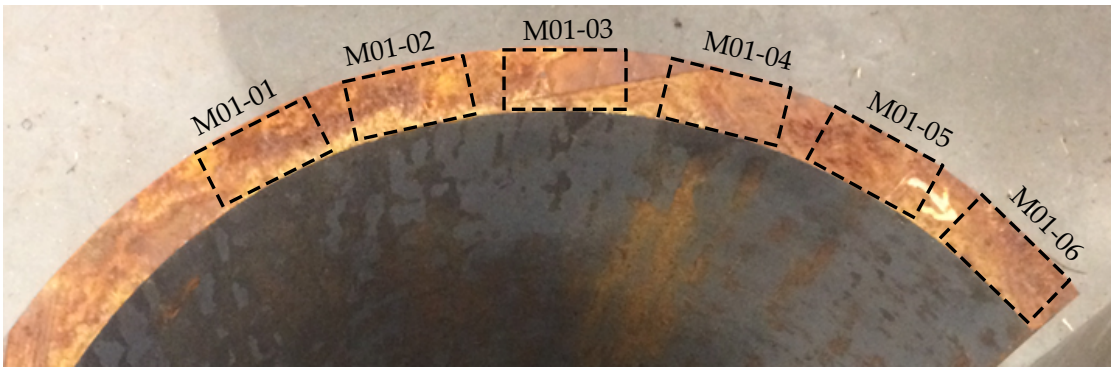

(b)

Figure 4.36: Pipe section from which the SENT specimens were extracted (a) pipe section (b) cutting plan for manufacturing SENT specimens

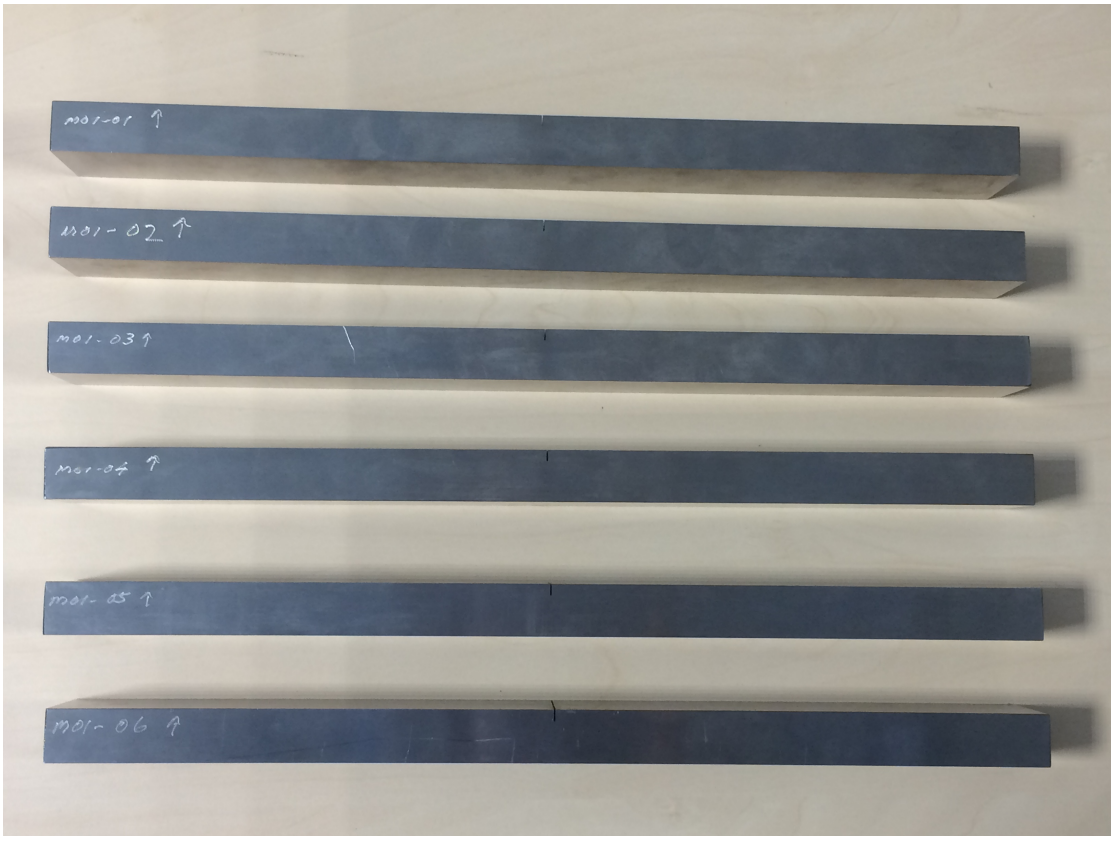

Figure 4.37: SENT specimens to be tested using multiple specimen method

Table 4.3: Actual dimensions of Set-1 SENT specimens with a nominal crack depth of $a_0/W = 0.35$

Specimen No.	W, mm	B, mm	a_0	a_0/W
M01-01	17	34	6.62	0.39
M01-02	17	34	6.57	0.39
M01-03	17	34	6.61	0.39
M01-04	17	34	6.85	0.40
M01-05	17	34	6.76	0.40
M01-06	17	34	6.69	0.39

Table 4.4: Actual dimensions of Set-2 SENT specimens with a nominal crack depth of $a_0/W = 0.15$

Specimen No.	W, mm	B, mm	a_0	a_0/W
M01-08	17	34	2.79	0.16
M01-09	17	34	2.89	0.17

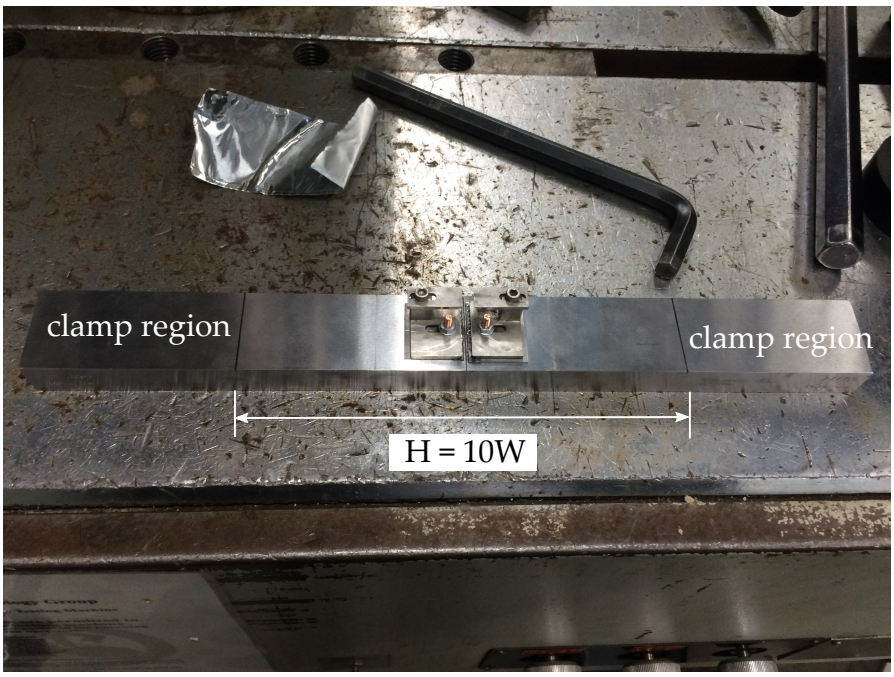

(a)

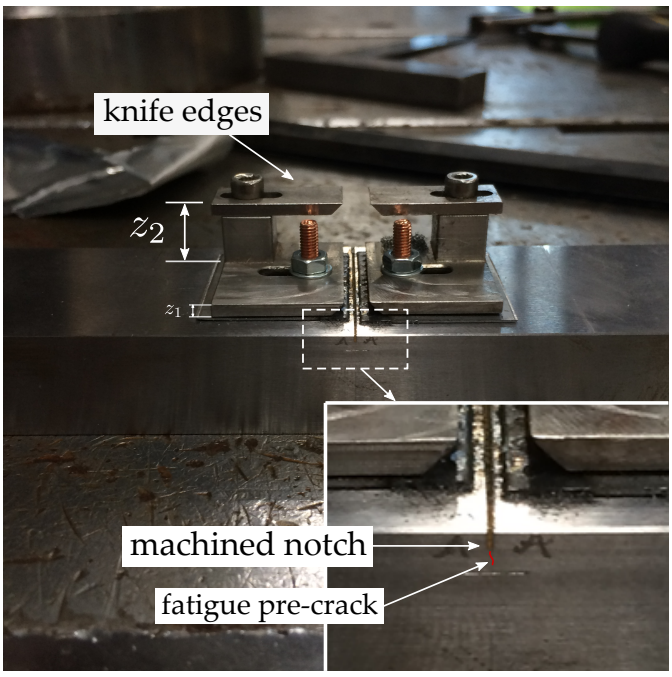

(b)

Figure 4.38: SENT specimen configuration: (a) global view of specimen configuration; (b) close-up view of the machined notch region

conducted. Similar to the tensile specimens reported in Chapter 3, speckle patterns were generated on the surface of the SENT specimens to capture deformation using DIC, as shown in Figure 4.39.

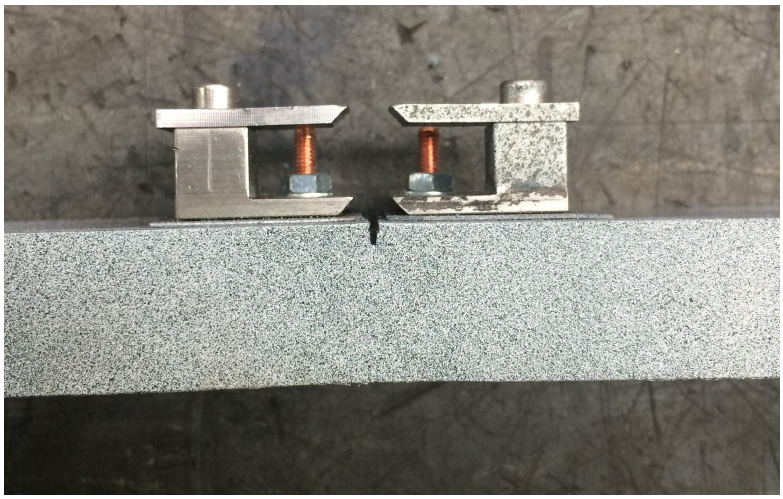

Figure 4.39: Speckle pattern applied to the surface of SENT specimens for DIC measurement

The specimens were tested in tension by clamping the specimens in the grips of a tensile test machine (INSTRON 8500 B107), as shown in Figure 4.40. Double-clip gauges were placed at the knife-edges to measure the clip gauge displacements, from which the CMOD and CTOD can be calculated. The CMOD was calculated from the displacement measurements via the equation given below:

$$\text{CMOD} = V_{p1} - \frac{Z_1}{Z_2 - Z_1}\left(V_{p2} - V_{p1}\right) \tag{4.4}$$

where V_p1 and ν_P2 are the plastic parts of the clip gauge displacements of the knife heights of Z_1 and Z_2, respectively.

The calculation of the J-integral is based on equations given in DNVGL-RP-F108 (DNVGL 2017), which takes the following form:

$$\begin{aligned} J &= J_{el} + J_{pl} \\ &= \frac{K^2}{E'} + \frac{\eta_p U_p}{B\,(W - a_0)} \end{aligned} \tag{4.5}$$

where J_{el} and J_{pl} are the elastic and plastic component of J, respectively; K is the elastic stress intensity factor at force applied to the specimen at the start of unloading; E' is the longitudinal elastic modulus in plane strain; η_p

is a dimensionless function of geometry; U_p is the plastic part of the load-CMOD curve;and a_0 is the initial crack depth. Like the J-integral, the CTOD is calculated as the sum of the elastic and plastic components, as follows:

$$\begin{aligned}\delta &= \delta_{el} + \delta_{pl} \\ &= \frac{(1-\nu^2)\,K_I^2}{m\sigma_y E} + V_{pl} - \frac{a_0 + Z_1}{Z_2 - Z_1}\left(V_{p2} - V_{p1}\right)\end{aligned} \tag{4.6}$$

where σ_y is the yield strength of the material in which the crack is located. The parameter m is close to 1 as indicated by limited FE analyses except for brittle fracture. Since these tests are used to generate an R-curve, the elastic component of CTOD is small, hence any errors in the assumption for the value of m have a negligible effect on the results. As shown in Equation 4.6, the elastic component of CTOD is determined from the elastic K, and the plastic component is calculated by extrapolating the readings from the pair of clip gauges back to the original fatigue pre-crack tip.

The R-curve line is fitted to the test data, either as a best-fit curve, or as a lower-bound, depending on the application requirement. The R-curve takes the following form:

$$J \text{ or } CTOD = m + I\,(\Delta a)^x \tag{4.7}$$

where m, I and x are constants with $I \geqslant 0$ and $0 \leqslant x \leqslant 1$, and m is the intercept on the Y axis and may be 0. According to BS 8571, the R-curve should be fitted to crack extensions between 0.2 mm and the maximum crack extension from the test data, or 20% of the specimens ligament ($W - a_0$). In the testing work presented in this chapter where multiple specimen method is used, the R-curve is usually fitted to a minimum of six qualified results within this range. The test reports (produced by TWI) showing the test parameters, specimen dimensions and test results are included in Appendix B. The DIC was used for each test, with a frequency of 1 Hz (one image per second) in the image capturing.

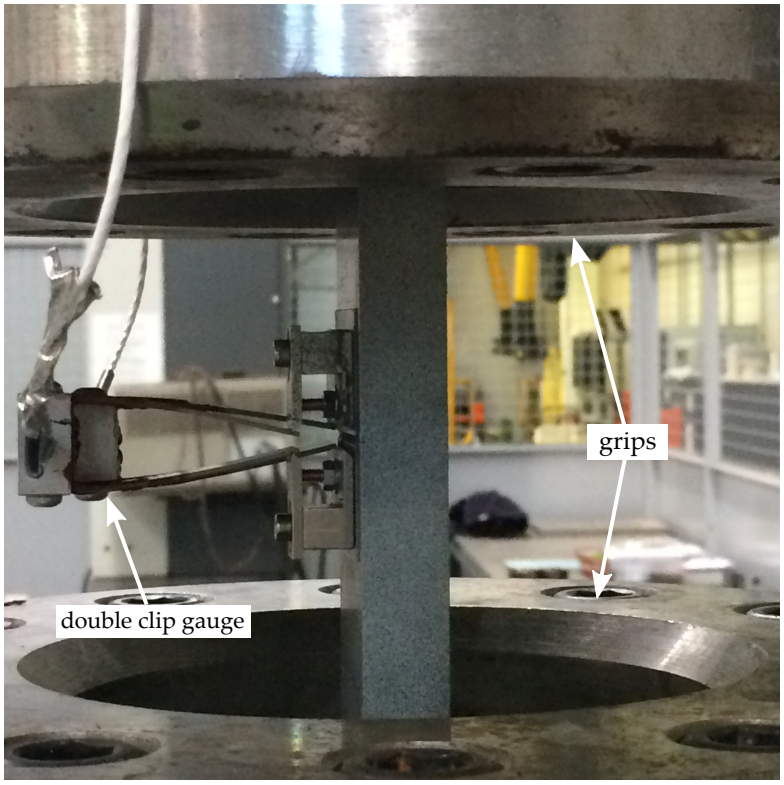

Figure 4.40: SENT specimen loaded using servo hydraulic testing machine

4.3.2 *Results*

4.3.2.1 *SENT test Set-1*

Figure 4.41 shows the Load-CMOD responses of six SENT specimens in test Set-01. All curves are observed to converge well and drop at different levels as each specimen was tested to different crack growth. Table 4.5 presents the CTOD and J values for each test, together with respective crack growth.

Table 4.5: Results of SENT fracture test Set-1 using multiple specimen method

Test No.	Δa	J, kJ/m^2	CTOD, mm
M01-01	1.965	1605.7	2.04
M01-02	0.248	390.8	0.70
M01-03	0.686	865.6	1.51
M01-04	1.438	1389.7	2.41
M01-05	1.096	1172.3	2.04
M01-06	0.592	781.0	1.34

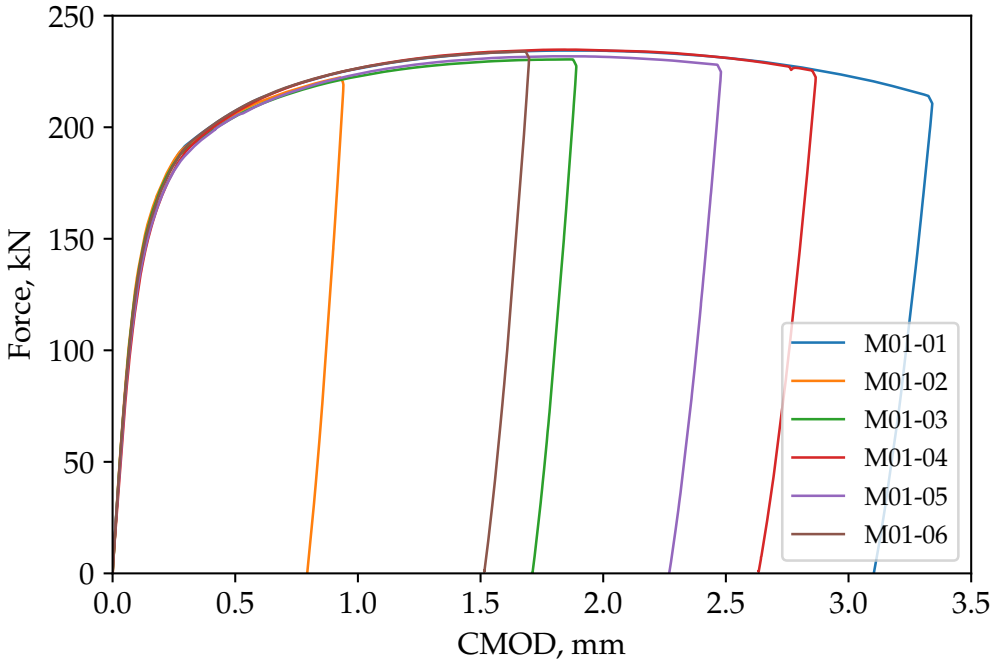

Figure 4.41: Force-CMOD responses of SENT specimens with nominal initial crack depth of $a/W = 0.35$

Using the curve fitting described Section 4.3.1, the R-curve of SENT Set-1 tests were obtained as follows:

$$J = -649.521 + 1756.704\Delta a^{0.379} \tag{4.8}$$

$$\delta = -0.875 + 2.794\Delta a^{0.417} \tag{4.9}$$

Figures 4.42 and 4.43 show the generated J-R curve and CTOD-R curve, respectively.

Figures 4.44 show the longitudinal strain maps respectively of the SENT specimen at various load levels in terms of CMOD. Since no propagating localisation bands were observed and the strains were found to localise in the crack region, only the strain maps near this region were shown. From the strain maps shown in Figures 4.44, it is shown that the strain pattern resembles the classic 'butterfly' pattern of the crack-tip plasticity and was found to increase in the magnitude and size when the applied load was increased. The strain maps were only shown up to load level in terms of CMOD equal to 0.607 mm at which

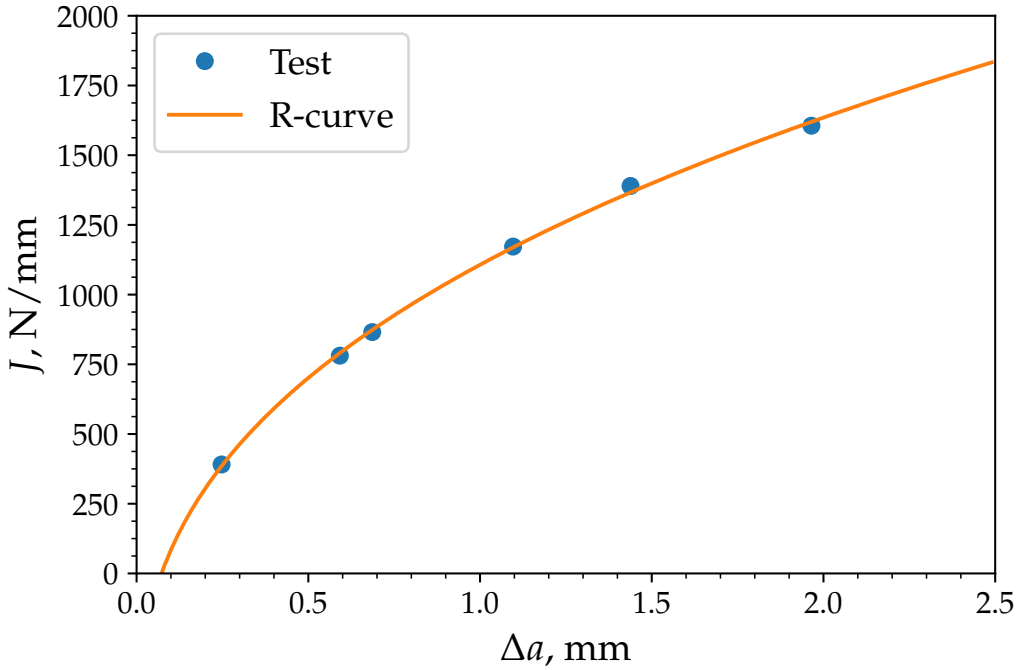

Figure 4.42: CTOD J-curves of SENT specimens with nominal crack depth of $a/W = 0.35$

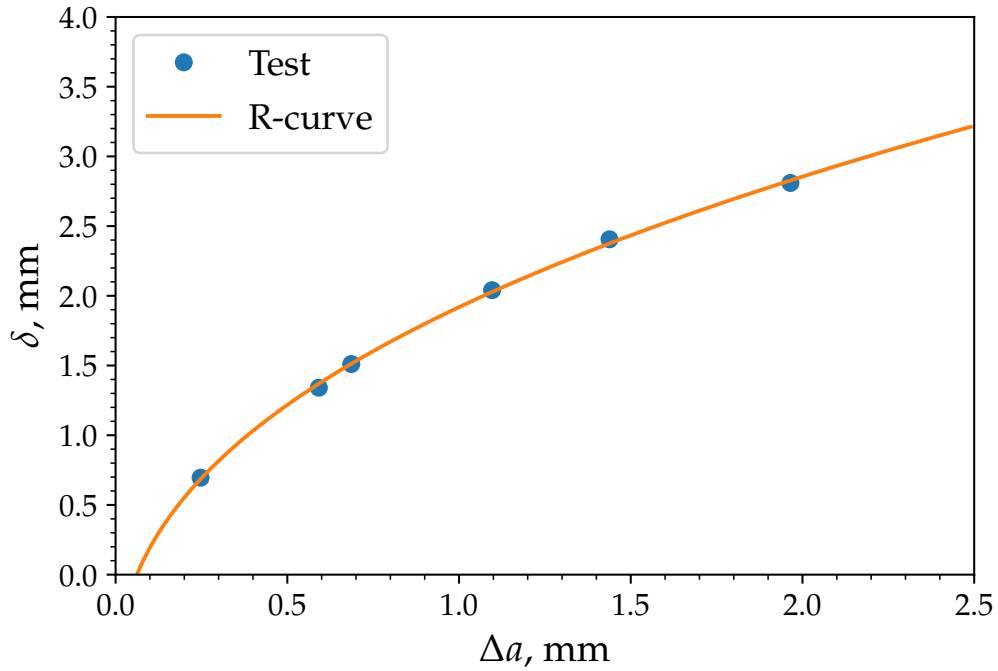

Figure 4.43: CTOD R-curves of SENT specimens with nominal crack depth of $a/W = 0.35$

very limited tearing was found to occur, which is based on the crack extension of specimen M01-02 (see Table 4.5; the total crack extension was mostly due to blunting, and possible a slight length of tearing). These strain distributions were then used to validate the FE analysis which did not explicitly simulate the ductile tearing. Beyond the CMOD levels for which the strain maps were presented herein, the strain localisation was observed to continuously develop in the crack-tip region, both in magnitude and size, until the termination of the test. It can be expected that upon the largest range of CMOD measured (as in M01-01), the specimen was expected to fail by plastic collapse due to gross plasticity in the uncracked ligament. For brevity, the strain maps for higher load levels were not reported. The distributions of Mises equivalent strain (ε_{eq}) of SENT specimen M01-08, which resembles closely its longitudinal strain maps shown in Figure 4.44, are not presented herein but included in Appendix C for conciseness.

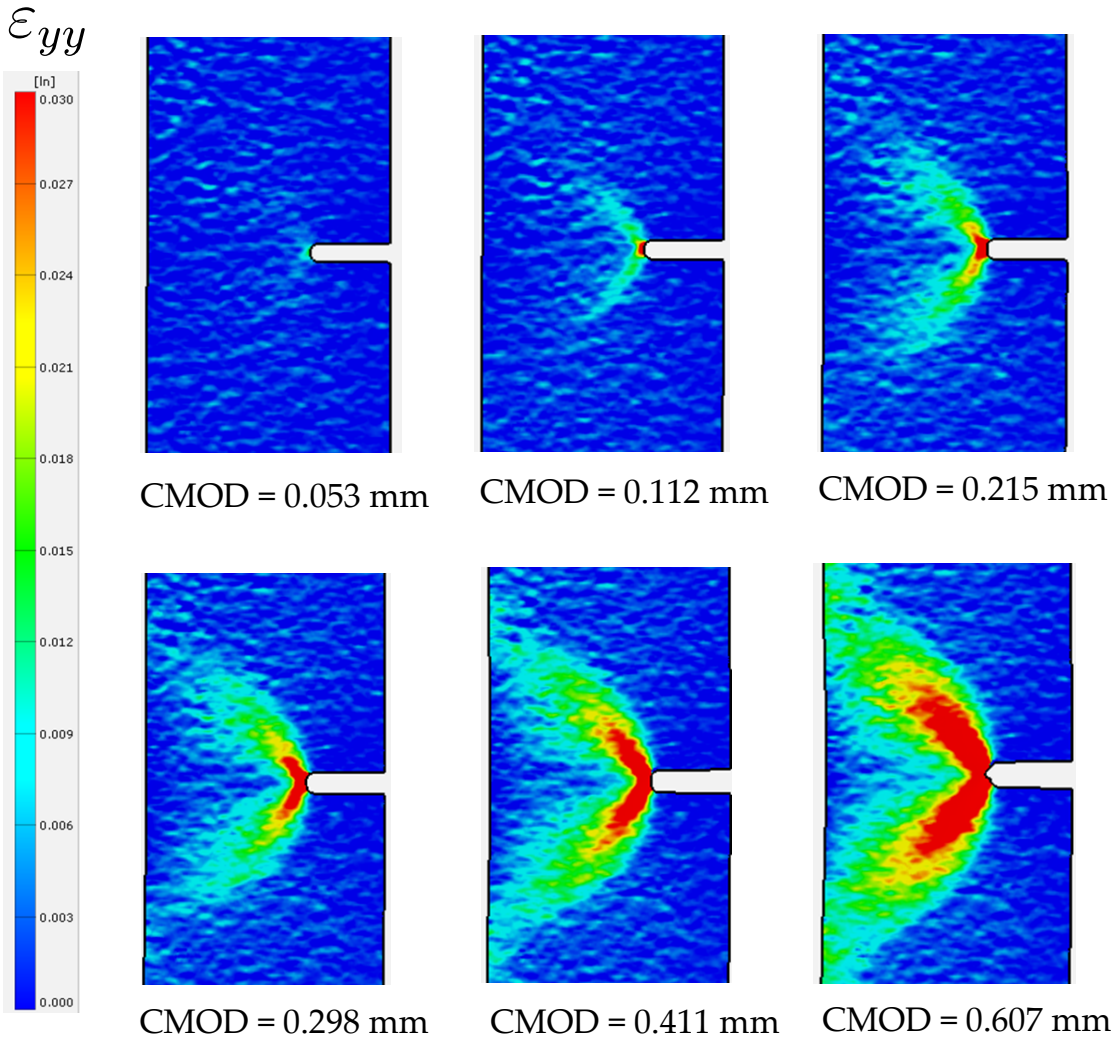

Figure 4.44: Longitudinal strain ε_{yy} maps of SENT test (Set-1) M01-02 captured by DIC

To show clearly the development of CMOD with applied loading, the CMOD versus the global strain extracted from a gauge length of 65 mm (illustrated in Figure 4.45) across the crack tip of the SENT specimen. Figure 4.50 shows the CMOD versus global strain (65 mm GL), which reinforces the observation that no Lüders bands propagation occurred and the CMOD increases monotonically and nearly linearly proportional to the global strain.

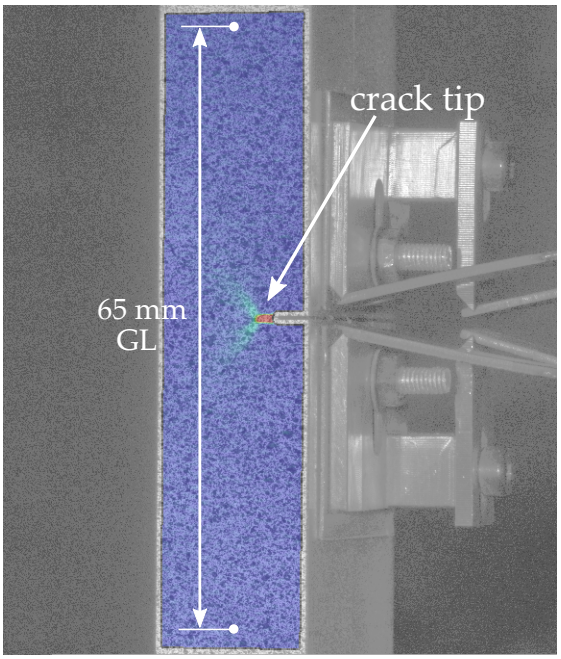

Figure 4.45: Gauge length for global strain extraction from SENT test Set-1 specimens

4.3.2.2 *SENT test Set-2*

Figure 4.47 shows the load-CMOD responses of the SENT test Set-2 (specimens M01-08 and M01-09). It can be seen that the load-CMOD responses of these two specimens initially overlapped and begun to deviate from each other when the globally-elastic regime was passed. In the plastic regime, the load measured of M01-08 is shown to lie above that of M01-09, which is likely due to the variance of the material properties around the pipe circumference from which the specimens were extracted.

Figures 4.49 shows the development of longitudinal strain. As can be seen, strain localisation or Lüders banding is found to occur, starting from the crack tip and then spreading towards both ends of the specimen. At CMOD $= 0.031$ mm, the specimen is globally elastic and very limited strain localisation can be observed at the crack tip. At the termination of the elastic regime on the

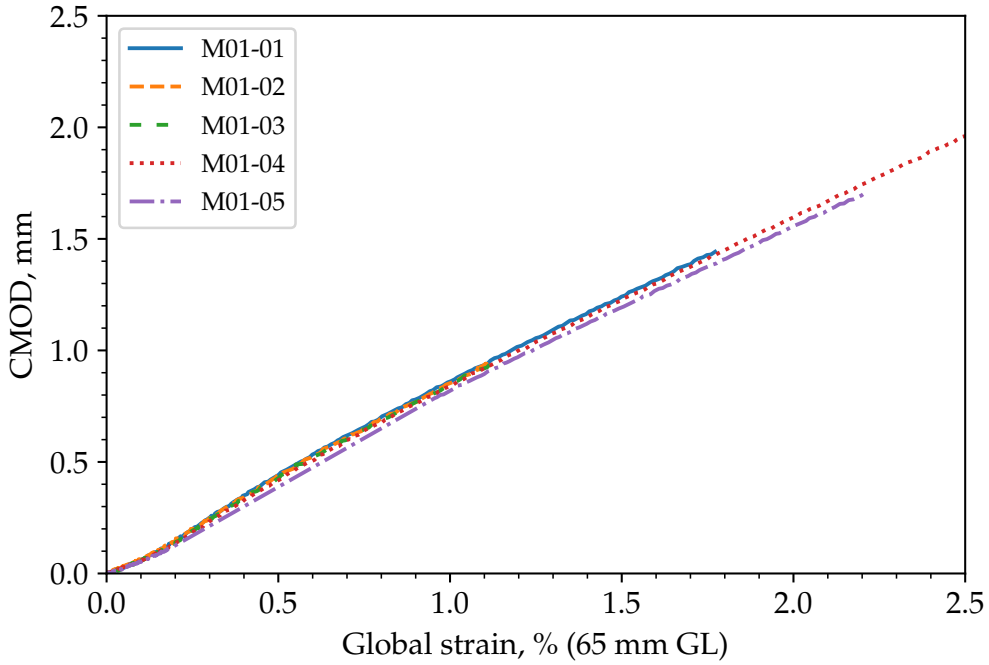

Figure 4.46: CMOD versus global strain (65 mm GL) of SENT test Set-2

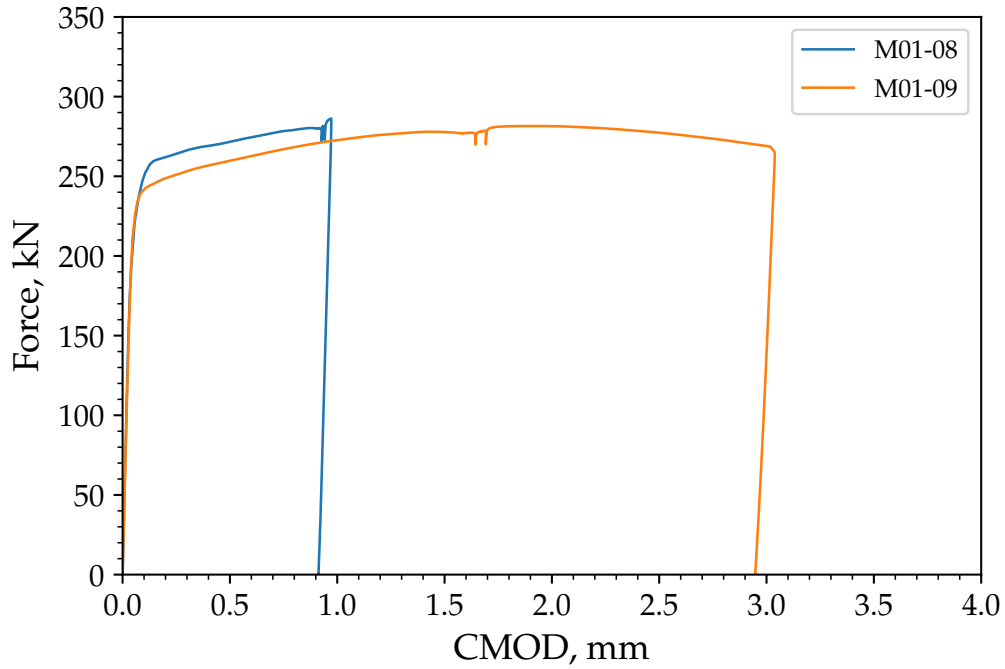

Figure 4.47: Force-CMOD responses of SENT specimens with nominal initial crack depth of $a/W = 0.15$

load-CMOD curve (CMOD = 0.145 mm), localised strain regime was found to emanate from the crack tip and spread to the opposite side at an inclination of about 45°. As applied load increases (CMOD=0.517 - 1.322 mm), the localised strain regime continued to develop, both in terms of magnitude and size, and propagated along the loading axis, towards both ends of the specimen. During the propagation of strain localisation, new bands were observed to initiate at the bottom (side opposite the crack) as the test proceeded. The bands that initiated at the bottom are shown to resemble the 'criss-cross' cluster pattern, which is similar to those observed by Wenman and Chard-Tuckey (2010), Hallai and Kyriakides (2011a), and Pokorny and Plkorny (2003). At CMOD=1.688 mm, the localisation bands were seen to have spread through the whole length (length between grips, or 'daylight') of the specimen, with a large area of increased strain localisation near the crack tip (strains above 4%). Again, due to the similarity in terms of strain patterns between the distributions of longitudinal and Mise equivalent strains, the Mises equivalent strain maps of SENT specimen M01-09 are included in Appendix C.

Similar to the CMOD versus global strain response of SENT test Set-1 presented earlier, the global strain for SENT test Set-2 was extracted over a gauge length of 80 mm due to larger size of the DIC monitoring frame. Figure 4.50 shows the CMOD versus global strain (80 mm GL).

4.4 NUMERICAL ANALYSIS OF SENT TESTING

4.4.1 *Material constitutive models*

Figure 4.51 shows the measured stress-strain curve of two round-bar tensile specimens extracted from the same pipe sample. The FE analyses adopted the average stress-strain curve and the average material properties (see Table 4.6).

The stress-strain curves used in FE simulation of SENT tests were shown in Figure 4.52. The 'Flat' curve is based on the average of the measured stress-strain curves with a flat stress plateau equal to R_{eL}. The UDU curves were constructed as described in Section 3.3.1 of Chapter 3 with respect to the 'Flat' curve with various softening modulus, namely $\bar{E}_L = 0.005$ (UDU-1), $\bar{E}_L = 0.015$ (UDU-2) and $\bar{E}_L = 0.025$ (UDU-3).

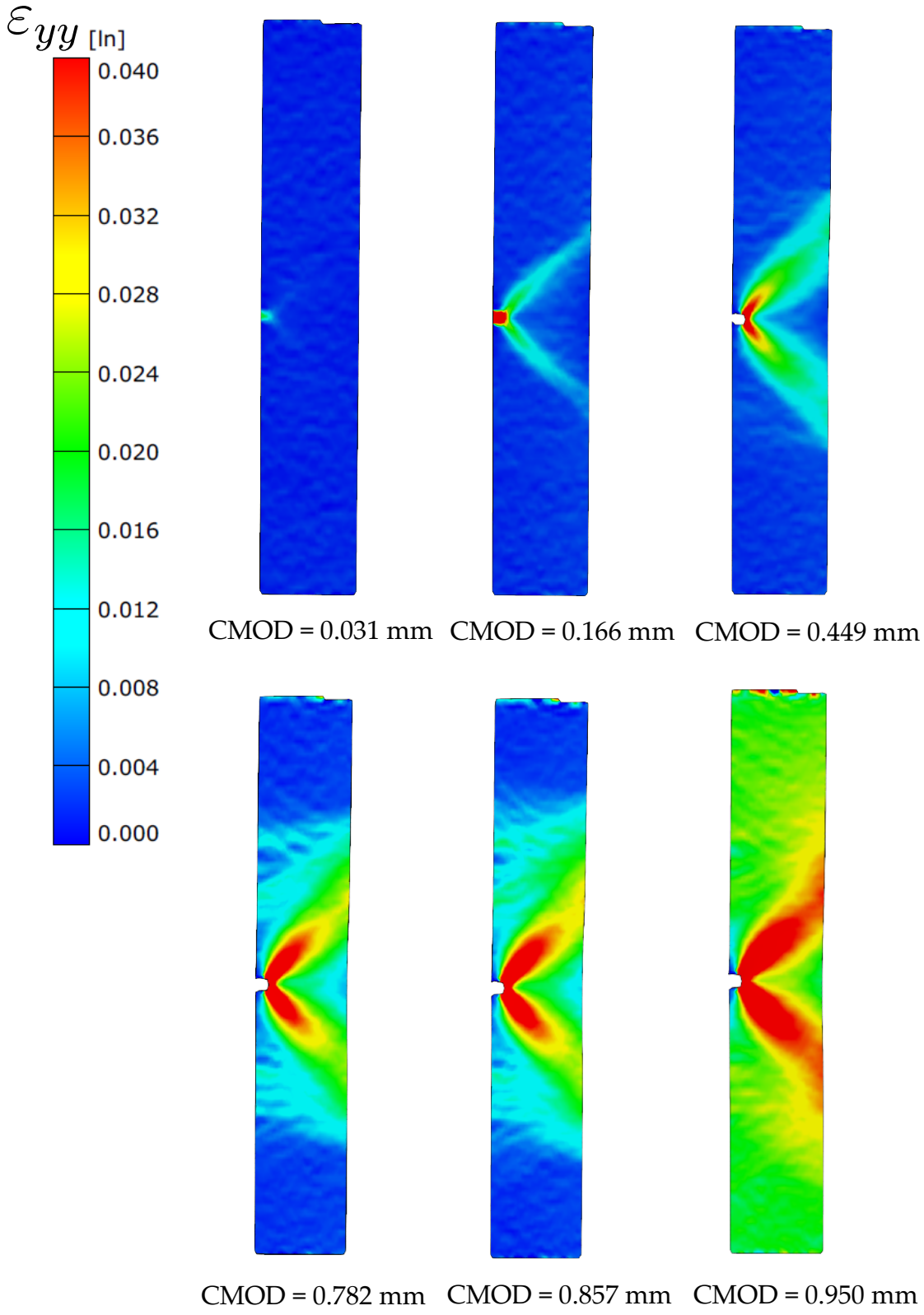

Figure 4.48: Longitudinal strain ε_{yy} maps of SENT test Set-2 (M01-08) captured by DIC

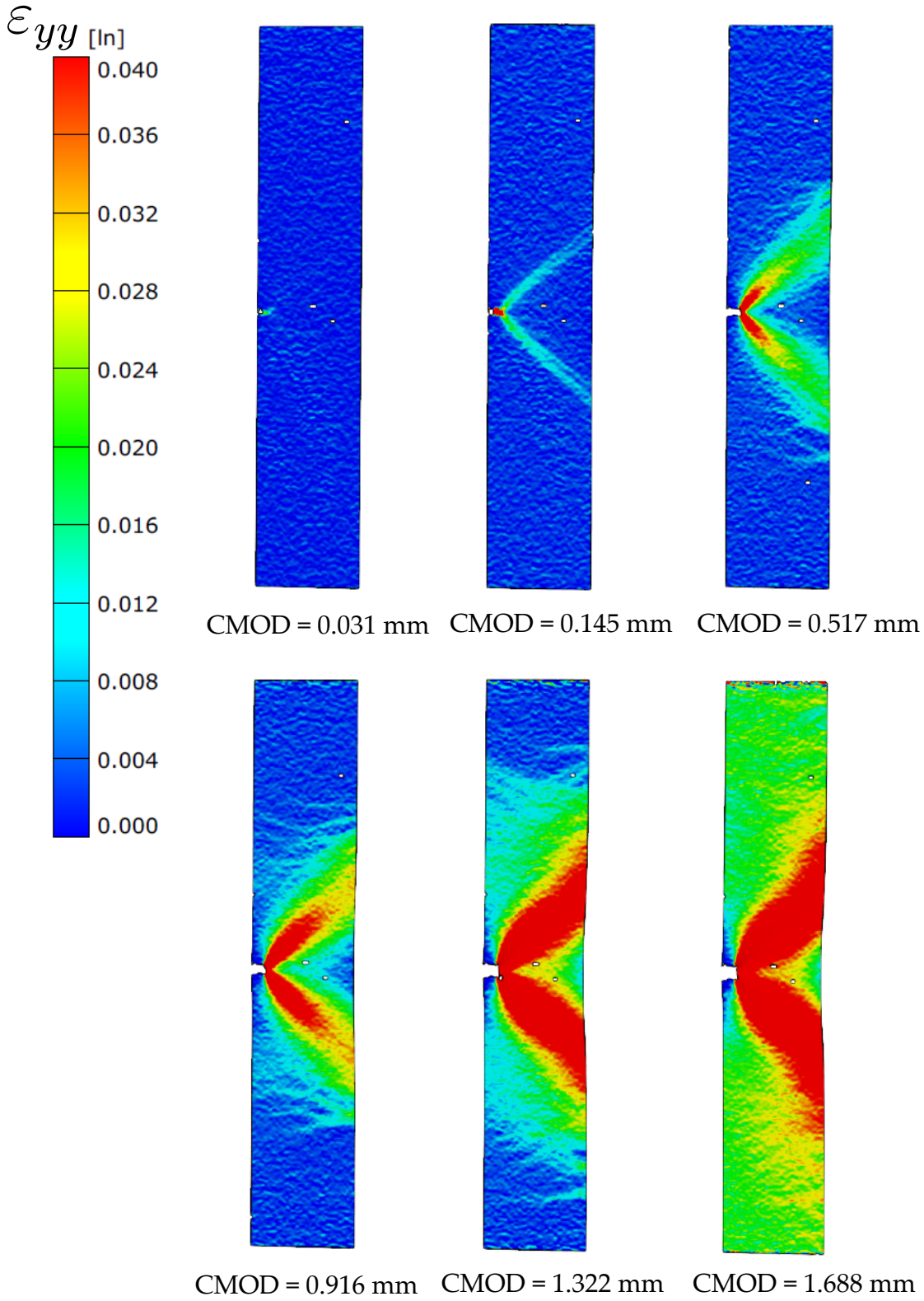

Figure 4.49: Longitudinal strain ε_{yy} maps of SENT test Set-2 (M01-09) captured by DIC

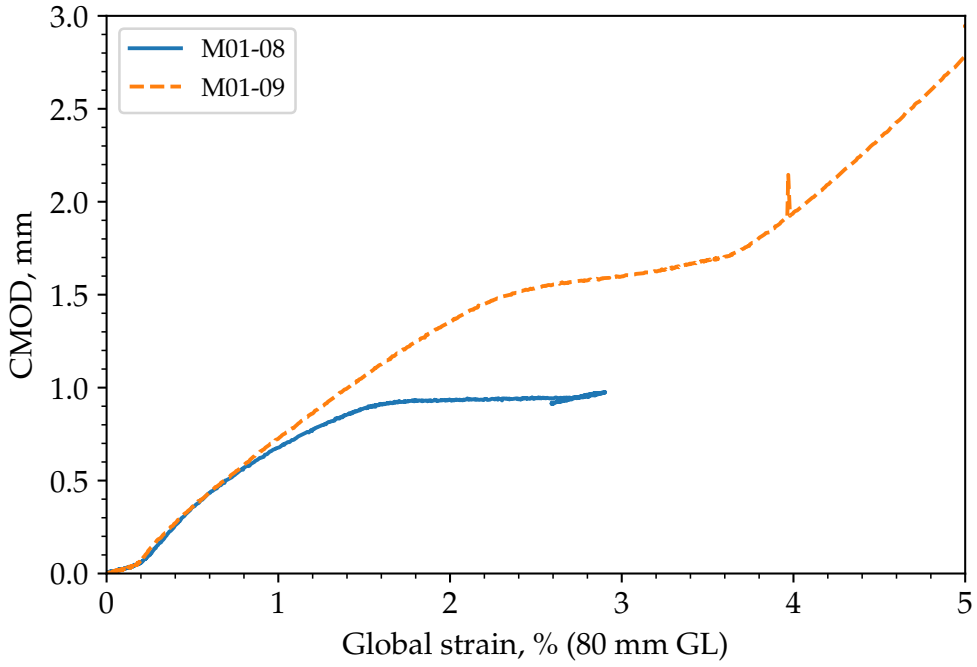

Figure 4.50: CMOD versus global strain (80 mm GL) of SENT test Set-2

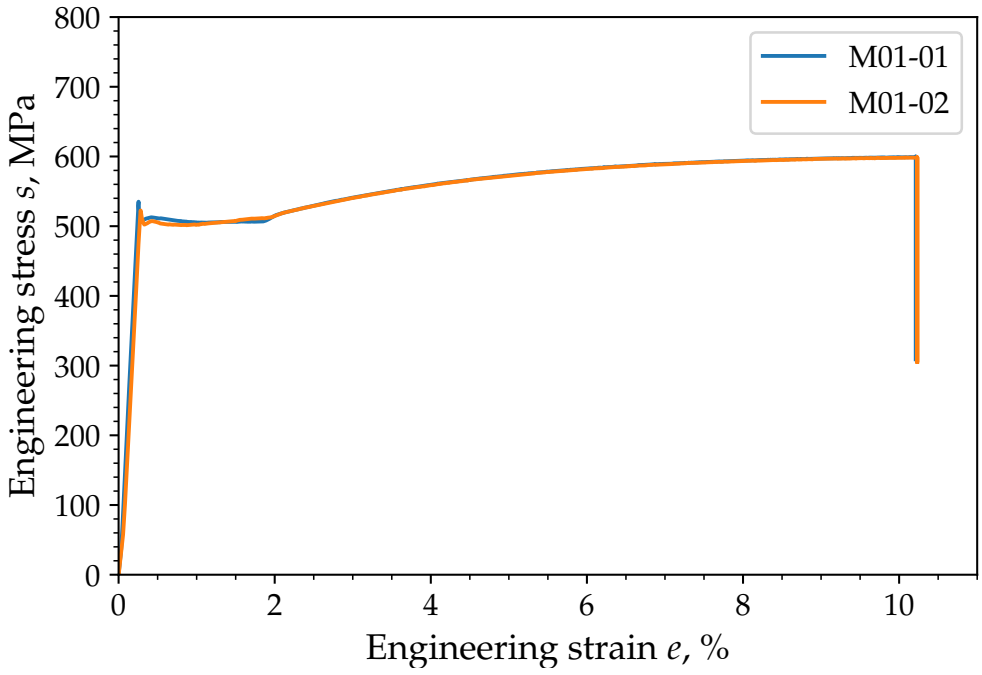

Figure 4.51: Measured stress-strain curves of the uniaxial round-bar tensile specimens

Table 4.6: Summary of average tensile properties measured by the round-bar tensile testing

Average material properties	
Young's modulus E, MPa	222553.5
0.2% proof stress, MPa	509.6
Plateau stress R_{eL}, MPa	507
Lüders strain, %	1.63

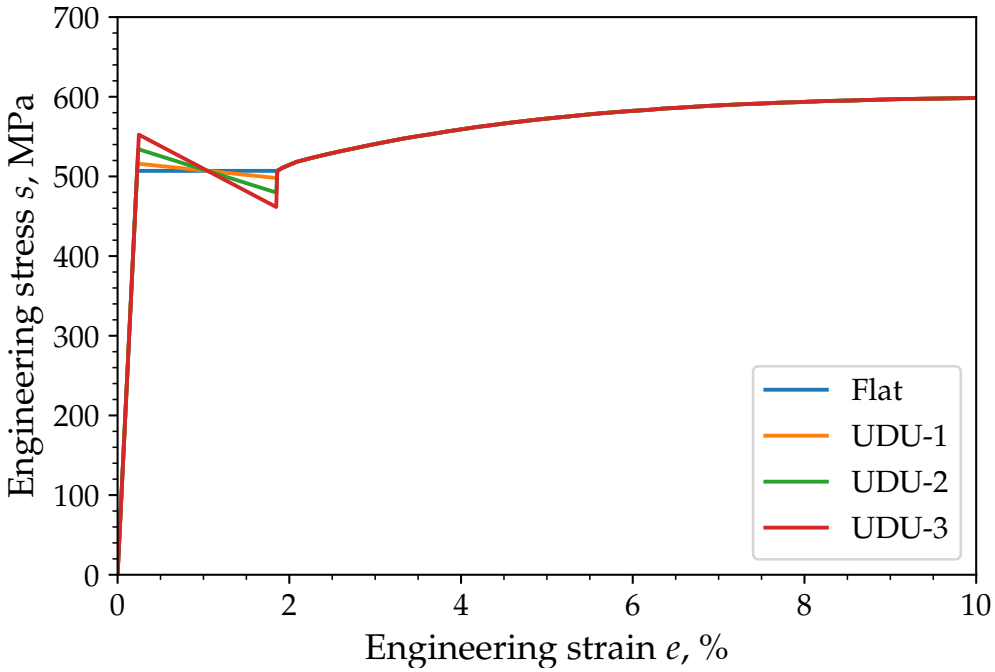

Figure 4.52: Stress-strain curves adopted in FE analyses of SENT specimens

4.4.2 *Finite element models*

FE models were generated for SENT test Set-1 and Set-2, respectively. The geometry of the models was based on M01-02 from Set-1 and M01-9 from Set-2. Figures 4.53 and 4.54 show the mesh configuration of the Set-1 and Set-2 SENT specimens, respectively. A quarter of the whole specimen was modelled due to symmetry boundary conditions. The crack was modelled as a notch with a blunted crack tip that is expected to facilitate the convergence. The initial radius (ρ_0) of the crack tip is 50 μm, which is sufficiently small to capture the crack-tip stress field and plasticity. The models were meshed with three-dimensional, 20-noded brick elements with quadratic interpolation (type C3D20R). The relatively fine mesh was applied in the crack-tip region, with 16 elements along the quarter annulus around the crack tip.

Since for Set-1 SENT model the deformation is expected to localised in the near-tip region and the uncracked ligament, the region distant from the crack tip was coarsely meshed with elements of larger sizes to avoid the excessive computational cost. For Set-2 SENT model, on the other hand, the relatively fine mesh was applied throughout the whole model to capture the propagation of strain localisation. The applied mesh is made isotropic with equal dimensions (1 mm) in each orientation, as shown in Figure 4.54, which helps to avoid biased results. The models were loaded in tension by applying a prescribed displacement to the nodes at the uncracked end. The nodes along the upper and lower edges at the uncracked end were not permitted to translate vertically to simulate the boundary conditions imposed by the grips in the experiment.

4.4.3 *Results and discussion*

4.4.3.1 *SENT test Set-1*

Figure 4.55 compares the load-CMOD response extracted from the FE analysis and those measured from the experiment. The numerically-calculated load-CMOD response generally agrees with those measured experimentally. A slight deviation can be observed around the elastic-plastic transition or the 'knee' region on the load-CMOD curve. This deviation may be due to variation in the material properties around the pipe circumference, which results in the

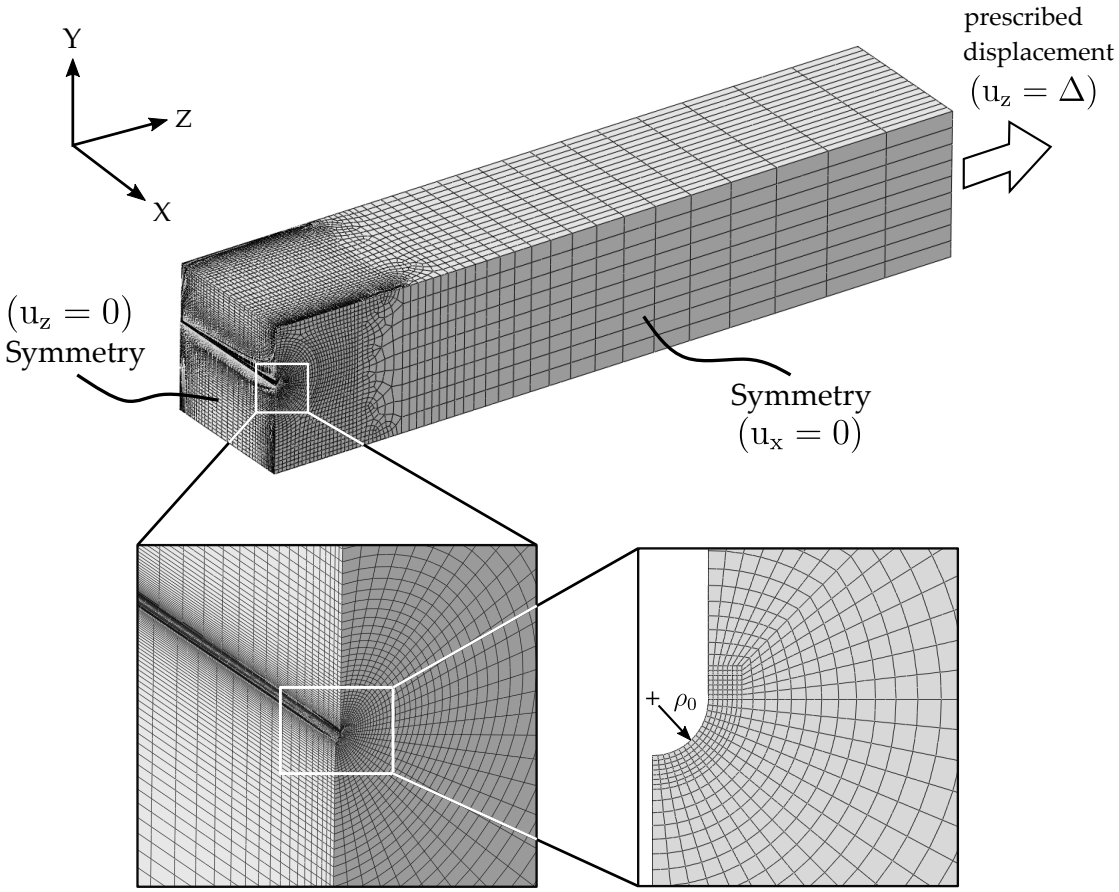

Figure 4.53: Mesh configuration and boundary conditions of FE model of SENT test (Set-1)

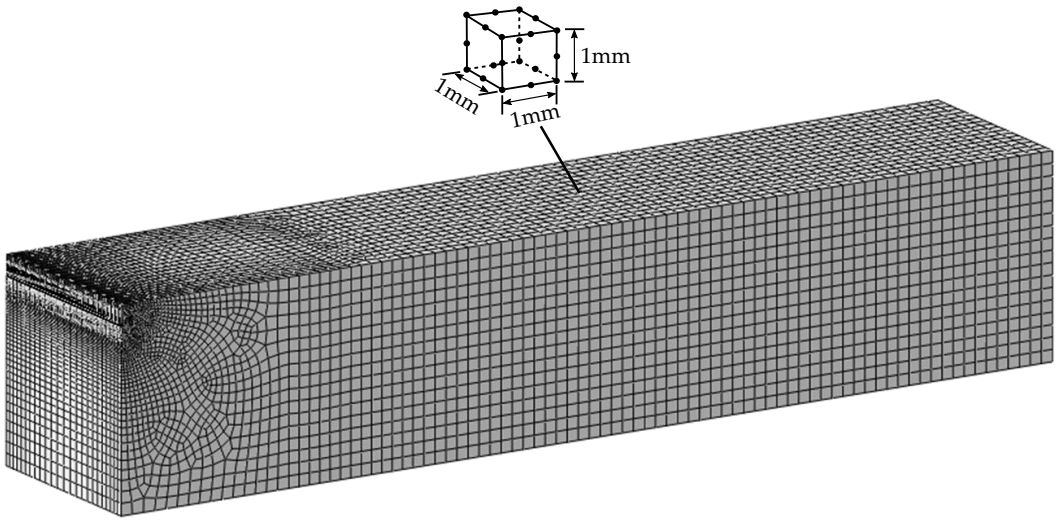

Figure 4.54: Mesh configuration and boundary conditions of FE model of SENT test (Set-2) with additional mesh refinement

difference between the material properties of the tensile specimens and those of the SENT specimens. Good agreement is noticed in the inelastic regime in the CMOD ranges of 0.5 mm to 2 mm. Beyond 2 mm CMOD, the FEAs start to deviate from the experiment, which is attributed to the adopted simulation technique that neglects the crack extension by tearing. As for the experiment, the crack extension reduces the stiffness of structure, and overpower the increase in stiffness due to strain hardening when the crack extension is significant, resulting in a decline of the loading bearing capacity and thus the applied load.

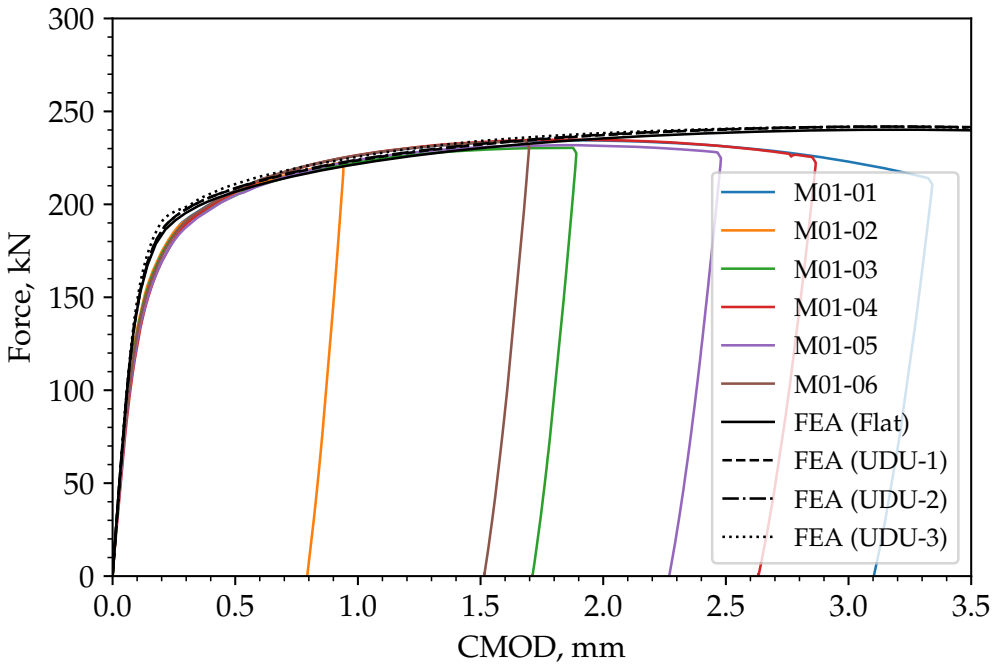

Figure 4.55: Comparison between the Load-CMOD responses calculated from FEA and those from the SENT tests

Looking closely at the elastic-plastic transition or 'knee' region on the load-CMOD curves, a slight 'bump' can be noticed. This is due to the result of Lüders behaviour. As for the FEA results, the load-CMOD curve calculated using the Flat stress-strain model does not show a 'bump', but a fairly smooth elastic-plastic 'round-house' transition. For FEA using UDU stress-strain models, a slight 'bump' can be observed and appears to be more pronounced for higher $\bar{E}_L$ (such as UDU-3).

Figures 4.56 to 4.61 show the longitudinal strain (ε_{yy}) in the crack-tip region of the SENT model at various CMOD levels, respectively. As stated earlier,

only the strain distribution in the crack region is of interest as the in the experiment the strain localisation was found to continuously develop in near the crack tip and the uncracked ligament, leading to excessive plastic straining of the uncracked ligament and ductile crack extension, rather than spreading to region far from the crack tip. Besides, the FE analyses did not explicitly simulate the crack extension by ductile tearing, the comparison between the FEA and experiment should ideally be made in the regime where no or limited ductile tearing occurred. Therefore, the strain distributions from FEA were compared with the experiment for CMOD range of 0.05 mm to 0.61 mm in which limited ductile tearing had occurred.

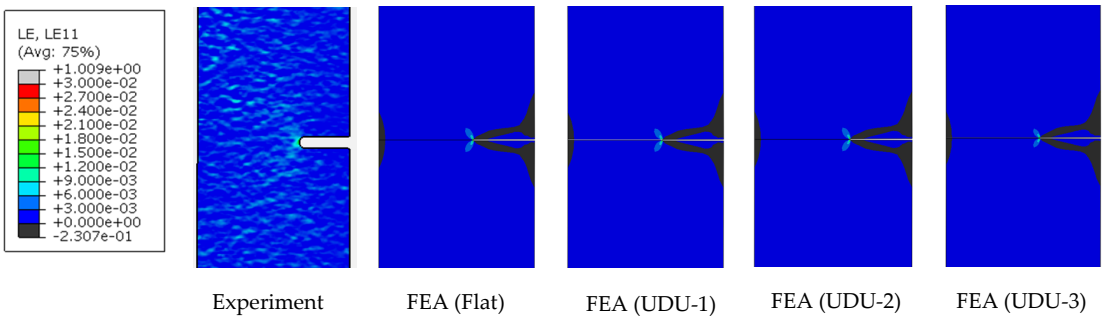

Figure 4.56: Comparison between the longitudinal strain map calculated from FEA and that from the SENT test at CMOD = 0.05

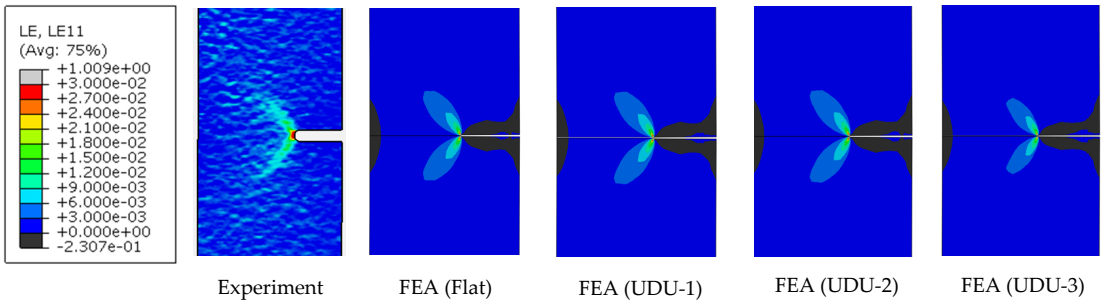

Figure 4.57: Comparison between the longitudinal strain map calculated from FEA and that from the SENT test at CMOD = 0.11 mm

From Figures 4.56 to 4.61, the ε_{yy} maps calculated by FEA using both 'Flat' and UDU stress-strain models all generally match those observed in the experiment at various CMOD levels examined. The size of the strain localisations and the magnitude of the strain distributions calculated from FEA generally agree those of the experiment. Despite the similarity in the ε_{yy} distributions among the FE models using different stress-strain curves, it can be noticed that the strain localisation tends to be more localised and contained in the model using a

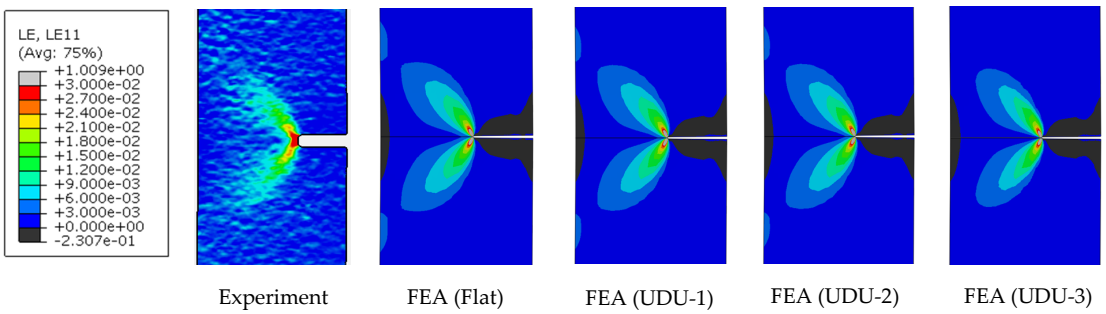

Figure 4.58: Comparison between the longitudinal strain map calculated from FEA and that from the SENT test at CMOD = 0.21 mm

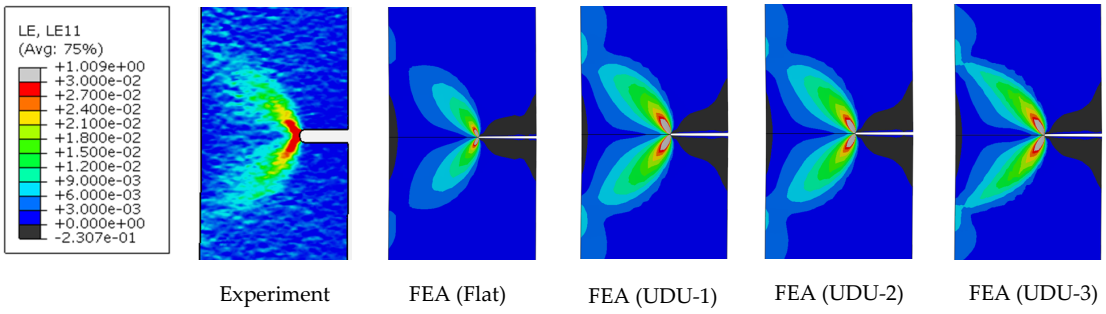

Figure 4.59: Comparison between the longitudinal strain map calculated from FEA and that from the SENT test at CMOD = 0.29 mm

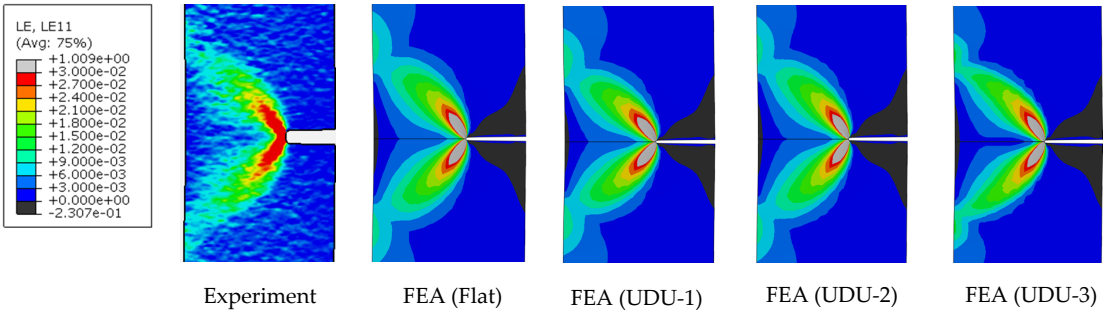

Figure 4.60: Comparison between the longitudinal strain map calculated from FEA and that from the SENT test at CMOD = 0.41 mm

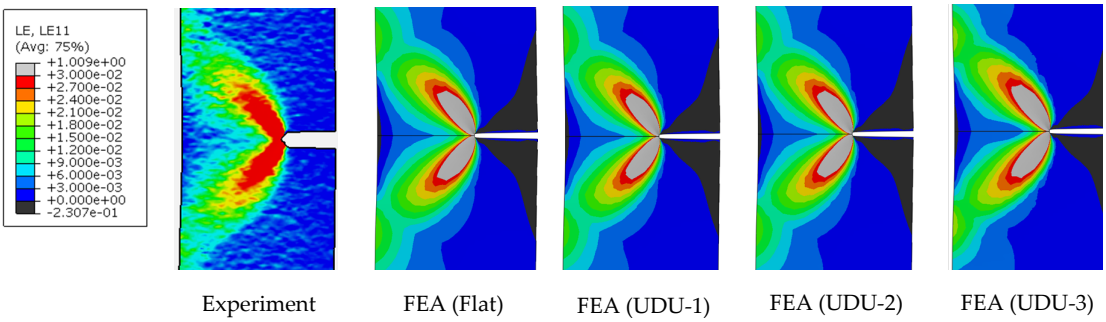

Figure 4.61: Comparison between the longitudinal strain map calculated from FEA and that from the SENT test at CMOD = 0.61 mm

stress-strain curve with a higher softening modulus or $\bar{E}_L$. Similar observations can be made from the ε^p_{eq} maps shown from Figures D.1 to D.6, which are included in Appendix D. It should be noted that the strain values calculated from the FEA shown in Figures D.1 to D.6 may be lower than those of the experiment as the strain maps extracted from the DIC are von Mises equivalent plastic strains including both elastic and plastic components.

4.4.3.2 *SENT test Set-2*

Figure 4.62 compares the load-CMOD response extracted from the FE analysis and those measured from the experiment. All load-CMOD responses calculated from FEA were shown to lay above those of the tests (both M01-08 and -09). This is may be due to the variations in tensile properties as the tensile specimens were extracted from different locations around the circumference than the SENT specimens. The SENT specimens themselves also see a deviation in the load-CMOD response because of the variation in material properties.

The numerically-calculated load-responses exhibit a plateau phase following the elastic regime and a transition region. Similar to what is observed in the load-CMOD responses of FEA of SENT Set-1 tests, the load-CMOD responses using UDU stress-strain laws are found to show a 'bump' at the elastic-plastic transition and the 'bump' is shown more prominent for model using higher softening modulus (such as UDU-2 and UDU-3). The model using 'Flat' stress-strain law, on the contrary, is found to generate a smooth elastic-plastic transition and a subsequent plateau.

As the plateau phase is about to terminate, slight unloading can be observed on the load-CMOD responses calculated using UDU stress-strain laws, which is aligned with the load-CMOD responses of the tests. This may be a result of the event that the Lüders band reaches the uncracked end of the specimen. Comparisons of longitudinal strain (ε_{yy}) maps calculated using FEA and those measured from the experiment (DIC) are shown from Figure 4.63 to 4.68.

From Figure 4.63, it is seen that all FEA models are globally elastic, and so as the test. Localised strain regime is found to initiate from the crack tip, as shown in Figure 4.64, with the strain band more localised for the stress-strain model using a higher softening modulus. As the crack loading (in terms of CMOD) increases, the localised strain regime continue to expand towards the clamped

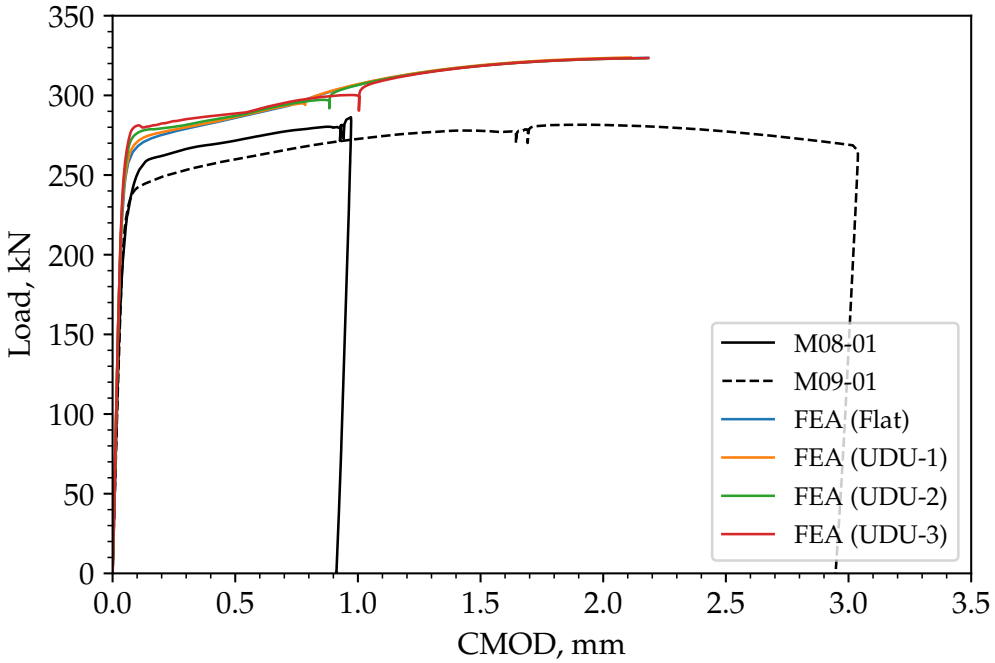

Figure 4.62: Comparison between the load-CMOD responses calculated from FEA and those from the SENT tests Set-2

ends, as can be seen in Figures 4.65 to 4.67. During the process, the model using 'Flat' stress-strain material law is found to show a generally uniform deformation except the region near the crack tip.

The models using UDU material laws were shown to exhibit Lüders banding, similar to that observed in the experiment. The patterns of the propagating band resemble that observed in the DIC with the exception that the bands observed in DIC exhibit a 'multi-pronged' pattern. This pattern observed in DIC may be due to the unevenness of the specimen, resulting in complex strain localisations. From Figures 4.66 to 4.68, the Lüders band front predicted using UDU with higher softening modulus is shown to propagate not as fast as those using a lower softening modulus. In particular, the localisation band simulated using UDU-3 material law only propagates to about one-third of the specimen length while those simulated using other material laws have spread through all the specimen length. This is aligned with the observation in Figure 4.62 that UDU with a higher softening modulus generates a longer load-CMOD plateau phase. Similar observations are found for the ε^{p}_{eq} maps, which are included in Appendix D (see Figures D.7 to 4.68). It should be noted that the

strain distributions therein from the DIC are the von Mises equivalent strain, comprising of both elastic and plastic strain components.

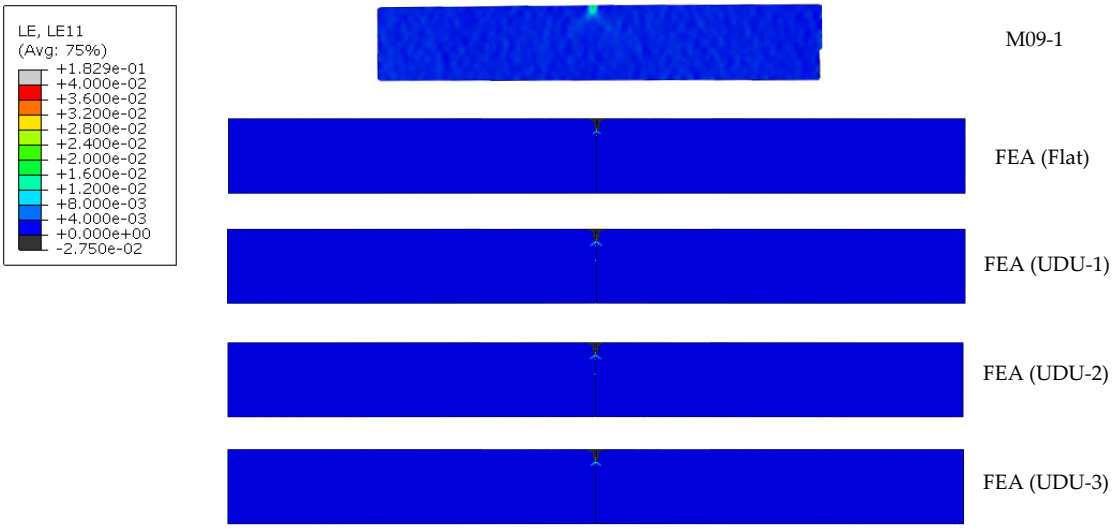

Figure 4.63: Comparison between the equivalent plastic strain map calculated from FEA and that from the SENT test (equivalent von Mises strain) at CMOD = 0.031 mm

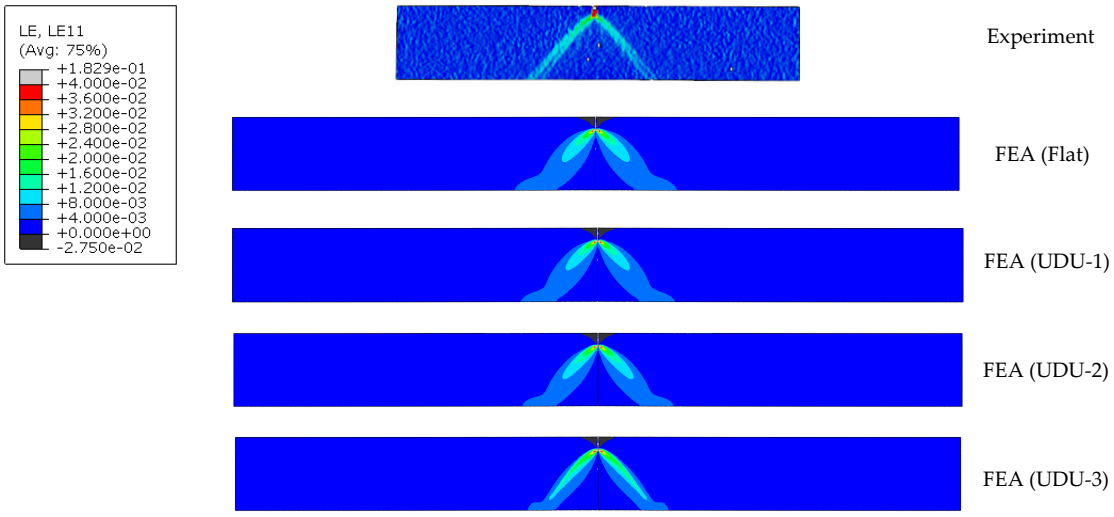

Figure 4.64: Comparison between the equivalent plastic strain map calculated from FEA and that from the SENT test (equivalent von Mises strain) at CMOD = 0.166 mm

Figure 4.69 shows the comparison of the CMOD versus global strain extracted from 80 mm GL for the experiments and FEA. It can be observed that the the higher CMOD values are obtained using a UDU stress-strain curve with a higher $\bar{E}_L$.

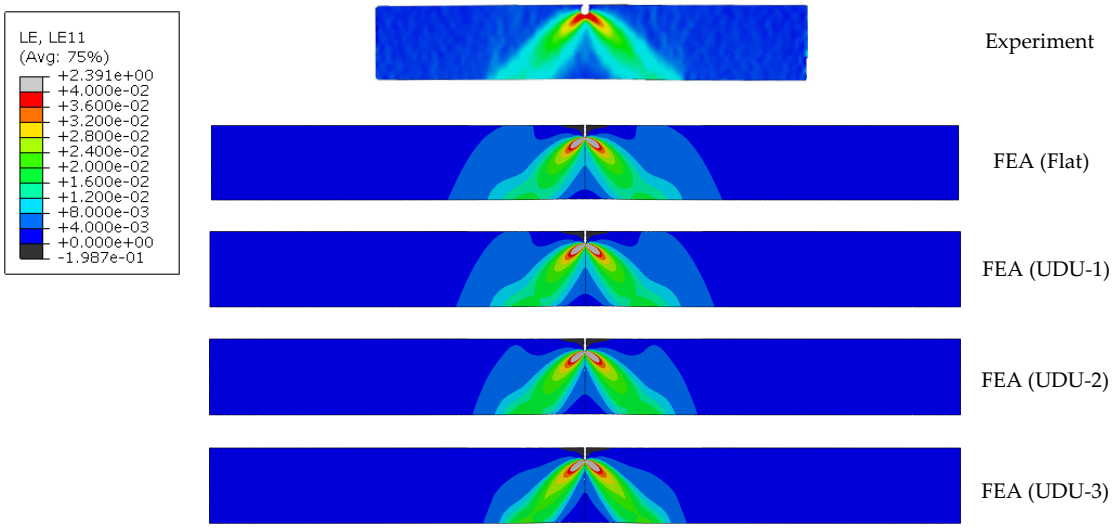

Figure 4.65: Comparison between the equivalent plastic strain map calculated from FEA and that from the SENT test (equivalent von Mises strain) at CMOD = 0.449 mm

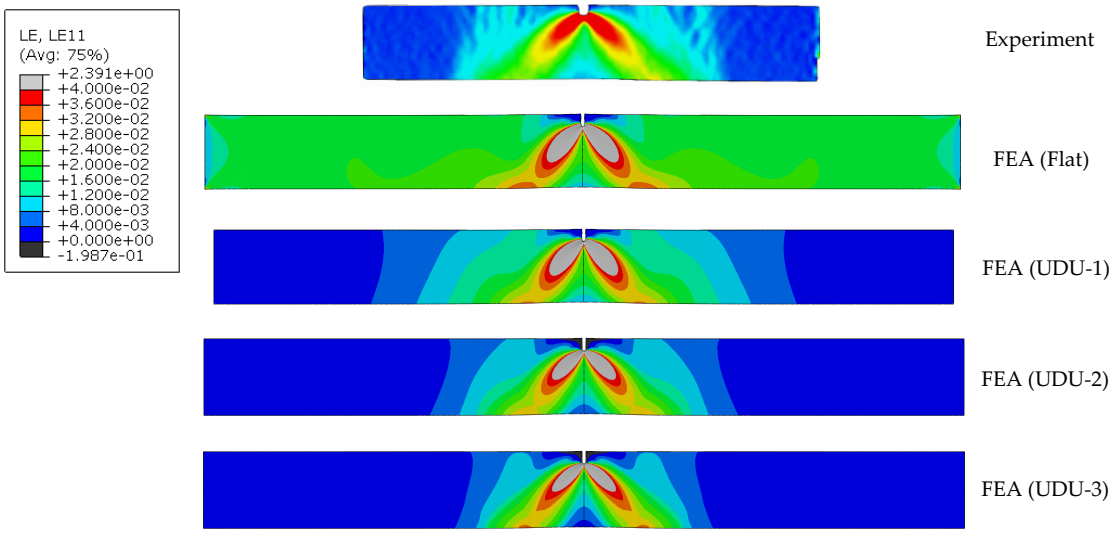

Figure 4.66: Comparison between the equivalent plastic strain map calculated from FEA and that from the SENT test (equivalent von Mises strain) at CMOD = 0.782 mm

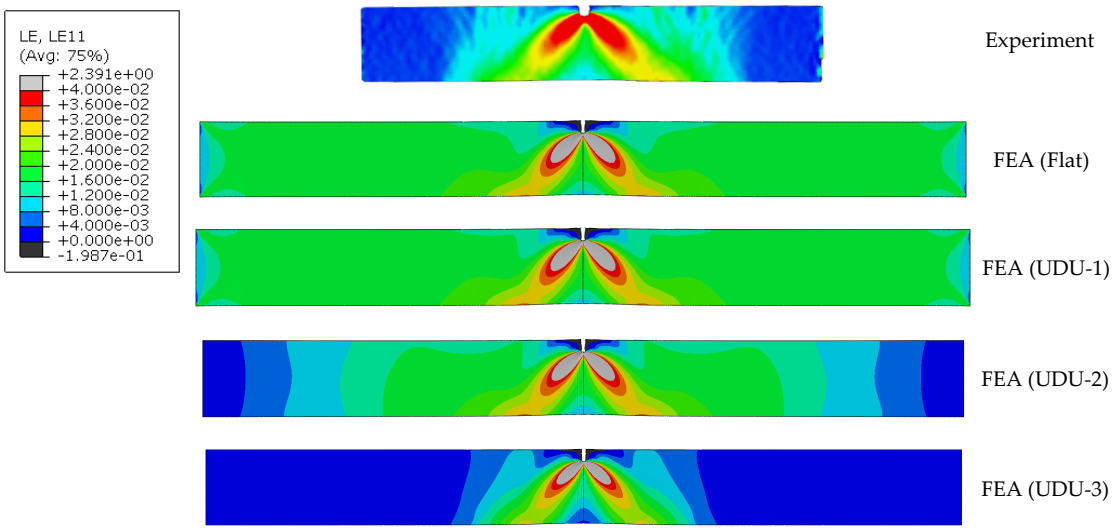

Figure 4.67: Comparison between the equivalent plastic strain map calculated from FEA and that from the SENT test (equivalent von Mises strain) at CMOD = 0.923 mm

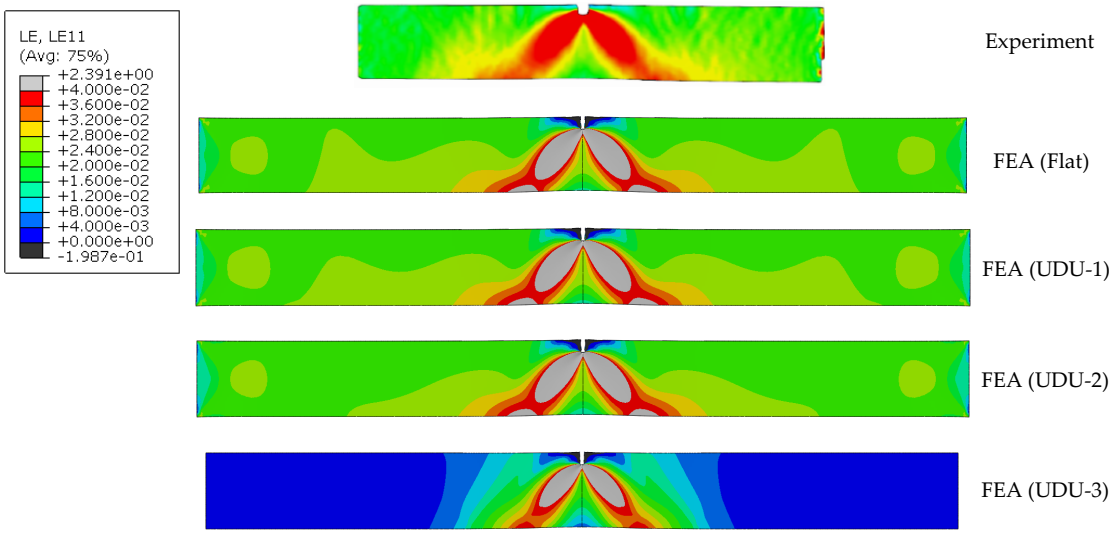

Figure 4.68: Comparison between the equivalent plastic strain map calculated from FEA and that from the SENT test (equivalent von Mises strain) at CMOD = 0.950 mm

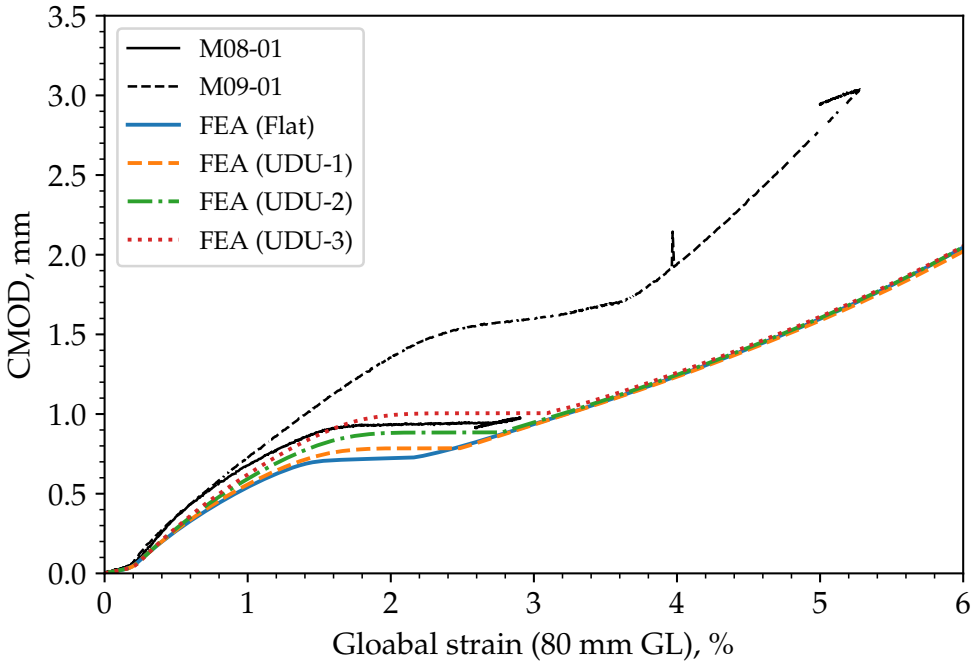

Figure 4.69: Comparison between the CMOD versus global strain (80 mm GL) responses calculated from FEA and those from the SENT tests Set-2

4.5 PARAMETRIC STUDY

From the results on SENT test Set-1 and -2 presented earlier in this chapter, it is indicated that the crack depth may have a significant effect on the development of strain localisation associated with Lüders banding. To obtain a better understanding in this regard, a parametric numerical analysis was performed to investigate how the crack depth affects the formation and propagation of Lüders bands in the SENT specimen. The stress-strain curve used in this parametric study was the UDU-2 (UDU material law with a normalised softening modulus $\bar{E}_L = 0.015$ as the use of it , in comparison with other material laws examined, best captures the strain localisations associated with Lüders banding observed in the experiment.

4.5.1 *Finite element models*

SENT specimens with various notch depths were modelled, with the dimensions shown in Table 4.7, covering notch depths ranging from $a/W = 0.1$ to $a/W = 0.5$. Similar mesh configuration and boundary conditions to those of FEA of

SENT experiment reported in Section 4.4.2 were applied in this parametric study.

Table 4.7: Dimensions of the FE models in the parametric study of SENT specimens

Model No.	Thickness B, mm	Width W, mm	a/W	Notch depth a, mm
1	34	17	0.1	1.7
2			0.2	3.4
3			0.3	5.1
4			0.4	6.8
5			0.5	8.5

4.5.2 *Results and discussion*

4.5.2.1 *Load-CMOD response*

Figure 4.70 compares the Load-CMOD response calculated from SENT models with various a/W values. Clearly, the SENT with larger a/W is found to have a higher level of load-CMOD responses. This is the result of the reduction of the cross-section area of the uncracked ligament, leading to a decrease in the structural stiffness of the SENT model. For SENT model with $a/W = 0.1$, the load-CMOD response is seen to have a prominent load peak, preceding a slight drop and then followed by a rise (strain hardening). The load peak is due to the Lüders effect, which was incorporated by use of the UDU material model, and is found to diminish as the a/W increases.

The occurrence of load plateau can be observed on the load-CMOD curves for $a/W = 0.1$ and $a/W = 0.2$. The load plateau is found relatively short for $a/W = 0.1$ than that for $a/W = 0.2$ as the SENT with $a/W = 0.1$ has a much less CMOD. A slight load bump is noticed for load-CMOD curve with $a/W = 0.2$, followed by a much longer and steadily rising load plateau. The occurrence of the load peak and the subsequent plateau becomes less prominent as the a/W increases, such as those for $a/W = 0.3$ and 0.4 where a slight load bump can be observed. For $a/W = 0.5$, the presence of load peak almost vanishes, rendering a smooth, power-law shaped load-CMOD curve.

A clear comparison of the global behaviour associated with Lüders effect is made in Figure 4.71 showing the CMOD versus global strain responses for

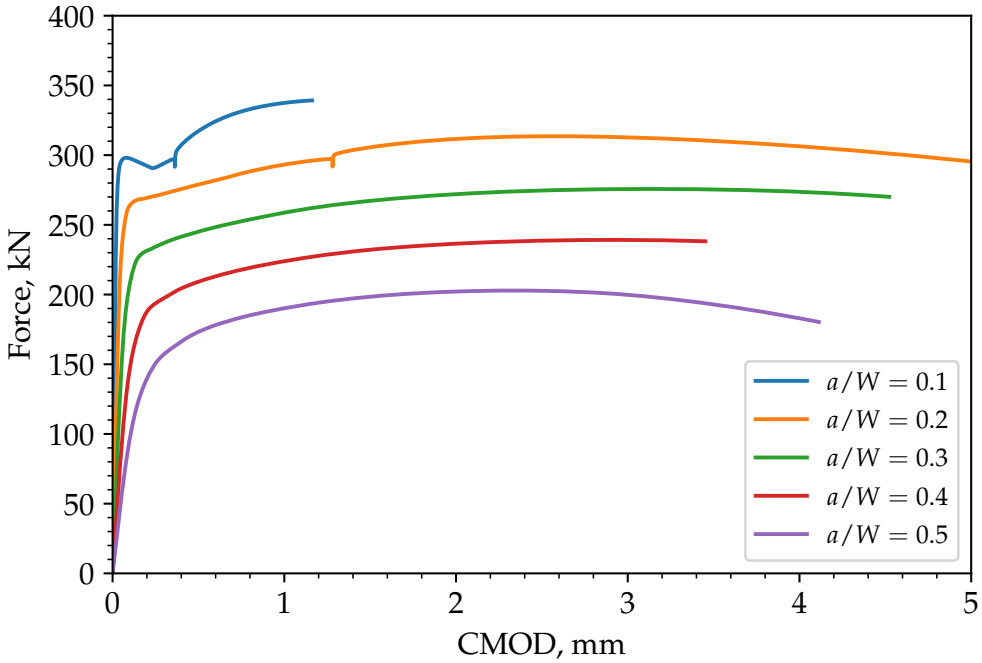

Figure 4.70: Load-CMOD responses of the SENT FEA models with various notch depths (a/W)

SENT models with various a/W values. From Figure 4.71, it is clearly shown that only CMOD versus global strain responses for $a/W = 0.1$ and $a/W = 0.2$ exhibit a CMOD plateau whereas those for $a/W = 0.3, 0.4$ and 0.5 appear linearly proportional to the global strain. This may suggest that the macroscopic phenomenon of Lüders banding, such as band propagation, may not occur in SENT models with $a/W = 0.3, 0.4$ and 0.5, but instead the plasticity may continuously develop in the notch region, leading to the occurrence of plastic collapse. Further details of the deformation of each FE SENT model were given in Section 4.5.2.2.

4.5.2.2 *Development of Lüders bands*

Figures 4.72 and 4.73, 4.74 and 4.75, 4.77 and 4.77, 4.78 and 4.79, and 4.80 and 4.81 show the progression of plasticity, in terms of equivalent plastic strain (PEEQ or ε^{p}_{eq}), in the mid-surface (symmetric plane) and the outer surface of the SENT model with $a/W = 0.1, 0.2, 0.3, 0.4$ and 0.5, respectively.

From the ε^{p}_{eq} distributions shown in these figures, it can be seen that as implied by the CMOD responses presented in Section 4.5.2.1, only SENT with $a/W = 0.1$ and 0.2 display the initiations and propagation of Lüders bands, as

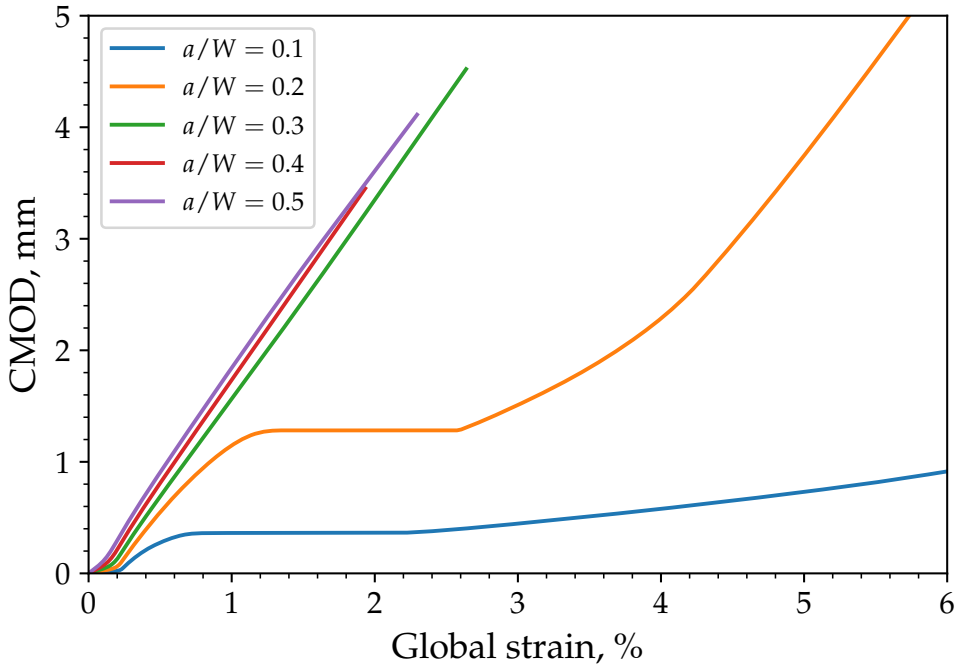

Figure 4.71: CMOD versus global strain responses of the SENT FEA models with various notch depths (a/W)

shown in Figures 4.72 to 4.75. Both models show a typical strain localisation that resembles that of the FEA of SENT test Set-2 in Section 4.4.3.2. The strain localisation is seen to initiate from the notch tip and then spread towards the uncracked ends of the model.

Models with $a/W = 0.3, 0.4$ and 0.5, as shown in Figures 4.76 to 4.81, are found to show strain localisations that only develop in the near-notch region and ligament until the models fail by plastic collapse. This phenomenon is similar to the observation in the SENT test Set-1 in which the actual notch depth (a/W) is about 0.4. The cause for this phenomenon may be that the notch is sufficiently deep such that the uncracked ligament is incapable of sustaining load equivalent to a global strain at which the Lüders band starts to propagate.

For all SENT models analysed, it is interesting to find that the plastic strain is found more localised at the notch tip when the Lüders band initiates in the mid surface (plane strain) than that in the outer surface (plane stress), which is aligned with the observation in Belotteau et al. (2009).

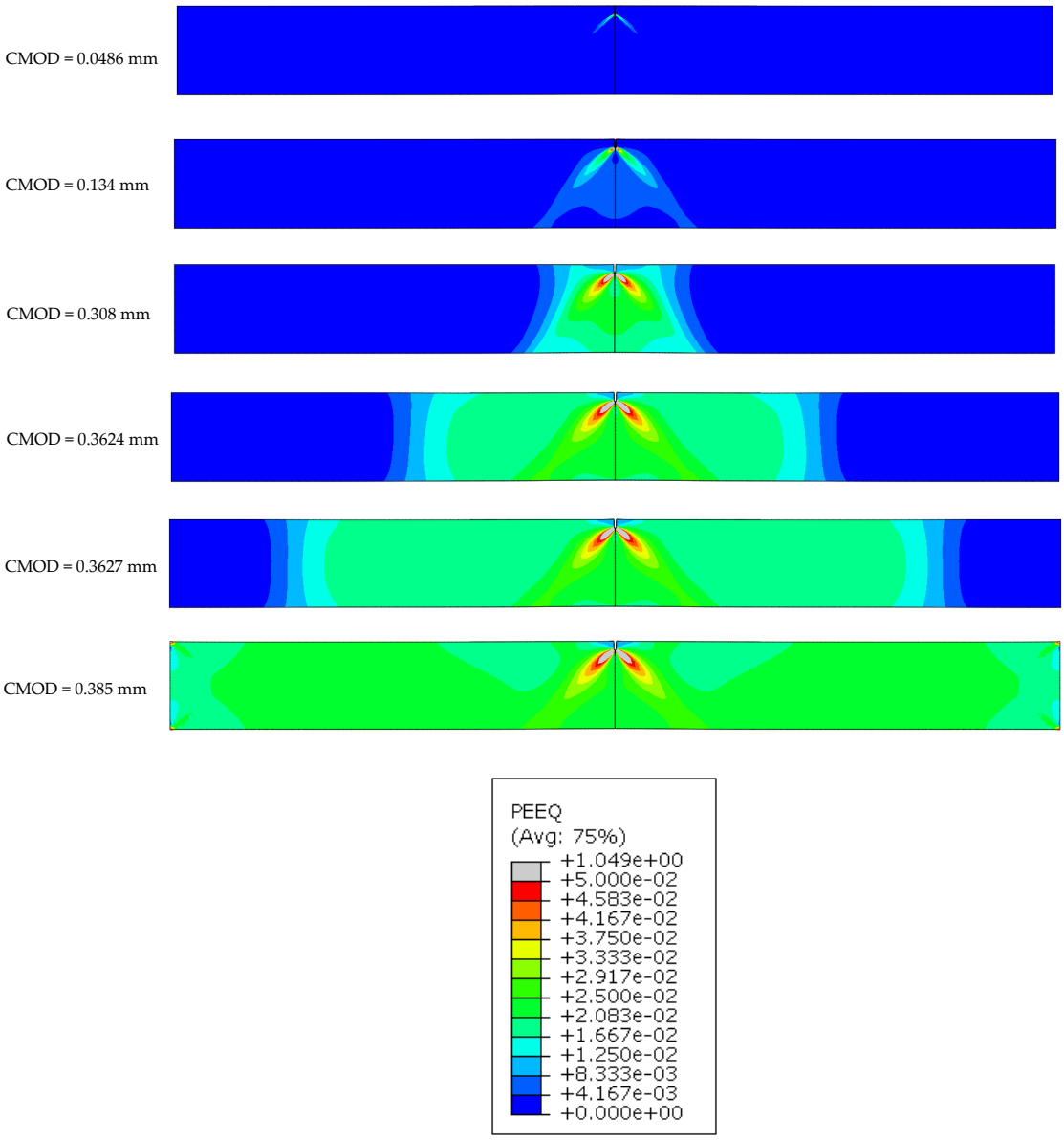

Figure 4.72: Equivalent plastic strain (ε^{p}_{eq}) distributions in the symmetric plane (plain strain) of SENT FE model with $a/W = 0.1$

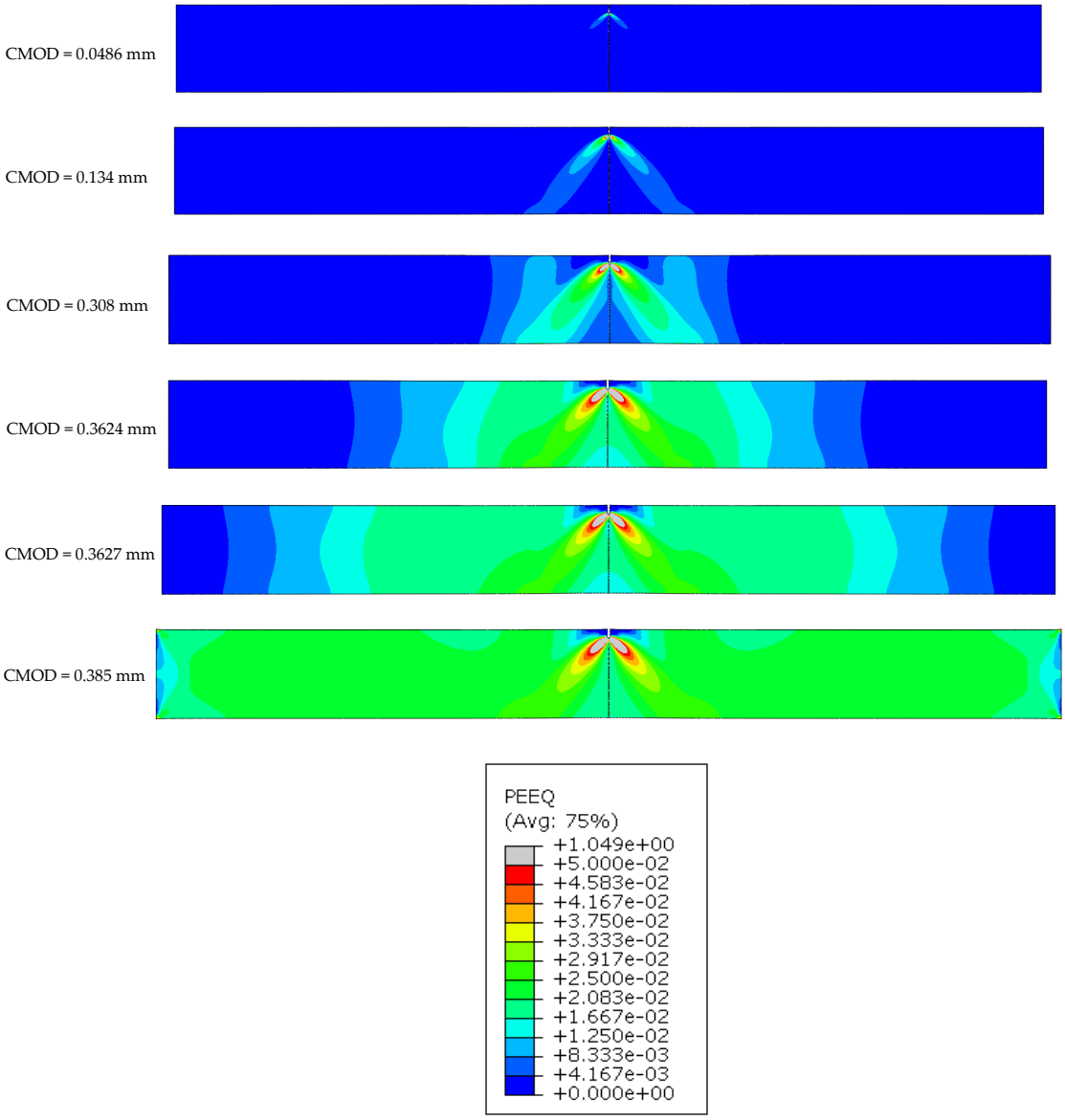

Figure 4.73: Equivalent plastic strain (ε^{p}_{eq}) distributions in the surface (plain stress) of SENT FE model with $a/W = 0.1$

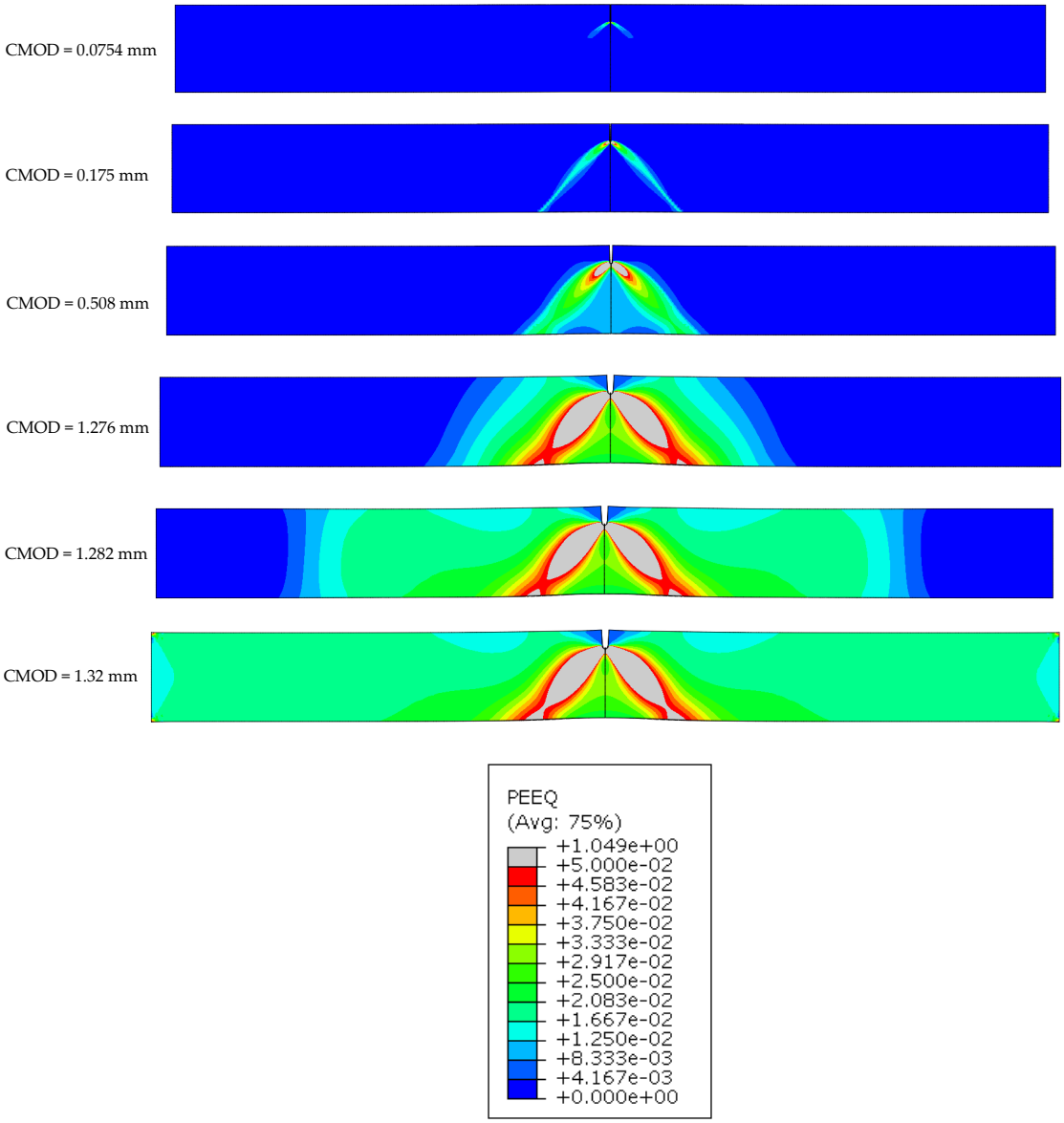

Figure 4.74: Equivalent plastic strain (ε^{p}_{eq}) distributions in the symmetric plane (plain strain) of SENT FE model with $a/W = 0.2$

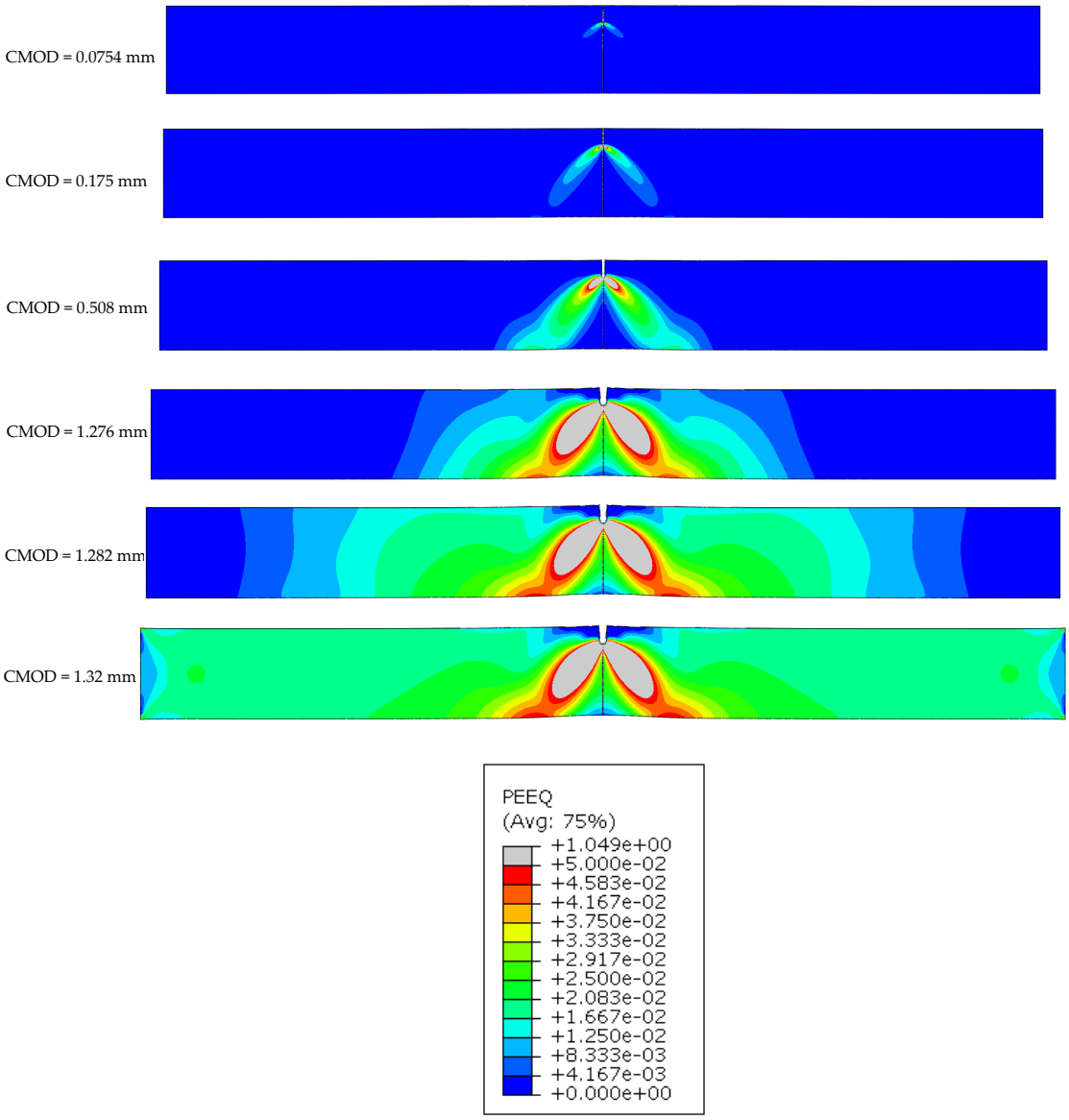

Figure 4.75: Equivalent plastic strain (ε^{p}_{eq}) distributions in the surface (plain stress) of SENT FE model with $a/W = 0.2$

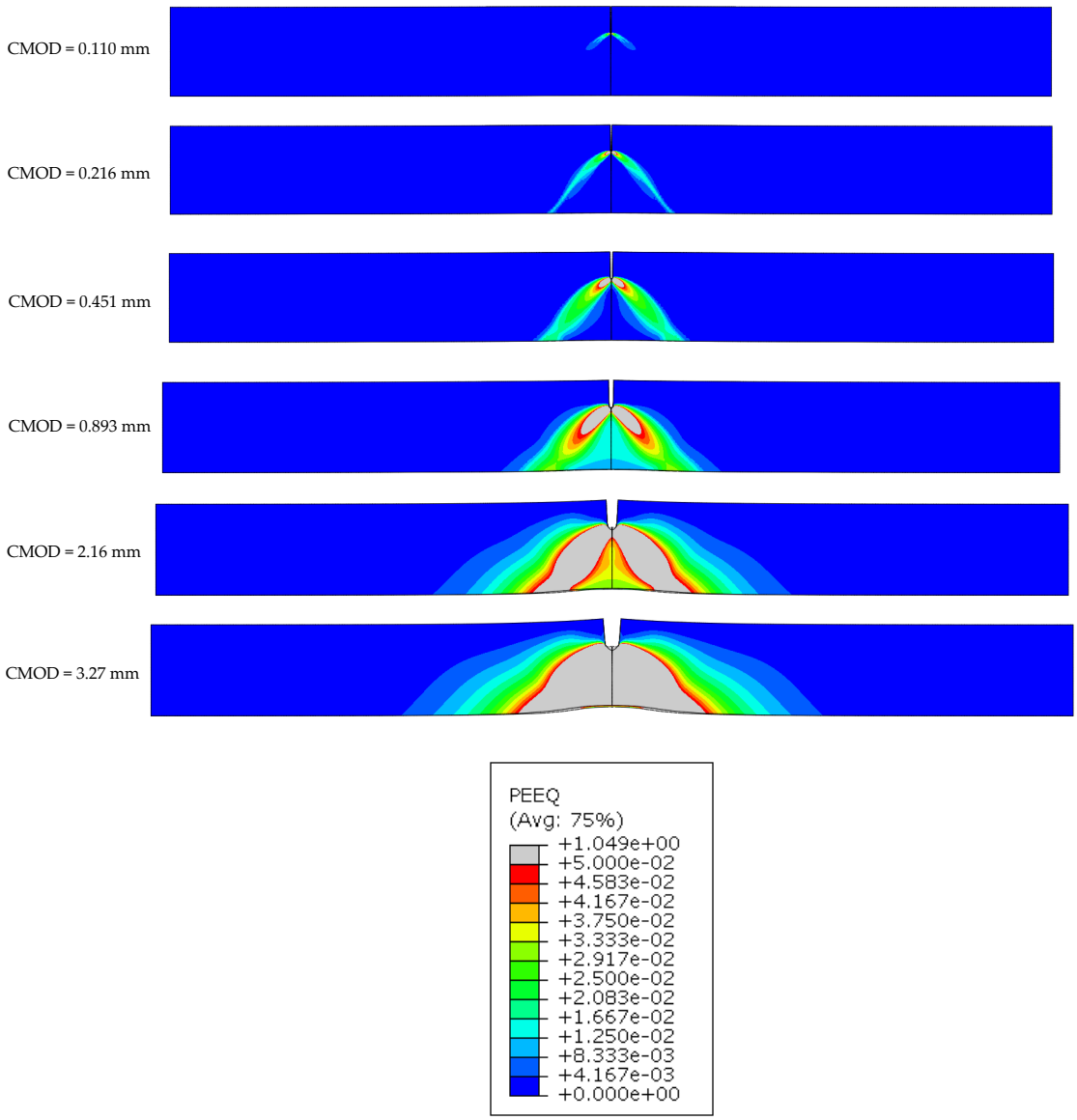

Figure 4.76: Equivalent plastic strain (ε^{p}_{eq}) distributions in the symmetric plane (plain strain) of SENT FE model with $a/W = 0.3$

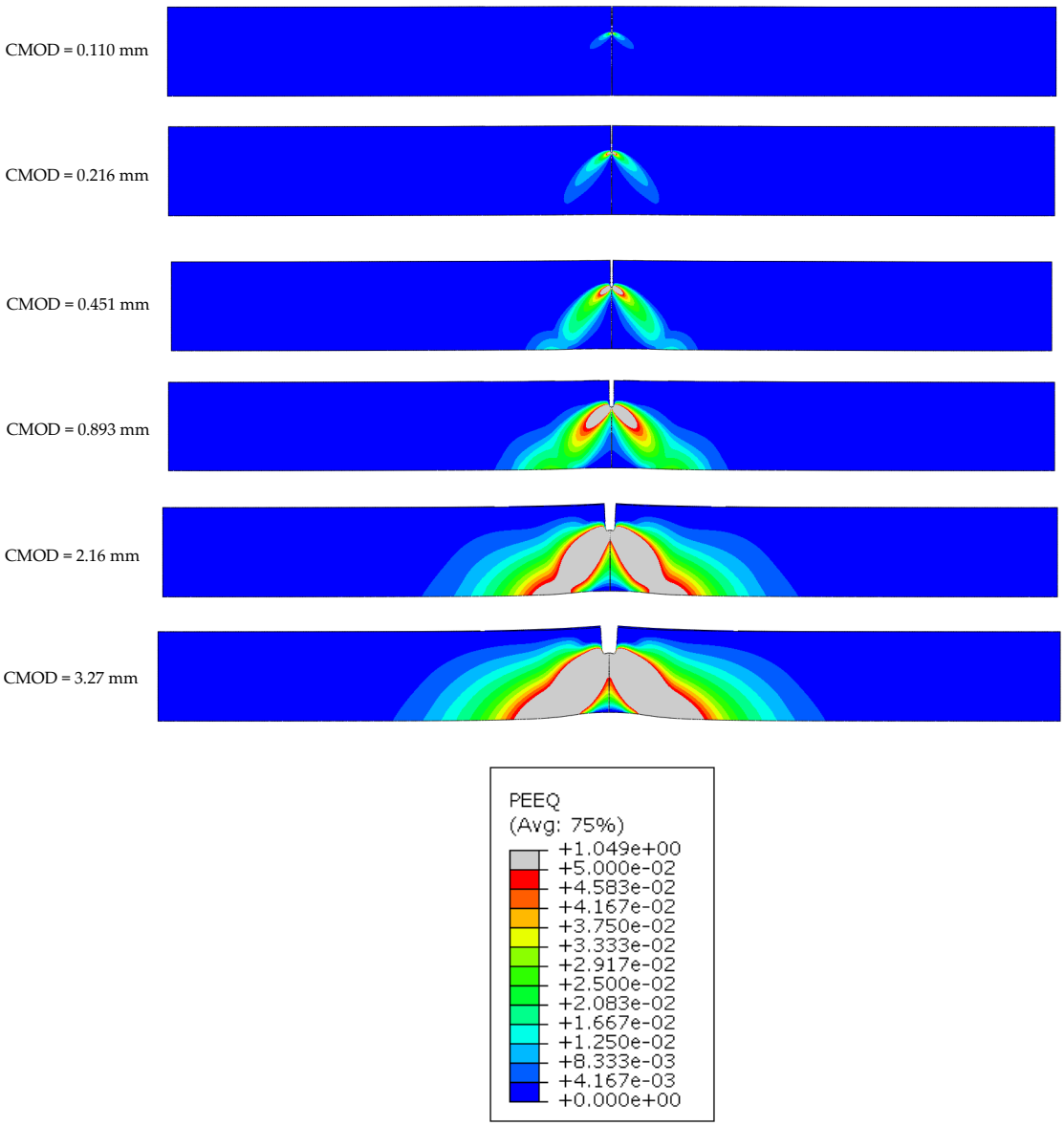

Figure 4.77: Equivalent plastic strain (ε^{p}_{eq}) distributions in the surface (plain stress) of SENT FE model with $a/W = 0.3$

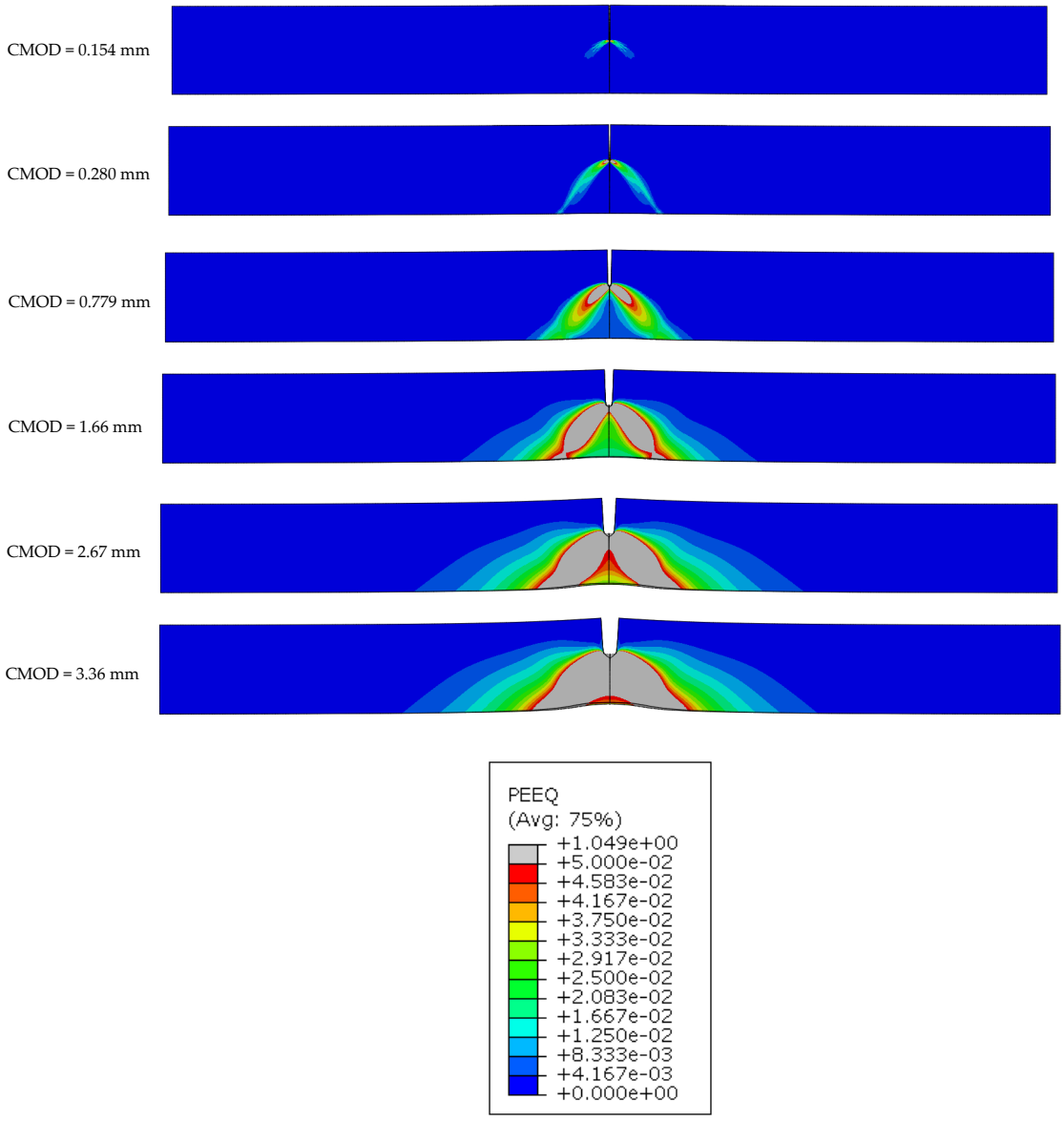

Figure 4.78: Equivalent plastic strain (ε^{p}_{eq}) distributions in the symmetric plane (plain strain) of SENT FE model with $a/W = 0.4$

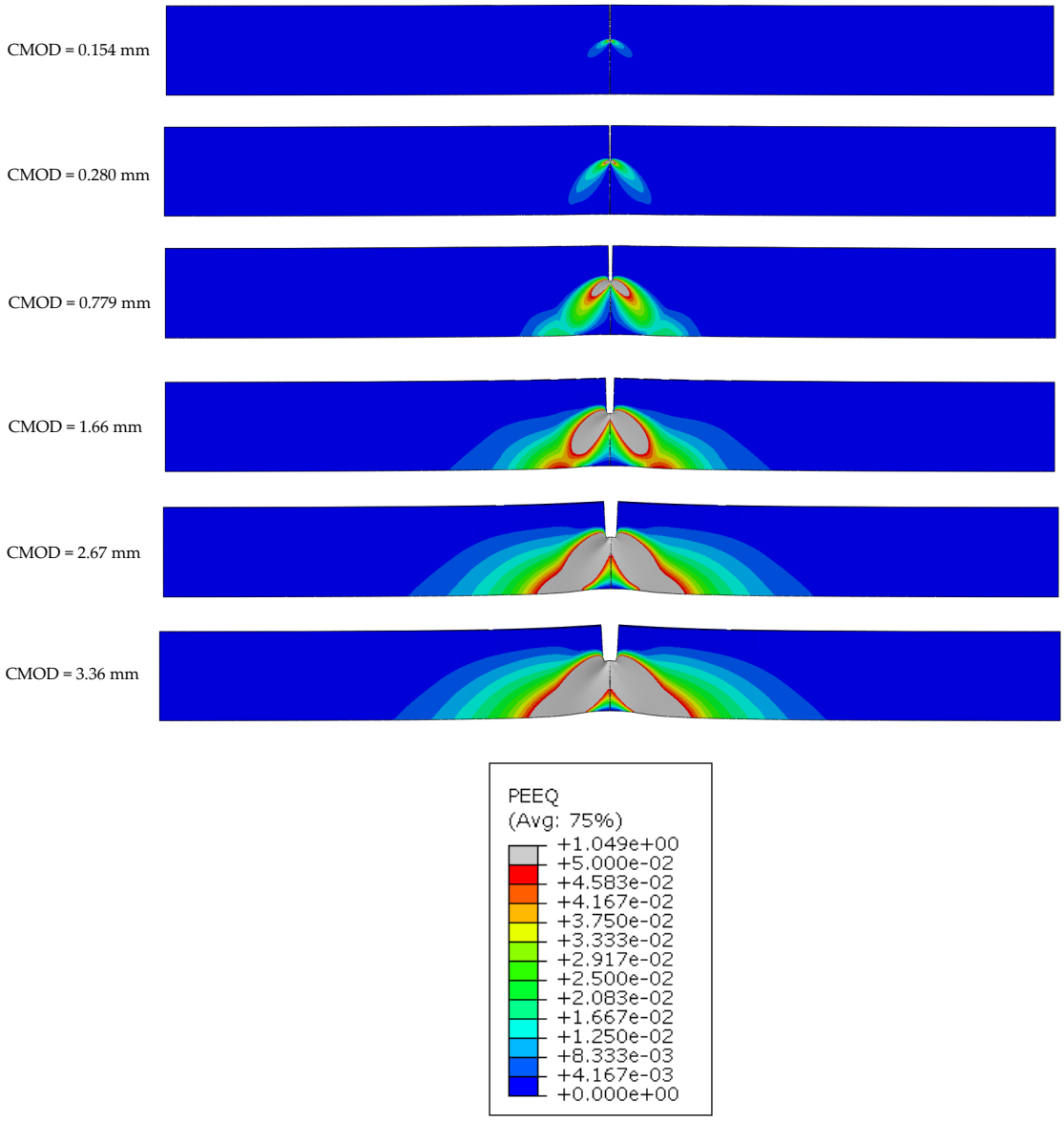

Figure 4.79: Equivalent plastic strain (ε^{p}_{eq}) distributions in the surface (plain stress) of SENT FE model with $a/W = 0.4$

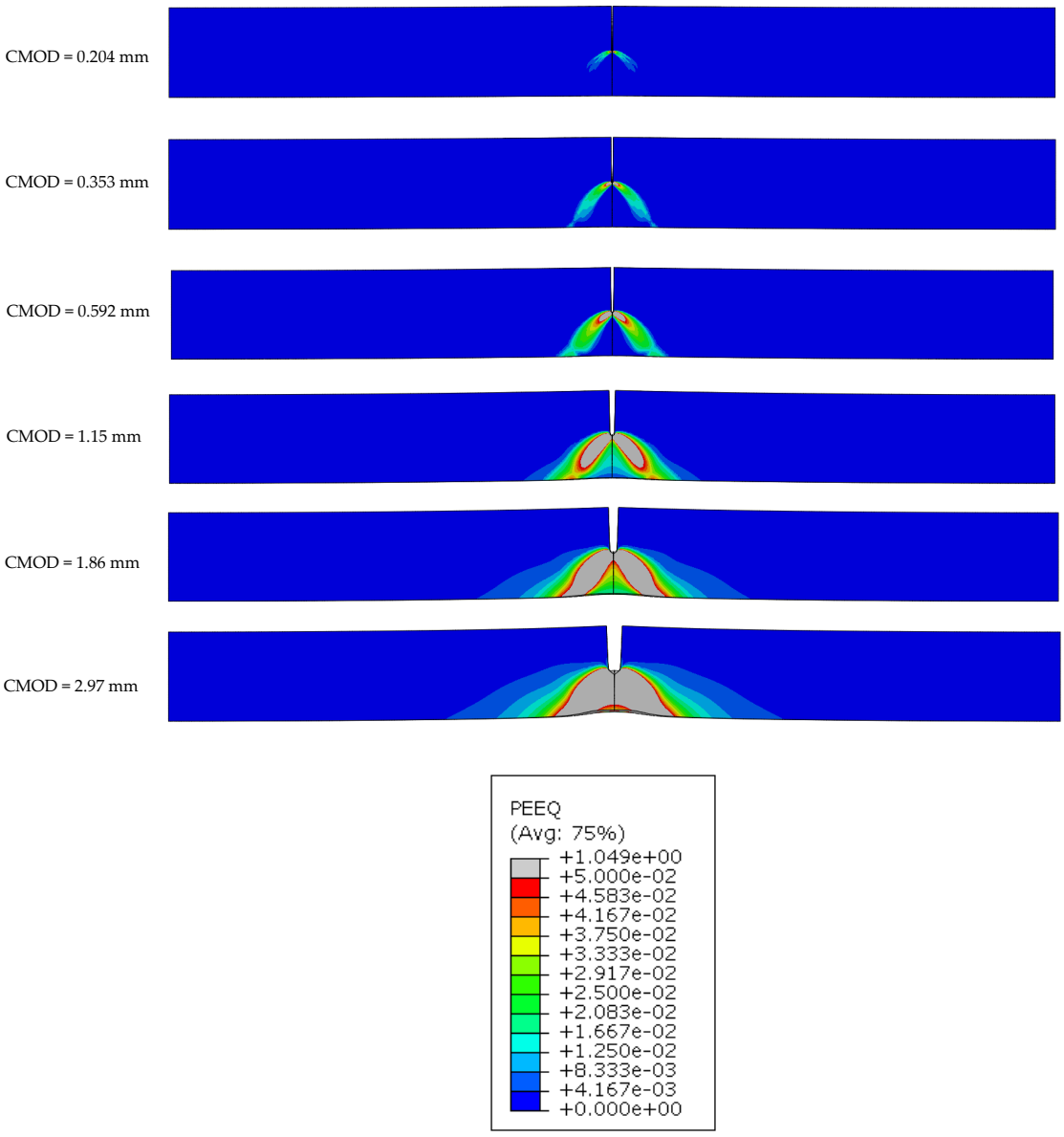

Figure 4.80: Equivalent plastic strain (ε^{p}_{eq}) distributions in the symmetric plane (plain strain) of SENT FE model with $a/W = 0.5$

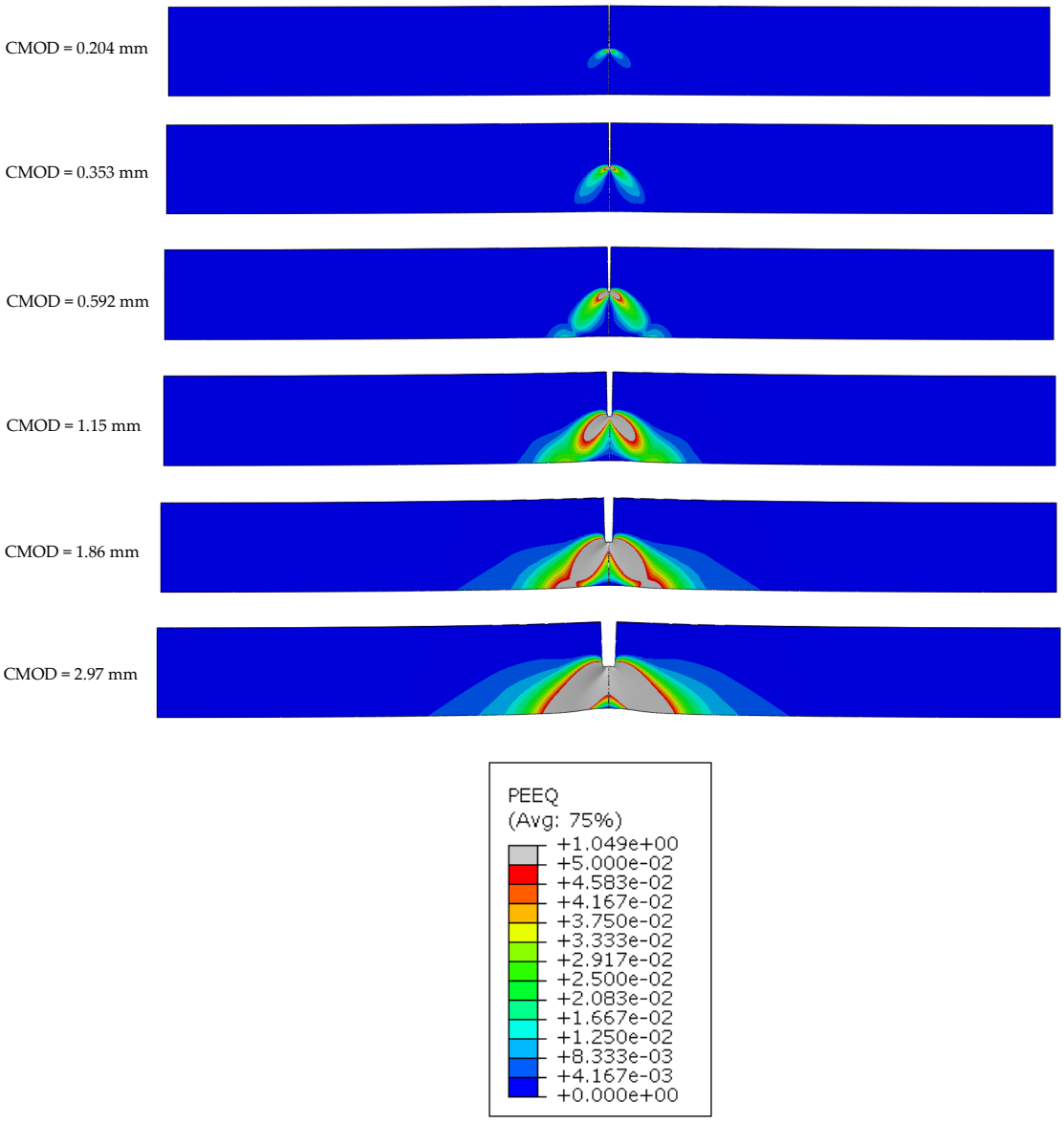

Figure 4.81: Equivalent plastic strain (ε^{p}_{eq}) distributions in the surface (plain stress) of SENT FE model with $a/W = 0.5$

4.6 SUMMARY

In this chapter, SENT tests with optimal notch size derived from numerical analyses of crack-tip constraint were carried out. DIC was employed to quantify the deformation of the SENT specimens. FE analyses were performed to identify the suitable material models, and parametric numerical analyses were conducted to investigate the notch size on the development of strain localization associated with Lüders banding. From the results presented, the following findings were found:

- SENT (2B $\times$ B) with a/W range of 0.3 to 0.4 is found best representative of the crack-tip in-plane constraint of that of cracked pipes subjected to combined axial straining and internal pressure. In terms of out-of-plane constraint, use of SENT (2B $\times$ B) may be more conservative than SENT (B $\times$ B).
- Use of the 'Flat' and UDU material models generate similar deformation pattern in SENT model with deeper notch ($a/W = 0.4$), but significantly different strain distributions in SENT model with a shallow notch ($a/W = 0.15$). Therefore, the necessity of the use of UDU model in capturing the strain localization associated with Lüders banding is less pronounced in FEA cases where notch size in SENT is sufficiently large such that the plastic deformation localises only in the notch region and no propagation of plastic bands occur.
- Change in notch size is found to significantly alter the development of plasticity localization associated with Lüders behaviour in SENT specimens.

5

NUMERICAL ANALYSIS OF X65 PIPES CONTAINING FLAWS SUBJECTED TO AXIAL PLASTIC STRAINING WITH LÜDERS PLATEAU

5.1 INTRODUCTION

As aforementioned in Chapter 2, in existing codified ECA procedures such as those given in BS 7910, DNVGL-RP-F108 and R6, the behaviour of materials containing a Lüders plateau is usually simplified as a stress-strain curve having a flat stress plateau (i.e. constant flow stress) over the Lüders strain phase, and the upper yield point is neglected. This type of stress-strain responses have been commonly used in other studies (Tkaczyk et al. 2009c; Pisarski et al. 2014; Tang et al. 2014). However, the failure of this type of stress-strain response in simulation of the macroscopic features of the Lüders band has been reported (Wang et al. 2017). It was found that FEA using the simplified stress-strain curve with a flat stress plateau resulted in an underestimate of the crack driving force by approximately 20% in comparison with the full-scale test results.

In this chapter, the numerical analysis of steel pipes containing a circumferential external surface flaw is presented, with a focus on the effect of the constitutive laws that represent the Lüders behaviour on the predicted crack driving force and the deformation behaviour of the cracked pipes. It was demonstrated that the effect of Lüders plateau in fracture analysis of cracked pipes can be properly evaluated provided that the correct constitutive law is utilised.

5.2 FEA OF STEEL PIPES CONTAINING FLAWS

FE models were created in accordance with the geometry and configuration of the full-scale tests carried out at TWI and reported by Pisarski et al. (2014). Both uni-axially and bi-axially loaded pipe tests were conducted in the full-scale test programme. In this chapter, the uni-axially loaded pipe test is analysed. The pipe reported had a length (2L) of 2000 mm, an outer diameter (OD) of 273.3 mm and an average wall thickness (t) of 18.4 mm. The pipe contained four notches that were machined using electric discharge machining (EDM). These notches had a constant depth and semi-circular ends. Each notch has a finite radius of 0.12 mm at the notch tip. The four notches were at cardinal points around the pipe circumference, namely the 0, 3, 6 and 12 o'clock positions. The notches at the opposite positions had identical sizes. FE simulations were performed for the notches at 3 and 9 o'clock each with a nominal size of 650 mm, and those at 6 and 12 o'clock each with a nominal size of 5×100 mm. In favour of brevity, the detailed analyses of the Lüders banding behaviour and the crack-tip field were presented for the 6×50 mm notch only since similar trends were observed for both 6×50 mm and 5×100 mm notches. Figure 5.1 illustrates the flaw configuration and pipe geometry.

To accurately simulate notch behaviour, the actual notch sizes were used in the FE analyses. Theses had average sizes of 5.68×50 mm, and 4.41×100 mm, respectively.

5.3 CONSTITUTIVE MODELS

The constitutive model used in this study is the so-called UDU stress-strain response. The model is an isotropic, J_2 type, elastic-plastic material law assuming incremental plasticity, and contains a segment of strain softening followed by conventional strain hardening. To the best of the author's knowledge, Kyriakides and Miller (2000) were among the first to use the UDU model to simulate strain localisation due to Lüders phenomenon in FE analysis. The UDU is a simplified approach used to fit to the experimentally determined stress-strain curve that contains a Lüders plateau. Figure 5.2 illustrates how the UDU fit is constructed.

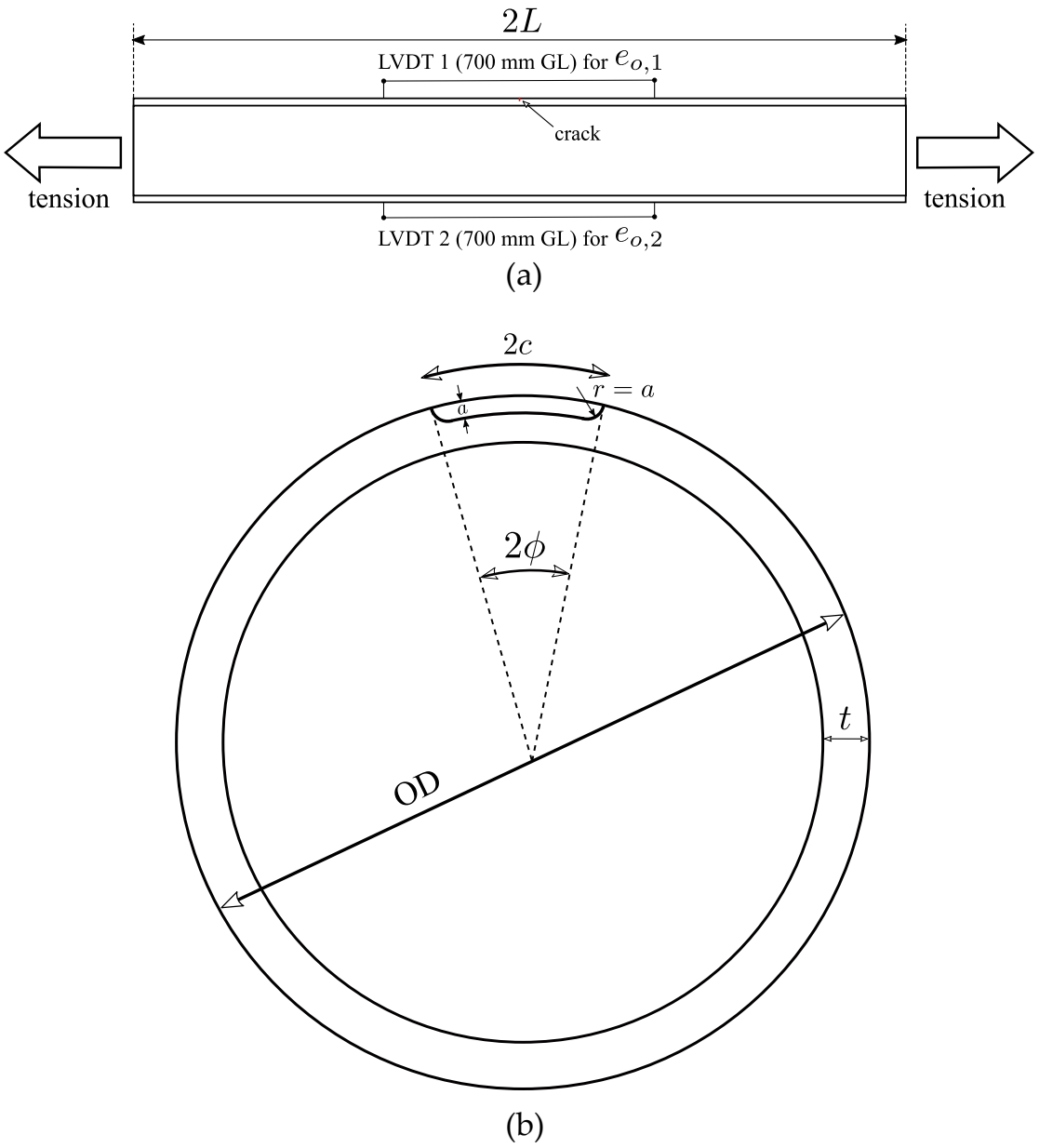

Figure 5.1: Schematic of the pipe containing a surface-breaking flaw: (a) geometric features of the pipe in the longitudinal view; (b)geometric features of the pipe cross-section containing an external surface-breaking flaw

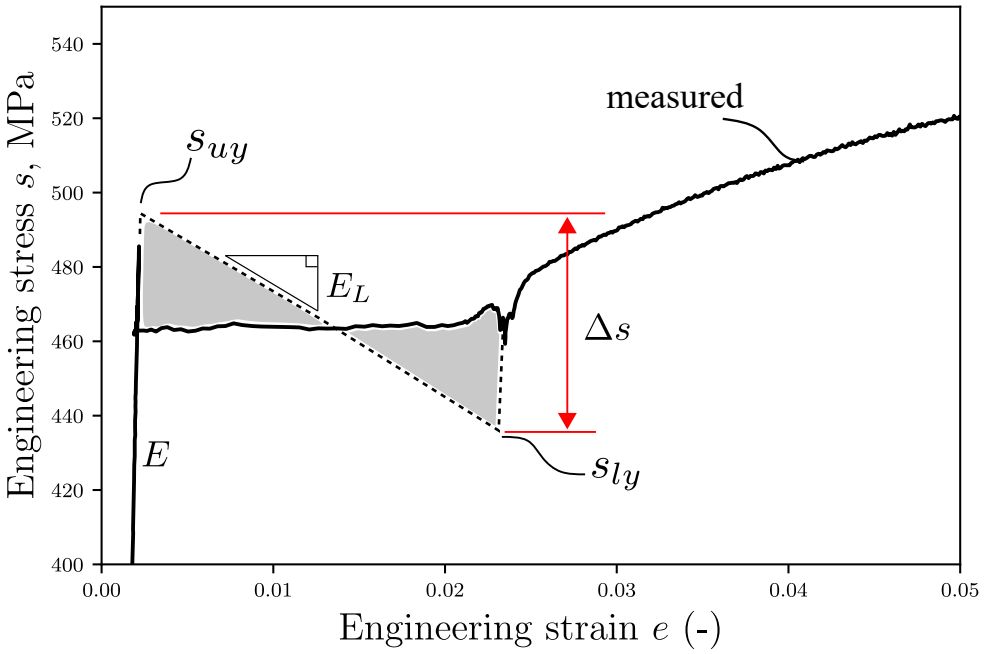

Figure 5.2: Illustrative schematic of the UDU stress-strain model

The fit consists of four branches, namely the linear-elastic, linear softening, linear hardening and the measured strain hardening branches. The fit is constructed such that the so-called Maxwell stress is equal to plateau stress (R_{eL}). Artificial upper and lower yield strengths are then created. A straight line joining these points creates two triangles above and below the Maxwell stress, as shown in Figure 5.3. According to the Maxwell equal area rule, the area of the two triangles are made equal. This requirement is to ensure that the dissipated energy remains unchanged during the Lüders phase. Accordingly, the upper yield stress (s_{uy}) and the lower yield stress (s_{ly}) can be determined as:

$$s_{uy} - R_{eL} = R_{eL} - s_{ly} = \frac{\Delta s}{2} \tag{5.1}$$

where Δs is the different between s_{uy} and s_{ly}, and can be related to the softening modulus (E_L) via:

$$E_L = -\frac{\Delta s}{\Delta e_L} = -\frac{s_{uy} - s_{ly}}{\Delta e_L} \tag{5.2}$$

where Δe_L is the length of Lüders plateau in terms of engineering strain. The material properties of the cracked pipe analysed in this work refer to those presented in Pisarski et al. (2014). The pipe is seamless to API 5L Grade X65 steel that exhibited a marked Lüders plateau with strain extent (Δe_L) of about 2%. Figure 5.3 shows the average engineering stress-strain curve of the X65 pipe, which neglected the upper yield stress that was observed in the tensile tests (Pisarski et al. 2014), with the UDU fit using different normalised softening modulus ($\bar{E}_L \equiv | E_L/E |$). The parameters of the constitutive models are shown in detail in Table 5.1.

Table 5.1: Parameters of material laws used in FEA of cracked pipes

Material law	E, GPa	R_{eL}, MPa	Δe_L, %	$\bar{E}_L$	$\Delta s/R_{eL}$
Flat	210	512	2.0	0	0
UDU-1				0.005	0.041
UDU-2				0.015	0.122
UDU-3				0.025	0.203

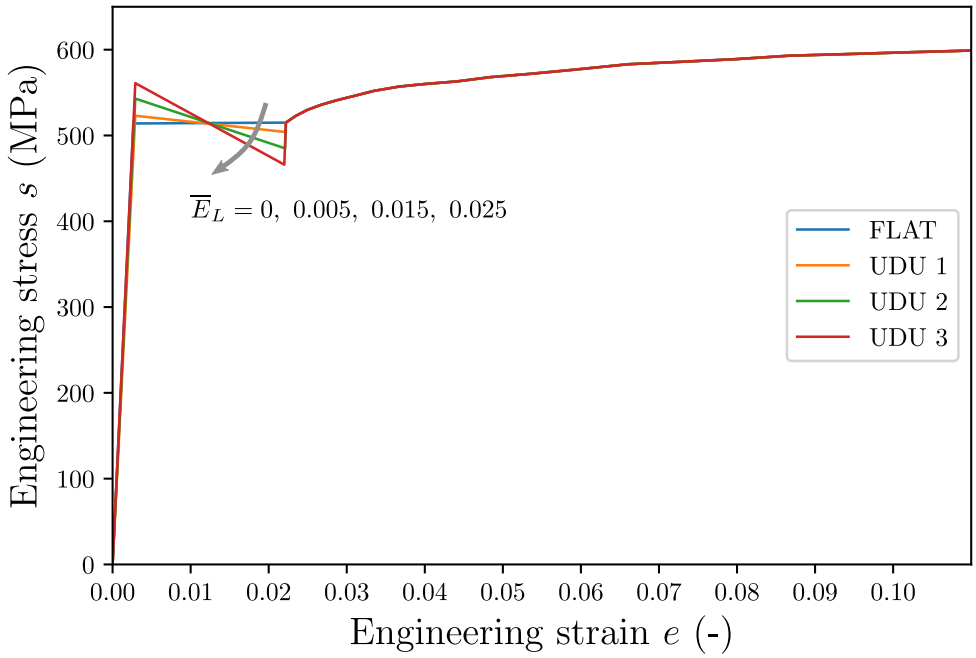

Figure 5.3: Constitutive models used in FE analyses

5.4 FE MODEL CONFIGURATION

The FE pipe model was constructed using the commercial FE software Abaqus 6.14. Only a quarter of the pipe (L = 1000 mm) was simulated due to the application of symmetry boundary conditions. The model was meshed with the three-dimensional, 20-node, quadratic elements with reduced integration (Abaqus type C3D20R). Figure 5.4 shows the mesh configuration utilised in the FE analysis, alongside the applied boundary conditions. Prescribed displacements were applied to the nodes at the uncracked end such that an average overall strain $e_{o,avg}$ of about 0.06 was obtained. A node at the bottom corner was fixed in the vertical direction to prevent the potential rigid body movement. The spider-web focused mesh using non-singular elements was applied to the crack tip. The mesh had 16 elements in a row along the half circumference. The bulk of the pipe was meshed with different density for different constitutive models. The stress-strain curve (in its engineering form) containing a flat stress plateau (denoted as 'Flat' in this paper) is expected to produce generally uniform deformation in the FE analysis because the corresponding true stress-true strain response of the Flat model has a monotonically increasing trend over the whole strain range. Therefore, a coarser mesh was used with a smooth mesh transition in which the longitudinal element length ranges from 10 to 200 mm. As for the UDU stress-strain response, a refined mesh was applied to the bulk of the pipe to capture the strain localisations due to Lüders plateau. The elements were applied through the pipe wall thickness with dimensions in other orientations (circumferential and longitudinal) being equal to those in the thickness direction. Such an isotropic mesh pattern was chosen to avoid potential directional bias of element arrangement. The mesh was derived from a mesh sensitivity study, which reproduced the Lüders banding pattern similar to that reported in literature (Aguirre et al. 2004; Kyriakides et al. 2008; Hallai and Kyriakides 2011b; Liu et al. 2015)

It is well-known that strain softening (or a negative tangent stiffness $\partial\Delta\sigma/\partial\Delta\epsilon$) in the constitutive law can result in spurious mesh sensitivity of FE results. The reason is that strain softening renders the governing partial differential equations (PDEs) ill-defined and the ellipticity of the PDEs lost, leading to non-uniqueness of the solution. To remove the induced mesh sensitivity, a mild

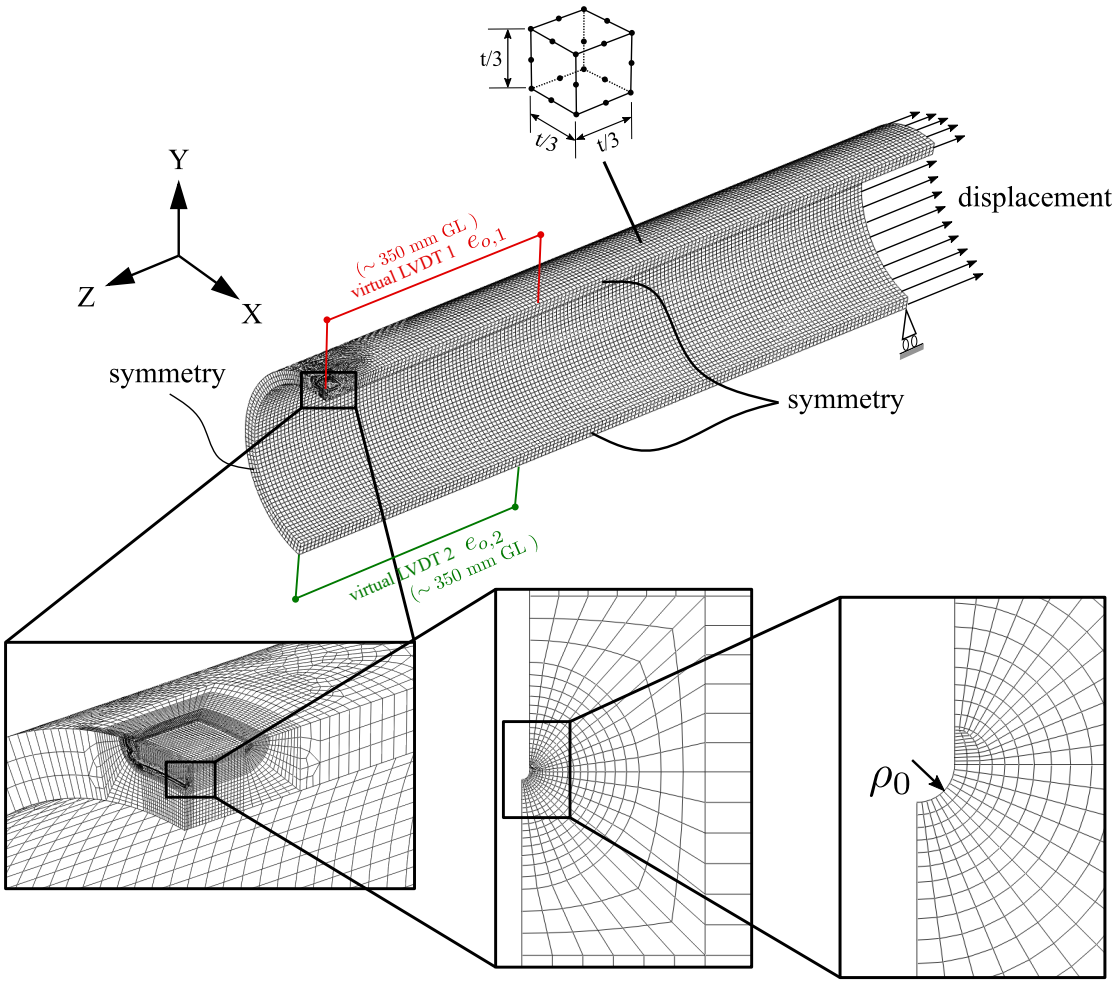

Figure 5.4: Mesh configuration of the circumferentially-flawed pipe FE model

strain rate dependence was applied (Needleman 1988). A simple power-law rate-dependence as described in Hallai and Kyriakides (2011b) and Liu et al. (2015) was used, which takes the following form:

$$\left(\frac{\dot{\varepsilon}^p}{\dot{\varepsilon}_0^p}\right) = \frac{\sigma}{_0\left(\varepsilon^p\right)} \tag{5.3}$$

where $\dot{\varepsilon}^p$ is the actual equivalent plastic strain rate, $\dot{\varepsilon}_0^p$ s the reference equivalent strain rate (assumed to be $10^{-4}s^{-1}$ in this work), $\sigma_0\left(\varepsilon^p\right)$ is stress corresponding to the applied plastic strain at the reference plastic strain rate, σ is the stress corresponding to the applied plastic strain at the actual plastic strain rate, and N is the exponent describing the strain rate dependence. In this work, N is taken as 0.001, which is deemed sufficient to reduce the mesh sensitivity while having marginal effect on the simulated behaviour. The strain rate-dependence was applied in Abaqus 6.14 via the yield ratio option.

A series of pipe models was generated to account for the effect of ductile tearing from the notches, which is elaborated in Section 5.4.1. Similar mesh strategy was used for other pipe models. The total element number of the refined mesh for analyses using UDU material model ranged from 69,872 (326,867 nodes) to 77,764 (359,850 nodes) depending on the specific crack dimensions.

The FE models were computed using an implicit time integration scheme and Newton-Raphson iteration. Geometric non-linearity and finite strain formulation were utilised. Loading parameters, such as the CTOD, load-displacement response and average overall strain were extracted. The average overall strain ($e_{o,avg} = \frac{1}{2}(e_{o,1} + e_{o,2})$) is defined as the mean value of the strain measured from virtual LVDT-1 ($e_{o,1}$) and LVDT-2 ($e_{o,2}$) located at the upper and lower edges of the pipe shown in Figure 5.5. The CTOD was calculated by using the 90°intercept definition proposed by Rice (1968). It is known that in finite strain analysis, J-integral often exhibits noticeable path-dependence, invalidating its use as a fracture parameter. Brocks and Scheider (2001) demonstrated the J at the outermost contours tend to converge and approach to the far-field J, and recommended to extract the J from the furthest contour that is also not in contact with the model boundary. However, in the present study the J-integral was not adopted as crack driving force due to the spurious path-dependence

even for the outermost contours. Figure 5.6 illustrates the locations of a total of 30 J contours determined. The innermost contour (i.e. contour 1) is along the notch, and the outmost one (contour 30) is closest to but in contact with the boundary of the model. It can be noticed in Figure 5.7 that the J curves from the outermost contours are initially well converged, and then start to diverge in the strain range $e_{o,avg} = 0.01\text{-}0.025$. A pronounced decreasing trend in the J is also observed, which is expected to be due to the strain softening. Strain softening is believed to invalidate the use of J as the fundamental assumption of J was violated (Brocks and Scheider 2001).

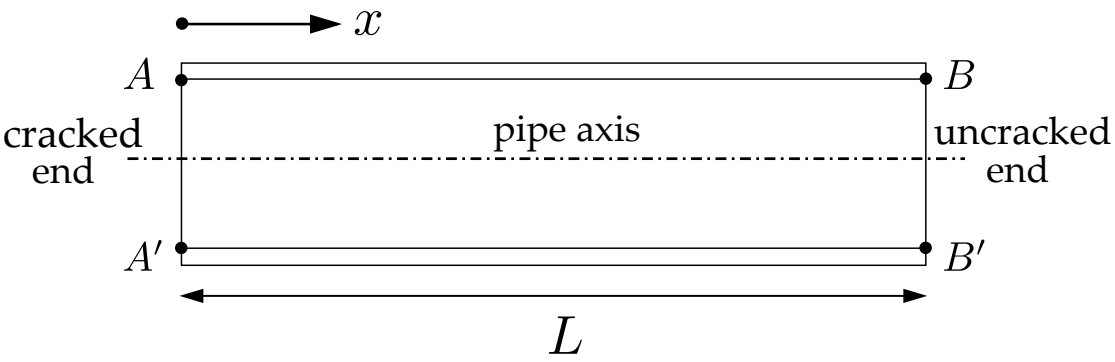

Figure 5.5: Paths AB and A'B' selected to extract the equivalent plastic strain distribution

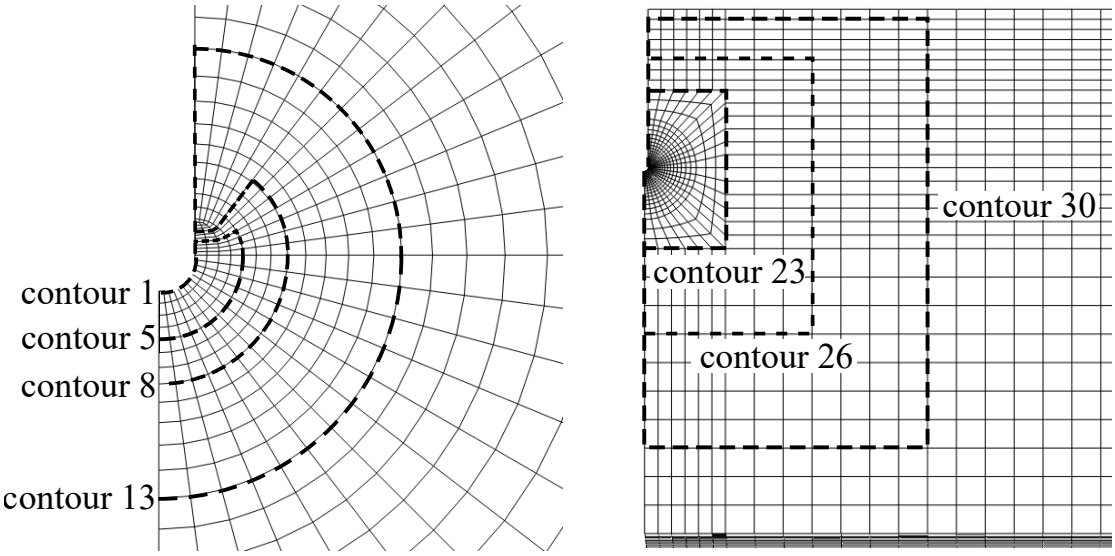

Figure 5.6: Illustration of the J contours at the crack tip and near-tip regions

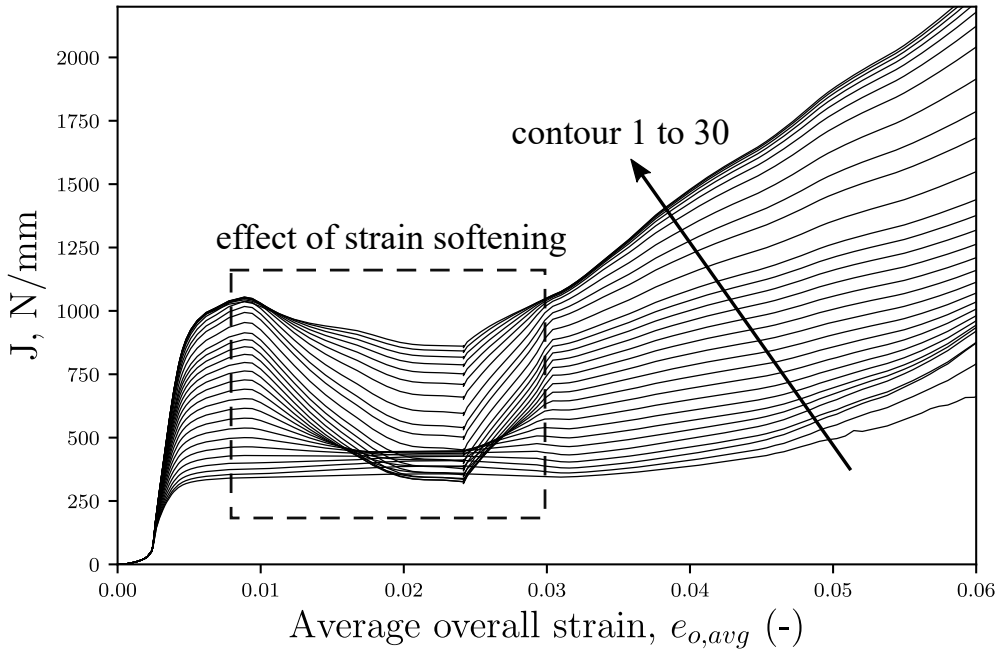

Figure 5.7: Calculated J-integral of cracked pipes for UDU model with $\overline{E}_L = 0.005$

5.4.1 *Consideration of ductile tearing*

In the pipe tests reported in Pisarski et al. (2014), ductile tearing occurred during the test. Ductile tearing increases crack depth which leads to a higher crack driving force than that with the initial crack depth. However, this effect cannot be explicitly captured in the FE analysis of a stationary crack. In order to incorporate the effect of ductile tearing in the crack driving force, the driving force mapping approach (Hertelé et al. 2012, 2014) was adopted in this work. The mapping approach requires a series of FE simulations to be conducted with crack depths ranging from the initial depth (a_0) to a prescribed final depth ($a_0 + \Delta a_n$). The predicted CTOD and crack extension can then be interpreted from the intersections between the crack growth resistance curve (R-curve) and a series of iso-strain CTOD curves. The iso-strain CTOD curves refer to the CTOD curves in a function of crack growth at a certain strain. The mapping approach has also been commonly used by researchers to predict crack extension and the strain capacity of pipeline girth welds (Fairchild et al. 2011a; Pisarski et al. 2014).

In the present study, simulations of crack depth $a = 5.68, 6, 7, 8$ and 9 mm were performed for 5.68×50 mm notch (actual sizes) were performed to incorporate the effect of ductile tearing. Iso-strain CTOD curves were constructed for an average overall strain $e_{o,avg}$ increasing from o with an increment of 0.0005 until a tangency with the R-curve was reached. The CTOD R-curve of the parent material was reported in Pisarski et al. (2014) as $\delta = 1.917\Delta a^{0.704}$. The iso-strain CTOD curves were established by applying fourth order curve fitting to the points $(CTOD_i, a_i)$ for the discrete crack depths. For example, two iso-strain CTOD curves for $e_{o,avg} = 0.03$ and $e_{o,avg} = 0.0435$ for 5.68×50 mm notch are shown in Figure 5.8. The iso-strain CTOD curve for $e_{o,avg} = 0.03$ intersects the R-curve at the point (6.528, 1.708), indicating the crack depth of 6.528 mm and the corresponding CTOD of 1.708 mm. The ductile instability was predicted to occur when the tangency between the iso-strain CTOD curve (when $e_{o,avg} = 0.0435$) and the R-curve was reached. Using the mapping approach, we have obtained a CTOD versus $e_{o,avg}$ curve with the actual CTOD values considering the effect of ductile tearing, as shown in Figure 5.8(b).

5.5 RESULTS

5.5.1 *Global deformation behaviour*

The load-displacement or the gross stress versus average overall strain (s-$e_{o,avg}$) response is an important indicator of the global behaviour of a deforming body. The gross stress is defined as the remote stress applied at the end of the pipe, which is expressed as:

$$s = \frac{F}{A} \tag{5.4}$$

where F is the applied force and A is the cross-section area of the uncracked end. Figure 5.9 shows the s-$e_{o,avg}$ response. The s-$e_{o,avg}$ response was defined as the average of the overall strains, i.e. $e_{o,1}$ (based on virtual LVDT 1) and $e_{o,2}$ (based on virtual LVDT 2). The s-$e_{o,avg}$ responses calculated using different stress-strain models exhibit similar trends with a stress plateau followed by strain hardening. The FE model with 'Flat' stress-strain curve produced the

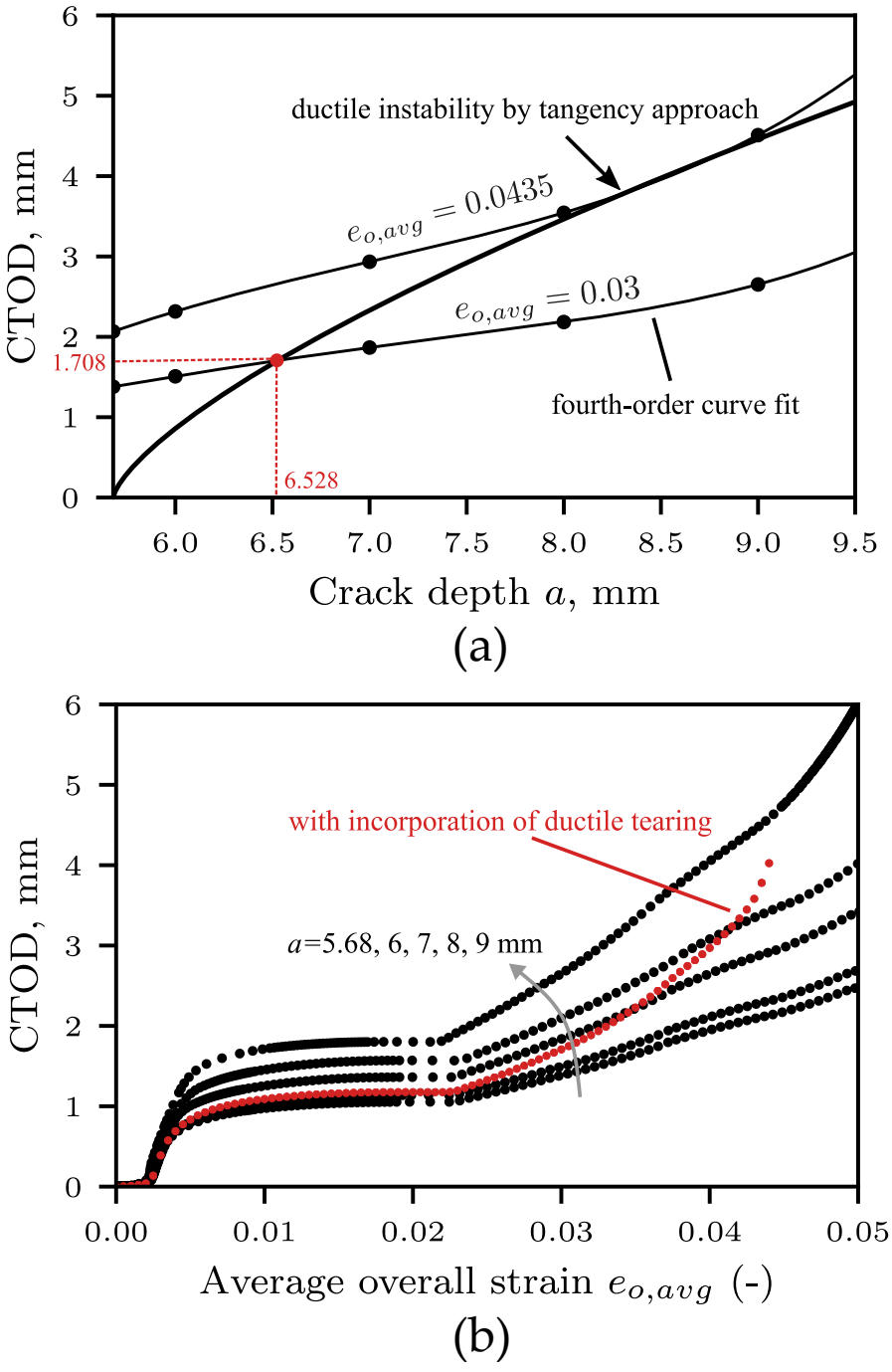

Figure 5.8: Incorporation of ductile tearing by driving force mapping and tangency approach

lowest stress plateau with stress magnitude of 512 MPa, which is 4.12% lower than the tested value. The height and length of the stress plateau is observed to increase with the increasing $\bar{E}_L$. This behaviour was also noted on pipes loaded in bending in the absence of flaws by other researchers (Hallai and Kyriakides 2011b). All global stress versus strain curves converge in the strain hardening regime subsequent to the Lüders plateau phase. A slight decrease in the global stress with some fluctuations is noticed after 1.5% strain for $\bar{E}_L = 0.015$ and after 2% for $\bar{E}_L = 0.025$ before strain hardening occurs in the simulation. This may be the result of the merge of propagating bands at several locations before the bands propagate to the end of the pipe.

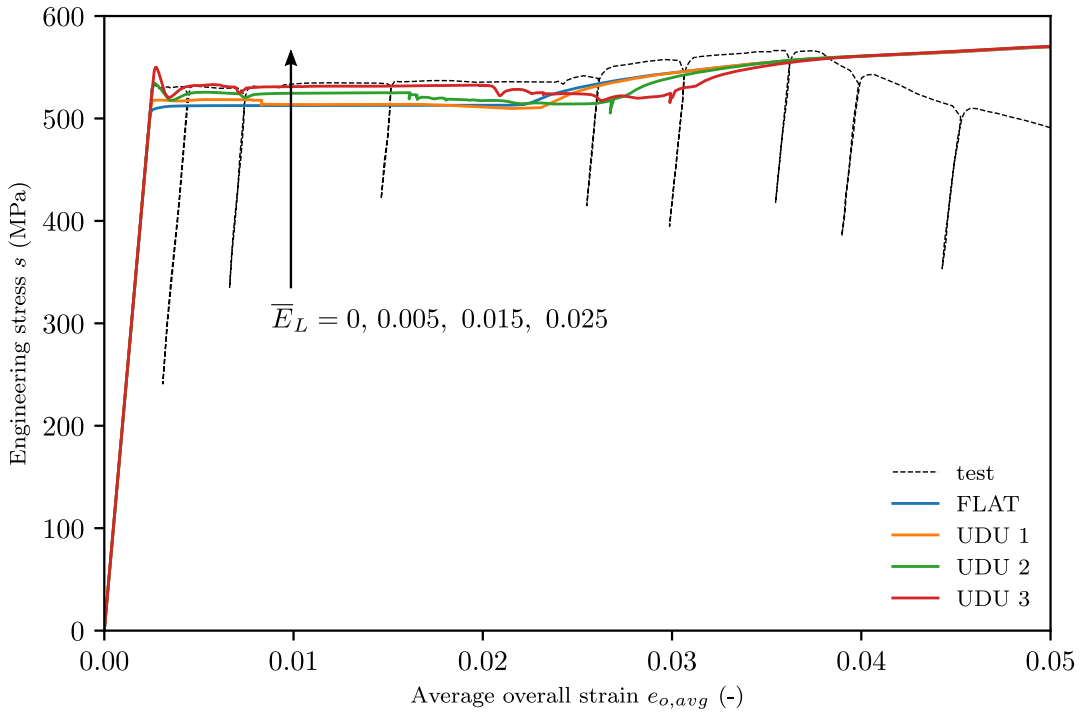

Figure 5.9: Comparison between global deformation behaviour (s-$e_{o,avg}$) calculated from FEA and that measured from full-scale test

Apart from the stress plateau, the E_L ratio also affects the yield point. As expected, the s-$e_{o,avg}$ curve calculated with the FLAT stress-strain model shows neither an upper yield point nor a stress drop. Similar behaviour is found for s-$e_{o,avg}$ response calculated with $\bar{E}_L = 0.005$ except that the stress slightly drops at about $e_{o,avg} = 0.008$. On the other hand, the s-$e_{o,avg}$ responses for $\bar{E}_L = 0.015$ and $\bar{E}_L = 0.025$, have noticeable upper yield stresses of 531 MPa and 548 MPa, respectively.

5.5.2 *Evolution of plasticity*

From the gross stress versus average overall strain (s-$e_{o,avg}$) curves, six configurations were selected for each stress-strain model to show the development of plastic deformation. Figure 5.10 shows the equivalent plastic strain (ε^{p}_{eq}) distributions on the deformed pipe for different $e_{o,avg}$ levels.

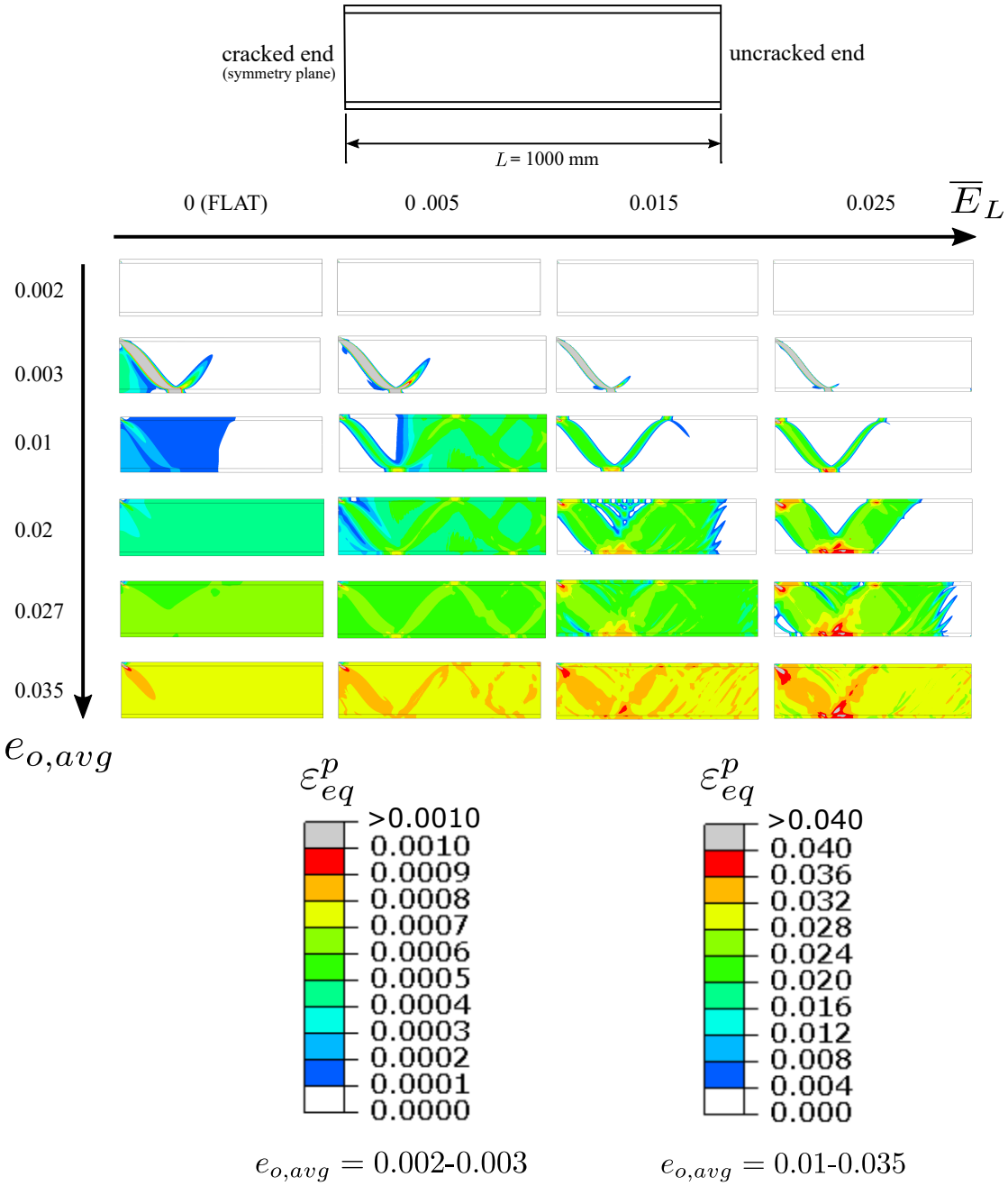

Figure 5.10: Equivalent plastic strain (ε^{p}_{eq}) contours of the simulated cracked pipe with different material models at various average overall strain ($e_{o,avg}$) levels

Initially, when $e_{o,avg} = 0.002$, the simulated pipe is globally elastic; indicated by the white colour covering the whole pipe. Limited plasticity is found to accumulate at the crack tip. At the onset of the elastic-plastic transition on the s-$e_{o,avg}$ curves, localised shear bands emanate from the crack tip, which is observed in all models. The width of the localised band tends to be narrower for the UDU model with a higher $\bar{E}_L$. This indicates that higher $\bar{E}_L$ leads to stronger strain localisation. Beyond $e_{o,avg} = 0.003$, the plasticity starts to spread to the elastically deformed parts of the pipe. When $e_{o,avg} = 0.01$, which is about one third of the stress plateau extent, prominent differences in the band patterns are observed. In the model using FLAT stress-strain curve, uniform plasticity is found to spread over the pipe, indicating homogeneous deformation. In contrast, the pipe models using UDU stress-strain curves exhibit inhomogeneous deformation, featuring propagating localised plastic band/bands. It is worth noting that FE model using $\bar{E}_L = 0.005$ yields more complex bands which initiated simultaneously at different locations of the pipe. When $\bar{E}_L = 0.005$ and 0.025, localised bands are formed near the cracked region, and propagate to the remainder of the pipe. When $e_{o,avg} = 0.02$, the pipe model using the Flat stress-strain curve continues to deform homogeneously. The models using UDU stress-strain curves still see propagation of localised plastic bands moving towards the elastically-strained parts of the pipes. The exception is noticed for model using $\bar{E}_L = 0.005$ where the bands have covered the whole pipe. When $e_{o,avg} = 0.027$, the pipes simulated with $\bar{E}_L = 0.005$ and 0.015 have proceeded into the globally strain hardening regime in which the pipes deform uniformly. With $\bar{E}_L = 0.025$, the band propagates through a majority of the pipe, and then starts to deform uniformly beyond $e_{o,avg} = 0.035$. It is indicated that the increase in $\bar{E}_L$ results in longer stress plateau, as shown in Figure 5.9.

To examine in further detail the evolution of plasticity in the pipe, the equivalent plastic strain (ε^p_{eq}) distributions along the upper and lower edges (denoted by the paths AB and A'B' respectively shown in Figure 5.5) are plotted against the normalised distance (x/L) along the pipe axis in Figures 5.11 and 5.12, respectively. From Figures 5.11 and 5.12, little plasticity is observed as the pipe is globally elastic when $e_{o,avg} = 0.002$. When $e_{o,avg} = 0.003$, prominent strain localisation associated with net section yielding occurring at the cracked end are observed.It can be noticed that more localised plasticity is produced

with a with a greater $\bar{E}_L$, which is indicated by the narrower width of the strain peak (bump) along paths AB and A'B' using a greater $\bar{E}_L$ when $e_{o,avg} = 0.003$. In addition, a greater $\bar{E}_L$ is generally shown to produce a higher peak value of ε^p_{eq}, though exception is noticed for $\bar{E}_L = 0.025$ due to the plasticity just reaching the bottom edge.

For $e_{o,avg}$ ranging from 0.01 to 0.035, ε^p_{eq} for the Flat strain-strain model is shown to remain nearly constant along both paths AB and A'B'. For pipes using the UDU models, noticeable heterogeneity in the ε^p_{eq} is observed. Apart from the observation that ε^p_{eq} for a greater E_L has a higher peak value in the localised shear band emanating from the crack, it is also noticed that the peak values of ε^p_{eq} in the pipes using the UDU models are significantly above those obtained using the Flat model. It can be therefore inferred that a greater $\bar{E}_L$ promotes strains and strain localisation in the near-tip region, and will consequently increase the crack driving force. When $e_{o,avg} = 0.035$, all pipe models are all well into the globally strain hardening regime, displaying nearly constant ε^p_{eq} in the locations away from cracked end.

5.5.3 *Crack driving force*

Figures 5.13 and 5.14 show the calculated CTOD versus strain ($e_{o,avg}$) in the cracked pipe with an average flaw sizes of 5.68×50 mm and 4.41×100 mm, respectively. The CTOD values calculated from the 'Flat' model and the UDU model with various softening parameters are compared with those measured in the full-scale tests. It is clear that using the Flat model in the FE analyses for the stationary crack under-predictes the CTOD for $e_{o,avg}$ above 0.005, while conservative CTOD values are predicted with the use of the UDU models. Using the UDU models, the CTOD sees a rapid increase at $e_{o,avg} = 0.005$, followed by a subsequent plateau. Increasing E_L is shown to result in a higher CTOD plateau and longer extent, which is analogous to the global stress-strain behaviour described in Section 5.5.1. Depending on the $\bar{E}_L$ ratios used, the CTOD plateau for various E_L values (0.005, 0.015 and 0.025) terminates at $e_{o,avg}$ of 0.0288, 0.0346 and 0.0376, respectively. As for the pipe containing a 4.41×100 mm flaw, significant improvement is observed with the use of the UDU model, as shown in Figure 5.14. The Flat model, however, considerably

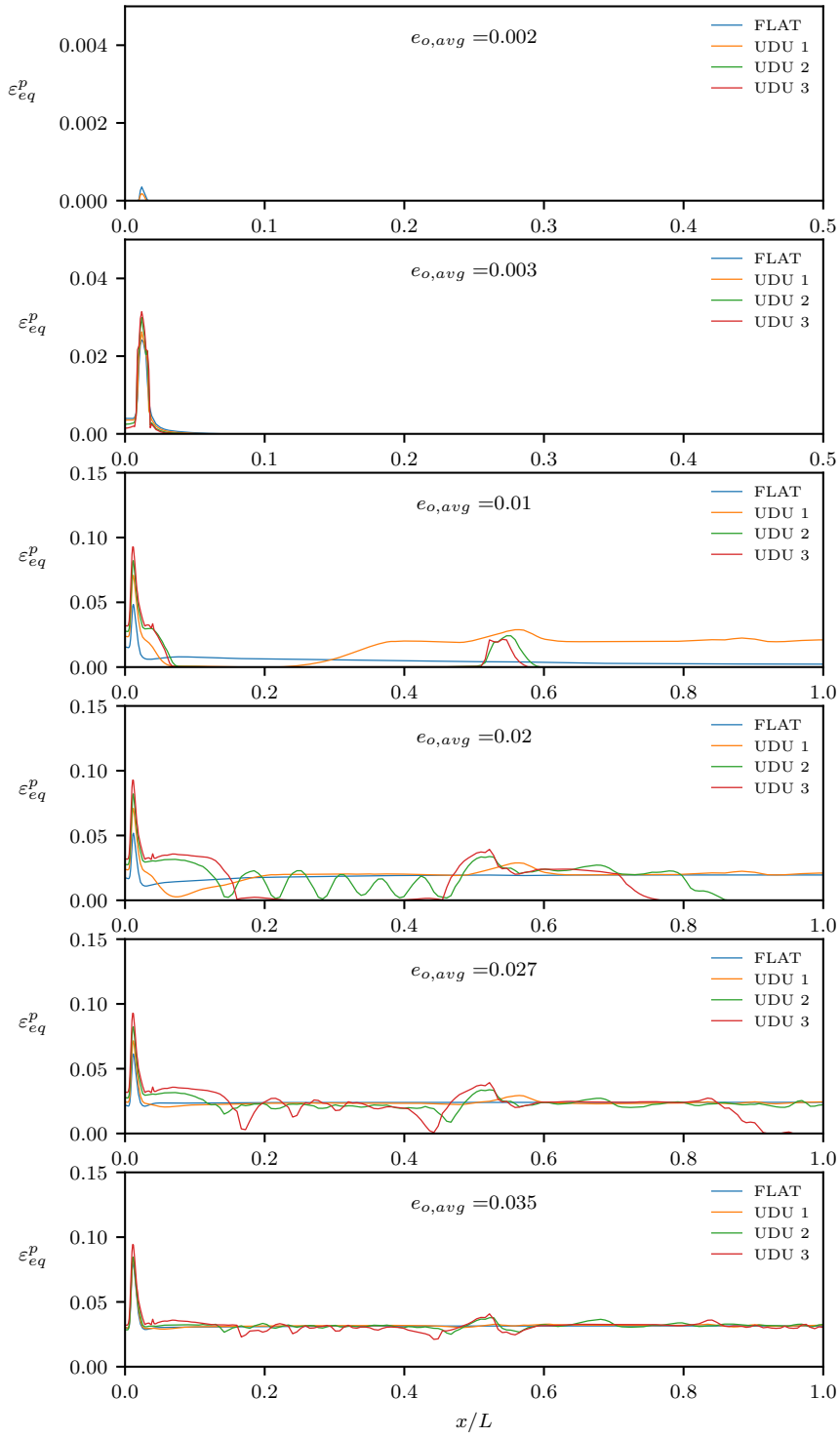

Figure 5.11: Equivalent plastic strain distribution along path AB in the pipes

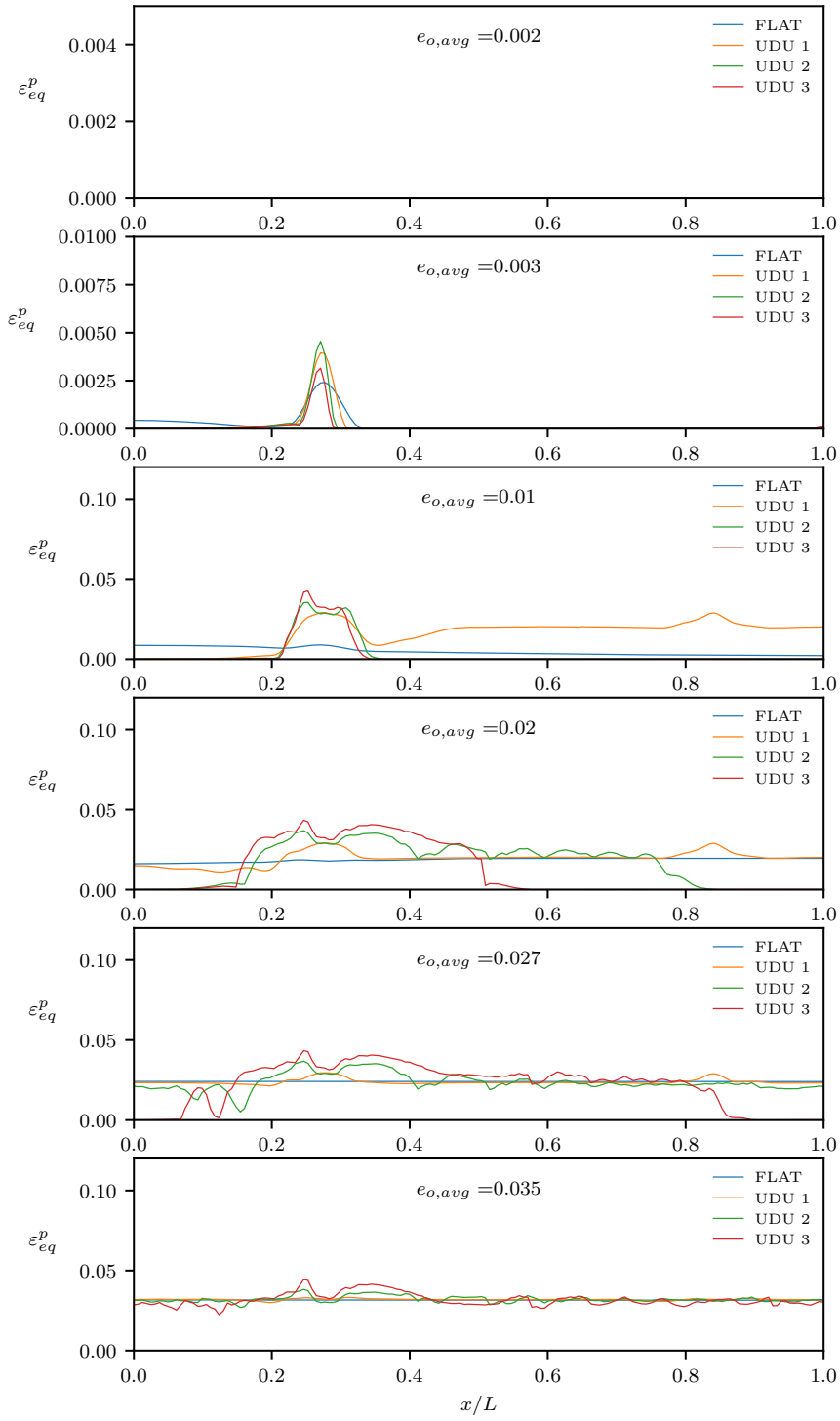

Figure 5.12: Equivalent plastic strain distribution along path A'B' in the pipes

under-predicts the CTOD. An widening gap between the FE analyses and test results is observed for $e_{o,avg}$ above 0.0325, which may be due to the assumption of a stationary crack which neglects crack extension by ductile tearing.

With the incorporation of ductile tearing in the FE analyses using the mapping approach, the deviation between the FE analyses and the test in the post-CTOD plateau regime is significantly reduced, as shown in Figure 5.15. In the post-plateau phase, the Flat model yields a greater CTOD than the UDU models. The reason of this may be that the CTOD predicted using the Flat model has the shortest plateau, and accordingly the effect of ductile tearing kicks in earlier than that using the UDU models. For pipes using the UDU models, the magnitude of the CTOD plateau is shown to increase with the increasing $\bar{E}_L$.

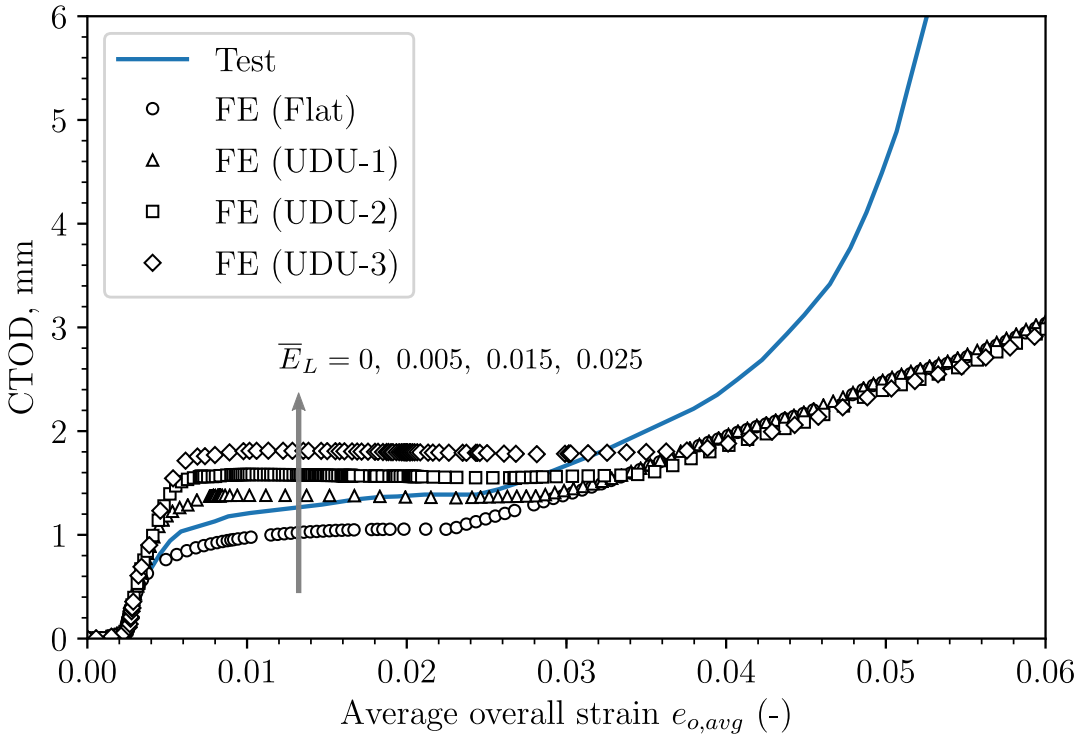

Figure 5.13: Comparison of CTOD for average flaw size 5.68 × 50 mm from full-scale test and FE analyses without consideration of ductile tearing

5.5.4 *Crack tip plastic zone*

To appreciate the cause of the deviations in the calculated CTOD with various material models, the plasticity and the stress field near the crack tip were investigated. Figures 5.16 to 5.19 depict the equivalent plastic strain (ε^{p}_{eq}) dis-

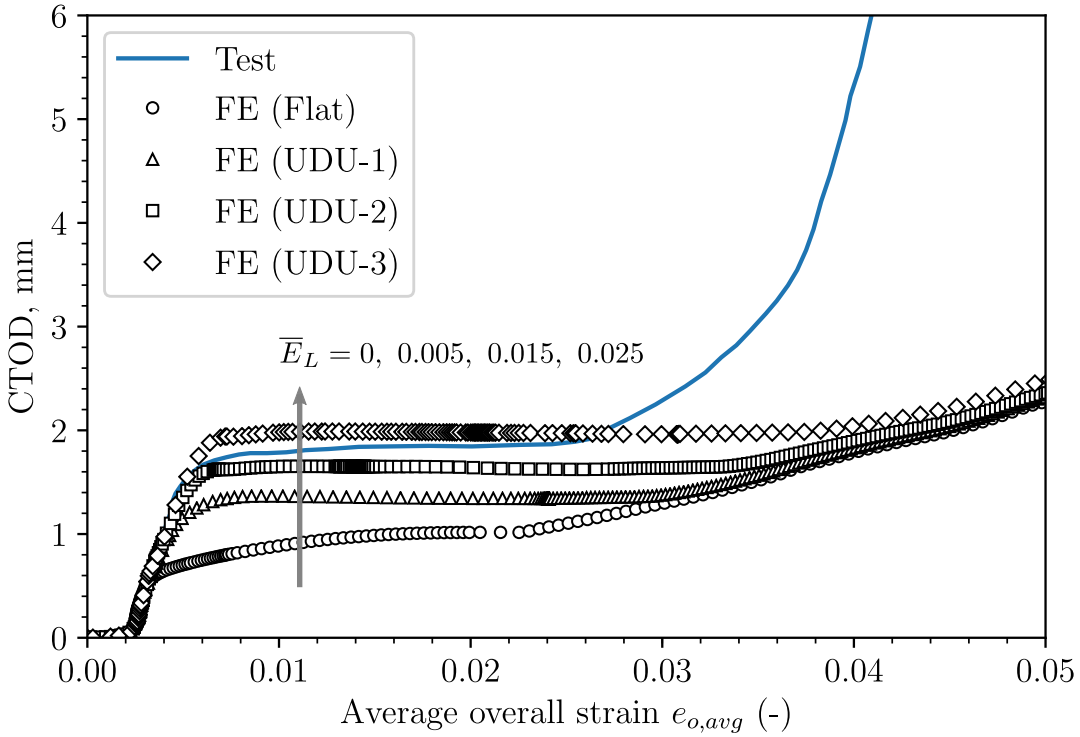

Figure 5.14: Comparison of CTOD for average flaw size 4.6 × 100 mm from full-scale test and FE analyses without consideration of ductile tearing

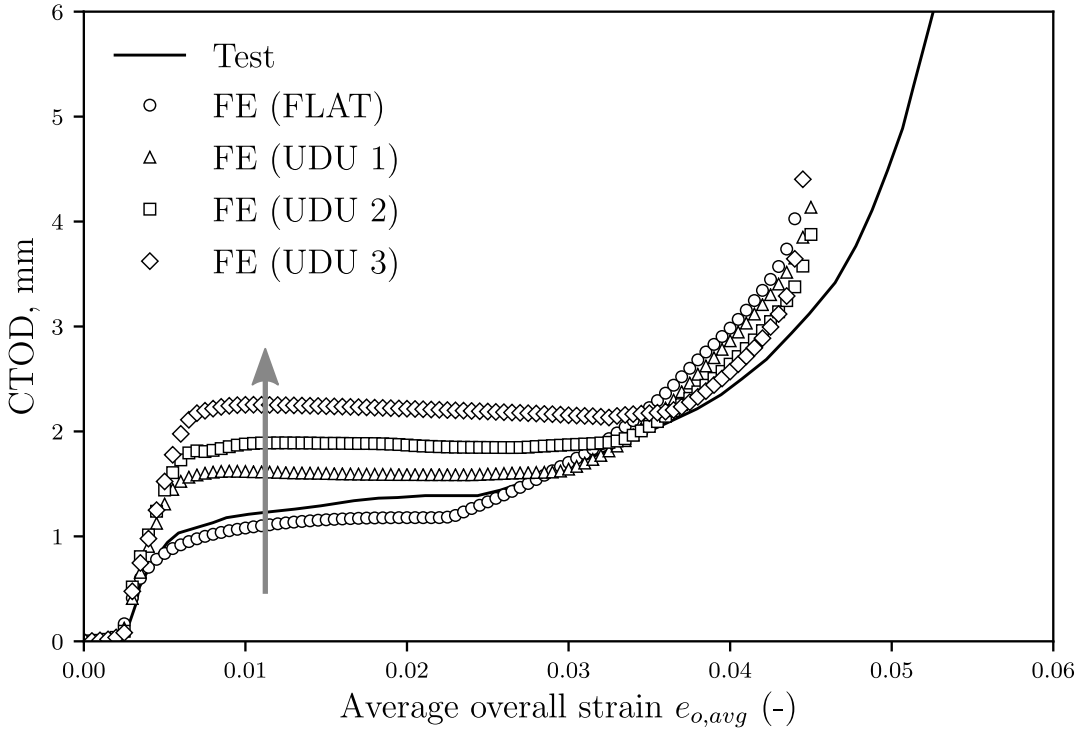

Figure 5.15: Comparison of CTOD for average flaw size 5.68 × 50 mm from full-scale test and FE analyses with consideration of ductile tearing

tributions ahead of the crack tip at the symmetry plane. For $e_{o,avg} = 0.002$ at which the pipe is globally elastic, a small plastic zone is formed near the crack tip. Clearly, the plastic zone of the pipes simulated using a greater $\bar{E}_L$ exhibits a mode localised plastic zone. It is worth noting that the ε^p_{eq} contours of FE models with $\bar{E}_L = 0.015$ and $\bar{E}_L = 0.025$ appear slenderer, more concentrated and branched. As shown in Figure 5.17, the plasticity has spread to the bottom of the pipes, and no pronounced difference is observed in terms of the shape of ε^p_{eq} contours near the crack tip among all pipe models. It can be noted that the distribution of higher plasticity regime (ε^p_{eq} above 0.02) is more widespread when higher $\bar{E}_L$ values are used. On the other hand, the sizes of ε^p_{eq} contours in pipe models using the UDU stress-strain curves remain almost unchanged. The reason is that the plastic bands are still propagating and the crack behaviour remains constant. Nevertheless, the crack will start opening further again after the bands have spread throughout the model.

5.5.5 *Crack tip stress and strain fields*

To understand the crack tip conditions during deformation with different material models, the stress and train fields near the crack tip were examined. Stress and strain components in the near-tip region were extracted based on a local polar coordinate system. Figure 5.20 illustrates the position and orientations of the stress and strain components defined in the local polar coordinate system.

Figures 5.21 and 5.22 present the crack-tip stress and strain fields at global strains (ε^p_{eq}) of 0.002 and 0.01, respectively. The stress components are normalised by a reference stress (denoted by σ_0) equal to the true stress of the upper yield point in the UDU models, and the radial distance is normalised by the CTOD (denoted by δ). The radial stress and strain distributions (i.e. Figure 5.21 (a), (c), (e) and (g))were extracted along the crack tip at $\theta = 0$. The angular stress and strain distributions (i.e. Figure 5.21 (b), (d), (f) and (h)) were extracted away from the crack tip at the normalised radial distance $r/\delta = 2$

From Figures 5.21(a) and 5.22(b), it is found that for $\varepsilon_{o,avg} = 0.002$ a higher E_L results in lower normalised crack opening stresses $\sigma_{\theta\theta}$ and radial stresses σ_{rr} along the ligament in the proximity to the crack tip. The influence of E_L on

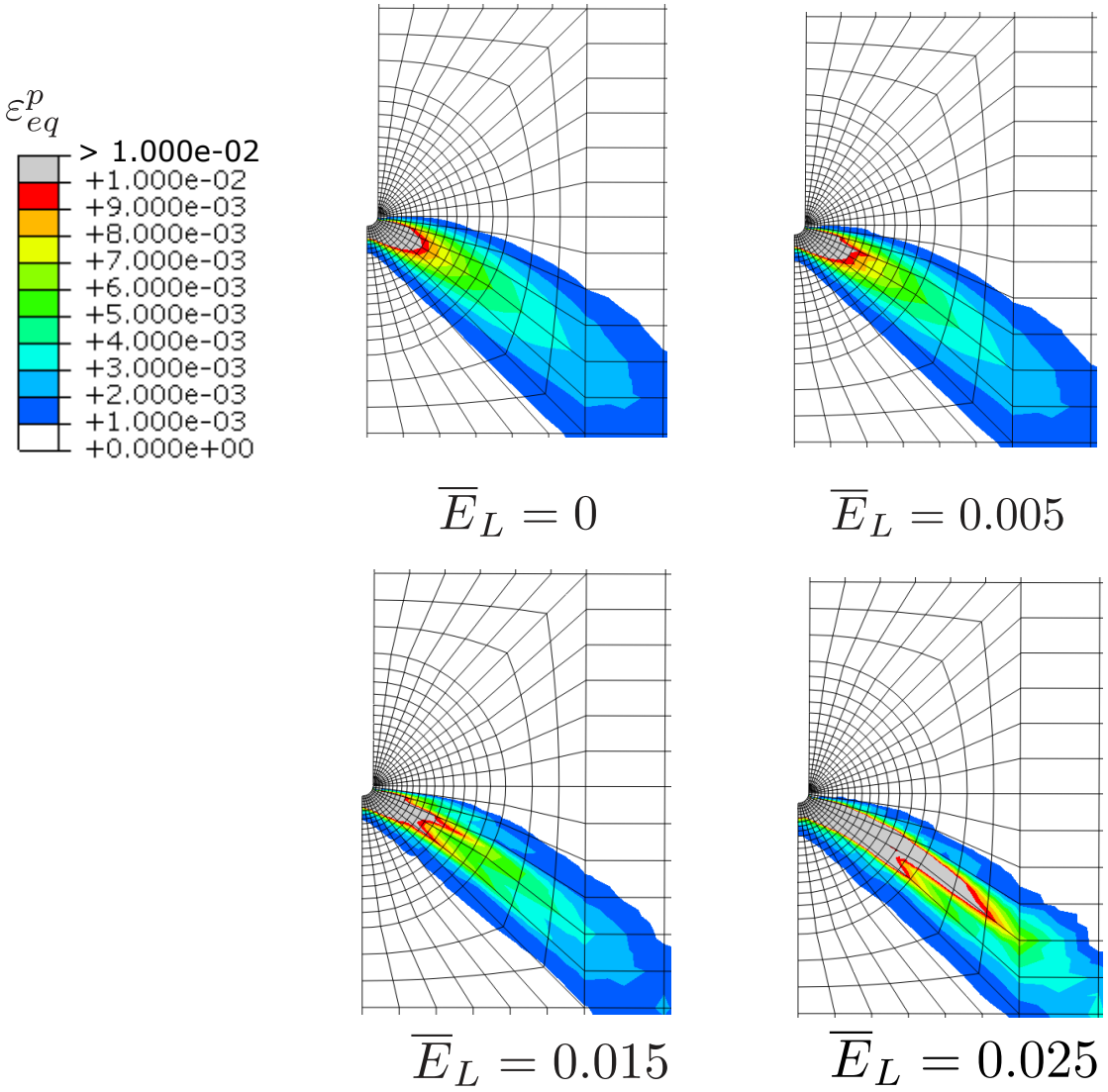

Figure 5.16: Equivalent plastic strain contours in the near-tip region at $e_{o,avg} = 0.002$ from FE analyses using different material models

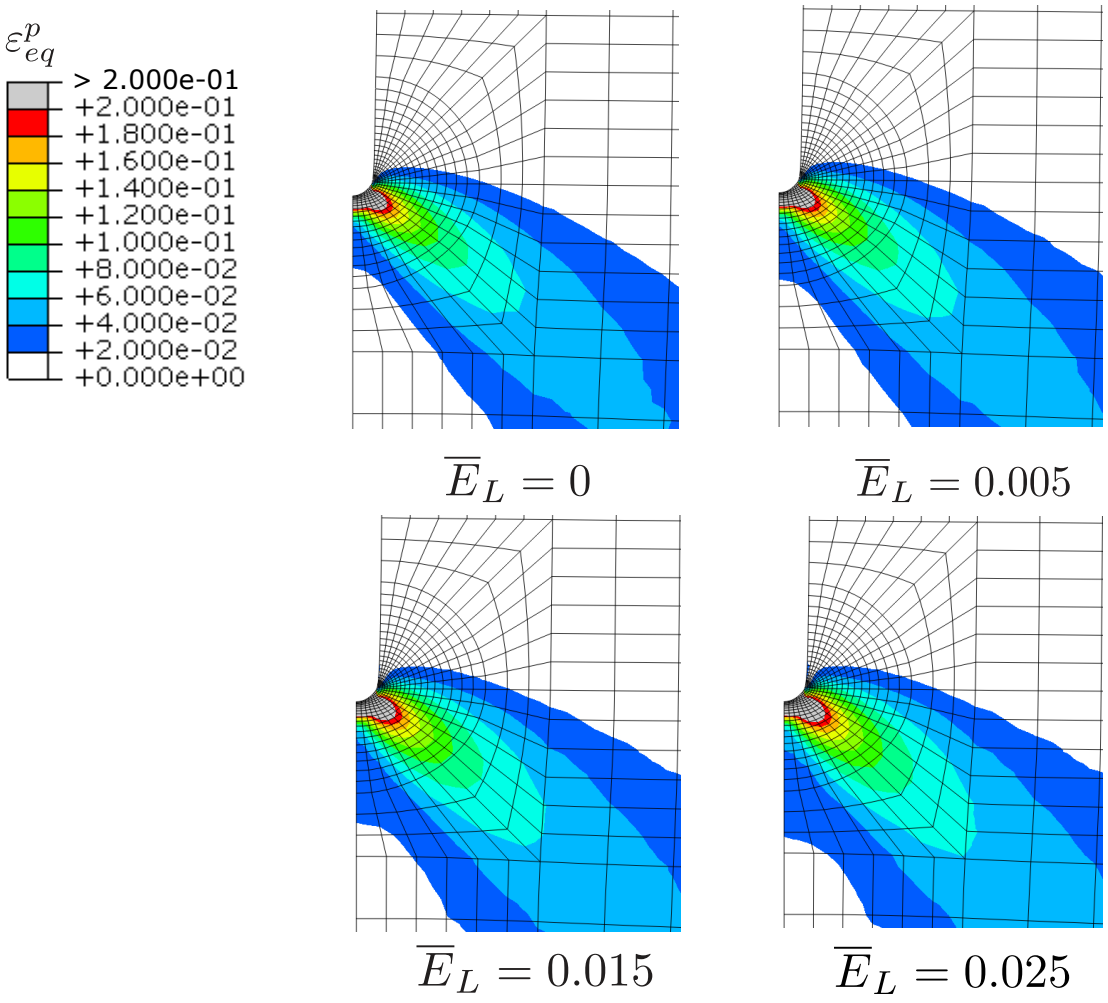

Figure 5.17: Equivalent plastic strain contours in the near-tip region at $e_{o,avg} = 0.003$ from FE analyses using different material models

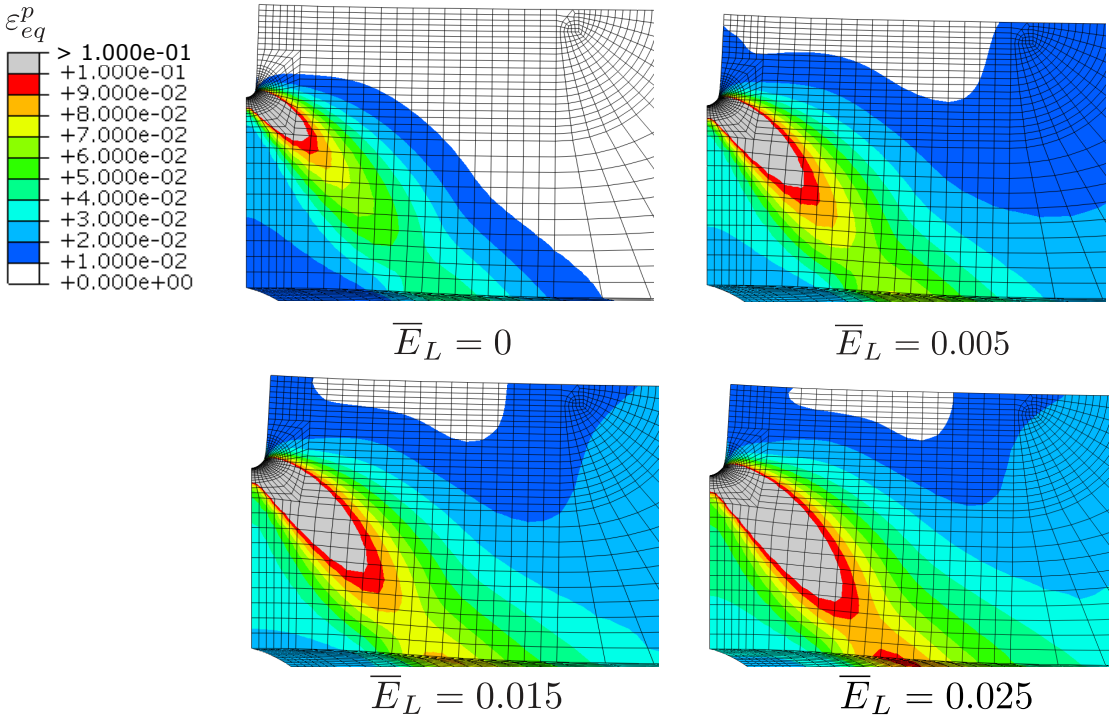

Figure 5.18: Equivalent plastic strain contours in the near-tip region at $e_{o,avg} = 0.01$ from FE analyses using different material models

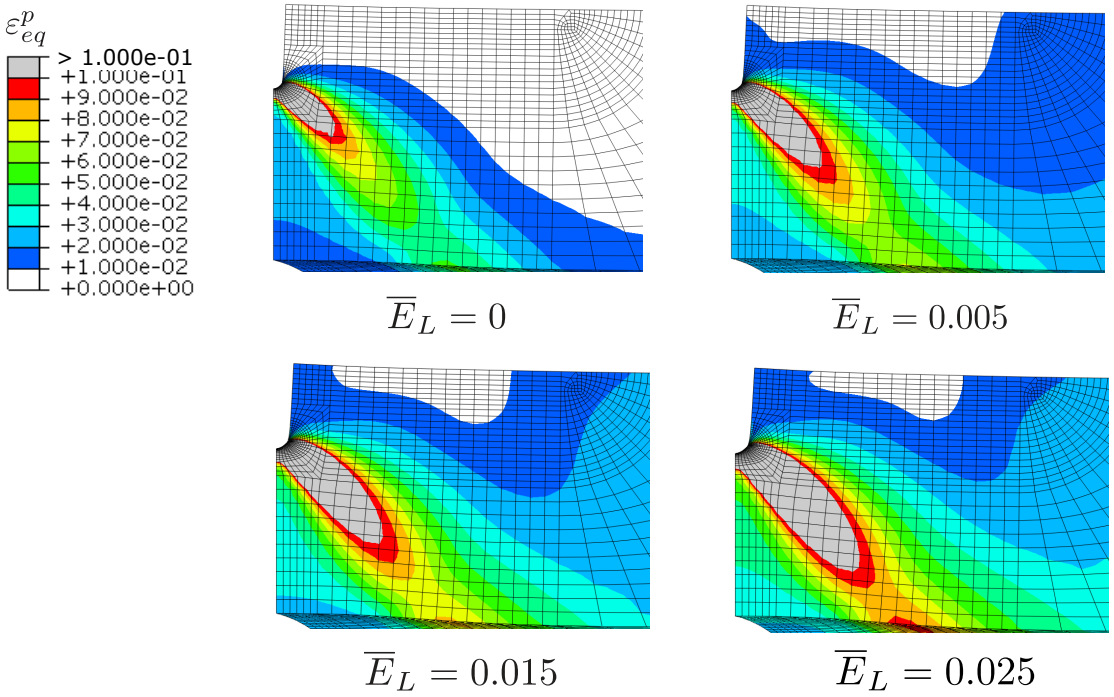

Figure 5.19: Equivalent plastic strain contours in the near-tip region at $e_{o,avg} = 0.02$ from FE analyses using different material models

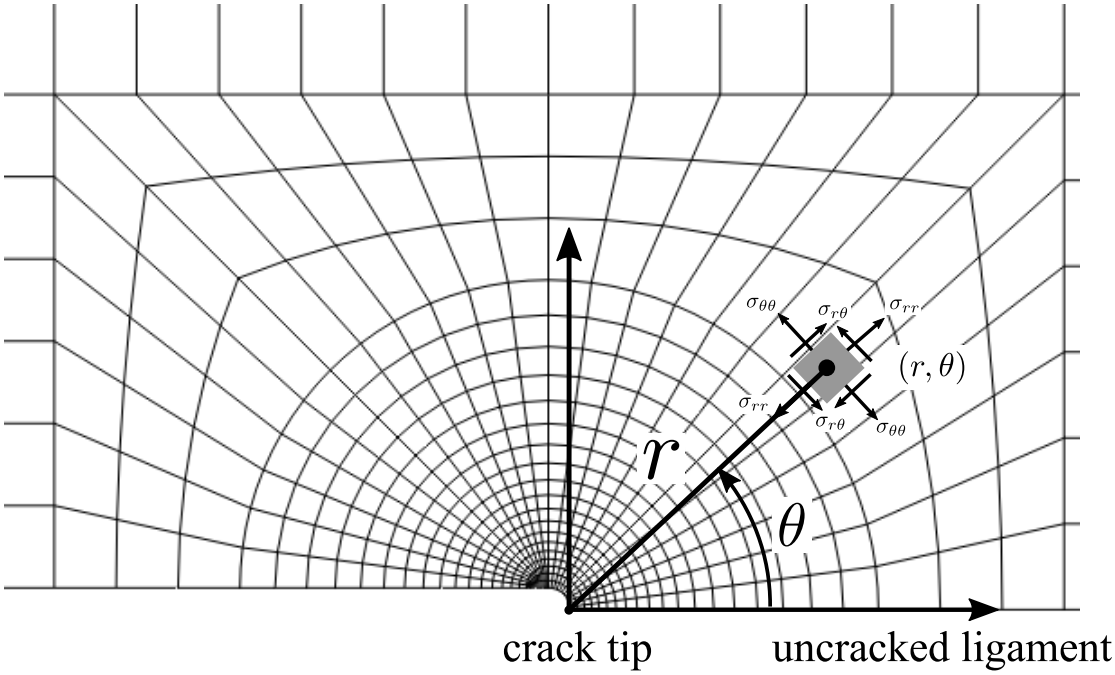

Figure 5.20: Local polar coordinate system defined originating at the crack tip

the angular distribution of stresses was shown to be similar, where a higher E_L results in lower tangential and radial stresses, as shown in Figure 5.21(b) and (d). From (e) and (f) in Figure 5.21, it is shown that an increase in E_L reduces the von Mises stress σ_e in both radial and angular directions. A dip is found in (e) at $r/\delta = 5$, particularly for the UDU model with a higher E_L. It is indicated that the Gauss point at that location is experiencing strain softening associated with Lüders instability. As for the radial distribution of ε^p_{eq} along the ligament, the material models are found to have marginal effect (see Figure 5.21(h)).

For $e_{o,avg} = 0.01$, it is also found that a higher E_L leads to lower radial distribution values of $\sigma_{\theta\theta}$ and σ_{rr}. However, the effect of E_L on the radial distributions of σ_e and ε^p_{eq} appears insignificant in that the Lüders instability has propagated to locations far from the near-tip region. The stress state in the near-tip region has well entered the strain hardening regime where all the material models investigated share the same hardening curve. Nonetheless, some deviations are observed in the angular distribution of σ_e and ε^p_{eq}, as presented in Figure 5.22(f) and (h). A higher E_L is found to produce higher values of ε^p_{eq} along the quarter annulus in the forward sector ahead of the crack tip, which suggests that large plastic deformation occurred in the near-tip region.

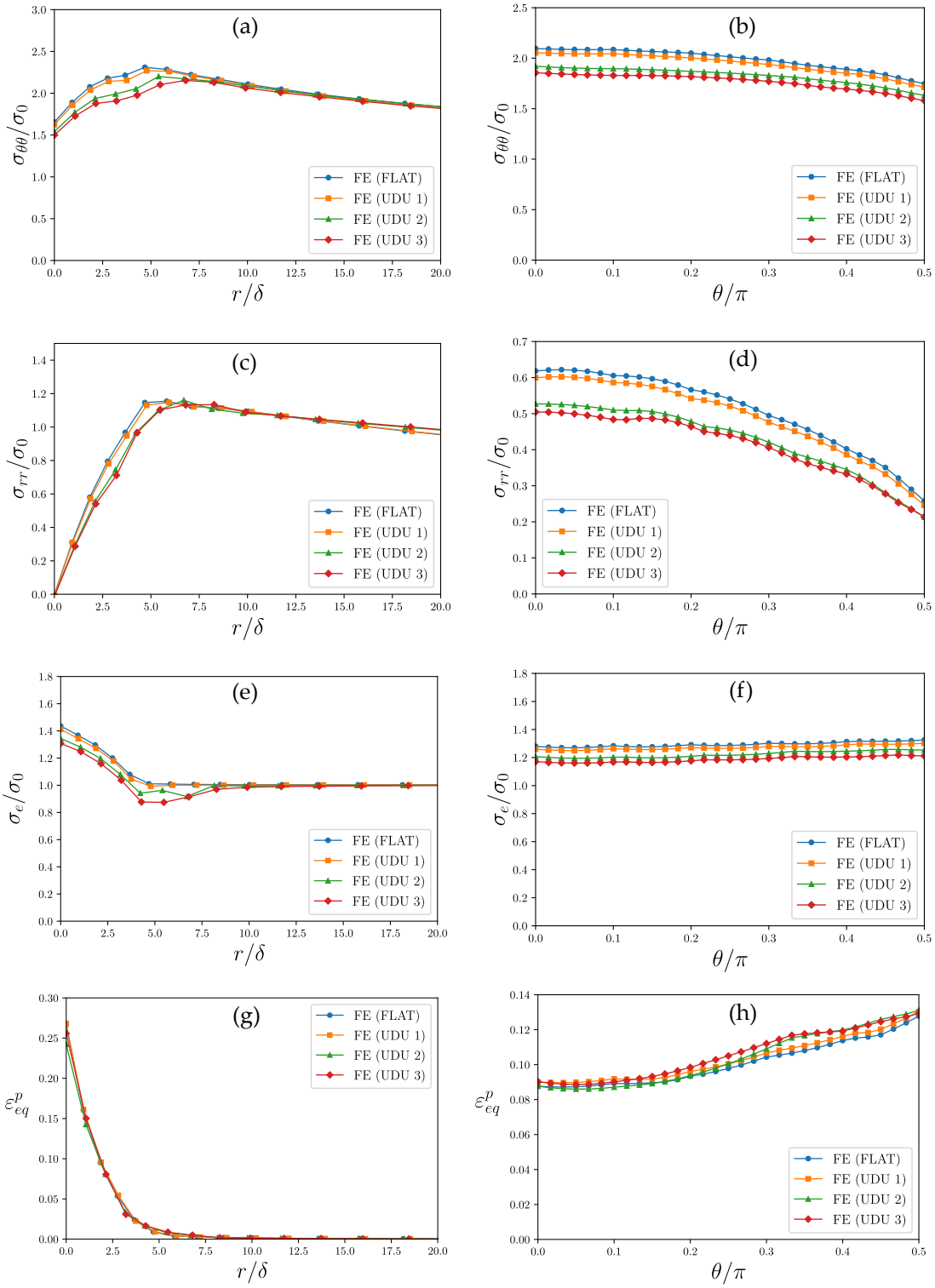

Figure 5.21: Crack-tip fields at $e_{o,avg} = 0.002$: (a) radial distribution of tangential stress component $\sigma_{\theta\theta}$, (c) radial stress component σ_{rr}, (e) von Mises effective stress σ_e and (g) equivalent plastic strain ε^p_{eq} at angle $\theta = 0$; angular distribution of (b) tangential stress component $\sigma_{\theta\theta}$, (d) radial stress component σ_{rr}, (f) von Mises effective stress σ_e and (h) equivalent plastic strain ε^p_{eq} at normalised radial distance $r/\delta = 2$

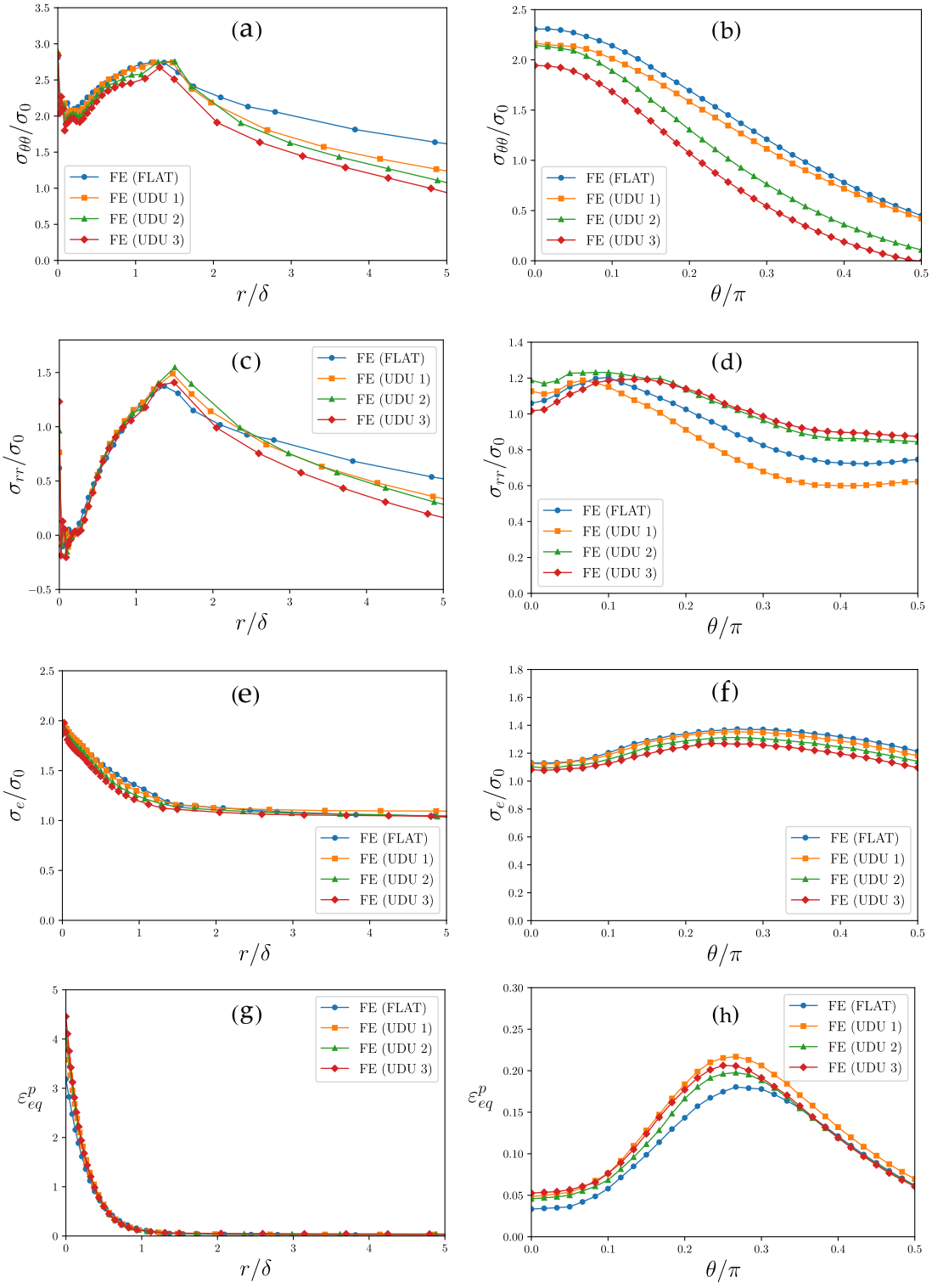

Figure 5.22: Crack-tip fields at $e_{o,avg} = 0.01$: (a) radial distribution of tangential stress component $\sigma_{\theta\theta}$, (c) radial stress component σ_{rr}, (e) von Mises effective stress σ_e and (g) equivalent plastic strain ε^p_{eq} at angle $\theta = 0$; angular distribution of (b) tangential stress component $\sigma_{\theta\theta}$, (d)radial stress component σ_{rr}, (f) von Mises effective stress σ_e and (h) equivalent plastic strain ε^p_{eq} at normalised radial distance $r/\delta = 2$

To investigate the effect of the stress-strain models on the stress triaxiality which is relevant to ductile fracture, the hydrostatic stress and triaxiality parameter ahead of the crack tip are extracted and plotted in Figures 5.23 and 5.24, respectively. The triaxiality parameter h is determined as:

$$h = \frac{\sigma_h}{\sigma_e} \tag{5.5}$$

where $\sigma_h = \sigma_{kk}/3$ is the hydrostatic or mean stress.

From Figures 5.23 and 5.24, it can be seen that at strains $e_{o,avg} = 0.002$ and 0.01, a higher $\bar{E}_L$ value gives a lower hydrostatic stress ahead of the crack tip. The stress triaxiality parameter h, however, exhibits a slight increase with increasing $\bar{E}_L$ at a normalised radial distance around 5, according to Figure 5.24(c). As for the angular distributions, both hydrostatic stress and triaxiality parameter are found to decrease with increaseing $\bar{E}_L$ for both strains $e_{o,avg} = 0.002$ and 0.01.

The above observations suggest that the UDU models with a higher $\bar{E}_L$ predict higher plastic strains but lower hydrostatic stresses and triaxiality parameter. The latter is believed to be relevant to ductile fracture. It is implied that the crack driving force may be affected by $\bar{E}_L$, and therefore use of a Flat model could potentially lead to under-estimation of crack driving force for flawed components made of Lüders-deforming materials.

5.6 DISCUSSION

5.6.1 *Effect of softening modulus on deformation of flawed pipes*

It is clear from Figures 5.10 to 5.19 and 5.21 to 5.24 that softening modulus has a noticeable effect on the evolution of plasticity, the crack-tip stress field and the crack driving force of the FE model of a cracked pipe. The strain softening, or a negative tangent stiffness ($\partial s/\partial e$) in the stress-strain curve is shown to be required to produce strain localisation associated with Lüders-type deformation. This was noted by (Shaw and Kyriakides 1997) during the simulation of the strain localisation in NiTi strips subjected to tensile loading. Therefore, it is indicated that the softening modulus plays an significant role in the occurrence of Lüders-type deformation of the cracked pipe model.

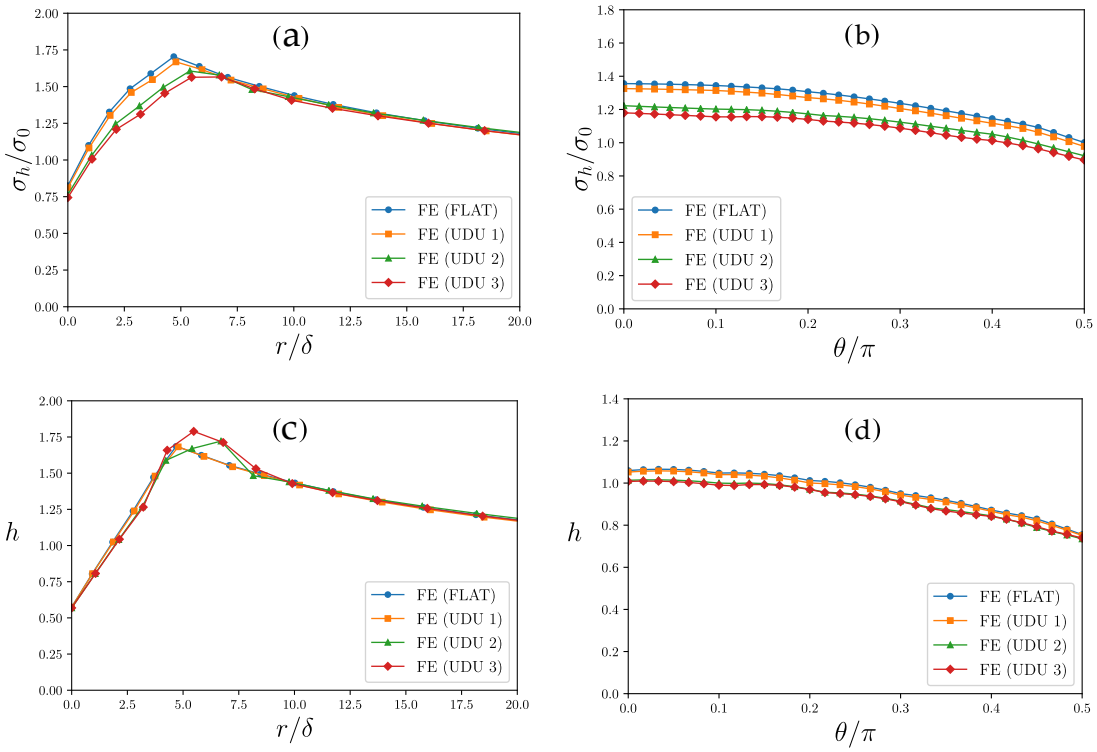

Figure 5.23: Crack-tip fields at $e_{o,avg} = 0.002$: Radial distribution of (a) hydrostatic stress, (b) triaxiality parameter; Angular distribution of (c) hydrostatic stress, (d) triaxiality parameter; at normalised radial distance $r/\delta = 2$

To further describe the effect of material laws on the produced band pattern in FEA, the images of the simulated bands at a certain strain level ($e_{o,avg} = 0.015$) were captured and shown in Figure 5.25. With higher value of $\bar{E}_L$, the nearly generated Lüders bands are found to appear sharper with a narrower band width. The propagating bands at the edge of the pipe using UDU-2 and UDU-3 material laws are observed to have a criss-cross or "fish-bone" pattern, which resembles that reported by Kyriakides et al. (2008), Aguirre et al. (2004), and Hallai and Kyriakides (2011b). For the model using UDU-1, a diffuse band front is observed, propagating from the uncracked end towards the other.

In the analysis of bent pipes/tubes in the presence of Lüders plateau (Aguirre et al. 2004; Kyriakides et al. 2008; Hallai and Kyriakides 2011b), the value of $\bar{E}_L$ seemed to have marginal effect on the global behaviour in terms of moment-rotation response when the selected $\bar{E}_L$ sufficed to simulate the localisation bands. As for the global behaviour of the uni-axial tensile strips, however, a noticeable deviations in the Lüders plateau phase was observed for various $\bar{E}_L$ adopted (Wang et al. 2017). It was found that a higher value of $\bar{E}_L$ leads to a greater magnitude of the stress plateau, which supports the effect of material

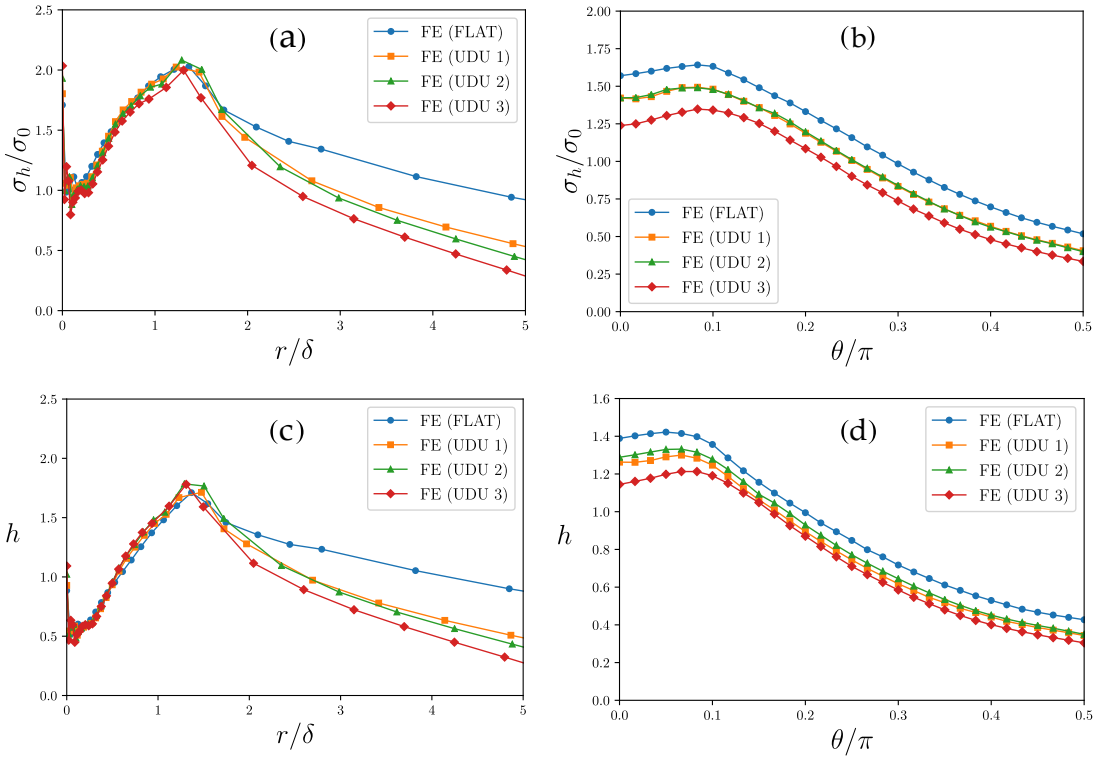

Figure 5.24: Crack-tip fields at $e_{o,avg} = 0.01$: Radial distribution of (a) hydrostatic stress, (b) triaxiality parameter; Angular distribution of (c) hydrostatic stress, (d) triaxiality parameter; at normalised radial distance $r/\delta = 2$

laws on the crack driving force reported in the current chapter. The effect of $\bar{E}_L$ on the crack driving force, in terms of CTOD versus strain response, seems more prominent than the global response of the pipe. A higher value of $\bar{E}_L$ results in stronger strain localisation, which in turn promotes the opening of crack. In addition, a higher $\bar{E}_L$ used in FEA also predicts a greater decrease in the crack opening stresses, therefore indicating a more significant loss of constraint ahead of the crack tip.

Hence, the parameters of the UDU material law, namely the softening modulus and the stress difference Δs, may need to be properly selected based on tensile testing programmes to yield appropriately conservative results in fracture assessment of cracked components.

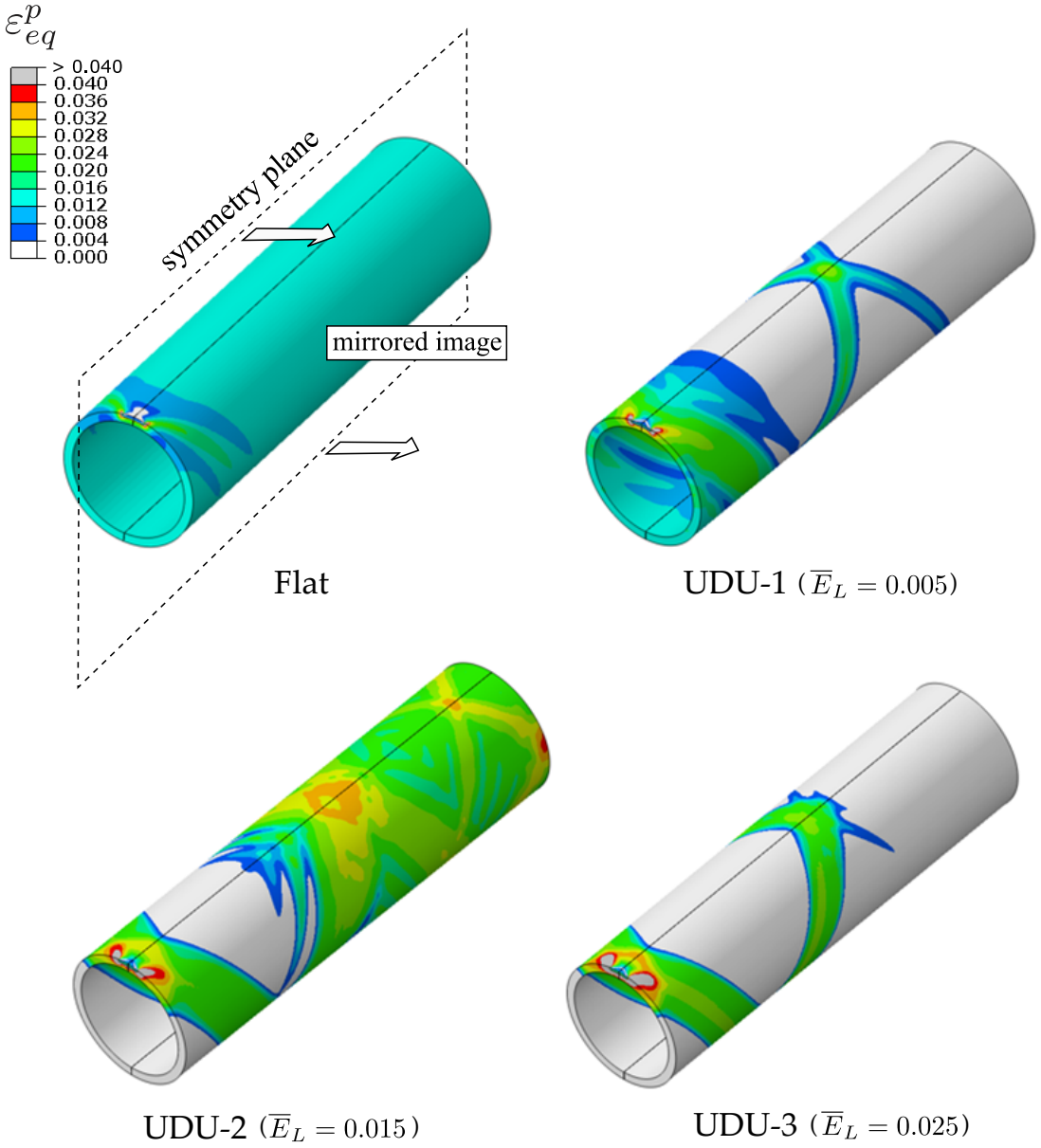

Figure 5.25: Illustration of Lüders band pattern simulated using different material laws

5.6.2 *Application of the UDU material law in fracture analysis of pipes containing crack-like flaws*

In this chapter, we have shown the efficacy of the UDU material law in the numerical analysis of cracked pipes in the presence of Lüders plateau. The UDU material law requires a number of FE analyses of the uni-axial tensile tests to be carried out. Then the softening modulus is fine-tuned based on the comparison of the numerically calculated global stress-strain behaviour against the experimentally measured one. Then the calibrated UDU material response is utilised in the FE analysis of components containing flaws.

Alternatively, a type of sandwich specimen described in Hallai and Kyriakides (2013) can be used to extract the underlying or real stress-strain response of the Lüders-deforming material. This type of specimen contains a strip of the discontinuously yielding material to be tested, sandwiched by two pieces of continuously yielding strips. The two strips of continuously yielding material are stiff enough to suppress the localised deformation of the material to be tested, forcing it to deform uniformly. Thus, the total stress-strain behaviour can be measured and the response of Lüders material can be derived by subtracting that of the continuously yielding material from the total response.

5.7 SUMMARY

In this chapter, an in-depth analysis of the fracture response of a seamless API X65 pipe containing a circumferential external surface flaw in the presence of Lüders plateau. In the simulation of Lüders behaviour using the UDU material law, it is shown that the softening modulus has a pronounced effect on the global response, Lüders band formation and propagation, and the crack-tip stress/strain fields in a cracked pipe. Based on the analysis and results reported in this chapter, the key findings are:

- An appropriate simulation approach of cracked pipes was demonstrated with the use of the UDU stress-strain model, featuring a segment of strain softening in the stress-strain curve used. This is presumed to have provided implications to the current codes and standards in the treatment of Lüders behaviour in the assessment of pipeline integrity.

- The stress-strain curve with a flat stress plateau is not capable of reproducing the strain localisation associated with Lüders bands in the pipes containing crack-like flaws. The UDU model containing a segment of strain softening, on the other hand, is shown to appropriately capture Lüders banding behaviour in a pipe containing a crack.
- The inclusion of strain softening in the stress-strain curve, such as the UDU material law, is shown capable of predicting a crack driving force that closely replicates that measured in a full-scale pipe test, with an appropriate level of conservatism (provided the effect of ductile tearing is incorporated in the analysis).
- The crack driving force is highly sensitive to the softening modulus adopted in the FE analysis. Therefore, the value of $\bar{E}_L$ should be carefully determined through tensile testing programmes in order to predict conservative crack driving force with a suitable level of conservatism.

6

NUMERICAL ANALYSIS OF X65 PIPES CONTAINING FLAWS SUBJECTED TO AXIAL PLASTIC STRAINING AND INTERNAL PRESSURE WITH LÜDERS PLATEAU

6.1 INTRODUCTION

Oil and gas pipeline in service are subjected to both axial straining imposed by geophysical events, and internal pressure due to the containment of the hydrocarbons. The pipe wall is subjected to combined tensile stress and hoop stress due to the internal pressure, resulting in a biaxial loading condition. Stress biaxiality changes the stress state in the yield surface, according to von Mises yielding criterion, and thus may alternate the yielding behaviour and Lüders band propagation. In this chapter, parametric FE analyses were performed to investigate the effect of internal pressure or biaxial loading on the development of Lüders banding as well as the crack-tip behaviour.

6.2 PARAMETRIC FE ANALYSIS

6.2.1 *Summary of FEA cases*

Table 6.1 shows the details of the parametric FEA, covering various flaw sizes and internal pressure levels. Since it is shown in Chapter 5 that the UDU stress-strain model with softening modulus $\bar{E}_L = 0.015$ outperforms other material models in terms of CDF prediction and simulation of Lüders banding behaviour. Hence, the same material model was adopted in the parametric FEA herein. As shown in Table 6.1, the flaw height (a) ranges from 3 to 7 mm and flaw length (2c) ranges from 10 to 100 mm (depending on the specific value of a

investigated), which are representative of the flaws in oil and gas pipelines. The internal pressure, in terms of hoop stress to yield stress ratio (σ_{hoop}/σ_y), ranges from 0 to 80%, covering both installation and operation conditions.

Table 6.1: FEA cases covering various flaw sizes and internal pressure levels

Flaw height a, mm	Flaw length 2c, mm	Internal Pressure (σ_{hoop}/σ_y)
3	10, 25, 50, 75, 100	0, 0.2, 0.5, 0.8
5	25, 50, 75, 100	
7	25, 50, 75, 100	

The FE models have a similar mesh configuration to that of the pipe models subjected to axial straining only reported in Chapter 5. The boundary conditions, however, were adjusted to closely replicate those imposed in the full-scale test reported in Pisarski et al. (2014). As shown in Figure 6.1, the simulation comprises two loading steps. In the first loading step (Loading Step 1), internal pressure is applied to the internal surface of the pipe while both the cracked end and uncracked end were fixed in the axial direction (same as the FE simulation reported in Chapter 5, the cracked end was fixed in axial direction due to symmetry boundary conditions). In the second loading step (Loading Step 2), while the internal pressure was maintained, the pipe was loaded in axial tension by applying a prescribed displacement to the nodes situated at the uncracked end. Same as the FE model in Chapter 5, the bottom node at the uncracked end was not permitted to translate vertically in order to prevent possible rigid body motion.

6.2.2 *Results*

6.2.2.1 *Global stress-strain response*

Figures 6.2 to 6.10 show the global stress-strain responses for all FE pipe models with various levels of internal pressure. Based on the global stress-strain behaviours for all flaw sizes, it is found that the internal pressure generally increases the axial stress over full strain range, particularly in the range after yield. The increase in stress is seen to be most prominent from axial straining only ($\sigma_{hoop}/\sigma_y = 0$) to combined axial straining and internal pressure

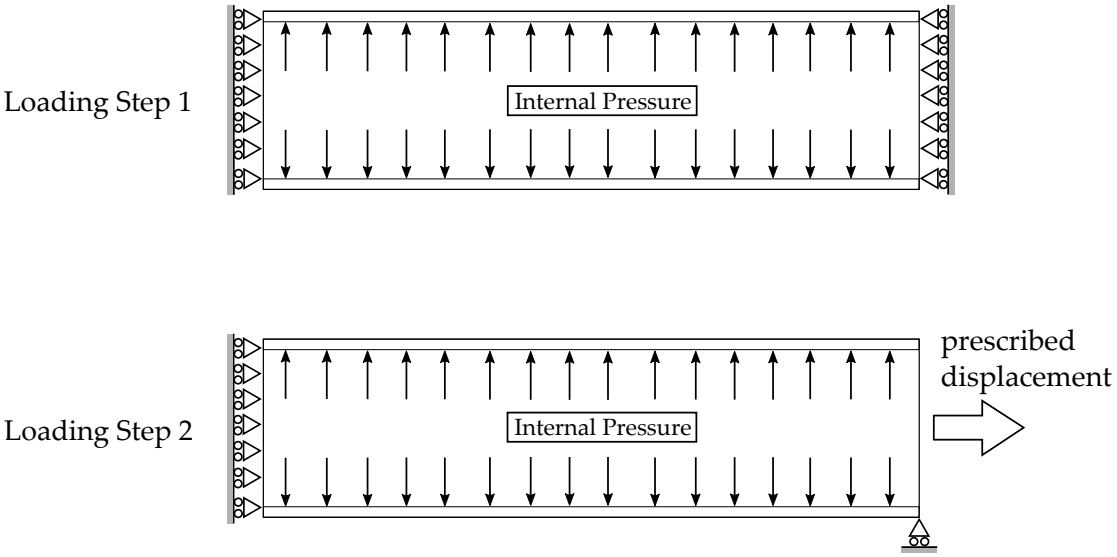

Figure 6.1: Schematic illustrating the loading steps in the FEA of cracked pipes subjected to axial straining and internal pressure

($\sigma_{hoop}/\sigma_y = 0$). From $\sigma_{hoop}/\sigma_y = 0.2$ to 0.5, the increase is found to be modest, and even slightly reduced from $\sigma_{hoop}/\sigma_y = 0.5$ to 0.8. This phenomenon can be explained by the von Mises yielding criterion and is elaborated in Section 6.3.

The effect of the internal pressure on the level of stress plateau is found in line with that on the axial stress levels. The length of the stress plateau, interestingly, is found to decrease as σ_{hoop}/σ_y increases. The reduction in the length of stress plateau is found slightest from $\sigma_{hoop}/\sigma_y = 0.5$ to 0.8.

6.2.2.2 *Crack driving force*

Figures 6.15 to 6.27 show the effect of internal pressure on the crack driving force (in terms of CTOD) for each flaw size. For the pipe with the same flaw sizes, a higher level of internal pressure is shown to result in a shorter CTOD plateau, which is aligned with the global responses reported in Section 6.2.2.1 in which the global stress plateau is found to be shorter for cases with a higher internal pressure level. As for the level of CTOD plateau, the CTOD plateau is not necessarily higher for greater internal pressure levels, and rather, interestingly, for cases with σ_{hoop} /sigma$_y$ of 0.5 and 0.8 has a lower height than those with $\sigma_{hoop}/\sigma_y = 0.2$ and those subjected to axial straining only. This may be due to the strain energy dissipated over the stress plateau, which for $\sigma_{hoop}/\sigma_y = 0.5$ and 0.8 is lower than that for $\sigma_{hoop}/\sigma_y = 0.2$, thus leading to less

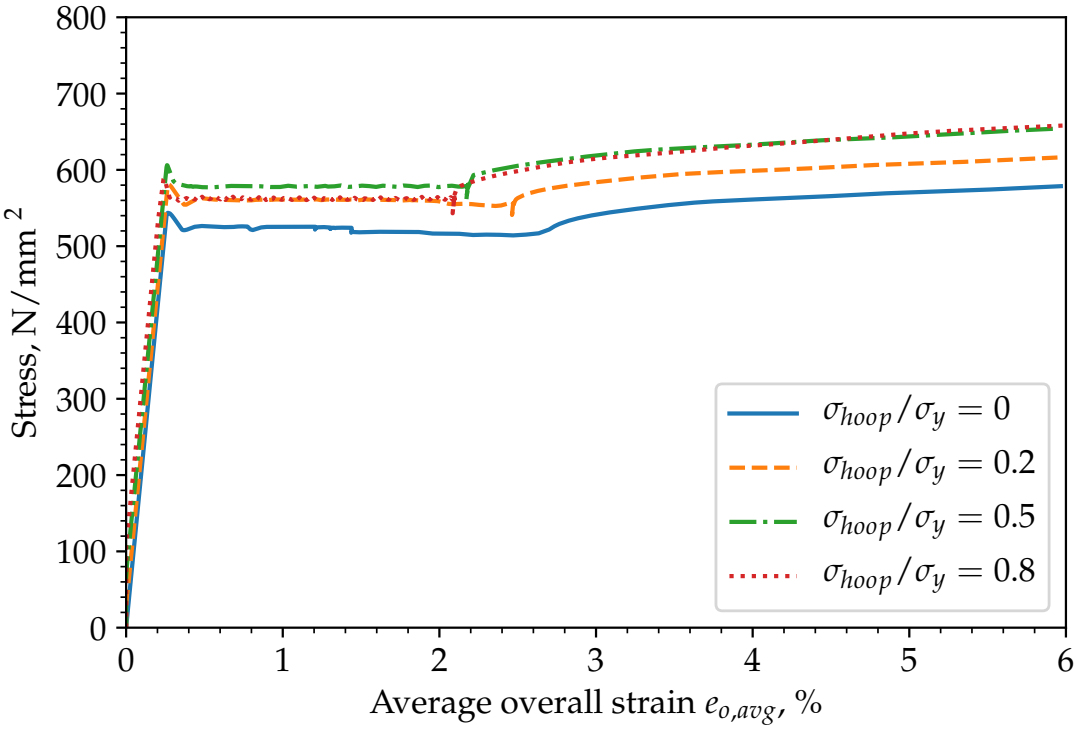

Figure 6.2: Global stress-strain response of FE pipe models with 3 × 10 mm circumferential flaw with various levels of internal pressure

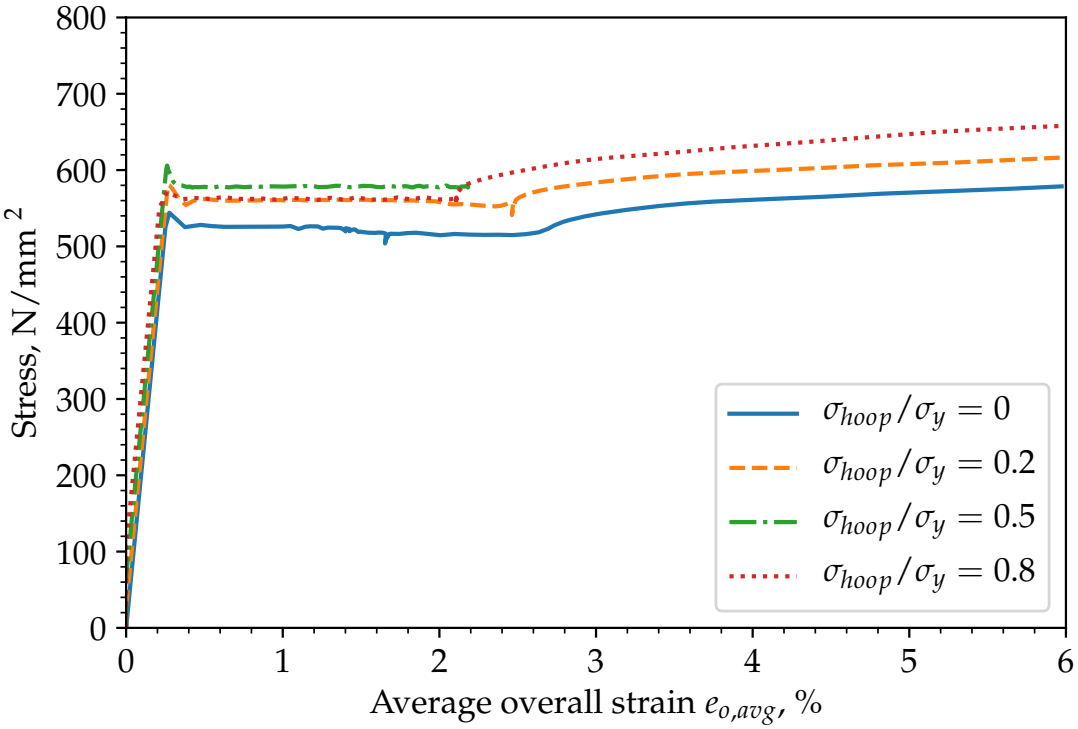

Figure 6.3: Global stress-strain response of FE pipe models with 3 × 25 mm circumferential flaw with various levels of internal pressure

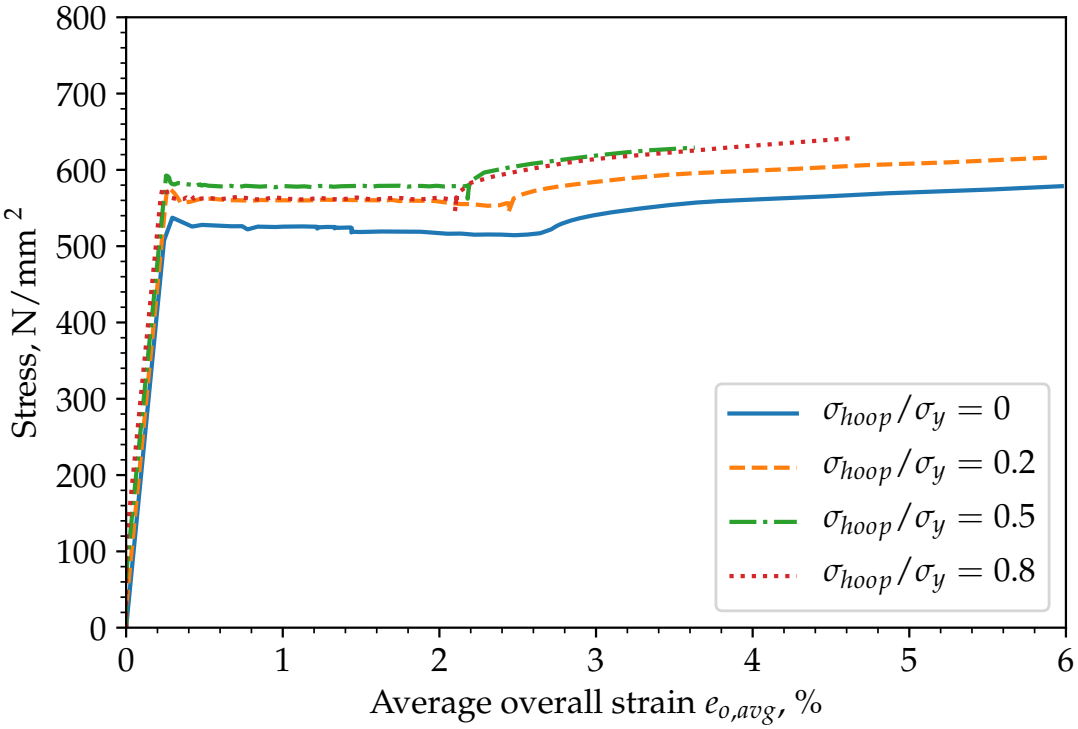

Figure 6.4: Global stress-strain response of FE pipe models with 3×50 mm circumferential flaw with various levels of internal pressure

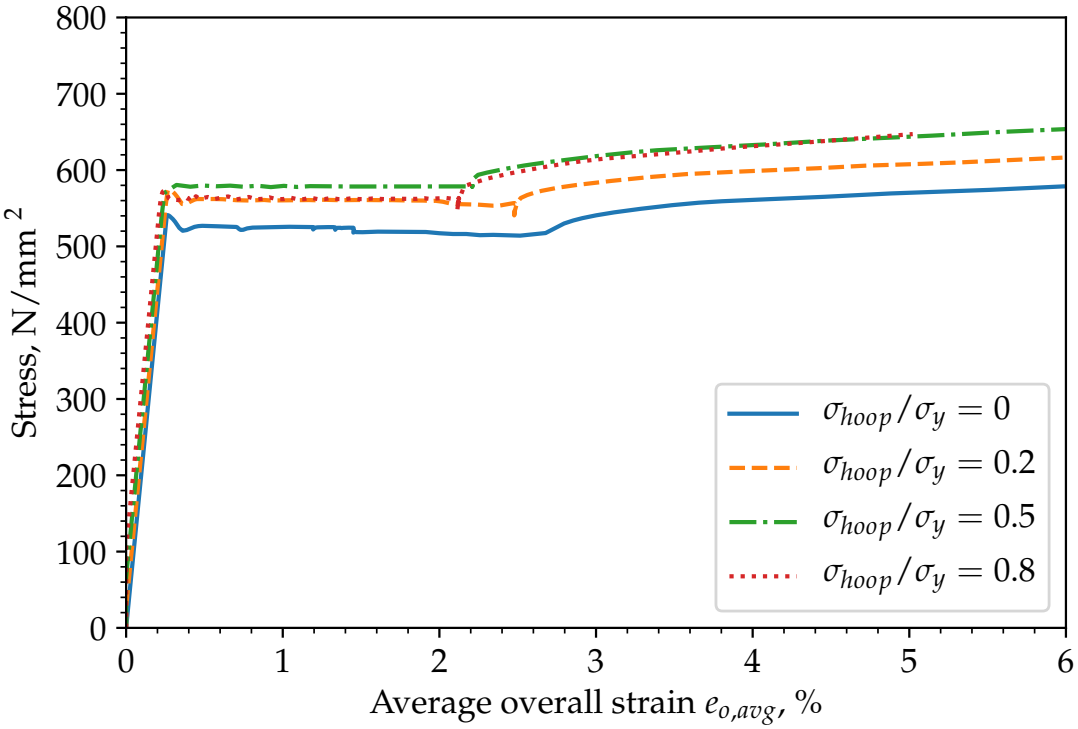

Figure 6.5: Global stress-strain response of FE pipe models with 3×75 mm circumferential flaw with various levels of internal pressure

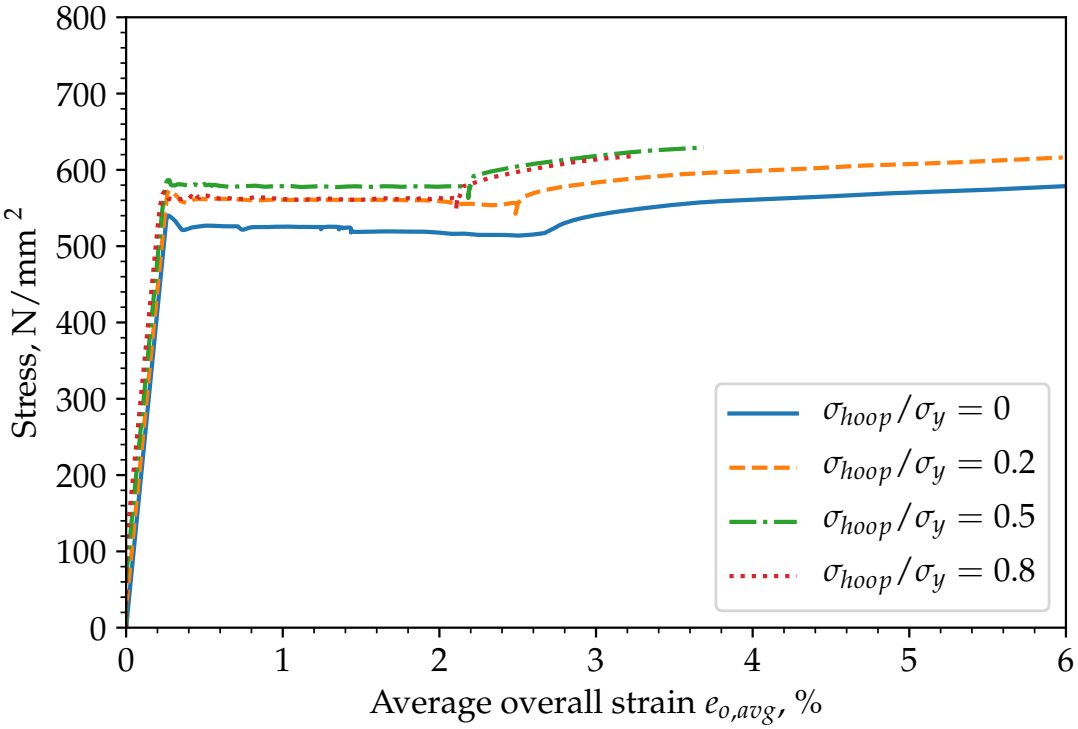

Figure 6.6: Global stress-strain response of FE pipe models with 3 × 100 mm circumferential flaw with various levels of internal pressure

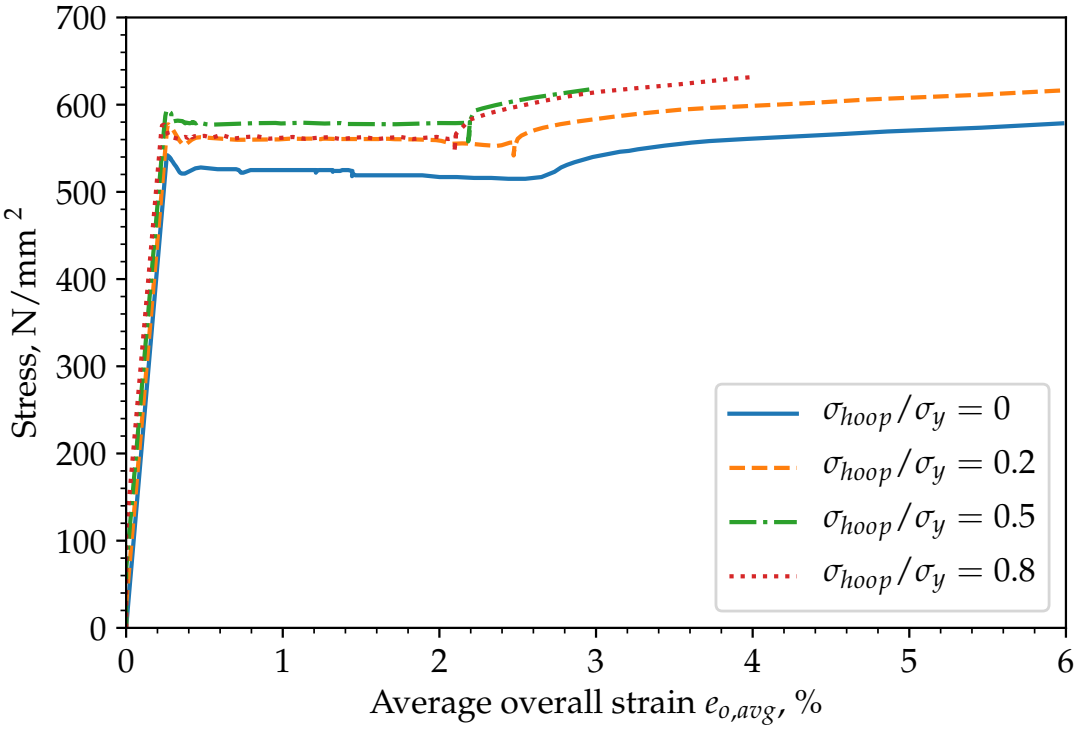

Figure 6.7: Global stress-strain response of FE pipe models with 5 × 25 mm circumferential flaw with various levels of internal pressure

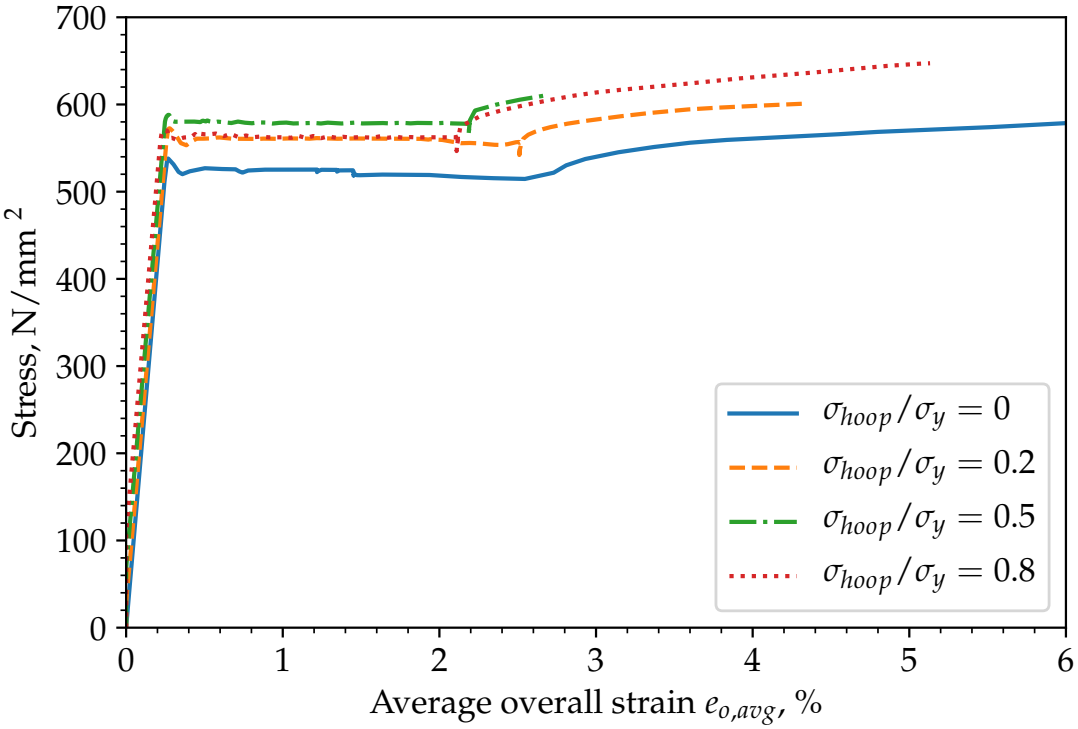

Figure 6.8: Global stress-strain response of FE pipe models with 5 × 50 mm circumferential flaw with various levels of internal pressure

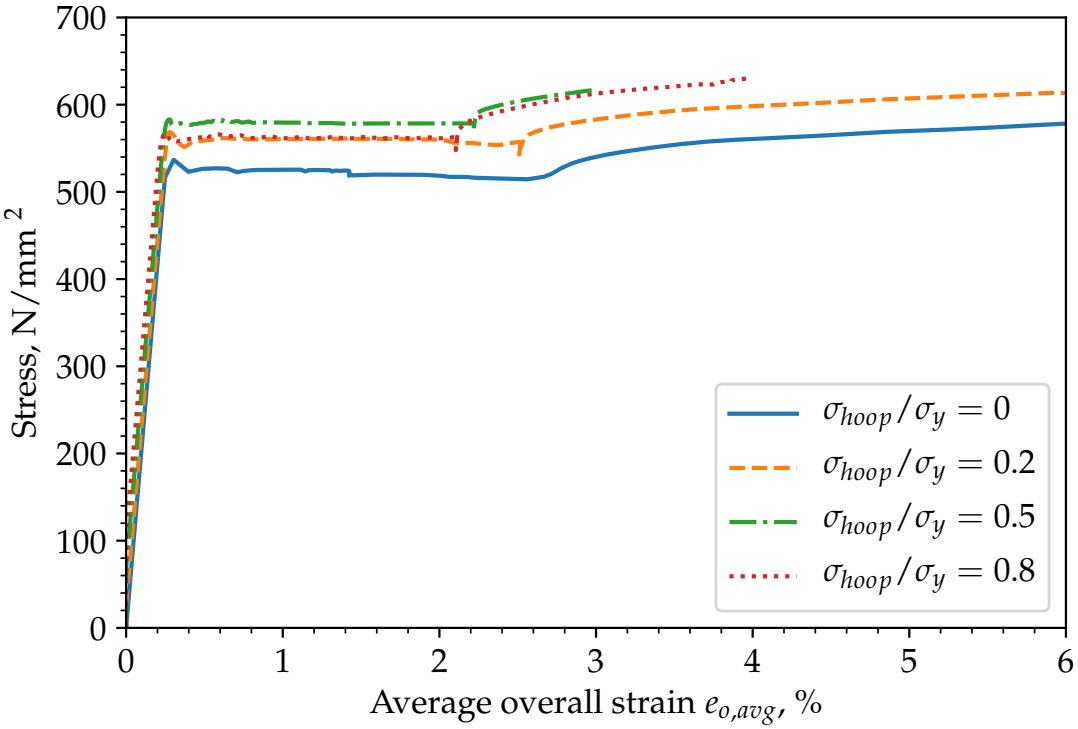

Figure 6.9: Global stress-strain response of FE pipe models with 5 × 75 mm circumferential flaw with various levels of internal pressure

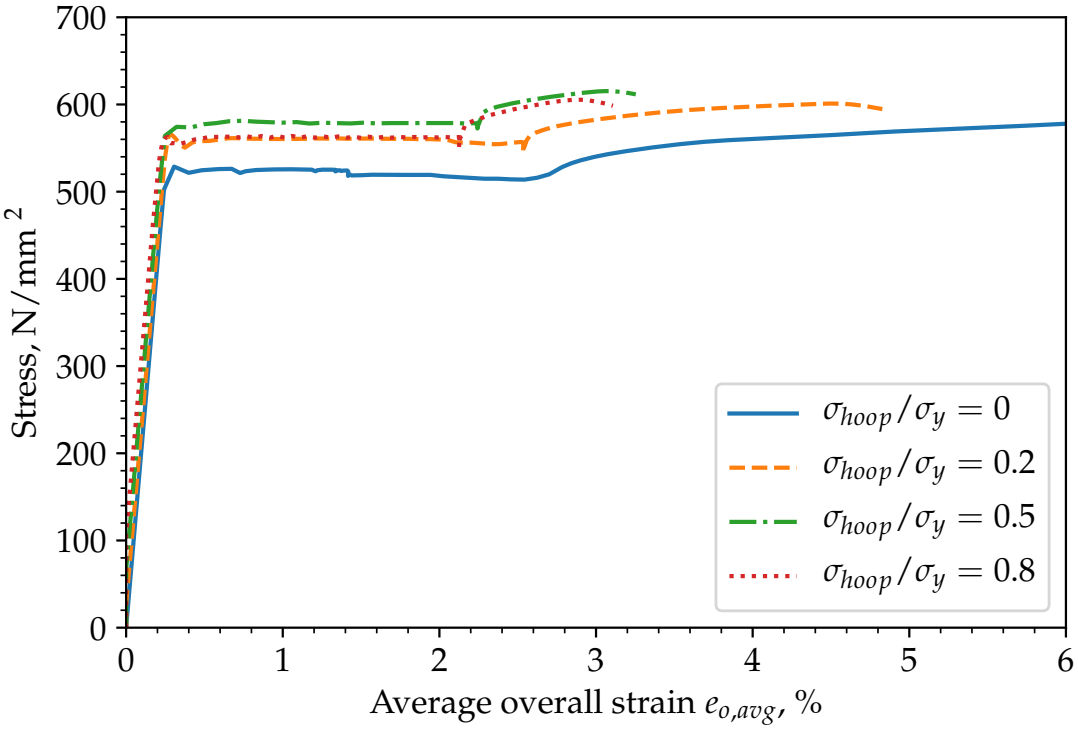

Figure 6.10: Global stress-strain response of FE pipe models with 5 × 100 mm circumferential flaw with various levels of internal pressure

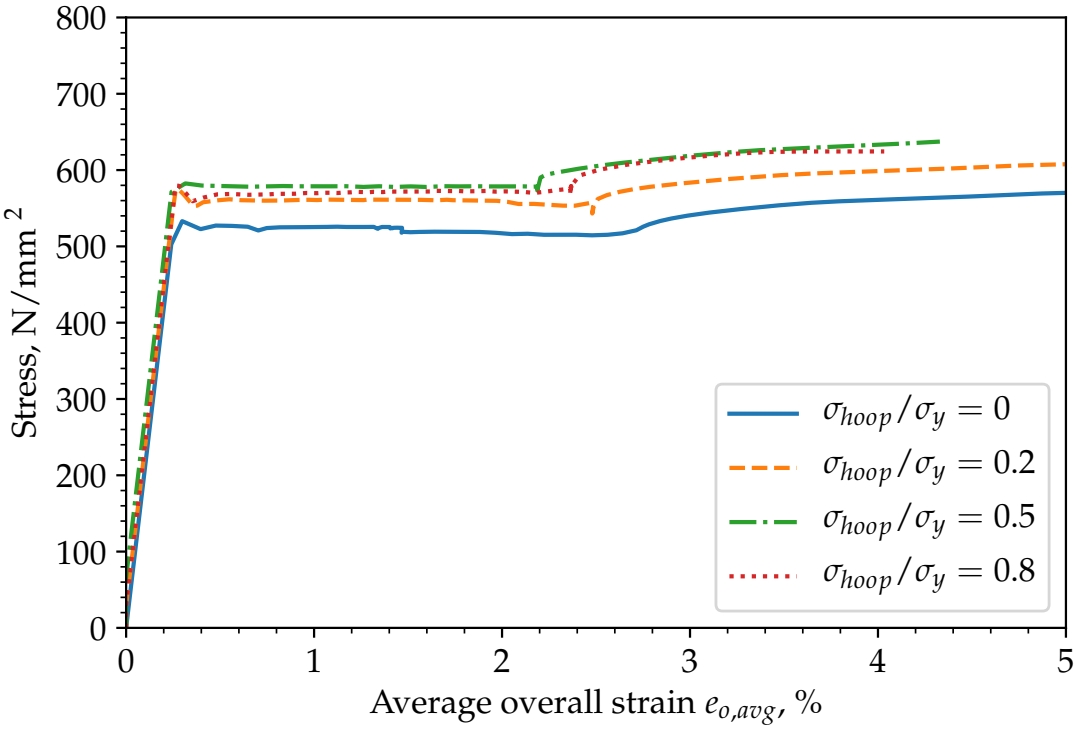

Figure 6.11: Global stress-strain response of FE pipe models with 7 × 25 mm circumferential flaw with various levels of internal pressure

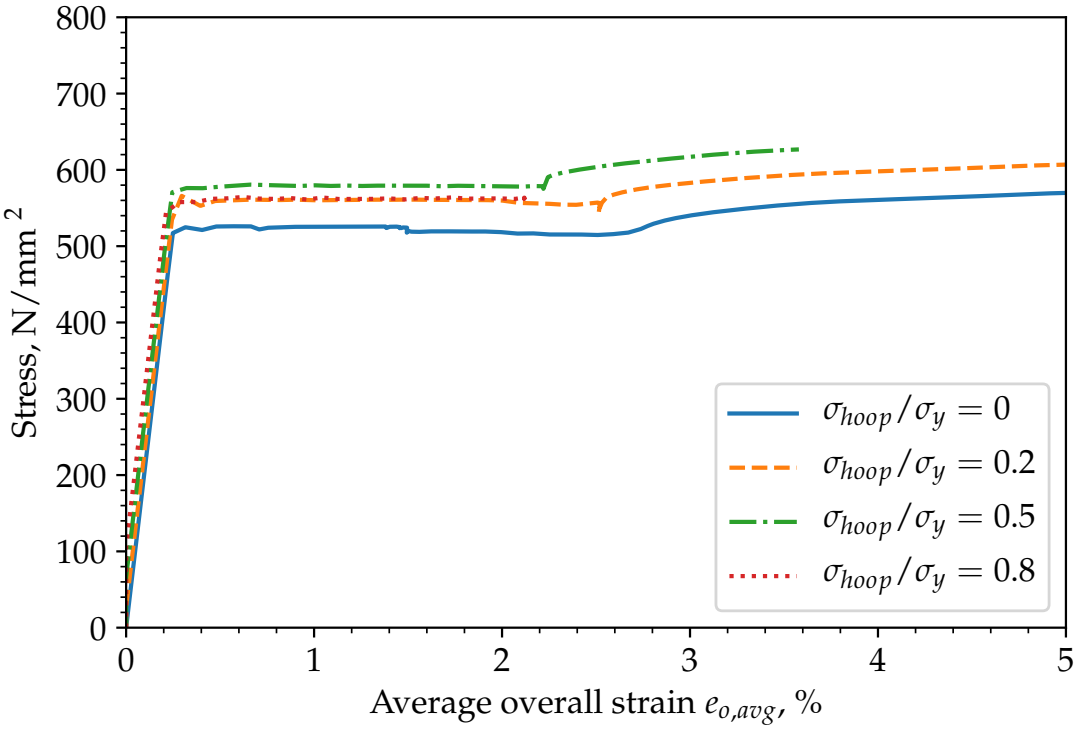

Figure 6.12: Global stress-strain response of FE pipe models with 7 × 50 mm circumferential flaw with various levels of internal pressure

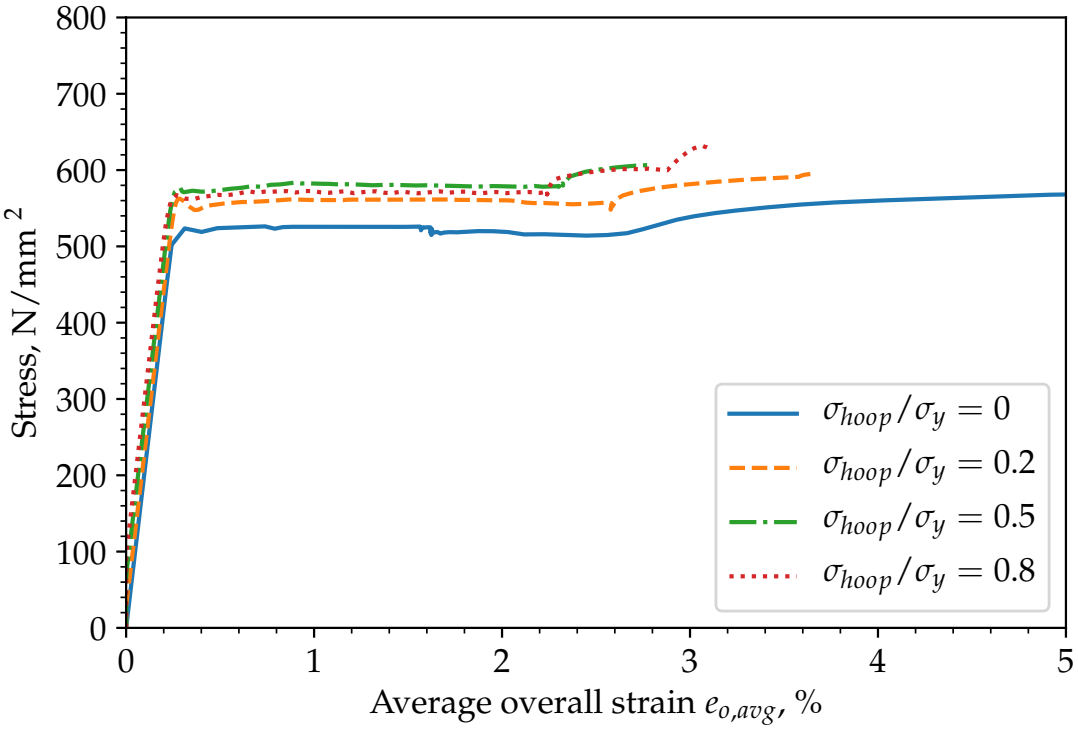

Figure 6.13: Global stress-strain response of FE pipe models with 7 × 75 mm circumferential flaw with various levels of internal pressure

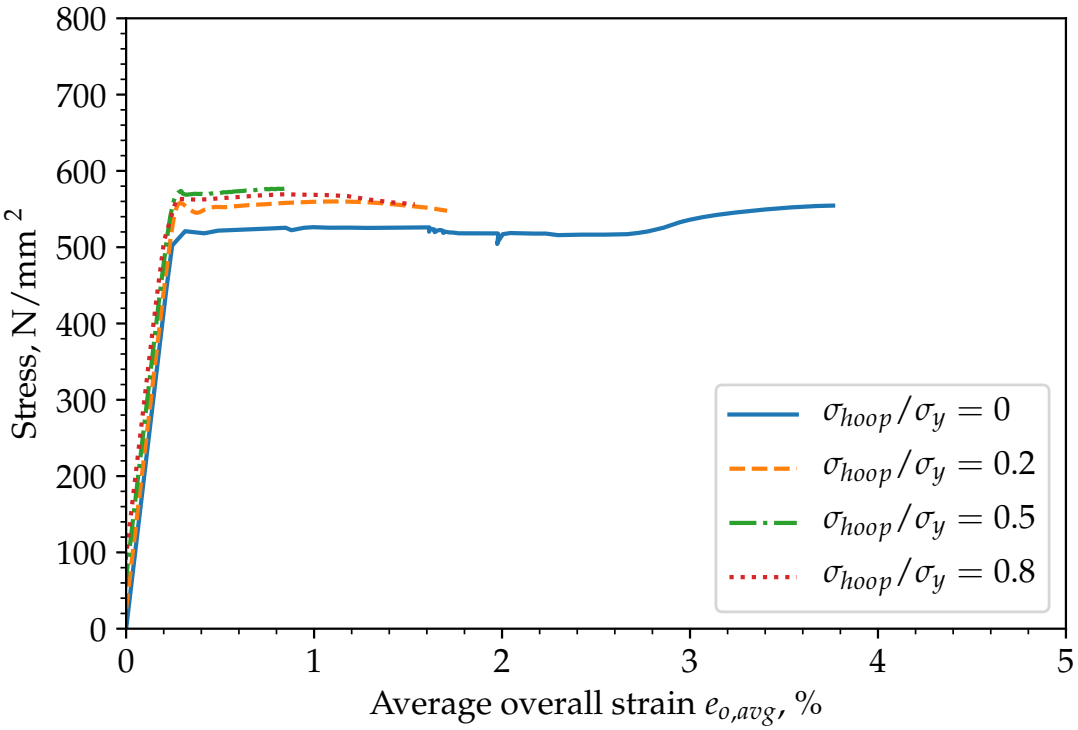

Figure 6.14: Global stress-strain response of FE pipe models with 7 × 100 mm circumferential flaw with various levels of internal pressure

extent of crack opening and hence lower value of CTOD. The CTOD level over the plateau phase is equal to that at the end of the Lüders plateau, therefore the lower dissipated strain energy at the end of plateau phase results in a lower CTOD level over the whole stress plateau. Beyond the end of CTOD plateau phase, the CTOD for $\sigma_{hoop} = 0.5$ and 0.8 starts to rise and then surpass those for $\sigma_{hoop} = 0$ and 0.2. The observation of the crack driving force is relevant to the strain energy dissipated, and further explanation is included in Chapter 6.3.

For larger flaws, such as those with $a = 3$ mm and $2c = 75$ - 100 mm, the plastic deformation is found to localise in the notch region and ligament only, resulting in premature necking and plastic collapse not long after the plateau phase, or (for flaw 7 × 100 mm) before the bands have fully spread through the remainder of the pipe. Consequently, the notch tip opens continuously with the applied loading, similar to that for continuously yielding materials, and lead to a relatively higher crack driving force at a low strain level.

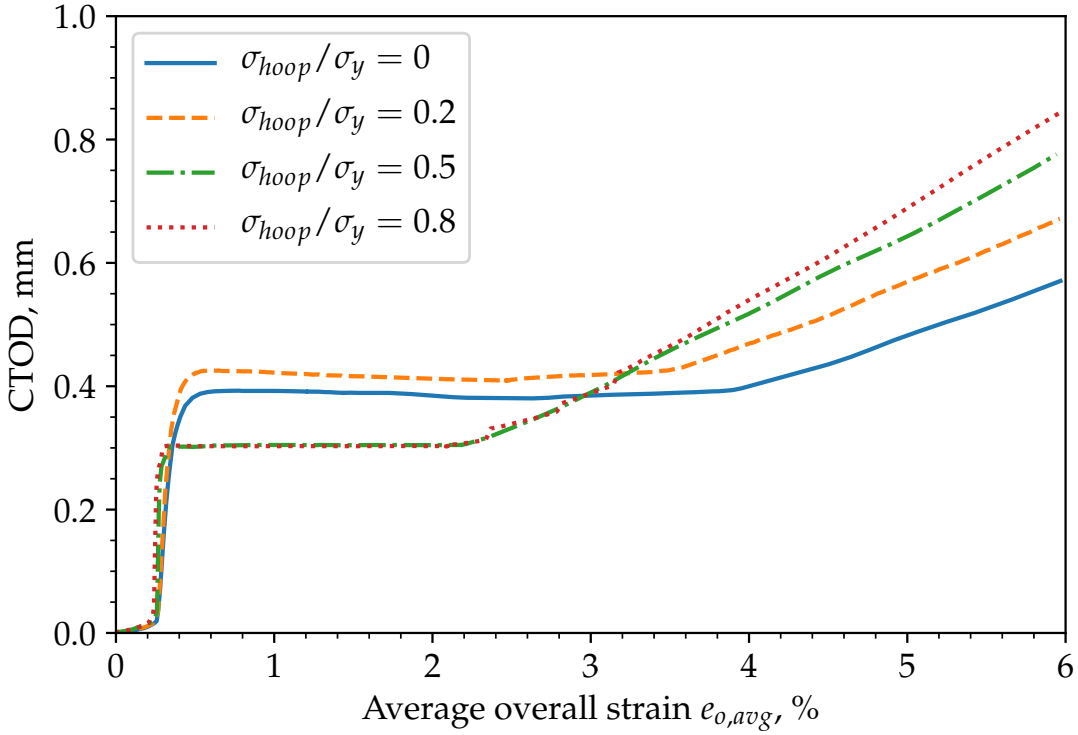

Figure 6.15: CTOD versus average overall strain of FE pipe models with 3×10 mm circumferential flaw with various levels of internal pressure

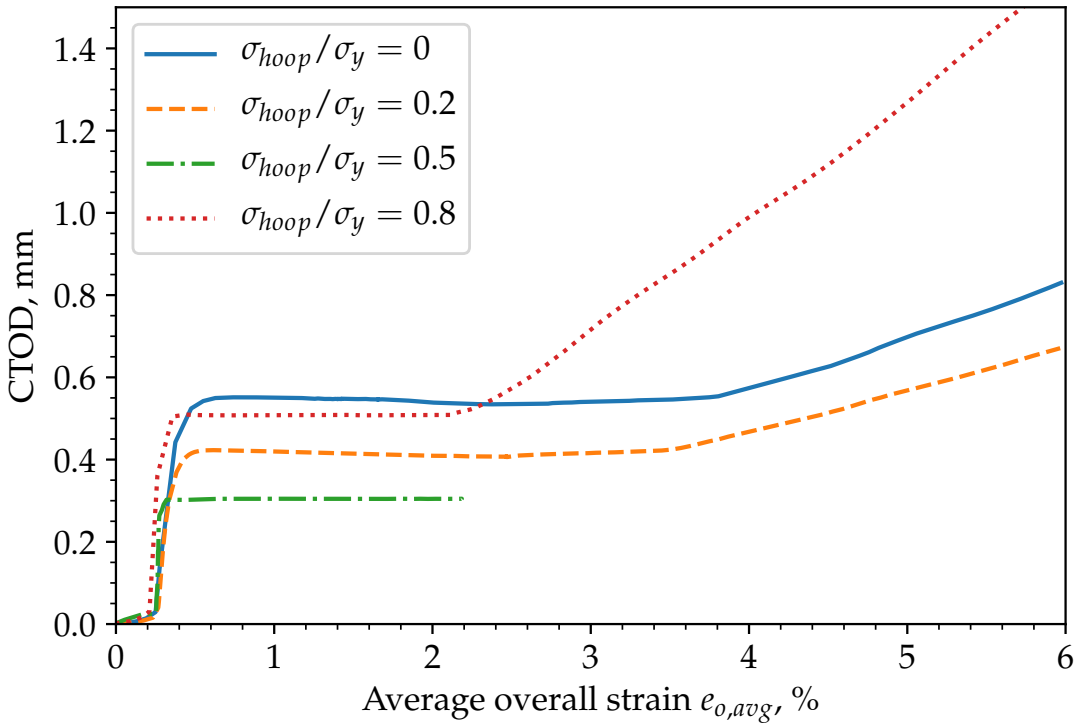

Figure 6.16: CTOD versus average overall strain of FE pipe models with 3×25 mm circumferential flaw with various levels of internal pressure

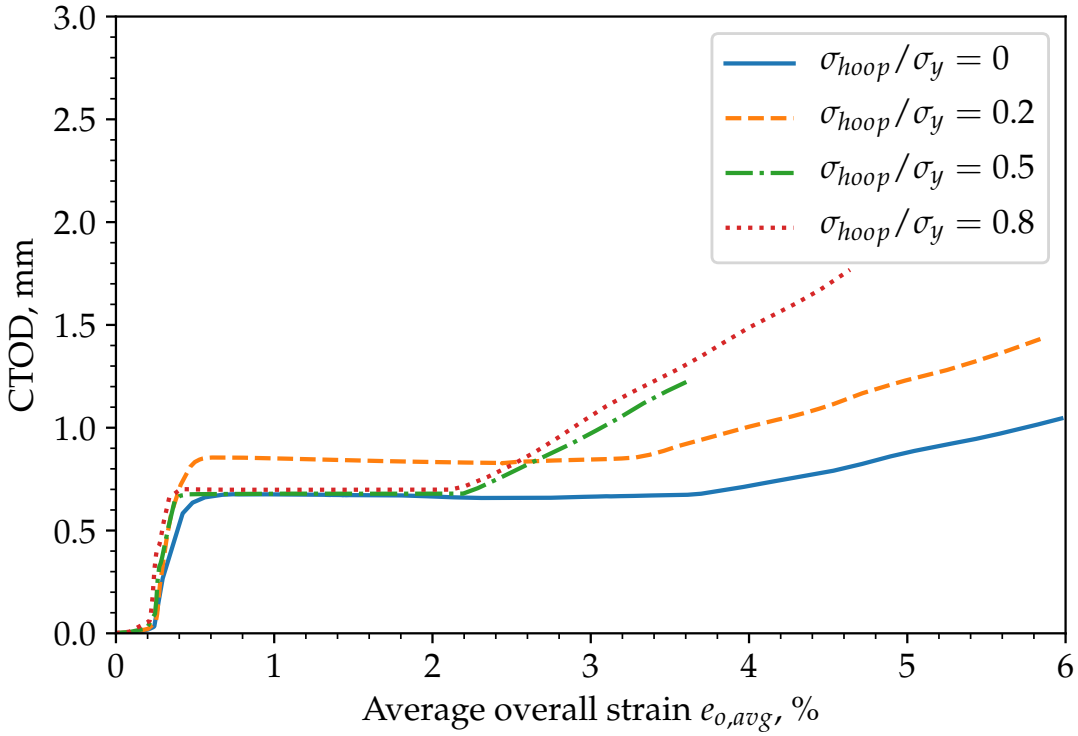

Figure 6.17: CTOD versus average overall strain of FE pipe models with 3×50 mm circumferential flaw with various levels of internal pressure

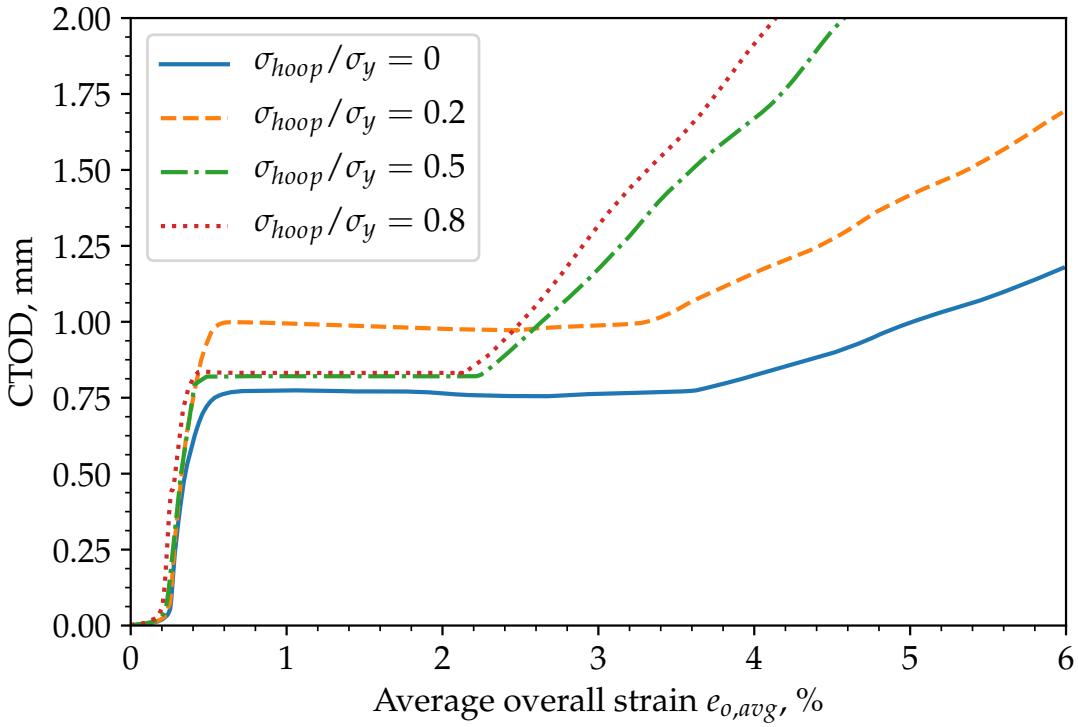

Figure 6.18: CTOD versus average overall strain of FE pipe models with 3×75 mm circumferential flaw with various levels of internal pressure

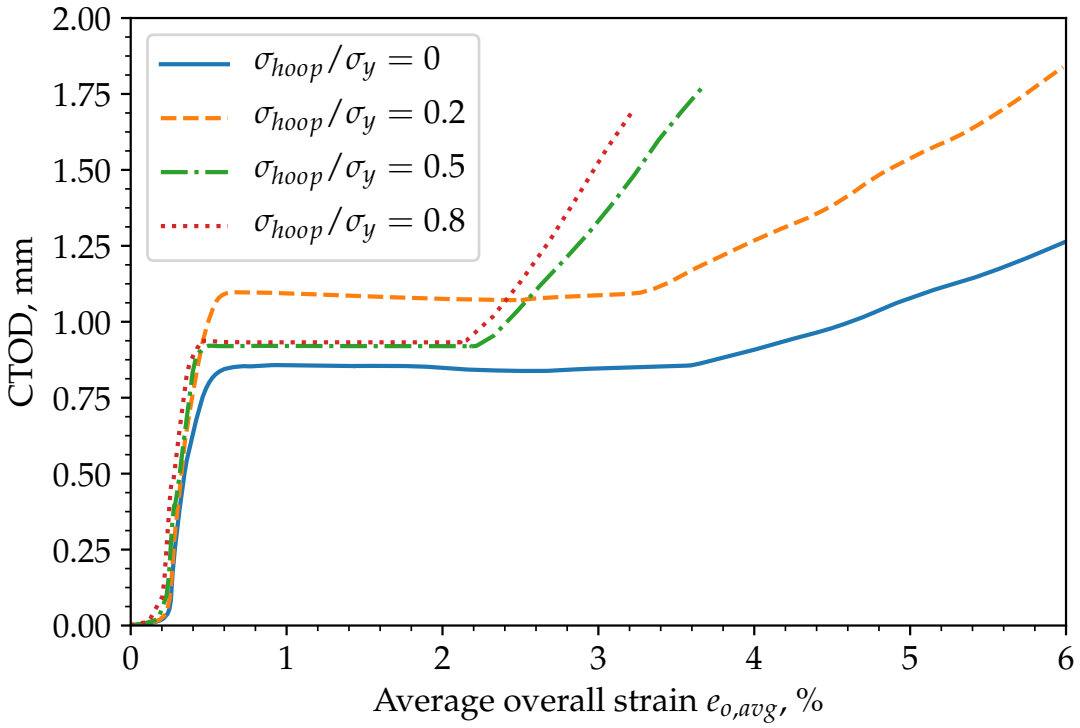

Figure 6.19: CTOD versus average overall strain of FE pipe models with 3×100 mm circumferential flaw with various levels of internal pressure

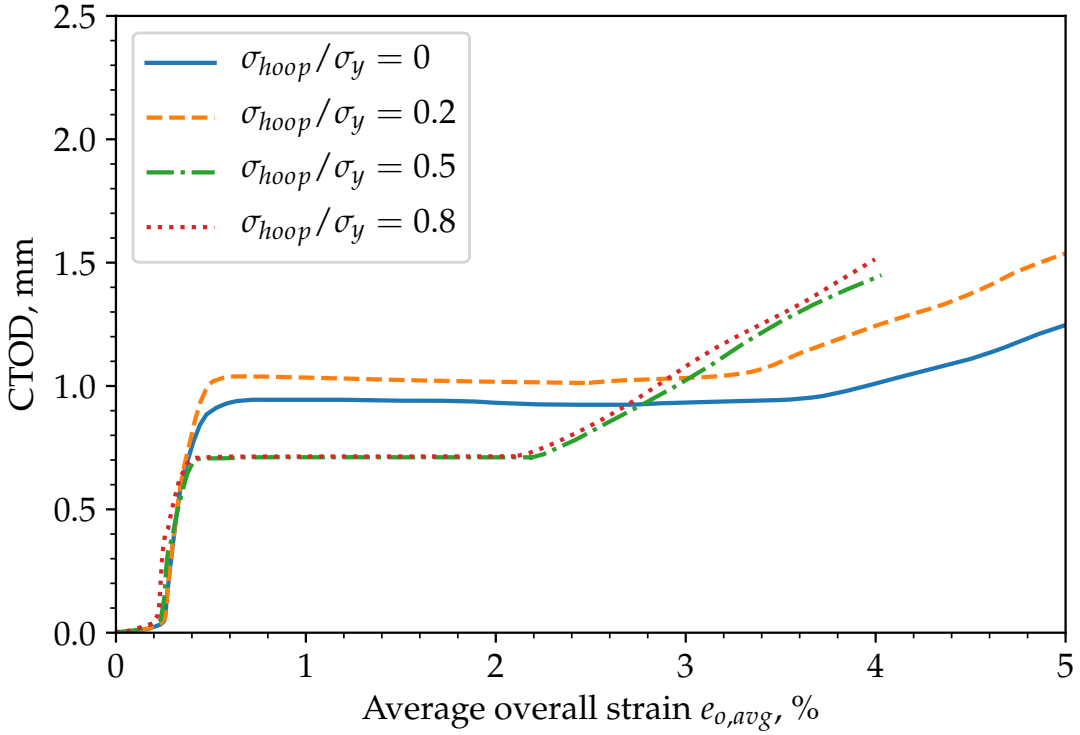

Figure 6.20: CTOD versus average overall strain of FE pipe models with 5×25 mm circumferential flaw with various levels of internal pressure

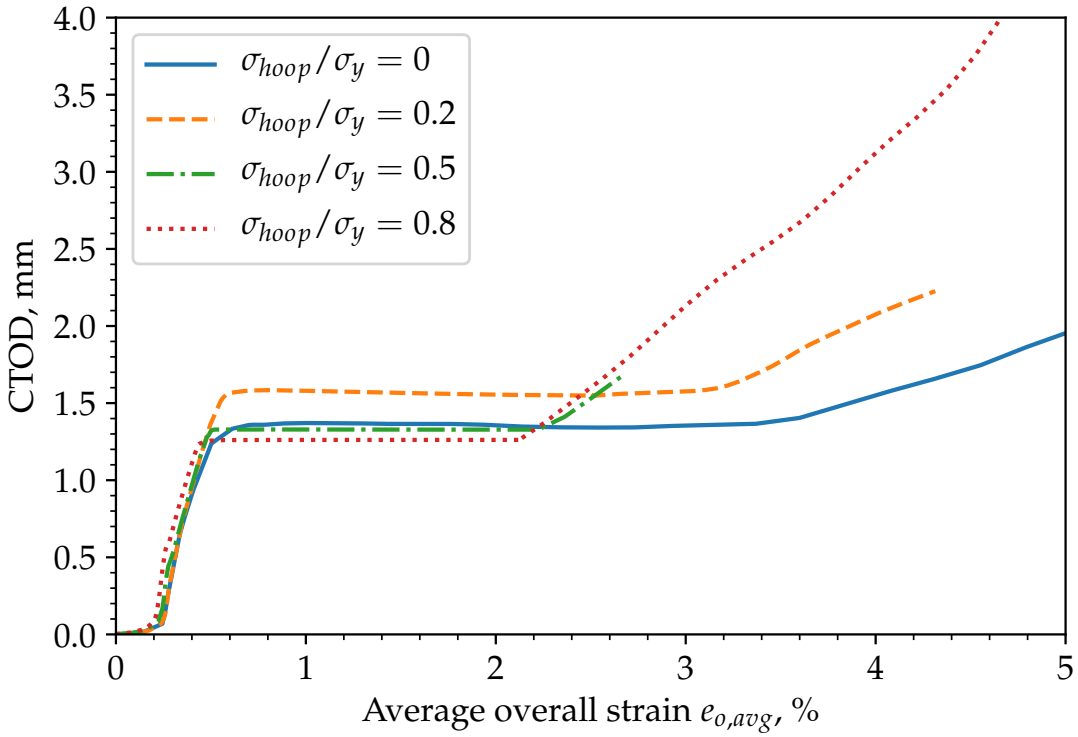

Figure 6.21: CTOD versus average overall strain of FE pipe models with 5×50 mm circumferential flaw with various levels of internal pressure

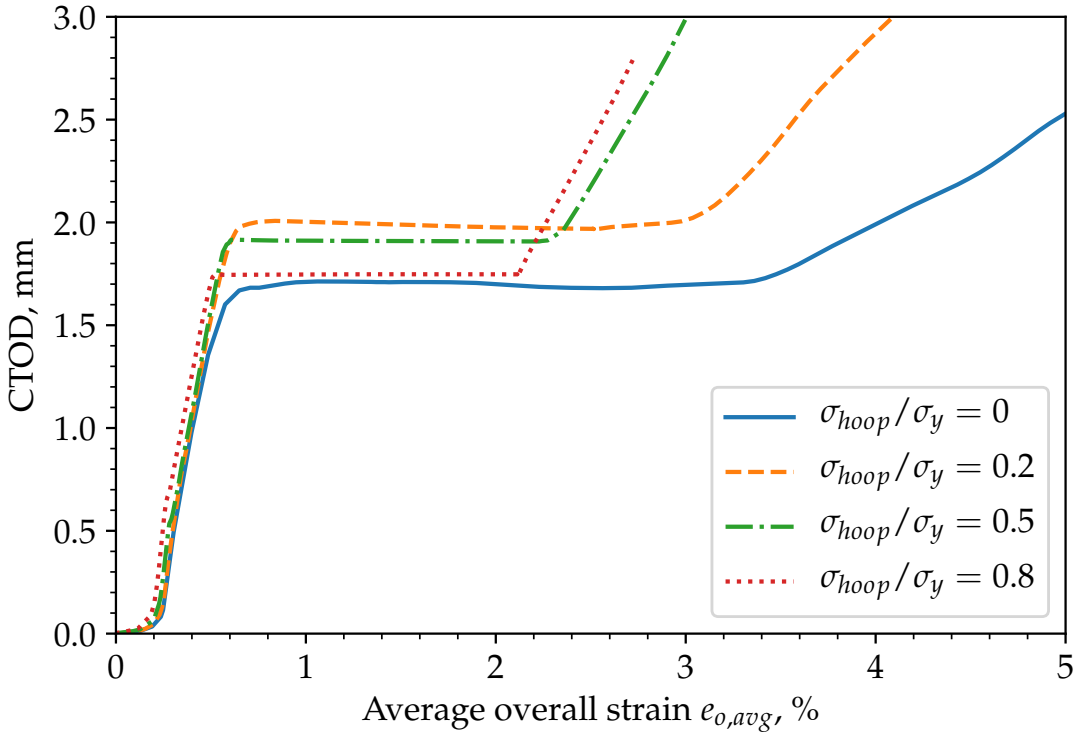

Figure 6.22: CTOD versus average overall strain of FE pipe models with 5×75 mm circumferential flaw with various levels of internal pressure

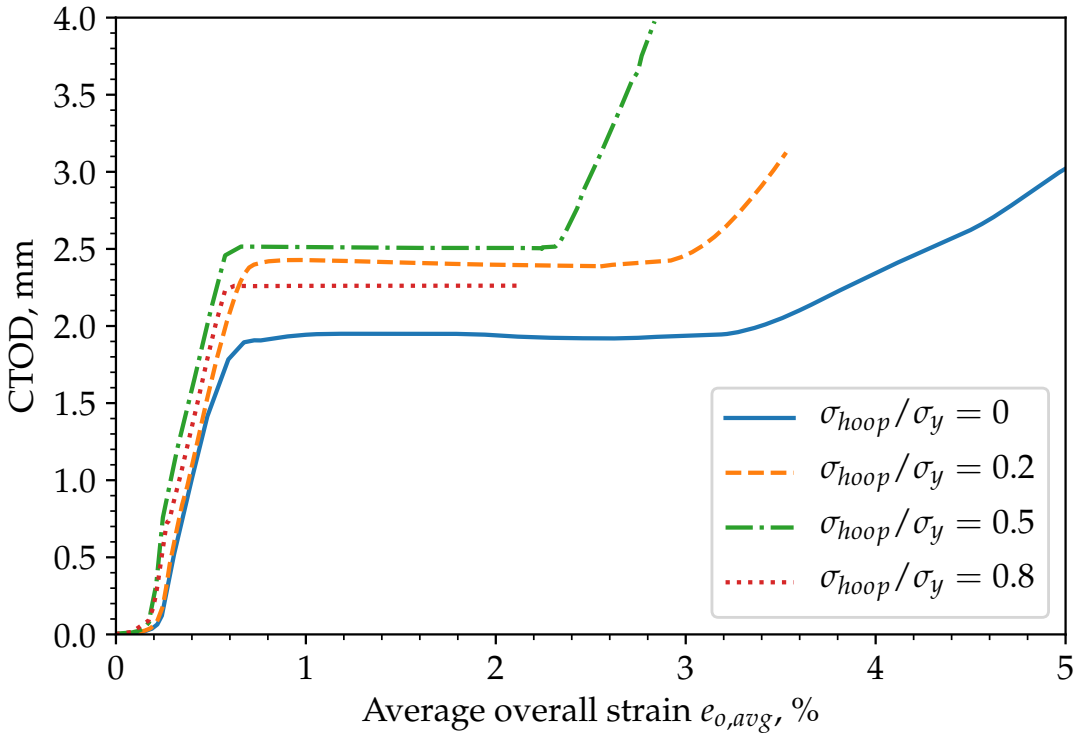

Figure 6.23: CTOD versus average overall strain of FE pipe models with 5×100 mm circumferential flaw with various levels of internal pressure

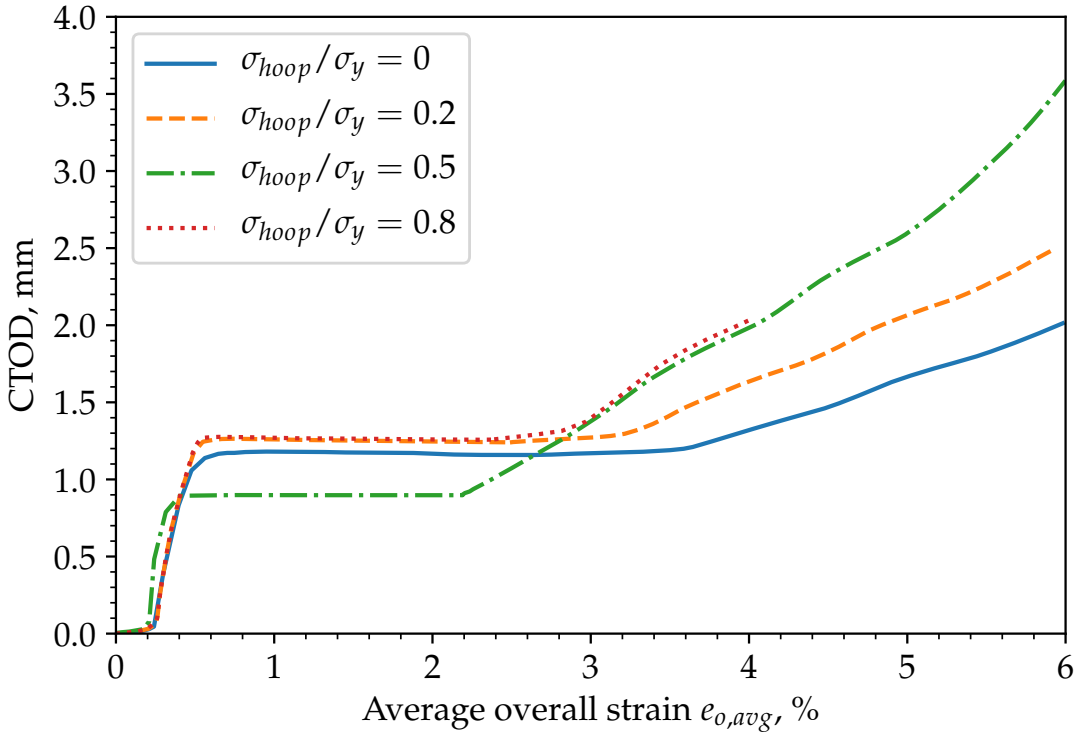

Figure 6.24: CTOD versus average overall strain of FE pipe models with 7×25 mm circumferential flaw with various levels of internal pressure

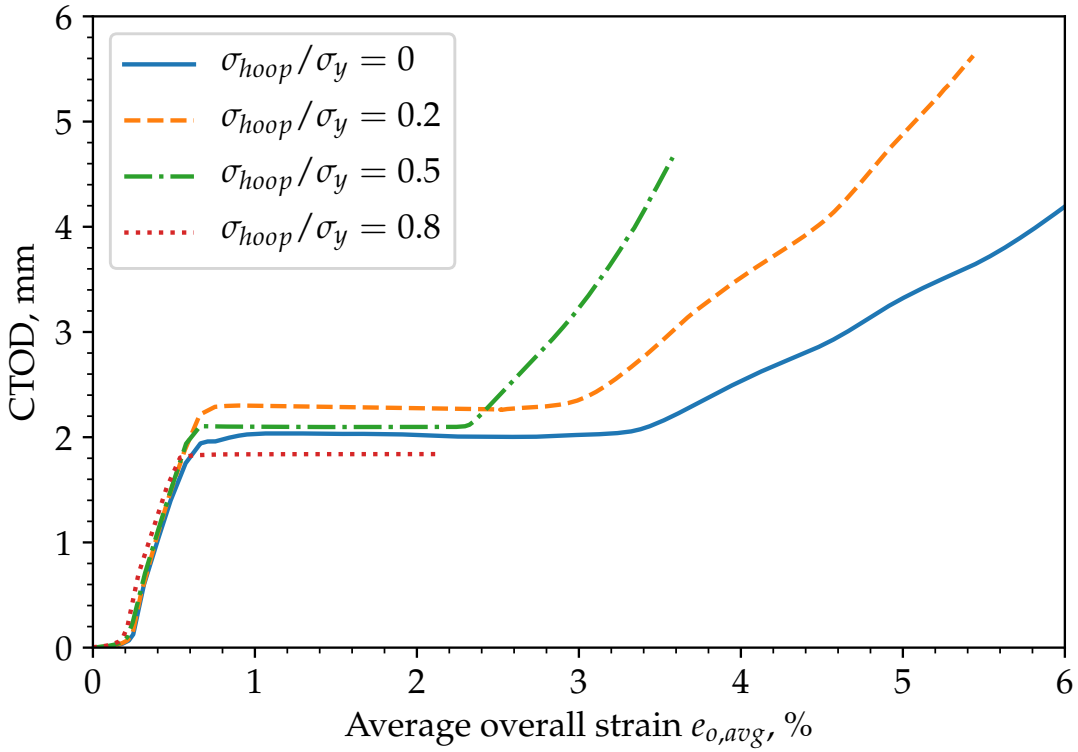

Figure 6.25: CTOD versus average overall strain of FE pipe models with 7×50 mm circumferential flaw with various levels of internal pressure

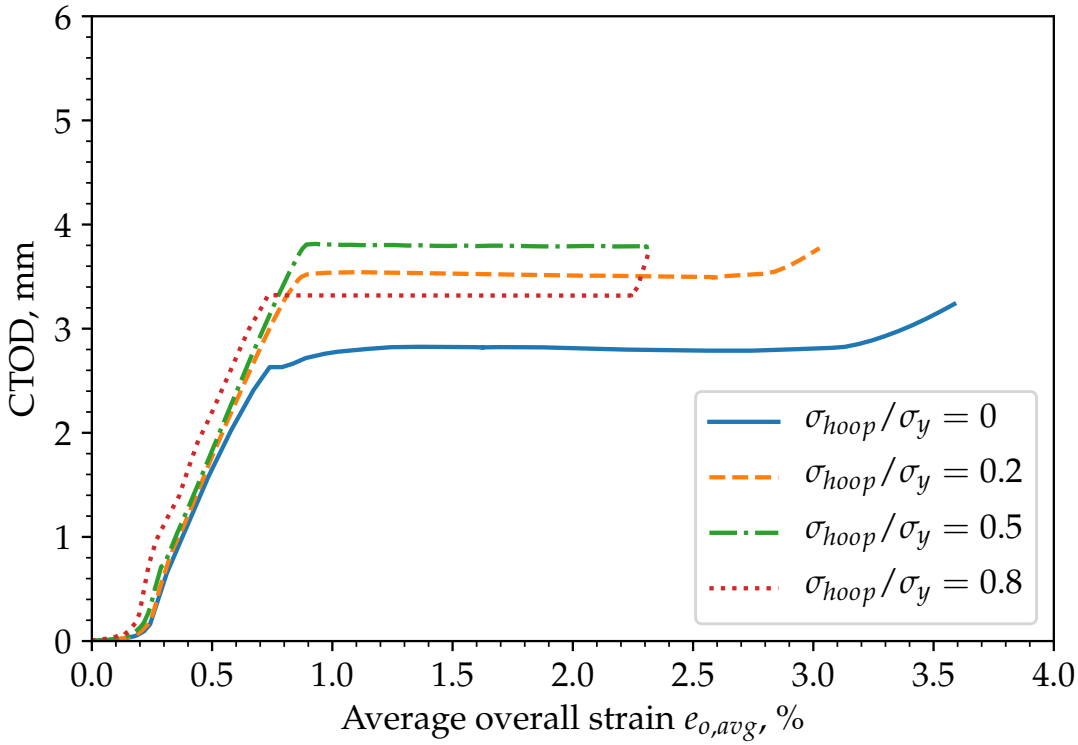

Figure 6.26: CTOD versus average overall strain of FE pipe models with 7×75 mm circumferential flaw with various levels of internal pressure

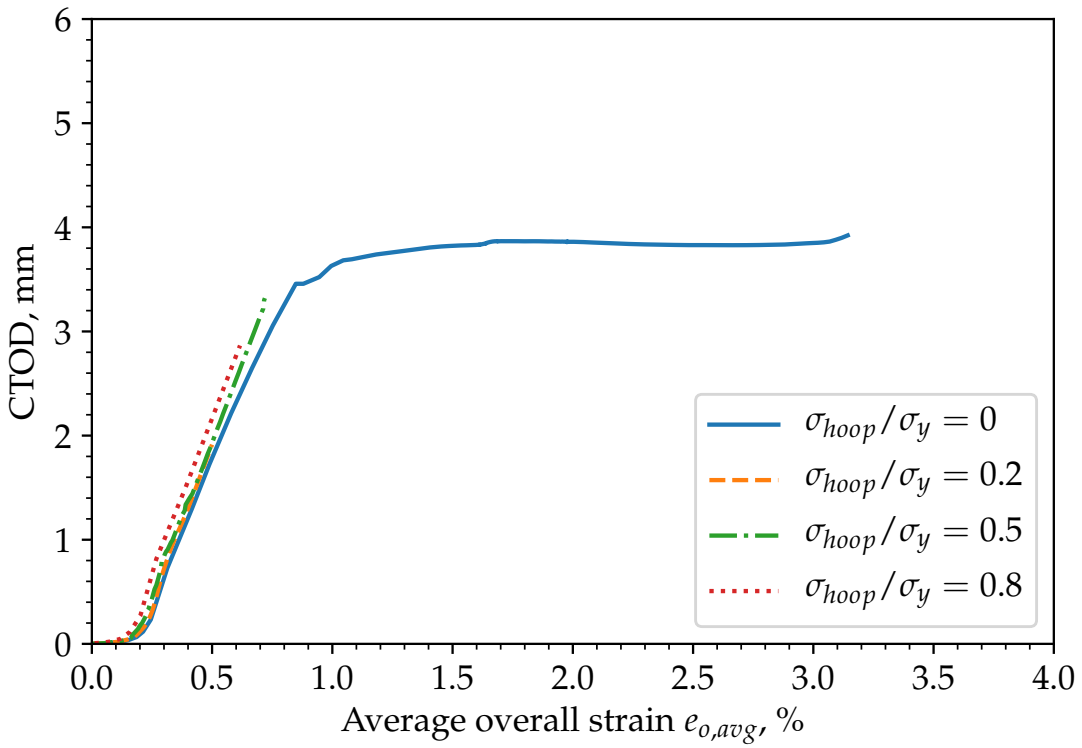

Figure 6.27: CTOD versus average overall strain of FE pipe models with 7 × 100 mm circumferential flaw with various levels of internal pressure

6.2.2.3 *Evolution of Lüders bands*

To demonstrate the effect of internal pressure on the evolution of Lüders bands, equivalent plastic strain (ε^{p}_{eq}) maps of representative cases are presented as most cases exhibit similar deformation behaviour. As the pattern of Lüders band progression are similar for most of the FE cases, the most representative ones for small and large flaws are presented, respectively.

Figures 6.28 to 6.33 compare the evolution of Lüders bands, in terms of equivalent plastic strain contour, in the pipe models containing a small flaw (3 × 10 mm) with different internal pressure level at selected strains. It can be readily noticed that the application of internal pressure alters the angle of inclination of Lüder band propagation. As shown in Figure 6.28, the average overall strain is 0.39% at which the pipe just started the plateau phase following the yield point and localised plastic bands were generated from the notch tip. The inclination angle of the band is about 52.7°with respect to the loading axis when the pipe is subjected to axial straining only ($\sigma_{hoop}/\sigma_y = 0$), and is found to increase to 58.3°when an internal pressure ($\sigma_{hoop}/\sigma_y = 0.2$) is applied, and up to 90°when the internal pressure is as high as $\sigma_{hoop}/\sigma_y = 0.5$ and beyond.

From Figures 6.29 to 6.32 that depict the pattern of Lüders band propagation simulated, the band development for $\sigma_{hoop}/\sigma_y = 0$ is found to be more complex than those for other internal pressure levels. For $\sigma_{hoop}/\sigma_y = 0$, bands are found to initiate at multiple locations, and spread back to the original location where the first band initiates after reaching the uncracked end of the pipe. For $\sigma_{hoop}/\sigma_y = 0.2$, 0.5, and 0.8, however, the band propagation is found to be more regular and simple, spreading from the cracked end to the uncracked end of the pipe. This may be attributed to the reinforcement of strain localisation induced by the application of internal pressure such that the localised deformation starting from the cracked end remains sufficiently large to maintain a single propagating band regime.

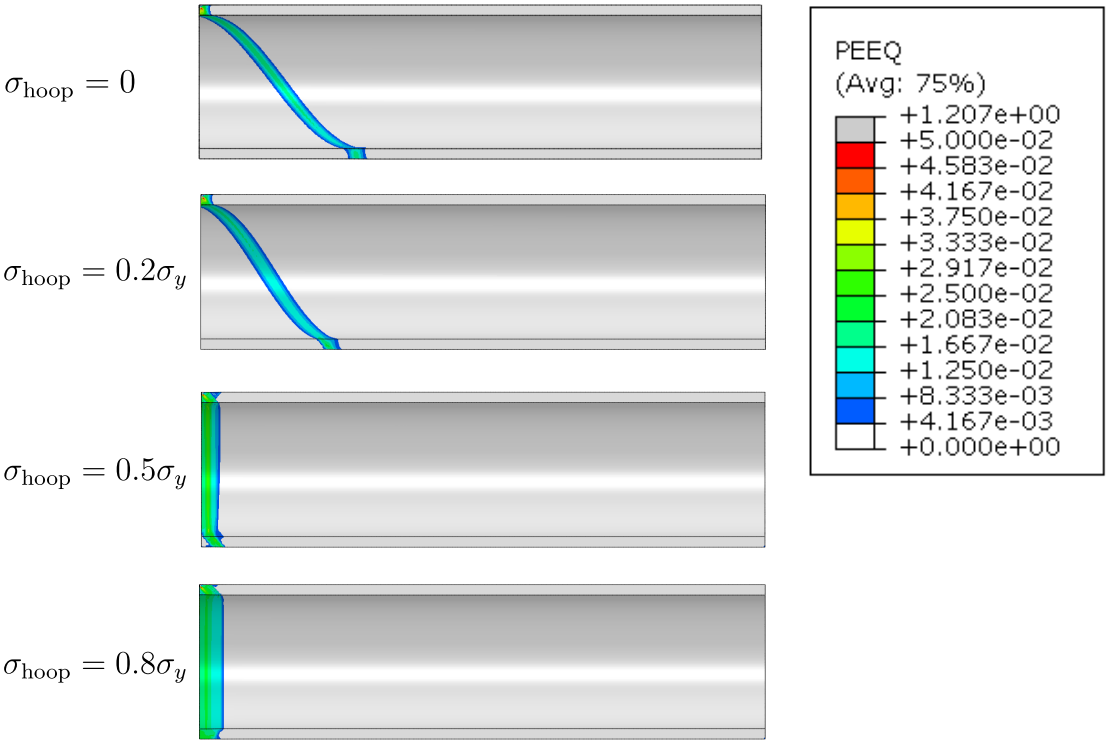

Figure 6.28: Equivalent plastic strain ε^p_{eq} (PEEQ) distribution of FE pipe model with flaw size 3 × 10 mm under various internal pressure levels at 0.39% global strain ($e_{o,avg} = 0.39\%$)

At $e_{o,avg} = 2.04\%$, as shown in Figure 6.32, the localisation bands are found to propagate through the majority of the pipe for $\sigma_{hoop}/\sigma_y = 0$ while the strain ($e_{o,avg} = 2.04\%$) is still distant from the Lüders strain ($e_L = 2.6\%$). The reason is that there are some parts of the pipe close to the cracked end remains plastically undeformed, which renders the overall strain over 700 mm gauge length across the flaw (350 mm from the flaw in the quarter FE model) equal to

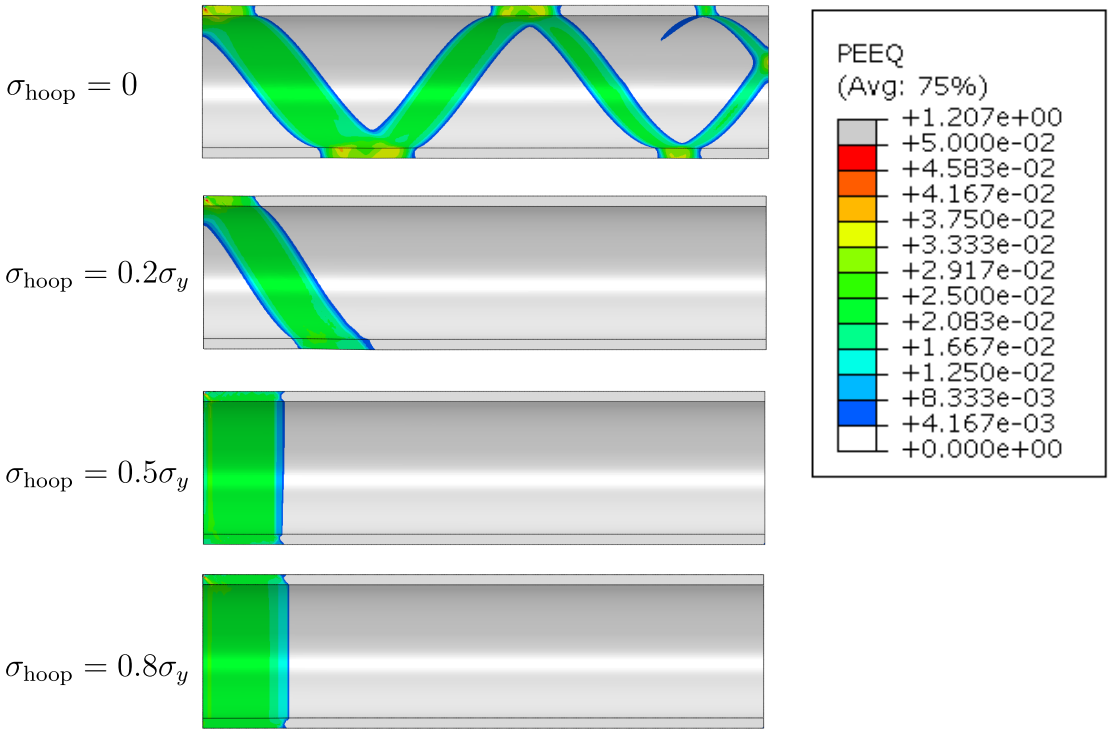

Figure 6.29: Equivalent plastic strain ε^{p}_{eq} (PEEQ) distribution of FE pipe model with flaw size 3 × 10 mm under various internal pressure levels at 0.98% global strain ($e_{o,avg} = 0.98\%$)

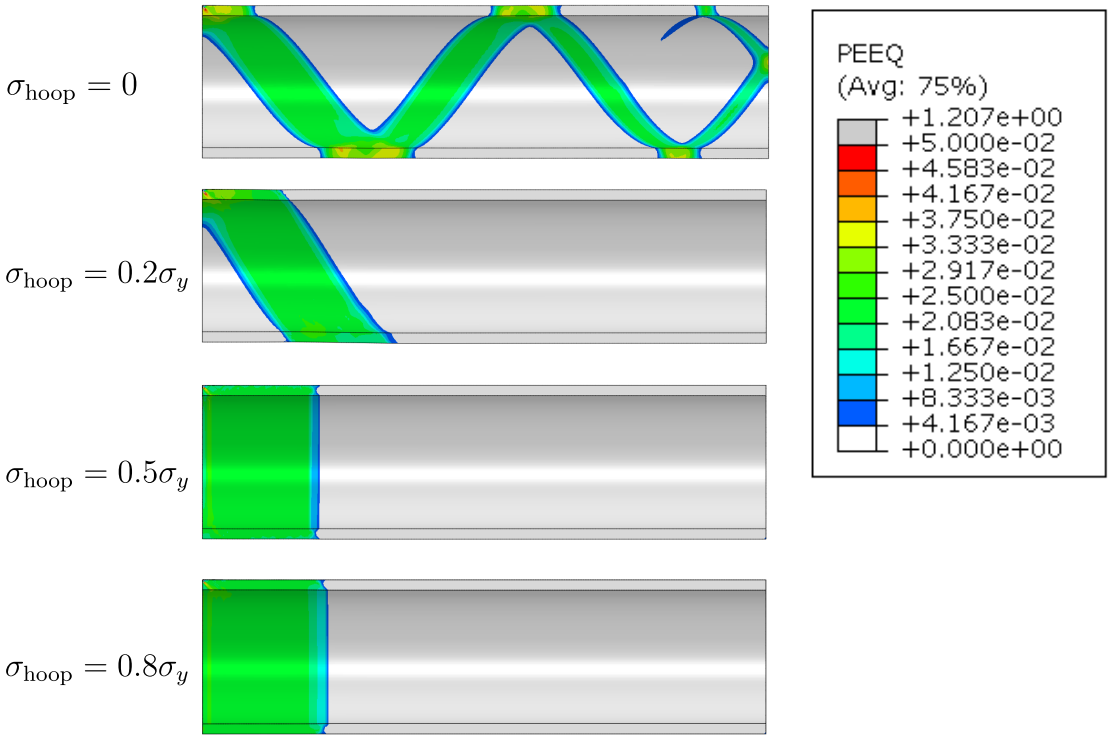

Figure 6.30: Equivalent plastic strain ε^{p}_{eq} (PEEQ) distribution of FE pipe model with flaw size 3 × 10 mm under various internal pressure levels at 1.31% global strain ($e_{o,avg} = 1.31\%$)

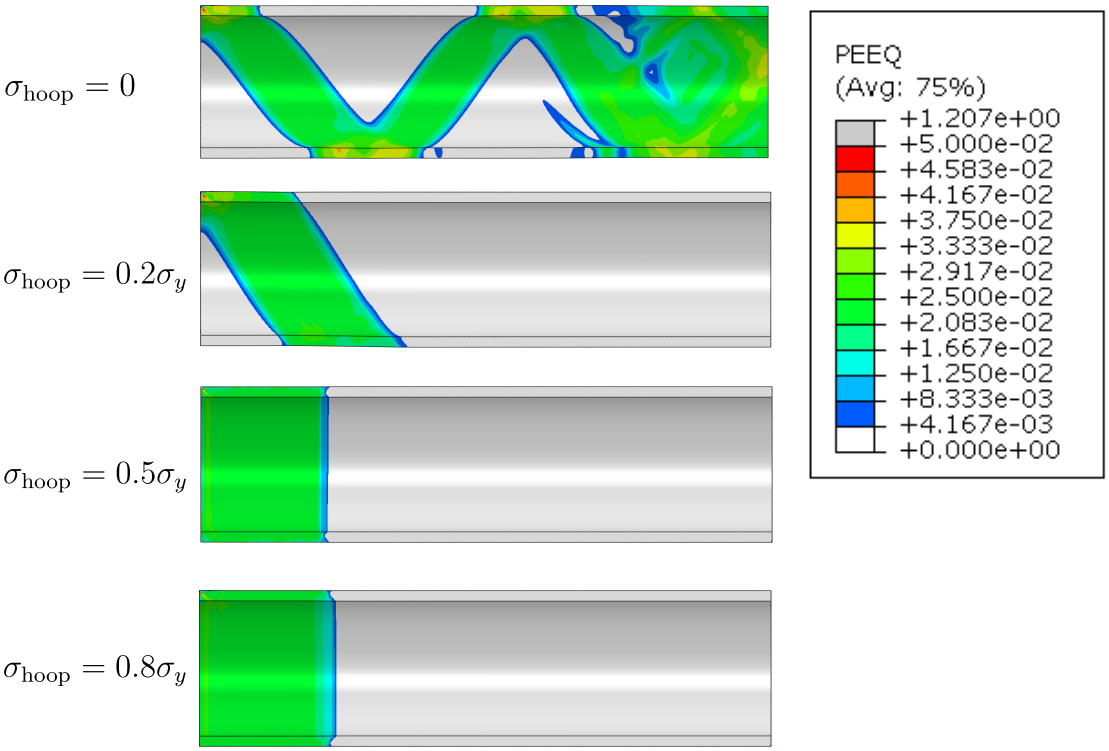

Figure 6.31: Equivalent plastic strain ε^{p}_{eq} (PEEQ) distribution of FE pipe model with flaw size 3 × 10 mm under various internal pressure levels at 1.44% global strain ($e_{o,avg} = 1.44\%$)

a lower strain value than the Lüders strain. For $\sigma_{hoop}/\sigma_y = 0.2$ - 0.8, the strain localisation band is seen to spread through a significant portion of the pipe. At $e_{o,avg} = 2.86\%$, as shown in Figure 6.28, the pipe models under all internal pressure levels are observed to have well entered the straining hardening regime in which the pipes deform uniformly.

The comparison of equivalent plastic strain contour for the pipe containing a large flaw (7 × 100 mm) are shown in Figures 6.34 to 6.36. For the case subjected to axial straining only ($\sigma_{hoop}/\sigma_y = 0$), Lüders bands are found to propagate. For the cases subjected to combined axial straining and internal pressure, significant plastic deformation is found to be localised around the ligament area before Lüders bands have spread to the region distant from the flaw, resulting in necking followed by plastic collapse. It is found that the band in the case with $\sigma_{hoop}/\sigma_y = 0.2$ has managed to propagate to some distance along the pipe axis, but the necking occurs due to considerable plastic straining in the ligament region.

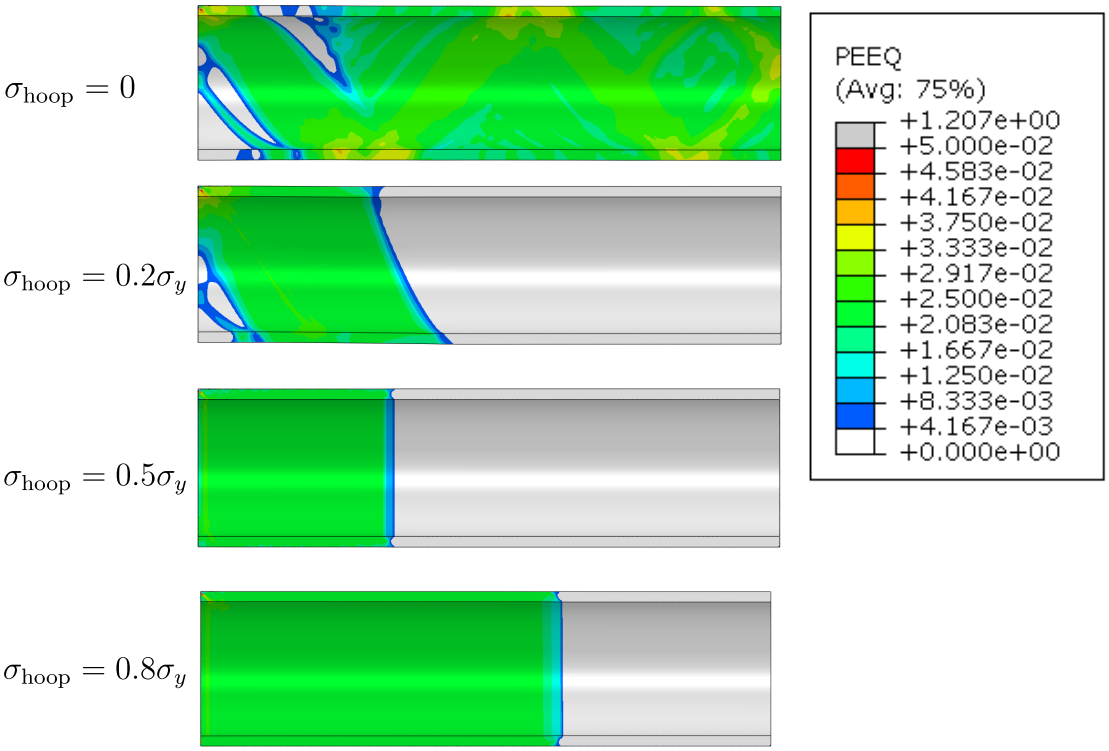

Figure 6.32: Equivalent plastic strain ε^p_{eq} (PEEQ) distribution of FE pipe model with flaw size 3 × 10 mm under various internal pressure levels at 2.04% global strain ($e_{o,avg} = 2.04\%$)

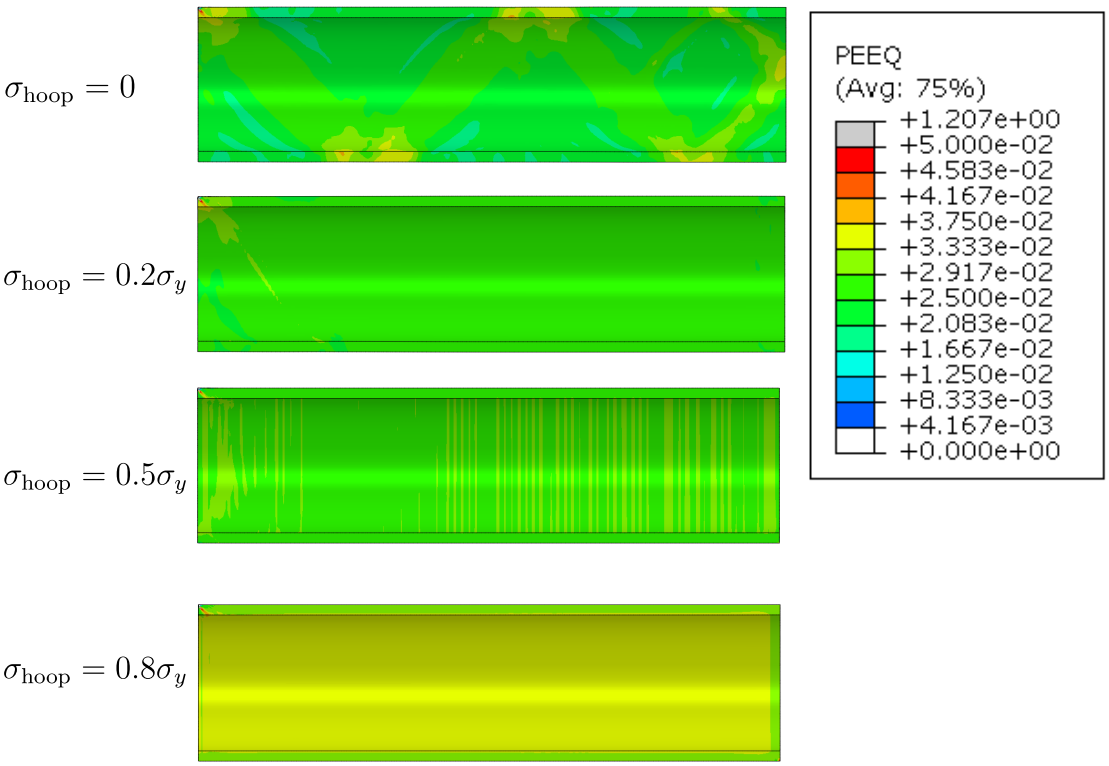

Figure 6.33: Equivalent plastic strain ε^p_{eq} (PEEQ) distribution of FE pipe model with flaw size 3 × 10 mm under various internal pressure levels at 2.86% global strain ($e_{o,avg} = 2.86\%$)

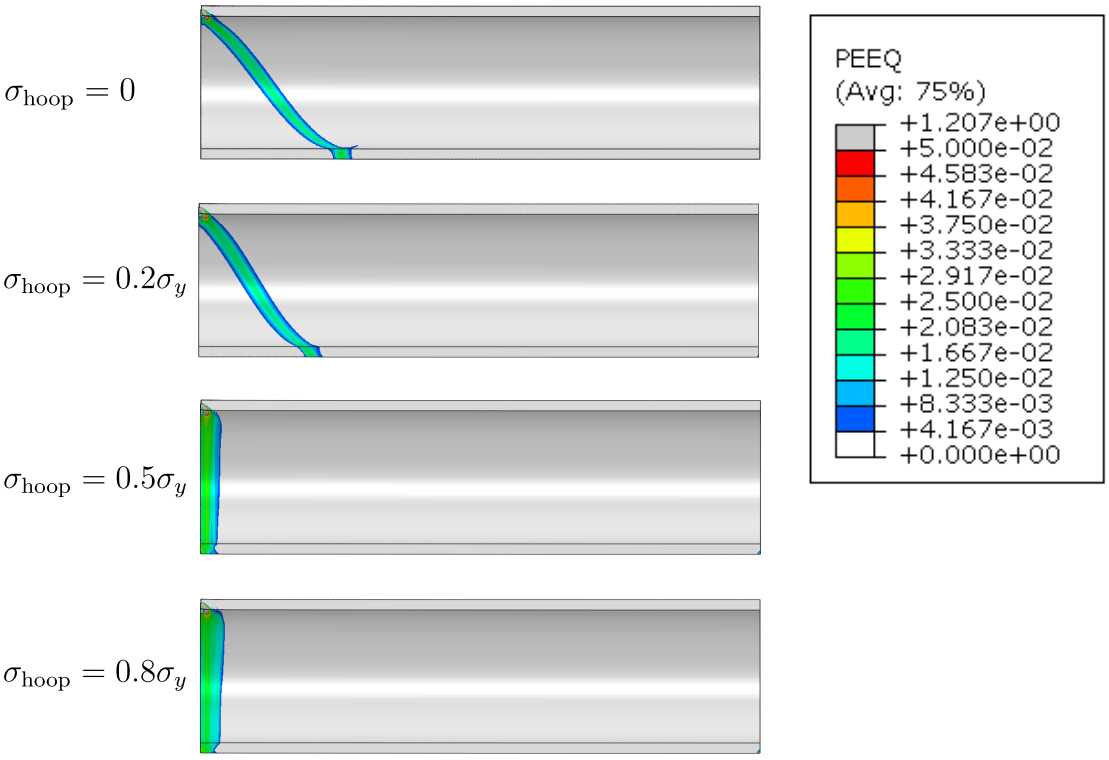

Figure 6.34: Equivalent plastic strain ε^{p}_{eq} (PEEQ) distribution of FE pipe model with flaw size 7 × 100 mm under various internal pressure levels at 0.4% global strain ($e_{o,avg} = 0.4\%$)

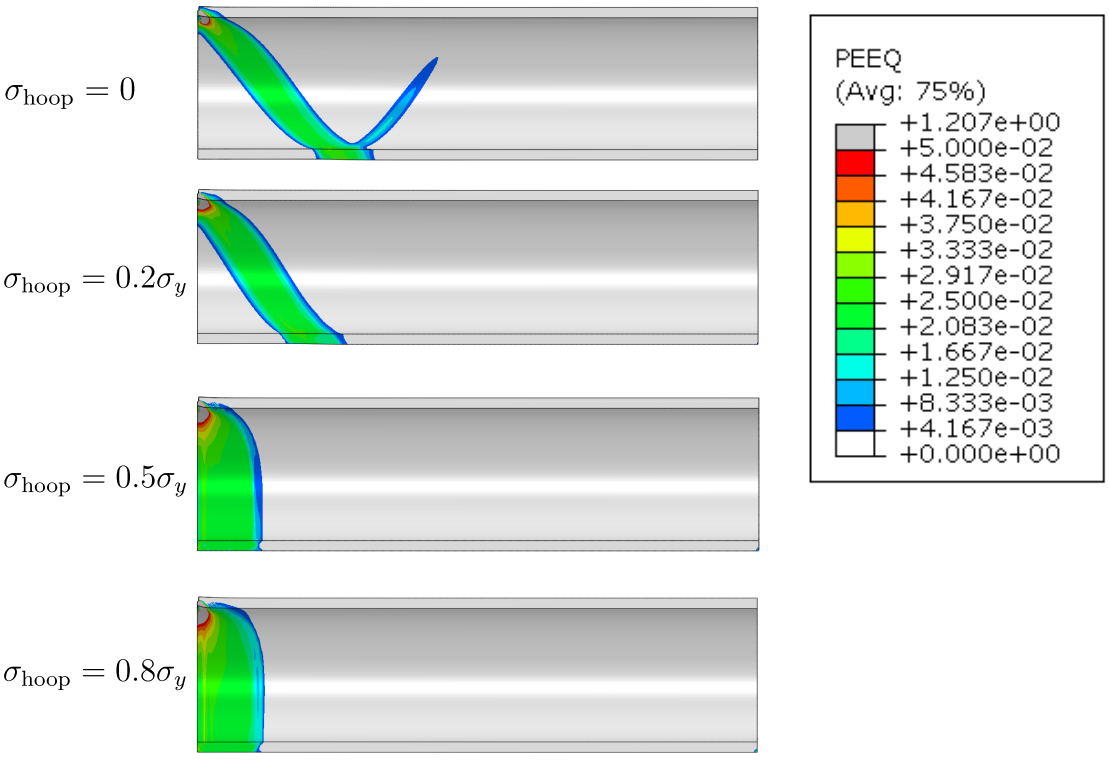

Figure 6.35: Equivalent plastic strain ε^{p}_{eq} (PEEQ) distribution of FE pipe model with flaw size 7 × 100 mm under various internal pressure levels at 0.8% global strain ($e_{o,avg} = 0.8\%$)

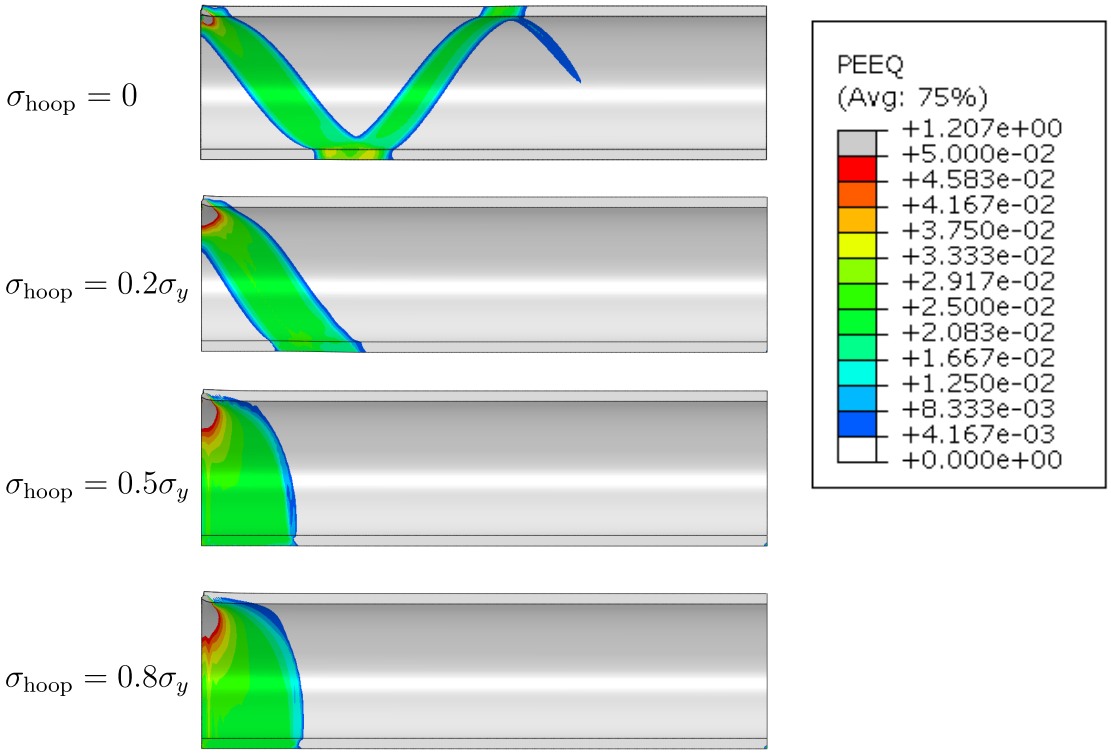

Figure 6.36: Equivalent plastic strain ε^{p}_{eq} (PEEQ) distribution of FE pipe model with flaw size 7 × 100 mm under various internal pressure levels at 1.1% global strain ($e_{o,avg} = 1.1\%$)

6.3 DISCUSSION

6.3.1 *Effect of internal pressure on global stress-strain response*

From the results reported in Section 6.2.2.1, the application of internal pressure is found to alter significantly the axial stress-strain behaviour of the pipes subjected to tensile loading. This has been noted by a number of researchers (e.g. Cosham and Macdonald 2015; Tyson et al. 2007; Berg et al. 2008; Abdulhameed et al. 2016; Østby et al. 2005; Wang et al. 2008) and is reckoned to be the cause for the change in the CDF, which will be elaborated in the subsequent section.

Figures 6.37 and 6.38 summaries the effect of internal pressure (in terms of σ_{hoop}/σ_y) on the stress level and extent of the Lüders plateau on the calculated gross stress-strain response for each flaw sizes. As illustrated in Figure 6.39, the parameters $s_{Plateau}$ and Δe_L are the average stress level and extent of the yield plateau, respectively.

As shown in Figures 6.37 and 6.38, the internal pressure is found to generally increase the stress level of the plateau but reduce its extent (Δe_L). Interestingly,

it is observed that the stress level during the plateau phase increases with the internal pressure up to $\sigma_{hoop}/\sigma_y = 0.5$. The increase is found to diminish and then saturate when $\sigma_{hoop}/\sigma_y = 0.5$, followed by a decline. This indicates the internal pressure has the maximum effect when the pressure-induced hoop stress is around half of the yield strength. The flaw sizes, on the other hand, are found to have marginal effects on the plateau stress level.

It can be noted that the normalised stress level ($s_{Plateau}/R_{eL}$) for all cases is above unity, even for cases with axial straining only. This implies that the calculated stress plateau from FEA using the UDU stress-strain model is above that of the measured stress-strain response, which is found in line with the observations on the global stress-strain behaviour of uniaxial tensile specimens and axially-strained pipes reported in Chapter 3 and 5, respectively.

For pipelines subjected to combined axial straining and internal pressure, the pipe wall is subjected to axial, radial and hoop stresses, as depicted in Figure 6.40. As the radial stress is negligibly small, the pipe is essentially in a biaxial stress state.

In the parametric FE study adopted the von Mises yield criterion (J_2 flow rule), which takes the following form:

$$\sigma_v = \sqrt{\sigma_{11}^2 - \sigma_{11}\sigma_{22} + \sigma_{22}^2 + 3\sigma_{12}^2} \tag{6.1}$$

When rephrased in terms of principal stresses in pipelines for which the radial stresses (σ_3) is negligible:

$$\sigma_v = \sqrt{\sigma_1^2 - \sigma_1\sigma_2 + \sigma_2^2} = \sqrt{\sigma_{axial}^2 - \sigma_{axial}\sigma_{hoop} + \sigma_{hoop}^2} \tag{6.2}$$

Figure 6.41 illustrates the effect of the hoop stress (σ_{hoop}) on the axial stress (σ_{axial}) in the light of von Mises yield criterion. It is found that σ_{axial} increases initially with σ_{hoop}, peaking at about $1.15\sigma_y$ when $\sigma_{hoop} = 0.58\sigma_y$, and then decreases. It can be therefore inferred that the effect of internal pressure on the axial stress-strain curve and thus the CDF peaks when σ_{hoop} is equal to $0.58\sigma_y$, and diminishes when σ_{hoop} is above $0.58\sigma_y$. During the plateau phase, the effect of internal pressure on the CDF is not completely the same as that on the global stress-strain response, which will be discussed in Section 6.3.2.

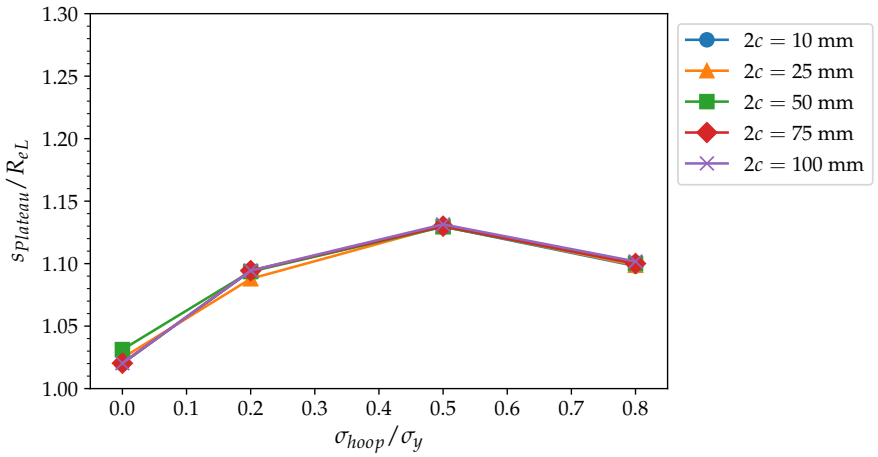

(a)

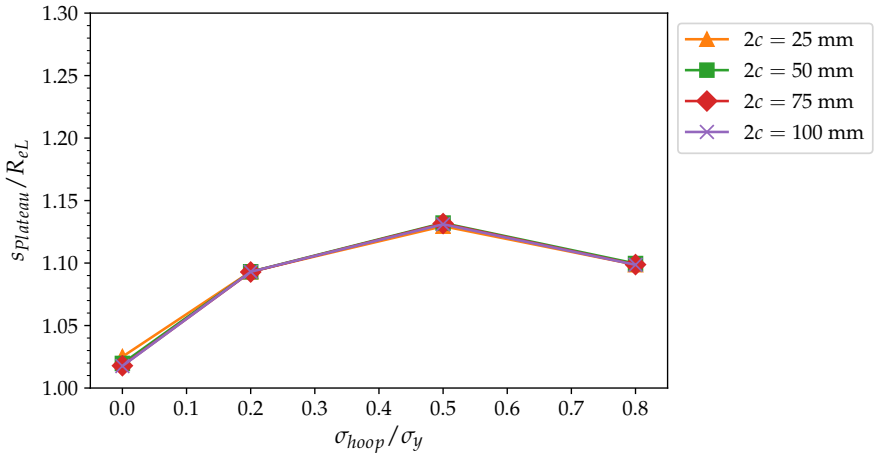

(b)

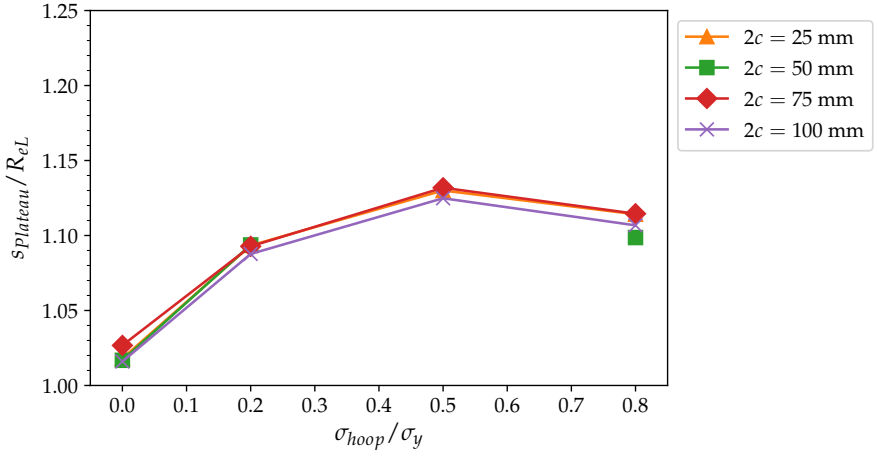

(c)

Figure 6.37: Effect of flaw sizes on the normalised gross stress ($s_{Plateau}/R_{eL}$) level during Lüders plateau phase of the cracked pipe with flaw height of (a) $a = 3$ mm, (b)$a = 5$ mm, and (c)$a = 7$ mm subjected to various levels of internal pressure

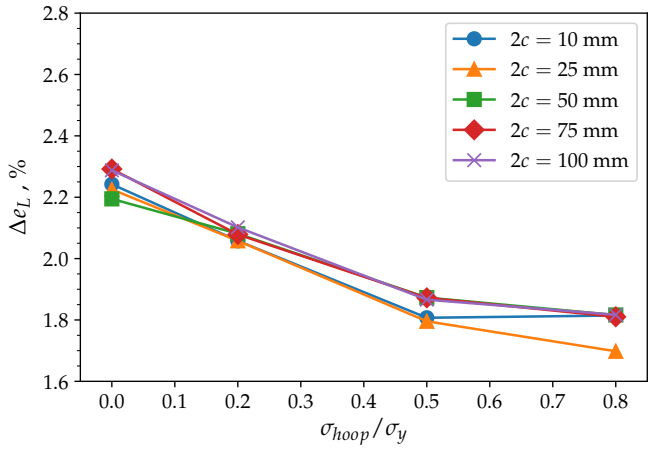

(a)

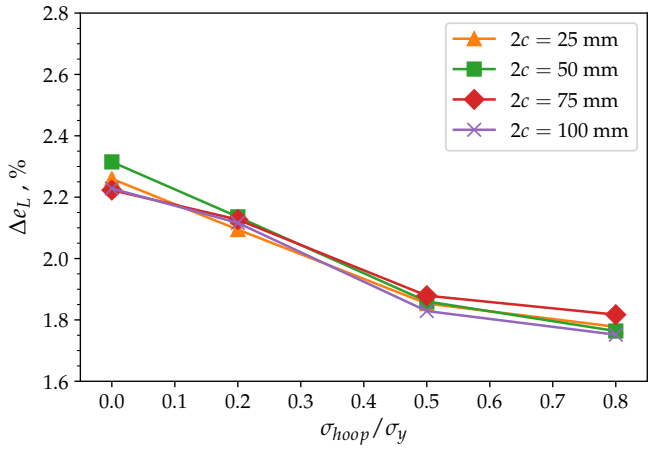

(b)

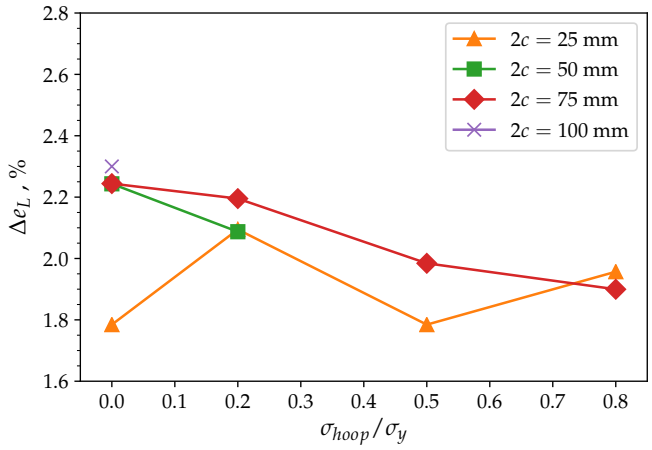

(c)

Figure 6.38: Effect of flaw sizes on extent of Lüders plateau (Δe_L) during Lüders plateau phase of the cracked pipe with flaw height of (a) $a = 3$ mm, (b)$a = 5$ mm, and (c)$a = 7$ mm subjected to various levels of internal pressure

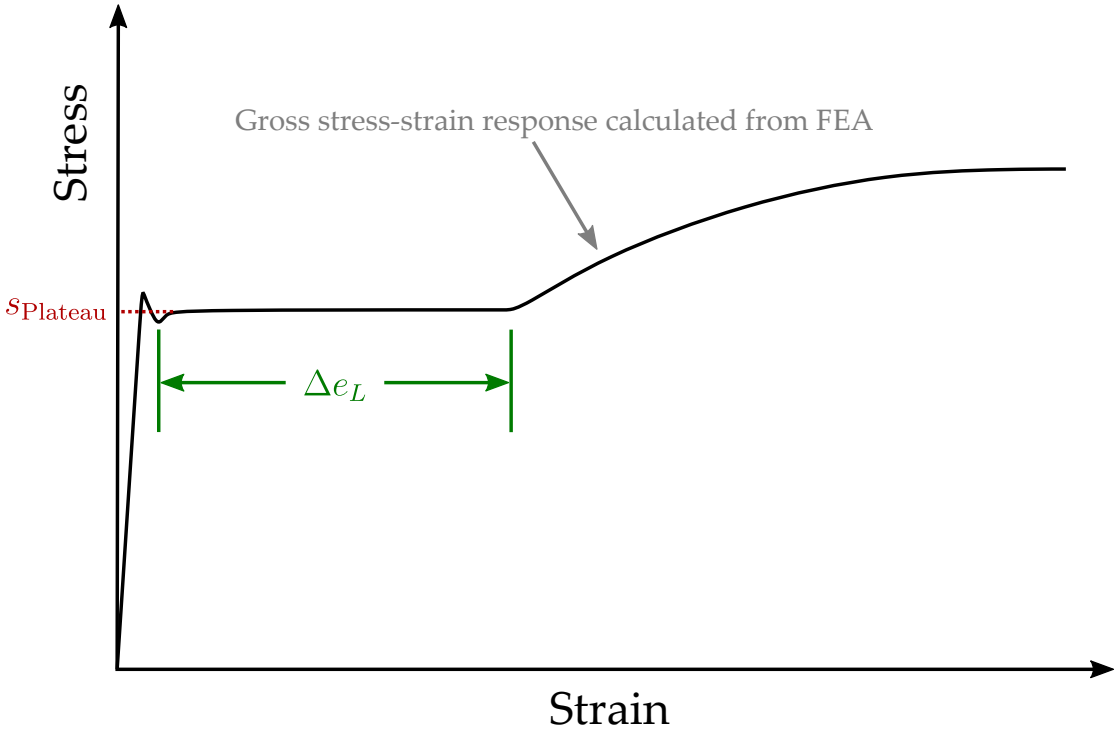

Figure 6.39: Schematic of the global stress-strain response calculated from the FEA with associated parameters

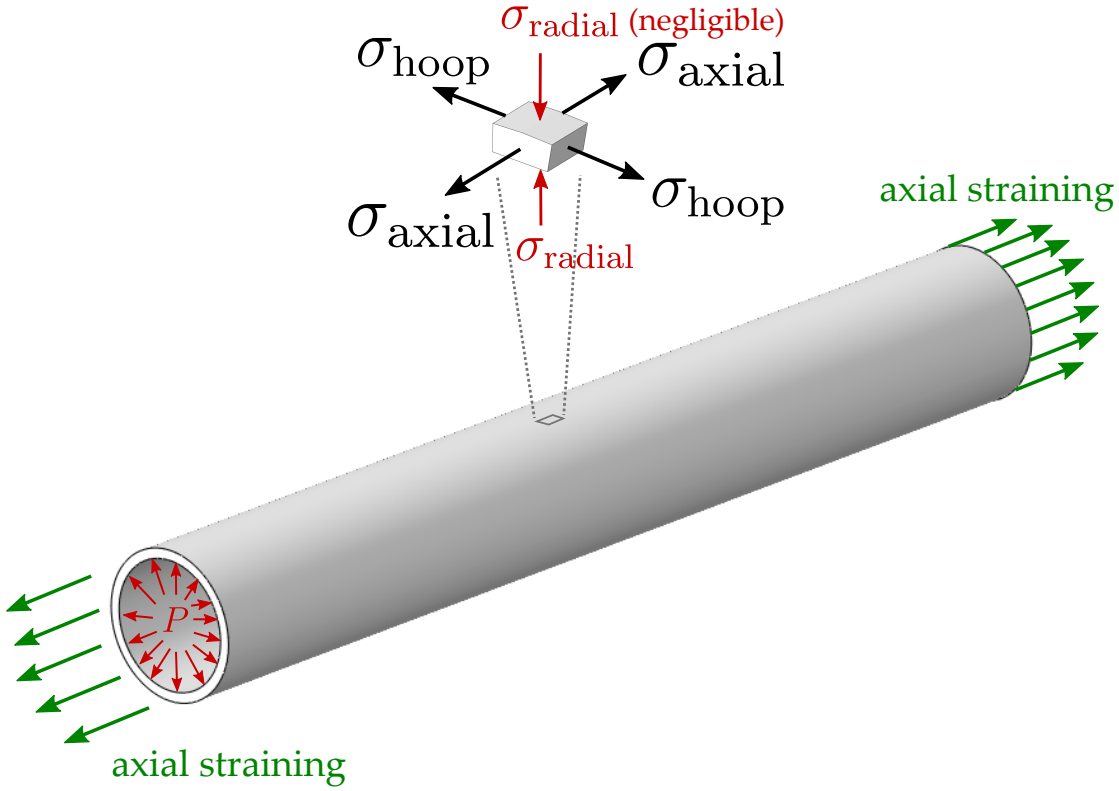

Figure 6.40: Stress state of a pipe subjected to combined axial straining and internal pressure

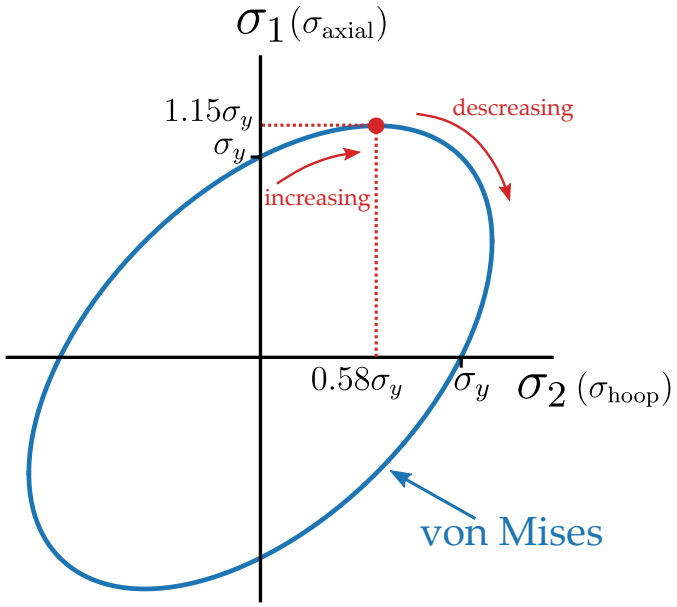

Figure 6.41: Schematic of the von Mises yield criterion illustrating the effect of hoop stress induced by internal pressure

6.3.2 *Effect of internal pressure on crack driving force*

As reported in Section 6.2.2.2, internal pressure has a significant effect on the CDF calculated from FEA. It is interesting to find that during the CTOD plateau phase the CDF increases at lower internal pressure levels (e.g. $\sigma_{hoop}/\sigma_y = 0.2$), whereas decreases at higher internal pressure levels (e.g. $\sigma_{hoop}/\sigma_y \leqslant 0.5$). After the CTOD plateau terminates, the CTOD calculated for a higher internal pressure at a given strain level is found to be higher than that for a lower internal pressure.

As aforementioned, such effect of internal pressure on the CTOD plateau level can be explained in the light of the strain energy dissipated. Recalling the definition of the energy release rate from Chapter 2, the energy release rate is related to the strain energy stored and the work done by an external force, as shown in the following equations:

$$\begin{aligned} G &= -\frac{d\Pi}{dA} \\ &= -\frac{d(U-F)}{dA} \\ &= -\frac{dU-dF}{dA} \\ &= -\frac{d(\int_0^{\Delta} P d\Delta)-dF}{dA} \end{aligned} \tag{6.3}$$

For an infinitesimal increment of crack growth, the increment of the work done by external force approaches to zero, thus the energy release rate (G) can be solely determined by the strain energy dissipated. The strain energy ($U = \int_0^\Delta P d\Delta$) is numerically equal to the area of the shape under the stress-strain or load-displacement response, as illustrated in Figure 6.42. It can be seen that from axial loading only ($\sigma_{hoop}/\sigma_y = 0$) to axial loading with internal pressure (pressure level 1, for example, $\sigma_{hoop}/\sigma_y = 0.2$), the strain energy U increases (i.e. $U_1 > U_0$). Notwithstanding that the length of the load plateau reduces, the increase in U due to an increased level of load plateau outbalances the decreases in U due to the reduction of plateau length. From pressure level 1 to level 2 (e.g. from $\sigma_{hoop}/\sigma = 0.2$ to $\sigma_{hoop}/\sigma = 0.5$, or from $\sigma_{hoop}/\sigma = 0.5$ to $\sigma_{hoop}/\sigma = 0.8$), the increase in the level of load plateau is less prominent while the shortening of the plateau length is relatively significant. Thus, the decrease in U due to shortening of the plateau length outweighs the increase in U due to heightened plateau level, resulting in a reduction of U ($U_1 < U_2$).

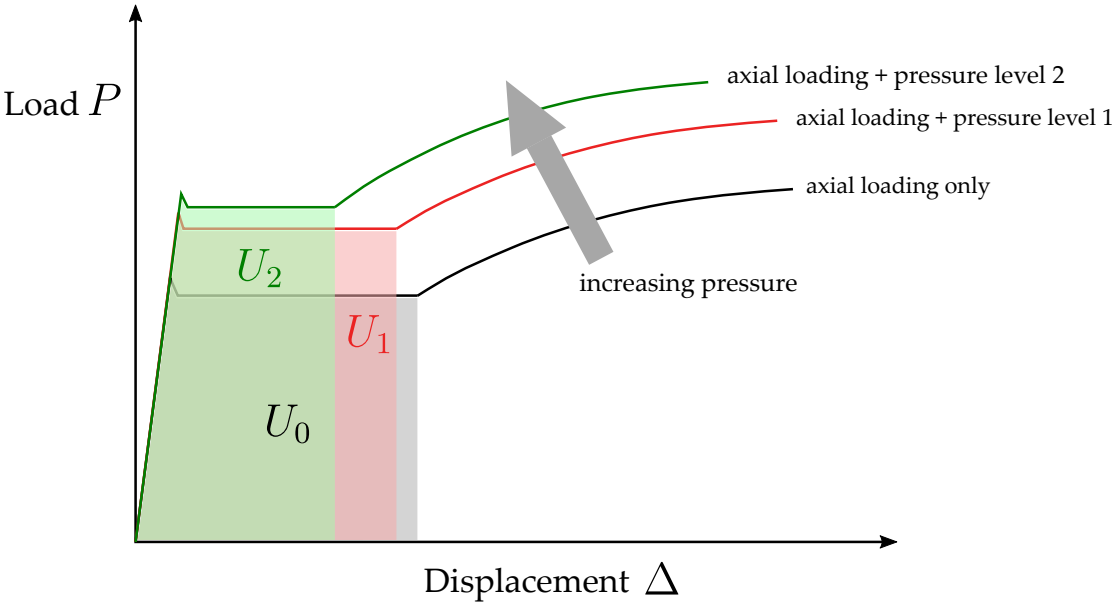

Figure 6.42: Schematic illustrating the effect of internal pressure on the strain energy of the cracked pipe

6.3.3 *Effect of flaw sizes on CDF plateau*

It is well-known that flaw sizes, in particularly the flaw depth, significantly increase the CDF at a given strain. Figure 6.43 and 6.44 show examples of the

effect of flaw sizes on the CDF. From Figure 6.43, it is interesting to observe that apart from enhancing the CDF, the increasing flaw depth slightly shortens the CTOD plateau. The increase in flaw length, on the other hand, is found to lengthen the CTOD plateau, as shown in Figure 6.44. The elongation of CTOD plateau appears more pronounced for shorter flaws (e.g. 2c = 10 - 25 mm) and marginal for longer flaws (e.g. 2c = 50 - 100 mm). When the flaw size is sufficiently large, such as 7×50 mm and 5×75 mm shown in Figures 6.43 (b) and 6.44 (b), respectively, the pipe fails by plastic collapse with the strain localisation propagating to region from the notch, resulting in a monotonically increasing CTOD.

The above results are just examples that were selected and re-organised from the CTOD versus strain results presented in Section 6.2.2.1. In view of conciseness, the results regarding the effects of flaw sizes on CDF for the remainder of the FE cases are not presented herein. Instead, the CTOD values in the Lüders plateau phase together with its extent for each case, which are of most interest, are summarised in Figures 6.45 and 6.46, respectively. The parameters $\delta_{Plateau}$ and $\Delta e_{\delta\ plateau}$ are defined as the average CTOD value and extent of the CTOD plateau, respectively, as illustrated in Figure 6.47 which is similar to the definitions for stress plateau as shown in Figure 6.39.

It can be seen from Figure 6.45 that the CTOD value during the plateau phase ($\delta_{Plateau}$) increases with the internal pressure (in terms of σ_{hoop}/σ_y) but decreases when σ_{hoop}/σ_y is above 0.2. Beyond $\sigma_{hoop}/\sigma_y = 0.5$, the internal pressure is found to have an insignificant effect on $\delta_{Plateau}$. The extent of the CTOD plateau ($\Delta e_{\delta plateau}$), as shown in Figure 6.46, shortens with the increase in σ_{hoop}/σ_y. It can be noticed that both the flaw height and flaw length reduce the extent of the extent of the CTOD plateau, with the effect of flaw height being more pronounced.

Table 6.2 summarises the presence of stress and CTOD plateau calculated from the FEA. It is found that most flaw sizes examined experienced the presence of the plateau phase in both global stress-strain and CTOD versus strain responses. For larger flaws, crack opened significantly during the plateau phase such that ligament necking occurs earlier than that for smaller flaws, either during the plateau phase or in the hardening phase immediately following the plateau. For instance, as shown in Figure 6.48, necking starts to occur in the

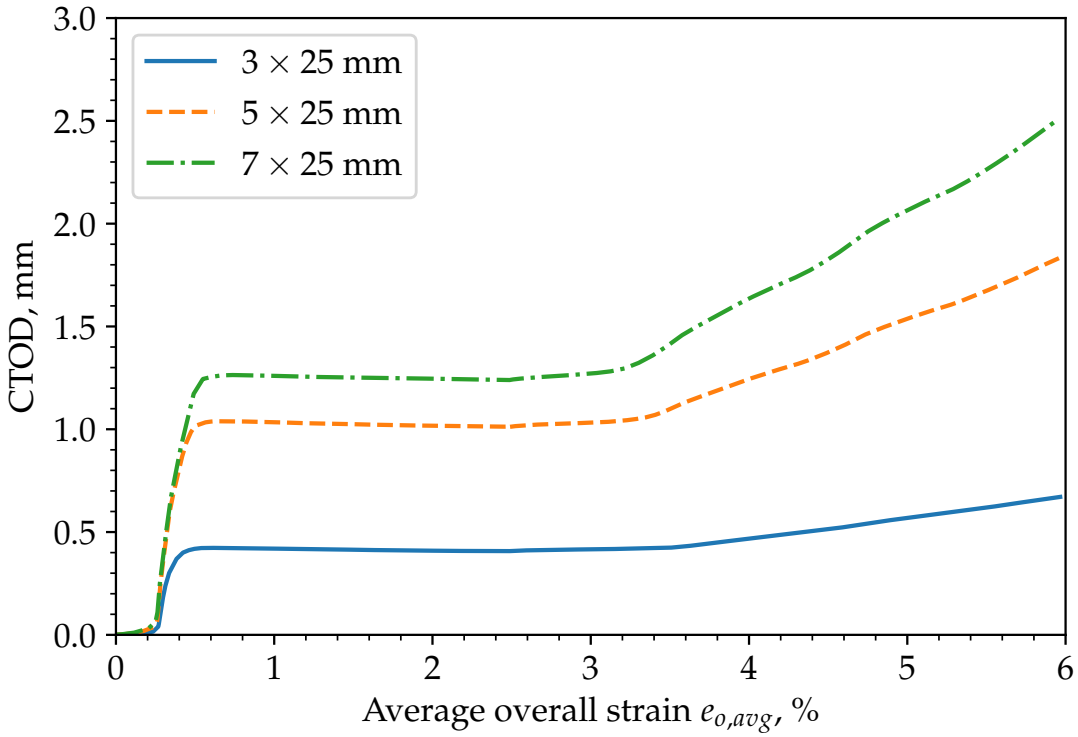

(a)

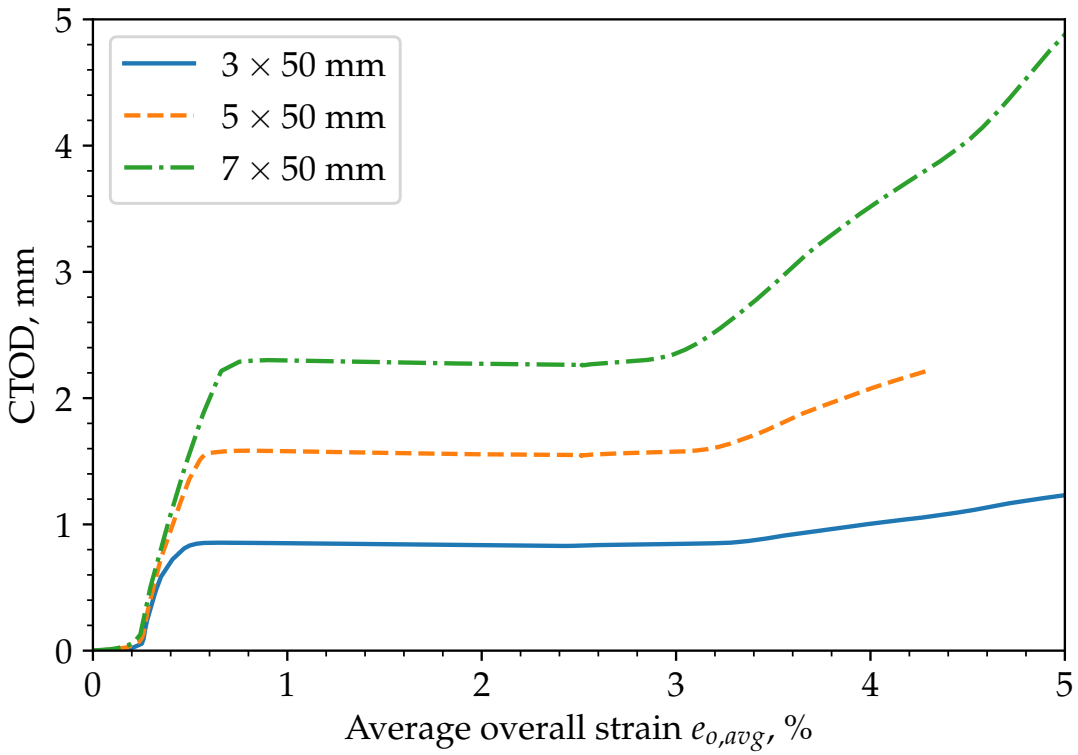

(b)

Figure 6.43: Effect of flaw depth on the CDF calculated from FEA for (a) 2c = 25 mm (b) 2c = 50 mm subjected to combine axial straining and internal pressure ($\sigma_{hoop}/\sigma_y = 0.2$)

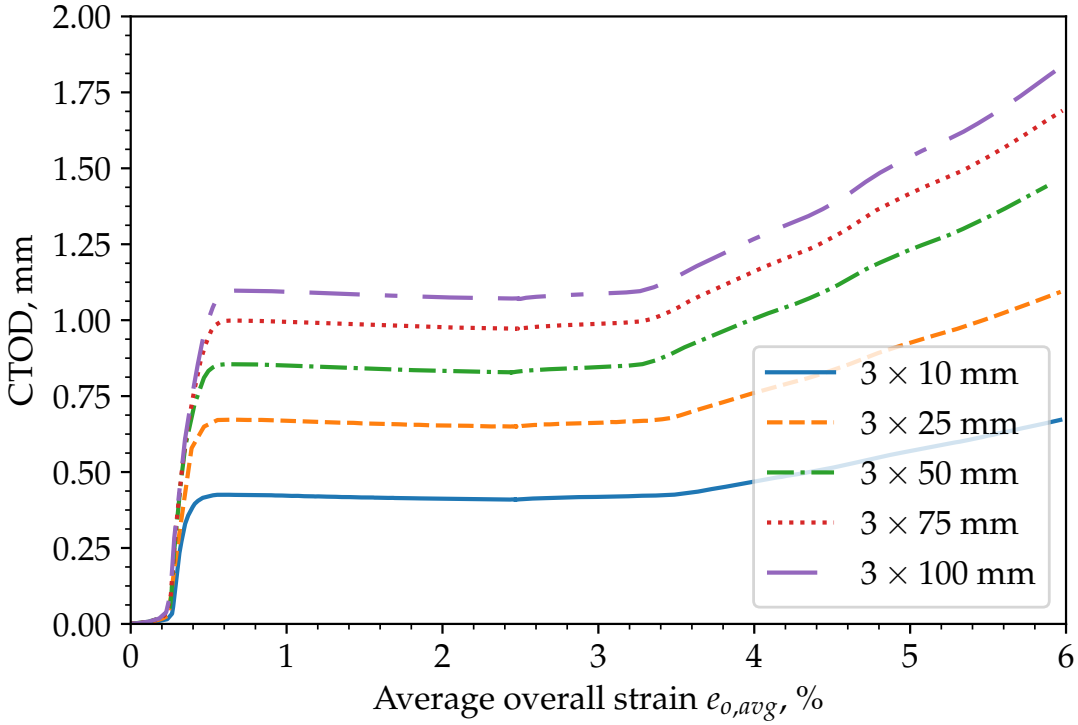

(a)

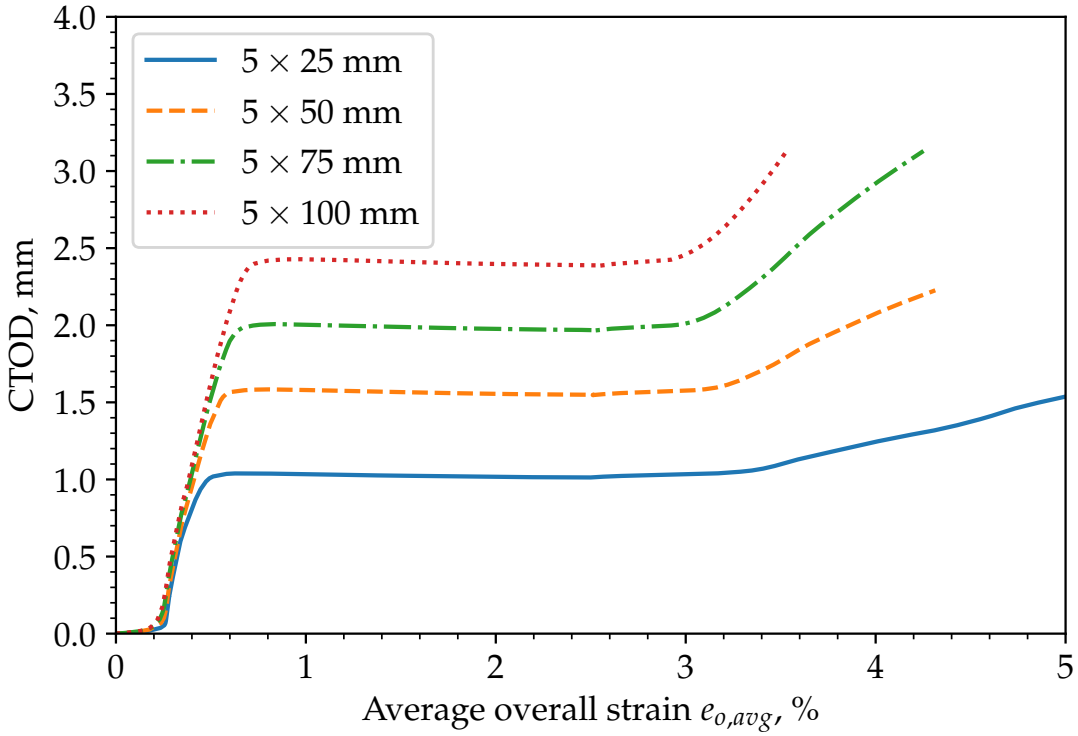

(b)

Figure 6.44: Effect of flaw length on the CDF calculated from FEA for (a) $a = 3$ mm (b) $a = 5$ mm subjected to combined axial straining and internal pressure ($\sigma_{hoop}/\sigma_y = 0.2$)

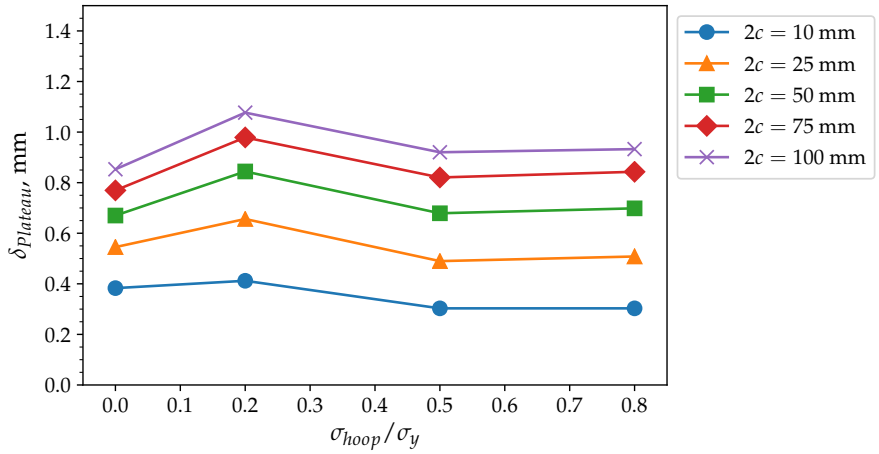

(a)

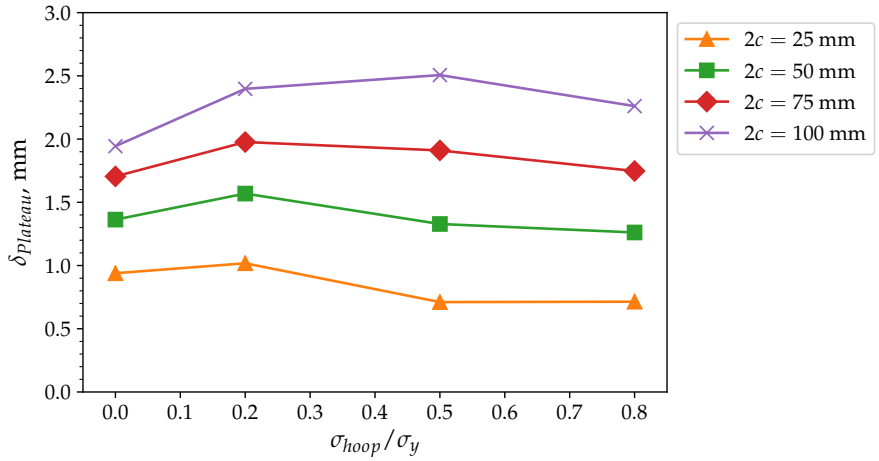

(b)

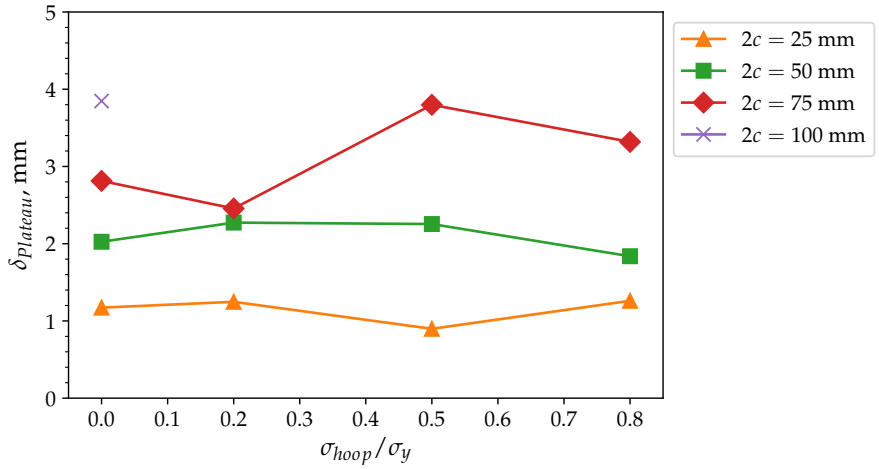

(c)

Figure 6.45: Effect of flaw sizes on the CTOD during plateau phase of the cracked pipe with flaw height of (a) $a = 3$ mm, (b) $a = 5$ mm, and (c) $a = 7$ mm subjected to various levels of internal pressure

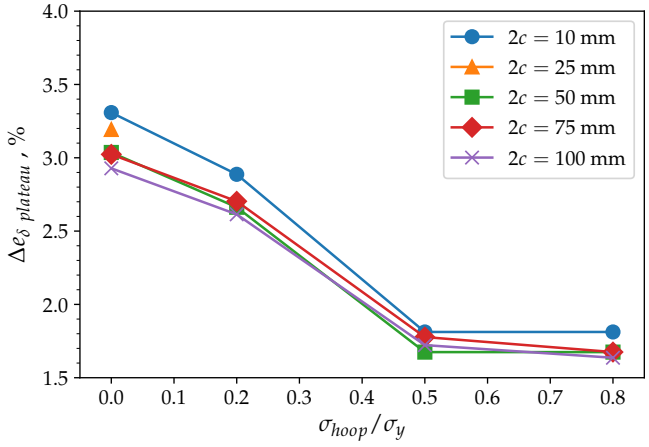

(a)

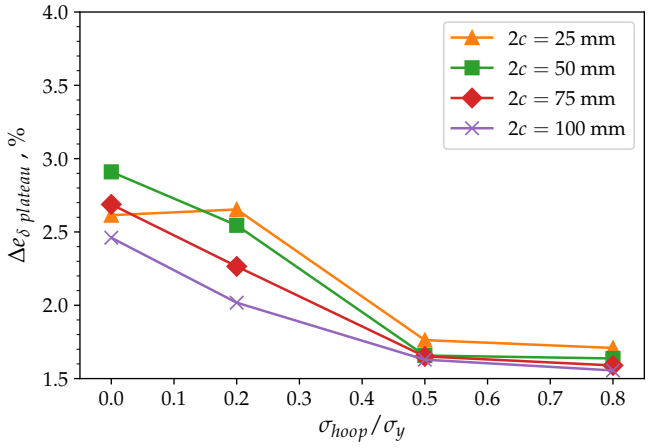

(b)

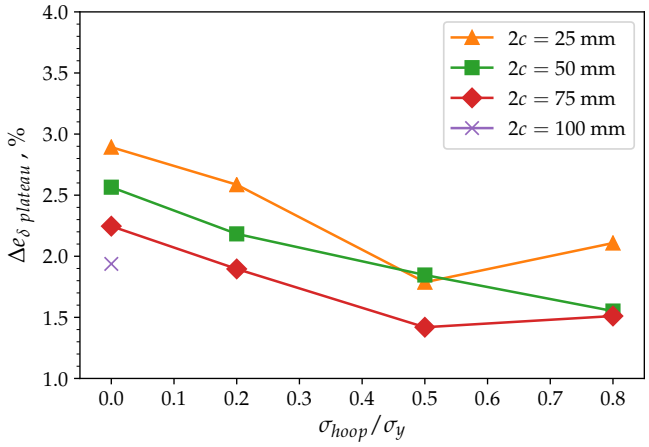

(c)

Figure 6.46: Effect of flaw sizes on the extent of CTOD plateau of the cracked pipe with flaw height of (a) $a = 3$ mm, (b) $a = 5$ mm, and (c) $a = 7$ mm subjected to various levels of internal pressure

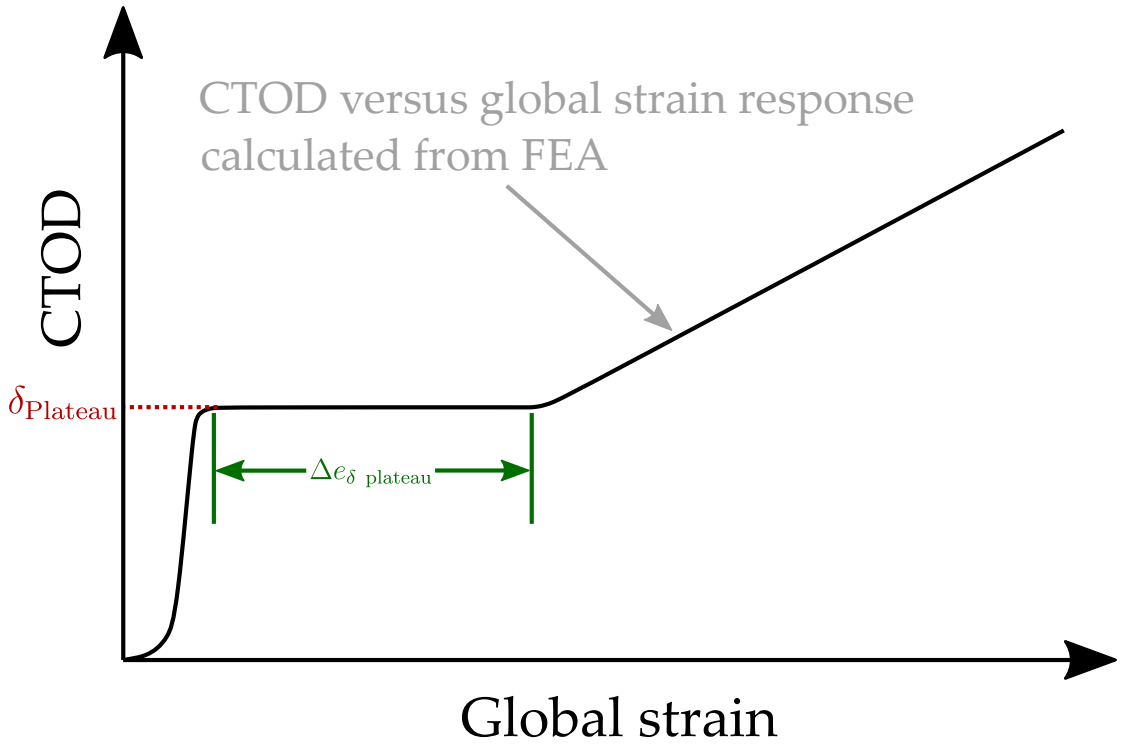

Figure 6.47: Schematic of the CTOD versus global strain response calculated from the FEA with associated parameters

pipe with flaw 7×75 mm subjected to internal pressure of $\sigma_{hoop}/\sigma_y = 0.5$ when the global strain is about 2.3%, not far from the end of the CTOD plateau, as as a result of significant crack opening and straining in the uncracked ligament (PEEQ is shown to be above 10% in the ligament region). For flaw 7×100 mm with internal pressure $\sigma_{hoop}/\sigma_y \geqslant 0.2$, necking was found to occur during the plateau phase before the strain hardening has started.

Table 6.2: Summary of CTOD and stress plateau calculated from FEA

Flaw sizes ($a \times 2c$), mm	σ_{hoop}/σ_y	Stress plateau	CTOD plateau
3×10	0	Yes (2.24%)	Yes (3.31%)
	0.2	Yes (2.06%)	Yes (2.89%)
	0.5	Yes (1.81%)	Yes (1.81%)
	0.8	Yes (1.81%)	Yes (1.81%)
3×25	0	Yes (2.23%)	Yes (3.19%)
	0.2	Yes (2.06%)	Yes (2.81%)
	0.5	Yes	Yes

Table 6.2 continued from previous page

Flaw sizes ($a \times 2c$), mm	σ_{hoop}/σ_y	Stress plateau	CTOD plateau
	0.8	Yes (1.70%)	Yes (1.74%)
3×50	0	Yes (2.19%)	Yes (3.04%)
	0.2	Yes (2.08%)	Yes (2.66%)
	0.5	Yes (1.87%)	Yes (1.72%)
	0.8	Yes (1.82%)	Yes (1.67%)
3×75	0	Yes (2.29%)	Yes (3.02%)
	0.2	Yes (2.08%)	Yes (2.70%)
	0.5	Yes (1.87%)	Yes (1.78%)
	0.8	Yes (1.81%)	Yes (1.68%)
3×100	0	Yes (2.29%)	Yes (2.93%)
	0.2	Yes (2.10%)	Yes (2.61%)
	0.5	Yes (1.87%)	Yes (1.72%)
	0.8	Yes (1.82%)	Yes (1.64%)
5×25	0	Yes (2.26%)	Yes (2.61%)
	0.2	Yes (2.09%)	Yes (2.65%)
	0.5	Yes (1.85%)	Yes (1.76%)
	0.8	Yes (1.78%)	Yes (1.71%)
5×50	0	Yes (2.31%)	Yes (2.91%)
	0.2	Yes (2.14%)	Yes (2.55%)
	0.5	Yes (1.86%)	Yes (1.66%)
	0.8	Yes (1.76%)	Yes (1.64%)
5×75	0	Yes (2.22%)	Yes (2.69%)
	0.2	Yes (2.13%)	Yes (2.27%)
	0.5	Yes (1.88%)	Yes (1.65%) *

* CTOD surged after plateau phase, leading to excessive crack opening and element distortion, followed by necking.

Table 6.2 continued from previous page

Flaw sizes ($a \times 2c$), mm	σ_{hoop}/σ_y	Stress plateau	CTOD plateau
5×100	0.8	Yes (1.82%)	Yes (1.59%) *
	0	Yes (2.23%)	Yes (2.46%)
	0.2	Yes (2.12%)	Yes (2.02%)
	0.5	Yes (1.83%)	Yes (1.63%) *
	0.8	Yes (1.75%)	Yes (N/A)
7×25	0	Yes (2.19%)	Yes (2.89%)
	0.2	Yes (2.09%)	Yes (2.59%)
	0.5	Yes (1.78%)	Yes (1.79%)
	0.8	Yes (1.96%)	Yes (2.11%)
7×50	0	Yes (2.24%)	Yes (2.03%)
	0.2	Yes (2.09%)	Yes (2.27%)
	0.5	Yes (1.85%)	Yes (1.63%)
	0.8	Yes (1.55%)	Yes (1.84%)
7×75	0	Yes (2.24%)	Yes (2.25%)
	0.2	Yes (2.20%)	Yes (1.90%)
	0.5	Yes (1.98%)	Yes (1.42%) *
	0.8	Yes (1.90%)	Yes (1.51%) *
7×100	0	Yes (1.43%)	Yes (1.94%)
	0.2	Yes (N/A) †	No (N/A) †
	0.5	Yes (N/A) †	No (N/A) †
	0.8	Yes (N/A) †	No (N/A) †

† CTOD surged during plateau phase, leading to excessive crack opening and element distortion, followed by necking.

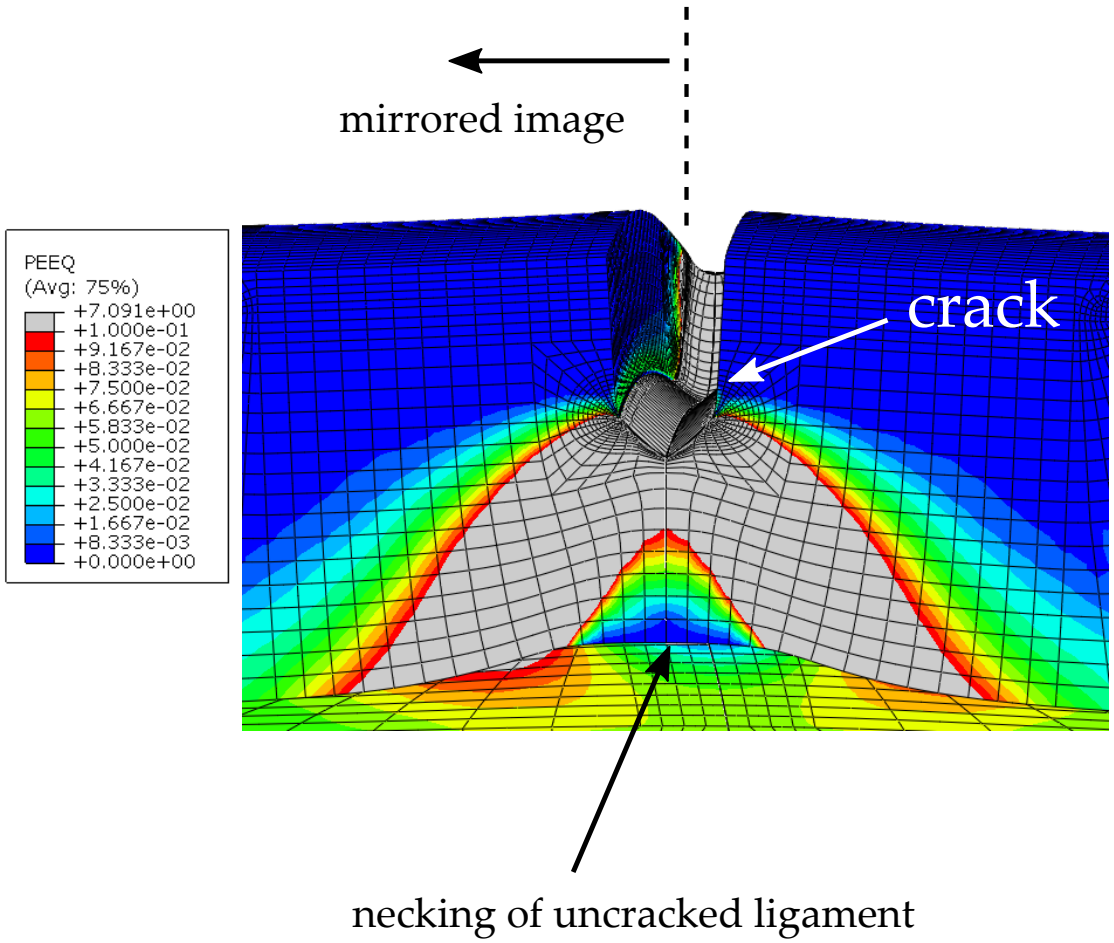

Figure 6.48: Illustration showing the necking in the uncracked ligament due to significant straining in the crack region (flaw 7×75 mm with $\sigma_{hoop}/\sigma_y = 0.5$ as an example)

6.4 SUMMARY

This chapter presents a parametric FEA study of circumferentially-flawed pipes made from Lüder-deforming material subjected to combined axial straining and internal pressure. The effect of internal pressure and the flaw sizes on the crack-tip behaviour and Lüders band development were investigated. Based on the results reported, the following conclusions can be drawn:

- For axially-loaded pipes containing crack-like flaws, the application of internal pressure alters the inclination angle of Lüders band propagation, and tend to yield a single propagating band regime by reinforcing the strain localisation that originates from stress concentrators (i.e. crack-like flaws).

- The internal pressure significantly enhance the CDF of the pipes containing crack-like flaws. During the Lüders plateau phase, however, the internal pressure increases the level of the CDF (in terms of CTOD) plateau for lower pressure ranges, while decreases the level of CDF plateau for higher pressure ranges.

- The effect of internal pressure on CDF and global structural behaviour peaks at around $\sigma_{hoop}/\sigma_y = 0.5$, and starts to diminish when σ_{hoop}/σ_y is above 0.5.

- When the flaw size is sufficiently large, the flawed pipe tends to fail by plastic collapse due to significant straining of the flawed section before the Lüders bands spread out. As a result, the plateau in CDF and global stress-strain responses cannot be observed, and the CDF increases monotonically with applied strain.

7

CONCLUSIONS AND RECOMMENDATIONS

7.1 SUMMARY

The research work reported in this thesis investigated the fracture behaviour of the API X65 seamless pipe containing a circumferential surface-breaking flaw made from a material exhibiting yield discontinuity. The investigation covers experiment of small-scale samples and FE analyses of both small-scale samples and pipes containing flaws. Optimal and simplified material models were identified based on experiments and FE analysis, and were utilised in the subsequent FE analysis of pipes containing flaws subjected to axial straining with and without internal pressure. The efficacy of the material model describing yield discontinuity, the effect of flaw sizes and internal pressure levels on the crack-tip behaviour and development of strain localisation associated with yield discontinuity were addressed.

7.2 CONCLUSIONS

Since the conclusions of each chapter are given at the end the respective chapters, the most prominent conclusions are put forward as follows:

- Most strain-based assessment methods do not explicitly consider the effect of Lüders plateau in the calculation of crack driving force.
- The stress-strain curve containing a flat stress plateau in its engineering stress-strain form is not capable of simulating the strain localisation associated with Lüders bands for both small-scale and full-scale test samples. Use of the stress-strain curve with a flat stress plateau in the FE

analysis of pipes containing flaws may result in a non-conservative crack driving force.

- Material models containing strain softening, such as the UDU stress-strain curve, are necessary to generate Lüders-type strain localisations observed in plain test specimens without flaws, and that in flawed samples such as fracture mechanics test specimens and pipes containing circumferential flaws. For flawed pipes, the use of UDU stress-strain curves were found to effectively capture the strain localisation due to Lüders behaviour, and predict crack driving force with suitable conservatism in comparison with the full-scale test data.

- The flaw sizes, in particular the flaw depth, has a significant effect on the development of strain localisation associated with Lüders bands in the small-small scale fracture toughness test specimens (i.e. SENT specimens) and the pipes containing circumferential surface-breaking flaws. Deeper flaws tend to render plastic deformation localised at the flaw region and the uncracked ligament, rather than propagate to regions far from the flaw, ultimately leading to plastic collapse of the ligament.

- The internal pressure alternates significantly the global stress-strain behaviour of the pipes containing circumferential flaws. The level of global stress plateau (Lüders plateau) increases with the application of internal pressure, and reduces slightly for higher internal pressure levels ($\sigma_{hoop}/\sigma_y \geqslant 0.5$). The extent of the stress plateau, on the other hand, decreases as the internal pressure increases, which is less prominent for higher in internal pressure levels.

- The internal pressure changes the development of strain localisation associated with Lüders bands. The internal pressure reinforces the strain localization in the near-tip region, and alters the inclination angle at which the Lüders band propagates.

7.3 RECOMMENDATIONS FOR FUTURE WORK

This thesis presents a comprehensive body of work, combining both experimental and numerical investigations of the fracture behaviour of X65 pipes

containing circumferential flaws in the presence of yield discontinuity. It is believed, however, the following additional research work may be a suitable follow-up:

- More sophisticated material models, such as the strain ageing model which yields a stress-strain curve with a nonlinear softening behaviour, could be employed in the numerical analysis. This type of material models may require a vast body of experimental programmes for calibration of the parameters of the constitutive models. Simplification of the constitutive models may be made to reduce the number of parameters as the strain ageing model was originally designated for simulating the PLC phenomenon, taking the effect of temperature, strain rate and the intrinsic mechanisms of dislocation interaction. In the assessment of pipelines made from materials exhibiting a Lüders plateau, however, such complex material model may not be necessary and further simplification and assumption could be made.

- To reinforce the understanding of the effect of biaxial stress state on the Lüders bands in structures with and without flaws, it would be useful to carry out biaxial loading tests (e.g. cruciform tests) on a plain plate and a plate containing a surface notch, coupled with DIC technique for strain measurement. Variance in biaxial stress ratio and notch sizes can be considered. Both continuous yielding and discontinuous yielding materials could also be used to investigate the effect of yield discontinuity on the plasticity development under a biaxial stress state.

- Explicit simulation of ductile crack growth can be incorporated using the damage model (such as the GTN model) to investigate the effect of yielding discontinuity on the ductile tearing of cracked pipes. This also allows a more accurate calibration with the test in which ductile crack growth occurs.

- It is suggested that metallurgic analysis, such as microscopy using scanning electron microscope (SEM) technique, be carried out to explore the fracture surfaces and the microstructures of the small-scale test specimens including tensile tests and fracture mechanics tests made from materials exhibiting yield discontinuity.

- Additional full-scale pipe tests subjected to axial straining with and without internal pressure may be desired. DIC technique can be employed to quantify the full-field deformation of the pipe containing surface flaws. FE analyses could be performed using the constitutive models calibrated, and then validated against the test data and DIC.

APPENDIX

A

TENSILE TEST REPORTS

ROUND TENSILE 23192 M12-01

Test date	14/05/2015
Technician	Jerry Godden
Test machine	INSTRON 8500 B107
Control mode	DISPLACEMENT
Test standard	BS EN ISO 6892-1

Client	
Project leader	E Eren
Investigator's signature	
Compiled by	J Godden
Signed	

SPECIMEN DETAILS

Initial diameter	9.96	mm
Initial XSA	77.913	mm²
Final XSA	16.260	mm²
Estimated Youngs modulus	228405	N/mm²
Poissons ratio	0.300	
Test temperature	22.0	°C
Extensometer gauge length	50.00	mm
Initial Gauge length	49.96	mm
Final gauge length	63.58	mm
Initial Stressing rate	13.868	N/mm²/S
Initial Straining rate	0.000061	Strain/S
Initial Dispacement rate	0.016577	mm/S

RESULTS

Strain %	Extension mm	Load kN	Stress N/mm²
0.1	0.172	39.75	510.2
0.2	0.222	39.93	512.5
0.5	0.372	39.55	507.6
1.0	0.622	39.39	505.5
2.0	1.125	40.75	523.0
UTS		46.75	600.0

Reduction in area	79.13	%
Elongation	27.26	%

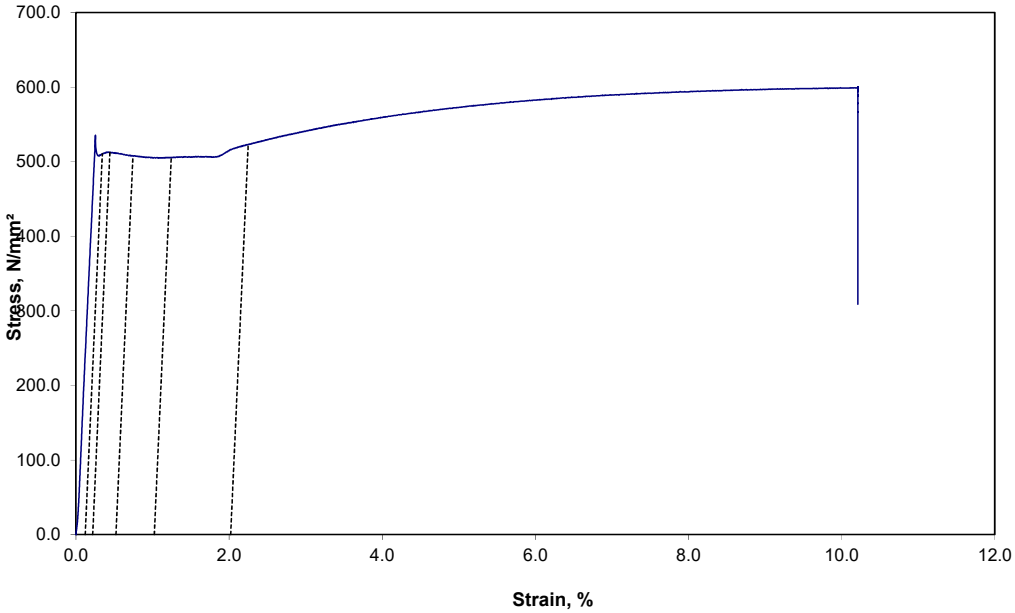

LVGENPLOT V 1.29 02-Apr-2015

14 May 2015 FI

ROUND TENSILE 23192 M12-02

Test date	14/05/2015
Technician	Jerry Godden
Test machine	INSTRON 8500 B107
Control mode	DISPLACEMENT
Test standard	BS EN ISO 6892-1

Client	
Project leader	E Eren
Investigator's signature	
Compiled by	J Godden
Signed	

SPECIMEN DETAILS

Initial diameter	10.05	mm
Initial XSA	79.327	mm²
Final XSA	16.117	mm²
Estimated Youngs modulus	216702	N/mm²
Poissons ratio	0.300	
Test temperature	22.0	°C
Extensometer gauge length	50.00	mm
Initial Gauge length	49.60	mm
Final gauge length	62.93	mm
Initial Stressing rate	14.159	N/mm²/S
Initial Straining rate	0.000066	Strain/S
Initial Dispacement rate	0.016644	mm/S

RESULTS

Strain %	Extension mm	Load kN	Stress N/mm²
0.1	0.186	40.01	504.4
0.2	0.237	40.18	506.6
0.5	0.386	39.78	501.4
1.0	0.637	40.07	505.1
2.0	1.140	41.55	523.7
UTS		47.51	598.9

Reduction in area	79.68	%
Elongation	26.88	%

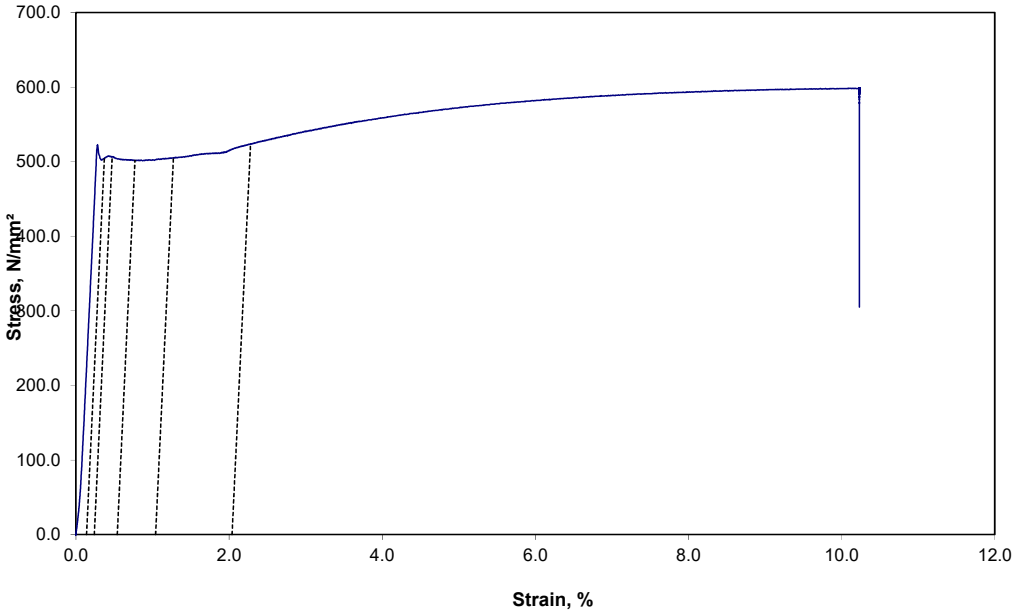

LVGENPLOT V 1.29 02-Apr-2015

14 May 2015 FI

FLAT TENSILE 24068 M01-02

Test date	12/04/2016
Technician	M Tinkler
Test machine	INSTRON 8500 B530
Control mode	DISPLACEMENT
Test standard	BS EN ISO 6892-1

Client	
Project leader	
Investigator's signature	
Compiled by	M. Tinkler
Signed	

SPECIMEN DETAILS

Initial Width	20.07	mm
Initial Thickness	5.01	mm
Initial XSA	100.551	mm²
Final XSA	22.995	mm²
Estimated Youngs modulus	222409	N/mm²
Poissons ratio	0.300	
Test temperature	20.0	°C
Extensometer gauge length	25.00	mm
Initial Gauge length	49.77	mm
Final gauge length	65.99	mm
Initial Stressing rate	6.406	N/mm²/S
Initial Straining rate	0.000029	Strain/S
Initial Displacement rate	0.009896	mm/S

RESULTS

Strain %	Extension mm	Load kN	Stress N/mm²
0.1	0.077	46.57	463.2
0.2	0.103	46.55	463.0
0.5	0.178	46.66	464.0
1.0	0.302	46.57	463.2
2.0	0.553	47.05	467.9
UTS		55.35	550.5

Reduction in area	77.13	%
Elongation	32.59	%

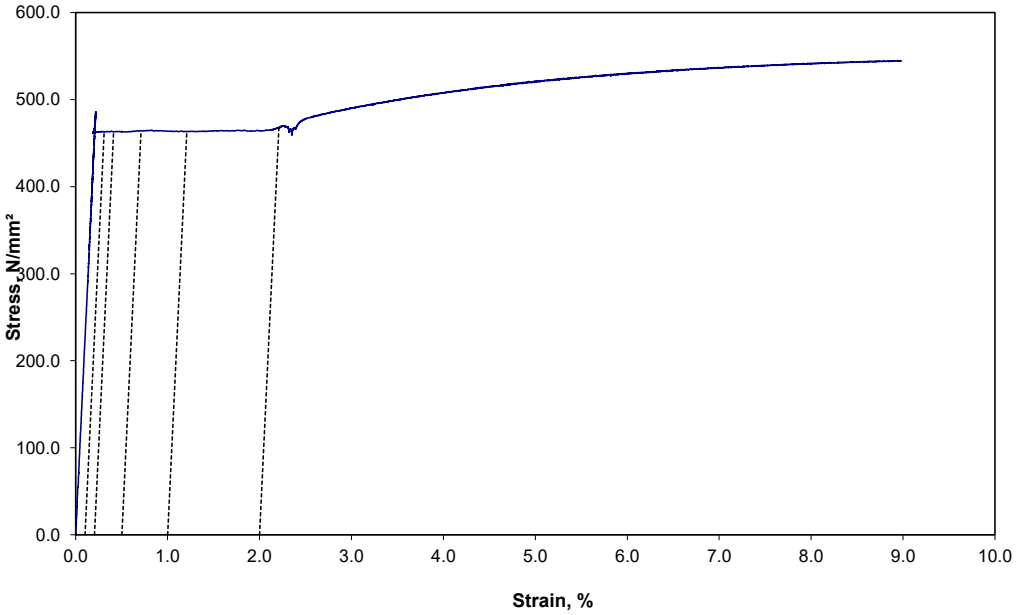

FLAT TENSILE 24068 M02-02

Test date	13/04/2016
Technician	M Tinkler
Test machine	INSTRON 8500 B530
Control mode	DISPLACEMENT
Test standard	BS EN ISO 6892-1

Client	
Project leader	
Investigator's signature	
Compiled by	M. Tinkler
Signed	

SPECIMEN DETAILS

Initial Width	14.27	mm
Initial Thickness	5.09	mm
Initial XSA	72.634	mm²
Final XSA	20.962	mm²
Estimated Youngs modulus	251660	N/mm²
Poissons ratio	0.300	
Test temperature	20.0	°C
Extensometer gauge length	25.00	mm
Initial Gauge length	49.70	mm
Final gauge length	54.36	mm
Initial Stressing rate	4.134	N/mm²/S
Initial Straining rate	0.000016	Strain/S
Initial Displacement rate	0.004187	mm/S

RESULTS

Strain %	Extension mm	Load kN	Stress N/mm²
0.1	0.076	37.21	512.3
0.2	0.102	37.58	517.4
0.5	0.178	38.39	528.6
1.0	0.304	39.81	548.1
2.0	0.557	41.45	570.6
UTS		44.88	617.9

Reduction in area	71.14	%
Elongation	9.38	%

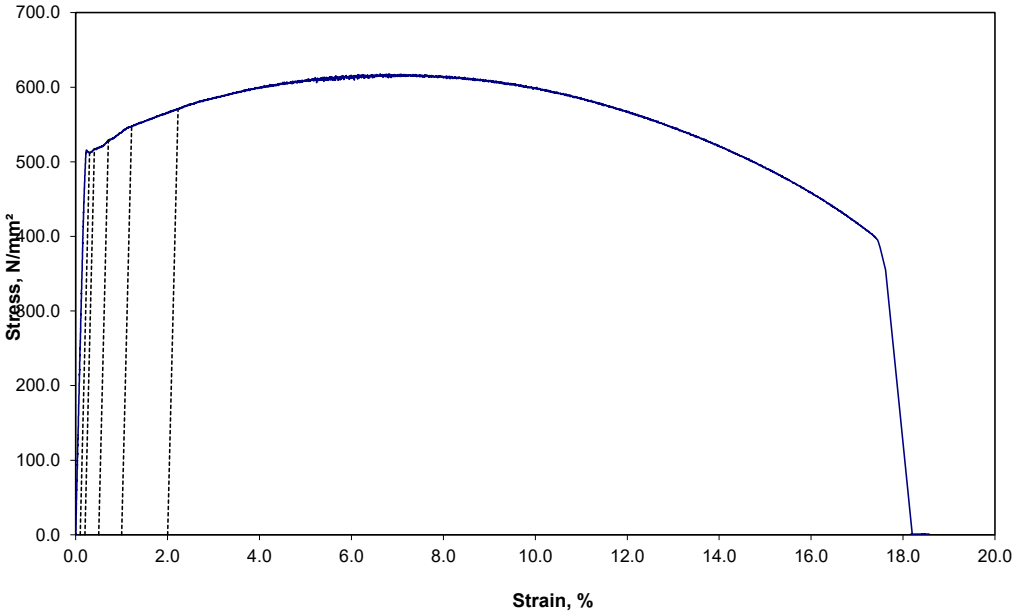

TWI Ltd, Granta Park, Great Abington, Cambridge, CB21 6AL, Cambridgeshire, UK, Tel 01223 899000

B

SENT TEST REPORTS

SENT FRACTURE TEST 24609 M01-01

Client
Project leader Signed:

Data source

Data logging program	LVGENLOG V 1.39 30-Jan-2017
Program used to calculate CTOD/J	LVGENPLOT V 1.44 26-Apr-2017
Calculation date of CTOD/J	19 May 2017

Specimen details

Material	API X65	
Specimen type	Subsize, SENT	
Crack plane orientation	X-Z	
Type of notch tip	Fatigue	
Notch tip location	Parent material	
Specimen width	17.010	mm
Specimen thickness	34.020	mm
Initial crack length	6.624	mm
Side-grooved?	NO	
Original PM 1 thickness	40.00	mm

Test details

Test standard(s)	BS8571:2014	
Test date	19/05/2017	
Test time	09:44:00	
Test technician	Phillip Cossey	Signed:
Test machine	INSTRON 8500 B107	
Test environment	AIR	
Test temperature	25.0	°C
Soak time @ test temperature	15.0	minutes
Knife edge heights	2.500, 12.500	mm
Knife edge spacing	2.00	mm
Initial K-rate	0.696	$MPa.m^{1/2}/s$
Length between grips	170.0	mm

TWI Ltd, Granta Park, Great Abington, Cambridge, CB21 6AL, Cambridgeshire, UK, Tel 01223 899000

Material properties

Yield strength for pre-cracking	463.0	MPa	Measured at RT
Tensile strength for pre-cracking	551.0	MPa	Measured at RT
Yield strength for testing	463.0	MPa	Measured at RT
Tensile strength for testing	551.0	MPa	Measured at RT
Poisson's ratio	0.3		Assumed
Young's modulus	210	GPa	Assumed

Fatigue details

Stress ratio, R	0.100	
Final force, F_f	13.00	kN
Final K	22.5	$MPa.m^{1/2}$
Fatigue temperature	21.0	°C
Loading span, S	68.0	mm

Analysis details

Lower knife edge height check	Warning !!! z/a > 0.2

Compiled by: Phillip Cossey **Signed:**

TWI Ltd, Granta Park, Great Abington, Cambridge, CB21 6AL, Cambridgeshire, UK, Tel 01223 899000

SENT FRACTURE TEST 24609 M01-01

Qualification checks to

(ISO 12135:2002 fig 8)	
Knife edge attachment spacing	**Pass**
(ISO 12135:2002 5.4.2.4.1)	
The stress ratio <= 0.1	**Pass**
(ISO 12135:2002 5.4.2.4.3)	
The final fatigue precracking force <= F_f	**Pass**
(ISO 12135:2002 5.7.5)	**Pass**
Initial K-rate between 0.2 MPa.m$^{0.5}$s^{-1} and 3.0 MPa.m$^{0.5}$s^{-1}	
(ISO 12135:2002 5.8.2)	
Minimum crack length (c)	**Pass**
Fatigue crack within evelope (d)	**Pass**
(BS8571:2014)	
a0/W Limit (9.1 b)	**Pass**
Crack shape (9.1 c)	**Pass**
Δa differences within in limit (9.1 d)	**Fail**
W/B Limit (5.2)	**Pass**
Length between the grips (5.2 Fig 4)	**Pass**

SENT FRACTURE TEST 24609 M01-01

Test date	19/05/2017
Technician	Phillip Cossey
Test machine	INSTRON 8500 B107
Control mode	Displacement

Client	00/01/1900
Project leader	00/01/1900
Investigator's signature	
Compiled by	Phillip Cossey

SPECIMEN DETAILS

Force, F	214.02	kN
Width, W	17.010	mm
Thickness, B	34.020	mm
Crack length, a_0	6.624	mm
Yield strength	463	MPa
Young's modulus	210	GPa
Poisson's ratio	0.300	
Test temperature	25.0	°C

RESULTS

δ	2.809	mm
K @ calculation point	94.9	MPa.m$^{1/2}$
F_{max}/F_Q	2.68	
K_Q	38.76	MPa.m$^{1/2}$
Total area under Force v CMOD	724.47	kNmm
J From CMOD to BS8571:2014 Eq 2 to 10	1605.73	kJ/m² (N/mm)
Plastic area Force vs CMOD	709.96	kNmm
Type of result	Unloading	
Test standard(s)	BS8571:2014	
Test qualified to standard(s)	YES	

LOWER CLIP GAUGE VALUES

Knife edge height	2.50	mm
Vg	3.503	mm
Vp	3.350	mm

UPPER CLIP GAUGE VALUES

Knife edge height	12.50	mm
Vg	4.214	mm
Vp	3.988	mm

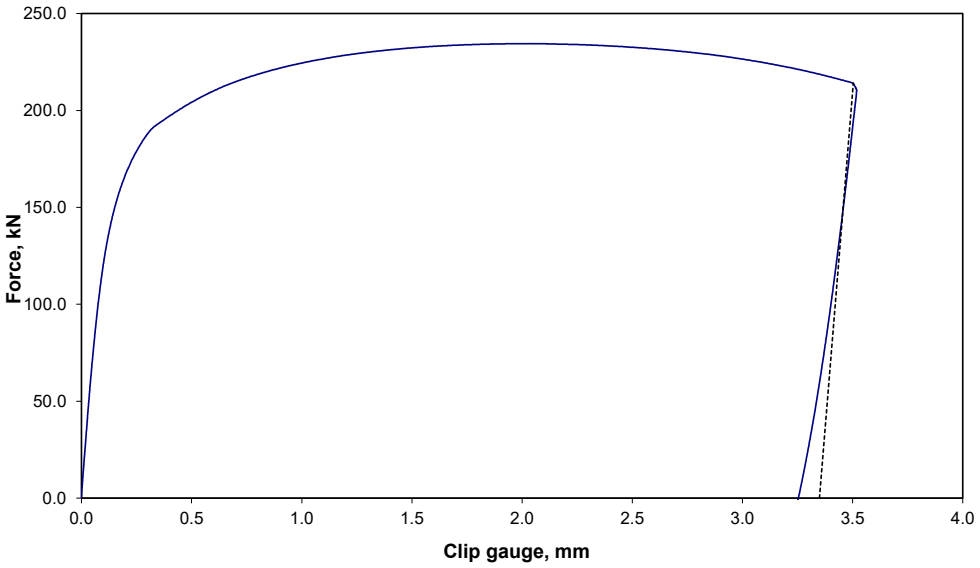

TWI Ltd, Granta Park, Great Abington, Cambridge, CB21 6AL, Cambridgeshire, UK, Tel 01223 899000

SENT FRACTURE TEST 24609 M01-01

Specimen width, W	17.010	mm
Specimen thickness, B	34.020	mm
Machined notch depth, M	3.620	mm
Machined notch width, N	0.320	mm
Surface crack length, a_{S1}	5.790	mm
Surface crack length, a_{S2}	5.810	mm
a_{max}	6.810	mm
a_{min}	6.160	mm

Diagram of fracture face

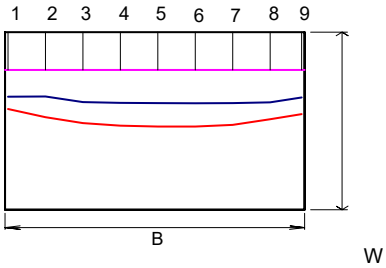

Comments

Measurement Line	Fatigue crack length a_0, mm	Slow stable crack extension + fatigue crack a_p, mm	Slow stable crack extension including stretch zone, Δ_a, mm
1	6.190	7.360	1.170
2	6.160	8.150	1.990
3	6.700	8.720	2.020
4	6.780	8.950	2.170
5	6.800	9.040	2.240
6	6.810	9.040	2.230
7	6.800	8.870	2.070
8	6.720	8.330	1.610
9	6.250	7.860	1.610
Weighted Average	**6.624**	**8.589**	**1.965**

Measured by: Phillip Cossey **Signed:**

SENT FRACTURE TEST 24609 M01-02

Client
Project leader Signed:

Data source

Data logging program	LVGENLOG V 1.39 30-Jan-2017
Program used to calculate CTOD/J	LVGENPLOT V 1.44 26-Apr-2017
Calculation date of CTOD/J	18 May 2017

Specimen details

Material	API X65	
Specimen type	Subsize, SENT	
Crack plane orientation	X-Z	
Type of notch tip	Fatigue	
Notch tip location	Parent material	
Specimen width	17.020	mm
Specimen thickness	34.000	mm
Initial crack length	6.569	mm
Side-grooved?	NO	
Original PM 1 thickness	40.00	mm

Test details

Test standard(s)	BS8571:2014	
Test date	17/05/2017	
Test time	15:16:00	
Test technician	Phillip Cossey	Signed:
Test machine	INSTRON 8500 B107	
Test environment	AIR	
Test temperature	25.0	°C
Soak time @ test temperature	15.0	minutes
Knife edge heights	2.500, 12.500	mm
Knife edge spacing	2.00	mm
Initial K-rate	0.687	$MPa.m^{1/2}/s$
Length between grips	170.0	mm

TWI Ltd, Granta Park, Great Abington, Cambridge, CB21 6AL, Cambridgeshire, UK, Tel 01223 899000

Material properties

Yield strength for pre-cracking	463.0	MPa	Measured at RT
Tensile strength for pre-cracking	551.0	MPa	Measured at RT
Yield strength for testing	463.0	MPa	Measured at RT
Tensile strength for testing	551.0	MPa	Measured at RT
Poisson's ratio	0.3		Assumed
Young's modulus	210	GPa	Assumed

Fatigue details

Stress ratio, R	0.100	
Final force, F_f	13.00	kN
Final K	22.3	$MPa.m^{1/2}$
Fatigue temperature	21.0	°C
Loading span, S	68.0	mm

Analysis details

Lower knife edge height check	Warning !!! z/a > 0.2

Compiled by: Phillip Cossey **Signed:**

TWI Ltd, Granta Park, Great Abington, Cambridge, CB21 6AL, Cambridgeshire, UK, Tel 01223 899000

SENT FRACTURE TEST 24609 M01-02

Qualification checks to

(ISO 12135:2002 fig 8)	
Knife edge attachment spacing	**Pass**
(ISO 12135:2002 5.4.2.4.1)	
The stress ratio <= 0.1	**Pass**
(ISO 12135:2002 5.4.2.4.3)	
The final fatigue precracking force <= F_f	**Pass**
(ISO 12135:2002 5.7.5)	**Pass**
Initial K-rate between 0.2 MPa.m$^{0.5}$s^{-1} and 3.0 MPa.m$^{0.5}$s^{-1}	
(ISO 12135:2002 5.8.2)	
Minimum crack length (c)	**Pass**
Fatigue crack within evelope (d)	**Pass**
(BS8571:2014)	
a0/W Limit (9.1 b)	**Pass**
Crack shape (9.1 c)	**Pass**
Δa differences within in limit (9.1 d)	**Fail**
W/B Limit (5.2)	**Pass**
Length between the grips (5.2 Fig 4)	**Pass**

SENT FRACTURE TEST 24609 M01-02

Test date	17/05/2017
Technician	Phillip Cossey
Test machine	INSTRON 8500 B107
Control mode	Displacement

Client	00/01/1900
Project leader	00/01/1900
Investigator's signature	
Compiled by	Phillip Cossey

SPECIMEN DETAILS

Force, F	222.31	kN
Width, W	17.020	mm
Thickness, B	34.000	mm
Crack length, a_0	6.569	mm
Yield strength	463	MPa
Young's modulus	210	GPa
Poisson's ratio	0.300	
Test temperature	25.0	°C

RESULTS

δ	0.695	mm
K @ calculation point	97.6	MPa.m$^{1/2}$
F_{max}/F_Q	2.49	
K_Q	39.21	MPa.m$^{1/2}$
Total area under Force v CMOD	174.00	kNmm
J From CMOD to BS8571:2014 Eq 2 to 10	390.80	kJ/m² (N/mm)
Plastic area Force vs CMOD	158.84	kNmm
Type of result	Unloading	
Test standard(s)	BS8571:2014	
Test qualified to standard(s)	YES	

LOWER CLIP GAUGE VALUES

Knife edge height	2.50	mm
Vg	1.003	mm
Vp	0.846	mm

UPPER CLIP GAUGE VALUES

Knife edge height	12.50	mm
Vg	1.299	mm
Vp	1.062	mm

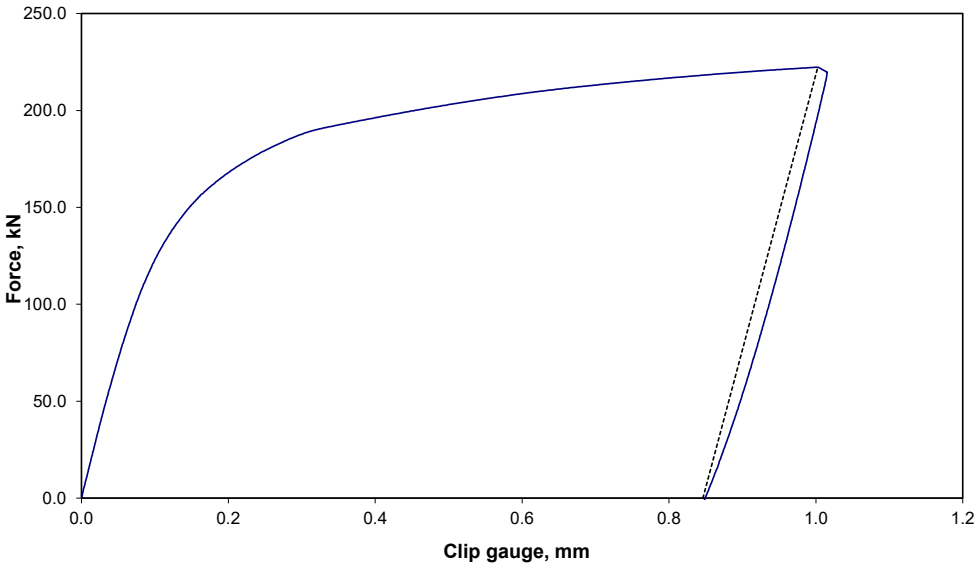

TWI Ltd, Granta Park, Great Abington, Cambridge, CB21 6AL, Cambridgeshire, UK, Tel 01223 899000

SENT FRACTURE TEST 24609 M01-02

Diagram of fracture face

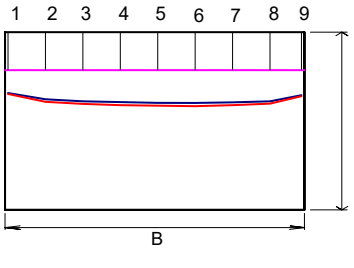

Specimen width, W	17.020	mm
Specimen thickness, B	34.000	mm
Machined notch depth, M	3.640	mm
Machined notch width, N	0.310	mm
Surface crack length, a_{S1}	5.780	mm
Surface crack length, a_{S2}	5.770	mm
a_{max}	6.780	mm
a_{min}	5.830	mm

Comments

Measurement Line	Fatigue crack length a_0, mm	Slow stable crack extension + fatigue crack a_p, mm	Slow stable crack extension including stretch zone, Δ_a, mm
1	5.830	5.920	0.090
2	6.420	6.680	0.260
3	6.620	6.870	0.250
4	6.700	6.990	0.290
5	6.770	7.030	0.260
6	6.780	7.090	0.310
7	6.710	7.000	0.290
8	6.620	6.850	0.230
9	6.040	6.130	0.090
Weighted Average	**6.569**	**6.817**	**0.248**

Measured by: Phillip Cossey **Signed:**

SENT FRACTURE TEST 24609 M01-03

Client
Project leader Signed:

Data source

Data logging program	LVGENLOG V 1.39 30-Jan-2017
Program used to calculate CTOD/J	LVGENPLOT V 1.44 26-Apr-2017
Calculation date of CTOD/J	18 May 2017

Specimen details

Material	API X65	
Specimen type	Subsize, SENT	
Crack plane orientation	X-Z	
Type of notch tip	Fatigue	
Notch tip location	Parent material	
Specimen width	17.020	mm
Specimen thickness	34.000	mm
Initial crack length	6.609	mm
Side-grooved?	NO	
Original PM 1 thickness	40.00	mm

Test details

Test standard(s)	BS8571:2014	
Test date	17/05/2017	
Test time	15:49:00	
Test technician	Phillip Cossey	Signed:
Test machine	INSTRON 8500 B107	
Test environment	AIR	
Test temperature	25.0	°C
Soak time @ test temperature	15.0	minutes
Knife edge heights	2.500, 12.500	mm
Knife edge spacing	2.00	mm
Initial K-rate	0.694	$MPa.m^{1/2}/s$
Length between grips	170.0	mm

TWI Ltd, Granta Park, Great Abington, Cambridge, CB21 6AL, Cambridgeshire, UK, Tel 01223 899000

Material properties

Yield strength for pre-cracking	463.0	MPa	Measured at RT
Tensile strength for pre-cracking	551.0	MPa	Measured at RT
Yield strength for testing	463.0	MPa	Measured at RT
Tensile strength for testing	551.0	MPa	Measured at RT
Poisson's ratio	0.3		Assumed
Young's modulus	210	GPa	Assumed

Fatigue details

Stress ratio, R	0.100	
Final force, F_f	13.00	kN
Final K	22.5	$MPa.m^{1/2}$
Fatigue temperature	21.0	°C
Loading span, S	68.0	mm

Analysis details

Lower knife edge height check	Warning !!! z/a > 0.2

Compiled by: Phillip Cossey **Signed:**

TWI Ltd, Granta Park, Great Abington, Cambridge, CB21 6AL, Cambridgeshire, UK, Tel 01223 899000

SENT FRACTURE TEST 24609 M01-03

Qualification checks to

(ISO 12135:2002 fig 8)	
Knife edge attachment spacing	**Pass**
(ISO 12135:2002 5.4.2.4.1)	
The stress ratio <= 0.1	**Pass**
(ISO 12135:2002 5.4.2.4.3)	
The final fatigue precracking force <= F_f	**Pass**
(ISO 12135:2002 5.7.5)	**Pass**
Initial K-rate between 0.2 MPa.m$^{0.5}$s^{-1} and 3.0 MPa.m$^{0.5}$s^{-1}	
(ISO 12135:2002 5.8.2)	
Minimum crack length (c)	**Pass**
Fatigue crack within evelope (d)	**Pass**
(BS8571:2014)	
a0/W Limit (9.1 b)	**Pass**
Crack shape (9.1 c)	**Pass**
Δa differences within in limit (9.1 d)	**Fail**
W/B Limit (5.2)	**Pass**
Length between the grips (5.2 Fig 4)	**Pass**

SENT FRACTURE TEST 24609 M01-03

Test date	17/05/2017
Technician	Phillip Cossey
Test machine	INSTRON 8500 B107
Control mode	Displacement

Client	00/01/1900
Project leader	00/01/1900
Investigator's signature	
Compiled by	Phillip Cossey

SPECIMEN DETAILS

Force, F	230.39	kN
Width, W	17.020	mm
Thickness, B	34.000	mm
Crack length, a_0	6.609	mm
Yield strength	463	MPa
Young's modulus	210	GPa
Poisson's ratio	0.300	
Test temperature	25.0	°C

RESULTS

δ	1.511	mm
K @ calculation point	101.9	MPa.m$^{1/2}$
F_{max}/F_Q	2.56	
K_Q	39.76	MPa.m$^{1/2}$
Total area under Force v CMOD	388.73	kNmm
J From CMOD to BS8571:2014 Eq 2 to 10	865.64	kJ/m² (N/mm)
Plastic area Force vs CMOD	372.20	kNmm
Type of result	Unloading	
Test standard(s)	BS8571:2014	
Test qualified to standard(s)	YES	

LOWER CLIP GAUGE VALUES

Knife edge height	2.50	mm
Vg	1.999	mm
Vp	1.836	mm

UPPER CLIP GAUGE VALUES

Knife edge height	12.50	mm
Vg	2.489	mm
Vp	2.247	mm

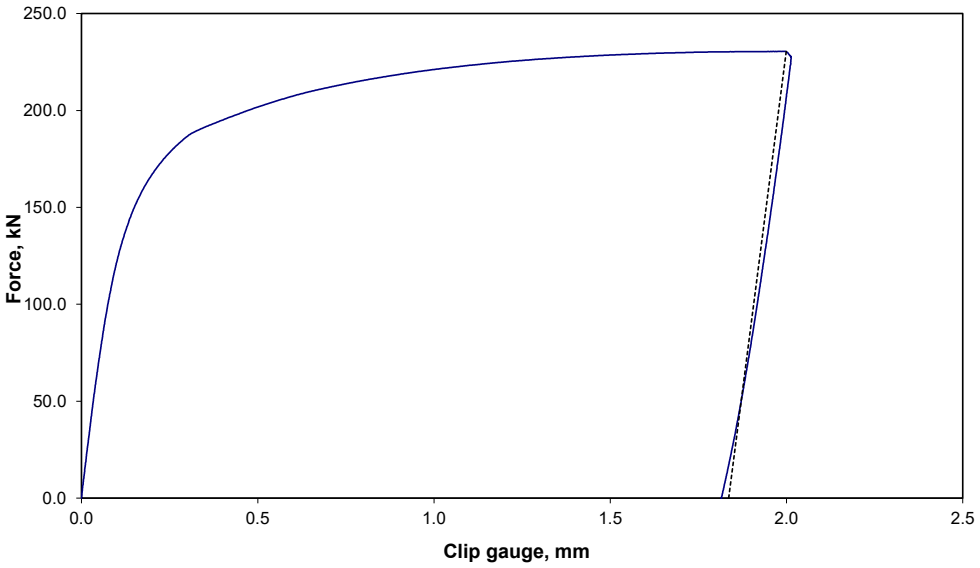

TWI Ltd, Granta Park, Great Abington, Cambridge, CB21 6AL, Cambridgeshire, UK, Tel 01223 899000

SENT FRACTURE TEST 24609 M01-03

Specimen width, W	17.020	mm
Specimen thickness, B	34.000	mm
Machined notch depth, M	3.680	mm
Machined notch width, N	0.320	mm
Surface crack length, a_{S1}	5.780	mm
Surface crack length, a_{S2}	5.770	mm
a_{max}	6.770	mm
a_{min}	5.930	mm

Diagram of fracture face

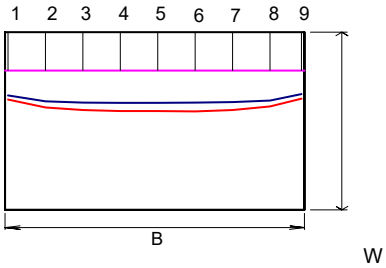

Comments

Measurement Line	Fatigue crack length a_0, mm	Slow stable crack extension + fatigue crack a_p, mm	Slow stable crack extension including stretch zone, Δ_a, mm
1	6.050	6.450	0.400
2	6.620	7.220	0.600
3	6.740	7.470	0.730
4	6.760	7.550	0.790
5	6.770	7.550	0.780
6	6.750	7.590	0.840
7	6.700	7.460	0.760
8	6.540	7.110	0.570
9	5.930	6.370	0.440
Weighted Average	**6.609**	**7.295**	**0.686**

Measured by: Phillip Cossey **Signed:**

C

MISES EQUIVALENT STRAIN MAPS OF SENT SPECIMENS CAPTURED BY DIC

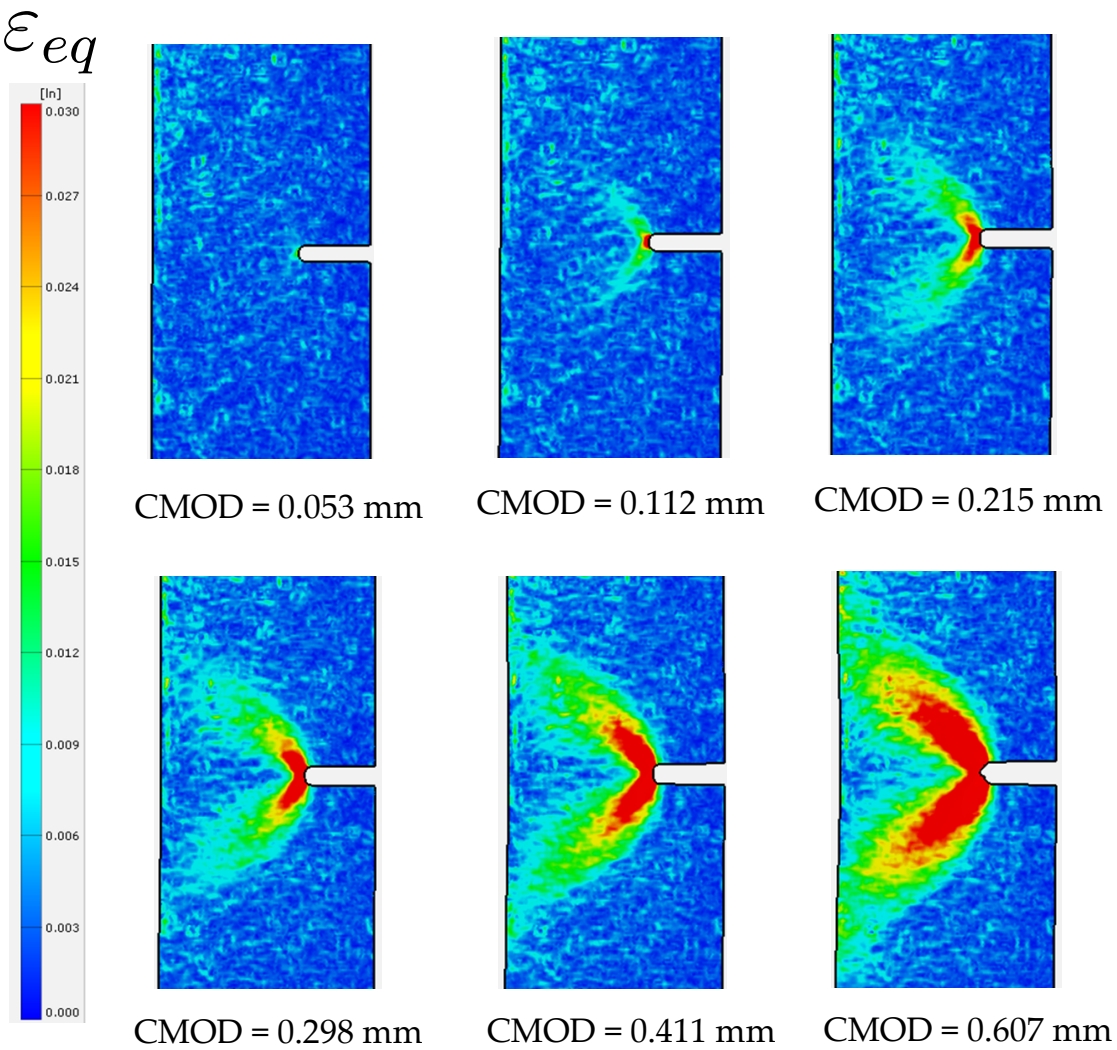

Figure C.1: Equivalent von Mises strain ε_{eq} maps of SENT test (Set-2) M01-02 captured by DIC

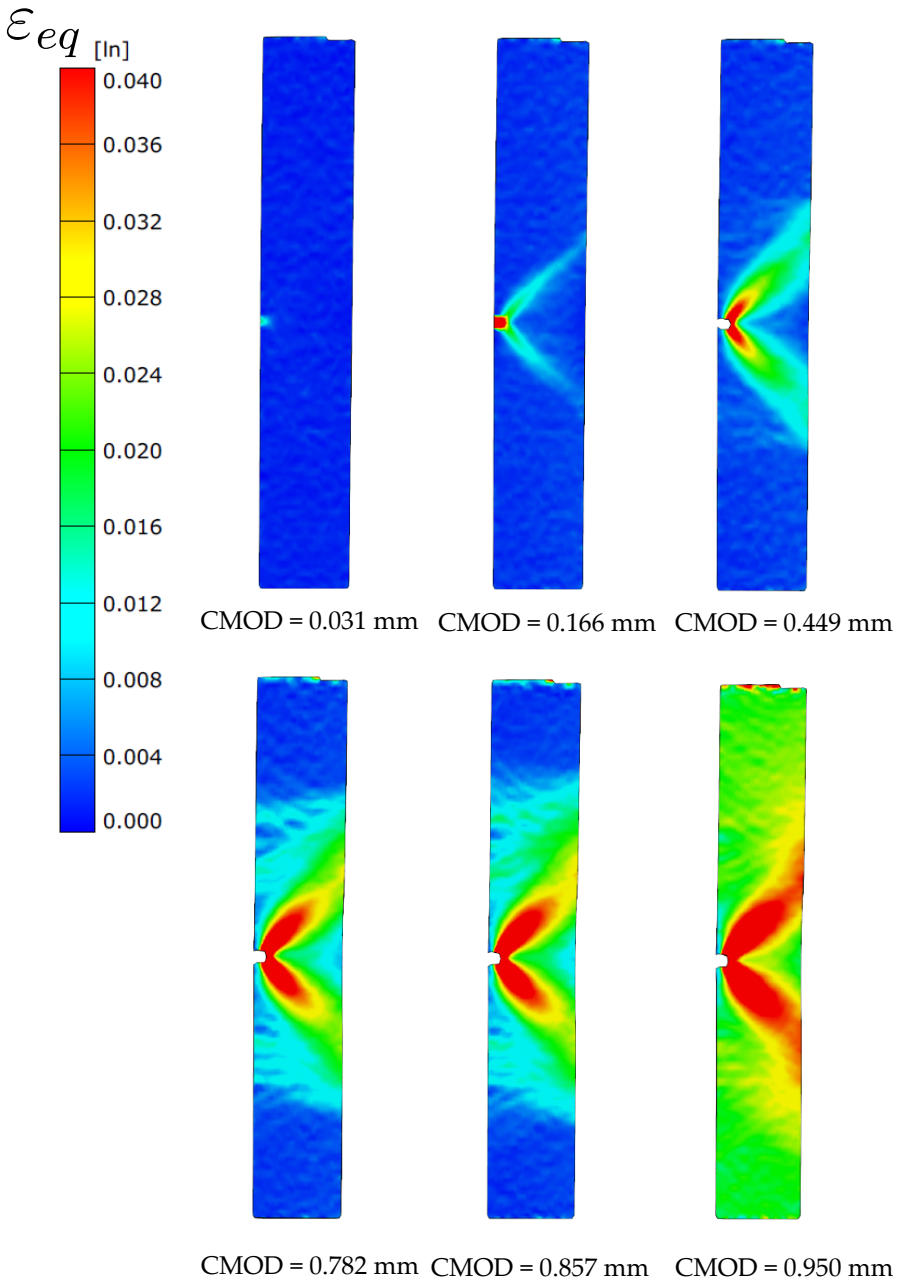

Figure C.2: Von Mises equivalent strain ε_{yy} maps of SENT test Set-2 (M01-08) captured by DIC

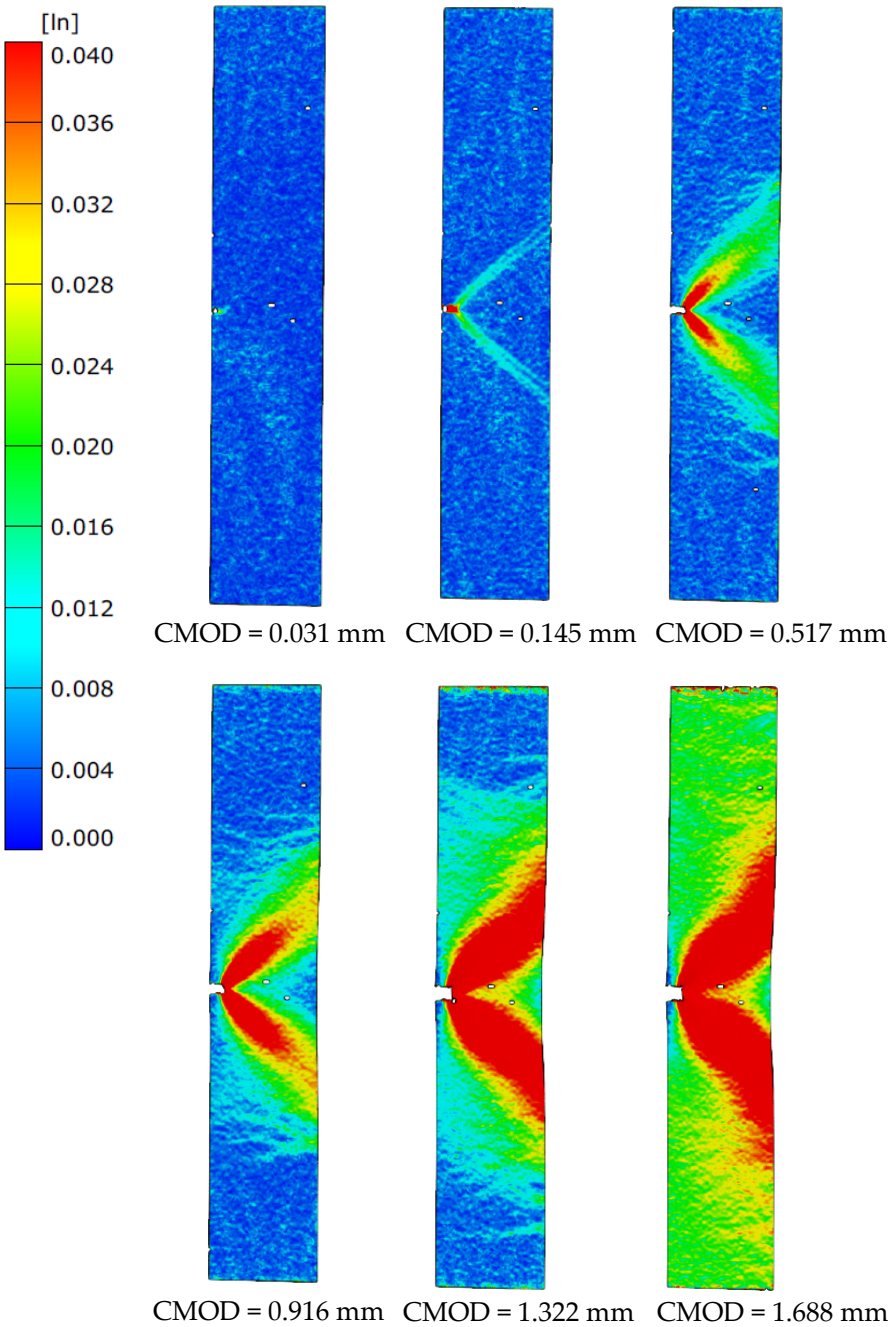

Figure C.3: Von Mises equivalent strain ε_{yy} maps of SENT test Set-2 (M01-09) captured by DIC

D

EQUIVALENT PLASTIC STRAIN MAPS OF SENT SPECIMENS CALCULATED FROM FEA

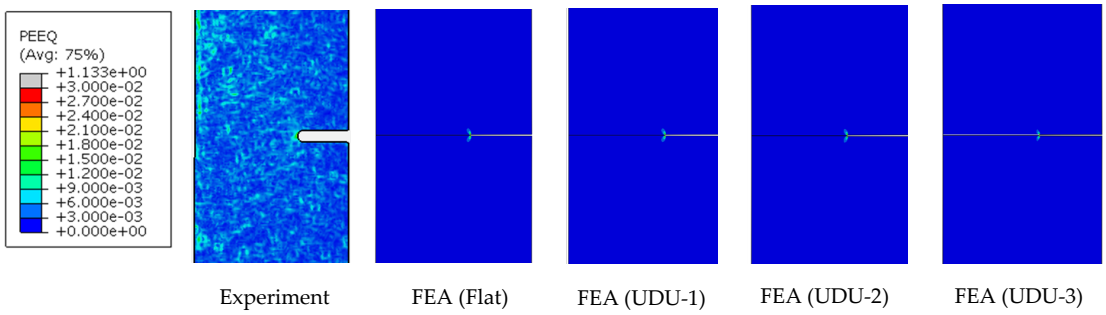

Figure D.1: Comparison between the equivalent plastic strain map calculated from FEA and that from the SENT test (equivalent von Mises strain) at CMOD = 0.05 mm

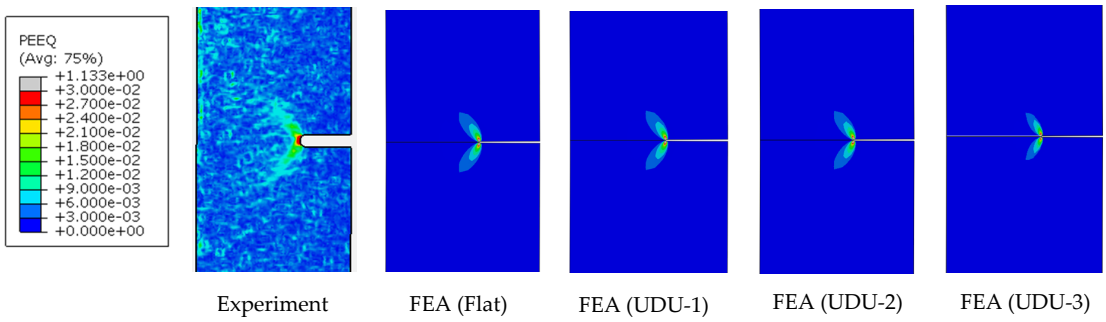

Figure D.2: Comparison between the equivalent plastic strain map calculated from FEA and that from the SENT test (equivalent von Mises strain) at CMOD = 0.11 mm

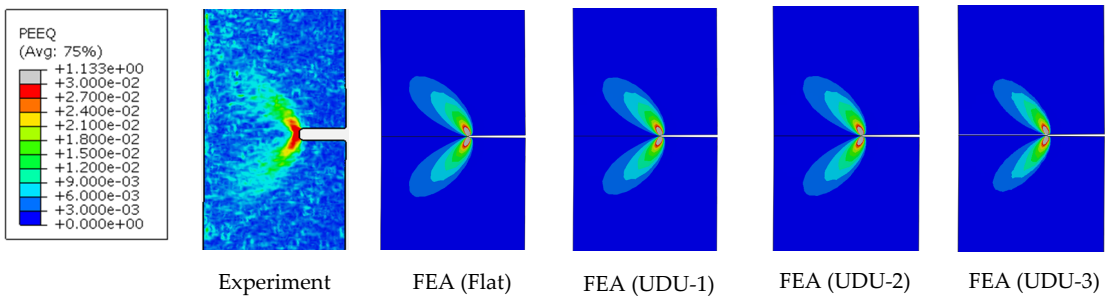

Figure D.3: Comparison between the equivalent plastic strain map calculated from FEA and that from the SENT test (equivalent von Mises strain) at CMOD = 0.21 mm

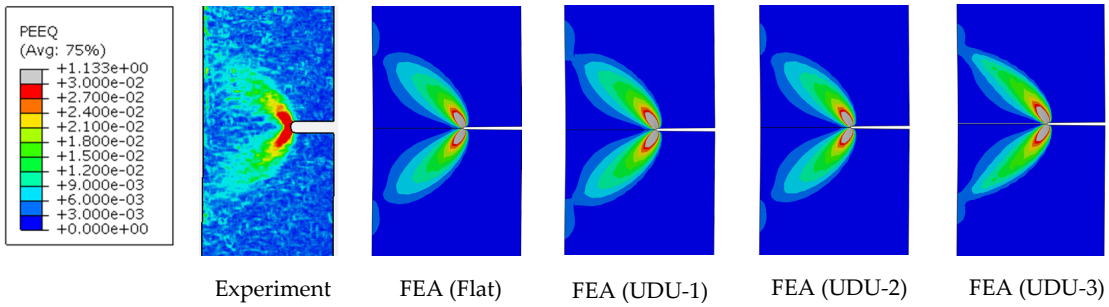

Figure D.4: Comparison between the equivalent plastic strain map calculated from FEA and that from the SENT test (equivalent von Mises strain) at CMOD = 0.29 mm

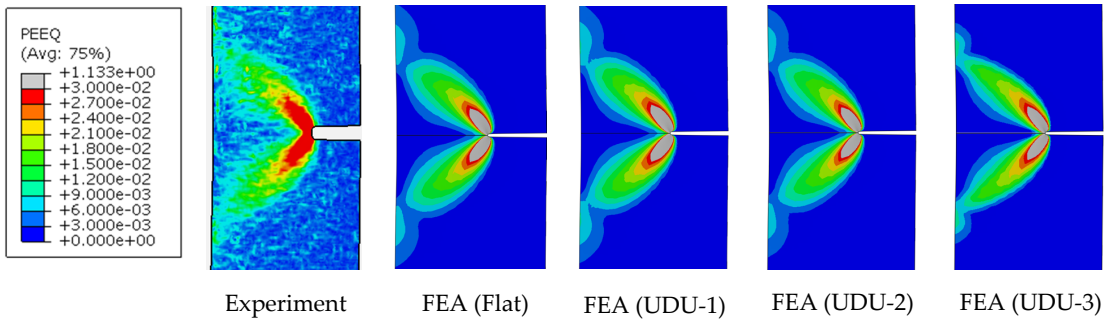

Figure D.5: Comparison between the equivalent plastic strain map calculated from FEA and that from the SENT test (equivalent von Mises strain) at CMOD = 0.41 mm

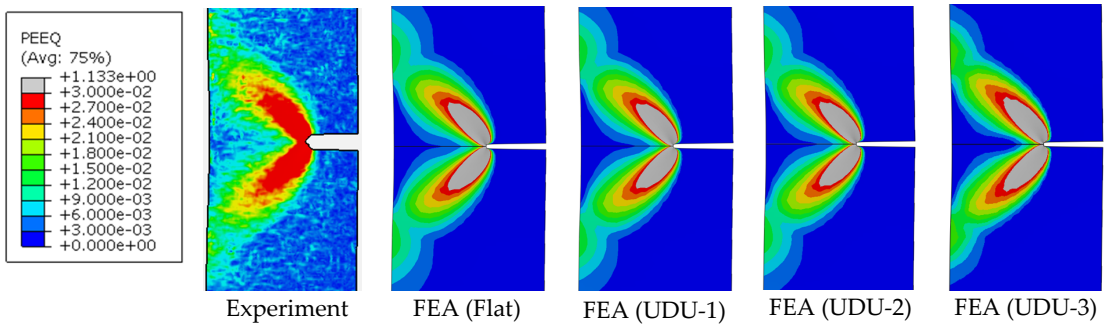

Figure D.6: Comparison between the equivalent plastic strain map calculated from FEA and that from the SENT test (equivalent von Mises strain) at CMOD = 0.61 mm

Figure D.7: Comparison between the equivalent plastic strain map calculated from FEA and that from the SENT test (equivalent von Mises strain) at CMOD = 0.031 mm

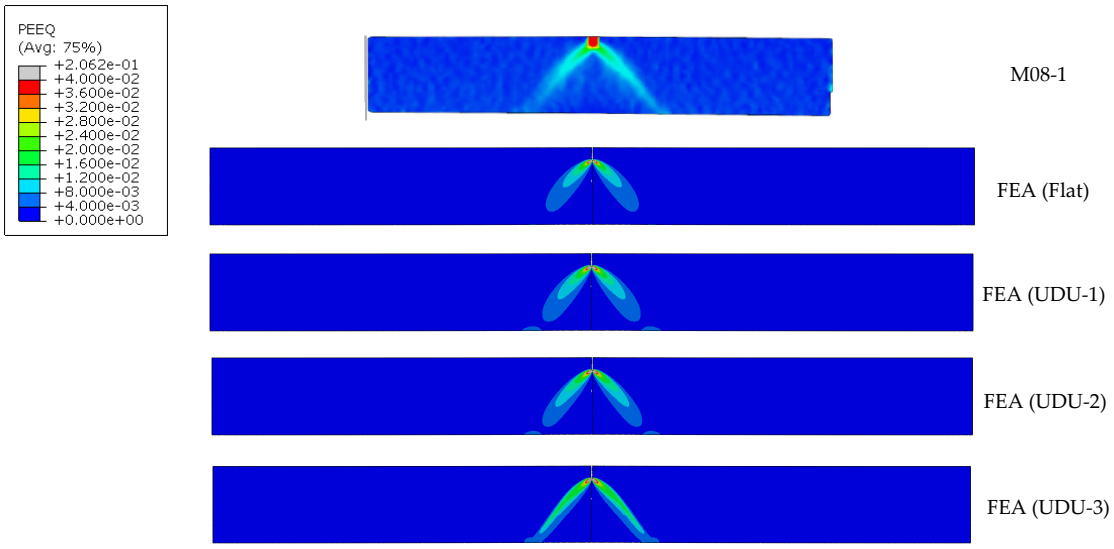

Figure D.8: Comparison between the equivalent plastic strain map calculated from FEA and that from the SENT test (equivalent von Mises strain) at CMOD = 0.166 mm

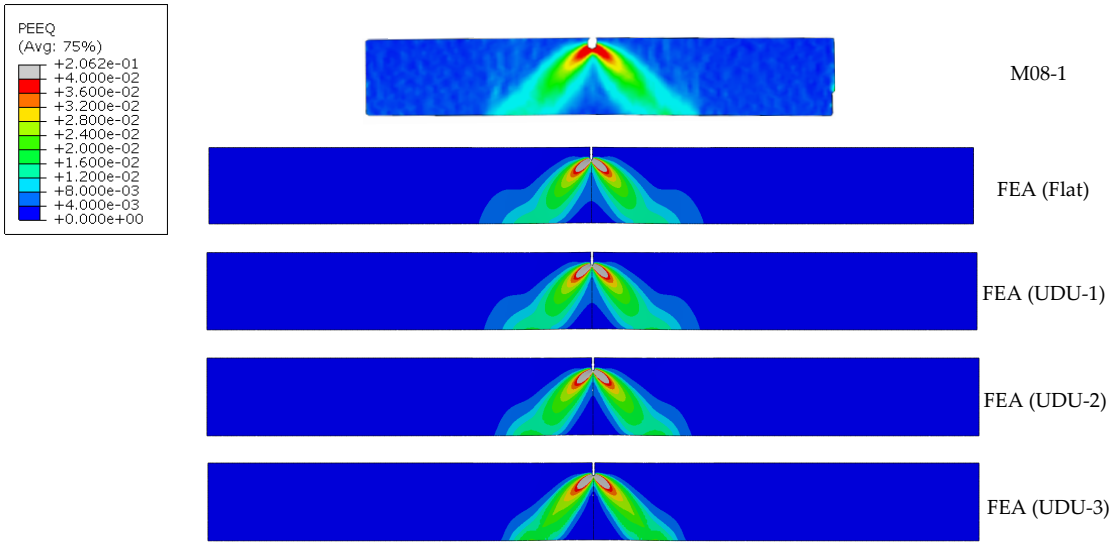

Figure D.9: Comparison between the equivalent plastic strain map calculated from FEA and that from the SENT test (equivalent von Mises strain) at CMOD = 0.449 mm

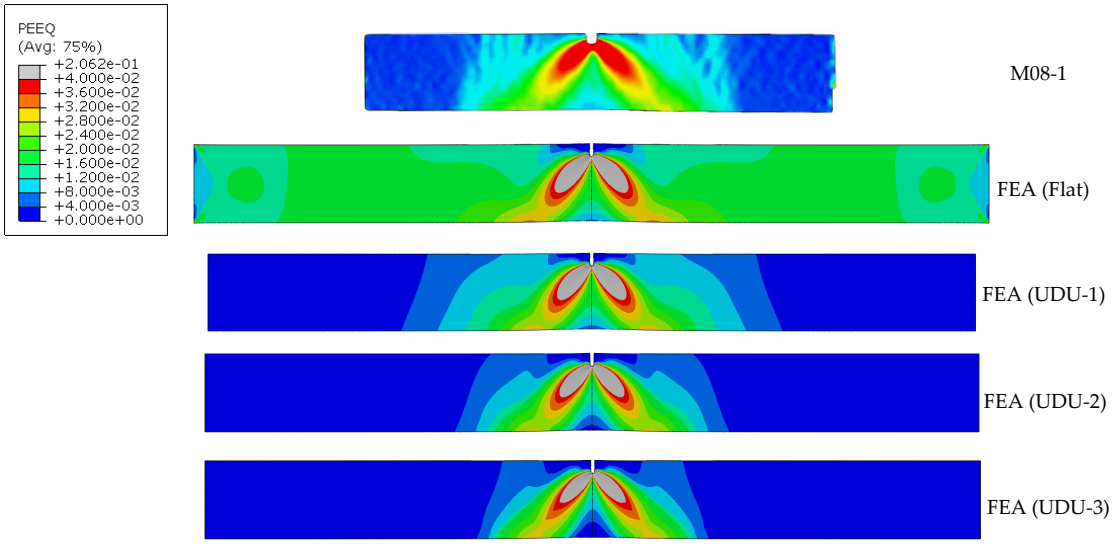

Figure D.10: Comparison between the equivalent plastic strain map calculated from FEA and that from the SENT test (equivalent von Mises strain) at CMOD = 0.782 mm

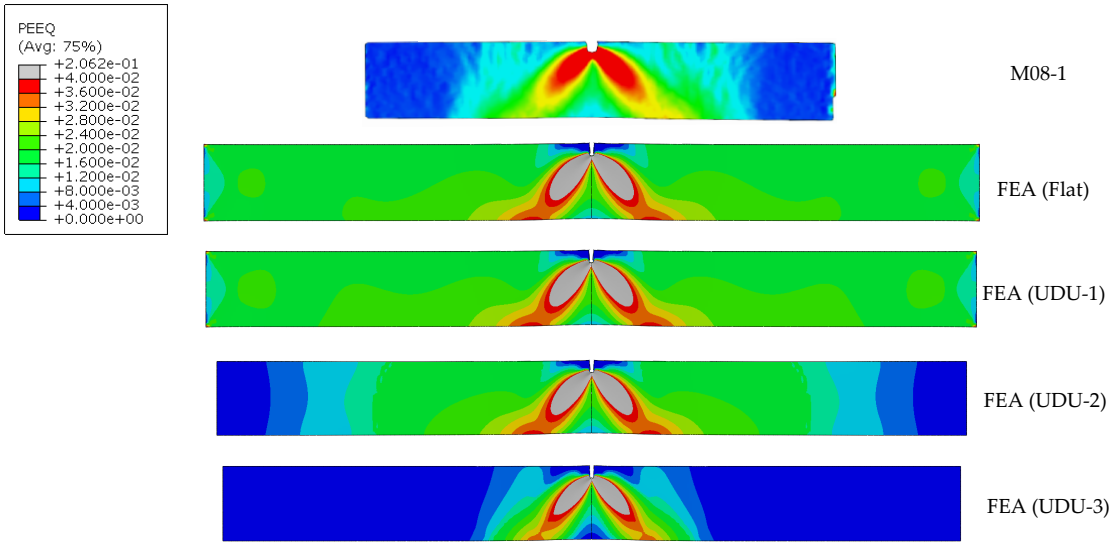

Figure D.11: Comparison between the equivalent plastic strain map calculated from FEA and that from the SENT test (equivalent von Mises strain) at CMOD = 0.923 mm

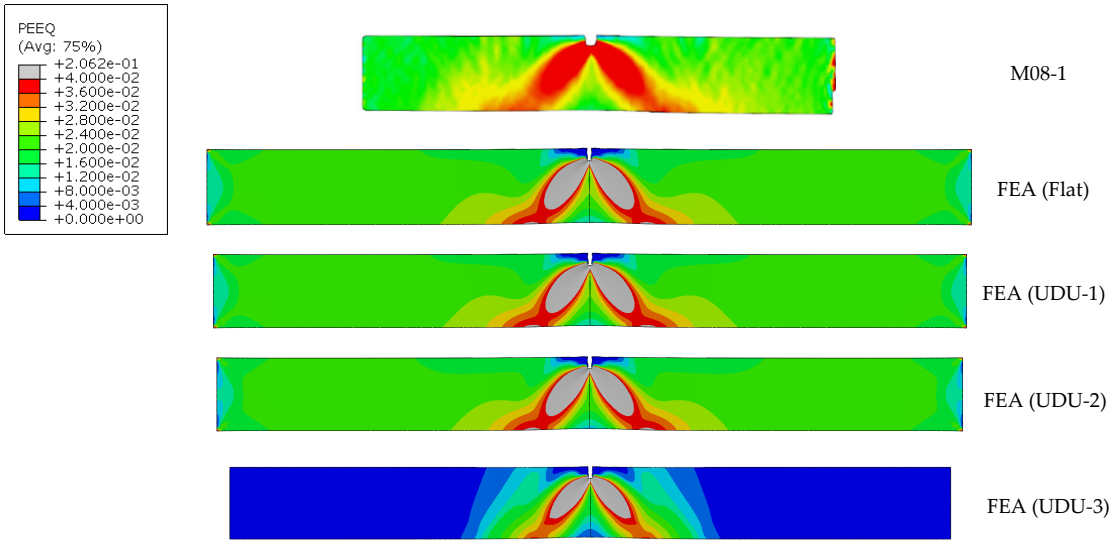

Figure D.12: Comparison between the equivalent plastic strain map calculated from FEA and that from the SENT test (equivalent von Mises strain) at CMOD = 0.950 mm

BIBLIOGRAPHY

Abdulhameed, D., C. Cakiroglu, M. Lin, R. Cheng, J. Nychka, M. Sen, et al. 2016. "The effect of internal pressure on the tensile strain capacity of X52 pipelines with circumferential flaws." *Journal of Pressure Vessel Technology* 138 (6).

Aguirre, F., S. Kyriakides, and H. Yun. 2004. "Bending of steel tubes with Lüders bands." *International Journal of Plasticity* 20 (7): 1199–1225.

Ainsworth, R. 1984. "The assessment of defects in structures of strain hardening material." *Engineering Fracture Mechanics* 19 (4): 633–642.

Ananthan, V., and E. Hall. 1991. "Macroscopic aspects of Lüders band deformation in mild steel." *Acta Metallurgica et Materialia* 39:3153–3160.

Anderson, T. 1988. "Ductile and brittle fracture analysis of surface flaws using CTOD." *Experimental Mechanics* 28 (2): 188–193.

API/ASME. 2016. *API 579-1/ASME FFS-1*. Standard.

Barrette, P. 2011. "Offshore pipeline protection against seabed gouging by ice: An overview." *Cold Regions Science and Technology* 69 (1): 3–20.

Beardsmore, D., J. Q. da Fonseca, J. Romero, C. English, S. Ortner, J. Sharples, et al. 2013. "Study of Lüders phenomena in reactor pressure vessel steels." *Materials Science and Engineering: A* 588:151–166.

Belotteau, J., C. Berdin, S. Forest, A. Parrot, and C. Prioul. 2006. "Mechanical Behavior Modeling in the Presence of Strain Aging." In *Fracture of Nano and Engineering Materials and Structures*, ed. by E. E. Gdoutos, 827–828. Dordrecht: Springer Netherlands.

– . 2009. "Mechanical behavior and crack tip plasticity of a strain aging sensitive steel." *Materials Science and Engineering: A* 526 (1): 156–165.

Belotteau, J. 2009. "Behavior and rupture of a C- Mn steel in the presence of aging under strain." Theses, Ecole Centrale Paris.

Berg, E., E. Østby, C. Thaulow, and B. Skallerud. 2008. "Ultimate fracture capacity of pressurised pipes with defects – Comparisons of large scale testing and numerical simulations." *Engineering Fracture Mechanics* 75 (8): 2352–2366.

Bloom, J. M. 1980. "Prediction of ductile tearing using a proposed strain hardening failure assessment diagram." *International Journal of Fracture* 16 (2): R73–R77.

Bratfos, H. 2002. "Use of strain-based ECA for the assessment of flaws in pipeline girth welds subjected to plastic deformations." In *Proceedings of the International Pipe Dreamers Conference*, 957–985. Yokohama, Greece: American Society of Mechanical Engineers.

Brocks, W., and I. Scheider. 2001. *Numerical aspects of the path-dependence of the J-integral in incremental plasticity*. Technical Report No. GKSS/WMS/01/08. Geesthacht, Germany.

BSI. 2013a. *Guide to methods for assessing the acceptability of aws in metallic structures*. Standard. British Standards Institution.

– . 2013b. *Method of test for determination of fracture toughness in metallic materials using single edge notched tension (SENT) specimens*. Standard. British Standards Institution.

Budden, P. 2006. "Failure assessment diagram methods for strain-based fracture." *Engineering Fracture Mechanics* 73 (5): 537–552.

Budden, P., and R. Ainsworth. 2012. "The shape of a strain-based failure assessment diagram." *International Journal of Pressure Vessels and Piping* 89:59–66.

Burdekin, F., and D. Stone. 1966. "The crack opening displacement approach to fracture mechanics in yielding materials." *Journal of Strain Analysis* 1 (2): 145–153.

Butler, J. 1962. "Lüders front propagation in low carbon steels." *Journal of the Mechanics and Physics of Solids* 10 (4): 313–318.

Cheaitani, M. 2016. *Validation of the proposed R6 strainbased FAD using pipe test data and FEA*. Tech. rep. TWI Member Report, Report No. 1075/2016.

Chiodo, M. S., and C. Ruggieri. 2010. "J and CTOD estimation procedure for circumferential surface cracks in pipes under bending." *Engineering Fracture Mechanics* 77 (3): 415–436.

Cosham, A., and K. A. Macdonald. 2015. "ECAs, FE and Bi-Axial Loading: A Critique of DNV-OS-F101, Appendix A." In *Proceedings of the ASME 2015 34th International Conference on Ocean, Offshore and Arctic Engineering*. 56529. St. John's, Newfoundland, Canada: American Society of Mechanical Engineers.

Cottrell, A., and B.A.Bilby. 1949. "Dislocation Theory of Yielding and Strain Ageing of Iron." *Proceedings of the Physical Society. Section A* 62 (1): 49–62.

Cravero, S., R. E. Bravo, and H. A. Ernst. 2008. "Evaluation of Crack Tip Constraint Effects on the Assessment of Pipes Subjected to Combined Loading Conditions." In *Proceedings of 2008 7th International Pipeline Conference*, vol. Volume 3, 607–615. Calgary, Alberta, Canada: American Society of Mechanical Engineers.

CSA. 2007. *Oil and Gas Pipeline Systems*. Standard. Calgary, Alberta: Canadian Standard Association.

Dahl, B., X. Ren, O. Akselsen, B. Nyhus, and Z. Zhang. 2018. "Effect of low temperature tensile properties on crack driving force for Arctic applications." *Theoretical and Applied Fracture Mechanics* 93:88–96.

Delwiche, D., and D. Moon. 1971. "Orientation of Lüders band fronts." *Materials Science and Engineering* 7 (4): 203–207.

DNVGL. 2017. *Recommended Practice DNV-RP-F108: Assessment of flaws in pipeline and riser girth welds*. Standard. Norway: DNV GL.

Dodds, R., M. Tang, and T. Anderson. 1993a. *Effects of Prior Ductile Tearing on Cleavage Fracture Toughness in the Transition Region*. Tech. rep. Rerpot No. UILU-ENG-93-2014. Urbana, Illinois: University of Illinois at Urbana-Champaign.

– . 1993b. "Numerical procedures to model ductile crack extension." *Engineering Fracture Mechanics* 46 (2): 253–264.

Dowling, A., and C. Townley. 1975. "The effect of defects on structural failure: A two-criteria approach." *International Journal of Pressure Vessels and Piping* 3 (2): 77–107.

Dugdale, D. 1960. "Yielding of steel sheets containing slits." *Journal of the Mechanics and Physics of Solids* 8 (2): 100–104.

Fairchild, D., M. MacIa, S. Kibey, X. Wang, V. Krishnan, F. Bardi, et al. 2011a. "A multi-tiered procedure for engineering critical assessment of strain-based pipelines." In *Proceedings of the International Offshore and Polar Engineering Conference*, 698–705.

Fairchild, D., M. Macia, S. Kibey, X. Wang, V. Krishnan, F. Bardi, et al. 2011b. "A Multi-Tiered Procedure For Engineering Critical Assessment of Strain-Based Pipelines." In *Proceedings of the Twenty-first (2011) International Offshore and Polar Engineering Conference*. Maui, Hawaii, USA: International Society of Offshore / Polar Engineers.

Fairchild, D., H. Tang, S. Shafrova, W. Cheng, and J. Crapps. 2014. "Updates to ExxonMobil's modelling approach for tensile strain capacity prediction." In *Proceedings of the Twenty-fourth (2014) International Offshore and Polar Engineering Conference*, 487–496. Busan, Korea: International Society of Offshore / Polar Engineers.

Fortes, M. A. 1984. "Constitutive equations for inhomogeneous plastic flow and application to Lüders band propagation." *Journal of Materials Science* 19 (5): 1496–1504.

Graff, S., S. Forest, J. Strudel, C. Prioul, P. Pilvin, and J. Béchade. 2004. "Strain localization phenomena associated with static and dynamic strain ageing in notched specimens: experiments and finite element simulations." 13th International Conference on the Strength of Materials, *Materials Science and Engineering: A* 387–389:181–185.

Griffith, A. 1920. "The Phenomena of Rupture and Flow in Solids." *Philosophical Transactions. Series A* 221:163–198.

Guo, W. 1993. "Elastoplastic three dimensional crack border field—I. Singular structure of the field." *Engineering Fracture Mechanics* 46 (1): 93–104.

Hallai, J. F., and S. Kyriakides. 2011a. "On the effect of Lüders bands on the bending of steel tubes. Part I: Experiments." *International Journal of Solids and Structures* 48 (24): 3275–3284.

– . 2011b. "On the effect of Lüders bands on the bending of steel tubes. Part II: Analysis." *International Journal of Solids and Structures* 48 (24): 3285–3298.

– . 2013. "Underlying material response for Lüders-like instabilities." *International Journal of Plasticity* 47:1–12.

Han, J., C. Lu, B. Wu, J. Li, H. Li, Y. Lu, et al. 2017. "Innovative analysis of Luders band behaviour in X80 pipeline steel." *Materials Science and Engineering: A* 683:123–128.

Harrison, R., K. Loosemore, and I. Milne. 1976. *Assessment of the Integrity of Structures Containing Defects*. Tech. rep. CEGB Report R/H/R6. UK: Central Electricity Generating Board.

Hertelé, S. 2012. "Coupled experimental-numerical framework for the assessment of strain capacity of flawed girth welds in pipelines." PhD thesis, Ghent University.

Hertelé, S., W. De Waele, R. Denys, and M. Verstraete. 2012. "Justification of the mapping approach for finite element modelling of ductile tearing." In *SUSTAINABLE CONSTRUCTION AND DESIGN*, 3:36–43. Ghent, Belgium: Ghent University, Laboratory Soete.

Hertelé, S., N. O'Dowd, K. V. Minnebruggen, R. Denys, and W. D. Waele. 2014. "Effects of pipe steel heterogeneity on the tensile strain capacity of a flawed pipeline girth weld." *Engineering Fracture Mechanics* 115:172–189.

Hutchinson, J. 1968. "Singular behaviour at the end of a tensile crack in a hardening material." *Journal of the Mechanics and Physics of Solids* 16 (1): 13–31.

Inglis, C. 1913. "Stresses in a Plate Due to the Presence of Cracks and Sharp Corners." *Transactions of the Institute of Naval Architects* 55:219–241.

Irwin, G. 1939. "Bearing Pressures and Cracks." *Journal of Applied Mechanics* 6:49–53.

– . 1948. "Fracturing of Metals." Chap. Fracture Dynamics, 147–166. Cleveland, OH: American Society for Metals.

– . 1961. "Plastic Zone Near a Crack and Fracture Toughness." *agamore Research Conference Proceedings* 4:63–78.

Jia, P., H. Jing, L. Xu, Y. Han, and L. zhao. 2016. "A modified reference strain method for engineering critical assessment of reeled pipelines." *International Journal of Mechanical Sciences* 105:23–31.

Jiang, D., S. Kyriakides, N. J. Bechle, and C. M. Landis. 2017a. "Bending of pseudoelastic NiTi tubes." *International Journal of Solids and Structures* 124 (Supplement C): 192–214.

Jiang, D., S. Kyriakides, C. M. Landis, and K. Kazinakis. 2017b. "Modeling of propagation of phase transformation fronts in NiTi under uniaxial tension." *European Journal of Mechanics - A/Solids* 64:131–142.

Johnston, W. G., and J. J. Gilman. 1959. "Dislocation Velocities, Dislocation Densities, and Plastic Flow in Lithium Fluoride Crystals." *Journal of Applied Physics* 30 (2): 129–144.

Kastner, W., E. Röhrich, W. Schmitt, and R. Steinbuch. 1981. "Critical crack sizes in ductile piping." *International Journal of Pressure Vessels and Piping* 9 (3): 197–219.

Kibey, S., X. Wang, K. Minnaar, M. Macia, D. Fairchild, W. Kan, et al. 2010. "Tensile strain capacity equations for strain-based design of welded pipelines." In *Proceedings of the Biennial International Pipeline Conference, IPC*, 4:355–363. American Society of Mechanical Engineers.

Kirk, M., R. Dodds, and T. Anderson. 1994. "An Approximate Technique for Predicting Size Effects on Cleavage Fracture Toughness (J_c) Using the Elastic T Stress." In *Fracture Mechanics: Twenty-Fourth Volume*. Philadelphia, PA: ASTM STP 905, American Society for Testing / Materials.

Kumar, V., and M. German. 1988. *Elastic-Plastic Fracture Analysis of Through-Wall and Surface Flaws in Cylinders*. Tech. rep. EPRI Report NP-5596. Palo Alto, CA: Electric Power Research Institute.

Kumar, V., M. German, and C. Shih. 1981. *An engineering approach for elastic-plastic fracture analysis*. Tech. rep. EPRI Report NP-1931. Palo Alto, CA: Electric Power Research Institute.

Kumar, V., M. German, W. Wilkening, W. Andrews, H. deLorenzi, and D. Mowbray. 1984. *Advances in elastic-plastic fracture analysis*. Tech. rep. EPRI Report NP-3607. Palo Alto, CA: Electric Power Research Institute.

Kyriakides, S., and J. Miller. 2000. "On the Propagation of Lüders Bands in Steel Strips." *Journal of Applied Mechanics* 67 (4): 64–654.

Kyriakides, S., and E. Corona. 2007a. "13 - Elements of Plasticity Theory." In *Mechanics of Offshore Pipelines*, ed. by S. Kyriakides and E. Corona, 336–360. Oxford: Elsevier Science Ltd.

– . 2007b. "2 - Offshore Facilities and Pipeline Installation Methods." In *Mechanics of Offshore Pipelines*, ed. by S. Kyriakides and E. Corona, 15–58. Oxford: Elsevier Science Ltd.

Kyriakides, S., A. Ok, and E. Corona. 2008. "Localization and propagation of curvature under pure bending in steel tubes with Lüders bands." *International Journal of Solids and Structures* 45 (10): 3074–3087.

Ling, Y. 1996. "Uniaxial true stress-strain after necking." *AMP Journal of Technology* 5:37–48.

Liu, M., Y.-Y. Wang, Y. Song, D. Horsley, and S. Nanney. 2012. "Multi-Tier Tensile Strain Models for Strain-Based Design: Part 2 — Development and Formulation of Tensile Strain Capacity Models." In *2012 9th International Pipeline Conference*, 415–425. 45158. Calgary, Alberta, Canada: American Society of Mechanical Engineers.

Liu, Y., S. Kyriakides, and J. F. Hallai. 2015. "Reeling of pipe with Lüders bands." *International Journal of Solids and Structures* 72:11–25.

Lüders, W. 1860. "Über die äusserung der elasticität an stahlartigen eisenstaben und stahlstäben, und über eine beim biegen solcher stäbe beobachtete molecularbewegung." *Dingler's Polytech. J.* 155:18–22.

Marais, A., M. Mazière, S. Forest, A. Parrot, and P. L. Delliou. 2015. "Influence of static strain aging on the cleavage fracture of a C–Mn steel." *Engineering Fracture Mechanics* 141:95–110.

McClintock, F. 1971. "CHAPTER 2 - PLASTICITY ASPECTS OF FRACTURE." In *Engineering Fundamentals and Environmental Effects*, 3:47–225. New York: Academic Press.

McCormick, P. 1988. "Theory of flow localisation due to dynamic strain ageing." *Acta Metallurgica* 36 (12): 3061–3067.

McMeeking, R., and D. Parks. 1979. "On criteria for J-dominance of crack-tip fields in large-scale yielding." In *Elastic Plastic Fracture*, 175–194. Philadelphia, PA: ASTM STP 668, American Society for Testing / Materials.

Nacar, A., A. Needleman, and M. Ortiz. 1989. "A finite element method for analyzing localization in rate dependent solids at finite strains." *Computer Methods in Applied Mechanics and Engineering* 73 (3): 235–258.

National Energy Board. 2016. "ARCHIVED - Part 3 Production, The transmission pipelines." https://https://www.neb-one.gc.ca/pplctnflng/mjrpp/archive/mcknzgs/rfd/rfdv1p3-eng.html.

Needleman, A. 1988. "Material rate dependence and mesh sensitivity in localization problems." *Computer Methods in Applied Mechanics and Engineering* 67 (1): 69–85.

Nourpanah, N., and F. Taheri. 2011. "Effect of L uders plateau on fracture response and toughness of pipelines subject to extreme plastic bending." 133 (5): 051701.

Nourpanah, N., and F. Taheri. 2010. "Development of a reference strain approach for assessment of fracture response of reeled pipelines." *Engineering Fracture Mechanics* 77 (12): 2337–2353.

O. Hall, E. 1970. "Yield Point Phenomena in Metals and Alloys." Chap. Yield Point Phenomena and their Theoretical Background, 1st ed., 1–64. New York: Springer US.

O'Dowd, N., and C. Shih. 1991. "Family of crack-tip fields characterized by a triaxiality parameter–I. Structure of fields." *Journal of the Mechanics and Physics of Solids* 39 (8): 989–1015.

– . 1992. "Family of crack-tip fields characterized by a triaxiality parameter–II. Fracture applications." *Journal of the Mechanics and Physics of Solids* 40 (5): 939–963.

Orowan, E. 1949. "Fracture and Strength of Solids." *Reports on Progress in Physics* 12 (1): 185.

– . 1956. "Onset of Fast Crack Propagation in High Strength Steel and Aluminum Alloys." *Sagamore Research Conference Proceedings* 2:289–305.

Østby, E. 2007. "Fracture Control - Offshore Pipelines JIP Proposal for strain-based fracture assessment procedure." In *Proceedings of the 17th International Offshore and Polar Engineering Conference*, 3238–3245. Lisbon, Portugal: International Society of Offshore / Polar Engineers.

Østby, E. 2005. "Fracture Control - Offshore Pipelines: New Strain-Based Fracture Mechanics Equations Including the Effects of Biaxial Loading, Mismatch, and Misalignment." In *ASME 2005 24th International Conference on Offshore Mechanics and Arctic Engineering*, 649–658. 41979. Halkidiki, Greece: American Society of Mechanical Engineers.

Østby, E., K. Jayadevan, and C. Thaulow. 2005. "Fracture response of pipelines subject to large plastic deformation under bending." *International Journal of Pressure Vessels and Piping* 82 (3): 201–215.

Pangeranlaut. 2016. "Pipeline Global Guckling/Upheaval Buckling/Sneaking." https://pangeranlaut.wordpress.com/2016/02/17/pipeline-global-gucklingupheaval-bucklingsneaking/.

Parise, L. F., C. Ruggieri, and N. P. O'Dowd. 2015. "Fully-Plastic Strain-Based J Estimation Scheme for Circumferential Surface Cracks in Pipes Subjected to Reeling." *Journal of Pressure Vessel Technology* 137, no. 4 (): 41204–41208.

Penning, P. 1972. "Mathematics of the Portevin-Le Chatelier effect." *Acta Metallurgica* 20 (10): 1169–1175.

Piobert, G., A. J. Morin, and I. Didion. 1842. "Commission des principes du tir." *Memorial de l'artillerie* 5:501–552.

Pisarski, H. 2011. "Assessment of Flaws in Pipe Girth Welds." In *CBMM-TMS International Conference on Welding of High Strength Pipeline Steels*. Araxá, Brasil.

Pisarski, H., S. Smith, and T. London. 2014. "Flaw Tolerance of Pipelines Containing Circumferential Flaws Subjected to Axial Straining and Internal Pressure - Tests and Analyses." *International Journal of Offshore and Polar Engineering* 24 (03): 199–205.

Pisarski, H., R. Phaal, I. Hadley, and R. Francis. 1994. "Integrity of steel pipe during reeling." In *Proceedings of the International Conference on Offshore Mechanics and Arctic Engineering*, 5:189–198. Houston, TX: American Society of Mechanical Engineers.

Pokorny, A., and J. Plkorny. 2003. "Fractographie. Macrographies et micrographies." *Techniques de l'ingénieur. Matériaux métalliques*, no. M4122: M4122–1.

Portevin, A., and F. Le Chatelier. 1923. "Sur un phénomène observé lors de l'essai de traction d'alliages en cours de transformation." *Comptes Rendus de l'Académie des Sciences Paris* 176:507–510.

EDF Energy. 2015. *Assessment of the integrity of structures containing defects*. Standard. Gloucester, UK: EDF Energy.

Rice, J. R. 1968. "A Path Independent Integral and the Approximate Analysis of Strain Concentration by Notches and Cracks." *Journal of Applied Mechanics* 35 (2): 379–386.

Rice, J., W. Drugan, and T. Sham. 1979. "Elastic-Plastic Analysis of Growing Cracks," vol. 700.

Rice, J. 1964. "A path independent integral and the approximate analysis of strain concentration by notches and cracks." *Journal of Applied Mechanics, Transactions ASME* 35 (2): 379–388.

Rice, J., and G. Rosengren. 1968. "Plane strain deformation near a crack tip in a power-law hardening material." *Journal of the Mechanics and Physics of Solids* 16 (1): 1–12.

Shaw, J., and S. Kyriakides. 1997. "Initiation and propagation of localized deformation in elasto-plastic strips under uniaxial tension." *International Journal of Plasticity* 13 (10): 837–871.

Shih, C., M. German, and V. Kumar. 1981. "An engineering approach for examining crack growth and stability in flawed structures." *International Journal of Pressure Vessels and Piping* 9 (3): 159–196.

Smith, S. 2012. "Development of the BS 7910 Failure Assessment Diagram for Strain Based Design With Application to Pipelines." In *Proceedings of the ASME 2012 31st International Conference on Ocean, Offshore and Arctic Engineering*, 431–436. 44908. Rio de Janeiro, Brazil: American Society of Mechanical Engineers.

Smith, S. D. 2018. "Consideration of a proposed SBAD method for BS7910." *International Journal of Pressure Vessels and Piping* 168:142–147.

Sutton, M. A., J.-J. Orteu, and H. Schreier. 2010. *Image Correlation for Shape, Motion and Deformation Measurements*. Springer US.

Sylwestrowicz, W., and E. Hall. 1951. "The Deformation and Ageing of Mild Steel." *Proceedings of the Physical Society. Section B* 64 (6): 495.

Tang, H., D. Fairchild, M. Panico, J. Crapps, and W. Cheng. 2014. "Strain capacity prediction of strain-based pipelines," vol. 4.

Tang, H., M. Macia, K. Minnaar, P. Gioielli, S. Kibey, and D. Fairchild. 2010. "Development of the SENT Test for Strain-Based Design of Welded Pipelines." In *Proceedings of the Biennial International Pipeline Conference, IPC*, 4:303–312. American Society of Mechanical Engineers.

Tkaczyk, T., N. O'Dowd, and K. Nikbin. 2011. "The effect of prestrain on ductile fracture toughness of reeled pipeline steels." *Journal of Pressure Vessel Technology, Transactions of the ASME* 133 (3).

Tkaczyk, T., N. P. O'Dowd, and K. Nikbin. 2009a. "Fracture Assessment Procedures for Steel Pipelines Using a Modified Reference Stress Solution." *Journal of Pressure Vessel Technology* 131, no. 3 (): 31409–31411.

Tkaczyk, T., N. P. O'Dowd, K. Nikbin, and B. P. Howard. 2009b. "A non-linear fracture assessment procedure for pipeline materials with a yield plateau." In *Proceedings of the 19th International Offshore and Polar Engineering Conference*, 100–109.

Tkaczyk, T., N. O'Dowd, K. Nikbin, B. Howard, et al. 2009c. "Fracture Assessment of Elastic-Plastic Steel Pipelines Subject to Multi-cycle Bending." In *Proceedings of The Nineteenth International Offshore and Polar Engineering Conference*. International Society of Offshore and Polar Engineers.

Towers, O., and S. Garwood. 1986. "Influence of Crack Depth on Resistance Curves for Three-Point Bend Specimens in HY130." In *Fracture Mechanics: Seventingth Volume*, 454–484. Philadelphia, PA: ASTM STP 905, American Society for Testing / Materials.

Tu, S., X. Ren, J. He, and Z. Zhang. 2018. "Numerical study on the effect of the Lüders plateau on the ductile crack growth resistance of SENT specimens." *International Journal of Fracture* 214 (2): 185–200.

Tyson, W., G. Shen, and G. Roy. 2007. "Effect of biaxial stress on ECA of pipelines under strain-based design," 3107–3113.

Wang, Y.-Y., M. Liu, Y. Song, M. Stephens, R. Petersen, and R. Gordon. 2011a. *Second generation models for strain-based design*. Tech. rep. Final report to US DOT and PRCI. Pipeline Research Council International.

Verstraete, M., W. D. Waele, R. Denys, K. V. Minnebruggen, and S. Hertelé. 2014. "Constraint analysis of defects in strength mismatched girth welds of (pressurized) pipe and Curved Wide Plate tensile test specimens." *Engineering Fracture Mechanics* 131 (Supplement C): 128–141.

Wang, H., C. Berdin, M. Mazière, S. Forest, C. Prioul, A. Parrot, et al. 2012. "Experimental and numerical study of dynamic strain ageing and its relation to ductile fracture of a C–Mn steel." *Materials Science and Engineering: A* 547:19–31.

Wang, L., E. Eren, B. Wang, and G. Wu. 2017. "Consideration of yield discontinuity in the elastic-plastic fracture analaysis of circumferentially flawed pipes." In *Proceedings of ASME 2017 Pressure Vessels and Piping Conference*, vol. 6A : Materials and Fabrication, V06AT06A035. Waikoloa, Hawaii, USA: American Society of Mechanical Engineers.

Wang, X., S. Kibey, H. Tang, W. Cheng, K. Minnaar, M. Macia, et al. 2011b. "Strain-based design—advances in prediction methods of tensile strain capacity." *International Journal of Offshore and Polar Engineering* 21 (1): 1–7.

Wang, Y.-Y., D. Horsley, and M. Stephens. 2008. "Preliminary Analysis of Tensile Strain Capacity of Full-Scale Pipe Tests With Internal Pressure." In *The Eighteenth International Offshore and Polar Engineering Conference*. Vancouver, Canada: International Society of Offshore / Polar Engineers.

Wang, Y.-Y., M. Liu, D. Horsley, and J. Zhou. 2006. "A Quantitative Approach to Tensile Strain Capacity of Pipelines." In *Proceedings of the Biennial International Pipeline Conference, IPC*, 3:545–552.

Wang, Y.-Y., M. Liu, Y. Song, M. Stephens, R. Petersen, and R. Gordon. 2011c. "Second generation models for strain-based design." *US DOT Contract No. DTPH56-06-T000014, final report to US DOT and PRCI*.

Wang, Y., W. Cheng, D. Horsley, A. Glover, D. Zoe, and M. McLamb. 2004. "Tensile strain limits of girth welds with surface-breaking defects - Part I: an analytical framework." In *Proceedings of the Fourth International Pipeline Technology Conference*, vol. 1.

Wells, A. 1961. "Unstable crack propagation in metals: cleavage and fast fracture." In *Proceedings of the crack propagation symposium*, vol. 1. 84. Cranfield, UK.

Wenman, M. R., and R. D. Plant. 2006. "Simple Model of Lüders Behaviour in a Novel Compact Tension Specimen for Investigation of Residual Stress Effects." In *Proceedings of ASME 2006 Pressure Vessels and Piping/ICPVT-11 Conference*, vol. 6: Materials and Fabrication, V06AT06A035. Vancouver, BC, Canada: American Society of Mechanical Engineers.

Wenman, M., and P. Chard-Tuckey. 2010. "Modelling and experimental characterisation of the Lüders strain in complex loaded ferritic steel compact tension specimens." *International Journal of Plasticity* 26 (7): 1013–1028.

Westergaard, H. 1939. "Bearing Pressures and Cracks." *Journal of Applied Mechanics* 6:49–53.

William D. Callister, D. G. R. 2007. *Materials Science and Engineering An Introdction*. 8th ed. NJ: John Wiley & Sons, Inc.

Williams, M. 1957. "On the Stress Distribution at the Base of a Stationary Crack." *Journal of Applied Mechanics* 24:109–114.

Wilson, D., B. Russell, and J. Eshelby. 1959. "Stress induced ordering and strain-ageing in low carbon steels." *Acta Metallurgica* 7 (9): 628–631.

Xu, J., Z. Zhang, E. Østby, B. Nyhus, and D. Sun. 2010. "Constraint effect on the ductile crack growth resistance of circumferentially cracked pipes." *Engineering Fracture Mechanics* 77 (4): 671–684.

Zahoor, A. 1989. *Ductile Fracture Handbook, Volume 1: Circumferential Through-wall Cracks*. Tech. rep. EPRI Report NP-6301-D. Palo Alto, CA: Electric Power Research Institute.

Zhang, B., and W. Guo. 2007. "Three-dimensional stress state around quarter-elliptical corner cracks in elastic plates subjected to uniform tension loading." *Engineering Fracture Mechanics* 74 (3): 386–398.

Zhang, S., P. McCormick, and Y. Estrin. 2001. "The morphology of Portevin–Le Chatelier bands: finite element simulation for Al–Mg–Si." *Acta Materialia* 49 (6): 1087–1094.

Zhao, J., W. Guo, and C. She. 2007. "The in-plane and out-of-plane stress constraint factors and KTTz description of stress field near the border of a semi-elliptical surface crack." *International Journal of Fatigue* 29 (3): 435–443.

Zhao, W., M. Chen, S. Chen, and J. Qu. 2012. "Static strain aging behavior of an X100 pipeline steel." *Materials Science and Engineering: A* 550:418–422.